Development and Application of Individual-based Models for Predicting Upstream Passage of European Fish

Thomas Edward Padgett

University of Leeds

Centre for Doctoral Training in Fluid Dynamics

Submitted in accordance with the requirements for the degree of

Doctor of Philosophy

September, 2020

For Katherine.

Intellectual Property Statement

The candidate confirms that the work submitted is their own, except where work which has formed part of jointly authored publications has been included. The contribution of the candidate and the other authors to this work has been explicitly indicated below. The candidate confirms that appropriate credit has been given within the thesis where reference has been made to the work of others.

The work in Chapter 3 of this thesis contains material from the jointly authored publication:

Padgett, T. E., Thomas, R. E., Borman, D. J., and Mould, D. C. (2020). Individual-based model of juvenile eel movement parametrized with computational fluid dynamics-derived flow fields informs improved fish pass design. *Royal Society Open Science*, 7(1):191505.

The co-authors provided ideas and guidance surrounding this work and aided with the writing of the paper. All scientific research contained in this work was undertaken by the candidate himself.

Acknowledgements

First, I say thank you to my supervisors: Robert Thomas, Duncan Borman, David Mould, and Richard Hardy; your individual expertise and guidance facilitated this work. Thank you for all the conversations over the past 5 years. I would also like to thank those academics not formally involved in the project: Jamie Dodd and Jon Bolland, who gave their time, sympathy, support, and perspective on the work. Thank you to JBA Consulting and JBA Trust for sponsoring this work. Thank you to the Environment Agency and Esk Energy (Yorkshire) Ltd for facilitating the field work.

Thank you to Claire and the rest of the CDT Fluid Dynamics team for your constant support. Thank you to my fellow postgraduates for all the conversations we've had. Thank you to my internal examiner, Cath Noakes, and external examiner, Beth Scott; your positivity and enthusiasm made the viva process enjoyable!

Thank you to my family and friends for your enthusiasm, support, and love. Thank you to my parents, for pushing me to pursue education throughout my life. Thank you to my Best Men, you're the best distraction I could ask for.

Above all, thank you to Katie, your unwavering support has been incredible - We finally did it.

Abstract

Anthropogenic alteration of rivers is ubiquitous and leads to fragmented river systems that restrict the passage of aquatic fauna. There are considerable efforts to facilitate unhindered migration through the installation of fish passage facilities. However, recent assessments suggest upstream passage efficiencies of 42%, and suggest that only 3% of rivers in Great Britain are fully connected. Decoding the behaviours that govern up-migrating fish responses to flow fields has been dubbed a high research priority that would allow for computational metrics of fish passage and a reduction in invasive experiments. The aim of this project was to develop cellular automata (CA), individual-based models (IBM), and computational fluid dynamic (CFD) models to predict the trajectories of up-migrating fishes and subsequently provide a method to computationally assess passage facilities.

Past work was critically assessed to determine: the appropriate CFD approach to quantify the flow through various domains, the hydrodynamic stimuli that influence fish responses, and the current state of fish path prediction models and their applications and limitations.

Multiple 2D CA and IBMs were developed to predict the passage efficiency of various eel tile configurations for juvenile European eels (*Anguilla anguilla*) using CFD-derived flow fields. Predictions compared well to a published values (76% vs. 74%) and suggested passage efficiency was highest for shallow slopes and low discharges. Results were extended to define maximum pass lengths and incorporated into an easy-to-use graphic.

A 3D IBM, `fishPy`, was developed to predict up-migration trajectories of brown trout (*Salmo trutta*) based fish responses to hydraulic stimuli. Artificial hydrodynamic domains were created using CFD and used to verify model function. A CFD model of a passage facility on the River Esk was created based on collected bathymetry data, and compared well to measured velocity data. The IBM was applied to the passage facility and compared against measured passage metrics and fish trajectories.

Overall, 2D and 3D models of up-migrating fishes were successfully developed and compared well to measured data. Potential areas for further research and development of the models are highlighted, including development of additional species modules for the 3D IBM.

Contents

List of Figures

List of Tables

Nomenclature

ABM	Agent Based Model(-ling)
ADV	Acoustic Doppler Velocimetry
ADCP	Acoustic Doppler Current Profiler
CA	Cellular Automaton / Cellular Automata
CFD	Computational Fluid Dynamics
CFL	Courant-Friedrichs-Lewy (criterion)
DNS	Direct Numerical Simulation
ELAM	Eulerian-Lagrangian Agent-based Method
IBM	Individual-based Model(-ling)
LES	Large Eddy Simulation
NFS	Numerical Fish Surrogate
PLIC	Piece-wise Linear Interface Construction
RANS	Reynolds-Averaged Navier-Stokes
Re	Reynolds Number
SO	Sensory Ovoid
SQD	Sensory Query Distance
THS	Total Hydraulic Strain
TI	Turbulent Intensity
TKE	Turbulence Kinetic Energy
UTM	Universal Transverse Mercator
VOF	Volume of Fluid
WFD	Water Framework Directive

Glossary of Terms for Elver Passage Models

`burst`	Burst swimming speed of current individual.
`burstTime`	Cumulative time spent at burst speed.
`checkStuck`	Method of `FEPM` [see p.89].
`createNeighours`	Method of used in each CA [see p.85].
`col`	Current column of individual.
`EEPM`	Exhaustion Elver Passage Model.
`FEPM`	Fallback Elver Passage Model.
`HEPM`	Heterogeneous Elver Passage Model.
`history`	Location history of current individual.
`id`	Identification number of current individual.
`location`	Current location of current individual.
`move`	Method used by each CA, modified between models [see p.85,89,90].
`passable`	Method used by each CA, modified between models [see p.86,92].
`pastColNumber`	Number of location sample to determine if an individual is "stuck".
`row`	Current row of individual.
`SEPM`	Simple Elver Passage Model.
`stuck`	Denotes whether current individual is "stuck".
`stuckIt`	Number of timesteps individual has spent "stuck".
`stuckItMax`	Maximum number of timesteps individual is allowed to be "stuck".
`timePerStep`	List of `timeReq` each timestep.
`timeReq`	Time required to make a move.
`threshold`	Distance that defines whether an individual is "stuck".
`velMag`	Magnitude of velocity at cell location.

Glossary of Key Terms for `fishPy`

`bodylength`	Total length of the individual.
`calcHeading`	Function to calculate heading of the individual [section 4.6.8].
`calcMoveMakeMove`	Function to execute final movement response [section 4.6.10].
`colAvoidance`	Collision avoidance rule [section 4.6.5].
`coordsCentroid`	Current location of the centre of the individual.
`determineCreationLocation`	Function to determine creation locations of individuals.
`deterReponse`	Function to determine response of an individual [section 4.6.10].
`failed`	List of individuals that have failed to pass through the domain.
`fishNum`	Total number of simulated fish.
`fishTimestep`	Timestep used within `fishPy`.
`followFlow`	Movement rule [section 4.6.1].
`G3D`	Passability matrix [section 4.3.1].
`heading`	Current directional heading of individual.
`initiative`	Ordered list of movement order of individuals.
`K3D`	Turbulence kinetic energy input data.
`memory`	Memory bias rule [section 4.6.6].
`minMaxEnergy`	Energy pathway selection rule [section 4.6.2].
`nx`, `ny`, `nz`	Number of data points in x,y,z.
`obAvoidance`	Obstacle avoidance rule [section 4.6.4].
`passabilityThreshold`	Threshold defining the minimum value of passability.
`passed`	List of individuals that have successfully passed through the domain.
`sensoryRange`	Range of sensory length measured in bodylengths.
`SQDx`, `SQDy`, `SQDz`	Sensory query distances in x,y,z.
`randomWalk`	Random walk rule [section 4.6.3].
`repulsionDist`	Distance threshold that triggers `colAvoidance`.
`swimBurst`,`swimSust`	Burst and sustained swimming speeds of individual.
`tkeAvoidance`	Turbulence avoidance rule [section 4.6.7].
`Tmax`	Maximum `fishTimestep`
`U3D`, `V3D`, `W3D`	Flow field input data in x,y,z.
`x`, `y`, `z`	Current location of individual in x,y,z.
`X3D`, `Y3D`, `Z3D`	Domain geometry input data in x,y,z.

Chapter 1

Introduction

1.1 Statement of the Research Question

Globally, rivers are regulated and modified for a variety of purposes. Anthropogenic alteration of rivers is implemented to control water levels, prevent sea water intrusion, facilitate human navigation, power mills, and to allow abstraction [Fuller et al., 2015]. More recently, rivers have been modified to power hydroelectric facilities through the construction of new structures or the retrofitting of existing ones. Historically, little attention was given to the environmental and ecological effects of altering the natural flow of rivers. This has led to a drastic decline in the populations of numerous aquatic species [e.g. Nicola et al. 1996, Laffaille et al. 2005, Hall et al. 2012] and, in some cases, the loss of entire species [Nilsson et al., 2005]. More recently, the impact of anthropogenic alteration has been studied in an attempt to quantify and subsequently better design hydraulic structures [e.g. Lucas and Frear 1997, Baras and Lucas 2001, Russon et al. 2011, Gauld et al. 2013, Piper et al. 2017]. In 2000, the European Union (EU) Water Framework Directive (WFD) came into force with the purpose of protecting and restoring aquatic environments in EU member states. The WFD mandated that all aquatic ecosystems must meet "good ecological status" by December 2015. This deadline has since been extended after a review in 2012 predicted that 47% of waters would not achieve this goal [European Commission, 2012].

A key proposed physical improvement is the requirement of unhindered longitudinal migration of aquatic species through the removal or easement of barriers to fish migration and the removal or modification of engineering structures. Where removal of hydraulic structures is impractical, barriers are eased through further anthropogenic modifications in the form of additional hydraulic structures known as fish passes. These are defined as in-stream structures designed to facilitate upstream migration of aquatic fauna [Armstrong et al., 2010]. There are numerous designs of fish passes which can be generally categorised as pool-type passes, slope-type passes, and lift-type passes. Furthermore, there are also structures designed to ease only downstream movement, including physical screens, surface bypasses, and bar racks [Noonan et al., 2012]. These devices function by diverting fish towards safe downstream routes and away from turbines. Numerous researchers have employed experiments to determine the efficiency of different surface bypass and fish pass designs under different conditions and with different techniques [Roscoe and Hinch, 2010, Foulds and Lucas, 2013].

There have been many experimental and computational studies on the quantifica-

tion of fluid flow within a range of different fish pass designs [e.g. Khan 2006, Ferrari et al. 2009, Andersson et al. 2012, Lindberg et al. 2013, Arenas et al. 2015]. Therefore, the hydraulics of these designs are generally well understood. However, the ecological efficiency of fish passes, defined as the number of successful passages divided by the number of attempts, can currently only be determined experimentally. This requires a large amount of time, resources, and is often invasive. Furthermore, it is difficult to assess the success of a given passage facility as there is a distinct lack of recommended performance criteria present in the literature [Silva et al., 2018] and ongoing monitoring of installations is often cost prohibitive. This is compounded by a difficulty in accurately measuring the number of attempts made by individuals that approached the structure (failure rate). These difficulties in measuring ecological efficiencies make the analysis of new fish pass designs costly and time-consuming. Furthermore, they make swift design iterations (or optimisation) of fish passes impossible. It is therefore unsurprising that fish pass efficiencies are consistently reported as low [Larinier and Travade, 2002b, Oldani et al., 2007, Roscoe et al., 2011, Brown et al., 2013]. Moreover, Noonan et al. [2012] found fish passage facilities had average upstream and downstream passage efficiencies of 41.7% and 68.5%, respectively; drastically lower than the recommendation of 90% to 100% made by Lucas and Baras [2008].

Defining and decoding the behavioural rules that govern up-migrating fish responses to ecohydraulic flow fields, with particular consideration to attraction flows, would allow for better design of passage facilities and has been dubbed a "high research priority" by Silva et al. [2018]. Simulation of the movement decisions of up-migrating fauna will give insight into fish migration pathways and potentially allow for more freedom in the design and operation of fish passage facilities. Similarly, it has the potential to allow for swift iterative design and optimisation of fish pass geometries to maximise passage efficiencies. Furthermore, the use of a computational model of fish passage would implement the governing principles of animal research: replacement, reduction, and refinement; known as the 3Rs [Russell and Burch, 1992, Fenwick et al., 2009]. Specifically, reducing, and in some cases replacing, the need for animal experiments. Multiple attempts have been made to computationally predict fish movements for a variety of cases and using a variety of methods [Goodwin, 2004, Blank, 2008, Abdelaziz, 2013, Plymesser, 2014, Gao et al., 2016]. These studies are reviewed in detail in section 2.8. However, none of the models developed in these studies are capable of modelling

the pathways of up-migrating fishes through a generalised domain. This makes them inaccessible to practitioners and restricts the possibility of their wide-spread use.

1.2 Research Aim and Developmental Tool Principles

This research aims to address knowledge gaps in fish behaviour in anthropogenically impacted rivers. In particular, this research aims to develop a functional software tool to be used by practitioners to understand up-migrating fish behaviour in lowland rivers. This tool will subsequently provide a method to assess the impact of ecohydraulic environments such as weirs and fish passes on up-migrating fishes. This will be achieved through the following objectives:

- Thorough review of literature to identify key hydrodynamic stimuli.
- Investigation of the applicability of agent-based modelling to predict juvenile eel behaviour in ecohydraulic environments through the development and application of simple 2D agent-based models.
- Application of the agent-based approach to develop an open-source tool to predict upstream migration trajectories of brown trout, through decoding fish responses to hydrodynamic stimuli into a behavioural ruleset.
- Individual verification of each behavioural rule through application of the tool to artificial flow environments.
- Exploration of the sensitivity of predicted trajectories to model parameters.
- Application of the developed model through an ecohydraulic domain and comparisons of predicted brown trout pathways against measured fish track data.

For this software tool to be useful to practitioners it must adhere to a number of developmental principles defined through an understanding of: the literature, client requirements, and good data practice. These principles are outlined in table 1.1 and act as drivers in developmental decisions throughout this research.

Table 1.1: The development principles designed to guide the development of the software tool.

No.	Principle	Description
1	Open source	Developing the model using open-source software increases its accessibility and encourages its usage.
2	Transparent	Transparency in the development and function of the tool increases its accessibility and allows others to further develop the tool.
3	Generalised	The tool needs to be applicable to any hydrodynamic environment that the user wishes to consider.
4	Spatially 3D	This ensures that the model does not limit the user and can assess trajectories in all axes.
5	Self-contained	The tool should function as a stand-alone tool with minimal software dependencies.
6	Modular	Developing the tool in a modular manner allows easy exploration of separate behavioural rules as well as facilitate the future incorporation of other additional species.
7	Individual Focus	The tool should focus on the passage and pathway of the individual; i.e. micro-scale, rather than that of a population; i.e. macro-scale.

1.3 Thesis Structure

Chapter 2 presents a literature review including: a brief summary of British fish species and their biology and conservation status, designs of typical fish pass facilities, an overview of the Reynolds-Averaged Navier-Stokes approach to computational fluid dynamics, the agent-based modelling approach, fish behaviour studies, and the current state of fish path prediction models.

Chapter 3 presents a viability study of agent-based modelling and its application to an ecohydraulic environment. In particular, this chapter considers the passage of juvenile European eels ascending a purpose-built anguilliform pass in a variety of configurations. Flow fields within each pass configuration are quantified using computational fluid dynamics. Passage efficiencies are predicted through the application of multiple custom-built two dimensional agent-based models and the novel application of established landscape connectivity metrics. Results are compared to published passage efficiencies and the implications for eel pass design are discussed. Lastly, the results are extended to consider theoretical maximum pass lengths, which are presented as charts

aimed at assisting practitioners in developing improved designs.

Chapter 4 presents the development of a three dimensional, temporally discrete, spatially continuous agent-based model to predict up-migration pathways of brown trout. The model predicts vector-based trajectories of individual heterogeneous fish based on their responses to stimuli within their local hydrodynamic environment. The decoded behavioural ruleset is detailed along with the tool structure, required environmental inputs, and user defined parameters. This chapter also presents a model of energy expenditure and a model of swim bladder buoyancy and their implementation within the tool.

Chapter 5 presents the verification of each behavioural rule and the sensitivity of predicted fish trajectories to tool parameters, in order to ensure tool functionality. Multiple artificial hydrodynamic environments, created and executed using computational fluid dynamics, are developed and converted into appropriate inputs for the software tool. A parameter sensitivity study is performed through the application of the tool to each artificial environment for each behavioural rule and the discussion of the predicted pathways.

Chapter 6 presents validation of the tool against measured velocity and fish track data at a study-site on the River Esk, North Yorkshire. This chapter details the study site and data collection methodology used to collect both geometric and velocity data. The process of converting collected geometric data to a usable computational fluid dynamics mesh is detailed along with the subsequent execution of the simulations to quantify study site velocity fields. Simulated and measured velocity data are compared to validate the computational fluid dynamics approach. Simulated fish pathways and published, measured fish tracks are compared to validate the software tool.

Chapter 7 discusses the research findings including: the use of two dimensional agent-based models and landscape connectivity metrics to passage of eels, the implications for eel pass design, the use of three dimensional agent-based models in predicting up-migration pathways through a generalised domain, the implications and usage of the software tool. It then presents limitations of the research, conclusions, and future work.

Chapter 2

Literature Review

This chapter discusses background theory and previous research required to understand models of up-migrating fishes. This chapter begins with a brief introduction to the causes and effects of river fragmentation, as well as common fish passage solutions employed to ease barriers to migration. Section 2.3 presents a non-exhaustive list of British fish species along with associated conservation statuses and migration types. These sections are presented to provide context to the research question.

In order to accurately model the movement of fish, it is important to understand the manner in which fish interact with their environment. Therefore, section 2.4 presents a brief introduction to fish biokinetics and their mechanosensory system. Similarly, in order to model the responses of fish to hydrodynamic cues, the fluvial environment that the fish inhabit must be quantified. This is done through the using of computational fluid dynamics (CFD), and therefore an introduction to CFD is presented in section 2.5. Cellular automata, individual-, and agent-based modelling approaches are used to develop the models within this thesis and therefore an introduction to these are presented in section 2.6. Section 2.7 presents a review fish behaviour studies, and summarises key identified hydraulic stimuli as well as observed responses to those stimuli. These are used to inform the behavioural rulesets outlined throughout this thesis. The final section of this chapter provides a thorough review of previous research in fish path prediction.

2.1 Anthropogenic Alteration of the Fluvial Environment

Rivers are a fundamental part of the natural environment, play host to a vast range of aquatic plants and animals, and are heavily relied upon by non-aquatic species through the provision of ecosystems services [Costanza et al., 1997]. Anthropogenic alteration of fluvial systems, sometimes referred to as river fragmentation, is ubiquitous in areas populated by humans [Dynesius and Nilsson, 1994]. Recent assessments have suggested that only 3.3% of rivers in Great Britain are fully connected, and only 1% of rivers in Great Britain do not feature anthropogenic alteration [Jones et al., 2019]. Historically, river systems were modified to control water levels, facilitate human navigation, power mills, or to permit abstraction. More recently, rivers have been exploited as a green energy source through the building of new hydroelectric structures or through retrofitting existing weirs. River alteration has severe ecological effects [i.e. van Puijenbroek et al. 2019]. It provides barriers to the upstream and downstream movements of

aquatic organisms and has been directly linked to declining populations and even the loss of entire species [Nilsson et al., 2005]. In addition, it can change the local river temperature, food availability, oxidation levels, and habitat access [Humborg et al., 1997, Nilsson and Berggren, 2000, Alo and Turner, 2005]. However, in lowland British rivers, weirs and the upstream and downstream reaches thereof provide significant niche habitats that would otherwise display minimal streamwise and cross-stream variations in velocities, depth, and substrate characteristics [i.e. Kröger et al. 2008]. The World Commission on Dams [2000] report similar benefits at large dams, some of which have been recognised as internationally important sites under the Ramsar Convention.

The European Union (EU) Water Framework Directive (WFD) mandates EU member states to improve all aquatic ecosystems and allow for unhindered longitudinal migration of aquatic species. Unhindered migration can be achieved through the removal or easement of barriers to fish migration. Examples of these are listed below.

- Weir and dam removal [Bednarek, 2001, Stanley and Doyle, 2003]. While the removal of weirs and dams has the effect of easing fish migration, it has been reported that there may be costly repercussions, such as the loss of niche habitats and increased mortality in downstream aquatic communities [Stanley and Doyle, 2003]. Furthermore, it is often impractical to remove some barriers as they are required for ecosystem services (i.e. water abstraction).

- Physical transportation of fish [Williams et al., 2005, Keefer et al., 2008]. There has been some attempt to aid migration by manually transporting fish around river fragmentation points. However, Keefer et al. [2008] found that this practice, over a 1 to 3 year period, severely impaired adult orientation and homing abilities compared to those left alone.

- Construction of fish passes [Clay, 1994, Cowx et al., 1998b]. Fish passes provide a migration solution that does not affect the niche habitats formed by river fragmentation, does not impact ecosystem services, and does not have the biological impact of hatchery programmes [Larinier and Marmulla, 2004]. For example, Calles and Greenberg [2005] found that densities of brown trout yearlings upstream of two nature-like fish-ways increased after their construction compared to control sites, which saw no change. The percent of fish successfully passing the fish-way was reported as $> 90\%$, but this metric only considers individuals

recorded at the bottom of the pass. After accounting for the number of fish that successfully located the pass (52%) the total efficiency of the fish-way is reduced to 48% [Calles and Greenberg, 2005]. Therefore, while nature-like fish-ways are beneficial to overcoming the fragmentation of rivers, the likelihood of successful passage is limited by the ability of the fish to locate the pass.

It is also worth mentioning that, while not strictly a form of migration easement, compensatory stocking is also used in many countries [see Ackefors et al. 1991, Eriksson and Eriksson 1993, Wanke et al. 2016]. This involves rearing fish in hatcheries before releasing them into the upper reaches of rivers. Literature suggests that hatchery-reared salmonids are significantly outperformed by wild salmonids [Saloniemi et al., 2004, Chittenden et al., 2008, Serrano et al., 2009] due to slower migration times, naïve anti-predator relations, and higher lipid concentrations [Weber and Fausch, 2003, Serrano et al., 2009].

2.2 Fish Pass Design

In ecological terms, a fish pass is a structure designed to facilitate the passage of fish past obstructions [Larinier and Marmulla, 2004]. In hydraulic terms, a fish pass is a structure designed to dissipate the kinetic energy of the flow [Kamula, 2001]. This dissipation is vital to the function of the fish pass so as to ensure that the water velocity is below the biokinetic capacity of the fish [Armstrong et al., 2010]. However, recent thought suggests that considering only energy dissipation and mean velocities is too simplistic and inefficient, and an understanding of turbulence within the pass is required to adequately facilitate passage [Silva et al., 2018] This is discussed in section 2.7.

There are several critical controls on fish-way design including water depth, discharge, length, gradient and velocity, all of which affect the species for which the pass is most suitable [Armstrong et al., 2010]. Crucially, different species require different hydraulic conditions, some of which are mutually exclusive [Larinier and Marmulla, 2004]. For this reason, practitioners are forced to design for particular species, the result of which is commonly a bias towards economically important species such as Atlantic salmon or other salmonidae [Noonan et al., 2012, Williams et al., 2012].

The hydraulic conditions (flow velocity, turbulence, etc.) within a fish-way are intrinsic to its overall performance. However, the flow field downstream of the fish

pass is also important as it influences the attraction of the fish to the entrance of the fish-way, known as the "attraction flow" [Armstrong et al., 2010]. However, little has been published to quantify the attraction flow [Gisen et al., 2016] and what guidelines are available are ambiguous [Katopodis, 2005]. It has been suggested that the flow rate, turbulence structure, velocity, and temporal and spatial derivatives of velocity at the fish-way entrance affect the attraction flow [Coutant, 1998, Goodwin et al., 2014, Burnett et al., 2016, Gisen et al., 2016]. Additionally, noise, scent, temperature, and oxygenation have also been suggested to be relevant [Williams et al., 2012]. However, little has been done to quantitatively isolate the influence of each, and many existing international guidelines are inconsistent [Weichert et al., 2013].

Fish pass designs can be split into three categories [Armstrong et al., 2010]:

- Pool-type passes, figure 2.1. These designs split the vertical distance to be passed into a series of pools of increasing height and are often augmented with notches, slots, or orifices [Larinier and Marmulla, 2004].
- Baffle passes, figure 2.2. Baffle pass designs utilise a relatively steep slope divided by various forms of baffle, down which water flows [Larinier and Marmulla, 2004]. The baffles are used to dissipate the kinetic energy of the water, reducing its velocity and facilitating the passage of fish [Armstrong et al., 2010].
- Lift passes. Lift passes attract fish into a finite space which is then lifted the required vertical distance where the fish are then released [Armstrong et al., 2010]. Since the primary focus of this project is British lowland rivers, lift passes will not be considered, as they are designed for large scale dams [Deutscher Verband für Wasserwirtschaft und Kulturbau, 1996].

2.2.1 Pool Passes

Pool-type passes are the oldest type of fish pass and have been used extensively across Britain, mainland Europe, and North America [Larinier and Marmulla, 2004]. They consist of a series of uniformly-spaced pools, with each pool slightly lower than the pool immediately upstream creating a series of stepped pools, with a traverse between each [Armstrong et al., 2010]. Each type of pool pass employs a slightly different design of traverse, which alters the hydraulic environment and the way in which fish move through the pass [see Maeno and Miyauchi 2001, Khan 2006, Liu et al. 2006, Quaresma

and Pinheiro 2014]. Pool-type passes have the advantage of being low maintenance and have the potential to be constructed with frequent, sharp changes of direction, allowing flexibility in their installation [Armstrong et al., 2010]. Furthermore, each pool offers the opportunity for migrants to rest between each energetic bout, therefore pool passes are accessible for a variety of fish with differing swimming capacities [Larinier and Marmulla, 2004]. Nevertheless, it is beneficial to minimise the total passage time as increased passage time has been related to unsuccessful passage due to energy depletion and exposure to predation [Caudill et al., 2007].

Pool and Traverse Passes

Pool and traverse-type passes, figure 2.1a, sometimes referred to as pool and weir passes, consist of a series of traverses between pools of different heights. Simple over-falls are used to connect pool to pool, through the formation of a nappe. These passes require fish to travel in the nappe and are therefore unsuitable for benthic and some benthopelagic species, and favour species with greater swimming performance [Armstrong et al., 2010]

Numerous experiments have been performed to study the flow structure of pool and weir passes [e.g. Hayashida et al. 2000, Maeno and Miyauchi 2001, Ead et al. 2004, Atsushi et al. 2008, Atsushi 2009, Abdelaziz et al. 2013, Duguay et al. 2017]. Abdelaziz et al. [2013] performed 2D, width-averaged RANS simulations of a pool and traverse pass, with the k–ε turbulence closure, and using a rectangular grid with a resolution of 0.1 m [see section 2.5]. Abdelaziz et al. [2013] found that the flow field of each pool was dominated by a region of up-welling near the downstream wall and a region of down-welling at the upstream wall, leaving a region of low velocity in the centre of the pool. The structure of the simulated flow field matched the experiments of Atsushi [2009], however the simulations suggested the largest velocities were experienced close to the upstream and downstream walls, whereas the experimental data shows that the largest velocities appear in the nappe over each weir [Abdelaziz et al., 2013]. Duguay et al. [2017] performed 3D RANS simulations of a pool and weir fish pass using the k-ε turbulence closure within OpenFOAM and FLOW-3D, using the volume of fluid method to track the free surface [see section 2.5]. Duguay et al. [2017] collected *in situ* instantaneous 3D velocity data within a single pool of the pool and weir fish pass using an acoustic Doppler velocimeter (ADV), with a sample frequency of $60Hz$ and collected

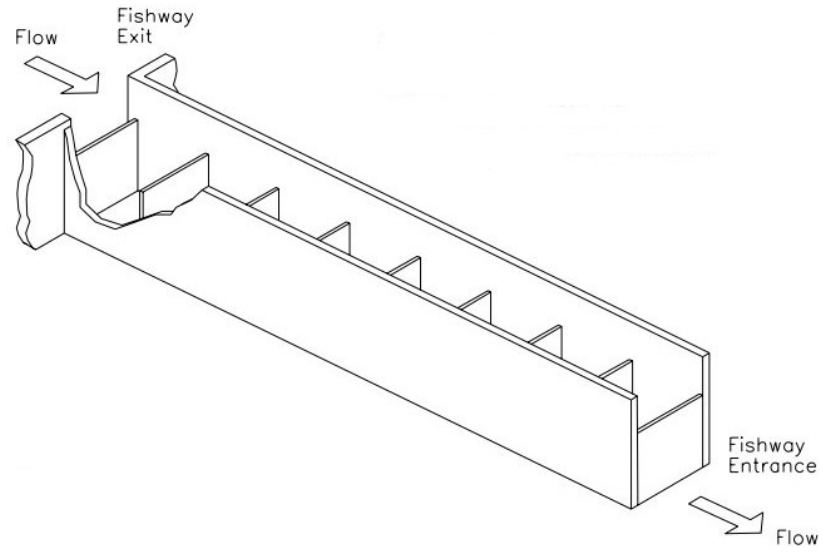

(a)

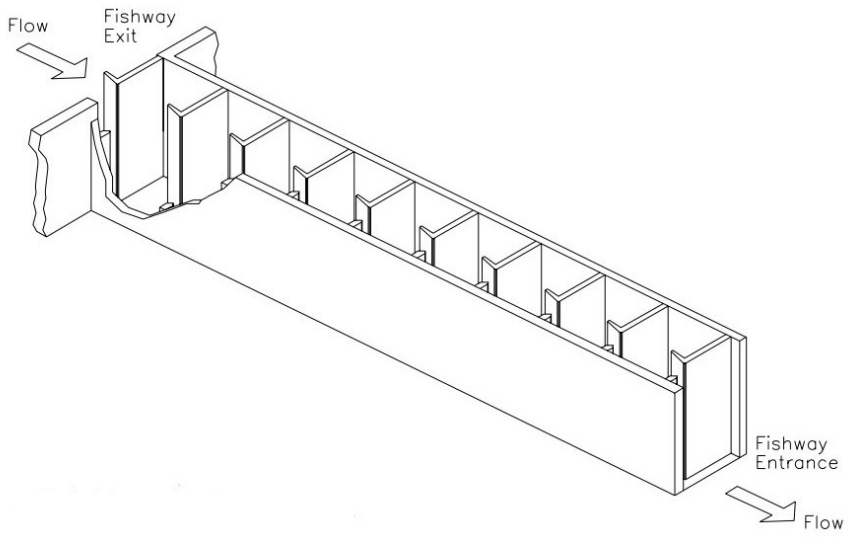

(b)

Figure 2.1: Schematics of (a) a pool and traverse fishway and (b) a vertical slot fishway, both adapted from Katopodis [1992]

over a period of $180s$. Duguay et al. [2017] found agreement between simulated and measured velocity data, turbulence kinetic energy, and water surface levels, although both models were unable to predict finer turbulence structures within the flow field. These results suggest that a 2D RANS CFD approach is not sufficient to accurately model the flow in a pool and traverse fish pass, but a 3D RANS CFD approach is capable of accurately predicting the water surface height and the velocity field.

Vertical Slot

Vertical slot fish passes are similar to pool and traverse passes but employ one or two vertical rectangular slots between pools [Armstrong et al. 2010; figure 2.1b]. This forms a jet of water at the outlet of each slot, dissipating the kinetic energy of the water through circulation around the axis perpendicular to the channel floor [Kamula, 2001]. The rectangular slots are often located off-centre and angled toward the centre of the lower pool to ensure that the resulting jet thoroughly mixes in the lower pool [see Rajaratnam et al. 1986, 1992]. Small baffles at the slot are sometimes used to ensure mixing [Rodríguez et al., 2006]. Vertical slot fish passes have the advantage of allowing passage at all parts of the water column, making them suitable for almost all aquatic species including benthic species and invertebrates [Larinier and Travade, 2002a, Armstrong et al., 2010].

The hydraulics of vertical slot fish passes have been extensively studied experimentally [Rajaratnam et al., 1986, 1988, 1992, Wu et al., 1999, Liu et al., 2006, Rodríguez et al., 2006] and, more recently, numerically in both two [Cea et al., 2007, Bermúdez et al., 2010, Chorda et al., 2010, Bombač et al., 2014, Gao et al., 2016, Quaranta et al., 2016] and three dimensions [Khan, 2006, Heimerl et al., 2008, Barton et al., 2009, Marriner et al., 2016]. Vertical slot fishways are thought to be tolerate large fluctuations in upstream water level as the flow structure in each pool is approximately independent of the upstream flow depth [Kamula, 2001, Heimerl et al., 2008]. For this reason a large number of numerical studies of vertical slot fish passes have employed a 2D, depth-averaged formulation. However, it has been demonstrated that each pool in a vertical slot fish pass has large regions of up-welling near the downstream slot and large regions of down-welling at the upstream slot [Khan, 2006]. Furthermore, Barton et al. [2009] found that the flow velocity through the slot is a function of the elevation, and Khan [2006] found that eddies are formed around the horizontal axis within pools.

These findings indicate that the velocity field within a vertical slot fish pass is strongly three-dimensional, and that a 3D RANS CFD approach is capable of predicting the hydraulics of the fish pass.

2.2.2 Baffle Passes

Baffle fish-ways are use relatively steep ($\approx 20°$), straight slopes with baffles used to dissipate the kinetic energy of the flow [Armstrong et al., 2010]. The principle of the baffle passes is to dissipate the kinetic energy of the flow through causing secondary flows and increasing turbulence through strategically positioned baffles [Larinier, 2002a].

With the exception of Larinier fish passes, there is a lack of studies to quantify the hydraulics of baffle fish passes. Furthermore, there is a distinct lack of computational investigations into the hydraulics of baffle fish-ways, likely due to their complex geometries and the associated complexities of CFD meshing. Unlike pool passes, baffle passes offer no respite to migrants and therefore they must pass the entire structure in a single attempt, making them better suited to stronger swimmers such as salmonidae [Larinier and Marmulla, 2004]. This limits the maximum length of baffle-type fish passes unless resting pools are introduced between lengths of pass [Larinier and Marmulla, 2004]. Additionally, baffle passes require a straight slope, meaning that they can only change direction via a resting pool, limiting the viability of their installation.

Baffle passes can be split into three types:

- Bottom-baffle fish-ways. These fish passes have baffles attached only on the bottom of the pass, which allows for wider fish-ways, giving versatility in discharge [Larinier, 2002a]. However, they cannot withstand large variations in upstream water level due to rapid increases in velocity with depth [Larinier, 2002a].

- Side-baffle fish-ways. These passes have baffles connected only to the sides of the fish pass and have the advantage of being able to withstand large variations in upstream water level and are the most efficient at kinetic energy dissipation Larinier [2002a] . However, side-mounted baffles are very prone to blockage and therefore require increased maintenance [Larinier, 2002a].

- Bottom- and side-baffle fish-ways. These passes have baffles placed on both the sides of the fish-way and the floor, and can withstand greater variations in up-

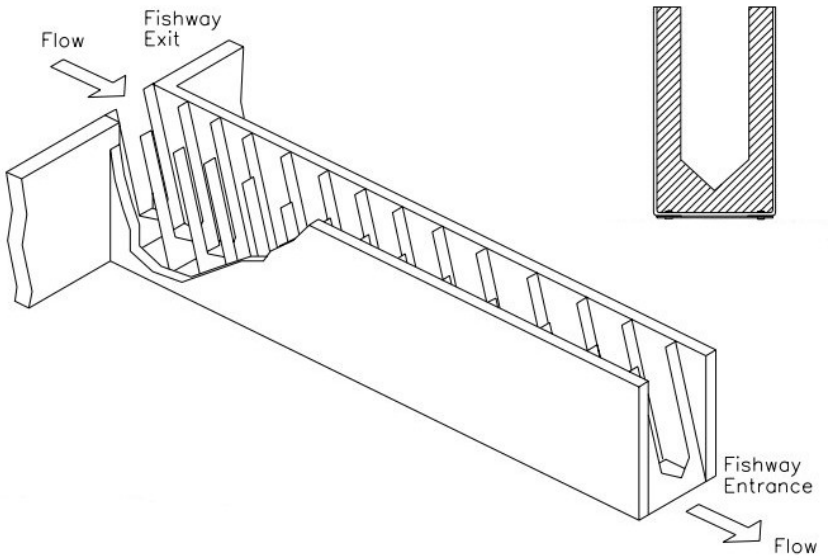

(a)

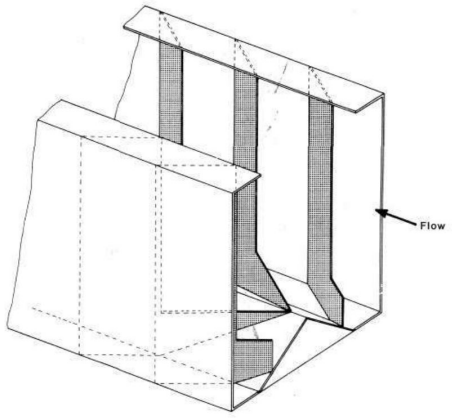

(b)

Figure 2.2: Schematics of two typical baffle/slope fish-ways. (a) Schematic of a Denil fish-way adapted from Katopodis [1992]. (b) Schematic of an Alaskan Denil fish-way from Beach [1984].

stream water level compared to bottom baffle fish-ways, but are limited in size as large baffles encroach on the swimming channel [Larinier, 2002a].

Denil Passes

The Denil fish pass (figure 2.2a) was originally developed by Denil [1909], and has subsequently been further developed by McLeod and Nemenyi [1941], White and Nemenyi [1942], and Fulton et al. [1953], among others. Within the fish pass are a series of symmetrical baffles attached to both the sides and bottom of the fishway and set at 45° to the channel slope [Armstrong et al., 2010], which transfer energy from the flow to the fish pass walls [Kamula, 2001]. Literature suggests that these fish passes are suitable for migratory salmonids when installed at large gradients (i.e. $\geq 15\%$) and can be utilised by coarse fish and lamprey by using shallower slopes (i.e. $\leq 15\%$) [Mallen-Cooper and Stuart, 2007, Fish Counters In Action, 2008, Armstrong et al., 2010]. However, Noonan et al. [2012] found in a recent review that Denil fish passes had the lowest aggregated passage efficiencies. Furthermore, there is a distinct lack of experimental and numerical quantification of flow within Denil passes in the literature.

Alaskan Denil

The Alaskan Denil fish pass, sometimes referred to as an Alaskan steeppass [Plymesser and Cahoon 2017; figure 2.2b], is designed to be robust for installation in remote areas [Carling and Dobson, 1992]. It was originally developed by Ziemer [1962] for Pacific salmon in Alaska and features symmetric baffles, perpendicular to the channel slope, and angled 60° toward the upstream direction [Larinier, 2002a]. This produces a hydraulic structure that is more efficient at energy dissipation than the Denil fish pass but is more likely to suffer from blockage [Larinier, 2002a]. Alaskan Denil fish-ways are narrow due to the wall-mounted baffles, and are installed at relatively steep angles (25-33% gradient) [Larinier, 2002a].

Plymesser [2014] and Plymesser and Cahoon [2017] performed 3D RANS simulations of an Alaskan steeppass using FLOW3D, and using the k-ε RNG turbulent closure and the VOF method to track free surface location [see section 2.5]. Plymesser [2014] found that predicted velocities compared well to velocities collected via an electromagnetic current meter (ECM), and water surface heights compared well to data measured by Haro et al. [1999]. This result suggests a 3D RANS approach using the k–ε RNG

turbulent closure and the VOF method is capable of accurately modelling the free surface and velocity field within a baffle-type fish-way.

Larinier

Sometimes referred to as the super-active baffle fish-way, the Larinier fish pass was originally developed by Larinier and Miralles [1981]. The pass uses a herringbone pattern of small baffles attached only to the bottom of the channel [Larinier, 2002a]. The Larinier pass is wide and shallow when compared to other baffle passes; and, unlike other baffles passes, the width of a Larinier pass is not limited by the hydraulic operation of the pass, only by the conditions at the installation site [Larinier and Marmulla, 2004]. Therefore, multiple prefabricated units of baffles can be placed side-by-side to meet the desired width, which can lead to very large attraction flows [Armstrong et al., 2010]. The hydraulics of Larinier fish passes have been studied experimentally, resulting in specific baffle geometries to obtain the desired flow conditions [Larinier and Miralles, 1981, Larinier, 1992, Larinier et al., 1994, Larinier, 2002a]. Furthermore, there are established relationships between the discharge per unit width (m^2s^{-1}) and the average velocity in the pass for a given combination of installation angle and baffle size [see Larinier 1992]. For example, for a gradient of 15%, $0.15m$ baffles, and a discharge per unit width between $0.2m^2s^{-1}$ and $1.3m^2s^{-1}$, the velocity can be calculated based on the work of Larinier [1992]:

$$c_1q^2 + c_2q + c_3 \tag{2.1}$$

where c_1, c_2, c_3 are empirically derived constants equal to $-0.0603, 0.7816$, and 1.0424, respectively.

2.2.3 Anguilliform Passes

In addition to pool passes and baffle passes, passes have also been designed to specifically aid the passage of eels (anguilliformes) (figure 2.3). Eels are catadromous [see section 2.3] and thus it is essential for them to migrate upstream and downstream at different life stages. However, eels cannot traverse vertical barriers that are greater than 50% of their body length [Cowx et al., 1998a]. Therefore, only larger adult eels can successfully navigate conventional fish-ways, and only if the velocities are low enough to facilitate passage. Eels are weak swimmers but can exploit boundary layers, crawl,

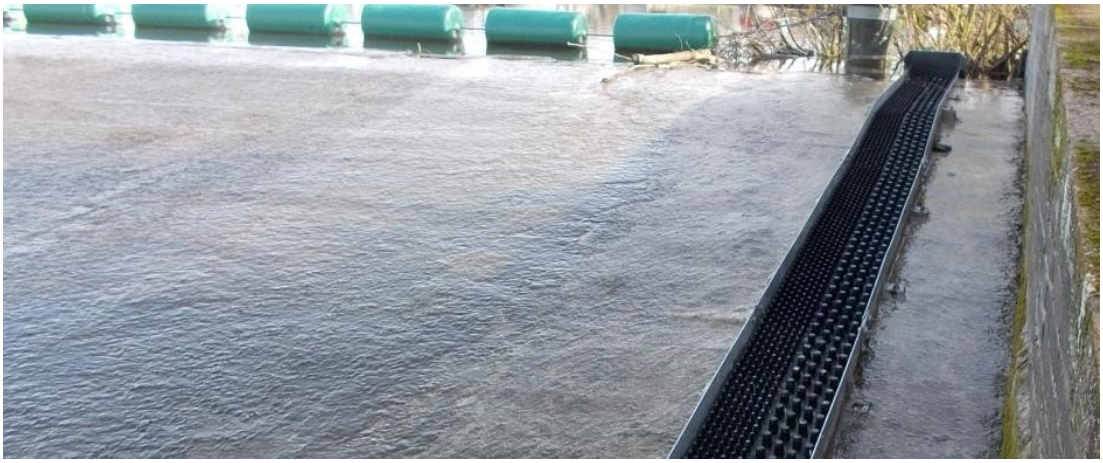

Figure 2.3: Image of an *in situ* eel pass installed on a weir

and cling to surfaces [Solomon and Beach, 2004]. Eel passes provide a wetted substrate on an inclined plane that provides purchase for eels to cling to and wriggle through [Armstrong et al., 2010]. Historically, the substrates used were often cheap items and fabric such as broom-heads [Environment Agency, 2011], trawl netting [Shotzberger and Strait, 2002], garden netting, burlap [Jackman et al., 2009], and geotextile matting [Environment Agency, 2011]. However, Voegtle and Larinier [2000] found that these materials were too abrasive and caused passing eels to lose a considerable amount of mucus. More recently, purpose-built synthetic substrates have become available that use a series of small, more-or-less rigid, vertical cylinders or studs attached to a base [i.e. Berry & Escott Engineering 2017, Milieu Inc. 2017, Terraqua Environmental Solutions 2017; figure 2.4]. These passes have been shown to successfully increase passage efficiency of eels and elvers from 0% to 67% when installed on a model Crump weir [Vowles et al., 2015]. As eels are inclined to cling to substrates, eel passes can be installed at large gradients, with successful passage recorded even at slopes of 45° [Environment Agency, 2011]. Eels tend to congregate in areas with slow velocities and so eel passes are commonly installed in these areas. Furthermore, it is necessary to ensure that upstream velocities are low to ensure that eels are not washed back downstream [Environment Agency, 2011]. Therefore, unlike other fish passes, eel passes do not require a substantial attraction flow and do not require large flow rates down the face of the eel pass [Armstrong et al., 2010].

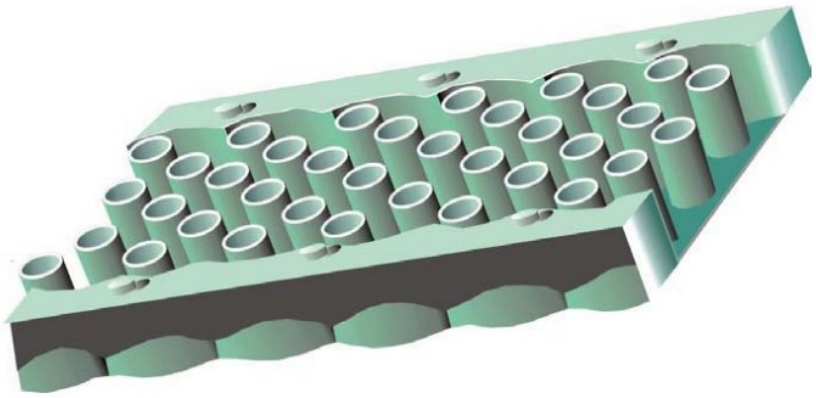

Figure 2.4: CAD render of a typical Milieu eel pass segment from Environment Agency [2011]

2.3 British Fish Species

The responses of fish to hydrodynamics and environmental cues are known to be species-specific [i.e. Silva et al. 2016] . Furthermore, the efficiency of fish passes depends on the species passing through the pass due to differences in size, biokinetic ability, and mechanosensory ability [Armstrong et al., 2010]. This section details example fish species that exist within British river systems to give context to the research question, as well as technical language used throughout the work.

Fish migrate within the river environment to feed or spawn, or to take refuge [Lucas and Baras, 2008]. Table A.1, located in Appendix A, gives a non-exhaustive list of British freshwater fish species including their common name, taxonomic name, International Union for Conservation of Nature (IUCN) Red List Status, family, migration type, and habitation zone. The IUCN has categorised the conservation status of species into nine categories ranging from least to most threatened: Not Evaluated (NE), Data Deficient (DD), Least Concern (LC), Near Threatened (NT), Vulnerable (VU), Endangered (EN), Critically Endangered (CR), Extinct in the Wild (EW), Extinct (EX). The IUCN use the term "Threatened" to refer to any species classified as Vulnerable, Endangered, or Critically Endangered. Migration types are split into six categories: Anadromous, Amphidromous, Catadromous, Non-migratory, Oceanodromous, and Potamodromous [Lucas and Baras, 2008]. Anadromous fish are born in freshwater and migrate to sea where they live most of their life before migrating back to freshwa-

ter to spawn [Brönmark et al., 2014]. Amphidromous fish are born in freshwater and drift into the ocean as larvae, migrating back into freshwater to grow into adults and spawn [Lucas and Baras, 2008]. Catadromous fish are born in the ocean and migrate to freshwater, where they live most of their lives before migrating back to the ocean to spawn [e.g Aarestrup et al. 2009]. Non-migratory fish spend all of their lives in the same reach of a river; for example nest building fish, such as Grayling. Oceanodromous fish migrate between different marine environments [Lucas and Baras, 2008]. Potamodromous fish spend all of their lives in freshwater. However, they are known to locally migrate over distances of the order of kilometres [e.g. Northcote 1997, Masters et al. 2002].

The section of the water column that the fish naturally inhabits is defined as "Zone". Demersal fish live and feed in the section of water just above the bed (benthic zone), and are sometimes referred to as bottom feeders. Demersal fish are split into two categories; benthic fish and benthopelagic fish. Benthic fish have negative buoyancy and lie on the bottom without actively maintaining station. Benthopelagic fish have neutral buoyancy. Pelagic fish live and feed in the pelagic zone, which encompasses the water column from the surface to near the demersal zone but away from the coast. Pelagic fish are not considered in this project as they do not venture inland at any time. Pelagic-Neritic refers to those species that also venture into the neritic zone, which is defined as relatively shallow coastal waters or river outflows.

2.4 Fish Biology

Fish interact with their environment in a manner that can be broken down into their ability to move through the environment (biokinetic capabilities), and their ability to perceive their environment through the mechanosensory system.

2.4.1 Fish Biokinetics

Fish locomotion is achieved through a combination of aerobic (red) muscles and anaerobic (white) muscles [Johnston, 1981]. The use of red muscles does not noticeably fatigue fish, whereas the use of white muscles fatigues fish [Johnston, 1981]. The biokinetic capability of fish can be separated into three distinct categories: sustained swimming, prolonged swimming, and burst swimming [Beamish, 1979]. Sustained swim-

ming uses only red muscles [Johnston, 1981] and is defined as locomotion that can be maintained for long periods of time ($>$ 200 minutes) without muscular fatigue [Beamish, 1979]. Prolonged swimming is defined as locomotion that can be maintained for between 20 seconds and 200 minutes and will end in fatigue [Beamish, 1979]. Burst swimming is defined as locomotion that can be maintained for short periods of time ($<$ 20 seconds), and encompasses the highest speeds attainable by the fish [Beamish, 1979]. Both prolonged and burst swimming modes use white muscles only [Johnston, 1981]. Biokinetic capabilities are species-specific and are also a function of fish body length and local water temperature [Clough and Turnpenny, 2001].

2.4.2 Fish Mechanosensory System

Fish have a complex sensory system evolved to navigate hydraulic environments. Montgomery et al. [1995] suggest that fish behaviour is mediated by a combination of all available sensory information. All fish have two mechanosenory subsystems which allow them to sense local hydrodynamics, the lateral line system and the inner ear [Montgomery et al., 1995]. In addition to these organs, many fish have a swim bladder that allows the fish to maintain near-neutral buoyancy [Lucas and Baras, 2000].

The lateral line is a sensory system that uses a series of neuromasts to detect water motion and pressure gradients [Bleckmann and Zelick, 2009]. Dijkgraaf [1963] describes the lateral line system as allowing fish to "touch at a distance" and Montgomery et al. [1995] suggest that this distance may be up to a body length from the fish. Neuromasts are sometimes referred to as "hair cell receptors". They are made up of mechanosensory hair cells which are sensitive to local water movements [Montgomery et al., 1995]. While the patterns and exact number of neuromasts are species-specific, fish generally have hundreds of neuromasts spread over their head, trunk, and tail [Montgomery et al., 1995]. These neuromasts are split into superficial neuromasts on the surface of the skin and sub-cutaneous "canal" neuromasts in fluid-filled canals connected to the skin surface via pores [Dijkgraaf, 1963]. Studies have shown that the lateral line plays an important role in predation [Janssen and Corcoran, 1993], and that the lateral line directly links to the Mauthner cell, which controls the escape reflex of the fish [Zottoli and Danielson, 1989]. The lateral line system has also been shown to play a significant part in rheotaxis, which is the behavioural tendency for fish to orientate themselves so that they are pointing upstream [Montgomery et al., 1997]. Rheotaxis is an important

evolutionary trait as it minimises the effort required by the fish to hold position when subjected to a current through drag reduction [Arnold, 1974]. Currents also carry both food and olfactory information that is best interpreted by fish when facing upstream [Montgomery et al., 1997].

The inner ear is formed from multiple otolithic end organs each of which contain mechanoreceptive sensory hair cells, as in the neuromasts of the lateral line, coupled with a specialised receptor surface known as the epithelia [Popper et al., 2005]. These end organs serve as an inertial system whereby stimuli cause motion of the fish relative to the otoliths due to the difference in densities between the two [Popper et al., 2003, 2005]. The relative motion of the fish body to each of the otoliths provides the fish with a three-dimensional perception of the motion of its body [Braun and Coombs, 2000]. The inner ear also provides the fish with hearing and gravity perception [Paxton, 2000].

Some fish have an internal organ known as the swim bladder [Jones, 1951]. The swim bladder is sensitive to hydrostatic pressure and can adjust its volume without adding to the mass of the fish, allowing it to effectively function as a ballast [Brawn, 1962]. This gives fish the ability to modify their own specific gravity [Alexander, 1966], allowing them to maintain near-neutral buoyancy [Lucas and Baras, 2000]. Therefore, the swim bladder enables the fish to conserve energy through removing the need for any active vertical force to be produced during rest and movement [Alexander, 1990]. The filling and emptying of the swim bladder is species-specific [see Jones 1951, Alexander 1971, and Vogel 1994]. The blood tends to a gaseous equilibrium with the local water through the exchange of gas in the gills [Randall and Daxboeck, 1984]. Generally, the gas in the swim bladder is regulated through exposure to blood, where diffusion of gas can occur between the two [Alexander, 1966]. The release of lactic acid by the adjacent "gas gland" produces carbon dioxide, which fills the swim bladder [Alexander, 1966]. Some fish have pneumatic ducts and have been observed releasing gas bubbles during ascent [Brawn, 1962]. The disadvantage of the swim bladder is that the filling and emptying of the swim bladder is a slow process, unless expelling gas [Jones, 1951]. This means that the swim bladder is ill-suited to rapid movements, such as in predation, where the fish would have to actively move. Rapid movement in the vertical axis under normal locomotion is unstable because, at its new depth, the fish would have to resist the buoyancy force through compensatory movement of its fins until its density has equalised through modification to the swim bladder [Jones, 1951].

2.5 Computational Fluid Dynamic Modelling

Computational fluid dynamics has gained popularity in ecohydraulics and ecological engineering in recent years in-line with the growing availability of computational resources [Ingham and Ma, 2005]. This section outlines the fundamentals of computational fluid dynamics (CFD) and describes the most popular approaches used in fish passage literature.

2.5.1 Fundamentals of Computational Fluid Dynamics

Fluid flow is modelled by applying a combination of Newton's second law to fluid motion and the physical principle of mass conservation [Anderson, 1995]. The continuity equation (2.2) stems from applying mass conservation to a finite fluid parcel, and states that the mass flow into and out of the finite parcel must equal the mass accumulation within the parcel [Pedlosky, 2013].

$$\frac{\partial \rho}{\partial t} + \frac{\partial \rho u_j}{\partial x_j} = 0 \tag{2.2}$$

where: ρ is the fluid density, u_j $(j = 1, 2, 3)$ are the components of the fluid velocity vector, x_j $(j = 1, 2, 3)$ are the components of the Cartesian spatial vector, and t is time.

Applying Newton's second law to fluid motion yields the Navier-Stokes equations (2.3), which describe the motion of a compressible Newtonian fluid in time and space [Anderson, 1995]. The equations state that the net force acting upon a finite fluid parcel must equal the mass of the element multiplied by its acceleration [Pedlosky, 2013].

$$\frac{\partial \rho u_i}{\partial t} + \frac{\partial \rho u_i u_j}{\partial x_j} = \frac{-\partial p}{\partial x_i} + \frac{\partial}{\partial x_j}\left(\frac{\mu \partial u_i}{\partial x_j}\right) + \rho F_i \tag{2.3}$$

where: $u_{i,j}$ $(i, j = 1, 2, 3)$ are the components of the fluid velocity vector, $x_{i,j}$ $(i, j = 1, 2, 3)$ are the components of the Cartesian spatial vector, the left hand side of the equation describes the inertial forces, $\frac{-\partial p}{\partial x_i}$ describes pressure forces, ρF_i describes external forces (i.e. gravity, Coriolis), and $\frac{\partial}{\partial x_j}\left(\frac{\mu \partial u_i}{\partial x_j}\right)$ describes the viscous forces, where μ is the dynamic viscosity of the fluid.

This non-linear system of equations forms the basis of most computational fluid dynamic (CFD) simulations [ANSYS, 2016]. This system is discretised using various numerical approximations, wherein the domain through which the fluid flow is considered is divided into a finite number of regions [Blazek, 2015]. Therefore, the flow

variations can be captured at each spatial point and each temporal step [Anderson, 1995].

For many fluid problems the Navier-Stokes equations can be simplified [Versteeg and Malalasekera, 2007]. For hydraulic flows, the water can be assumed to be incompressible (i.e. $\frac{\partial u_i}{\partial x_i} = 0$) [Ingham and Ma, 2005]. This leads to the incompressible Navier-Stokes equation:

$$\frac{\partial u_i}{\partial t} + \frac{\partial u_i u_j}{\partial x_j} = \frac{-\partial p}{\partial x_i}\frac{1}{\rho} + \frac{\partial}{\partial x_j}\left(\frac{\nu \partial u_i}{\partial x_j}\right) + F_i \tag{2.4}$$

where ν is the kinematic viscosity of the fluid.

2.5.2 Reynolds Averaged Navier-Stokes Equations

The Reynolds averaged Navier-Stokes (RANS) approach is the most widely used method of computationally predicting fluid flow in ecological engineering and fish passage literature [see Andersson et al. 2012, Feurich et al. 2012, Kim et al. 2012, Abdelaziz et al. 2013, Bombač et al. 2014, Marriner et al. 2014, Plymesser 2014, Quaresma and Pinheiro 2014, Gao et al. 2016, Quaranta et al. 2016, Plymesser and Cahoon 2017, Stamou et al. 2018, Klopries and Schüttrumpf 2020]. Other approaches such as Large Eddy Simulation (LES) [Sagaut, 2006] and Direct Numerical Simulation (DNS) [Moin and Mahesh, 1998] can yield higher accuracy. However, these methods are infrequently used within ecological engineering due to their higher computational expense.

The RANS approach considers the time-averaging of the Navier-Stokes equations [Anderson, 1995]. These equations are derived through Reynolds decomposition, which assumes that the instantaneous flow parameters can be split into the mean and fluctuating components, i.e. $u_i = \bar{u_i} + u_i'$ and $p = \bar{p} + p'$ [Ingham and Ma, 2005]. This results in the RANS equations (2.5) and (2.6). This assumption requires the mean value to be time-averaged over an interval which is large compared to the turbulent time scale [Anderson, 1995].

$$\frac{\partial \rho}{\partial t} + \frac{\partial \rho \bar{u_i}}{\partial x_i} = 0 \tag{2.5}$$

$$\rho \bar{u_j}\frac{\partial \bar{u_i}}{\partial x_j} = \rho \bar{F_i} + \frac{\partial}{\partial x_j}\Big(- \bar{p}\delta_{ij} + 2\mu \bar{S_{ij}} - \rho\overline{u_i' u_j'}\Big) \tag{2.6}$$

where δ_{ij} is the Kronecker delta; and S_{ij} is the mean strain-rate tensor defined as:

$$\bar{S_{ij}} = \frac{1}{2}\left(\frac{\partial \bar{u}_i}{\partial x_j} + \frac{\partial \bar{u_j}}{\partial x_i}\right) \tag{2.7}$$

The $-\rho\overline{u_i' u_j'}$ term in the RANS equations denotes the Reynolds shear stresses due to the fluctuating velocity field [Ingham and Ma, 2005]. This term contains additional unknowns introduced through the averaging process and is a non-linear term which requires additional modelling, termed a turbulence model, to close the equations [Ingham and Ma, 2005]. There are many established turbulence models in the literature, ranging from simplistic algebraic (zero-equation) models that do not solve additional equations, to non-linear, multi-equation models [Chen, 1997]. The turbulence model used is dependent upon the problem being solved and the computational expense that the user can tolerate [Ingham and Ma, 2005]. The turbulence closure models most commonly used in fish passage and ecological engineering literature are discussed in section 2.5.3.

2.5.3 Turbulence Closure Models

This section describes the turbulence models that occur most frequently in ecohydraulic and ecological engineering literature, namely the k–ε and k–ω models and their variants. Each of these turbulence closure models are two-equation linear eddy viscosity models that introduce and solve two additional transport equations to capture the turbulent properties of the flow [Wilcox, 1993]. Eddy viscosity models, such as the k–ε and k–ω models, solve for the eddy viscosity in order to satisfy the Boussinesq assumption [Boussinesq, 1877, Wilcox, 1993]:

$$-\rho\overline{u_i' u_j'} = 2\mu_t S_{ij} - \frac{2}{3}\rho k \delta_{ij} \tag{2.8}$$

where μ_t is the eddy viscosity, k is the turbulent kinetic energy, δ_{ij} is the Kronocker delta, and S_{ij} is the mean strain-rate tensor, defined in equation 2.7.

Standard k–ε Model

The standard k–ε model has seen fair usage in fish passage literature [e.g. Andersson et al. 2012, Abdelaziz 2013, Quaranta et al. 2016]. The k–ε model represents eddy viscosity through the turbulent kinetic energy, k, and the turbulent energy dissipation, ε, governed by: [Launder and Spalding, 1974].

$$\mu_t = c_\mu \rho \frac{k^2}{\varepsilon} \tag{2.9}$$

where c_μ is an empirical dimensionless constant; recommended as $c_\mu = 0.09$ [Versteeg and Malalasekera, 2007].

The turbulent kinetic energy, k, and the turbulent energy dissipation, ε are obtained through the introduction of two transport equations:

$$\frac{\partial}{\partial t}(\rho k) + \frac{\partial}{\partial x_i}(\rho k u_i) = \frac{\partial}{\partial x_j}\left[\left(\mu + \frac{\mu_t}{\sigma_k}\right)\frac{\partial k}{\partial x_j}\right] + G_k + G_b - \rho\epsilon - Y_M + S_k \tag{2.10}$$

$$\frac{\partial}{\partial t}(\rho \epsilon) + \frac{\partial}{\partial x_i}(\rho \epsilon u_i) = \frac{\partial}{\partial x_j}\left[\left(\mu + \frac{\mu_t}{\sigma_\epsilon}\right)\frac{\partial \epsilon}{\partial x_j}\right] + C_{1\epsilon}\frac{\epsilon}{k}(G_k + G_b) - C_{2\epsilon}\rho\frac{\epsilon^2}{k} + S_\epsilon \tag{2.11}$$

where $C_{1\epsilon}$, $C_{2\epsilon}$, σ_k, and σ_ϵ are empirical dimensionless constants with recommended values of 1.44, 1.92, 1.0, and 1.3, respectively [Launder and Spalding, 1974]; G_k and G_b represent the production of k due to the mean velocity gradients and buoyancy, respectively [ANSYS, 2016]; Y_M represent the contribution of compressibility; and S_k and S_ϵ are user-defined source terms [ANSYS, 2016].

The k–ε closure offers robustness and reasonable accuracy for a manageable computational power. However, it suffers from an insensitivity to adverse pressure gradients and boundary layer separation [ANSYS, 2016]. Furthermore, it can overestimate turbulent viscosity due to the assumption that the turbulence fluctuations are isotropic, which can result in delayed onset separation over smooth surfaces and under-prediction of the size of the separation zone [Ingham and Ma, 2005]. Nevertheless, Quaranta et al. [2016] found that the k–ε model performed well when applied to a vertical slot fishway and compared favourably against measurements taken by Rajaratnam et al. [1986]. Similarly, Andersson et al. [2012] found that the k–ε model performed well in predicting the velocity field within the tailrace channel and confluence area downstream of a hydroelectric power plant, and compared well to ADCP data.

Re-Normalisation Group k–ε Model

The Re-Normalisation Group (RNG) k–ε model has seen significant usage in fish passage literature [e.g. Kim et al. 2012, Feurich et al. 2012, Plymesser 2014, Stamou et al.

2018]. The RNG k–ε model was developed by Yakhot et al. [1992] through the re-normalisation of the Navier-Stokes equations. This yields a refined form of the k–ε model which includes a new transport equation for the turbulent energy dissipation, ε:

$$\frac{\partial}{\partial t}(\rho k) + \frac{\partial}{\partial x_i}(\rho k u_i) = \frac{\partial}{\partial x_j}\left[\left(\mu + \frac{\mu_t}{\sigma_k}\right)\frac{\partial k}{\partial x_j}\right] + G_k + G_b - \rho\epsilon - Y_M + S_k \tag{2.12}$$

$$\frac{\partial}{\partial t}(\rho\epsilon) + \frac{\partial}{\partial x_i}(\rho\epsilon u_i) = \frac{\partial}{\partial x_j}\left[\left(\mu + \frac{\mu_t}{\sigma_\epsilon}\right)\frac{\partial \epsilon}{\partial x_j}\right] + C_{1\epsilon}\frac{\epsilon}{k}(G_k + G_b) - C_{2\epsilon}\rho\frac{\epsilon^2}{k} - R_\epsilon + S_\epsilon \tag{2.13}$$

where σ_k, σ_ϵ, $C_{1\epsilon}$, and $C_{2\epsilon}$ are explicitly derived constants equal to 0.7194, 0.7194, 1.42, and 1.68, respectively; and R_ϵ is:

$$R_\epsilon = \frac{C_\mu \rho \eta^3 (1 - \frac{\eta}{\eta_0})}{1 + \beta\eta^3}\frac{\epsilon^2}{k} \tag{2.14}$$

where: η_0 is an explicitly derived constant equal to 4.38, β is an empricially derived constant equal to 0.012, $\eta = \frac{Sk}{\epsilon}$, and $S = (2S_{ij}S_{ij})^{\frac{1}{2}}$ [Yakhot et al., 1992].

The eddy viscosity is then calculated in the same manner as for the standard k–ε model (2.9) but C_μ is explicitly derived using RNG theory and equal to 0.0845 [Yakhot et al., 1992].

The RNG k–ε model has been shown to better predict the reattachement point of flow over a backward facing step compared to the standard k–ε model [Speziale and Thangam, 1992, Yakhot et al., 1992]. Furthermore, Stamou et al. [2018] found that the RNG k–ε model was able to better predict the turbulence characteristics within a vertical slot fishway compared to the standard k–ε model. Similarly, Quaresma and Pinheiro [2014] found the RNG k–ε gave good agreement with both the Smagorinsky LES Model and ADV measurements within a pool-type pass with submerged orifices.

k–ω Model

The k–ω model solves for the Reynolds shear stresses by solving for the turbulent kinetic energy, k, and the specific dissipation rate, ω [see Wilcox 1993]. The eddy viscosity is then determined through:

$$\mu_t = \alpha^* \rho \frac{k}{\omega} \tag{2.15}$$

The coefficient α^* is dependant on the version of k-ω in use [Ingham and Ma, 2005] and dampens the turbulent viscosity to create a low-Reynolds-number correction [ANSYS, 2016]. The value of $\alpha*$ generally takes the form [ANSYS, 2016]:

$$\alpha^* = \alpha^*_\infty \left(\frac{\alpha^*_0 + \frac{Re_t}{R_k}}{1 + \frac{Re_t}{R_k}} \right) \tag{2.16}$$

where $Re_t = \frac{\rho k}{\mu \omega}$, and R_k, α^*_0, and α^*_∞ are constants equal to 6.0, 0.024, and 1, respectively [ANSYS, 2016].

The k-ω model solves for the turbulent kinetic energy, k, and the specific dissipation rate, ω, through the introduction of two transport equations:

$$\frac{\partial}{\partial t}(\rho k) + \frac{\partial}{\partial x_i}(\rho k u_i) = \frac{\partial}{\partial x_j}(\Gamma_k \frac{\partial k}{\partial x_j}) + G_k - Y_k + S_k \tag{2.17}$$

$$\frac{\partial}{\partial t}(\rho \omega) + \frac{\partial}{\partial x_i}(\rho \omega u_i) = \frac{\partial}{\partial x_j}(\Gamma_\omega \frac{\partial \omega}{\partial x_j}) + G_\omega - Y_\omega + S_{omega} \tag{2.18}$$

where Y_k and Y_ω are the turbulent dissipation of k and ω; S_k and S_ω are user-defined source terms, Γ_k and Γ_ω are the effective diffusivity of k and ω defined by $\Gamma_k = \mu + \frac{\mu_t}{\sigma_k}$ and $\Gamma_\omega = \mu + \frac{\mu_t}{\sigma_\omega}$, respectively, where σ_k and σ_ω are the turbulent Prandtl numbers for k and ω and are constants equal to 2.0 [ANSYS, 2016], and G_k and G_ω are the production of k and ω defined by:

$$G_k = -\rho \overline{u'_i u'_j} \frac{\partial u_j}{\partial x_i} = \mu_t S^2 \tag{2.19}$$

$$G_\omega = \alpha \frac{\omega}{k} G_k \tag{2.20}$$

where S is defined as in the k–ε model, and the coefficient α is given by:

$$\alpha = \frac{\alpha_\infty}{\alpha^*} \left(\frac{\alpha_0 + \frac{Re_t}{R_\omega}}{1 + \frac{Re_t}{R_\omega}} \right) \tag{2.21}$$

where R_ω, α_∞ and α_0 are constants equal to 2.95, 0.52, and 0.i̇, respectively [ANSYS, 2016].

The standard (Wilcox) k–ω model suffers from an over-sensitivity to the free stream boundary condition, which can lead to significant variation in the predicted fluid flow [Wilcox, 1988]. This is somewhat corrected in subsequent models [i.e. Wilcox 1993] but still performs poorly in stagnation regions [Ingham and Ma, 2005].

k–ω Shear Stress Transport Model

The k–ω Shear Stress Transport (SST) model combines the standard k–ω model with the standard k–ε model [Menter, 1993, 1994] and has seen some success in fish passage literature [e.g. Chorda et al. 2019, Klopries and Schüttrumpf 2020]. The model applies the standard k–ω model to near-wall regions and applies the standard k–ε model to the free shear layers [Ingham and Ma, 2005]. This is achieved through the implementation of two blending functions, F_1 and F_2 [ANSYS, 2016]. These blending functions are applied to the effective diffusitivites, Γ_k and Γ_ω, the turbulence production of ω, G_ω, and the turbulence dissipation of ω, Y_k [Menter, 1993]. Furthermore, an additional term, D_ω is introduced to the transport equation for ω which represents a cross-diffusion term resulting from the blending of the two models [ANSYS, 2016].

This blending results in a robust turbulence closure model which overcomes the insensitivity of the standard k–ε model to boundary layer separation and removes the sensitivity of the standard k–ω model to the free stream [Ingham and Ma, 2005]. The k–ω SST model is known to yield better results when applied to aerofoils and adverse pressure gradient flows compared to the standard k–ε model and standard k–ω model [Menter, 2009]. This model is popular in engineering and ecological problems due to its increased accuracy and reliability over both the standard k–ε and standard k–ω models and its manageable computational requirements [ANSYS, 2016]. Chorda et al. [2019] found the k–ω SST model to give a good prediction of the free surface location and velocity field within a vertical slot fish pass compared to optical and ADV measurements taken by Tran et al. [2016]. Furthermore, when applied to the same mesh, Chorda et al. [2019] found the k–ω SST model to give comparable results to the Smagorinsky LES Model [see Smagorinsky 1963] while requiring 73% of the CPU time (128 versus 175 CPU hours per 1 second of flow time).

2.5.4 Approaches to Free Surface Modelling

Hydraulic fluid problems often consider the flow of water through a domain that also contains air. Therefore, as both water and air are immiscible, there must exist a sharp interface between the two fluids. This section introduces the most common methods of free surface interface modelling in ecohydraulic literature, namely the rigid lid approximation and the volume of fluid method.

The Rigid Lid Approximation

The rigid lid approach assumes that the water-air interface can be modelled as a rigid ceiling. This approach has found success in ecohydraulic literature [e.g. Kwan et al. 2011, Andersson et al. 2012, Marjoribanks et al. 2014, 2017]. Furthermore, Andersson et al. [2013] found the rigid-lid approximation to give good predictions of the free surface location for an emptying reserviour with a submerged outlet compared to measured data. However, this approach is only valid if the deformation of the water surface is less than 10% of the depth of the channel [Rodriguez et al., 2004] and is therefore not suitable for assessing fish passes.

The Volume of Fluid Method

The Volume of Fluid (VOF) method [Hirt and Nichols, 1981] is one of the most established techniques used to model hydraulic free surface flows and is the most commonly used method in fish passage literature [e.g. Feurich et al. 2012, Kim et al. 2012, Marriner et al. 2014, Quaresma and Pinheiro 2014, Stamou et al. 2018, Chorda et al. 2019]. The VOF method is based on an Eulerian mesh and introduces a volume fraction variable, α, which is applied to each cell [Hirt and Nichols, 1981]. The VOF method then solves fluid flow for two or more immiscible fluids by solving a single set of momentum equations and tracking the volume fraction within each cell [Hirt and Nichols, 1981]. An α value of 0 denotes a cell containing only `fluid1`, commonly air; whereas an α value of 1 denotes a cell containing only `fluid2`, commonly water [Hirt and Nichols, 1981]. The free surface must exist within cells with values between 0 and 1 and is generally taken along the surface where the volume fraction is equal to 0.5 [Hirt and Nichols, 1981]. Mathematically, this is expressed as:

$$\alpha = \begin{cases} 0, & \text{cell contains only } \texttt{fluid1} \\ 1, & \text{cell contains only } \texttt{fluid2} \\ 0 < \alpha < 1, & \text{cell contains interface} \end{cases} \tag{2.22}$$

The Volume of Fluid method introduces a new transport equation for the volume fraction (2.23). The two immiscible fluids are considered as a single fluid throughout the domain. The fluid properties for this single fluid are calculated for a given cell based on weighted averages of the fluids present in the cell (2.24). Therefore the calculated

properties are equal to each fluid in their respective regions and vary only across the interface.

$$\frac{\partial \alpha}{\partial t} + \frac{\partial \alpha u_j}{\partial x_j} = 0 \tag{2.23}$$

$$\rho = \alpha \rho_1 + (1 - \alpha)\rho_2 \tag{2.24}$$

where: ρ is the cell fluid density; ρ_1 is the density of `fluid1`; ρ_2 is the density of `fluid2`.

Gravity and surface tension effects at the interface are included with the $\rho \bar{F}_i$ term of the RANS equations (2.6) when using the VOF method. The volume fraction can be solved via either implicit or explicit formulation [ANSYS, 2016]. Explicit formulation allows the fluid interface to be approximated using Geo-Reconstruct, a piece-wise linear approach to representing the interface within a cell, which yields greater accuracy compared to other interface interpolation schemes [see Hirt and Nichols 1981, Youngs 1982].

2.5.5 Turbulence Descriptors

Turbulence is an important phenomena that influences the behaviour of fish [e.g. Coutant 1998, Silva et al. 2011, Tullos and Walter 2015, Piper et al. 2015, 2017, Quaranta et al. 2017; section 2.7]. Therefore it is important to understand how turbulence can be quantified in order to model its influence on simulated fish decisions. There are many parameters that can be used to quantify turbulence in space, known as turbulence descriptors. This section defines the turbulence descriptors most commonly used in fish passage literature.

Reynolds Number

The Reynolds Number, denoted Re, is a dimensionless number defined by the ratio between inertial forces and viscous forces within a flow, equation (2.25) [Tansley and Marshall, 2001]. The Reynolds number is indicative of the expected flow pattern within a fluid flow and can be used to approximate the global turbulence level within a domain, as opposed to the other turbulence descriptors in this section, which can define the local turbulence level..

$$Re = \frac{UL}{\nu} \tag{2.25}$$

where U is the flow velocity; L is a turbulence length scale dependent upon the flow geometry and often taken as flow depth for river applications [Bates et al., 2005], and ν is the kinematic viscosity of the fluid.

Reynolds Shear Stress

A simple turbulence descriptor is the Reynolds shear stress (2.26), as it appears in the RANS equations (2.6). This is appropriate due to the common usage of the RANS approach in ecohydraulics [e.g. Quaranta et al. 2016, Stamou et al. 2018, Chorda et al. 2019, among others]. Physically, this term in a symmetric tensor which describes the turbulent momentum fluxes in three dimensions [Wilcox, 1993].

$$\tau_{ij} = R_{ij} = -\rho\overline{u_i' u_j'} \tag{2.26}$$

Turbulence Kinetic Energy

Another turbulence descriptor is the turbulence kinetic energy, k, of a flow (2.27), sometimes denoted as TKE, which describes the kinetic energy of turbulent fluctuations per unit mass. This measure is useful due to the prevalence of k–ε and k–ω turbulence closure models in fish passage literature, in which the TKE is already calculated.

$$k = \frac{1}{2}\left(\bar{u_x'^2} + \bar{u_y'^2} + \bar{u_z'^2}\right) = \frac{1}{2}u_i'^2 \tag{2.27}$$

Turbulent Intensity

The turbulent intensity, I, denotes the root-mean-square of the turbulent velocity fluctuations divided by a reference velocity i.e. the Reynolds averaged mean velocity of the flow:

$$I = \frac{u'}{U} \tag{2.28}$$

where $u' = \sqrt{\frac{1}{3}u_i'^2} = \sqrt{\frac{2}{3}k}$ and $U = \sqrt{U_i^2}$.

Turbulence Dissipation

Turbulence dissipation, ϵ, is the rate that the turbulence kinetic energy is dissipated through conversion to internal thermal energy [Wilcox, 1993]. This is useful due to the common usage of the k–ε and RNG k–ε turbulence closure models, in which ϵ is already calculated.

$$\epsilon = \nu \overline{\frac{\partial u_i'}{\partial x_k} \frac{\partial u_i'}{\partial x_k}} \tag{2.29}$$

Spatial Velocity Gradient Tensor

The spatial velocity gradient tensor describes the gradient of each component of the fluid velocity with respect to changes in each spatial dimension, (2.30). The spatial gradient of velocity is a description of the fluid shear stresses [Goodwin, 2004]. The spatial velocity gradient tensor comprises the linear deformation, rotation, and angular deformation experienced by the fluid [Nestler et al., 2008].

$$\mathbf{J} = \nabla \mathbf{u} = \frac{\partial u_i}{\partial x_j} = \begin{bmatrix} \frac{\partial u_x}{\partial x} & \frac{\partial u_x}{\partial y} & \frac{\partial u_x}{\partial z} \\ \frac{\partial u_y}{\partial x} & \frac{\partial u_y}{\partial y} & \frac{\partial u_y}{\partial z} \\ \frac{\partial u_z}{\partial x} & \frac{\partial u_z}{\partial y} & \frac{\partial u_z}{\partial z} \end{bmatrix} \tag{2.30}$$

Nestler et al. [2008] introduced a "total distortion metric" through the summation of the absolute values of each spatial velocity gradient (2.31), termed the total hydraulic strain. This summarised value provides an easily comparable value describing the overall fluid shear at a point in space.

$$\begin{aligned} S = \sum \left| \frac{\partial u_i}{\partial x_j} \right| = \left| \frac{\partial u_x}{\partial x} \right| + \left| \frac{\partial u_x}{\partial y} \right| + \left| \frac{\partial u_x}{\partial z} \right| + \left| \frac{\partial u_y}{\partial x} \right| + \\ \left| \frac{\partial u_y}{\partial y} \right| + \left| \frac{\partial u_y}{\partial z} \right| + \left| \frac{\partial u_z}{\partial z} \right| + \left| \frac{\partial u_z}{\partial y} \right| + \left| \frac{\partial u_z}{\partial z} \right| \end{aligned} \tag{2.31}$$

2.6 Agent-based Modelling

Agent-based modelling (ABM) is an adaptive, bottom-up approach to solving complex phenomena, which has seen increasing popularity in recent decades [Tang and Bennett, 2010, Crooks and Heppenstall, 2012]. ABM considers the disaggregation of a system

into multiple components (agents) each of which are given their own characteristics and allowed to act autonomously and interact with each other [Crooks and Heppenstall, 2012]. It is thought that deconstructing a complex system in this way will allow the behaviour of the entire system to emerge through the simpler agents [Macal and North, 2010]. This methodology lends itself to real world systems that can be characterised by continuous changes in space and time, as agents are often allowed to act autonomously in both space and time. Agent-based models have been used in ecology [Tang and Bennett, 2010], transportation [Nourinejad and Roorda, 2016], engineering [Abebea et al., 2016], economics [Fagiolo et al., 2007], government policy [Kremmydas, 2012], and the social sciences [Conte and Paolucci, 2014].

2.6.1 General Formulation of Agent-Based Models

An agent-based model has two fundamental components: it must contain multiple agents, and these agents must exist within an environment [Crooks and Heppenstall, 2012]. Agents are simple individuals that represent real-world entities. Agent behaviour is controlled through a framework that determines a response to a given stimulus [Tang and Bennett, 2010, Crooks and Heppenstall, 2012]. This framework means agents are intrinsically autonomous entities; they can act and make decisions without external direction [Macal and North, 2010].

Furthermore, agents generally have multiple internal properties which describe the agent and its behaviours, figure 2.5. These properties can vary between agents and therefore agents can display heterogeneity. An agent's internal properties are referred to as "agent attributes". Macal and North [2010] identify a number of what they consider essential characteristics of agents:

- **An agent is wholly self-contained.** Agents must be distinguishable from one another and their attributes must be explicit.
- **An agent must be autonomous.** Agents must function independently within the environment and in their interactions with other agents.
- **An agent must have variable states.** An agent is an adaptive entity and therefore their internal states must be able to change to reflect the agent's current situation.

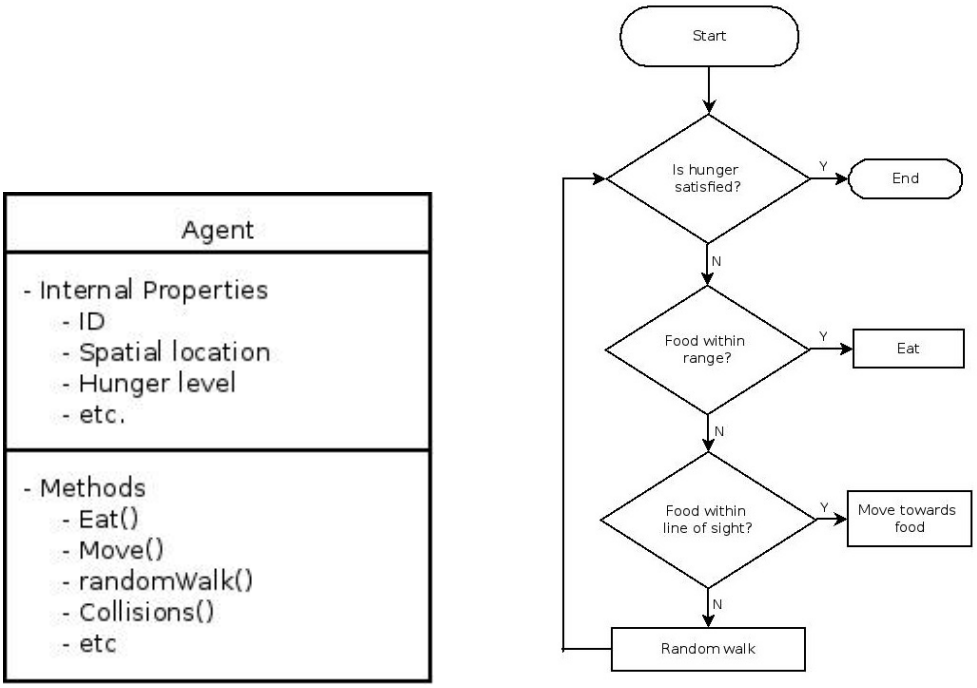

(a) (b)

Figure 2.5: Representative structure of the function of an agent including a) UML diagram of an agent with internal properties and methods, and b) A flow chart depicting a simple decision framework. [After Tang and Bennett 2010].

- **An agent is social.** Agents must be capable of interactions with other agents that will influence their behaviour.

An agent's behaviours are the result of the agent's various internal decision-making processes, termed "agent methods" [Macal and North, 2010], which are based on fixed or learned rules and driven by encountered stimuli.

Agents exist within an environment that defines the space in which agents can operate and also dictates the flow of information, figure 2.6. Environments provide stimuli to agents which cause behavioural responses [Grimm and Railsback, 2005]. Environments can be multi-dimensional depending on the system that is being modelled [Tang and Bennett, 2010]. Similarly, environments can exist purely to provide the spatial location of agents, or can provide a wealth of spatial information [Crooks and Heppenstall, 2012]. Agents within an environment may be spatially explicit (i.e. have a specific location) or can be spatially implicit (i.e. their exact location is irrelevant)

[Bian, 2003, Alam and Geller, 2012]. Environments can be either spatially continuous or spatially discrete, depending on whether an object-based or grid-based approach is used [Bian, 2003, Grimm and Railsback, 2005].

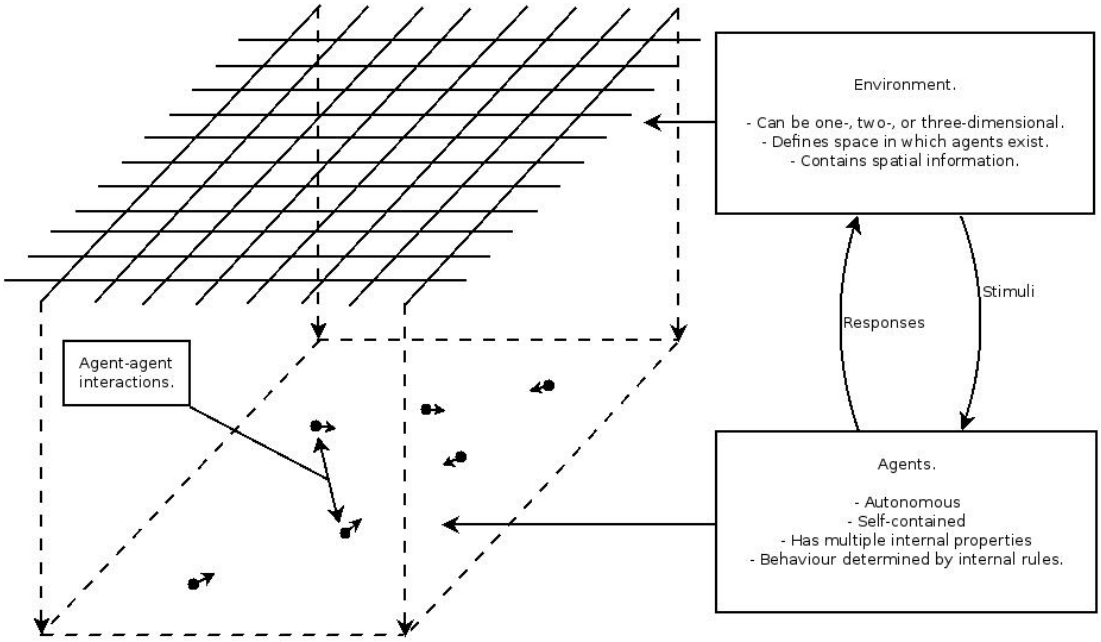

Figure 2.6: Schematic of agents and their environment; depicting the stimuli-response relationship between an agent and their environment, as well as agent-agent interactions.

As agent-based models are generally used to model real world dynamic systems, environments are generally modelled as temporally discrete, with (typically uniform) timesteps used to define the passage of time [Tang and Bennett, 2010]. The temporal and spatial resolutions of the ABM must be appropriately chosen to accurately model the dynamics of the real world system. Bennett and Tang [2006] suggested that the Courant-Friedrichs-Lewy (CFL) criterion [Courant et al., 1967] is suitable to determine the appropriate temporal resolution based on the movement rate of individuals per timestep. The CFL criterion states that no parcel of information should move more than the spatial resolution of the grid within a single timestep, (2.32).

$$|v|\Delta t \leq \Delta x \tag{2.32}$$

where $|v|$ is the velocity of the information parcel (or agent), Δt is the temporal resol-

ution, and Δx is the spatial resolution.

Satisfying this relationship ensures the balance between the spatial and temporal resolutions of the simulation; i.e. information does not travel faster through space than time [Bennett and Tang, 2006]. This can be simplistically stated as "an agent should not move more than the spatial resolution in a single timestep". To satisfy this relationship, either the spatial resolution must be fixed and the appropriate timestep selected, the timestep fixed and the appropriate spatial resolution selected, or the agent velocity artificially limited within a given timestep. If the maximum velocity of all agents is known, selection of the spatial and temporal resolutions becomes trivial. However, if the maximum velocity is unknown, selection of the temporal resolution becomes more laborious.

At each timestep an agent may perceive a stimulus. This is formally defined as an event and can be internal (change of an agent's internal state) or external (change in local environmental conditions) [Tang and Bennett, 2010]. Similarly, an event may be caused by an internal stimulus (self-stimulating) or caused by an external stimulus, such as the presence of a predator [Grimm and Railsback, 2005]. Events trigger the activation of an agent's internal rules, which determine the agent's behaviour [Tang and Bennett, 2010]. Depending on the complexity of an agent, multiple events may occur in the same timestep, which can trigger multiple agent methods [e.g Goodwin et al. 2006]. If multiple rules are simultaneously activated the agent may display all the resulting behaviours, or some combination of the resulting behaviours [e.g. Bennett and Tang 2006, Heppenstall et al. 2006, Gao et al. 2016]. However, if rules are implemented within a hierarchical structure, some of the behaviours may overrule other behaviours [e.g. Goodwin et al. 2006]. For example, if an animal is searching for food due to hunger and encounters both prey and predator, the presence of the predator could overrule the drive for food.

The environment also describes how the agents are connected to one another, termed the model's connectedness or the model's topology [Tang and Bennett, 2010, Crooks and Heppenstall, 2012]. The topology is important as it determines who can transfer information to whom [Macal and North, 2010]. Models are generally implemented with neighbourhood or adjacency rules, which control how agents interact with each other, figure 2.7. Cellular Automata (CA) are a good example of the importance of neighbourhood rules. CA are a type of model closely related to ABM wherein the environment is

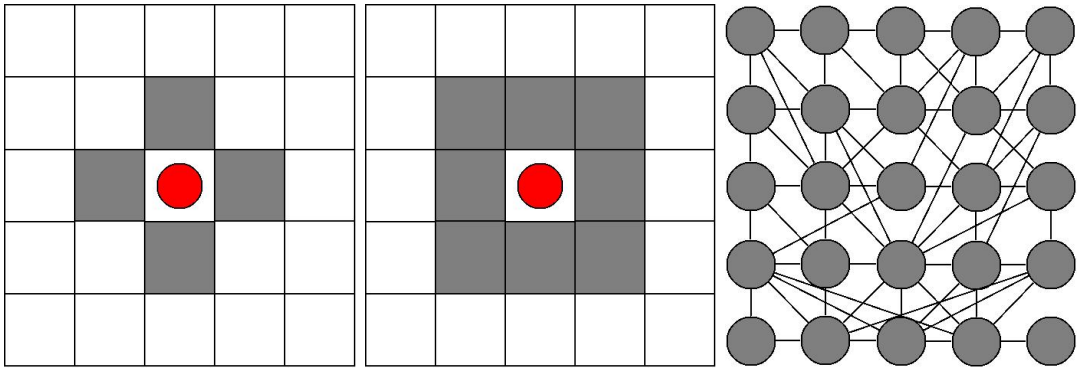

(a) (b) (c)

Figure 2.7: Example neighbourhood topologies. (a) First order von Neumann neighbourhood. Red denotes agent location, grey denotes neighbours. (b) First order Moore neighbourhood. Red denotes agent location, grey denotes neighbours. (c) Network topology. [After Iltanen 2012].

divided into regularly spaced cells on a grid or lattice [Crooks and Heppenstall, 2012]. Critically, CA do not use agents. Instead the cells within the environment, termed the automata, are given a single internal state (or attribute) [Iltanen, 2012]. The locations of the cells are constant but their internal states are determined by the state of one or more of that state's neighbours [Benenson and Torrens, 2004].

A good example of CA is Conway's Game of Life [Gardner, 1970] wherein a cell lives or dies (internal state 1 or 0, respectively) based on its number of living neighbours. Too few living neighbours and the cell dies due to underpopulation; too many living neighbours and the cell dies due to overpopulation [Gardner, 1970]. The model is formulated as a two-dimensional uniform grid, where each cell has eight neighbours. This is known as a Moore neighbourhood; specifically, it is a first order Moore Neighbourhood [Tang and Bennett, 2010], figure 2.7b. Other topologies include von Neumann neighbourhoods wherein an agent has only 4 neighbours (figure 2.7a), and network-based neighbourhoods wherein nodes are connected to one another either statically or dynamically, figure 2.7c. Networks are used to define neighbourhoods in a more general manner, and have been used to model social space rather than physical space [e.g. Alam and Geller 2012].

2.6.2 Advantages and Limitations of ABMs

Historically, dynamic systems (particularly ecological and geographical systems) have been modelled using top-down approaches wherein variables are described with differential equations [Crooks and Heppenstall, 2012]. Agent-based modelling provides an alternative bottom-up modelling approach, which offers some advantages over traditional approaches. Firstly, equation-based models are deterministic; meaning that for given initial data the result will always be the same [Bernard et al., 1999]. In contrast, agent-based models are inherently stochastic due to the adaptive, decision-making capacity of agents; therefore multiple futures are possible for the same initial condition [Crooks and Heppenstall, 2012]. Furthermore, the interactions between agents can be complex, non-linear, and discontinuous; therefore ABMs can be used to describe systems where traditional approaches would fail [Bonabeau, 2002]. Secondly, agent-based modelling is a disaggregated approach to modelling a system, therefore it is possible to design a heterogeneous population [Crooks and Heppenstall, 2012]. This allows for atypical behaviours to be simulated alongside regular behaviours as well as interactions between the two [Bonabeau, 2002]. This is in contrast to equation-based models which tend to smooth out fluctuations, and therefore only capture averaged behaviour [Crooks and Heppenstall, 2012].

Crooks and Heppenstall [2012] suggest that ABMs also have the advantage in that they can often provide the user with an explanation of the result due to the bottom-up approach. Similarly, Bonabeau [2002] suggests that agent-based models provide a natural description of a system, which aids in the explanation of the resulting behaviour. Bonabeau [2002] summarised the systems in which agent-based modelling offer the most advantages over equation-based approaches:

1. Where aggregate behaviour cannot be clearly defined;
2. When the complexity of individual behaviour within the system is such that formulation of equation-based models become intractable.;
3. When the system is more intuitively described by activities rather than processes; and
4. When it is more appropriate to strategically apply stochasticity to the system rather than arbitrarily applied as with equation-based approaches.

Agent-based modelling is thus particularly well suited to the modelling of dynamic systems that require flexibility in their solution. Furthermore, Crooks and Heppenstall [2012] suggests that ABMs are best used when a certain level of the complexity of the system under consideration is unknown and therefore understanding the system requires exploration.

However, agent-based modelling has limitations which must be considered. Firstly, the formulation of an ABM is a balance of abstraction: if too abstract, the model may miss important factors or behaviour; if too detailed, the model will be over-constrained and limited in its function [Crooks and Heppenstall, 2012]. Therefore subjective judgement of the level of abstraction and the importance of variables is crucial to the formulation of an agent-based models. Secondly, systems that describe the behaviour of conscious entities have an inherent potential to be irrational [Bonabeau, 2002], which can be difficult to quantify and justify [Crooks and Heppenstall, 2012]. Thirdly, validation and calibration are challenging processes for agent-based models [see Crooks et al. 2008, Ngo and See 2012]. There is some confusion in the literature over best practices with respect to validation [see Kopec et al. 2010]. Ngo and See [2012] suggest a four-step, standardised approach to ABM validation consisting of:

1. **Face validation.** This step considers qualitative assessment of the results and poses the question: "do outputs match reality?" and is referred to as "conceptual validation".

2. **Sensitivity analysis.** This assesses the impact of each parameter on individual behaviours as well as overall model outputs.

3. **Calibration.** This is the process of determining an appropriate range of values for each parameter through tuning the model to fit real data (qualitatively or quantitatively).

4. **Output validation.** This is the final step wherein model outputs are graphically or statistically compared to a real dataset.

This approach provides a thorough process including both verification (steps one and two) and validation (steps three and four), and leads to a fully realised model [Ngo and See, 2012]. That being said, it has been suggested that "the validity of a model should not be thought of as a binary event (i.e. a model cannot simply be classified as

valid or invalid); a model can have a certain degree of validity" [Crooks and Heppenstall, 2012, p. 93]. Validation remains a difficult and open challenge [Lamperti et al., 2018], exacerbated by a lack of access to high quality data [Crooks and Heppenstall, 2012]. Nevertheless, Crooks and Heppenstall [2012] state that "the fundamental motivation for modelling arises from a lack of full access to data relating to a phenomenon of interest. The development of agent-based models offers a means to increase the utility of simulation models" [Crooks and Heppenstall, 2012, p. 98].

2.7 Fish Behaviour Studies

This section considers the wealth of literature that aims to determine the hydrodynamic parameters that affect the movement decisions of various species of fish during upstream migration, split into themes identified within the literature. However, there are many conflicting conclusions within the literature, which may be attributed to differing fish species, bodylengths, or the inherent randomness of animal decisions. In addition, Lacey et al. [2012] suggest that these conflicting results are partly due to many authors attributing behaviours to turbulence, but lacking quantification of turbulence. In response, Lacey et al. [2012] introduced the "IPOS" framework to categorise turbulence into: "Intensity", "Periodicity", "Orientation", and "Scale". However, this framework has not been adopted by many and so the issue persists. Therefore, it is difficult to gain insight into precisely which parameters correlate with specific fish behaviours. Furthermore, even if fish movement decisions are found to correlate with hydraulic parameters, proving causation is challenging.

2.7.1 The Effect of Average Flow Velocity on Fish Behaviour

The local average velocity has been identified as a key parameter in determining the behaviour of up-migrating fishes as it provides stimulation to the fish to allow for rheotaxis, as well as providing directional information for migration [see section 2.4.1 and Montgomery et al. 1997]. Furthermore, a larger local average velocity downstream of a fish pass, relative to the river flow, is important to ensure an "attraction flow", although quantification of "attraction flow" remains vague [Katopodis, 2005, Castro-Santos et al., 2009].

The local flow field also generates hydrodynamic resistance on any up-migrating

fish, dictating the energetic cost of movement [Quaranta et al., 2017]. Furthermore, if the magnitude of the flow field is such that the energetic cost of up-migration is consistently too high, individuals will fail due to fatigue [Quaranta et al., 2017]. Up-migrating fishes are known to utilise lower velocity regions to shelter from high velocity regions, known as "flow refuging", thus temporarily lowering their energetic cost [Liao, 2007, Silva et al., 2011]. For example, Smith et al. [2005] found that juvenile rainbow trout (*Oncorhynchus mykiss*) chose laboratory flume locations with average streamwise, cross-stream, and vertical velocities lower than the average within the flume. Although a subsequent study found the volitional density of juvenile rainbow trout within the flume increased with increasing discharge, and hence mean velocity [Smith et al., 2006].

Up-migrating fishes have also been observed to lower their energetic cost through pathway selection. Kane et al. [2000] found Chinook salmon (*Oncorhynchus tshawytscha*) and Coho salmon (*Oncorhynchus kisutch*) up-migrating through Alaskan culverts consistently chose pathways that resulted in lower energy expenditure than the average. This was expanded upon by Blank [2008] who demonstrated that measured up-migrating fish paths through culverts closely matched calculated minimum energy pathways determined using drag equations introduced by Webb [1971a,b, 1975] [see section 2.8.1]. Furthermore, Silva et al. [2009] observed up-migrating Iberian barbel (*Luciobarbus bocagei*; Cyprinidae family) through an indoor pool and orifice-type fishway and noted that individuals passing via the submerged orifices were observed to pass close to the edges of the orifice, presumably to avoid the fastest velocities in the core of the jet formed through the orifice. A subsequent study by Silva et al. [2010] identified significant negative correlation between both time-to-pass and passage success, and mean water velocity, and suggested that the larger velocities resulted in higher energy expenditure and therefore increased failures due to fatigue.

Therefore, locally-larger fluid velocities are important to provide directional information and attraction [Montgomery et al., 1997, Katopodis, 2005]. However, fish are also attracted to locally-lower fluid velocities to minimise energetic costs [Kane et al., 2000, Smith et al., 2005]. Therefore, it can be surmised that Salmonidae are attracted to both locally-higher and locally-lower average velocities, dependent upon the fluid environment.

2.7.2 The Effect of Turbulence on Fish Behaviour

Turbulence has been shown to play an important role in the path selection of fish [e.g. Coutant 1998, Silva et al. 2011, Tullos and Walter 2015, Piper et al. 2015, 2017, Quaranta et al. 2017]. However, there are conflicting results on the effects of turbulence on fish behaviour within the literature, which has been attributed to differences in turbulence between studies [Lacey et al., 2012]. Furthermore, the response to turbulent parameters is thought to be species-specific, size-specific, and dependent on the migration status of an individual; i.e. down-migrating Salmonidae have a different goal to up-migrating fish of the same species and therefore are attracted/repelled to different turbulence parameters [see Goodwin et al. 2014 vs. Gisen 2018].

The presence of turbulence has been shown to increase the energetic cost of locomotion [Liao, 2007], and, in extreme cases, can cause damage to the fish [Odeh et al., 2002]. This extends to fish passes, where it has been shown that individuals are more likely to fail passage if the turbulence energy in the pass is too high [Bermúdez et al., 2010, Marriner et al., 2014]. Counter-intuitively, fish have also been shown to exploit turbulence generated by structures or other fish to reduce locomotive costs [Hinch and Rand, 2000, Liao et al., 2003].

Therefore, the precise quantification, or definition, of turbulence is significant in the resultant attraction or repulsion [Liao, 2007]. Therefore, the following sections categorise studies based on the turbulence descriptors used.

The Effect of Reynolds Shear Stress on Fish Behaviour

The Reynolds shear stress, τ, is a symmetric tensor that describes the turbulent momentum fluxes in three dimensions [Wilcox, 1993]. Smith et al. [2005] found that juvenile rainbow trout (*Oncorhynchus mykiss*) chose flume locations with lower-than-average average τ_{uv} and τ_{uw}, computed using 3D, ADV-collected instantaneous velocities. Similarly, Silva et al. [2010, 2011, 2012] found significant negative correlations between the Reynolds shear stress and transit time and passage success for Iberian barbel (*Luciobarbus bocagei*; Cyprinidae family) through two configurations of an experimental, full-scale pool-and-orifice-type fish-way, computed using 3D, ADV-collected instantaneous velocities. Duarte et al. [2012] studied the upstream passage of two neotropical species of fish (*Leporinus reinhardti* and *Pimelodus maculatus*, families Anostomidae and Pimelodidae, respectively) through a vertical slot fish-way, and found that both

species chose pathways with near-zero Reynolds shear stress. These findings suggest that up-migrating fishes select holding stations and migration pathways that minimise exposure to Reynolds shear stress.

The Effect of Turbulence Kinetic Energy and Turbulence Intensity on Fish Behaviour

The turbulence kinetic energy, k, is a measure of the mean kinetic energy of turbulent fluctuations per unit mass, characterised by the root-mean-square of the velocity fluctuations. The turbulence intensity, I, is a non-dimensionalised form the turbulence kinetic energy and hence these turbulence descriptors are present together.

Smith et al. [2005, 2006] found that juvenile rainbow trout (*Oncorhynchus mykiss*) chose flume locations with lower-than-average average k, computed using 3D, ADV-collected instantaneous velocities. Similarly, Cotel et al. [2006] found that brown trout (*Salmo salar*) chose locations with lower-than-average levels of I within the Maple river in Michigan, calculated using ADV-collected instantaneous velocities. However, Cotel et al. [2006] noted that individuals preferred to occupy lower sections of the water column where one can assume shear is increased due to wall effects. This result suggests that fish select regions where turbulence is reduced, but will expose themselves to higher turbulence in order to move closer to the river bed, presumably to minimise exposure to predation. Furthermore, Duarte et al. [2012] studied the upstream passage of two neotropical species of fish (*Leporinus reinhardti* and *Pimelodus maculatus*, families Anostomidae and Pimelodidae, respectively) through a vertical slot fish-way, and found that both species preferred pathways with "low to zero" k.

These results suggest that up-migrating fishes select holding stations and migration pathways that minimise exposure to k. However, Goettel et al. [2015] sought to demonstrate that western blacknose dace (*Rhinichthys obtusus*, Cyprindae family) selected pathways through a turbulent flume that minimised their exposure to turbulence conditions (quantified by turbulence kinetic energy). However, qualitative comparisons of contours of k and videography-measured fish paths indicated that fish did not preferentially seek lower k, but rather chose pathways that with consistent levels of k, i.e. between lower and upper thresholds, although the value of these thresholds was not elucidated. This is similar to the findings of Gao et al. [2016] and Tan et al. [2018] who found that trout (species not specified) and silver carp (*Hypophthalmichthys mo-*

litrix) selected pathways through a vertical slot fish-way with k values between 0.1 and $0.35m^2s^{-2}$, and 0.02 and $0.035m^2s^{-2}$, respectively. These findings suggest that while fishes may not explicitly seek to minimise k and I when selecting a pathway, they may be repelled from regions of "high" or "low" k or I, although precise quantification of these thresholds is challenging. Furthermore, Goettel et al. [2015] suggested that fish use turbulence levels as a navigational guide, and are attracted to low spatial turbulence gradients (i.e. $\frac{\partial k}{\partial x_i}$) in order to minimise encounters with detrimental turbulence conditions.

Silva et al. [2010, 2011] found significant negative correlations between k and I, and the transit time of Iberian barbel (*Luciobarbus bocagei*; Cyprinidae family) through an offset pool-and-orifice fish-way, computed using 3D, ADV-collected instantaneous velocities. Furthermore, Silva et al. [2012] reported that all individuals spent a larger percentage of time within "low turbulence" regions, characterised by lower-than-average k and I, which may be due to the associated reduction in energetic costs. Silva et al. [2012] also found that reducing the average water velocity within the pass by introducing a "deflector" downstream of each orifice, caused an increase in the average and maximum k and I values and resulted in a significant reduction in passage efficiency (69.5% to 35%). This demonstrates that average velocity alone does not control passage, and that velocity fluctuations, characterised by turbulence kinetic energy or turbulence intensity are significant factors.

2.7.3 Fish Preference for High Velocity or High Turbulence

One can surmise from the literature discussed thus far that fish are both attracted to and repelled by relatively large velocities, and both attracted to and repelled by high turbulence levels, depending upon the local hydraulic environment. There are limited studies that assess the interaction between velocity and turbulence, and fewer still that quantify fish preference between high velocity and high turbulence. Those that are available are discussed in this section.

Smith et al. [2005] assessed the volitional density of two size classes, large (average length $90mm$) and small (average length $44mm$), of juvenile rainbow trout (*Oncorhynchus mykiss*) when given the choice between a high velocity channel or a high turbulence channel, for a range of discharges (0.026, 0.048, 0.066, 0.083, and $0.111m^3s^{-1}$). Smith et al. [2005] quantified turbulence within each channel using k and τ, computed

Table 2.1: Measured hydraulic parameters within the low-velocity, high-turbulence channel for each discharge treatment, taken from Smith et al. [2005].

Discharge (m^3s^{-1})	k (m^2s^{-2}) $\times 10^{-3}$	τ_{uv} (Pa)	τ_{uw} (Pa)	$\bar{u}$ (ms^{-1})
0.026	1.128	11.67	13.97	0.0501
0.048	2.718	21.54	26.84	0.0725
0.066	5.566	67.96	52.41	0.0976
0.083	7.641	105.66	70.82	0.1217
0.111	14.666	314.19	98.76	0.1685

using 3D, ADV-collected instantaneous velocities, tables 2.1 and 2.2.

Smith et al. [2005] found no significant difference in volitional density of either size class for the lowest discharge ($0.026m^3s^{-1}$), and found that increasing discharge to $0.048m^3s^{-1}$ and $0.066m^3s^{-1}$ led to a significantly higher density of large fish within the high-velocity, low-turbulence channel, but no significant difference in the choice of the small fish was found. At a discharge of $0.083m^3s^{-1}$, significantly more large fish chose the high-velocity channel and significantly more small fish chose the high-turbulence channel; whereas at the highest discharge value ($0.111m^3s^{-1}$) no significant difference between either group was reported [Smith et al., 2005].

The results indicated that both groups had a preference for the high-velocity channel until the mean velocity in the channel overcame a threshold, after which individuals then opted for the high-turbulence channel [Smith et al., 2005]. This velocity threshold reportedly occurred at approximately $0.24ms^{-1}$ ($\approx 5.5BLs^{-1}$) for the small group and at approximately $0.40ms^{-1}$ ($\approx 4.4BLs^{-1}$) for the large group, reflecting the stronger swimming ability of the larger fish.

Goettel et al. [2015] observed the pathways selected by 49 western blacknose dace (*Rhinichthys obtusus*, Cyprindae family), with an average bodylength of $65mm$, through a turbulent flume for three discharges: 0.0029, 0.0034, $0.0043m^3s^{-1}$. Goettel et al. [2015] quantified turbulence within the flume using k and τ, computed using 3D, ADV-collected instantaneous velocities, and reported that the average and maxima of both turbulence descriptors increased with increasing discharge.

Goettel et al. [2015] reported that all fish preferentially chose to move to regions where k and τ were similar to their current location ($\pm 10\%$ of current value) for all

Table 2.2: Measured hydraulic parameters within the high-velocity, low-turbulence channel for each discharge treatment, taken from Smith et al. [2005].

Discharge (m^3s^{-1})	k (m^2s^{-2}) $\times 10^{-3}$	τ_{uv} (Pa)	τ_{uw} (Pa)	$\bar{u}$ (ms^{-1})
0.026	0.158	1.07	0.67	0.1201
0.048	0.291	3.27	1.94	0.1717
0.066	0.407	3.44	2.01	0.2474
0.083	0.599	6.86	3.37	0.2965
0.111	0.966	7.29	5.02	0.4037

discharge treatments, despite these locations representing only $\approx$ 31% of the total available movement locations. Goettel et al. [2015] found that fish tended to selected pathways that skirted the edges of the regions of highest k, τ, and u, but chose to enter regions of high k and τ in order to minimise their exposure to high velocities ($> 0.14ms^{-1}$, $> 2.2BLs^{-1}$). This suggests that high relative levels of k, τ, and u are repulsive to fish, but fish prioritise avoidance of high u. This finding agrees with findings of Smith et al. [2005] at higher discharges but is conflicting for lower discharges even when velocities are expressed as a function of bodylength, which suggests that avoidance prioritisation is dependent upon the magnitudes of the hydraulic parameters and that upper velocity thresholds are species-specific. Goettel et al. [2015] concluded that fish selected pathways based on upper and lower thresholds of k and τ, regardless of discharge, but did not elucidate the values of these turbulence thresholds.

2.7.4 Summary of Hydraulic Effects on Fish Behaviour

The local average velocity has been shown to be a key parameter for the selection of up-migration pathways in fishes, as it provides rheotaxis stimulation, directional information [Montgomery et al., 1997], and determines the hydrodynamic resistance fishes must overcome Quaranta et al. [2017]. Therefore, exposure to larger velocities increases drag, passage time, and fatigue, resulting in a higher chance of failure [Quaranta et al., 2017].

Literature has shown that fish prefer lower local velocities in order to reduce energetic costs [Kane et al., 2000, Smith et al., 2005, 2006, Liao, 2007, Blank, 2008, Silva

et al., 2009, 2011], but also require large local velocities to provide "attraction flow" and navigational information [Katopodis, 2005, Castro-Santos et al., 2009, Armstrong et al., 2010]. Therefore, the velocity magnitude preference of a passing fish is likely dependent on the local fluid environment, although precise quantification is not elucidated. Furthermore, it is likely that the definitions of "low" and "high" velocity are species-, and bodylength-specific.

High relative turbulence has been shown to increase the energetic cost of locomotion [Liao, 2007], increases the liklihood of failed passage through fish passes [Bermúdez et al., 2010, Marriner et al., 2014] and, in extreme cases, can cause damage to the fish [Odeh et al., 2002]. The Reynolds shear stress, τ, has been shown to be useful in predicting passage success through a pool-and-weir fish-way [Silva et al., 2010, 2011, 2012] and a vertical slot fish-way [Duarte et al., 2012], and that fish tend to avoid regions of high relative τ [Goettel et al., 2015]. Literature has shown that turbulence kinetic energy, k, and turbulence intensity, I, can be used as predictors for volitional density [Smith et al., 2005, 2006, Cotel et al., 2006, Silva et al., 2012], and that fishes avoid regions of high relative k and I [Duarte et al., 2012, Goettel et al., 2015, Gao et al., 2016, Tan et al., 2018]. Furthermore, Goettel et al. [2015] found that passing fish did not strictly minimise their exposure to k, and τ, but selected pathways that minimised their spatial gradients (i.e. $\frac{\partial k}{\partial x_i}$ or $\frac{\partial \tau}{\partial x_i}$).

In summary, fish have been shown to minimise energy expenditure by selecting pathways with lower local velocities, however larger relative velocities are required to provide directional information and attraction. Fish are repelled from high relative k, τ, and u, where the thresholds are species-, and bodylength-specific, and dependent upon the local hydraulics. Therefore, fish pathway selection is a trade-off between exposure to high local turbulence, and exposure to high local velocity. The findings of Goettel et al. [2015] suggest that, while high relative levels of k, τ, and u are repulsive, fish prioritise avoidance of high u, over k or τ. However, the findings of Smith et al. [2005] suggest the reverse; i.e. fish prioritise avoidance of high k and τ, over avoidance of high u. The results discussed here only show correlations between movement decisions and fluid flow parameters, as proving causation is challenging. Nevertheless, the literature discussed in this section provides the foundations for pathway prediction models, which have the potential to reveal behavioural patterns.

2.8 Fish Path Prediction

Predicting the movement of individuals and their responses to hydrodynamic cues is essential to determining a computational metric of fish passes, which can then be used to assess fish pass designs without the need for physical experimentation. This section considers the computational models that have been developed to predict fish trajectories through in-stream structures.

2.8.1 The work of Blank [2008], Abdelaziz [2013], and Plymesser [2014]: The Energy Expenditure Approach

This section presents literature which considers fish path selection using a concept of minimum energy pathways. It has been suggested that natural selection will favour animals that move efficiently [Shepard et al., 2013]. This efficiency is evident in many forms including physiological [Tucker et al., 1970], biomechanical [Dickinson et al., 2000], and behavioural [Pyke, 1984, Wall et al., 2006, Nathan et al., 2008]. Moreover, the quantification of energy expenditures in space, via the creation of "energy landscapes" has been demonstrated to aid in understanding volitional movement and spatial distributions of imperial cormorants (*Phalacrocorax atriceps*) when assuming efficient movements [Wilson et al., 2012]. Similarly, Kerr et al. [2016] suggest that space usage for brown trout (*Salmo trutta*) is dictated by a need to minimise the costs of swimming and McElroy et al. [2012] found that pallid sturgeon (*Scaphirhynchus albus*) consistently chose pathways with lower than average energy costs. Blank [2008], Abdelaziz [2013] and Plymesser [2014] applied these approaches of energy expenditure quantification and energy conservation to predict fish pathways by assuming fish tend to minimise their energy expenditure (i.e. take the path of least resistance).

Blank [2008] developed a model of energy expenditure of cutthroat trout (*Oncorhynchus clarkii*) through culverts. This was done through observation of the paths taken by approximately 322 captured cutthroat trout through a culvert relative to markers placed along the culvert side walls [Blank, 2008]. The flow in the culvert was then quantified using 3D CFD and validated using 3D ADV measurements [Blank, 2008]. The energy expended along each measured fish path was then quantified by balancing propulsive and drag forces, a method proposed by Vogel [1994]. Blank [2008] extended the analysis by creating an algorithm that selects a fish path node by node with a requirement to always movement upstream, and with multiple random starting

points. This was used to determine minimum and maximum energy paths by selecting nodes with the corresponding minimum or maximum velocity values. The calculated minimum energy path coincided with a large number of the observed fish movements. The quantification of minimum energy paths for different fish-ways can be combined with biokinetic data for different fish species and used to determine which fish-ways are most suitable for which species.

Abdelaziz [2013] developed a numerical model for simulating fish movements based on a framework that combines random-walk movements with the minimum energy expenditure concept, as used by Blank [2008]. The model employs a discrete particle-based method to simulate individual fish. Hydraulic data was obtained through 3D CFD using the standard k–ε closure and the VOF method [Abdelaziz, 2013]. The model makes use of the sensory ovoid as used by Goodwin et al. [2006] to define the local sensing range of an individual [Abdelaziz, 2013]. The model also includes a "turbulence check" step before assessing velocities at upstream nodes, which applies a turbulence avoidance model when the turbulence is deemed "high". Abdelaziz [2013] assume that the velocity gradient is directly indicative of the turbulence level and therefore uses this value as a proxy. This assumption is weakly justified and risks oversimplification of a complex environment. The turbulence avoidance model weights the probability of the individual's movement to heavily bias regions with lower values of turbulence and continues the bias for a fixed number of decisions (named the "forget-time-period") after encountering turbulence above the threshold. The turbulence threshold and the forget-time-period are calibrated to match measured observations. Abdelaziz [2013] then applied a moving average filter to the final predicted fish path to smooth the output which better matched measured data. Abdelaziz [2013] validated the predicted paths using the fish paths observed by Blank [2008]. The energy expenditure was then calculated for the final, smoothed fish path using the method outlined by Blank [2008]. Note that the Blank [2008] and Abdelaziz [2013] models do not include any measure of fatigue or available fish energy.

Plymesser [2014] expanded on the work of Blank [2008] by developing a model of energy expenditure of American Shad (*Alosa sapidissima*) moving through an Alaskan Denil fish pass, and included two measures of fatigue. Plymesser [2014] performed 3D CFD simulations of a full-scale Alaskan Denil fishway using the RNG k–ε turbulent closure and VOF method. Simulations were validated using time-averaged 3D velocity

data measured in a full scale experimental Alaskan Denil fish pass using an ADV with a frequency of 25 Hz, sampled over a two minute interval [Plymesser, 2014]. The improved model included two calculations of fatigue as functions of swim speed. Fatigue was determined first using the prolonged fish swimming mode. It was also calculated using a "percentage fatigue" value at each time step, as described by Castro-Santos [2006], which allowed switching between swimming modes. These two models of fatigue were calibrated against measured fish paths collected by Haro et al. [1999]. The models were bidirectionally validated, although the second model better conformed to the measured fish paths.

The Blank [2008], Abdelaziz [2013] and Plymesser [2014] models can be used to predict fish pathways by assuming the fish will only follow a path of a certain energy expenditure (i.e. minimum energy path). However, these models do not consider the direct influence of hydrodynamic and environmental cues on fish behaviour, which may be important in accurately predicting the movement of fish and the probability of fish locating the pass in a timely manner.

2.8.2 The work of Goodwin [2004] and Goodwin et al. [2006, 2014]: The Numerical Fish Surrogate Model

Goodwin [2004] developed an Eulerian-Lagrangian Agent-based Method (ELAM) model, termed the Numerical Fish Surrogate (NFS), to predict the movement of out-migrating (down-migrating) juvenile salmon at large hydropower dams in the Pacific Northwest, USA. The model was subsequently developed further by Goodwin et al. [2006, 2014]. The NFS model is based on the Strain-Velocity-Pressure (SVP) hypothesis, introduced by Goodwin [2004], which assumes that the downstream navigation of migrants is principally based on three metrics of the predominant hydrodynamics of the river: logarithmically-scaled local hydraulic strain (scaled with respect to the acclimatised ambient strain), the local time-averaged flow velocity, and the local hydrostatic pressure. It is assumed that individuals have preferences of strain, velocity, and pressure, with upper and lower limits, although the limits are not discussed [Goodwin et al., 2014]. The speed of movement of an individual increases with exposure to strains close to the upper limit, and is bound by the swimming capability of the individual [Goodwin et al., 2014]. Goodwin [2004] suggests that the authenticity of the SVP hypothesis is supported by various fish behaviour observations, although neither verification, valida-

tion, nor calibration are explicitly stated. The SVP hypothesis covers each of the main hydrodynamic stimuli perceived by the mechanosensory system of the fish: hydraulic strain is sensed by canal neuromasts, velocity is sensed through superficial neuromasts, and hydrostatic pressure is sensed through the swim bladder. An individual assesses the local hydrodynamic gradients and moves to a new location based on its defined preferences using a biased correlated random walk [Goodwin et al., 2014]. The individual is able to move to any point in 3D space and is not limited to mesh points, i.e. spatially continuous [Goodwin et al., 2014]. The range of the local hydrodynamics that can be assessed is a function of the body length of an individual [Goodwin et al., 2014]. Goodwin [2004] introduced the sensory ovoid and sensory query distance (SQD) which defines the hydrodynamic detection range, and thus the nodes within the environment that an individual considers before making a movement decision. This is based on the sensing distance of the lateral line organ and is hence based on fish body length, typically 2 to 3 times the body length of the individual Goodwin [2004].

The NFS model requires spatially-distributed velocity, pressure, and their gradients. The ELAM model has been used exclusively with the Unsteady, Unstructured RANS (U^2RANS) CFD code, developed by Lai [2000]. However, due to its use of contravariant space to interpolate data, the NFS requires data to be on structured grids although the conversion between grids and any potential loss of data is not discussed [Goodwin et al., 2014]. The U^2RANS code uses the k–ε turbulence model to solve for Reynolds stress [Jones and Launder, 1972]. The NFS model is computed in serial with the CFD, therefore the two codes are not coupled [Goodwin et al., 2014]. This means that any effect that the fish have on the flow field is not modelled. None of the literature that uses the NFS model discuss grid independence studies and instead opt to validate CFD results against measured data [see Goodwin 2004, Goodwin et al. 2006, Weber et al. 2006, Nestler et al. 2008, Goodwin et al. 2014]. The U^2RANS approach solves for transient (unsteady) flow, but it is not clear whether the output flow fields are averaged prior to applying the NFS model or whether the model is applied directly to the unsteady data [Goodwin et al., 2006]. If the former, Goodwin et al. [2006] neglect to discuss the temporal-averaging process and pseudo-steady state assumption. If the latter, Goodwin et al. [2006] neglect to discuss the potential temporal-dependency of the fish paths or sensitivity to the duration and temporal resolution of the unsteady data. Moreover, none of the related literature discuss any verification or sensitivity of the

NFS model to any of the parameters, threshold values, or flow field inputs. Therefore, the capability of the model to accurately and precisely predict fish pathways is not clear.

Weber et al. [2006] used the NFS model to evaluate the performance of alternative designs of juvenile downstream fish passage facilities, reporting that the model was able to identify which designs performed best. However, it is worth noting that these results were not validated with experimental data as the authors assumed the NFS model was reliable. Furthermore, the NFS model does not consider any environmental cues such as light or temperature, and does not offer any justification for these omissions. The model is also not publicly available, meaning that practitioners are unable to use the model to better design fish passage structures, and results can not be independently verified. Furthermore, the model is not designed for predicting upstream fish passage, nor has it been applied to a lowland river system, and is therefore does not meet the criteria that this project aims to fulfil.

2.8.3 The Gao et al. [2016] Model

Gao et al. [2016] developed an agent-based model to simulate the upstream movement of individual fish through a typical vertical slot fish pass. The flow field in the fish-way was quantified using a 2D depth-averaged numerical model using the Reynolds-Averaged Navier-Stokes (RANS) equations with the two-equation k–ε turbulent closure [Gao et al., 2016]. However previous results [see section 2.2.1] suggest that the flow structure in vertical slot fish-ways are 3D therefore 2D simulations will produce incorrect or incomplete results. Furthermore, the resulting flow fields are not validated against any measured data, which brings into question their reliability.

The trajectories of two trout of unspecified species, as collected by Rodriguez et al. [2011], were overlain over outputted time-averaged contours of velocity magnitude, velocity field, turbulence kinetic energy, turbulent eddy dissipation, and strain rate. Gao et al. [2016] found that the trajectory of neither individual correlated with the mean velocity magnitude or mean velocity field. However, the trajectories show that both fish avoid regions in which the turbulent kinetic energy exceeds 0.35 m^2s^{-2} or is less than 0.1 m^2s^{-2}. Gao et al. [2016] found no correlation between fish movements and the turbulent eddy dissipation, and crucially no correlation between fish movement and hydraulic strain, which is in direct opposition to the findings of Goodwin et al.

[2006]. This suggests that the hydrodynamic preferences are species-specific or life-stage-specific (i.e. migrating downstream versus migrating upstream).

The model developed by Gao et al. [2016] evaluates the turbulence kinetic energy in each local cell and the cell with the preferred value is selected. If two cells are equally appealing, the most upstream cell will be selected [Gao et al., 2016]. This can be thought of as a way to simulate rheotaxis in the individual. Therefore, assuming acceptable values of turbulence kinetic energy, the individual will always move upstream and only fall back downstream if unacceptable hydrodynamics are detected. Although the implication of "fallback" behaviour is not discussed, nor is the severity of the fallback justified [Gao et al., 2016]. The model assumes a constant fish velocity of 1 ms^{-1} and therefore does not account for energy expenditure or burst swimming capabilities [Gao et al., 2016]. The constant fish velocity is noted as being "close to observed movements", however it is not explicitly validated against any measured data. Furthermore, it is questionable to use a constant fish speed in a turbulent environment with largely fluctuating velocities. The model developed by Gao et al. [2016] is based on the measured trajectories of two trout. This brings into question the validity of the results given the small sample size. This is compounded when considering the difference in the two measured fish paths [see Rodriguez et al. [2011]]. Gao et al. [2016] performed 2D depth-averaged CFD simulations whereas literature suggests that the hydraulics of vertical slot fish-ways are not independent of depth [Khan, 2006, Barton et al., 2009, Marriner et al., 2014]. Furthermore, Gao et al. [2016] cite the turbulence kinetic energy as one of the main drivers for their model, although the vertical velocity component is neglected. Therefore, the correlation of the fish trajectories and turbulent kinetic energy may vary significantly when simulated in 3D. This would not be surprising as it has been shown that vertical slot fish-ways experience regions of up-welling and down-welling, which would induce significant vertical strain components [Khan 2006; see section 2.2.1].

2.8.4 The work of Gisen [2018]: The ELAM-de Model

Gisen [2018] modified the NFS model based on the work of Goodwin et al. [2014] to create a model of upstream directed fish migration termed the ELAM-de model. The ELAM-de model is based upon the same model framework as used in the NFS and therefore is spatially-continuous and makes use of the sensory ovoid assumption

[Goodwin et al., 2014, Gisen, 2018]. However, the ELAM-de model contains a new three-behaviour ruleset derived from flume-based movement data of brown trout, and is validated and calibrated against these data [Gisen, 2018]. Furthermore, a measure of motivation versus fatigue is implemented within the model, which defines whether an individual moves, holds station, or drifts [Gisen, 2018]. These motivation and fatigue values are determined based on the "spatial stagnation" of an individual; i.e. the longer an individual moves for the greater the fatigue value and the lesser the motivation value [Gisen, 2018]. The rate of change of fatigue and motivation is determined through coefficients, the value of which are not discussed, nor subject to sensitivity analyses [Gisen, 2018].

The ELAM-de model was developed to accept fluid flow data on unstructured polyhedral meshes output by OpenFOAM and is therefore dependent upon the use of this software to create input data [Gisen, 2018]. The openFOAM tools `blockMesh` and `snappyHexMesh` were used to generate meshes and transient simulations were executed using `interFoam` with the k–ω SST turbulence model [Gisen, 2018]. No investigation of mesh-dependency was presented however Gisen [2018] validates the results against measured ADV data. As with the NFS model, it is unclear whether the output flow fields are temporally-averaged prior to being used as model inputs or whether the ELAM-de model accepts unsteady data. If the former, Gisen [2018] neglects to discuss the temporal-averaging process and pseudo-steady state assumption. If the latter, Gisen [2018] neglects to discuss the potential temporal-dependency of the fish paths or sensitivity to the duration and temporal resolution of the unsteady data. Furthermore, Gisen [2018] reported that output fish trajectories were sensitive to the OpenFOAM version, chosen OpenFOAM libaries, and OpenFOAM compiler version [Gisen, 2018]. However, Gisen [2018] did not give reasoning, nor recommendations on "correct" versions to use. Furthermore, the ELAM-de model makes use of 3D unstructured meshes, but Gisen [2018] does not discuss the interpolation scheme used to determine environmental data at arbitrary spatial locations, which is complex for unstructured data.

2.8.5 The Tan et al. [2018] Model

Tan et al. [2018] presented a 2D agent-based model to predict upstream migration pathways of silver carp (*Hypophthalmichthys molitrix*) through a laboratory-based vertical slot fish-way. Tan et al. [2018] collected fish trajectory data via videography, using a

uniform reference grid of 25 cells (5x5) attached to the bed of each pool of the vertical slot fish-way. Furthermore, water velocity data were collected in a single pool using an ADV, and assumed to be representative of every pool [Tan et al., 2018]. Tan et al. [2018] found fish spent most time in cells with TKE values of $0.02 - 0.035m^2s^{-2}$, velocity magnitude (denoted V by Tan et al. 2018) of $0.16 - 0.4ms^{-1}$, and strain rates (SR) of $1.8 - 4.0s^{-1}$. It is not clear if the velocity considered is a component or the velocity magnitude.

Flow field data were created through the execution of 3D CFD using the RANS approach with the RNG k–ε turbulence closure, although the interface capturing scheme is not discussed [Tan et al., 2018]. The Tan et al. [2018] model was developed to compute 2D fish movements and therefore Tan et al. [2018] extracted data along an xy-plane, assumed to be horizontal to the bed. It is unclear whether these data were instantaneous or temporally averaged, or taken at a given depth or depth-averaged. It is curious that Tan et al. [2018] selected to compute 2D flow fields given that the flow structure in vertical slot fishways are thought to be 3D and feature regions of strong up-welling and down-welling [see section 2.2.1 and Khan 2006].

The Tan et al. [2018] model makes use of the sensory ovoid concept introduced by Goodwin [2004], although, as the model is 2D, it is referred to as the sensory circle. The Tan et al. [2018] model assesses the fitness (termed the "comprehensive probability") of each mesh cell along the boundary of the sensory circle. In each mesh cell, for each of the three hydraulic parameters (TKE, V, SR), the Tan et al. [2018] model determines a metric based on a Gaussian probability distribution weighted with the difference between the actual and "ideal" hydraulic parameter, where the "ideal" is assumed to be the range stated earlier, equation 2.33. The fitness is then determined as a weighted average of these metrics, equation 2.34, biasing towards the known (global) upstream direction. The Tan et al. [2018] model therefore requires *a priori* knowledge of the global upstream direction, and is only applicable to environments in which the velocity field is predominately in a single direction.

$$f(x_i) = \frac{1}{\sqrt{2\sigma_s}} e^{-\frac{(x_i - \mu_{si})^2}{2\sigma_s^2}} \tag{2.33}$$

$$F = \sum_{i=1}^{n} W_i f(x_i) \tag{2.34}$$

where $f(x_i)$ is the "probability" of stimuli i, x_i is actual value of stimulus i, μ_{si} is the

preferred value of stimulus i, F is "comprehensive probability" (fitness) of the cell, W_i is the weighting of stimulus, i, and the sum of W is 1.

An individual then moves towards the cell with the largest fitness, with a constant velocity (although this value is not explicitly stated). The values of the fitness weightings are stated ($W_{TKE} = 0.412, W_V = 0.391, W_{SR} = 0.197$) but no validation, justification, nor calibration is discussed; although Tan et al. [2018] state that the model was calibrated against 10% of the collected fish paths. Furthermore, the outputs of the Tan et al. [2018] model were validated against the remaining 90% of measured fish paths and shown qualitatively to compare favourably.

2.8.6 The work of Zielinski et al. [2018], Gilmanov et al. [2019], and Finger et al. [2020]

Zielinski et al. [2018] developed a 3D agent-based model to predict pathways of upmigrating fish based on path selection to minimise energetic cost. The Zielinski et al. [2018] model assumes individuals only move upstream (implicit rheotaxis) and uses the percentage fatigue model, developed by Castro-Santos [2005], as a proxy for energy expenditure (as used by Plymesser 2014). Swimming performance parameters for each individual are assigned randomly from distributions of swim speed-fatigue time curves, normalised by the body length of the individual Zielinski et al. [2018]. The Zielinski et al. [2018] model is spatially-discrete and therefore fish were constrained to CFD mesh nodes. At each timestep fish move to their neighbouring upstream node that results in the lowest increase in fatigue, which is determined randomly in cases where the lowest increase in fatigue is shared between nodes. The increase in fatigue is calculated as [Zielinski et al., 2018]:

$$\Delta F = \begin{cases} \frac{\Delta t}{T} \times 100\%, & U_{res} \geq U_{sus} \\ 0, & U_{res} \leq U_{sus} \end{cases} \tag{2.35}$$

where ΔF is the percentage fatigue increase, Δt is the time required to swim to the selected node calculated as $\Delta t = \frac{l}{U_g}$, l is the distance between nodes, U_g is the optimal ground speed of the individual, T is the endurance of the fish, U_{res} is the resultant water velocity that the fish must overcome.

Interestingly, Zielinski et al. [2018] chose to modify the velocity field within the model each timestep by selecting velocities at each node from normal distributions

constructed from the mean velocities (U, V, W) and using the velocity fluctuations (u', v', w') as the standard deviations. This stochastically adds turbulence to the model rather than attempt to explicitly capture behavioural responses to turbulence.

Zielinski et al. [2018] subsequently applied the model to a typical lock-and-dam on the Mississippi River. The flow field was quantified 3D unsteady flow field data using CFD with a transient RANS approach, using the standard k–ε turbulence closure, employing unstructured tetrahedral meshing, and using the rigid-lid approximation [Zielinski et al., 2018]. The result was considered pseudo-steady once the difference between instantaneous velocity fluctuations about the mean were an order of magnitude less than the mean [Zielinski et al., 2018]. No mesh dependency investigation was undertaken, however the CFD was qualitatively validated against velocity data collected via ADCP [Zielinski et al., 2018].

Zielinski et al. [2018] calculated passage metrics for silver carp (*Hypophthalmichthys molitrix*), bighead carp (*Hypophthalmichthys nobilis*), and lake sturgeon (*Acipenser fulvescens*), but did not compare these to measured passage efficiencies and therefore the success of the model is unclear. Zielinski et al. [2018] did not perform any validation of the model against measured fish paths nor bulk fish passage metrics and therefore confidence in the results is lacking. Furthermore, Zielinski et al. [2018] reported that the flow field had to be artificially modified through the creation of false-boundaries in areas where no upstream pathway was available, such as downstream of the sluice gates, due to the tendency for fish to become "stuck". This modification suggests that the model neglects the issue of fish being able to adequately locate passages and not become confused by in-stream barriers, and likely artificially inflates the predicted passage efficiency.

Zielinski et al. [2018] carried out a brief sensitivity analysis and found that passage efficiency was significantly decreased when maximum percentage fatigue was lowered from 100% to 50%, but was insensitive when increased to 200%. This suggests passage was limited by the structure rather than the capacity of the fish. Zielinski et al. [2018] also found that using a static velocity field did not significantly change the overall passage efficiency, suggesting this additional feature was not necessary.

Gilmanov et al. [2019] later modified the model to allow fish to move between mesh nodes in smaller steps, rather than moving between nodes in one movement. However, at each timestep, fish could still only assess the percentage fatigue increase at mesh

nodes, and therefore the model cannot be considered as spatially continuous. However, this adaptation allows a fish to change its direction more frequently and therefore update its minimum fatigue algorithm more frequently, and was found to result in smoother fish paths and increased passage efficiencies compared to the original model [Gilmanov et al., 2019]. This modification allow eases the dependency of the model upon the computational mesh, but does not entirely remove it. However, as with the original model, validation of the results was not discussed and therefore the legitimacy of the model is unclear.

Finger et al. [2020] applied the fish fatigue model to a Lock and Dam located on the Upper Mississippi River, Hastings, Minnesota, USA. Finger et al. [2020] tagged and tracked 112 Common carp (*Cyprinus carpio*) through the domain and compared measured and predicted data. Finger et al. [2020] quantified the flow field at the study site for discharges of 1274 and $1727 m^3 s^{-1}$, representing the flow conditions experienced by the tagged carp, following the methodology used by Zielinski et al. [2018]. The fish fatigue model [Zielinski et al., 2018, Gilmanov et al., 2019] was then applied to each velocity field using ten groups of 500 fish randomly seeded downstream of the lock-and-dam. Finger et al. [2020] reported passage efficiencies of 0% and 2% for the tagged fish and virtual fish at a discharge of $1274 m^3 s^{-1}$, respectively; and 6% and 30% for the tagged fish and virtual fish at a discharge of $1727 m^3 s^{-1}$, respectively. While demonstrating agreement at the lower discharge level, the results suggest the model overestimates the passage efficiency for the higher discharge level. This overestimation suggests that minimum energy pathways are insufficient to capture the aggregate behaviour of common carp. Furthermore, it is possible that the real carp became followed local minimum energy pathways but became confused in areas where no upstream pathway was available, something that the fatigue model artificially suppresses. Lastly, the sensitivity of the model to the number of agents was no explored, and therefore it is possible that the model may require more agents to capture bulk behaviours, particularly given the size of the domain.

2.8.7 Summary of Published Fish Path Prediction Models

This section has summarised the current approaches to modelling fish pathways in the literature, and has demonstrated that this is an active field of research. Available approaches range from the simpler work of Blank [2008], Abdelaziz [2013], Plymesser

[2014], Gao et al. [2016] through to the more advanced models of Goodwin et al. [2014], Gisen [2018], Zielinski et al. [2018]. However, there are many differences and similarities between approaches that are briefly highlighted here:

- Each model features a different behavioural ruleset, but all of them can be summarised as a combination of attraction to some hydrodynamic parameters, and repulsion from others.
- Each model explicitly uses the local water velocity as a stimulus, with the exception of the Gao et al. [2016] model which implicitly uses local water velocity in the form of implied rheotaxis. This demonstrates the importance of the local water velocity as a stimulus.
- Implicit rheotaxis is a theme in many of the models due to its simplistic nature [i.e. Blank 2008, Abdelaziz 2013, Plymesser 2014, Gao et al. 2016, Tan et al. 2018]. However, this approach limits the utility of the model by assuming that the domain has a single dominant flow direction, and assumes that, at any arbitrary point in space or time, a passing fish has this information.
- Blank [2008], Abdelaziz [2013], Plymesser [2014], Zielinski et al. [2018] each found success in the use of the concept of minimum energy expenditure with different energy quantification metrics. This demonstrates the utility of a minimum energy approach.
- Each model uses turbulence as a stimulus, with the exception of Blank [2008] and Plymesser [2014]. Tan et al. [2018] and Gao et al. [2016] use TKE as their turbulence descriptor, Goodwin et al. [2014] and Gisen [2018] use the spatial acceleration gradient, Abdelaziz [2013] uses the spatial velocity gradient, and Zielinski et al. [2018] implemented turbulence stochastically via a temporally-varying velocity field based on computed velocity fluctuations.
- Gilmanov et al. [2019] demonstrated that spatially-continuous modelling is more complex and computationally expensive versus spatially-discrete modelling, but yielded greater accuracy.
- Arguably the most advanced model is that of Goodwin et al. [2014], which is unique in that there's a large wealth of tracking and flow field data available to

calibrate and validate the model, and it has been in development for nearly two decades. The Goodwin et al. [2014] model considers down-migrating salmonidae and therefore it not suitable to determining up-migration pathways. Gisen [2018] utilised the framework of the Goodwin et al. [2014] model and developed a new motivation/fatigue ruleset to model up-migrating salmonidae. However, Gisen [2018] developed the model to work only with OpenFOAM, reducing the utility of the model, and reported that output fish trajectories were sensitive to the OpenFOAM version. Furthermore, there's a comparatively small amount of tracking and flow field data available with which to develop, calibrate, and validate against for up-migrating salmonidae.

- The majority of the models neglect to present sensitivity investigations, or calibration data, and where presented they are often incomplete, reflecting the associated difficulties with validation of agent-based models [see Crooks et al. 2008, Ngo and See 2012].

- The majority of the models implement behaviour based on behavioural thresholds or limits to define fish preferences of hydraulic parameters, but many neglect to explicit state threshold values nor subject these thresholds to sensitivity analyses.

Details of the specific approaches, functions, and findings of each model are discussed within the relevant chapter discussions later in this work. It is summarised that, while there are multiple established models in the literature, none of the current approaches are sufficient to fulfil the aims and objectives of this work. The development and open source distribution of such a model would enable engineers and practitioners globally to computationally assess fish pass structures and their placement; which would result in more efficient designs, better connected river systems, and be well aligned with the EU WFD.

Chapter 3

A Viability Study of European Eels Ascending Eel Tiles, using 2D Agent-Based Models and Landscape Ecology Metrics

3.1 Introduction

Chapter 1 outlined the developmental principles for this research, section 1.2. This chapter develops multiple cellular automata (CA) models and a single agent-based model (ABM) to assess the viability of this approach to modelling upstream passage of fish. Specifically, it considers the quantification of the passage efficiency, or connectivity, of an anguilliform fish pass with passing juvenile European eels. The velocity field within each pass is quantified using CFD. The passage efficiency is assessed through the development of multiple custom-built CA and ABMs as well as through employing several existing metrics originally developed to assess landscape connectivity.

The European eel (*Anguilla anguilla*) is a catadromous species, and therefore must migrate upstream as a part of their life cycle. They are born in the Sargasso Sea and transported as larvae along the Gulf Stream arriving on the Atlantic coast of Europe after a 9 month journey [van Ginneken and Maes, 2005]. On arrival, the larvae metamorphose into elvers and begin to migrate upriver [Tesch, 2004] where they can live for up to 50 years before migrating back to the Sargasso Sea to spawn [Poole and Reynolds, 1998]. Recruitment of elvers across Europe has suffered a 95% reduction since the early 1980s and has been officially listed as a critically endangered species on the International Union for Conservation of Nature (IUCN) Red List since 2014 [Moriarty, 1986, 1996, Jacoby and Gollock, 2014]. This decline has been partly attributed to the reduced connectivity of hydrosystems across Europe due to an increase in the number of in-stream barriers, particularly to the upstream migration of elver [Moriarty and Dekker, 1997, Feunteun, 2002]. Common fish passage solutions, such as the Larinier pass or vertical slot fish-ways are inefficient and inappropriate for the upstream passage of European eels [Knights and White, 1998, Feunteun, 2002] due to their low swimming performance and their inability to jump out of the water [Solomon and Beach, 2004].

Anguilliform-specific passage facilities have been developed to compliment common fish passage solutions. Anguilliform-specific fish passes make use of the tendency for eels to utilise lower velocity regions near-bed, and have been shown to be effective in enabling their passage [Briand et al., 2005, Piper et al., 2012, Vowles et al., 2015]. These eel passes are comprised of relatively steep ascent ramps that provide a wetted substrate designed to facilitate eel passage [Porcher, 2002]. Historically, the substrates used were often cheap, robust items such as rocks, aggregates, branches [Knights and White, 1998], trawl netting [Shotzberger and Strait, 2002], burlap [Jackman et al.,

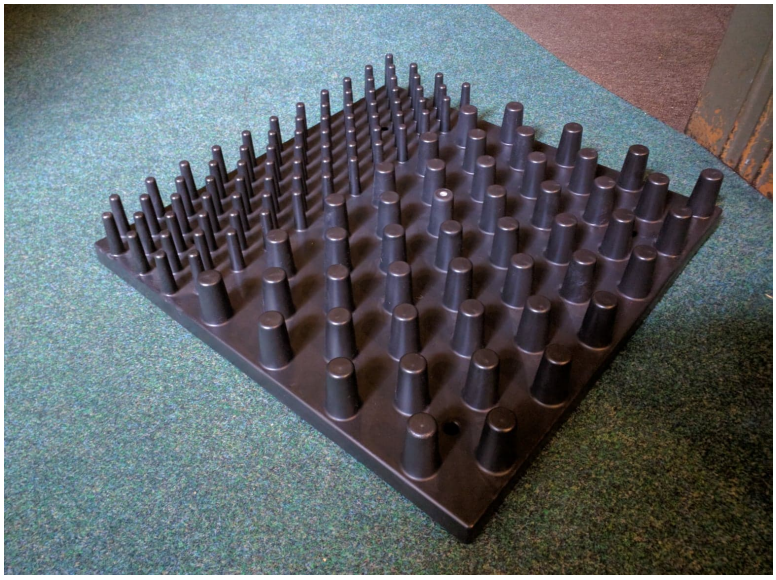

Figure 3.1: Typical eel tile produced by Berry & Escott [Berry & Escott Engineering, 2017].

2009], and geotextile matting [Knights and White, 1998, Environment Agency, 2011]. However these materials were found to be too abrasive and caused passing eels to lose a considerable amount of their protective mucus [Voegtle and Larinier, 2000]. The mucus layer protects the fish from abrasion and invading pathogens [Archer, 1979]. Furthermore, it helps to maintain the fish's osmotic and ionic integrity by regulating the influx and efflux of water and salt between the fish and the surrounding water. Loss of this layer may result in the death of the fish [Archer, 1979].

In more recent times, purpose-built, synthetic substrates have become available, figure 3.1. These use a series of small, more-or-less rigid, vertical cylinders or studs attached to a base to reduce the energy of the flow and provide the substrate for eels to pass [i.e. Milieu Inc. 2017, Berry & Escott Engineering 2017, Terraqua Environmental Solutions 2017]. These are generally available as modular "tiles" which can be placed beside one another to create cost-effective passes of varying geometry. This type of purpose-built "eel tile" is considered throughout this chapter.

3.1.1 Vowles et al. [2015]: A Case Study

Vowles et al. [2015] considered the passage efficiency of elver over a model crump weir

with and without the installation of an eel pass constructed from dual-density, studded Berry & Escott eel tiles [Berry & Escott Engineering, 2017]. These tiles feature $50mm$ high studs of two different tapered diameters and centre-to-centre spacings: $14.8mm$ at the base tapering to $11.7mm$ at the top, with a centre-to-centre spacing of $45.45mm$ and $29.6mm$ at the base tapering to $23.4mm$ at the top, with a centre-to-centre spacing of $83.3mm$. The dual density of studs is designed to allow for the passage of different sizes of eels, as smaller eels may struggle to pass the faster velocities present between the large studs, and larger eels cannot fit between the smaller studs. The tiles used in the experiments were 0.3 m wide and featured an approximately 2:1 ratio of large studs to small studs.

A model crump weir was placed within an open channel flume. The flume measured $12m$ long, $0.3m$ wide, and $0.4m$ deep. The crump weir measured $0.25m$ tall and $0.3m$ wide with an upstream angle of $26.6°$ and a downstream angle of $11.5°$, resulting in a downstream face of length $1.25m$. Experiments were conducted for two cases; the control, where the eel tiles were not present; and the treatment, where the eel tiles were installed. During the treatment case, the eel tiles covered the full width of the weir, with each stud density occupying an equal amount of space.

A constant discharge of $1.0\times10^{-3}m^3s^{-1}$ was reported, which equates to a discharge per unit width of $3.33\times10^{-3}m^2s^{-1}$ [Vowles et al., 2015]. This discharge has significant uncertainty since the mean inflow velocity was reported to be $8.0 \pm 6.1mms^{-1}$, which yields a discharge per unit width of $2.22\times10^{-3} \pm 1.70\times10^{-3}m^2s^{-1}$ [Vowles et al., 2015]. Water velocities were measured upstream and downstream of the weir using an electromagnetic flow meter, reportedly at 60% water depth [Vowles et al., 2015]. Furthermore, velocities on the downstream face were measured using the flow meter for the control case but use of the flow meter was obstructed in the treatment, therefore average flow velocities in the pass were measured by recording the time taken for 5 mL of India ink to flow down the downstream face [Vowles et al., 2015]. Table 3.1 shows the reported mean velocities for the modified and treatment cases upstream, within, and downstream of the pass.

Mean water velocity decreased upstream and increased downstream of the weir in the treatment case compared to the control case. Furthermore, the average water velocity on the face of the weir decreased during the treatment case. However, the velocity measurements are presented with error bars which vary from approximately 60% up to

Table 3.1: Measured velocities upstream, downstream, and on the face of a crump weir with and without the applied eel tile as reported by Vowles et al. [2015]

Case	Upstream	Downstream	Within the Pass
Control	0.0103 ± 0.0064	0.0711 ± 0.0884	0.574 ± 0.173
Treatment	0.0080 ± 0.0061	0.1000 ± 0.0952	0.347*

* No error given.

124% of the presented value, and therefore their reliability should be questioned. Furthermore, measuring the average velocity in through the pass using the transit time of India ink is unreliable, particularly as the authors neglect to detail the pathway taken by the ink. Therefore, it is unclear whether the reported value pertains to the velocity through the large studs, small studs, or some combination of both.

It is worth discussing these velocities in terms of the passing elvers. Clough and Turnpenny [2001] suggest that an elver measuring 0.072 m has a maximum burst speed of 0.47 ms^{-1}. Therefore, the average velocity given for the control case (0.574 ms^{-1}) suggests that the flow is too fast for any of the passing elvers, who would be overcome by the encountered water. The average velocity given for the treatment case (0.347 ms^{-1}) is less than this critical velocity and thus suggests that passage is possible.

Vowles et al. [2015] conducted 10 trials, each of 10 minutes length, for each of the two test cases. Trials were conducted during daylight hours in May of 2013. Each trial considered the upstream movement of a group of 30 elver released 2.2 metres downstream of the weir crest (approximately 1 metre downstream of the downstream end of the weir). Mean elver length was reported as 71.73 ± 3.87 mm, based on length measurements of 10% of the total population. Each group was allowed to acclimatise to the flume water temperature ($21.8 \pm 0.96°C$) for a minimum of 1 hour before the start of the trial, and were removed from the flume at the end of each trial. An individual fish was used in one trial only.

Vowles et al. [2015] defined the passage efficiency as the number of successes divided by the total number of attempts. The authors found that, during the control case, the mean number of attempts and successes were 30.4 (±13.0) and 0.0, respectively. During the treatment case, the mean number of attempts and successes were 29.9 (±6.1) and 20.0 (±4.6). Therefore, the mean passage efficiencies were 0% and 67% for the control

and treatment cases, respectively. Furthermore, the authors found that more elver successfully passed the smaller, denser studs; with passage efficiencies of 58.7% and 41.3% for the small and large studs, respectively. Therefore, either the elver had an increased attraction to the hydraulics of the smaller studs, the elver found the hydraulics of the smaller studs easier to overcome, or some mixture of both. The hydraulics of an eel tile is not quantified in the literature, and therefore one can only presume that the average velocity in the smaller, denser studs is less than that of the larger studs.

The work done by Vowles et al. [2015] suggests that the installation of eel tiles to existing crump weirs may increase connectivity of hydro-systems. However, the geometry of in-stream barriers vary largely and one cannot presume that the installation of eel tiles to other structures would give similar results. Furthermore, the work gives rise to the question of appropriate installation angles for eel passes. Solomon and Beach [2004] describe anguilliform-specific passage solutions as a trade off between restricting water velocities to a comfortable range for ascending eels (i.e. shallow installation angle), versus restricting the overall length of the pass (i.e. steep installation angle); particularly at in-stream barriers with large hydraulic heads. In practice, the installation angles of eel passes vary massively, ranging from 12° up to 60° [Solomon and Beach, 2004]. In theory, a pass should be installed at the steepest angle possible while not hindering movement. However, there is little literature which assess the passage efficiency of an eel pass and even less which consider the how the installation angle affects the passage efficiency. Current guidance for installation angles mostly arise from the observations of practitioners and the recommendations of manufacturers; which one could argue are not fully justifiable, repeatable, free from bias, nor empirically sound. Therefore, eel passes are complex structures and it is unlikely that a single pass geometry would be appropriate for all scenarios. Therefore, more work is required to understand how the geometry of the eel pass and the age range of the expected eels affects the passage efficiency.

3.1.2 Chapter Aim

This chapter aims to elucidate the effect of installation angle and discharge on the passage efficiency of an eel pass constructed of Berry & Escott eel tiles [Berry & Escott Engineering, 2017] for a range of lengths of elver. Furthermore, this chapter aims to demonstrate the potential for simple cellular automate and agent-based models to be

applied to model passage in complex ecohydraulic domains. This is achieved through the following objectives:

- Use a three dimensional free surface CFD modelling approach to quantify the velocity field within multiple eel pass configurations, using installation angles of 8°, 11°, 14°, 17°, and 20° and discharges per unit width of $1.67\times10^{-3}m^2s^{-1}$, $3.3\dot{3}\times10^{-3}m^2s^{-1}$, and $5.0\times10^{-3}m^2s^{-1}$.
- Development of multiple cellular automata and agent-based models to assess upstream passage of elvers.
- Application of developed models and established landscape connectivity metrics to each eel pass configuration.

3.2 Quantifying the Near-Substrate Velocity Field of a Typical Eel Pass

Successful passage of hydraulic structures is governed in part by the velocity field that exists within the hydraulic domain. If too high, ascending fauna may be unable to overcome the water velocity and fail to pass. Therefore it is important when modelling passage to quantify the pass hydraulics. This section outlines the methodology used to quantify the velocity field of each pass configuration.

3.2.1 Computational Fluid Dynamics Methodology

A 3D CFD model was constructed using ANSYS Fluent version 17.2. In order to simplify the CFD model, only the smaller studs were simulated and it was assumed that the larger studs had a negligible effect on the velocity field of the smaller studs. The smaller studs were chosen as these were found by Vowles et al. [2015] to be favoured by passing elver. As the hydraulics of these eel tile have not been investigated in the literature, it is difficult to understand ratio of water flowing between the smaller studs, compared to the larger studs. In this study, we assume that the flow rate ratio is approximately equal to the ratio of stud spacings (45 mm vs 83 mm), and therefore it is assumed that the flow is split 83:45 in favour of the larger studs. Furthermore, symmetry boundary conditions are used to reduce the domain to approximately one third of the original width of the small studs.

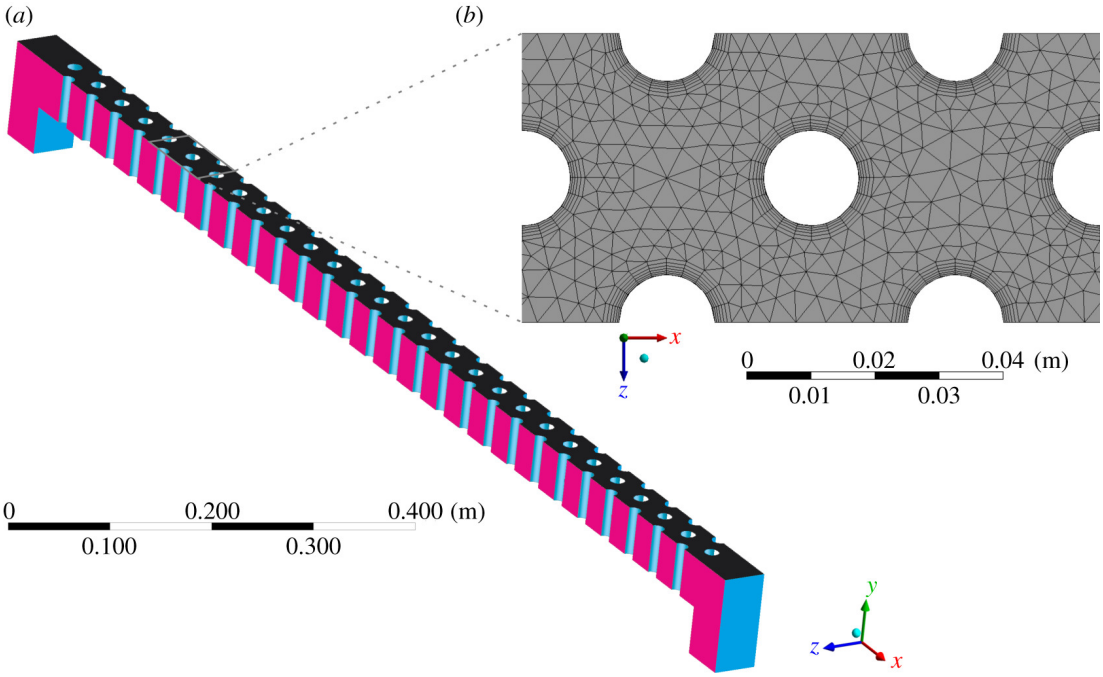

Figure 3.2: (a) Isometric view of the CFD domain. Cyan/light grey denotes no-slip boundary condition, magenta/dark grey denotes symmetry boundary condition and black denotes pressure outlet boundary condition and (b) magnified planform view highlighting the unstructured tetrahedral mesh and grid refinement near studs and walls. Water flows in the positive x direction.

Meshing was performed using ANSYS Meshing where an unstructured tetrahedral mesh approach was employed due to the geometry of the domain. The resulting mesh features approximately 906000 cells with average and maximum cell characteristic lengths of $1.5mm$ and $7mm$, respectively. Inflation layers were applied to the bed and to each stud. Each inflation layer consisted of 5 sub-layers which increased in size by a factor of 1.2 times the previous sub-layer (specified growth rate of 1.2). This ensured an increase in cell density close to the bed and the studs and ensured a smooth transition between the boundary ($0.4mm$ cells) and the main flow ($1.0mm$ cells). Water entered the domain through a velocity inlet positioned upstream of the eel tile and leaves the domain through a pressure outlet located downstream of the pass. The bed of the pass is defined at $y = 0$. Symmetry boundary conditions are applied in the cross-stream direction. All other boundaries are defined as walls with the no-slip boundary condition

and a roughness of 0.

The simulations were performed using the unsteady, incompressible, Reynolds Averaged Navier-Stokes (RANS) equations [see section 2.5.2]. Turbulence was modelled using the k–ω SST model. This was chosen as it is known to accurately capture flow separation over smooth surfaces, particularly compared to all forms of the k–ε model [Menter, 1993, ANSYS, 2016]. The SIMPLE pressure-velocity coupling scheme is used [Patankar and Spalding, 1972]. The free surface location is approximated using the volume of fluid (VOF) method with Piecewise Linear Interface Construction (PLIC) interface capturing scheme [see section 2.5.4], and the free surface is assumed to exist along the surface $\alpha = 0.5$. This approach was chosen as Ducrocq et al. [2017] found that the combination of the k–ω SST model and the VOF method gave good predictions of the free surface and the velocity field around a semi-submerged cylinder compared with optical measurements and particle tracking velocimetry. Similarly, Chorda et al. [2019] simulated the flow across a steep-sloped ramp covered with staggered, semi-submerged cylinders using the combination of the k–ω SST model and the VOF method. Chorda et al. [2019] found that the k–ω SST model was able to accurately predict the mean free surface location and the mean velocity field compared to optical and ADV measurements [taken by Cassan et al. 2014 and Tran et al. 2016, respectively].

Second order upwind discretisation of momentum, turbulence kinetic energy, and specific dissipation rate are used. A constant timestep $\Delta t = 0.0005$ seconds is used. A maximum limit of 100 iterations per time step is imposed. The convergence criteria for the non-dimensional residuals of u_x, u_y, and u_z, turbulent kinetic energy, k, and specific turbulence dissipation rate, ω is defined as 10^{-5}. Assuming an average velocity through the pass of $0.35ms^{-1}$, as reported by Vowles et al. [2015]; a residence time of approximately 4 seconds was calculated. Therefore, a total flow time of 10 seconds is defined to allow the flow to become pseudo-steady and give sufficient time for temporal averaging. A gravity term is applied to the model with components in both the x and y directions to define the installation angle. A parametric study is undertaken using installation angles of 8°, 11°, 14°, 17°, and 20° and discharges per unit width of $1.67\times10^{-3}m^2s^{-1}$, $3.3\dot{3}\times10^{-3}m^2s^{-1}$, and $5.0\times10^{-3}m^2s^{-1}$ for a total of configurations of eel pass, including the case as used by Vowles et al. [2015]. This allows for comparison to published experimental data and the exploration of the effect of installation angle and flow rate on passage efficiency.

3.2.2 Mesh Independence Study: Eel Tiles

A mesh independence study was undertaken for the eel tile installed at 11° with a discharge per unit width of $3.3\dot{3}\times10^{-3}m^2s^{-1}$. An unstructured tetrahedral meshing approach was employed for three densities of mesh; coarse, medium, and fine, table 3.2.

Table 3.2: Approximate mesh resolutions used for eel tile mesh independence study.

Mesh	Number of Elements
Coarse	$\approx 650,000$
Medium	$\approx 906,000$
Fine	$\approx 1,300,000$

Fluid flow was modelled using the approach outlined in section 3.2.1 with a reduced timestep size of $\Delta t = 0.0002$ seconds due to the increased mesh resolution. Solutions were analysed over a vertical sampling line located in the centre of the pass (i.e. $z = 0.0225m$) and exactly between the final and penultimate studs (i.e. $x = 1.17m$). Temporally-averaged velocity magnitude was used to evaluate the three meshes, figure 3.3. The medium and fine meshes agree well whereas the coarse mesh severely under-predicts the near-bed water velocity. This result suggests that the medium mesh accurately resolved the velocity field, and therefore is appropriate to use for further studies.

3.2.3 Results of the CFD

Figure 3.4 shows the free location after 10 seconds of flow time with contours of streamwise velocity, u, for an eel pass installed at 11° with a discharge per unit width of 3.33 $\times10^{-3}m^2s^{-1}$. The results show that the streamwise velocity was reduced in regions that contain studs, i.e. the studs reduce the flow velocity.

The results are as expected for a turbulent flow through a series of semi-submerged vertical cylinders and show that the streamwise velocity was reduced in regions that contain studs and stagnation points are scene on the upstream face of each stud, figure 3.4. Therefore the studs succeeded in reducing the flow velocity and hence the energy of the flow. Furthermore, the flow converges and accelerates between studs, causing peaks in the streamwise velocity. This is corroborated by figure 3.5b, which shows the streamwise-averaged streamwise velocity peaks at approximately $0.37ms^{-1}$ at the

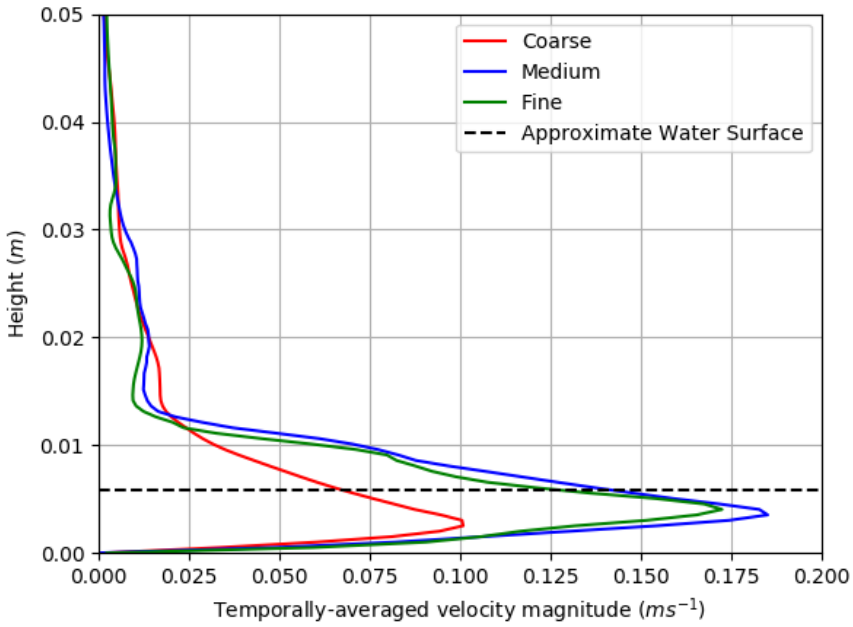

Figure 3.3: Height versus temporally-averaged velocity magnitude over a vertical sampling line located at $x = 1.17m$, $z = 0.0225\ m$, black dashed line denotes average water surface located at y $= 5.3\ mm$.

quarter and three-quarter width locations, coinciding with the absence of studs, and decreases to a minimum of approximately $0.26ms^{-1}$ in stud locations, coinciding with the no-slip boundary condition. The spacing between studs is such that there is strong interaction between wakes and the proceeding stud, so there is insufficient time or space for a Kármán vortex street to develop [Moulinec et al., 2004, Tong et al., 2014]. The average streamwise velocity ($0.299ms^{-1}$) compares well to the value reported by Vowles et al. [2015] ($0.347ms^{-1}$). However, the authors measured this value using the transit time of 5 mL of India ink to flow through the pass, a method of questionable accuracy. Furthermore, the authors do not discuss the pathway taken by the ink, and therefore it is impossible to know if their reported velocity is for the small studs, large studs, or some combination of both.

For the Vowles et al. [2015] case, the simulated flow field yields Reynolds numbers of 1740 or 4550 using the mean flow depth and the stud diameter as the length scale, respectively. Therefore the flow is fully turbulent [Moulinec et al., 2004, Tong et al.,

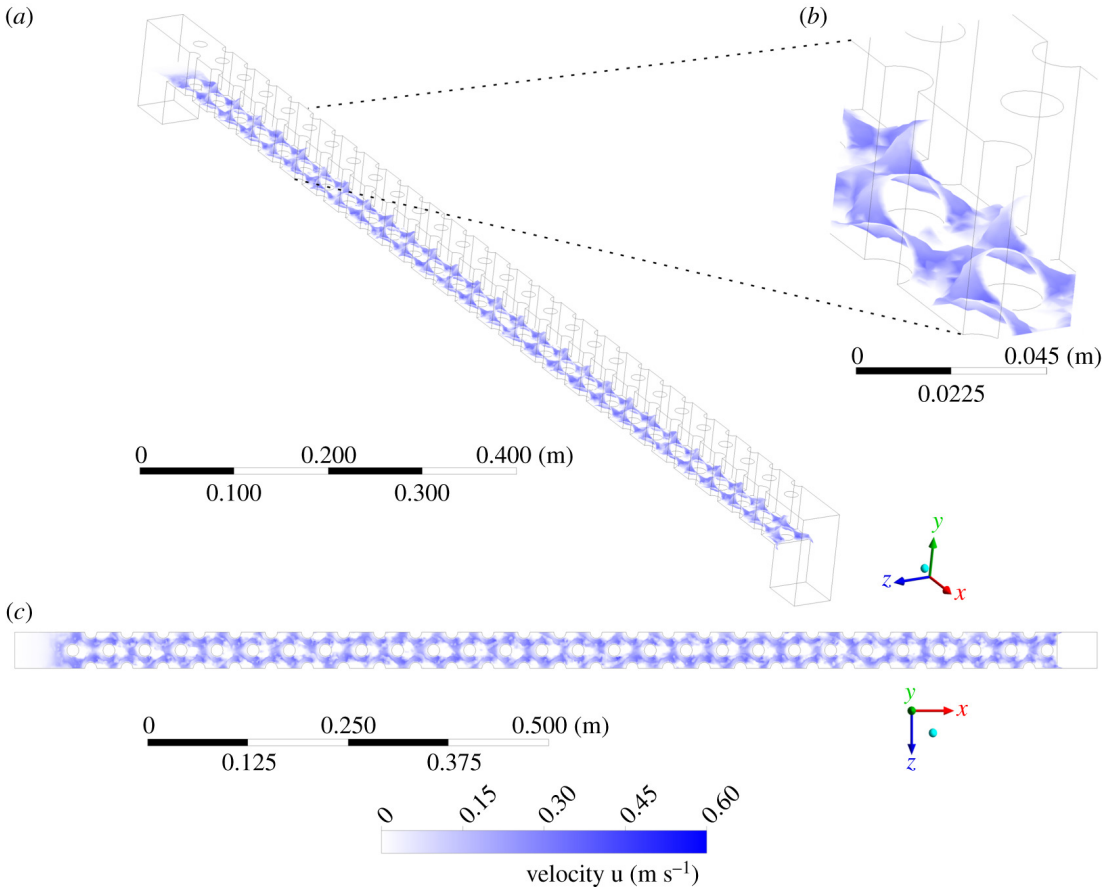

Figure 3.4: (a) Isometric, (b) magnified isometric and (c) plan views of the pass with an installation angle of 11° and a discharge per unit width of $3.33\times10^{-3}m^2s^{-1}$, with overlain free surface after 10.0 s of flow time. The free surface is overlain with contours of velocity magnitude at the free surface; the velocity contour scale is consistent across the three views. The domain has been cropped to increase ease of viewing. Water flows in the positive x direction.

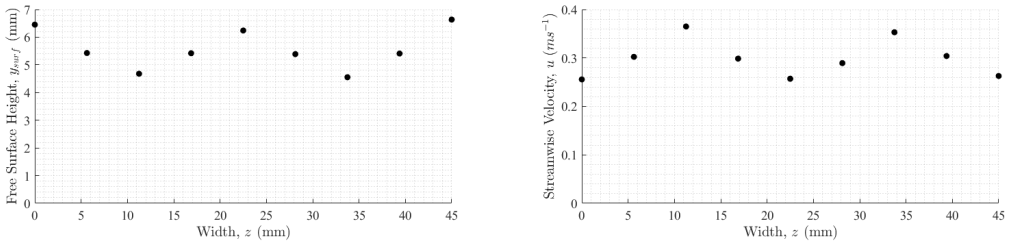

(a) (b)

Figure 3.5: a) Streamwise-averaged free surface height, $\bar{y_{surf}}$, and b) Streamwise-averaged streamwise water velocity, $\bar{u}$ against cross-stream location for the eel pass configuration as used by Vowles et al. [2015]; temporally averaged between $8s$ and $10s$ of flow time.

2014]. Furthermore, the simulated flow is fully turbulent for all eel pass configurations, with Reynolds numbers ranging from 660 or 2320 for the 8°, $1.6\dot{7}\times10^{-3}m^2s^{-1}$ case to 3070 or 5800 for the 20°, $5.0\times10^{-3}m^2s^{-1}$ case using the mean flow depth and stud diameter as the length scale, respectively.

Figure 3.5a shows the streamwise-averaged free surface height against the cross-stream location. The free surface is high at the boundary $z = 0$ and decreases to a minimum at a quarter of the pass width, before increasing back to a peak at the centreline of the pass; i.e. $z = \max(z)/2$. Similar results are seen from the centreline to the border $z = \max(z)$. These peaks and troughs in the free surface height correspond to the average presence and absence of studs, respectively, across the width of the pass. For example, there are a greater number of studs along the streamwise centreline of the pass, which causes the free surface height to increase. The symmetry in free surface height is expected due to the symmetry of the pass geometry, and gives confidence to the results. The average free surface height within the pass was approximately 5.58 mm, compared to 5 mm, reported by Vowles et al. [2015]. The methodology used by Vowles et al. [2015] is not discussed and therefore a comparison of results is difficult.

3.3 Measures of Connectivity

3.3.1 Preparing the Data for Connectivity Assessment

Once the simulations were completed, the near-substrate velocity field was extracted from each resulting dataset, in order to prepare the data for use with both the landscape connectivity metrics and the CA and IBM. As the landscape connectivity metrics can only assess temporally-independent, spatially two dimensional data, the CA and IBM were built such that they made use of the same input dataset. This was done to ease comparison and to simplify the model development.

In order to reduce the velocity field to spatially two dimensional, a plane parallel to the bed of the eel pass was extracted from the domain for each configuration. This plane was taken at 3 mm from the bed as this was found to have the highest near-bed velocities and therefore represents a worse case scenario for the up-migrating elver. The extracted two dimensional velocity fields were then temporally averaged across a time period of 2 seconds from 8 to 10 seconds of flow time, inclusively. These values were chosen as it was identified that the flow had become pseudo-steady at 8 seconds in all configurations. Increasing the temporal resolution and the duration over the data are averaged would benefit the accuracy of the results, however this was infeasible due to digital storage constraints. Finally, each of the datasets were mirrored in the cross-stream direction to approximately match the width of the domain to the width of the small stud area of the pass used by Vowles et al. [2015].

Each of the spatially two dimensional, temporally-averaged velocity fields were then converted to regularly spaced, uniform grids of $0.5mm$ through the use of triangulation-based linear interpolation. Classified versions of each of these datasets were then created by assessing the velocity in each cell and classifying them in three categories: “passable”, “impassable”, and “boundary”. A passable cell is defined as a cell wherein the velocity is less than a critical value, which is dependant upon the size of elver being considered. An impassable cell is defined as a cell wherein the velocity is above this threshold. A boundary cell is defined as a cell without a velocity that elver can never physically pass through, such as the studs of the domain. The velocity thresholds are determined based on the burst speed of elver of different sizes at a water temperature of $21.8°C$ during the spring, given by the SWIMIT program developed by Clough and Turnpenny [2001]. The burst speed was chosen as this is the maximum velocity at which the fish

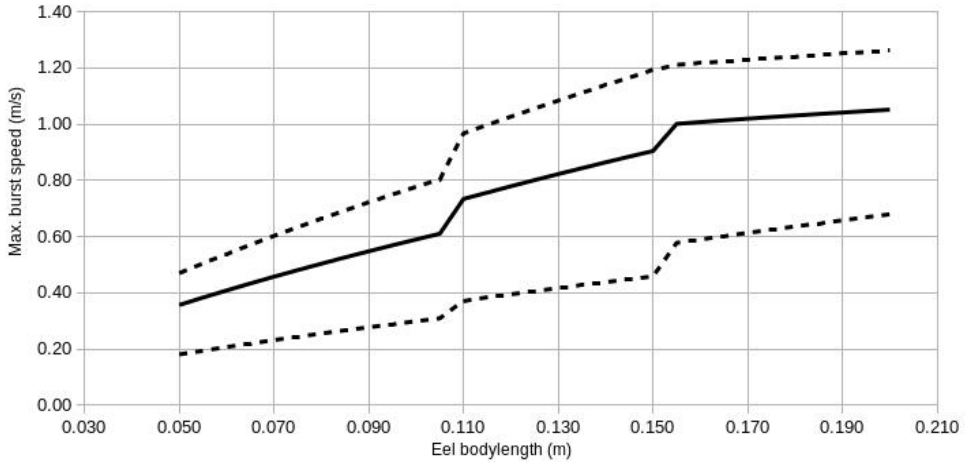

Figure 3.6: Graph of burst speed against elver length. Data taken from SWIMIT for a water temperature of $21.8°C$ during spring [Clough and Turnpenny, 2001]. Dotted lines show 10 and 90% confidence intervals. Solid line shows mean value.

can swim and therefore represents their best chance of successfully migrating through the domain. Figure 3.6 shows the determined burst speed against elver length as given by SWIMIT. Six different sizes of elver were considered; 0.05, 0.06, 0.07, 0.08, 0.09, and 0.1 m. This range was chosen as it encompasses the largest and smallest length of immigrating elvers recorded at an example European coastal region, Den Oever in Holland [Deelder, 1984]. The result is a "binary map" of the domain that shows which cells a given elver can pass [see figure 3.7 for example binary maps]. These binary maps constituent a simplistic proxy for the "landscape mosaic" approach as conventionally used in landscape ecology [see Noss 1991 or Forman 2014]. The 10%, 50%, and 90% confidence intervals were extracted from SWIMIT for each elver bodylength and used to classify the datasets. Therefore 18 binary maps were considered for each of the 15 configurations of eel pass, resulting in a total of 270 classified domains. The binary maps for other eel pass installations and for the 10% and 90% burst swimming speed confidence intervals are presented in Appendix B.

3.3.2 Landscape Connectivity Metrics

Landscape connectivity metrics are quantitative tools using by ecologists to assess the spatial patterns of heterogeneous environments over a number of scales; particularly when considering anthropogenic activities that may disrupt ecological processes

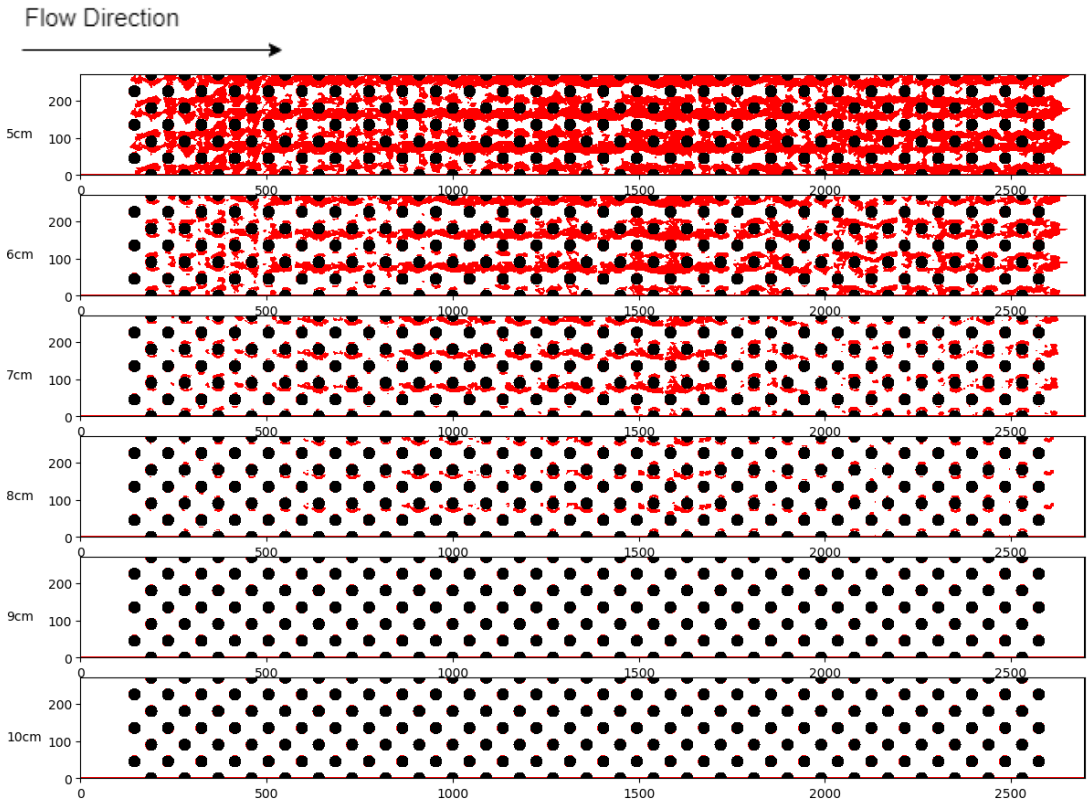

Figure 3.7: Example binary maps for an eel pass installed at 17° with a discharge per unit width of $5.0\times10^{-3}m^2s^{-1}$ for all elver lengths, using the mean burst swimming speed. Axes denote pixels. White denotes passable cells, black denotes boundary cells, and red denote impassable cells. Elver lengths denoted on the left hand side.

[Turner, 1989, Gustafson, 1998]. These metrics are applied to spatially two dimensional "landscape mosaics", which consist of multiple habitat (or patch) types. The quantification of landscape-level patterns is important as it is generally accepted that ecological processes are linked to ecological patterns at coarse spatial scales. Landscape metrics are well integrated into land management and decision making frameworks [Turner, 1989, Gustafson, 1998, Rudnick et al., 2012].

The patterns found in landscapes are dependent upon the scale at which the landscape is represented [Gergel and Turner, 2017]. Therefore, it is important to ensure that the landscapes to be assessed are of a scale representative of the perspective of the target species. Generally, landscape connectivity metrics are used to study large areas, however there is no reason that these metrics are any less applicable to the scale of domain considered here; provided that the resolution of the spatial discretisation is sufficiently high.

In landscape ecology, the term "connectivity" can refer to *structural connectivity*, which considers only the physical landscape; and *functional connectivity*, which considers the effects of the physical landscape on the movement of organisms. In other words, structural connectivity is landscape-specific whereas the functional connectivity is both landscape- and species-specific [Gergel and Turner, 2017]. Herein, only structural connectivity metrics are considered. However, the landscape is defined such that each patch is species-dependent; i.e. passable or impassable. Therefore the results obtained are dependent on both the landscape (pass geometry) as well as the target species, and can therefore be thought of as measures of functional connectivity.

It is envisaged that while each of the landscape ecology metrics assesses the aggregation of a landscape, the results can be used as proxies for the connectivity, or passability, of a fish pass domain. For example, a pass domain with a high aggregation of passable cells denotes an overall high passability, or a pass with a high measure of disconnectedness denotes a low overall passability.

Six established landscape connectivity metrics were used to assess the connectivity of each of the resulting binary maps, with three defined patch types: "passable", "impassable", and "boundary". Assessments were performed through the use of the FRAGSTATS v4.2 spatial analysis software package [McGarigal et al., 2012]. The metrics employed are: Number of Passable Patches (`NPP`), Percentage of Like Adjacencies (`PLADJ`), Patch Cohesion Index (`COHESION`), Contagion (`CONTAG`), Landscape Division

Index (DIVISION), and Splitting Index (SPLIT). The CONTAG metric was computed using passable and impassable patches and excluding the boundary patches; whereas each of the other metrics were computed using only the passable patches.

When considering landscape connectivity metrics, it is important to note the neighbourhood rules used. FRAGSTATS allows the users to select either a first order von Neumann neighbourhood or a first order Moore neighbourhood [see section 2.6.1]. Limiting each of the calculations to only 4 neighbours (von Neumann) will fail to capture patch aggregation that relies on diagonal adjacencies. This is overcome by the use of an 8 neighbour neighbourhood (Moore). Both are valid approaches but one must note and be consistent regarding which neighbourhood definition is used. In this study, only first order Moore neighbourhoods (8 neighbours) are considered.

Three of the six metrics; PLADJ, COHESION, and CONTAG, quantify the connectedness of an environment. For example, an environment consisting of larger, aggregated patches will result in a larger connectedness. The PLADJ metric (3.1) considers the number of pixel edges of the focal cell type, i, that border other pixels of the same type as a fraction of all pixel edges of the focal type [Gardner and O'Neill, 1991]. This value ranges from 0%, when there are no two cells of the focal patch type bordering each other; to 100%, when the entire domain consists solely of the focal patch type. The PLADJ metric quantifies only the spatial distribution of patches and does not consider their interconnectivity [McGarigal, 2015].

$$\texttt{PLADJ} = 100 \left[\frac{\sum_{i=1}^{m} g_{ii}}{\sum_{i=1}^{m} \sum_{k=1}^{m} g_{ik}} \right] \tag{3.1}$$

where: g_{ii} is the number of cell edges shared by pixels of patch type i based on the double count method; g_{ik} is the number of cell edges shared by pixels of types i and k based on the double count method; and m is the number of patch types present in the domain.

The COHESION metric (3.2) is an extension of the PLADJ metric but considers the summation of the perimeters of each patch divided by the summation of the area-weighted perimeters of each patch [Schumaker, 1996]. The COHESION value tends to 0 as the number of pixels of the focal type decreases and becomes less connected. The COHESION metric considers only the spatial distribution of patches and does not consider

their interconnectivity.

$$\texttt{COHESION} = 100\left(\frac{\sqrt{Z}}{\sqrt{Z}-1}\right)\left[1-\frac{\sum_{i=1}^{m}\sum_{j=1}^{n}p_{ij}^{*}}{\sum_{i=1}^{m}\sum_{j=1}^{n}p_{ij}^{*}\sqrt{a_{ij}^{*}}}\right] \tag{3.2}$$

where: p_{ij}^{*} is the perimeter of patch ij in terms of the number of pixel edges; a_{ij}^{*} is the area of patch ij in terms of the number of pixels; Z is the total number of pixels in the domain, excluding boundary cells.

The CONTAG metric (3.3) was first introduced by O'neill et al. [1988] and subsequently corrected by Li and Reynolds [1993]. It quantifies the extent to which patch types are aggregated as a percentage of the maximum possible aggregation. It can be thought of as the product of two probabilities. Firstly, the probability that a randomly chosen pixel belongs to patch type i; and secondly the probability that a pixel of patch type i has a neighbour of patch type k. This metric not only quantifies the spatial distribution of patches within the landscape, but also captures their interconnectivity. The CONTAG metric is widely used in landscape ecology due to its straightforward nature [McGarigal, 2015] and its ability to capture the aggregation of categorical maps effectively [Turner, 1989].

$$\texttt{CONTAG} = 100\left[1+\frac{\sum_{i=1}^{m}\sum_{k=1}^{m}\left[P_i\frac{g_{ik}}{\sum_{k=1}^{m}g_{ik}}\right]\ln\left(P_i\frac{g_{ik}}{\sum_{k=1}^{m}g_{ik}}\right)}{2\ln m}\right] \tag{3.3}$$

where: P_i is the proportion of the domain belonging to patch type i; g_{ik} is the number of edges between pixels of patch type i and k, using the double count method; and m is the number of patch types in the domain excluding the boundary.

The other three landscape metrics used in this study; NPP, DIVISION, and SPLIT, quantify the disconnectedness of an environment. For example, an environment consisting of many small, fragmented patches will result in a large disconnectedness. The NPP metric is the simplest of the landscape connectivity metrics, and counts the raw

number of passable patches within a given domain (3.4). An environment featuring no passable patches is by definition impossible to pass. However, one can assume an environment featuring a large number of passable patches represents a highly fractured landscape and would therefore have a low connectivity. Therefore, a well connected domain will likely have a low NPP value, but must be greater than 0. However, that is not to say that all low NPP values represent well connected environments.

$$\texttt{NPP} = n_i \tag{3.4}$$

where: n_i is the number of patches in the landscape of patch type i (in this case, only the passable patches are considered).

The DIVISION and SPLIT metrics were both introduced by Jaeger [2000] and are strongly linked. The DIVISION metric is defined as the probability that two randomly chosen pixels are not located in the same non-dissected area. The SPLIT metric is defined as the number of patches resulting from dividing the landscape into patches of equal size such that the new landscape configuration has a DIVISION value equal to the original landscape configuration [see Jaeger [2000]]. These two metrics conventionally quantify the graininess of the environment; that is, the frequency of fine-grained patches versus coarse-grained patches. The DIVISION metric is bound between 0 and unity. It is reduced to 0 when the environment consists of a single patch, and reaches its maximum of 1 when every pixel belongs to a separate patch. The SPLIT metric is bound to a minimum of 1, which occurs when the landscape consists of a single patch. The upper bound is equal to the square of the total number of cells, i.e. Z^2, which occurs when every cell belongs to a different patch.

$$\texttt{DIVISION} = 1 - \sum_{i=1}^{m}\sum_{j=1}^{n}\left(\frac{a_{ij}}{A}\right)^2 \tag{3.5}$$

$$\texttt{SPLIT} = \frac{A^2}{\sum_{i=1}^{m}\sum_{j=1}^{n} a_{ij}^2} \tag{3.6}$$

where: a_{ij} is the area of patch ij; A is the total area of the landscape.

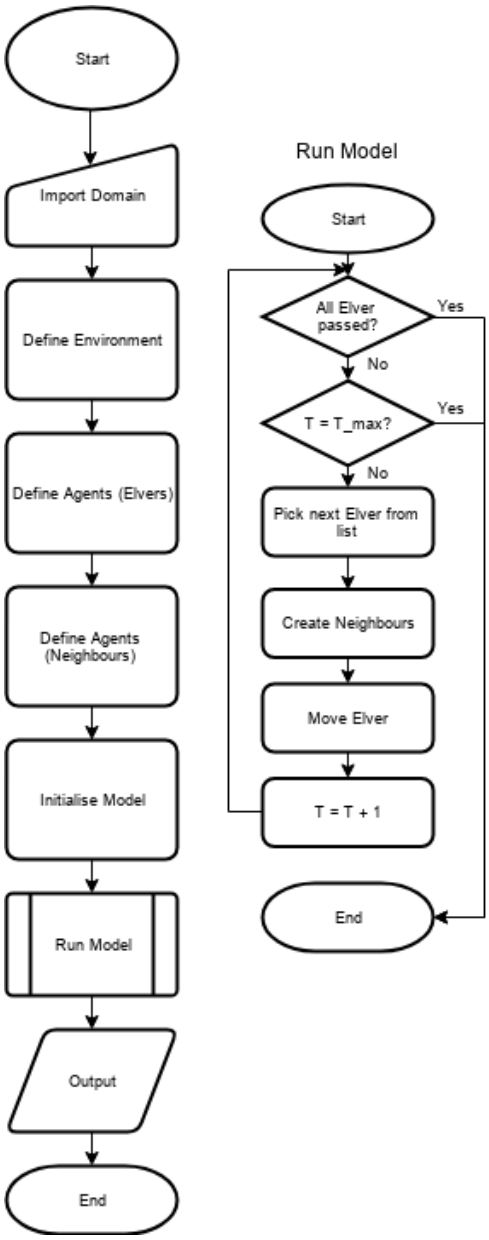

Figure 3.8: Flowchart detailing the basic underlying structure used by each of the CA/IB models to describe upstream passage of elver through a typical eel pass.

3.3.3 Development of Cellular Automata and Agent-based Models

Four models of increasing complexity were developed to model the upstream passage of elvers through the classified domains outlined in section 3.3.1. All four of the models are built in Python 3.6, and each are freely available from the University of Leeds Data Repository [Padgett and Thomas, 2019]. Each of the models measure the passability of an eel pass using the same basic structure, and output the number of successful and unsuccessful passage attempts. The first three models (denoted `SEPM`, `FEPM`, and `EEPM`) are cellular automata models, whereas the fourth model, `HEPM`, is an agent-based model. In all cases elvers are created at the downstream-most end of the domain and move upstream through the domain based on model-specific rulesets. As each of the models build on the previous model; this section will outline the basic structure shared by all the models and then subsequently highlight the differences between each of the models and their rulesets. The basic structure of each of the models is outlined in figure 3.8. The first agent-based model, the Simple Elver Passage Model `SEPM`, is the most simple and has no additional functionality and therefore functions as below.

Simple Elver Passage Model (`SEPM`)

Firstly, the environment in which the agents operate is defined by importing the classified domains. These domains are then preprocessed to ensure that the boundaries describing the stud locations are correct and to encase the domain in a continuous boundary to ensure no agents attempt to leave the domain. Secondly, the creation area for the agents is defined as all rows in the downstream-most column. This ensures a con-

Table 3.3: Basic agent (elver) attributes used by all four of the elver passage CA/IB models.

Attribute	Description
`id`	Identification number.
`row`	Current row. Integer. Updated every timestep.
`col`	Current column. Integer. Updated every timestep.
`location`	Current location, defined by row and column. Updated every timestep.
`history`	Array of location history for the agent. Updated every timestep. Used to output agent trajectory.

sistent streamwise starting point for all agents. Agents (elvers) are defined as a python class with a number of class variables (agent attributes), which describe the properties of the specific agent; and class methods (agent methods), which govern the behaviour of the agent. The basic agent attributes and methods are given in tables 3.3 and 3.4, respectively, along with a short description of each. Elvers are assumed to occupy only one cell at any one time and move one cell per timestep. Furthermore, the each of the agent-based models assume an inherent motivation to pass the domain. Therefore all of the following models can be thought of as a number of separate passage attempts by individual elvers. Fishes are known to acquire knowledge from each other through social learning, which can include migration and route selection [Brown and Laland, 2003]. However, it is difficult to quantify learned behaviours within a CA framework and therefore, to simplify model development, none of the elver passage models include any form of agent-agent interactions. Implementation of social learning between fishes in agent-based models remains unexplored in the literature, and therefore the model implications of this assumption are not clear.

Table 3.4: Basic agent (elver) methods used by all four of the eel CA/IB models.

Method	Description
`createNeighbours`	This method creates a list of the agent's neighbours using a first order Moore neighbourhood. It also compiles three lists of the passable upstream neighbours, passable cross-stream neighbours, and passable downstream neighbours. These are calculated using the neighbour method, `passable` and are stored as agent attributes. These lists are overwritten each time this method is executed.
`move`	This method selects a neighbour to move to based on the lists of passable neighbours; prioritising upstream neighbours, then cross-stream neighbours, then downstream neighbours.

Similarly, neighbours are defined as a separate python class whose attributes and methods are given in table 3.5. On the surface it may seem unnecessary to define neighbours in this manner as the passability of a cell could instead be directly interrogated by the elvers. However, by defining the neighbours as a class of their own, methods and attributes can be assigned to each neighbour which allows for more complex interactions. This is explored further in subsequent models. Furthermore, neighbours defined

in this manner can be easily created and deleted as required.

Table 3.5: Basic neighbour attributes and methods used the eel CA/IB models.

Attribute/method	Description
`id`	Identification number.
`row`	Row. Integer.
`col`	Column. Integer.
`location`	Location, defined by row and column.
`passable`	This method determines if the neighbour is passable by interrogating the data value at the neighbours location within the environment matrix. If this value is equal to 10, the neighbour is passable; else it is impassable.

Once each component of the model is defined, a simulation can be initialised. In its most basic form the initialisation creates a user-defined number of elvers within the domain. The spawn area is defined at the downstream-most column of the domain; wherein each agent is allocated a random row upon creation. Random values are handled using the `random` python module which uses the Mersenne Twister to produce pseudo-random numbers with a periodicity of $2^{19937} - 1$ [see Matsumoto and Nishimura [1998] for details of Mersenne Twister algorithm].

After the model has been initialised, the main loop is executed. This loop runs until all of the elvers have passed the domain or until a maximum number of timesteps is reached. At each timestep, each elver in the domain is sequentially selected and allowed to move once based on their surroundings using the methods outlined in table 3.4. As the landscape connectivity metrics use a first order Moore neighbourhood, it is sensible to use the same neighbourhood rule in the agent-based models. Therefore elver assess the passability of their 8 neighbours and may potentially move diagonally. Figure 3.9 shows an example of an agent moving through a domain. An elver is said to have successfully passed the domain once it passes column 25. This was chosen as velocities were consistently low in this region and therefore posed little resistance to the passing fish.

While simplistic, the `SEPM` was seen to adequately model the upstream movement of the agents through a given domain, as designed. However, during operation it was observed that agents could get "stuck" within the domain upon encountering regions of impassable cells. Figure 3.10 shows a diagram depicting an elver becoming stuck with

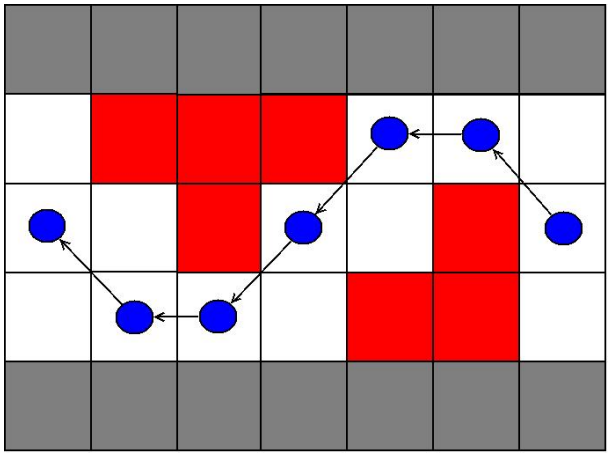

Figure 3.9: Diagram depicting example movement of an elver through a domain. The elver is represented by the blue circle. White cells are passable; red cells are impassable; grey cells are boundary.

a domain. This occurs due to the prioritisation of upstream cells. It was thought that in practice a passing elver would move back downstream upon encountering a high velocity region; rather than attempt to pass *ad infinitum*. The second agent-based model was created to incorporate this "fallback" behaviour.

Fallback Elver Passage Model (`FEPM`)

Fallback behaviour was implemented through the addition of multiple new attributes and methods, outlined in table 3.6. At every timestep, after an agent has moved, the `checkStuck` method is executed. This method assesses a number of past locations defined by `pastColsNumber`, and compares the column values (i.e. streamwise location). If the difference between the maximum and minimum column values is found to be less than `threshold`, the agent is deemed to be stuck. If the agent is found to be stuck, the `stuck` attribute is modified to reflect this and the `stuckIt` attribute is reset to zero. Furthermore, the `move` method is altered to switch the neighbourhood movement priorities if the `stuck` attribute is `True`; causing the agent to prioritise moving downstream, then cross-stream, then upstream. Each time the `move` method is executed whilst `stuck` = `True`, the counter, `stuckIt`, is increased. Once this counter reaches `stuckItMax`, the agent is assumed to no longer be stuck (`stuck` = `False`), and hence the movement priorities are reverted. The `FEPM` introduces several new

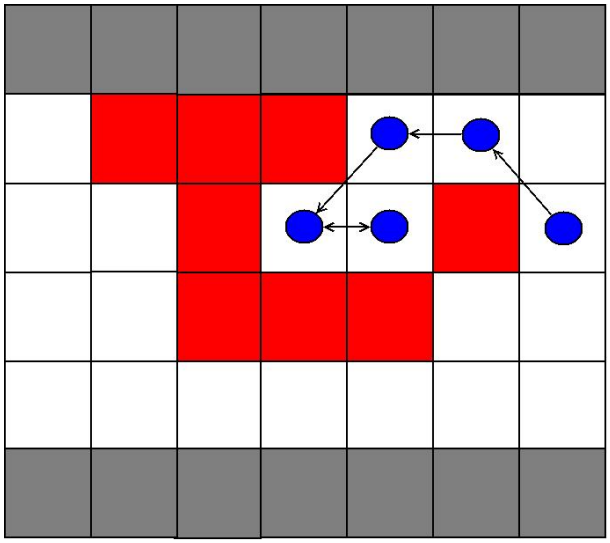

Figure 3.10: Diagram depicting example case of an elver becoming stuck with a region of impassable cells. The elver is represented by the blue circle. White cells are passable; red cells are impassable; grey cells are boundary.

variables which define the function of the `checkStuck` method. As these are user defined variables, a sensitivity study was carried out to ensure the results were not overly dependent on the value of these variables [see section 3.3.4].

This methodology effectively allows an elver to make an additional attempt to pass the domain once it becomes stuck. This means that agents no longer fail due to becoming caught in small regions of impassable cells or obstacles. However, if no clear path is present, the agent will still fail. Furthermore, `FEPM` did not adequately account for exhaustion; i.e. unless the maximum number of cell-to-cell moves was exceeded, an agent would continue to make passage attempts *ad infinitum*. Similarly, while fall back behaviour has been observed in eels and elver [Bolland, 2018], in was ultimately decided that the implementation of fallback within the model was not reflective of real behaviour. This is because an elver exposed to velocities above its burst speed (i.e an impassable cell) would be overcome by the momentum of the water and subsequently washed downstream, rather than make a conscious decision to retreat a set distant [Bolland, 2018].

Table 3.6: Additional/modified agent attributes and methods used in by the `FEPM`.

Attribute	Description
`stuck`	Boolean denoting whether or not the agent is defined as "stuck".
`stuckIt`	Count of the number of timesteps that the agent has been "stuck".
`StuckItMax`	Maximum number of timesteps an agent is allowed to be "stuck" before reverting to normal behaviour.
`pastColsNumber`	Number of previous timesteps over which to sample location data.
`threshold`	The threshold distance that defines whether an agent is "stuck". Must be greater than 2 and less than `pastColsNumber`.
`checkStuck`	This method checks whether the agent is stuck by assessing the agent's location over a past number of timesteps (controlled by `pastColsNumber`). If the range of streamwise locations (i.e. occupied columns) is less than `threshold`, the agent is defined as "stuck".
`move`	This method is modified to first operate differently in the case that `stuck` = `True`. In this case, the movement priorities are reversed, i.e. prioritising downstream neighbours, then cross-stream, then upstream neighbours.

Exhaustion Elver Passage Model (`EEPM`)

The third agent-based model removed the fallback behaviour implemented in `FEPM` and instead implemented a model of exhaustion. This exhaustion metric is based on the assumption that each elver is travelling at its burst speed and hence can only maintain its speed for a maximum of $20s$ [Clough and Turnpenny, 2001]. New attributes and methods were introduced to model the exhaustion, table 3.7. Crucially, upon importing the classified domain, the velocity magnitude map is also imported. This allowed neighbours to be assigned temporally-averaged velocities interpolated at the neighbours location. The `move` method is modified to calculate the relative speed of the agent based on its value of `burst` and the destination neighbour's value of `velMag`. Rather than average across the velocity at the current location and the velocity at the destination, it was decided that only the velocity magnitude of the destination was to be used to calculate the relative velocity. This was chosen as it simplified the required calculations and it is assumed that the velocities at the current location and the destination are approximately equal, which is acceptable as long as the resolution

Table 3.7: Additional agent attributes used in by the EEPM.

Class	Attribute	Description
elver	burst	Burst speed of the agent.
elver	timeReq	Time required to make a move, based on the relative speed and distance covered.
elver	timePerStep	List of timeReq values at each step.
elver	burstTime	Cumulative time spent travelling at burst speed.
neighbour	velMag	Magnitude of the temporally-averaged velocity interpolated at the cell location.
elver	move	Modified to calculate relative speed of the individual based on its burst speed and local velocity. Relative speed and distance covered during the move are used to calculate the time required to make the move, which is then totalled and stored. This value is used to define when the individual becomes exhausted.

of the spatial discretisation is sufficiently high. The time required for the agent to make its move, timeReq, is calculated based on the relative speed of the agent and the distance moved. A cumulative total of the time taken, denoted burstTime is calculated and stored. If this value exceeds $20s$, the agent is considered to have become exhausted and hence fails to pass the domain.

While EEPM does not solve the issue of the elver becoming "stuck" near impassable regions, it does adequately model their eventual exhaustion. This is reflective of the elver being overcome by the momentum of the water and being washed downstream, although it does not capture their subsequent passage attempt. However, if one were to instead view the model as a number of individual passage attempts rather than a number of individual elvers, implementation of fallback behaviour becomes unnecessary.

Heterogeneous Elver Passage Model (HEPM)

All three of the cellular automata models presented to this point have assumed that each agent has exactly the same burst speed, e.g. the population is homogeneous. This is not representative of reality due to the natural variation of the ability of organisms. Therefore the fourth model, HEPM, builds on the EEPM and overcomes this assumption of a homogeneous population by assigning a burst swimming speed to each elver upon

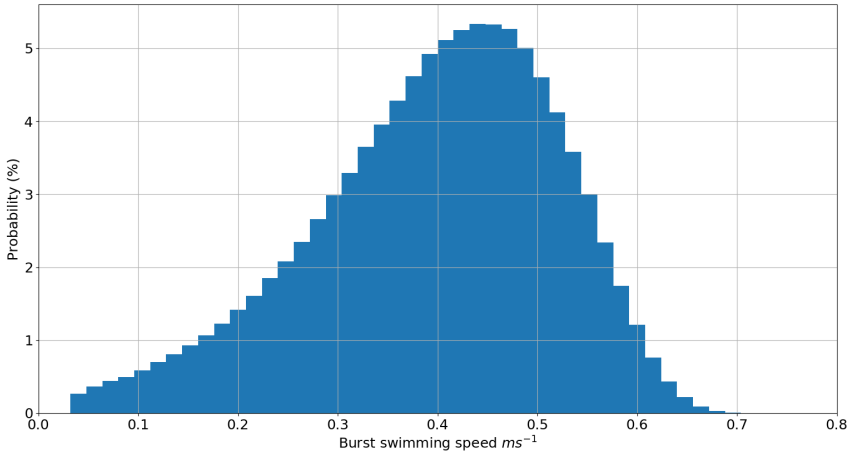

Figure 3.11: Histogram displaying the inverse lognormal distribution describing the range of burst swimming speeds for an elver of length of 0.07 m swimming in spring with a water temperature of 21.8°C, extracted from SWIMIT [Clough and Turnpenny, 2001], using 50 discrete bins.

creation within the domain. In order to determine the distribution of burst swim speeds, the data presented in the SWIMIT program [Clough and Turnpenny, 2001] were extracted. An inverse lognormal distribution, figure 3.11, was found to fit the extracted burst speed data for each length of elver. This distribution was used to randomly assign a burst speed to each elver upon creation, thus creating a heterogeneous population of elvers, better capturing the natural variation of swimming abilities within a population of elver of a given length.

This new functionality makes the pre-classified domains redundant as the passability of a given cell is now dependent upon the ability of the approaching elver and therefore must be calculated within the simulation. Therefore the `HEPM` instead requires the full velocity map as an input, examples of which are given in appendix B. Table 3.8 gives the modified attributes and methods used by `HEPM`.

3.3.4 Sensitivity Analyses of the Agent-based Models

Each of the four agent-based models rely on user-defined variables which may affect the results of each model. It is therefore important to understand the sensitivity of the results to each of the variables and ensure that the results are not significantly altered due to variable values. Figure 3.12a shows the relationship between the success

Table 3.8: Additional/modified agent attributes and methods used by the HEPM.

Class	Method	Description
elver	burst	Now assigned a burst speed from an inverse log-normal distribution for the size of elver considered.
neighbour	passable	This method is updated and requires an input of the burst of the current elver, and compares this to the velMag value of the cell, if velMag is less than burst, the cell is passable.

percentage of $0.07m$ elver through a given pass and the number of agents used in each simulation (solved using HEPM). It shows that the success percentage generally increased with increasing number of agents but levels off when the number of agents reaches 1000. More agents will result in a longer run time, and therefore 1000 agents are used for each simulation as this is the smallest value that does not significantly influence the results.

Figure 3.12b shows the relationship between the success percentage for $0.07m$ elver passing the same pass and the maximum number of timesteps allowed (solved using HEPM, with 1000 agents). It shows that if the timesteps are limited to 2000, 0% of the agents successful pass the domain. This is because the minimum required number of steps to pass is approximately equal to the length of the domain in terms of pixels (2700). Furthermore, the success percentage became approximately constant after 10000 timesteps. Therefore, 10000 timesteps are used for all simulations. It is worth noting that for EEPM and HEPM, if all agents were to pass or fail before the maximum number of timesteps is reached, the simulation will end early. Therefore, there is no disadvantage to setting the maximum number of timesteps much higher than required. However, when considering SEPM and FEPM, the simulation only finishes once either the maximum number of timesteps is reached or all agents pass as there is no failure mechanic implemented.

The FEPM relies on 3 additional variables that control the initiation of the fallback behaviour: stuckItMax, pastColNumber, and threshold. The effect of varying these parameters are shown in figures 3.13a, 3.13b, and 3.13c, respectively. The success percentage is seen to firstly increase with increasing values of stuckItmax until a value of 50 where it begins to decrease. At low values of stuckItMax agents aren't given enough time moves to effectively fallback. However at higher values, agents are forced

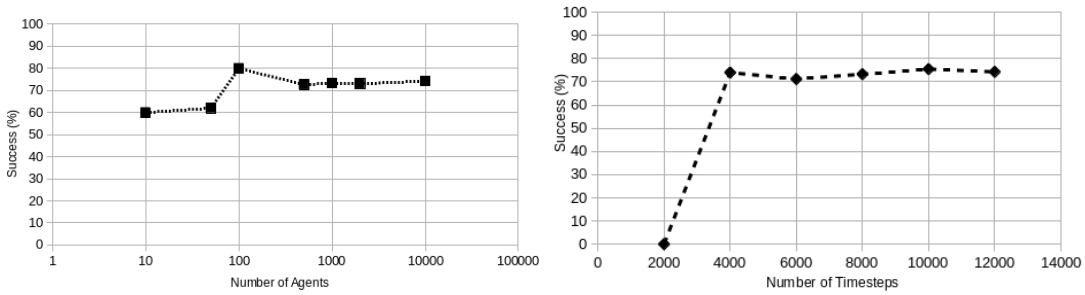

(a) (b)

Figure 3.12: Success percentage for the passage of elver of length $0.07m$ through an eel pass inclined at 11° with a discharge per unit width of $3.3\dot{3}\times10^{-3}m^2s^{-1}$, solved using the `HEPM`. a) Sensitivity to number of agents (using 10000 timesteps). b) Sensitivity to number of timesteps (using 1000 agents).

to fallback for too many moves. This result suggest that a value of between 30 and 50 is appropriate and doesn't artificially reduce the number of successful passages. A value of 30 is used in all `FEPM` simulations. The success percentage is approximately independent of `pastColsNumber`. A value of 20 is used in all `FEPM` simulations. The successful passage of agents is heavily dependent on the value of `threshold`, particularly relative to the value of `pastColsNumber`. The larger the `threshold` value, the more likely the individual is falsely classified as "stuck". This is shown by the sharp decline in success percentage for `threshold` values larger than 10. A `threshold` value of 2 is used in all `FEPM` simulations.

3.4 Validation of Connectivity Metrics

This section considers the comparison between each of the proposed metrics with the work of Vowles et al. [2015]. Vowles et al. [2015] assessed the passage of elver of bodylength $0.07173 \pm 0.00387m$ through an eel pass installed at an angle of 11° to the horizontal, and with a discharge per unit width of $3.3\dot{3}\times10^{-3}m^2s^{-1}$. The authors reported an average of 29.9 ± 6.1 passage attempts per trial, with a corresponding average of 20.0 ± 4.6 successful passages per trial. This gives a resulting average passage efficiency of 66.89%. Note that each trial was conducted with 30 agents and therefore the success percentage was 66.67%.

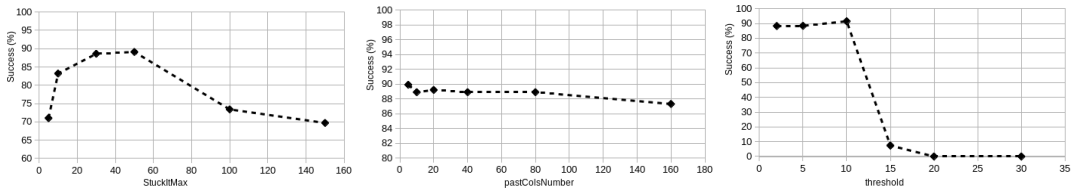

(a) (b) (c)

Figure 3.13: Success percentage for the passage of elver of length $0.07m$ (mean burst speed) through an eel pass inclined at 17° with a discharge per unit width of $5.0\times10^{-3}m^2s^{-1}$, solved using the `FEPM`. a) Sensitivity to the maximum number of timesteps the agent is "stuck" before reverting to normal behaviour `stuckItMax`. b) Sensitivity to number of previous timesteps over which to sample location data, `pastColsNumber` c) Sensitivity to the `threshold` defining whether an individual is stuck, using a `stuckItMax` of 30 and `pastColsNumber` of 20.

Vowles et al. [2015] also report that elvers found more success with ascending the small studs compared to the large studs. The authors reported an average of 12.3 ± 3.47 attempts per trial and an average of 8.3 ± 2.6 successful passes per trial for elvers ascending the large studs. Furthermore, the authors reported an average of 14.1 ± 4.86 attempts per trial and an average of 11.7 ± 2.9 successful passes per trial for those ascending the small studs. This suggests individual passage efficiencies for the large and small studs of 67.48% and 82.98%, respectively. However, Vowles et al. [2015] also report 3.5 ± 1.65 attempts per trial up the "centre" of the pass; with no corresponding successful passes. Given the geometry of the pass, these attempts must be attributed to either the small studs or the large studs, and it is therefore curious that the authors would instead choose to attribute them to the "centre" of the pass. If one were to instead evenly distribute these additional attempts to the large and small studs, the average attempts per trial become 14.05 and 15.85, respectively. This results in reduced passage efficiencies of 59.07% and 73.82% for the large and small studs, respectively.

This study considers only the quantification of the flow field through the small studs and therefore, it is apt to compare each of the connectivity metrics to the reported passage efficiency for the small studs, rather than for the entire eel pass. Table 3.9 shows the calculated connectivity measures for 0.07 m elvers passing the eel tile using the flow rate and installation angle used by Vowles et al. [2015]. For clarity in comparison, the

three measures of the disconnectedness of the domain have been converted to percentage connectedness. Note that $(1-\texttt{DIVISION})\times 100$ is mathematically identical to $(\frac{1}{\texttt{SPLIT}})\times 100$. Furthermore, note that the formulation of the HEPM means that it is inherently creating a heterogeneous population of agents and therefore is not limited to using the 10, 50, or 90% burst speed values.

Table 3.9: Results of each connectivity metric for an eel pass inclined at 11° with a discharge per unit width of $3.3\dot{3}\times10^{-3}m^2s^{-1}$ for passing elver of size 0.07 m, for the 10%, 50%, and 90% burst swim speed values.

	Burst Speed Percentiles		
Connectivity Measure	10%	50%	90%
PLADJ (%)	98.28	98.28	84.41
COHESION (%)	100.00	100.00	98.83
CONTAG (%)	100.00	99.96	21.86
NPP (%)	1	4	1598
DIVISION (%)	0.29	0.29	0.94
SPLIT (%)	1.41	1.41	16.68
$(\frac{1}{\texttt{NPP}})\times 100$ (%)	100.00	25.00	0.06
$(1-\texttt{DIVISION})\times 100$ (%)	71.16	71.16	5.99
$(\frac{1}{\texttt{SPLIT}})\times 100$ (%)	71.16	71.16	5.99
SEPM (%)	100.00	100.00	0.00
FEPM (%)	100.00	100.00	0.00
EEPM (%)	100.00	100.00	0.00
HEPM (%)		75.50	
Vowles et al. [2015] (%)		73.82	

Table 3.9 shows that none of the landscape connectedness metrics score the domain with a value comparable to the findings of Vowles et al. [2015], and neither does the modified NPP metric. The modified version of both the DIVISION and SPLIT metrics offer a value of 71.16% for the 50% burst swim speed, which is fairly comparable to the value found by Vowles et al. [2015]. It was expected that this value would increase for the 10% burst swim speed, but this is not the case, even though the theoretical upper bound of both metrics is 100%. This raises some question of the reliability of

this metric. This result is also seen for the PLADJ metric. However, with the exception of those cases, each of the landscape connectivity metrics generally show the correct trend of increasing connectivity with increasing burst swim speed.

The SEPM, FEPM, and EEPM suggest 100% of individuals with the top 10% and 50% burst speeds could pass, whereas those with a burst speed equal to the top 90% could not pass at all. This suggests that, assuming a heterogeneous population with a Gaussian distribution of burst swim speeds, between 50% and 90% of the population would be able to pass, which agrees with the experimental data. This is further indicated by the result of the HEPM, which shows that 75.50% of a heterogeneous population of $0.07m$ elvers successfully passed the domain. Note that this is using the inverse lognormal distribution shown in figure 3.11. This value compares well to the average value of 73.82% found by Vowles et al. [2015], and gives confidence in the ability of the HEPM in predicting passage success.

When comparing these results, one must consider that the elver populations used by Vowles et al. [2015] are on average larger ($0.07173m$) than those using in the simulations ($0.07m$), and are not uniform in size (standard deviation of $0.00387m$) unlike those used in the simulations. Furthermore, the size distribution of elver used in the experiments was not published, and therefore it is difficult to understand the exact burst swimming capabilities of those elvers. It is also worth considering that the individuals used in the simulations are programmed to have an inherent motivation to navigate upstream; whereas the same cannot be said for individuals in reality. It is unfortunate that more data are not available for comparison and validation of the models and metrics presented here, as this would give more confidence in the validity of the metrics. This highlights the lack of experimental data published in the literature and the significant need for more.

Comparisons between the published data and the outputs of the 10 connectivity measures presented here suggest that the HEPM adequately predicts the percentage of successful passages through the domain as used by Vowles et al. [2015]. This metric is therefore used to explore the passage efficiency of the eel pass geometry for other installation angles and flow rates. Furthermore, each of the other metrics are also applied to the new domains to understand their behaviour and compare the results to those of the HEPM and it is theorised that these connectivity measures may afford simplistic proxies for the passability of a domain after some degree of calibration or

modification.

3.5 Eel Tile Connectivity Results

This section outlines the results of applying the 6 landscape connectivity metrics and the 3 cellular automata to each of the 270 binary maps. For clarity, only the results found for the mean burst swimming speeds are shown. Results for the 90% and 10% confidence intervals of the burst swimming speed can be found in Appendix B. Furthermore, due to the formulation of the agent-based model, `HEPM`, it is not necessary to apply it to the binary maps as the agent population is heterogeneous. Therefore, `HEPM` is applied only to the 90 pre-classified velocity maps.

3.5.1 Landscape Connectivity Results

Figures 3.14, 3.15, and 3.16 show the 6 landscape connectivity metrics for a range of passing elver sizes and for a range of pass installation angles for discharges per unit width of $1.6\dot{7}\times10^{-3}m^2s^{-1}$, $3.3\dot{3}\times10^{-3}m^2s^{-1}$, and $5.0\times10^{-3}m^2s^{-1}$, respectively. These results shown are obtained using only the mean burst swimming speeds for each elver length. The 3 measures of connectedness; `PLADJ`, `COHESION`, and `CONTAG`, each decrease with increasing installation angle and increase with increasing elver bodylength for all discharges (figures 3.14a, 3.14b, 3.14c, 3.15a, 3.15b, 3.15c, 3.16a, 3.16b, and 3.16c). Similarly, the 3 measures of disconnectedness; `NPP`, `DIVISION`, and `SPLIT`, each increase with increasing installation angle and decrease with increasing elver bodylength for all discharges (figures 3.14d, 3.14e, 3.14f, 3.15d, 3.15e, 3.15f, 3.16d, 3.16e, and 3.16f). Furthermore, all connectedness metrics decreased with increasing flow rate and all disconnectedness metrics increased with increasing flow rate. These results show that the landscape connectivity metrics succeed in capturing the correct general trends with regards to increasing elver size, flow rate, and installation angle.

There are however some anomalous results. Figures 3.16a and 3.16c show that, for a discharge per unit width of $5.0\times10^{-3}m^2s^{-1}$, the least connected landscape is for the case of an installation angle of 17° and a passing elver size of 0.05 m, rather than an installation angle of 20°. Similarly, figure 3.16d shows that the installation angle of 17° is found to have a higher number of passable patches for passing 0.05 m elver than an installation angle of 20°, suggesting it is more fragmented.

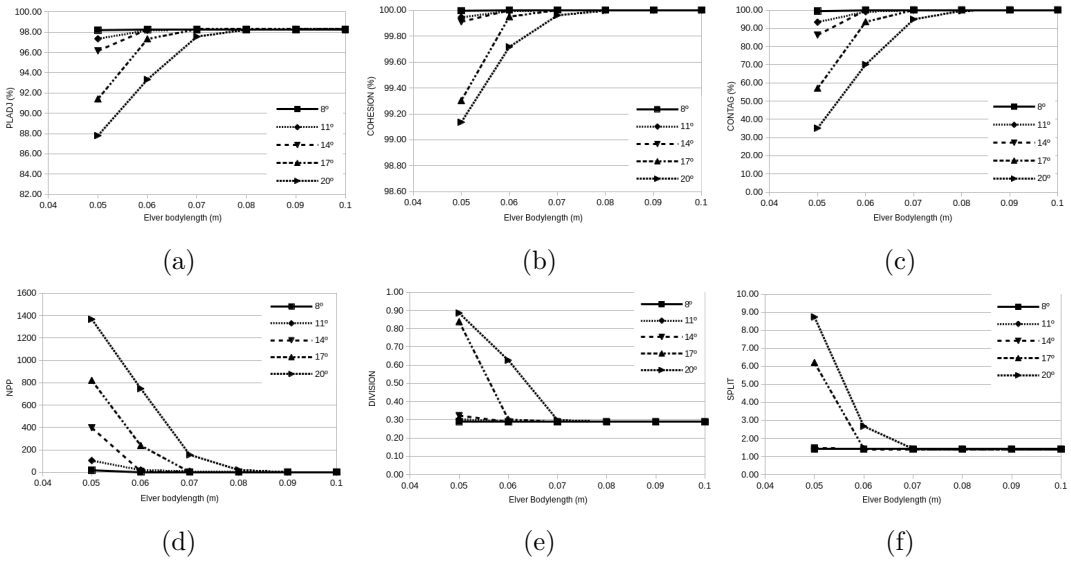

Figure 3.14: Six landscape connectivity metrics applied to an eel pass for five installation angles using a) `PLADJ`, b) `COHESION`, c) `CONTAG`, d) `NPP`, e) `DIVISION`, and f) `SPLIT`. Results shown are for a discharge per unit width of $1.6\dot{7}\times10^{-3}m^2s^{-1}$ and for a range of passing elver sizes, using only the mean burst swimming speeds.

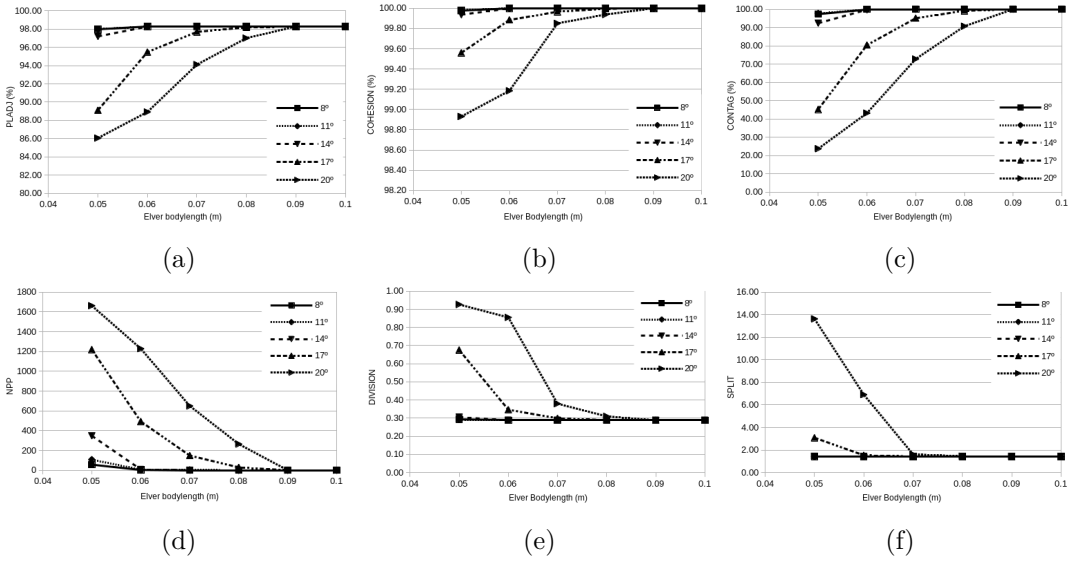

Figure 3.15: Six landscape connectivity metrics applied to an eel pass for five installation angles using a) `PLADJ`, b) `COHESION`, c) `CONTAG`, d) `NPP`, e) `DIVISION`, and f) `SPLIT`. Results shown are for a discharge per unit width of $3.3\dot{3}\times10^{-3}m^2s^{-1}$ and for a range of passing elver sizes, using only the mean burst swimming speeds.

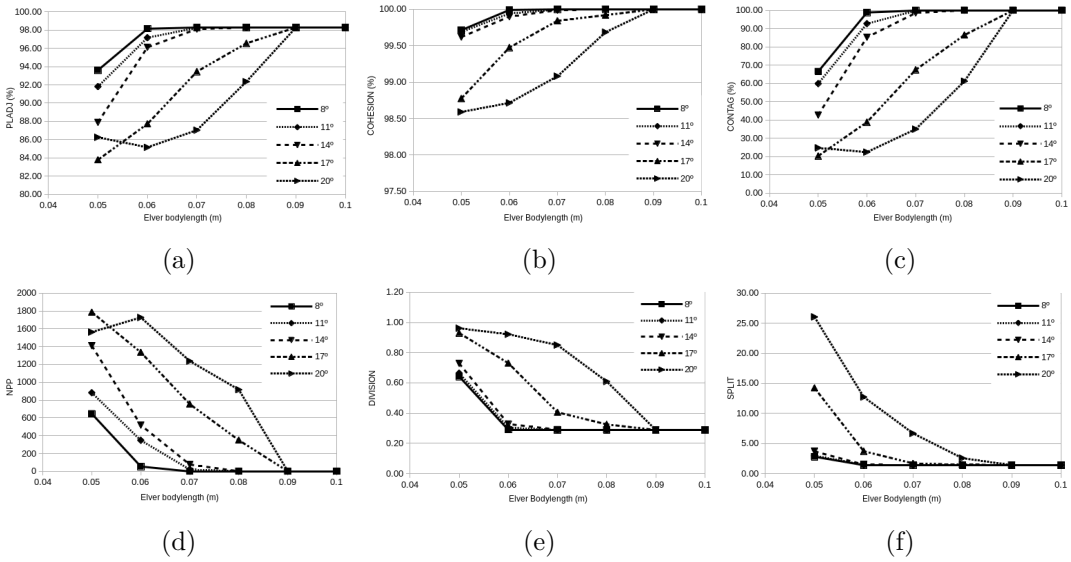

Figure 3.16: Six landscape connectivity metrics applied to an eel pass for five installation angles using a) `PLADJ`, b) `COHESION`, c) `CONTAG`, d) `NPP`, e) `DIVISION`, and f) `SPLIT`. Results shown are for a discharge per unit width of $5.0{\times}10^{-3}m^2s^{-1}$ and for a range of passing elver sizes, using only the mean burst swimming speeds.

3.5.2 Results of Agent-based Models

Figures 3.17, 3.18, and 3.19 show the resulting passage successes for each configuration of eel tile for passing elvers using the mean burst speeds for each length between 0.05 and 0.1 m using `SEPM`, `FEPM`, and `EEPM`, respectively. The results show that each model successfully captures the expected general trends; i.e. passage success increases with increasing elver length, decreasing flow rate, and decreasing installation angle. However, there are a number of unexpected results, such as that shown by figure 3.17a, which suggests that for an elver of 0.05 m, an installation angle of 14° is more passable than one installed at 11°. Similarly, figure 3.17c suggests an installation angle of 11° is more easily passed than one of 8° for an elver length of 0.05 m. Figure 3.20 shows the results of the passability of each configuration of eel tile for elver between 0.05 and 0.1 m solved using the `HEPM`. These results also display the same general trends as shown in the previous figures.

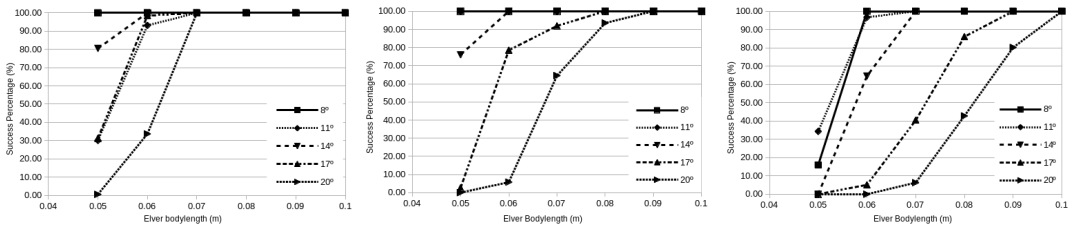

(a) (b) (c)

Figure 3.17: Results of the SEPM applied to 5 installation angles for the passage of elver between 0.05 and 0.1 m using only the mean burst swimming speeds, for discharges per unit width of a) $1.6\dot{7}\times10^{-3}m^2s^{-1}$, b) $3.3\dot{3}\times10^{-3}m^2s^{-1}$, and c) $5.0\times10^{-3}m^2s^{-1}$.

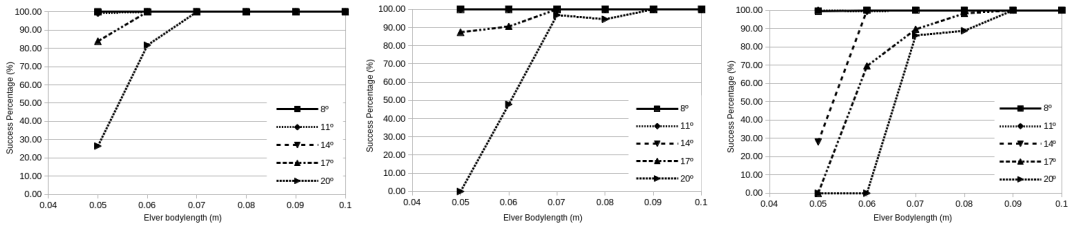

(a) (b) (c)

Figure 3.18: Results of the FEPM applied to five installation angles for the passage of elver between 0.05 and 0.1 m using only the mean burst swimming speeds, for discharges per unit width of a) $1.6\dot{7}\times10^{-3}m^2s^{-1}$, b) $3.3\dot{3}\times10^{-3}m^2s^{-1}$, and c) $5.0\times10^{-3}m^2s^{-1}$.

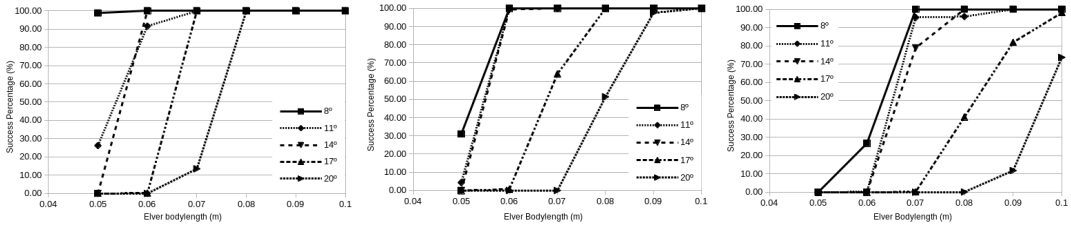

(a) (b) (c)

Figure 3.19: Results of the EEPM applied to five installation angles for the passage of elver between 0.05 and 0.1 m using only the mean burst swimming speeds, for discharges per unit width of a) $1.6\dot{7}\times10^{-3}m^2s^{-1}$, b) $3.3\dot{3}\times10^{-3}m^2s^{-1}$, and c) $5.0\times10^{-3}m^2s^{-1}$.

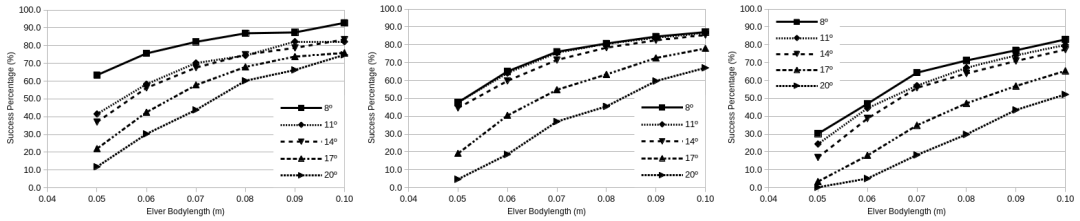

(a) (b) (c)

Figure 3.20: Results of the HEPM applied to five installation angles for the passage of elver between 0.05 and 0.1 m, for discharges per unit width of a) $1.6\dot{7}\times10^{-3}m^2s^{-1}$, b) $3.3\dot{3}\times10^{-3}m^2s^{-1}$, and c) $5.0\times10^{-3}m^2s^{-1}$.

3.6 Discussion

This study is the first to attempt to computationally assess the upstream passability of eel tiles for juvenile European eels. The results of the CFD show agreement with mean velocities and flow depths reported by Vowles et al. [2015] and therefore show promise in simulating the flow patterns through eel tiles. No previous studies have quantified the detailed flow fields within eel tiles and therefore it is difficult to thoroughly validate small-scale flow features. However, the k–ω SST model has been shown to give good predictions of the free surface location and velocity field around a series of semi-submerged cylinders [Ducrocq et al., 2017, Chorda et al., 2019]. More accurate results could be produced using Reynolds stress models, LES, or DNS [see Benhamadouche and Laurence 2003] but these models introduce significant computational cost and associated convergence issues [Ingham and Ma, 2005] and this level of complexity is not required as eels and elvers react to larger-scale flow structures [Piper et al., 2012, 2015]. Furthermore, the influence of any finer-scale turbulent structures yielded by the more complex models would be dampened by the temporal averaging required to create input datasets for the CA and agent-based models.

Two dimensional planes parallel to the bed offset at a distance of 3 mm were extracted from the computed velocity fields for each configuration of eel pass. This was done as the landscape connectivity metrics are only applicable to spatially two dimensional data. This also simplified the development of the cellular automata and agent-based models. Furthermore, the extracted spatially two dimensional velocity fields were temporally-averaged over a 2 second time period from 8 to 10 seconds

of flow time. As no previous studies have quantified the detailed flow fields within eel tiles, it is difficult to know whether this time period is sufficient to capture the unsteady features of the flow. However, this time period was chosen to maximum the time over which the data were averaged, but was limited by computational restrictions and digital storage restrictions. The resulting velocity fields are simple representations of the complex fluid flow within an eel pass. However, they allow for the assessment of passage efficiencies using relatively simple metrics and without requiring the use of live animals. Extending the domains to spatially 3D and transient would better represent the fluid environment within the domain, but would vastly increase the complexity of the CFD, cellular automata and agent-based models, and would restrict the usage of the landscape ecology metrics.

The work presented in this chapter investigates the influence of discharge per unit width, installation angle, and fish length on the passage efficiency of eel tiles and suggests that passability decreases for increasing discharge and installation angle; a result which corroborates previous research [Solomon and Beach, 2004]. This result is expected as the ability to successfully pass is intrinsically-linked to the water velocity within the pass, which increases with flow rate and installation angle. This result provides some evidence that all the metrics are performing sensibly.

3.6.1 Discussion of Landscape Metrics

The landscape connectivity metrics all show the expected general trends; e.g. increasing connectivity for increasing elver length, decreasing installation angle, and decreasing flow rate. However, it is unlikely that the metrics in their current state offer any practical results that can be used by practitioners. Furthermore, each of the landscape connectivity metrics suffer from an inability to assess whether a given domain contains a fully connected pathway from the downstream-most end to the upstream end. This is due to the fact that the landscape metrics are by definition assessing the aggregation of the passable regions, and do not consider pathways. This can be somewhat combated by dividing the chosen connectivity metric by the corresponding `NPP` value, as we can assume that low values of `NPP` reflect a less fractured domain and therefore a greater chance of a continuous pathway through the domain. Furthermore, each of the landscape metrics are very sensitive to the defined swimming ability for the given size used to create the classified domains. This could be overcome by assessing multiple classified

domains for any given elver length, where each domain is classified relative to a percentage of the range of the minimum and maximum burst swimming ability for the chosen elver length. A weighted average of these can be calculated based on the frequency of occurrence of the given burst swim ability within a heterogeneous population. This is beyond the scope of this work but does highlight the potential for landscape ecology metrics to be used as simplistic proxies, particularly if they can be calibrated against experimental data. This is not explored here as the available experimental data are not sufficient to adequately calibrate any of the landscape metrics.

3.6.2 Discussion of Cellular Automata and Agent-based Models

The `SEPM` over-predicted the passage efficiency for the Vowles et al. [2015] case, but did succeed in demonstrating realistic trends for the passage of elvers over all configurations of eel pass (figure 3.17). However, there are a number of unexpected results which suggest that higher installation angles provide a more easily passed domain [see figure 3.17a and 3.17c]. These results are likely a flaw with the `SEPM` methodology rather than a realistic result or a flaw in the CFD methodology as they are not reflected in the results of any of the other models. A comparison between `SEPM` and `FEPM` shows that the passability increases for all configurations and elver lengths when the agents are allowed to fallback and make multiple attempts [see figures 3.17 and 3.18]. However, the rule is heavily dependent on the values of `pastColNumber`, `threshold`, and `stuckItMax` each of which, while investigated in a sensitivity analysis, are difficult to justify from an ecological perspective. Furthermore, it is thought that in reality, if an elver became stuck during an ascent within an eel pass, it is likely to be washed downstream and out of the pass and then begin again at the downstream-most end of the pass [Bolland, 2018]. Therefore, the `FEPM` attempts to model an unnecessary behaviour, resulting in an artificial increase in the passage efficiency of each pass configuration. In comparing `SEPM` to `EEPM` it is seen that, for all pass configurations and elver lengths, the passability decreases when the exhaustion model is implemented. For example, the `SEPM` predicted a passage efficiency of 78.5% for elver of 0.06 m navigating an eel pass installed at 17° with a discharge per unit width of $3.3\dot{3}\times10^{-3}m^2s^{-1}$, figure 3.17b, whereas this the `EEPM` predicts a value of 0% for the same case. This suggests that even with relatively shallow installation angles (17°) and a relatively short length of pass (1.25 m), elvers are becoming exhausted due to the water velocities that they encounter within the

pass. This demonstrates the importance of passage duration and length in controlling passage efficiency and supports the statement of Solomon and Beach, 2004, p. 12 that "...we must take account not just of maximum swimming speed, but also of the ability to maintain certain swimming speeds for long enough to ascend a pass that may be many metres in length".

The `SEPM`, `FEPM`, and `EEPM` are very sensitive to the defined swimming ability of the agents used to classify the domains. Each of these agent-based models simulate an homogeneous population of elvers. This results in polarised results (i.e. close to zero or close to 100% successful passages) since it is likely that it one automaton can pass, all can pass and vice versa. This is overcome by the formulation of `HEPM` which captures the natural variation in the swimming performance of elvers of the same length, i.e. introduces heterogeneity. A comparison of the results of the `EEPM` and the `HEPM` shows that introducing the heterogeneous population produces consistently less extreme results for all elver lengths and configurations. Furthermore, the `HEPM` produces a result within 2.5% of that found by Vowles et al. [2015], which gives confidence to the findings. It would be interesting to compare the results of the `HEPM` against experimental data for other installation angles and discharges, but this is not possible due to a lack of experimental data.

A comparison of figures 3.20a and 3.20b shows that the `HEPM` predicts that for installation angles of 11° and 14°, reducing the discharge per unit width from $3.3\dot{3}\times10^{-3}m^2s^{-1}$ to $1.6\dot{7}\times10^{-3}m^2s^{-1}$ creates a marginally less passable domain for all lengths of elvers. However this is not found to be true for the other 3 installation angles, figure 3.21. These results may be indicative of an insufficient time period over which the CFD results were temporally-averaged, which could be overcome through averaging over a longer time period.

The cellular automata and agent-based models are limited as none of them account for many other factors important in successful passage such as predation within the pass or the ability for elver to locate the pass within a timely manner [Environment Agency, 2011]. Furthermore, each of the models assume all elvers are inherently motivated to ascend the pass; a variable which is difficult to quantify in practice. Furthermore, as the considered elver are less than 0.1 m in length, it is possible that they could exhibit climbing behaviour within the pass [Legault, 1988]. Similarly, eels of all sizes are known to exhibit crawling behaviour to utilise low velocity regions, allowing for

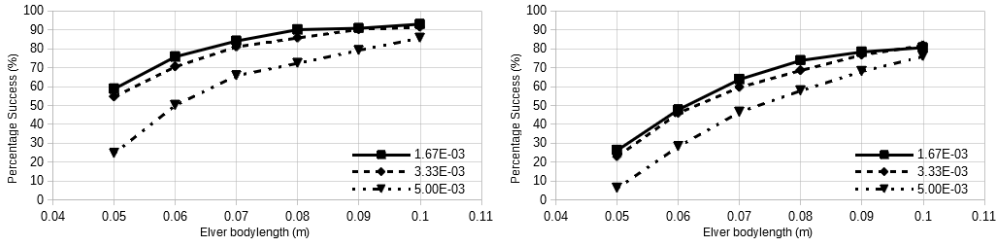

(a) (b)

Figure 3.21: Comparison of passage efficiency through an eel pass installed at a) 14° and b) 17° over a range of elver bodylengths (m) and flow rates per unit width (m^2s^{-1}). Solved using the `HEPM`.

respite from the main flow. However, Vowles et al. [2015] reported that while they expected to see these behaviours, elvers opted not to do this and instead attempted to ascend the eel tiles as quickly as possible using their burst swimming capabilities. Therefore, climbing was not implemented in any of the models. However, this remains an avenue for research, but is not considered in this work. Podgorniak et al. [2015a,b] suggest that, during climbing, cognitive processes are more important in the passage of obstacle by eels than metabolic capacities. Similarly, Podgorniak et al. [2016] suggested that climbing elver display inherent "personality types", and that those that displayed the best climbing ability tended to be of a more aggressive "personality". Therefore, if climbing behaviour were to be added to the model, an implementation of variable motivation may be necessary, such as that used by Gisen 2018, which could be a function of additional heterogeneity in the form of random, inherent "personalities" or an "aggression" factor.

Regardless of these limitations, the results show that the CA and AB models are better measures of passability than the landscape connectivity metrics, due in part to their inherent ability to overcome the issue of finding a continuous pathway through the domain. Furthermore, the results presented herein show that even the simple cellular automata models are able to output realistic data and trends and the ABM (`HEPM`) results compare favourably to the result found by Vowles et al. [2015]. This suggests that, even given their limitations and simplistic formulation, 2D cellular automata and agent-based models are well-suited to assessing the passage efficiency of fish passes.

3.6.3 Theoretical Maximum Passage Lengths

Although each eel tile configuration considered in this chapter are of equal length (1.25m), it is possible to estimate the maximum length of pass possible for an individual to successfully ascend for each configuration. This is done by using the time taken to ascend the 1.25 metre pass of the given configuration and the knowledge that the burst speed of an individual can only be maintained for 20 seconds. In addition, one must assume that the flow velocities and depths do not vary significantly along the pass.

The results of the `HEPM` are summarised within graphs of pass length against installation angle for three lengths of elvers; $0.05m$, $0.07m$, and $0.09m$, figure 3.22. These data are presented in the hopes of assisting practitioners with developing improved eel pass designs. For example, for a given eel pass installation angle and a chosen passage efficiency, a practitioner can select a pass length and read off the maximum permissible discharge per unit width that elvers of the target length can tolerate. Furthermore, for a length of eel pass and a chosen installation angle, a practitioner can estimate the likely passage efficiencies resulting from an imposed range of discharges per unit width or flow depths at the eel pass entrance. It is worth noting however, that given elvers are able to employ climbing when it is not possible for them to ascend a pass using anguilliform swimming alone, the passage efficiencies presented here are conservative estimates. Conversely, the burst swimming speeds of elvers utilised in this chapter are extracted from the SWIMIT software using the "spring" seasonal setting, which was found to yield values approximately twice that of the "summer/autumn" setting [Clough and Turnpenny, 2001]. This suggests that these estimated passage efficiencies will be significantly lower during summer and autumn. Furthermore, the effect of temperature on the burst swimming speed of elvers is not clear in the literature. Lee et al. [2003] found that the burst swimming speed of sockeye salmon (*Oncorhynchus nerka*) against temperature follows an "inverted-U-shape", where the burst speed increased with temperature to a maximum at approximately $16°C$, followed by a steady decline. Therefore, this suggests that the simplistic seasonal setting available within SWIMIT may not be sufficient to accurately capture the role of temperature in determining passage efficiency.

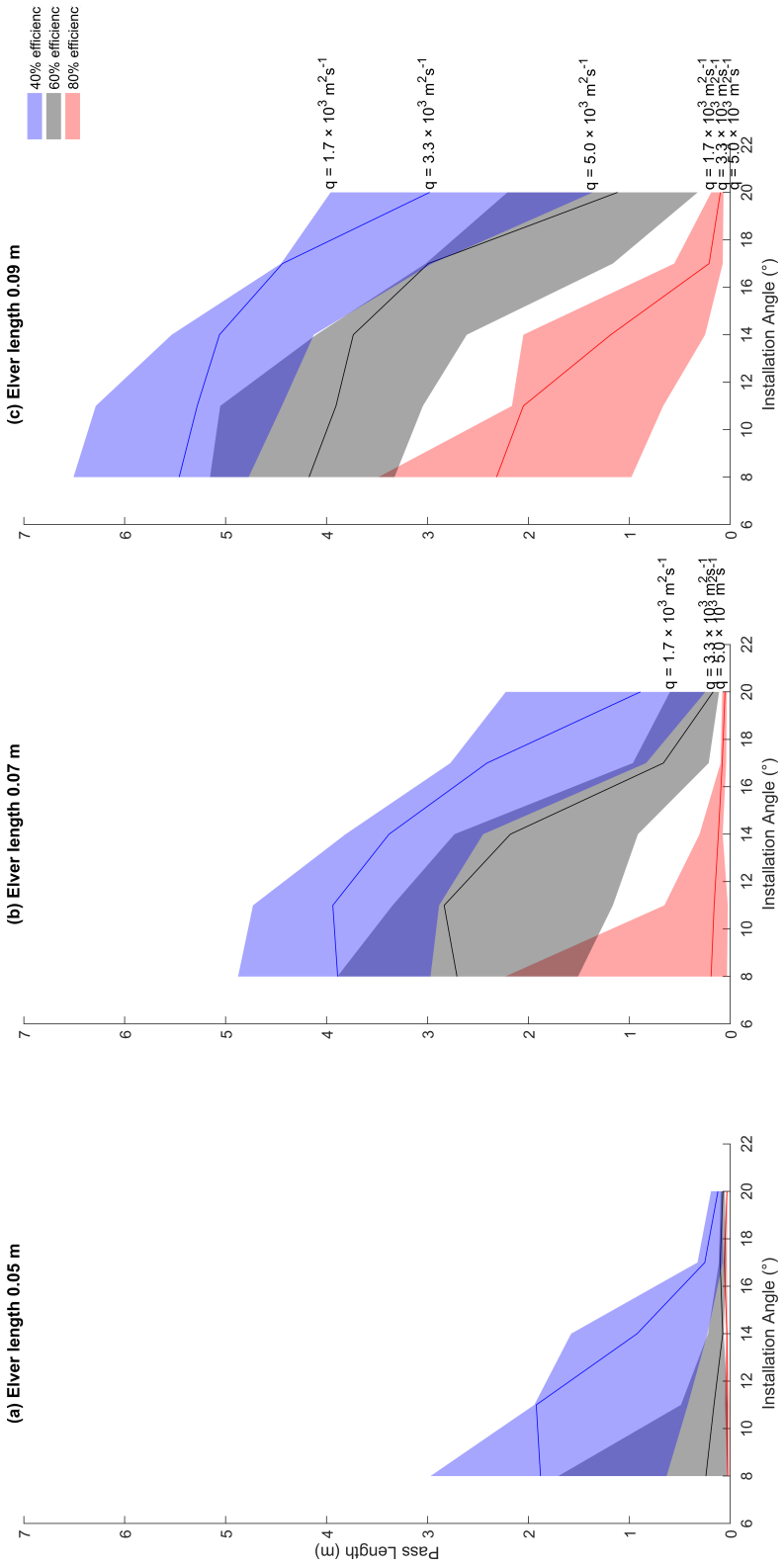

Figure 3.22: Plots of pass length against installation angle at 40%, 60%, and 80% passage efficiencies for elvers of length 0.05 m, 0.07 m, and 0.09 m for discharges per unit width of 1.67×10^{-3} m^2s^{-1}, 3.33×10^{-3} m^2s^{-1}, and 5.00×10^{-3} m^2s^{-1}.

3.6.4 Comparison to Current Guidelines

Although the models herein are simple their outputs compare well to experimental data. Extending the models to other eel tile configurations give insight into the installation of eel tiles, which can be compared to current guidelines. Guidance on the design and implementation of eel and elver passes in the UK is provided by Solomon and Beach [2004]. The authors note that the installation angle of a pass depends upon the chosen pass substrate, and ranges from 10° to 55°. However, they do not recommend specific angles for each substrate [Solomon and Beach, 2004]. Some examples of successful passages are presented, including some installed between 40° and 52°. However, only the raw number of successful passages is reported, rather than a measure of the efficiency, meaning that the passes may not be as successful as they seem. This lack of data is likely due to the impracticality of accurately measuring failed passages. Furthermore, the bodylengths of the passing eels are not divulged and therefore comparisons to the results found in this study aren't appropriate. The results found in this study show that for all bodylengths and flow rates, the success percentage decreases with increasing installation angle. Interestingly, for an angle of 20°, the `HEPM` suggests a passage efficiency of less than 15% for 0.05 m elver, regardless of discharge, which one can assume will only decrease further with increasing angle.

Solomon and Beach [2004] also suggest that the appropriate length of an eel pass is entirely governed by the hydraulic head that must be overcome and the chosen installation angle. Furthermore, the authors note that resting places are often incorporated into passes, but no investigations studying their effectiveness were identified [Solomon and Beach, 2004]. The exhaustion of the passing eels is not explicitly discussed. However, in the agent-based models, the exhaustion of passing elvers significantly reduces the number of successful passages for all configuration of pass [see figures 3.17 and 3.19]. This would only be exacerbated by an increase in pass length for similar flow rates and installation angles as the passing eels would have to combat potentially higher velocities over a prolonged time period. Therefore the length of a pass, or at the very least the length of pass between two resting pools, should be governed in part by the swimming ability of the passing eels. Furthermore, as the swimming ability of eels is intrinsically linked to their bodylength, the design of an eel pass should be dictated by the bodylength (and hence life-stage) of the target eels. The life-stage of the expected up-migrating eels is related to the geographical location of the pass and its proximity

to the ocean.

These considerations are not currently covered by UK guidance. It is proposed that current UK guidance should be modified to explicitly refer to the expected minimum bodylength (earliest life-stage) of the passing eels when discussing installation angle of passes. Additionally, the exhaustion of passing eels should be explicitly considered when discussing both installation angle and pass length. Furthermore, more work is needed to understand the impact of installation angle, flow rate, and length on the passage efficiency of eel passes for a range of eel bodylengths.

3.7 Conclusion

The work presented in this chapter has succeeded in computationally assessing the velocity fields in a variety of configurations of eel pass, consisting of eel tiles manufactured by Berry & Escott Engineering [2017]. Furthermore, the effects of varying installation angle and flow rate on the passage efficiency of each pass configuration was explored through the use of landscape connectivity metrics and custom cellular automata and agent-based models. All metrics showed realistic results with passage efficiency decreasing due to the increase in velocity resulting from increased installation angle and discharge. The landscape connectivity metrics succeeded in capturing general trends in passage efficiency, but all compared relatively poorly against the Vowles et al. [2015] result with the possible exception of $(1 - \texttt{DIVISION}) \times 100$. All of the landscape connectivity metrics suffered from an inability to discern between a pass with a fully passable pathway from inlet to outlet, and one without. The cellular automata and agent-based models inherently overcome this problem. Each of the four models produced realistic trends, such as decreasing passage with increasing discharge, with the more complex `HEPM` comparing very well to the available experimental data for the configuration used by Vowles et al. [2015].

This chapter has shown that landscape ecology metrics, when coupled with CFD, have the potential to be used as simple proxies of passability, but require significant modification and calibration such as that suggested in section 3.6.1; which is severely limited by a lack of experimental data. The work presented here also shows that applying even simple cellular automata and agent-based models to complex ecohydraulic systems can result in realistic behaviours and trends. Furthermore, the `HEPM`, the most complex of the models presented, was able to predict successful passage to within 2.5%

of experimental data. This result was achieved as each model was tailored to this exact domain and target species. This methodology is evidently capable of yielding accurate results. However, it does not meet the overall aim of this research, outlined by the principles given in section 1.2, namely the development of a generalised tool for practitioners to assess passage efficiencies [see table 3.10]. To achieve this, the model must not be tailored to a specific problem geometry, nor hard-coded for a specific species. In addition, it should be extended to be spatially 3D in order to ensure it can be applied to any ecohydaulic domain.

Table 3.10: A comparison of the eel CA/IB models and the established tool developmental principles.

No.	Principle	Achieved
1	Open source	Each of the agent-based models were built using Python 3.6 and are freely downloadable from the University of Leeds Data Repository [Padgett and Thomas, 2019]. Each model requires an input velocity field in the form of an ascii file and is therefore not limited to a specific CFD software.
2	Transparent	The work presented herein is published in Royal Society Open Science [Padgett et al., 2020] and the associated data from the paper; including the simulated flow fields, the `HEPM`, and the `FEPM`, are openly available from the University of Leeds Data Repository [Padgett and Thomas, 2019]
3	Generalised	Each of the agent-based models described in this chapter are built specifically for the flow fields presented herein. Therefore none of the models are generalised.
4	Spatially 3D	As the models require on input 2D flow fields, movement in depth in not considered. Therefore, none of the models are spatially 3D.
5	Self-contained	Each of the models are built solely within Python 3.6 and do not require any additional software. Furthermore, the only required Python packages are: `numpy`, `random`, and `csv`.
6	Modular	The `HEPM` is the only ABM presented herein which models elver as a Python class in their own right. This partially covers the modular requirement as further classes could be added to introduce other species to the code. However, the code would still require extensive modification as elvers are assumed to be the passing species in the definition of various other parameters.
7	Individual Focus	The `HEPM` is the only ABM presented herein which includes any amount of heterogeneity within the population.

Chapter 4

Development of `fishPy`, A Three Dimensional Agent-based Model for the Upstream Movement of Salmonidae

4.1 Introduction

The work in chapter 3 demonstrated the potential of cellular automata and agent-based models applied to up-migrating juvenile eels through a specific ecohydraulic environment. In order to address all of the outlined tool principles these models need to be extended to a generalised tool. However, this is difficult for cellular automata and individual based models due to their simplicity and focus on populations rather than individuals (macroscale versus microscale). Therefore, a new model is required, which models each individual as this will allow for a complex ruleset, more agent autonomy and heterogeneity, and a true decision-making framework. To validate such a model requires data on the movement of individual fish, with a high spatio-temporal resolution. Data of this type and quality are sparse across species, but non-existent for eels. Therefore, the current chapter and subsequent chapters consider a different species.

The salmonid family are commercially significant. Furthermore, salmonidae are anadromous and therefore their successful up-migration is vital to their sustained population. This makes them a family of interest. Due to this, various studies have been undertaken to understand their biology and lifecycle [e.g. Mills 1989, Crisp 2008, and Quinn 2018]. Although sparse, data exists on the trajectory of individual salmonids, particularly brown trout (*Salmo trutta*) [e.g. Rodriguez et al. 2011 and Dodd et al. 2018]. Together, this means agent-based modelling is a viable approach to understanding the up-migration pathways for this species. There are multiple agent-based models of fish in the literature, including the well-established NFS model [Goodwin et al., 2014]. However, there is currently no model in the literature which meets the aim of this work, and therefore there remains a gap in the literature [see section 2.8].

This chapter presents the development of an open-source model to predict the up-migration pathways of brown trout (*Salmo trutta*), due to availability of validation data. The model predicts vector-based trajectories of individual, heterogeneous fish in continuous three-dimensional space, based on individual responses to stimuli from their local environment. The hydrodynamic environment in which agents exist is defined by multiple three-dimensional matrices defining all *a priori* data fields, such as velocity, pressure, and geometric data. These matrices are populated through the execution and subsequent interpolation of three-dimensional computational fluid dynamics. It is hoped that the model will enable practitioners and designers to optimise fish passage facilities and reduce the need for invasive physical experiments.

4.1.1 Chapter Aim

The aim of this chapter is to develop an open-source agent-based model to predict upstream migration trajectories of brown trout, henceforth referred to as `fishPy`. This model is developed with significant consideration of the developmental tool principles, outlined in section 1.2. The model considers the response of an individual to hydrodynamic stimuli, and how these responses can be decoded into a ruleset. This is achieved through a number of objectives outlined below:

- Application of the agent-based modelling approach to predicting fish trajectories. This is broken down into the following steps:
  - Determination of key hydrodynamic stimuli through a thorough review of the literature;
  - Determination of the approach to representing the environment;
  - Definition of key attributes for representing an individual as an agent;
  - Determination of the model structure by combining the agent and environment representations; and
  - Determination of maximum timestep.
- Creation of a model to understand energy expenditure of each individual.
- Creation of a model to understand the effect of the swim bladder on the trajectory of an individual.
- Determination of a behavioural ruleset based on defined key hydrodynamic stimuli.

4.2 Potential Hydraulic Stimuli

As discussed in section 2.7, there have been many studies on the effects of hydrodynamic stimuli on fish behaviour. The key hydrodynamic stimuli, their impact, and the study sources are summarised in table 4.1, along with the relevant `fishPy` rule and subsection corresponding to each stimulus.

In addition to the stimuli outlined in table 4.1, Duarte et al. [2012] suggest movement choices of neotropical fishes (*Leporinus reinhardti* and *Pimelodus maculatus*)

through a vertical slot fish-way strongly correlate to the local Reynolds shear stress. Duarte et al. [2012] found that both species preferred regions of "low to zero" Reynolds shear stress. However, a definition of "low to zero" is not given by Duarte et al. [2012]. A similar study for salmonidae was not found, although Odeh et al. [2002] reported that Reynolds shear stress value above 50 Nm^{-2} can cause injury to migrating salmonidae. Interesting Duarte et al. [2012] also note that the movement choices of both species of neotropical fish, coincide with regions of "low to zero" streamwise and cross-stream velocity fluctuations. One can also assume that these regions also feature "low to zero" turbulence kinetic energy, given its definition [see section 2.5.5]. Therefore, Reynolds shear stress is not explicitly included in the `fishPy` model, but rather implicitly included through the inclusion of the velocity fluctuations within the turbulence kinetic energy, as well as inclusion of the spatial velocity gradients within the `minMaxEnergy` rule.

4.3 Agent-based Approach to Modelling Fish Behaviour

An agent-based model has two constituent components; agents and an environment [Macal and North, 2010]. Agents are heterogeneous, autonomous entities capable of collecting and processing information and subsequently capable of making and executing decisions. Therefore, `fishPy` is developed with an emphasis on modelling from the point of view of the individual in question. Agents exist within an environment that provides data to the agent and with which the agents can interact [Crooks and Heppenstall, 2012]. In `fishPy`, the model is formulated with individual fish representing the model agents. These individuals interact with each other as well as their environment. In `fishPy`, the environment is represented as a spatially three-dimensional discrete grid where each grid point contains local hydraulic and environmental information.

Any fauna existing within a hydrodynamic environment exerts a force upon the environment during locomotion; thereby changing the hydrodynamic environment with every movement [Montgomery et al., 1995]. It was decided that `fishPy` would not be coupled with CFD; i.e. the codes would execute serially. This means that the fish have no effect upon the hydrodynamic environment. This drastically simplifies the development of the model and does not limit its usage to a single software, solver, or turbulence model. Furthermore, this decision allows the required environment to be constructed using experimental data in place of a CFD output.

Table 4.1: Identified key hydraulic stimuli and their corresponding `fishPy` rule.

Stimulus	Findings	Sources	Rule/Function	Section
Mean Velocity	Provides directional information (attraction flow) and governs rheotaxis response (direction).	Coutant [1998] Montgomery et al. [1997]	`followFlow` `calcHeading`	4.6.1 4.6.8
Mean Velocity	Governs hydrodynamic resistance.	Khan [2006] Blank [2008]	`deterResponse` `calcMoveMakeMove`	4.6.10
Local Velocity	Fish preference for minimum drag and/or minimum energy pathways.	Kerr et al. [2016] Tullos and Walter [2015] Smith et al. [2005] Blank [2008] Abdelaziz [2013] Plymesser [2014]	`minMaxEnergy`	4.6.2
Local Velocity	Fish require attraction flow to locate fish passes.	Armstrong et al. [2010]	`minMaxEnergy`	4.6.2
Local Velocity	Salmonidae attracted to higher velocities when up-migrating and down-migrating.	Gisen [2018] Goodwin et al. [2014]	`minMaxEnergy`	4.6.2
Turbulence Kinetic Energy	Brown trout chose regions with lower TKE in a flume environment.	Smith et al. [2005]	`tkeAvoidance`	4.6.7
Turbulence Kinetic Energy	Trout and carp tended to prefer regions with TKE within the ranges of 0.1 to 0.35 m^2s^{-2} and 0.02 to 0.035 m^2s^{-2} when passing a vertical slot fishway, respectively.	Gao et al. [2016] Tan et al. [2018]	`tkeAvoidance`	4.6.7
Spatial Velocity Gradients	Juvenile down-migrating fish preferred regions with hydraulic strain between an upper and lower limit.	Goodwin et al. [2014] Abdelaziz [2013]	`minMaxEnergy`	4.6.2

4.3.1 Representing the Environment

Within `fishPy`, the environment is represented as a spatially three-dimensional discrete grid where each grid point contains local hydraulic and environmental information. These hydraulic and environmental parameters are required user inputs. The required variables are listed in table 4.2. As `fishPy` is executed independently, the environment data can come from any source; i.e. any solver, any turbulence model, or even experimental methods. This is done for flexibility of the user. Similarly, the model does not prescribe a spatial resolution of the input environment data. This is done to allow greater freedom to the user. However, the user should be aware that, much like any model, the models outputs rely upon its inputs. That is to say that a poor quality input will produce a poor quality output. A study of the dependence of simulated fish trajectories on the grid resolution of the environment is given in section 5.5.

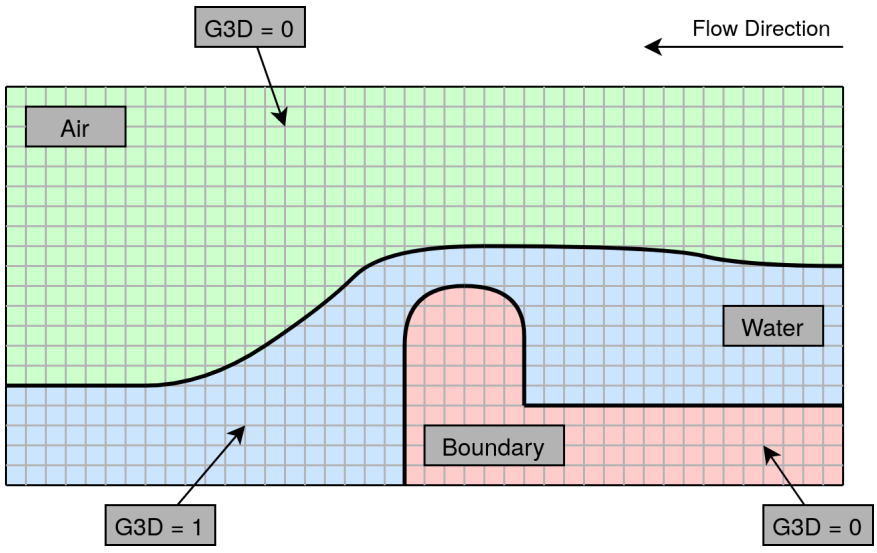

Figure 4.1: Schematic depicting 2D flow over an object, demonstrating the formulation of the `G3D` matrix, denoted by the overlain grey grid. The red and green areas denote the boundary and air, respectively, which fish can never enter and therefore `G3D` = 0 for these nodes. The blue area denotes the water and therefore `G3D` = 1 for these nodes.

The geometry of the domain is handled by the "passability" matrix, termed `G3D`, figure 4.1. This matrix is a series of Boolean values that describes whether the corresponding spatial node is passable (value = 1) or impassable (value = 0) to an individual.

For example, a node that exists above the free surface (i.e. $\alpha < 0.5$ if VOF is used) would be impassable. Similarly, a node outside of the domain would be impassable. This method allows for domains with complex geometries to be modelled simply.

Table 4.2: Required environment inputs for `fishPy`.

Name	Information	Format	Units
`sp`	Spatial resolution	Float	m
`nx`	Num. of points (X)	Integer	n/a
`ny`	Num. of points (Y)	Integer	n/a
`nz`	Num. of points (Z)	Integer	n/a
`X3D`	Location (X)	Matrix [nx,ny,nz], float	m
`Y3D`	Location (Y)	Matrix [nx,ny,nz], float	m
`Z3D`	Location (Z)	Matrix [nx,ny,nz], float	m
`U3D`	Avg. Velocity (X)	Matrix [nx,ny,nz], float	ms^{-1}
`V3D`	Avg. Velocity (Y)	Matrix [nx,ny,nz], float	ms^{-1}
`W3D`	Avg. Velocity (Z)	Matrix [nx,ny,nz], float	ms^{-1}
`P3D`	Avg. Pressure	Matrix [nx,ny,nz], float	Pa
`K3D`	Turbulence Kinetic Energy	Matrix [nx,ny,nz], float	m^2s^{-2}
`G3D`	Geometric Data	Matrix [nx,ny,nz], Boolean	n/a

Hydrodynamic fauna exist within a temporally-dependent environment wherein their local hydrodynamics are constantly varying. However, `fishPy` is built only to function with temporally-averaged environment data. This is to simplify the model and its input requirements, and to avoid the possibility of temporally-dependent fish trajectories; where individuals perform differently depending on their start time. Similarly, a temporally-varying environment would introduce issues of temporal resolution dependency. Furthermore, the required total time for the input environment data would depend upon the passage time of the slowest individual. Therefore, investigations would require a certain amount of guesswork to determine the total time and temporal resolution required for the desired domain. Therefore, a core assumption of this work is that a temporal changes in the hydraulic passage environment are not significant to influencing fish behaviour and that a temporally-averaged hydraulic environment provides sufficient information to determine fish movement decisions. This assumption is significant but necessary, due to the complications outlined above, and is an area of research which could be pursued in the future, but is outside the scope of this work.

4.3.2 Representing Fish as Agents

Within `fishPy`, individual fish are represented as agents. These are self-contained, heterogeneous, autonomous entities that interact with their environment and make decisions based on internal rules. In this work, these agents have a number of internal states, or attributes, which define them, table 4.3. Individuals are assigned attributes upon creation. Some attributes vary throughout the simulation, such as location and heading; whereas others are fixed throughout, such as bodylength. Many of these attributes rely upon user inputs, therefore the required non-environment user inputs are detailed in table 4.4. Simulated trajectory dependency on `fishTimestep` and `sensoryRange` are given in section 5.5.

The `fishNum` variable is used to define the size of the simulated population. The `bodylength_mean` and `bodylength_deviation` variables define the normal distribution of bodylengths for the population. Upon creation, each individual is assigned a number of attributes. Firstly, it is given an identification number. It is then assigned a location, which defines `x`,`y`,`z`, and `coordsCentroid`. The method used to determine where an individual is created is discussed in section 4.3.4. The initial heading of the individual is calculated as the opposite direction to the local velocity vector at the location the individual is created. This is done to simulate rheotaxis. The heading in subsequent timesteps is defined following the method in section 4.6.8.

Each individual is also assigned a `bodylength` randomly taken from the normal distribution of the bodylengths of the population. The `bodywidth` and `bodyheight` of the individual are calculated based on the work of Tonkin et al. [2013], equations 4.1 and 4.2, respectively. These values are used to model the physical size of the individual.

$$W = 0.08571 \times L + 1.42885 \times 10^{-3} \tag{4.1}$$

$$H = 0.21875 \times L - 1.875 \times 10^{-3} \tag{4.2}$$

where: W is the `bodywidth` of the individual in m; L is the `bodylength` of the individual in m; and H is the `bodyheight` of the individual in m.

The wetted area (or surface area) of the individual is calculated based on the work of Haefner and Bowen [2002], equation 4.3. This value is used to estimate the drag experienced by the individual, discussed in section 4.4.

$$A_s = \alpha L^{\beta} \tag{4.3}$$

where: A_s is the wetted area of the individual in m; and α and β are empirically derived constants equal to 0.465 and 2.11, respectively.

Lastly, the individual is assigned a mass based on the work of Milewski and Brown [1994], equation 4.4. Milewski and Brown [1994] report that the relationship is acceptable for brown trout of length $> 150mm$. This value is used to approximate buoyancy effects, discussed in section 4.5.

$$M = 10^{-4.867+2.96 \log L} \tag{4.4}$$

where: M is the mass of the fish in grams; and L is the `bodylength` of the fish in mm.

As individuals are not infinitesimal points, it is important to model their physical size. Once the `bodylength`, `bodywidth`, and `bodyheight` of the individual are calculated the full physical extent of the individual is calculated, figure 4.2. This is done by determining the location of the extent of the individual in each direction, modelled in the fish axis. Specifically, the `bodylength`, `bodywidth`, and `bodyheight` are used to determine the location of the extent of each individual in each axis, denoted `coordsNose`, `coordsTail`, `coordsLeft`, `coordsRight`, `coordsTop`, and `coordsBottom`. The fish axis is defined by its heading, where `coordsCentroid` represented the axis origin, positive x is the heading direction, positive y is the left (port) side of the individual, and positive z is upwards. The sensory ovoid for the individual, originally introduced by Goodwin [2004], is then defined based on the `sensoryRange` and the `bodylength`. The ovoid is defined by the sensory query distances: `SQDx`, `SQDy`, and `SQDz`, which denote the distance over which the individual can detect hydrodynamic information in the x,y, and z directions in the fish axis. In `fishPy`, `SQDx` and `SQDy` are defined as `bodylength` $\times$ `sensoryRange`, where the `sensoryRange` is set to 1.0 [see section 5.5.3]. An individual's sensory perception is weaker above and below itself, which is reflected in `SQDz` which is defined as $0.25 \times$ `bodylength` $\times$ `sensoryRange`. The extent of the sensory ovoid of an individual is shown in figure 4.2. A sensitivity analysis of fish trajectories to `sensoryRange` is given in section 5.5.3.

Each individual is assigned a burst swimming speed, `swimBurst`, and a sustained swimming speed, `swimSust`, based on its `bodylength`. These are calculated based on the work of Scruton et al. [1998], Clough and Turnpenny [2001], and Peake [2008]; equations 4.5 and 4.6 [see figure 4.3]. These empirically-derived equations are based

Table 4.3: Agent attributes assigned to each individual upon creation within `fishPy`.

Attribute	Description	Units
`id`	Identification number	n/a
`x`	x location of centroid of the individual.	m
`y`	y location of centroid of the individual.	m
`z`	z location of centroid of the individual.	m
`coordsCentroid`	Coordinates of the centroid of the individual - defined as [`x`,`y`,`z`]	m
`bodylength`	Total length of the individual	m
`bodywidth`	Total width of the individual	m
`bodyheight`	Total height of the individual	m
`mass`	Mass of the individual	kg
`SQDx`	Sensory query distance in the x direction using the fish axis.	m
`SQDy`	Sensory query distance in the y direction using the fish axis.	m
`SQDz`	Sensory query distance in the z direction using the fish axis	m
`swimBurst`	Burst swimming speed	ms^{-1}
`swimSust`	Sustained swimming speed	ms^{-1}
`wettedArea`	Measure of the surface area of the fish	m^2
`heading`	Direction that the fish is pointing	Unit vector.
`movementWeights`	Weightings of behaviours	List of percentages.
`coordsNose`	Coordinates of the individual's nose - i.e. the extent of the fish in positive x in the fish axis.	m
`coordsTail`	Coordinates of the individual's tail - i.e. the extent of the fish in negative x in the fish axis.	m
`coordsLeft`	Coordinates of the individual's left side - i.e. the extent of the fish in positive y in the fish axis.	m
`coordsRight`	Coordinates of the individual's right side - i.e. the extent of the fish in negative y in the fish axis.	m
`coordsTop`	Coordinates of the individual's top - i.e. the extent of the fish in positive z in the fish axis.	m
`coordsBottom`	Coordinates of the individual's bottom - i.e. the extent of the fish in negative z in the fish axis.	m

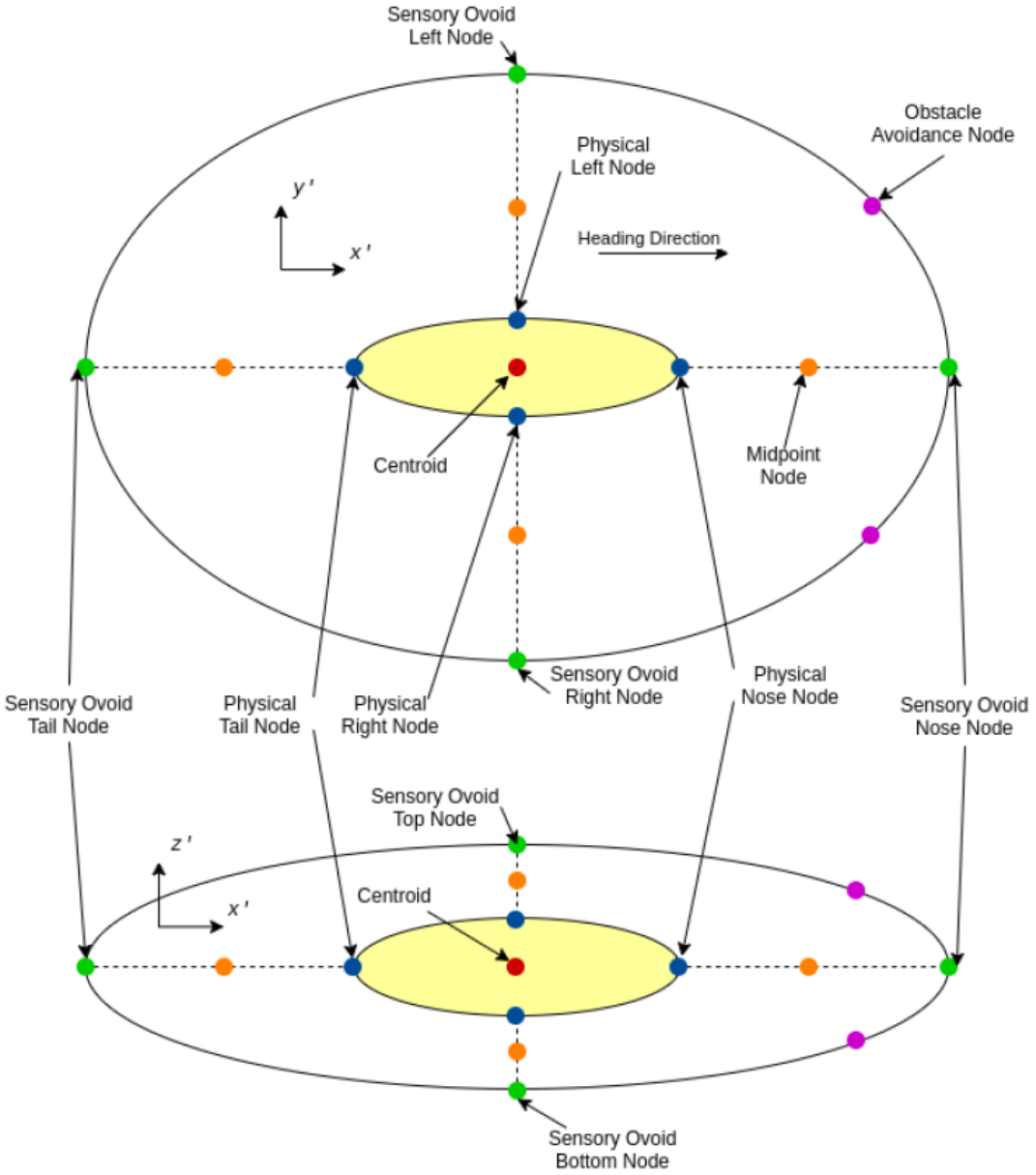

Figure 4.2: Schematic of an example virtual fish, denoted in yellow, showing a planform and side view. The centroid is denoted in red. Physical nodes are denoted in blue. Sensory ovoid nodes are denoted in green. Sensory ovoid midpoint nodes are denoted in orange. Obstacle avoidance nodes are denoted in pink. Fish axis denoted in each case.

Table 4.4: Required non-environment inputs for `fishPy`

Name	Format	Default value	Units
`fishTimestep`	Float	0.1	s
`Tmax`	Integer	n/a	n/a
`fishNum`	Integer	n/a	n/a
`sensoryRange`	Float	1.0	bodylengths
`repulsionDist`	Float	`max`(bodylengths)/2	m
`bodylength_mean`	Float	n/a	m
`bodylength_deviation`	Float	n/a	m
`spawnZoneXmin`	Float	n/a	m
`creationZoneXmax`	Float	n/a	m
`creationZoneYmin`	Float	n/a	m
`creationZoneYmax`	Float	n/a	m
`creationZoneZmin`	Float	n/a	m
`creationZoneZmax`	Float	n/a	m
`targetZoneXmin`	Float	n/a	m
`targetZoneXmax`	Float	n/a	m
`targetZoneYmin`	Float	n/a	m
`targetZoneYmax`	Float	n/a	m
`targetZoneZmin`	Float	n/a	m
`targetZoneZmax`	Float	n/a	m

on eight research studies of brown trout swimming speeds for a mean length of $0.161m$ (range: $0.05m$ to $0.35m$) and a mean water temperature of $8.3°C$ (range: $5.0°C$ to $15.0°C$). As swimming performance versus temperature has been shown to follow an "inverted-U-shape" [see Lee et al. 2003], it follows that equations 4.6 and 4.5 are only applicable for temperatures between $5.0°C$ and $15.0°C$.

$$\texttt{swimBurst} = 0.305 + 6.1L - 0.05742 \tag{4.5}$$

$$\texttt{swimSust} = 4.8L + 0.02T \tag{4.6}$$

where: L is the `bodylength` of the individual in m; and T is the water temperature in $°C$, taken as $10°C$ in all calculations.

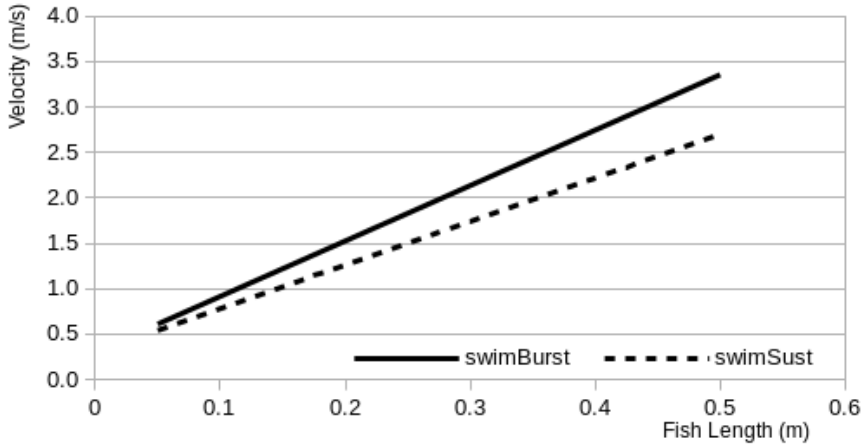

Figure 4.3: Burst swimming and sustained swimming speeds against fish bodylength. Calculated based on the work of Scruton et al. [1998], Clough and Turnpenny [2001], Peake [2008], equations 4.5 and 4.6.

4.3.3 Axis Transformations

The behavioural ruleset of each individual is based within Lagrangian space and the environment is represented in Eulerian space. Therefore, it is important to convert between the global axis; determined by the environmental data, and the axis of each individual, dubbed the fish axis. This is done by assuming that the x direction in the fish axis, dubbed x', is defined by the `heading` of the individual. Furthermore, it is defined that the z' axis must always be the closest axis to z (i.e. the individual must always been angled less than 45° to the global horizontal axis), and the roll of the individual is zero in relation to the global axis. These three criteria are sufficient to define a new axis based on any `heading` direction. These assumptions are appropriate given that the model is applied to natural river systems where variations in the z direction are not significant. Implementation of this axis system, while computationally inexpensive, imposes a limit that the input environmental data must have its negative z direction aligned with the direction of gravity.

4.3.4 The Structure of `fishPy`

Figure 4.4 details the general structure and function of `fishPy`. The code can be thought of as four separate sections or stages. These are: the problem definition, the

initialisation, the main loop, and the outputs. The problem definition stage includes the user defining all user inputs. These include the required environment data, table 4.2, and the required non-environment data, table 4.4.

In the initialisation phase, the model sequentially creates individuals up to the value of `fishNum`. Upon creation, each individual is assigned a number of attributes, as described in section 4.3.2. Each individual is also placed within the `creationZone`, a bounding box defined by the user [see table 4.4]. This `creationZone` must exist entirely inside the domain. Individuals are randomly placed within the domain via the `determineCreationLocation` function, which randomly picks an x,y, and z location within the `creationZone`, using the `random.uniform` function in Python. This location is assessed based on the `G3D` matrix to ensure it is an acceptable location. If the location is unacceptable, the process is repeated for that individual a maximum of 10 times, before moving on to the next individual. If fish-fish interaction is enabled (i.e. `colAvoidance` is enabled) individuals are placed ensuring they are not within `repulsionDist` from any other individual. If the `creationZone` is not large enough to accommodate the entire population, the code will place as many as it can, warn the user that the entire population will not be simulated, then execute.

The user must also define the region in which fish are understood as having successful "passed" the domain. This region is named the `targetZone` and is defined as a bounding box [see table 4.4]. If an individual enters this box they are considered to have passed through the domain and are removed from the simulation. They are subsequently added to the list, `passed`, which defines successful individuals. At the end of each timestep the `failCheck` function is executed to check whether the current individual has failed. This is assessed based on two criteria; firstly, whether the averaged velocity magnitude is zero, and secondly, whether the individual has moved outside of the bounds of the domain as represented by `G3D`. If either of these criteria are met, the individual is deemed to have failed and is subsequently moved to the `failed` list.

The main loop runs until either all fish have passed or failed, noted by their existence within the `passed` and `failed` lists, or until a maximum number of timesteps, `Tmax`, is reached. The latter condition is included only to ensure the code fails gracefully, and generally `Tmax` should be defined large enough so as to not affect fish trajectories. At each main loop timestep, each fish makes a single movement in an order defined by the `initiative` list. This list is determined at each timestep based on the distances moved

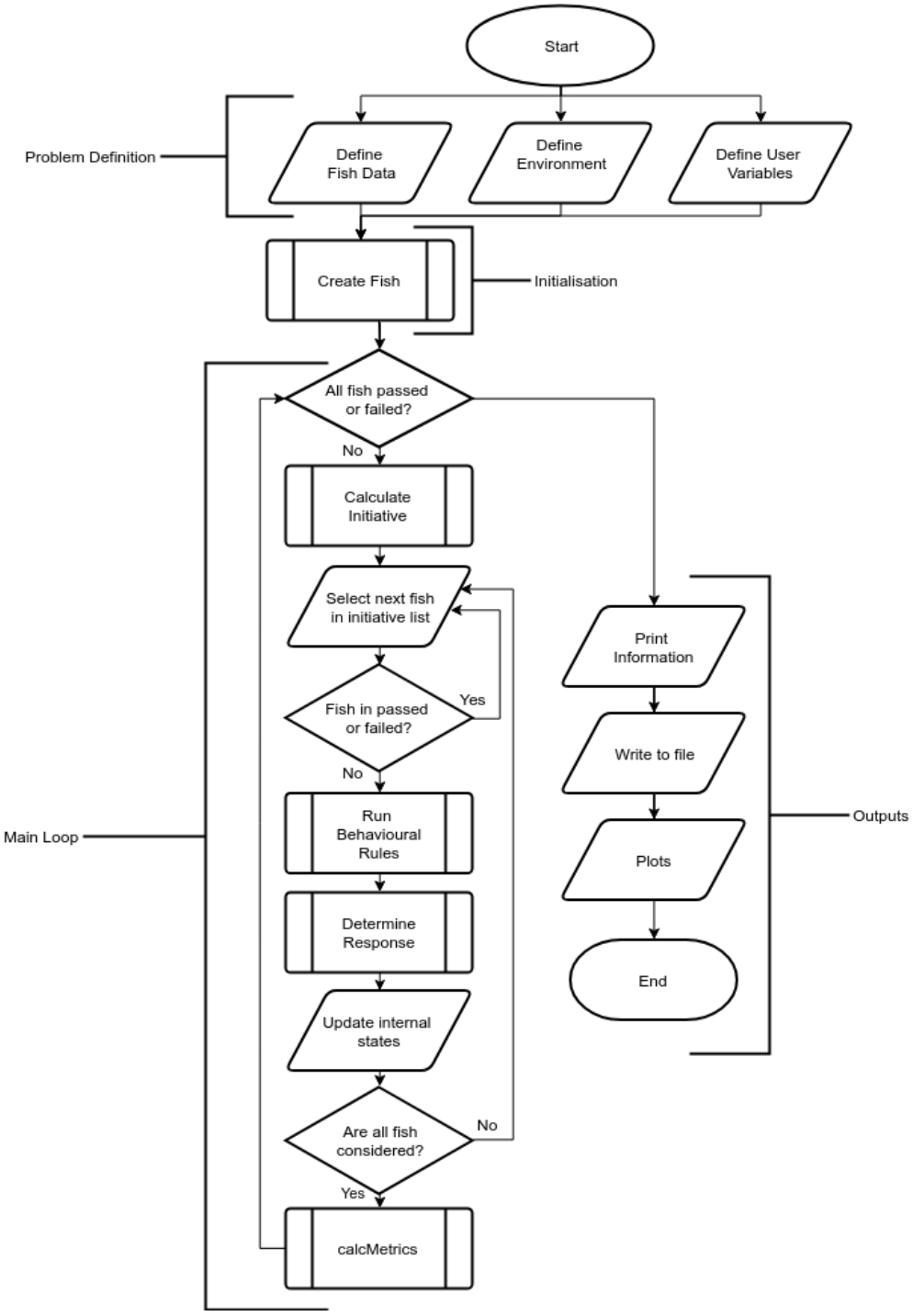

Figure 4.4: Flowchart denoting the general structure and function of `fishPy`. Note that `passed` and `failed` refer to Python lists of the individuals that have successfully passed the domain and failed to pass the domain, respectively.

by each individual in the previous timestep. During the first timestep, the `initiative` list is defined as the list of individuals in the order they are created. Each individual moves based on the result of their behavioural ruleset, discussed in section 4.6.

The environment within `fishPy` is represented by spatially discrete data. However, individuals are free to move in a spatially continuous manner (i.e. between nodes). This was done to allow additional freedom to individuals and to mitigate against the use of larger spatial resolutions in the environment data. To accomplish this `fishPy` uses a three-dimensional linear grid-based interpolation scheme `RegularGridInterpolator`, a part of the `scipy` Python package. This allows an individual to query the value of any environmental variable at any point in three-dimensional space. This interpolation is also used to determine the passability value for any location in the domain from the `G3D` matrix. This means at some locations the passability will be between 0 and 1. Therefore a threshold value (`passabilityThreshold`) was required to determine what value of `G3D` denoted the interface between passable and impassable regions. The value of `passabilityThreshold` was varied between 0.5 and 0.01. Larger values resulted in a reduction in the near-wall geometry, which triggered individuals to avoid walls due to an artefact of the `passabilityThreshold` value rather than due to a behavioural rule. This artefact was reduced with decreasing values of `passabilityThreshold`, and was eliminated at a value of 0.1. Therefore, the `passabilityThreshold` was set to 0.1. Any location with a passability greater than this threshold is classed as passable, and any location with a passability less than this threshold is classed as impassable.

After a response is determined, the individual's internal states, such as location and heading, are updated. The method used to calculate the heading is discussed in section 4.6.8. After each individual has moved a number of metrics are calculated including the current time taken, the cumulative energy expended, and the total distance moved. The method used to calculate the energy expended is detailed in section 4.4. Once all individuals have either passed or failed, or `Tmax` has been reached, the simulation ends and passage metrics as well as the movement history of each individual are written to file.

4.3.5 Temporal Sensitivity & Maximum Decision Timestep

The timestep defines the jump between discrete time points within the simulation. The larger the timestep the smaller the computation expense for a given time period. How-

Table 4.5: Calculated maximum decision timesteps (`fishTimestep`) for a number of example cases within `fishPy`.

`bodylength` (m)	`swimSust` (ms^{-1})	min($\|\mathbf{U}\|$) (ms^{-1})	max(`fishTimestep`) (s)
0.15	0.92	0.0	0.245
		0.2	0.313
0.25	1.40	0.0	0.268
		0.2	0.313
0.5	2.60	0.0	0.288
		0.2	0.313
0.75	3.80	0.0	0.296
		0.2	0.313
1.0	5.0	0.0	0.300
		0.2	0.313

ever, decreasing the timestep will increase the accuracy of the simulation. Therefore, there is a trade-of between accuracy and computational expense. The model framework is defined such that it is straightforward to vary the timestep size. This enables a study of the sensitivity of the model to the timestep [see section 5.5], and also enables any future users to modify the tool to fit their requirements. Furthermore, a timestep maximum is imposed to ensure environmental information is not overlooked. An individual moving within any domain can sense all environmental data within their sensory ovoid. If the individual were to move far enough in a single timestep that the new sensory ovoid does not overlap the original sensory ovoid (in Eulerian space), some information has been neglected. This can cause individuals to move through objects or otherwise miss potentially important environmental data. This is a form of the CFL criterion as discussed in section 2.6.1. Therefore an individual should be limited in its movement via imposing a maximum limit on the decision timestep.

This maximum is calculated for the case of an individual moving at its sustained speed (`swimSust`) with an opposing fluid velocity equal to the minimum velocity magnitude within the wetted domain. This case represents the largest ground speed of an individual in a single timestep, assuming that it is moving upstream, and therefore represents the largest distance moved in a single timestep. One may think that the burst speed (`swimBurst`) should be considered, however, within `fishPy` an individual only

opts to move at burst speed if the local velocity is greater than its sustained swimming speed, resulting in an overall smaller Eulerian distance moved. If the maximum speed multiplied by the decision timestep causes the individual to move such that it's new centroid is outside of its previous sensory ovoid, then the timestep must be reduced. Furthermore, if a population of individuals is used, the `bodylength` and `swimSust` of the largest individual must be used. This can be expressed mathematically as equation 4.7.

$$\max(\texttt{fishTimestep}) < \frac{TSL}{(\texttt{swimSust} - \min|\mathbf{U}|)} \tag{4.7}$$

where: TSL is the total sensing length of the largest individual in the population, equal to $\frac{\texttt{bodylength}}{2} + \texttt{SQDx}$.

Table 4.5 shows some example maximum decision timesteps for a variety of sizes of individuals. Interestingly, as the `swimSust` value scales with the `bodylength` of an individual, the maximum timestep remains roughly constant for a given minimum velocity magnitude, within the domain. If the `fishTimestep` is defined as greater than this value, `fishPy` will continue to execute but the user may suffer from stability issues or unnatural movements.

The definition of the maximum decision timestep is done to ensure stability and the flow of information within the model. It does not suggest that the model is insensitive to the timestep if the timestep is less than the maximum. It is impractical to quantify the temporal sensitivity of the model for a general case as sensitivity to the timestep will depend upon the flow field and geometry considered. Therefore, a timestep sensitivity study, such as that presented in section 5.5, should be undertaken to ensure independence of the results for a given case.

4.4 Modelling Energy Expenditure

Quantification of the energy expended by up-migrating individuals is considered in this section. Many species of salmon cease feeding before commencing migration and rely on stored energy for all movements [Khan, 2006]. This means that an up-migrating individual has a finite amount of energy which must last the entire duration of migration. Therefore quantification and reduction of the energy required to pass through anthropogenic facilities is important in ensuring unhindered longitudinal migration. The energy

expended by each individual is modelled using the method detailed by Khan [2006] and subsequently by Blank [2008]. The method assumes that the main force acting upon an individual is hydrodynamic drag. Therefore the energy expended by an individual can be expressed as the culminated drag force that is experienced by the individual. An equation for the drag force is derived from boundary layer theory and is analogous to the conventional drag equation [Behlke, 1991, Vogel, 1994], equation 4.8.

$$\boldsymbol{F} = \frac{1}{2} C_d \rho A_S (\boldsymbol{U_w} - \boldsymbol{U_f})^2 \tag{4.8}$$

where: C_d is the fish drag coefficient; ρ is the water density; A_S is the wetted area of the fish; $\boldsymbol{U_w}$ is the local water velocity; $\boldsymbol{U_f}$ is the fish velocity.

The drag coefficient, C_d, can be described as in equation 4.9, where C_f is the frictional component of the drag coefficient.

$$C_d \approx 1.2 C_f \tag{4.9}$$

where, for turbulent flows, the frictional component can be described as:

$$C_f = 0.074 Re^{-0.2} \tag{4.10}$$

where the local Reynolds number for the individual is:

$$Re = \frac{\rho(\boldsymbol{U}_w - \boldsymbol{U}_f) L}{\mu} \tag{4.11}$$

where: L is the individual's bodylength; ρ is the density of water; and μ is the kinematic viscosity of water.

The energy expenditure of an individual can then be calculated as

$$E = \int_0^S |\boldsymbol{F}| \, dS \tag{4.12}$$

Where S is the fish path.

In terms of code implementation, the energy equation, (4.12), is discretised and the drag force is calculated for each timestep. Assuming that the water density, ρ, and the wetted surface area of the individual, A_S, are constant, the following equation can be written for the energy expended per timestep, i:

$$E_i = \alpha \rho A_S \sum_{i=1}^{n} (\boldsymbol{U}_{w,i} - \boldsymbol{U}_{f,i})^2 Re_i^{-0.2} \Delta d_i \tag{4.13}$$

Where E_i is the energy expended by the individual during timestep i; α is a constant equal to 0.0444; $\boldsymbol{U}_{w,i}$ is the velocity of the water during timestep i; $\boldsymbol{U}_{f,i}$ is the individual's velocity during timestep i; Re_i is the local Reynolds number in timestep i, and Δd_i is the distance travelled in timestep i.

It is difficult to verify that this methodology accurately calculates the energy expended by an individual. Furthermore, only the wetted area A_s is a function of the species considered. This is questionable as it is known that swimming type, such as anguilliform or subcarangiform, have varying levels of efficiency and required effort, naturally resulting in a change in energy expended over similar distances. Similarly, the local water temperature is known to affect the energy expenditure, and is not considered within equation 4.12. However, the methodology outlined here may not provide an exact number but does provides an analogous metric, used to compare between different pathways taken by an individual.

4.5 Modelling the Swim Bladder

As discussed in section 2.4.2, most fish have swim bladders which allows individuals to modify their density. This regulates the buoyancy of the individual, reducing its energy expenditure by reducing the need for a vertical component of the swimming vector. An investigation into modelling of the swim bladder was undertaken based on the work of Alexander [1966] and Strand et al. [2005]. This modelling process is detailed in appendix C. This approach was extended to determine the exact volume of the swim bladder at a snapshot in time, based on current and previous depths. However, a simple model of the swim bladder was implemented in `fishPy` to determine the significance of the swim bladder in upstream river migrations, rather than the vertical marine migrations considered by Strand et al. [2005]. The simple model assumed the volume of the swim bladder was constant and determined upon creation based on the initial depth of the individual. The buoyancy experienced by the individual was calculated at each timestep. These buoyancy values were tracked over the course of multiple trajectories and found to never exceed 1×10^{-9} N. This meant that trajectories were near-independent of the swim bladder influence and so it was decided that complex modelling of the swim bladder volume was unnecessary.

A simple model of the swim bladder is implemented within `fishPy` to demonstrate

the negligible effect of buoyancy; facilitating future development of the code, such as future species models or the application of `fishPy` to marine datasets. The `fishPy` implementation of the swim bladder is:

1. Upon creation an individual is assigned a swim bladder volume. This volume is determined as the required volume to ensure neutral buoyancy at the creation depth of individual.

2. At each timestep the buoyancy is calculated based on equation C.2, located in appendix C.

3. The resultant movement vector is then determined and applied to the individual.

This function demonstrates the negligible buoyancy forces over the time-scales considered within `fishPy` (i.e. $\mathcal{O}(1.0)$ seconds). Crucially, the swim bladder is implemented with static volume; therefore neither passive nor active gas transfer processes are modelled. This means that an individual always tends towards the depth at which it was created.

4.6 Behavioural Ruleset

This section details the behavioural ruleset that governs the movement decisions of each individual. The ruleset is defined in a modular manner with no dependencies between rules. This allows individual rules to be turned on or off without affecting the output of other rules. The formulation of each rule is based on a thorough literature review. This is summarised in table 4.1 which cross references key literature findings with each behavioural rule. Furthermore, vision is known to play a key part in the navigation of fish [Liao, 2007] but is not explicitly implemented within `fishPy`, as hydraulic stimuli are the focus. However, vision is implicitly implemented within some of the housekeeping rules such as collision avoidance, covered in section 4.6.9. Each rule outputs a movement direction (unit vector). These outputs are used to determine the final behavioural response, detailed in section 4.6.10. Furthermore, sensitivity studies for a number of the parameters introduced in this section are presented in chapter 5.

4.6.1 Rule 1: `followFlow`

Rule 1, `followFlow`, forms the basis of an individual's attempt to move upstream. The rule determines the local upstream direction based on the local bulk flow, allowing for simulation of rheotaxis and fundamental upstream movement. This is achieved through sampling U,V, and W at the 6 nodes that make up the physical representation of the individual as well as at the 12 sensory ovoid nodes [see figure 4.2]. These are then averaged to determine the average velocity direction, local to the individual, which is assumed to be representative of the inverse of the local upstream direction. The spatial averaging of the local velocities is weighted based on the magnitude of the velocities, i.e. faster flows have more influence over the determined velocity direction. This is done to effectively reduce the influence of any secondary or tertiary flows in the local area, as these an not representative of the local bulk flow. This is not to say that secondary or tertiary flows are insignificant, but that they are not considered within this rule, and instead considered within sections 4.6.2 and 4.6.7.

The velocity magnitudes across the physical representation nodes are also averaged to determine the velocity that the individual must overcome. This rule then returns a unit vector in the opposite direction to the average local velocity direction as well as the average velocity magnitude. This rule results in the individual moving upstream without any requirement for knowledge of the geometry of the domain in question. Furthermore, this rule does not rely on flow in a certain axis, as long as the negative z direction of the input environmental domain aligns with gravity.

4.6.2 Rule 2: `minMaxEnergy`

Rule 2, `minMaxEnergy`, takes inspiration from the work of Blank [2008], Abdelaziz [2013], and Plymesser [2014] by implementing a minimum energy selection process. However, as discussed in section 2.8.1, modelling the local minimum energy pathway requires knowledge of the entire flow field and, more importantly, is insufficient when considering domains with flow reversal, stagnation, or recirculation zones. Conversely, literature also suggests that up-migrating salmonids are attracted to high flows [Banks, 1969, Lundqvist et al., 2008, Thorstad et al., 2008]. Therefore, this rule includes cases in which the individual's preference is switched between searching for the minimum energy path, searching for the maximum energy path, and not actively searching for either. This captures the different behaviours undertaken based on the individual's

surroundings. It is theorised that, when exposed to a simple flow field, an individual will search for the minimum energy pathway, i.e. search for lower velocity magnitudes. If the individual experiences a sufficiently large lateral negative fluid shear; i.e. the rate of change of the fluid velocity in the local hydrodynamic environment, it will cease seeking the minimum velocity region. It is theorised that a large negative fluid shear denotes the presence of high turbulence, and that continuing to search for lower velocity regions will tend the individual into the turbulence. Use of the fluid shear value is inspired by the work of Goodwin [2004], Goodwin et al. [2006] and Nestler et al. [2008].

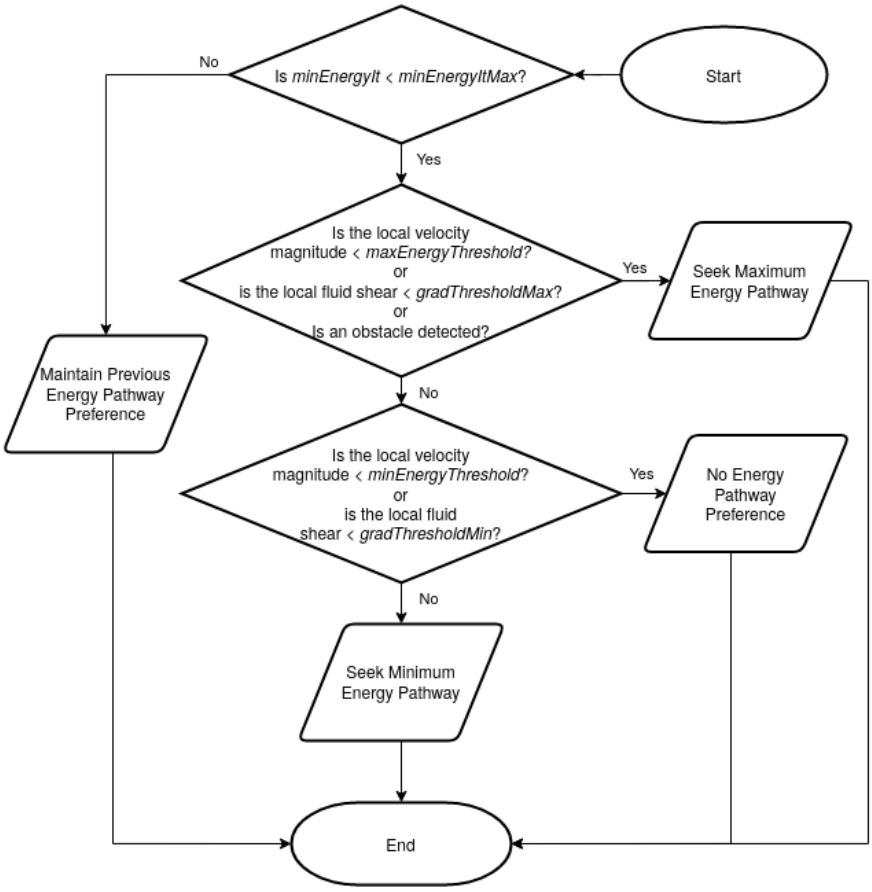

Figure 4.5: Flowchart denoting the structure of the `minMaxEnergy` rule.

If the local average velocity magnitude or fluid shear are found to be below an additional threshold, or the individual senses the presence of an obstacle, the individual will switch to seeking maximum velocities. The presence of an obstacle is determined

by querying the output of `obAvoidance` [section 4.6.4]. This is done as these events represent a hydrodynamic environment that are detrimental to the individuals passage (i.e. stagnation or high turbulence regions). This is aligned with the findings of Smith et al. [2005] and Smith et al. [2006], who found that brown trout consistently chose faster, lower turbulence regions opposed to slower, higher turbulence regions ["turbulence" defined by Smith et al. [2005] as increased u', v', w', TKE, and τ; see section 2.7.2]. Regions of stagnating flow are detrimental as it is important for the individual to be exposed to relatively significant flow velocities to determine the correct upstream direction, in line with the known requirement for an "attraction flow" often referred to in policy documents and literature [see section 2.7.1]. Therefore if, when seeking lower velocities, the average velocity magnitude becomes suitably low, the individual will cease searching for lower velocity regions.

The default behavioural case considers the individual searching for the local minimum energy pathway, figure 4.5. If the individual encounters a velocity magnitude less than `minEnergyThreshold` or a lateral fluid shear less than `gradThesholdMin`, the case is switched and the individual ceases searching for the local minimum energy pathway. Moreover, if the individual encounters an obstacle, a velocity magnitude less than `maxEnergyThreshold` or a lateral fluid shear less than `gradThresholdMax`, the case is switched and the individual will begin searching for the local maximum energy pathway; i.e. larger local velocities. To limit constant reversion back and forth between the three states, a counter is included so that when an individual encounters an event triggering a search for higher velocities, the individual will search for higher velocities for a minimum number of timesteps before accepting a change in behaviour, effectively dampening sharp changes in behaviour. The minimum number of timesteps between case switches is controlled by the `minEnergyItMax` variable, which is defined as $\frac{\texttt{minEnergyTimeMax}}{\texttt{fishTimestep}}$; where $\texttt{minEnergyTimeMax} = 2.0s$. Therefore, at its most frequent, the behavioural case for a given individual can switch once every two seconds. As with many behavioural parameters, it is difficult to determine an exact expression for `minEnergyTimeMax` and therefore, sensitivity to this value could be determined in future work.

Individuals assess the velocity at eight nodes that describe the region of the sensory ovoid in front of the individual. As the heading direction is controlled by the known "extended local" upstream direction, considering only the region in front of the indi-

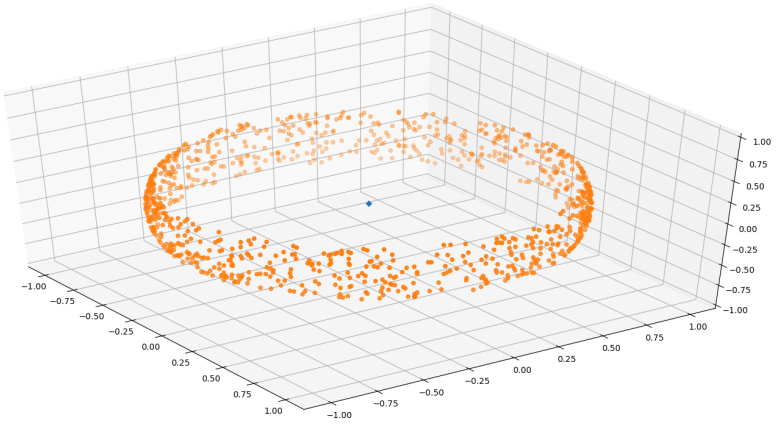

Figure 4.6: Scatter plot showing 1000 example points (orange) generated by the `randomWalk` function from an initial location, shown in blue. These points, in reference to the initial location, describe the resulting movement direction.

vidual removes the option for an individual to move backwards, even if this location would present an attractive option. This is important as movement backwards is unlikely to constitute the minimum energy pathway. Once the eight nodes are assessed, the location of the minimum (or maximum) velocity magnitude is determined and the unit vector describing the direction of this node is calculated. This unit vector is then returned as the output of the rule. The sensitivity of the model to the values of the thresholds discussed in this chapter are explored in section 5.5.1.

4.6.3 Rule 3: `randomWalk`

Random walk theory is a classical method used to study motion. First studied by Brown [1828], and subsequently by Einstein [1905], Pearson [1905], and Rayleigh [1905]. Random walk theory has since been explored and applied to a multitude of animal types [see Codling et al. 2008 for a thorough review].

Random walk theory is applied to individuals within `fishPy`. This introduces stochasticism to the model, aids in capturing the fickle nature of decision-making, and can represent processes not explicitly modelled [Grimm and Railsback, 2005, Gisen, 2018]. An uncorrelated, biased random walk is used by individuals. The function randomly selects two variables; a yaw angle, ϕ, and a pitch angle, θ; using the python `random` package. The pitch angle is limited to allow for maximum pitch magnitude of

10 degrees (0.175 radians), to eliminate unnatural vertical movements. This limitation is in rough agreement with the maximum angle of natural riverine slopes. These two angles describe a point in three dimensional space (using a nominal radius of 1), which is used to define a unit vector direction from the current location to the point [see figure 4.6]. This unit vector is returned as the behavioural output denoting the biased random walk; noting that the magnitude of the movement is handled after the direction is established.

4.6.4 Rule 4: `obAvoidance`

This rule adds additional obstacle avoidance abilities to each individual. This is done by assessing the passability (`G3D`) of five locations in front of the individual, named "query points", to search for obstacles. These query points exist within the sensory ovoid and are shown by figure 4.2.

The individual interrogates the `G3D` matrix at each query point and stores the corresponding value. If all of the query points are found to be impassible, the location of each of the query points are temporally moved closer to the individual (by a factor of 0.67). This reduction step is executed a maximum of 10 times, after which further reductions were found to have negligible impact. After querying the points, and determining at least one passable point, the average location of the passable points is calculated. A unit vector describing the direction towards the average passable location is determined. If all query points are impassable or all query points are passable, the unit vector is reduced to zero to indicate the individual's lack of preference.

4.6.5 Rule 5: `colAvoidance`

This rule ensures no two individuals occupy the same physical space. Individuals assess the Euclidean distance between their own centroid and the centroid location of all other individuals in the domain. If any individual is within `repulsionDist` of the active individual, the unit vector describing the direction is calculated and stored. The average direction of influencing individuals is calculated and a unit vector describing the opposite direction is given as the output.

Due to using this methodology, if an individual is flanked equally by other individuals on either side, and those individuals are within `repulsionDist` and therefore activate the collision avoidance behaviour, the `colAvoidance` rule will result in a zero

magnitude unit vector output for the middle individual. Whereas, the results will move the left-most individual more to the left, and the right-most individual more to the right.

It was decided to include this behaviour as a defined behavioural rule in its own right, rather than include it within the `housekeeping` functions. This decision was made as the foundation of the behaviour (and its implementation) lend themselves to modelling schooling behaviour, which is expected to be required for other species in the future of the `fishPy` model. However, this is not required for brown trout.

4.6.6 Rule 6: `memory`

This rule models the individual's memory of the main velocity direction. It is thought that trout migrating upstream would not make harsh changes in direction over small time periods. This thinking forms the basis of this behavioural rule, which gives influence to the previous movement direction in the current timestep. This has the effect of increasing an individual's tendency to continually move in the same direction, rather than relying significantly on the current local hydrodynamic environment. With each execution of `followFlow`, the local velocity unit vector, averaged over the sensory ovoid, is calculated. This value denotes the local flow direction and is stored within an array of directions representing the memory of the individual. The length of this array, denoted `numMemory`, is determined as:

$$\texttt{numMemory} = \frac{\texttt{memoryTime}}{\texttt{fishTimestep}} \tag{4.14}$$

where `memoryTime` is the time period of which the individual "remembers", the value of this variable is explored in section 5.4.6. This array is then averaged over to determine the individual's perception of the average upstream direction. Therefore, at each timestep, the `memory` rule outputs the average upstream direction that the individual remembers.

4.6.7 Rule 7: `tkeAvoidance`

Rule 7 takes inspiration from the work of Gao et al. [2016] and Smith et al. [2005] and considers the preference of an individual to avoid regions of high turbulence kinetic energy. Smith et al. [2005] suggest that brown trout choose regions with low relative TKE, whereas Gao et al. [2016] suggests they opt for regions with a *tke* within the

range of 0.1 to $0.35 m^2 s^{-2}$ (or Jkg^{-1}). This rule uses a formulation of both by selecting a pathway that minimises local turbulence kinetic energy but only if the individual senses a value above $0.35\ m^2 s^{-2}$.

The rule functions in a manner similar to the `minMaxEnergy` rule. If the local turbulence kinetic energy exceeds $0.35\ m^2 s^{-2}$, the individual assesses the TKE at 8 nodes that describe the region of the sensory ovoid in front of the individual. This ensures that the individual does not move backwards, as it is assumed that the`heading` represents the upstream direction. Once the 8 nodes are assessed, the location of the minimum turbulence kinetic energy is determined and the unit vector describing the direction of this node is calculated. This unit vector is then returned as the rule output.

4.6.8 Calculation of the `heading`

Upon creation an individual's `heading` is calculated as the opposite direction to the local average velocity vector without any `memory` influence as the `memory` array only contains the upstream direction at the current timestep. In future timesteps the heading is calculated based on the current local upstream direction (weighting 1.0), the upstream direction from memory (weighing 1.5), and the direction moved in that timestep (weighting 0.5). This tends the individual to point its nose upstream, simulating rheotaxis. This is done to ensure that an individual's `heading` in a given timestep is not dominated by the local velocity direction, as this can cause harsh, unnatural changes in heading.

4.6.9 Housekeeping

In addition to the described novel behavioural ruleset, there are a number of additional functions which have been grouped together with the term "housekeeping" rules. These ensure code functionality. They are not described in detail as they are not associated with fish behaviour but ensure that the physics of the system are not compromised. This includes a calculation of buoyancy forces based on the work of Alexander [1966], Strand et al. [2005], detailed in section 4.5. It also includes collision avoidance measures for walls, and functions to ensure individuals don't enter dry cells.

4.6.10 Determining a Behavioural Response

Once the behavioural rules have been executed for the given individual, the output of each behavioural rule are compiled into the `runResults` array. It is important to note that each element of this array contains a direction for the individual to move in rather than a vector. A behavioural response is then determined via a weighted average of these results, where the weighting is controlled by the `movementWeights` array, an example of which is given in equation 4.15. After averaging, the result is then converted to a unit vector to maintain its representation of direction. The `movementWeights` array contains the weight applied to the output of each behaviour rule, and is calculated for each individual upon creation. At creation, the `movementWeights` array is given by equation 4.15.

$$\texttt{movementWeights} = [0.2, 0.1, 0.05, 0.15, 0.2, 0.2, 0.1] \tag{4.15}$$

where $\texttt{movementWeights}[N]$ represents the weighting applied to the output of rule N, and the sum of $\texttt{movementWeights} = 1$.

During each timestep, the weighting for the `minMaxEnergy` rule can vary. This is done to give more influence to the search for the local maximum energy path, as this is an escape behaviour, equation 4.16. If the individual is searching for the local minimum energy path, the weighting is set to 0.1. If the individual is not actively seeking, the weighting is set to zero. If the individual is searching for the maximum energy path, the weighting is set to $0.5 - 0.1(\texttt{fishTimestep} \times \texttt{minEnergyIt})$. This gives a large influence to the rule upon first switching to searching for larger velocities to model the importance of moving away from potentially dangerous situations. This influence then slowly reduces as the danger subsides, equation 4.16. This formulation is akin to the repulsion behaviour in the NFS model [Goodwin et al., 2014]. As the weighting of the `minMaxEnergy` rule can vary, the `movementWeights` array is re-normalised within each timestep to ensure that the weightings sum to 1.0 [see i.e. figure 4.7].

$$W_{energy} = \begin{cases} 0.1, & \text{if seeking min. energy} \\ 0.5 - 0.1(\texttt{minEnergyIt}\Delta t), & \text{if seeking max. energy} \\ 0.0, & \text{otherwise} \end{cases} \tag{4.16}$$

where $W_{\texttt{minManEnergy}}$ is the weighting assigned to the output of the `minMaxEnergy` rule, `minEnergyIt` is the number of timesteps since the behavioural case switch, and Δt is the `fishTimestep`.

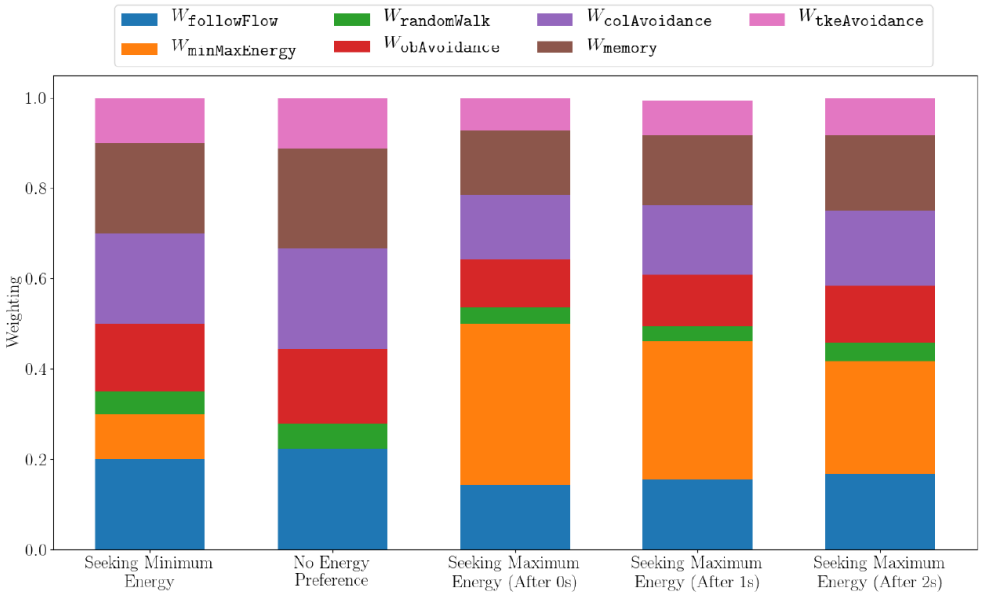

Figure 4.7: Visualisation of the distribution of the `movementWeights` array for five cases

Once a direction is determined, the actual movement of the individual is handled by the `calcMoveMakeMove` function. The speed that the individual moves at depends upon the local average velocity magnitude (`AvgMagVel`) that the individual must overcome. If this value is above the `swimSust` of the individual, the individual switches to swimming at burst speed (`swimBurst`), but otherwise opts to use its sustained speed. Furthermore, if `AvgMagVel` is more than the `swimBurst` of the individual, then the speed of the individual is set to zero and the individual is considered to be retreating. Mathematically, this is expressed as equation 4.17. This effectively represents the individual succumbing to the water velocity and retreating downstream. This retreat (or fallback) behaviour continues for a number of timesteps controlled by the `fallbackItMax` variable. This is mathematically equal to setting the weighting of each rule to zero.

$$S = \begin{cases} 0.0, & \text{if } \texttt{AvgMagVel} \geq \texttt{swimBurst} \\ \texttt{swimBurst}, & \text{if } \texttt{swimSust} \leq \texttt{AvgMagVel} \leq \texttt{swimBurst} \\ \texttt{swimSust}, & \text{otherwise} \end{cases} \tag{4.17}$$

where: S is the individual's speed for the current timestep; and `AvgMagVel` is the velo-

city magnitude averaged across the individual's physical nodes.

The actual movement is then defined as the summation of the move directions multiplied by the individual's speed and the averaged velocity vector of the local water which must be overcome. This is then multiplied by the decision timestep. Mathematically, this is expressed as equation 4.18.

$$\texttt{moveVector} = ((\texttt{moveDirection} \times S) + \texttt{avgVecVel}) \times \texttt{fishTimestep} \tag{4.18}$$

As the direction of the movement of the individual is based upon the unit vector of the weighted average of the `runResults` array, it is possible for this average to result in a direction dominated by unnatural vertical movement. This happens in cases where the outputs of two rules effectively cancel each other out in x and/or y. These cases are rare but are caught by an exception function. This function checks to see if the averaged `runResults` direction is dominated by vertical movement. If this is the case, the z component is set to zero and a new unit vector is determined.

4.7 Discussion on the Development of fishPy

This chapter has summarised the development, structure, and function of `fishPy` and has detailed the specific ruleset used to predict pathways taken by up-migrating brown trout. This section presents a discussion on the development of `fishPy`. Firstly, decisions, assumptions, and simplifications made during the model development are discussed. Secondly, model uncertainties and limitations are discussed. In both cases, the model is discussed in comparison to other published models.

4.7.1 Discussion on Agent-based Modelling Approach for Determining Up-migration Pathways

Agent-based modelling is well suited to determining up-migration pathways in fish, evidenced by multiple established models in the literature. This is due to its inherent formulation of agents and environment and its emphasis on the individual rather than the population. This section discusses the decisions, simplifications, and assumptions made during the development of the model.

Discussion on Temporally-dependent Flow and Coupling to Computational Fluid Dynamics

Literature suggests that fish react to hydrodynamic stimuli collected from their local environment. However, it is unclear whether fish react to temporally-averaged values (i.e. mean velocity, $\bar{U}$) or instantaneous or fluctuating values (i.e. u_i or u'), or some combination of both. It was decided in the early stages of this work that `fishPy` would only consider temporally-averaged environmental data. This was done as the inclusion of temporally-dependent data would drastically increase the complexity of the model. Furthermore, due to the novelty of the research, it was unclear whether this increase in complexity would produce significantly different results. None of the established models of fish passage prediction utilise temporally-dependent flow fields. Furthermore, Zielinski et al. [2018] implemented stochastic velocity fluctuations within their model, but found insignificant differences in over passage efficiencies compared to using a static flow field. The inclusion of temporally-dependent data would, for better or worse, result in temporally-dependent fish pathways. That is to say that resulting trajectories would depend upon the exact start time of the individual in relation to the start time of the environment data, and therefore passage success metrics may also be temporally-dependent. The sensitivity of the model and its metrics to this would become domain-dependent and significantly difficult to quantify. Moreover, the required duration of the temporally-dependent environment data would be difficult to quantify without knowing in advance the time required for an individual to pass the domain. This issue could be overcome by coupling the fish path prediction code to the computational fluid dynamics code. This was considered in the early stages of the research but ultimately decided against due to the increased complexity, resultant software (CFD) dependencies, user unfriendliness, and drastic increases to computational and time expenses for each simulation. Furthermore, uncoupled code allows for the environmental input data to be collected experimentally rather than limit the input to CFD results, expanding the utility and usefulness of the model top practitioners. The inclusion of temporally-dependent data has not been sufficiently considered in the literature and is therefore a possible avenue for further research but is beyond the scope of this work.

Discussion on Spatially Continuous Model Formulation

Unlike the cellular automata and individual-based models developed and presented within chapter 3, fishPy is spatially continuous. That is to say that, while the environmental input data is discrete, individuals are free to move continuously within the environment rather than limited to moving between mesh nodes. It was thought that while this decision increased the complexity of the model, it would allow fish greater freedom within a given domain and reduce the dependence of trajectories to the input grid. However, this is difficult to quantify and therefore it is difficult to know if the increased complexity was necessary. Although, Gilmanov et al. [2019] found a spatially continuous formulation of the Zielinski et al. [2018] model resulted in greater accuracy compared to the original spatially discrete model. This spatially continuous formulation of fishPy was achieved through using RegularGridInterpolator, a three-dimensional linear grid-based interpolation scheme within the scipy Python package. The spatially continuous formulation of fishPy coupled with the RegularGridInterpolator function allowed for full usage of the sensory ovoid in determining fish behaviour, wherein points located on the surface of the ovoid are queried for data rather than using the closest node approximation used by Gao et al. [2016]. However, this could be improved by sampling data along continuous lines rather than using discrete points, or sampling over the entire surface of the ovoid, thus producing better spatial averages. Sampling over the entire surface of the sensory ovoid has not been considered in the literature and is a possible avenue for further research, however it was deemed too computationally demanding and therefore was not considered in this work.

Discussion on Ruleset Definition and Decision Framework

The rules were developed based on a thorough literature review [see sections 2.7, 2.8, and 4.2] and were implemented in a modular, transparent manner. The rules simulate a combination of rheotaxis, energy pathway selection, obstacle avoidance, and turbulence avoidance.

Adequate simulation of rheotaxis has been shown to be significant in the literature [see section 2.8 and Montgomery et al. 1997]. This significance is increased for fishPy due to the developmental principle of creating a generalised model; i.e. a model that can be applied to any domain [see table 1.1 in section 1.2]. The explicit calculation of the upstream water direction, coupled with the conversion between global and individual

axes, implemented in `fishPy` allows the model to be applied to any domain. This is in contrast with many of the established models which can only be applied to domains where the flow is dominated by flow in the positive x direction or a global upstream direction is known to individuals *a priori*, severely limiting their usefulness [i.e. Blank 2008, Abdelaziz 2013, Plymesser 2014, Gao et al. 2016, Tan et al. 2018, Zielinski et al. 2018].

Goodwin et al. [2014] and subsequently Gisen [2018] limit random movements within the NFS and ELAM-de models, respectively. In particular, both impose limits of 20° in the horizontal direction and 10° in the vertical. It was found during the development of `fishPy` that no horizontal limitation was required, but that a limit of 10° in the vertical within the `randomWalk` rule gave qualitatively better results compared to observations of fish movements.

The concept of the minimum energy pathway is not in itself novel [i.e. Blank 2008, Abdelaziz 2013, Plymesser 2014, Zielinski et al. 2018]. However, Goodwin et al. [2014], and subsequently Gisen [2018] have demonstrated that attraction to larger velocities and accelerations (which represent the maximum energy pathway) can assist in predicting fish paths. Gisen [2018] suggested that simple energy savings rules are generally unsuitable to predicting upstream migration. However, Abdelaziz [2013] demonstrated that the minimum energy concept can predict upstream pathways of salmonidae through a culvert and compared well to measured data. Therefore, `fishPy` implements the minimum energy concept instead under the assumption that sometimes fish select the path of least resistance to conserve energy, such as when traversing a channel or culvert [see Abdelaziz 2013], but at other times selecting higher energy routes is more beneficial. Therefore, `fishPy` assumes that an individual actively switches between seeking lower velocities, not actively seeking, and seeking larger velocities [see section 4.6.2]. Switching between behavioural cases is controlled by thresholds of velocity magnitude as well as spatial velocity gradients (i.e fluid strain), based on the work of Goodwin et al. [2014]. This approach is novel and combines the minimum energy pathway concept with attraction to larger velocities and repulsion from large fluid strains used by Goodwin et al. [2014] and the biasing towards large accelerations used by Gisen [2018].

Gao et al. [2016] and Tan et al. [2018] have shown that, within a vertical slot fishway, the TKE can be indicative of route selection by trout and carp, respectively. Therefore,

fishPy includes a turbulence avoidance rule [see section 4.6.7] using the threshold value defined by Gao et al. [2016]. It is not clear whether this threshold value is appropriate in all cases, however, no other studies offer a different point of view. However, the validity of this rule is discussed more in later chapters.

While it is known that each hydrodynamic stimuli affects fish behaviour [see section 4.2], the difficulty in determining the specific influence of each is significant. For this reason, the final behavioural response of each individual, each timestep, is determined through a weighted averaged of the outputs of each rule [see section 4.6.10]. The weightings are controlled by the movementWeights array, which allows for easy modification to the influence of each rule, and therefore lends itself to calibration against experimental data. This approach is similar to that of Tan et al. [2018] who use a weighted average to determine location fitnesses. Gisen [2018] determines a behaviour based on a motivation/fatigue measure which is a function of distance moved over time; whereas fishPy, like most other models, assumes an inherent, constant motivation to migrate upstream, which Castro-Santos and Haro [2010] note is well-justified for salmonidae.

Discussion on Modelling from the Perspective of the Individual

Throughout the development of the model, the emphasis has been placed on understanding and modelling from the perspective of the individual. In some ways, this can limit prediction of pathways. For example, for a given domain, one could calculate the exact minimum energy pathway that successfully passes the domain. This would reveal the optimal route through the domain, but in reality would require a fish to have prior knowledge of the entire domain and its flow field. Therefore the sensory ovoid concept introduced by Goodwin [2004] is of vital importance and ensures proper sensory perception. Although it is known to be linked to the bodylength of the individual [Montgomery et al., 1995, Goodwin et al., 2006], exact quantification of the size of the sensory ovoid is difficult.

Discussion of Timestepping within fishPy

In an agent-based model, the timestep can generally be defined in one of two ways. The first is to prescribe a constant explicit timestep such as that used by Goodwin et al. [2014], Gao et al. [2016], Gisen [2018] and Tan et al. [2018]. The second is to use a varying implicit timestep such as that used in the elver passage models described in

chapter 3, wherein fish move a predetermined distance per step. This approach is also used by Abdelaziz [2013] and Zielinski et al. [2018]. Both are valid approaches, but a constant explicit timestep lends itself to a spatially-continuous model, whereas an implicit timestep lends itself to a spatially-discrete model. Therefore, `fishPy` handles timestepping using a constant explicit timestep.

The disadvantage of using a constant explicit timestep is that, to ensure model stability, a maximum timestep size is required [see section 4.3.5]. Within `fishPy`, this is a function of the lowest water velocity magnitude within the domain, which is assumed to coincide with the highest ground speed of an individual. However, this formulation could unnecessarily limit the timestep in regions of faster flow where fish are moving at a lesser ground speed. This could be overcome by varying the timestep and defining local timestep maxima. In theory this would reduce computational cost by reducing the necessary number of timesteps. However, it would increase the complexity of the code and could result in asynchronous movements between individuals. Another option to reduce computational expense is by setting a timestep maximum based on the average water velocity magnitude in the domain and then implementing a sub-timestep in regions where the ground speed exceeds a threshold determined by the maximum timestep value. This would reduce the overall maximum timestep and only solve smaller timesteps when required. A similar process is suggested by Goodwin et al. [2014] but not implemented. This approach was considered but decided against as the computational expense of a constant timestep within `fishPy` was deemed small enough.

4.7.2 Discussion on Limitations and Uncertainties of `fishPy`

Predicting behaviour using agent-based models is challenging due to the the inherent random and irrational nature of behaviour and decision-making [Bonabeau, 2002]. Furthermore, behaviour is often difficult to quantify and justify [Crooks and Heppenstall, 2012]. This is no different for `fishPy`, and therefore it is important to both verify model functionality and compare predictions to published data, addressed in chapters 5 and 6, respectively. Similarly, it is difficult to justify the threshold values used within many of the rules implemented within `fishPy`, and many of the published models give very little justification for the thresholds used. For example, it is likely that many threshold values are related to the bodylength of the individual, due to its role in determining

the swim speeds of the individual. However, this is not implemented as it is difficult to quantify and is not entirely covered within the literature. This lack of specific data within the literature is likely due to the difficulties associated with experimentally defining the behavioural reactions to exact values of hydrodynamic parameters, compounded by the significant task of proving causation rather than correlation. With the exception of `tkeAvoidance`, which takes its threshold value from the work of Gao et al. [2016], each threshold is value is determined through sensitivity analyses and qualitative assessments, addressed in chapter 5.

The `fishPy` model has a number of limitations. Firstly, the model has limited heterogeneity within its agents as an individual of a given bodylength will always have the same sustained and burst speeds. However, it was shown in chapter 3 that heterogeneity within the swim speed was important to capture the dynamics of the entire population. However, this is partially overcome within `fishPy` through using a population of individuals which are assigned bodylengths from a distribution. This indirectly assigns a distribution of swim speeds. Swim speed distributions, such as that used by the `HEPM` within chapter 3, could be implemented in the future but they are not considered in the present work. Secondly, fish within `fishPy` may not leave the water (defined as $\alpha \geq 0.5$ within the VOF formulation). However, brown trout with bodylengths $\leq 150mm$ and $\geq 150mm$ have been shown to be able to leap vertical gaps up to 33 cm and 40 cm, respectively [Holthe et al., 2005]. Therefore, it is likely that `fishPy` will underestimate passage efficiencies through domains where leaping is beneficial, such as across low-head weirs or through some types of fish passes. To implement leaping in `fishPy`, momentum conservation, gravity, species- and bodylength-specific leaping abilities, and a new formulation of the passability matrix (`G3D`) would also need to be implemented, vastly increasing the complexity of the model. Leaping could be implemented in the future but they are not considered in the present work. Lastly, there are a number of non-hydrodynamic stimuli that are known to affect behavioural responses in fish but are not considered in `fishPy` such as predator-prey relationships, noise, scent, temperature, and oxygenation [see chapter 2]. These are not implemented in `fishPy` as the model considers only hydrodynamic stimuli. However, due to the modular formulation of `fishPy`, additional environmental data (i.e. light, water temperature) could easily be added to the model in future versions, allowing for new rules determining responses to these new stimuli.

4.7.3 Conclusion to the Development of `fishPy`

This chapter has detailed the development of `fishPy`. In particular, the seven behavioural rules that constitute the governing ruleset. Each rule outputs a unit vector, which is then input into a decision making function. This ultimately determines the behavioural response of an individual. The behavioural rules are:

- Rule 1: `followFlow`. Move in the opposite direction to the determined local average velocity vector, weighted with velocity magnitudes to bias towards larger magnitudes.
- Rule 2: `minMaxEnergy`. Contains three distinct behavioural cases:
  - a) Seek the local minimum energy pathway - i.e. bias movement direction towards locally minimum velocities.
  - b) Have no energy preference if local hydrodynamic environment is already preferable.
  - c) Seek the local maximum energy pathway - i.e. bias movement direction towards locally maximum velocities, which represents the bulk of the flow.
- Rule 3: `randomWalk`. Move in a random direction, limited to 10° in vertical direction.
- Rule 4: `obAvoidance`. Bias movement vector in opposite direction to any established obstacles.
- Rule 5: `colAvoidance`. Move in the opposite direction to any other individuals within `repulsionDist`.
- Rule 6: `memory`. Move in the opposite direction to the spatially averaged local velocity vector, temporally-averaged across the memory of the individual.
- Rule 7: `turbulence`. Bias movement away from turbulent areas, where a turbulent region is defined as TKE $>$ threshold.

The developmental tool principles, introduced in section 1.2, were consulted throughout the development of the `fishPy` tool. These principles have ensured good practice and a focus on the end user and open-source nature of the tool, in line with client

expectations. The principles are reiterated in table 4.6, along with how they are considered within the development of the `fishPy` tool.

Table 4.6: A comparison of the fishPy tool against the established developmental tool principles.

No.	Principle	Achieved
1	Open source	The fishPy tool was programmed in Python 3.6, and has been developed to work with OpenFOAM and Paraview. However, the pre-processing required for a fishPy input is currently achieved within MATLAB. The fishPy tool and the MATLAB pre-processor script are available from University of Leeds Data Repository [Padgett, 2020].
2	Transparent	Development, verification, sensitivity analyses, and an application of the fishPy tool are included in this work. Furthermore, the codes are openly available from University of Leeds Data Repository [Padgett, 2020].
3	Generalised	The fishPy code is almost entirely generalised; with the only requirement that the global z axis of the user input dataset is parallel to the gravity direction.
4	Spatially 3D	The fishPy model is spatially three dimensional.
5	Self-contained	Built in Python 3.6 and has no other dependencies.
6	Modular	The fishPy tool is developed in a modular manner, with the species contained within a class. This facilitates expansion of the code to include other classes (species) with their own behavioural rules.
7	Individual Focus	The fishPy tool treats each simulated fish as an individual and features heterogeneity within the population of fish. Furthermore, the sensing of all environmental data and the behavioural rules are executed from the point of view of the individual, and make no assumptions of outside knowledge.

Chapter 5

Verification and Sensitivity Analyses of `fishPy`

5.1 Introduction

The previous chapter detailed the approach, structure, and behavioural ruleset of `fishPy`. The `fishPy` tool is developed with emphasis on the outlined developmental tool principles [see table 1.1 in chapter 1]. Therefore, in line with the transparency principle, this chapter details the verification of the function of `fishPy` on a rule-by-rule basis. Verification is intrinsic to the development of a model[Crooks et al., 2008], yet very few of the published fish path prediction models present any verification processes or results [see section 2.8]. However, verification is considered part of the greatest challenge of agent-based modelling [Crooks et al., 2008]. This chapter also details the sensitivity of predicted fish trajectories to various model parameters. Sensitivity analyses evaluate one chosen parameter at a time, in isolation, and assess how changing this parameter affects model outputs and in some cases model stability. All of the published fish path prediction models use prescribed parameters to govern fish behaviour and define the environment. However, only Goodwin et al. [2014], Gisen [2018] and Zielinski et al. [2018] present any consideration for sensitivity of predicted fish trajectories to any defined parameter or threshold.

Verification and sensitivity analyses were enabled through the design and execution of a variety of CFD verification datasets. These verification datasets are hypothetical fluid environments and are not based on real systems; they exist ensure that the `fishPy` model is functioning as expected and to assess model sensitivity. As such their accuracy is not explored, nor are they compared to experimental data.

5.1.1 Aim

The aim of this chapter is to perform verification of each behavioural rule described in chapter 4 to ensure that each rule is functioning as intended. Furthermore, this chapter also aims to perform a number of sensitivity analyses to explore and understand the dependency of model outputs on the value of key parameters.

This is achieved through the following objectives:

- Development and execution of a number of CFD verification datasets, tailored specifically to the verification of each rule.
- Application of a modified `fishPy` to each verification domain to verify each behavioural rule separately.

- Execution of a number of sensitivity analyses of key parameters:
  - `minMaxEnergy` parameters
  - Decision timestep
  - Sensory range
  - Interpolated spatial resolution

5.2 Verification Domains

In order to verify the behavioural ruleset, multiple verification datasets were created. Each of these were created using openFOAM 4.1, and are detailed in this section. These domains are simple geometries designed as test beds for `fishPy`. Therefore, the CFD results are not validated, nor is the dependency of the results on the mesh explored. Each of these CFD datasets presents a unique hydrodynamic environment tailored to testing the functionality of each rule. The behavioural rules are:

- Rule 1: `followFlow`. Move in the opposite direction to the determined local average velocity vector, weighted with velocity magnitudes to bias towards larger magnitudes.
- Rule 2: `minMaxEnergy`. Seek local minimum or maximum energy pathway, or have no preference, depending on local hydraulics (behaviour controlled by `minMaxEnergy` parameters).
- Rule 3: `randomWalk`. Move in a random direction, limited to 10° in vertical direction.
- Rule 4: `obAvoidance`. Bias movement vector in opposite direction to any established obstacles.
- Rule 5: `colAvoidance`. Move in the opposite direction to any other individuals within `repulsionDist`.
- Rule 6: `memory`. Move in the opposite direction to the spatially averaged local velocity vector, temporally-averaged across the memory of the individual.
- Rule 7: `turbulence`. Bias movement away from turbulent areas, where a turbulent region is defined as TKE $>$ threshold.

The first dataset, `veriSetA`, considers flow in a straight channel with a parabolic velocity profile, and was designed to verify the `followFlow` rule and to test the `minMaxEnergy` rule when biasing towards the local minimum energy pathway. The second dataset, `veriSetB`, considers flow in a straight channel featuring an obstacle, which constricts the flow and causes a wake region downstream of the obstacle. Two additional datasets were created, `veriSetB2` and `veriSetB3`, which are variations on `veriSetB` and consider a larger and smaller obstacle, respectively. These were designed to verify the `obAvoidance` and `turbAvoidance` rules, and to test the `minMaxEnergy` rule when biasing towards the local maximum energy pathway. The third dataset, `veriSetC`, considered flow around a cylinder within a straight channel, and was designed to verify the `obAvoidance` rule. No specific dataset was designed to test the `colAvoidance` and `randomWalk` rules as these can be verified using any domain.

5.2.1 Verification Domain 1: `veriSetA`

The first verification dataset, termed `veriSetA`, considers water flowing through an open channel; $32m$ long, $4m$ wide, and $4m$ deep, figure 5.1. This domain was created as a simple example hydrodynamic environment that a virtual fish would need to pass. The geometry was created and meshed using the `blockMesh` utility within openFOAM with a regular uniform grid of hexahedral elements with a spatial resolution of $0.1m$, resulting in a mesh size of approximately 500000 cells. A figure showing the mesh is included in appendix D.

The volume of fluid method is used, which is implemented using the `interFoam` solver within openFOAM. Furthermore, a transient RANS approach was employed with the k–ω SST closure used [see section 2.5.3]. Residual tolerances were taken as 1×10^{-8} for all cases. Second order numerical schemes are used in all cases, table 5.1. Gravity is set to 9.81 ms^{-2} and acts in the negative z direction. Values of ω and k at the inlet were selected based on equations 5.1 and 5.2, [Menter, 1993].

$$\frac{U_\infty}{L} < \omega < 10\frac{U_\infty}{L} \tag{5.1}$$

where U_∞ is the expected freestream velocity (ms^{-1}), and L is the length scale for the domain (m).

$$10^{-5}\frac{U_\infty^2}{Re_L} < k < 0.1\frac{U_\infty^2}{Re_L} \tag{5.2}$$

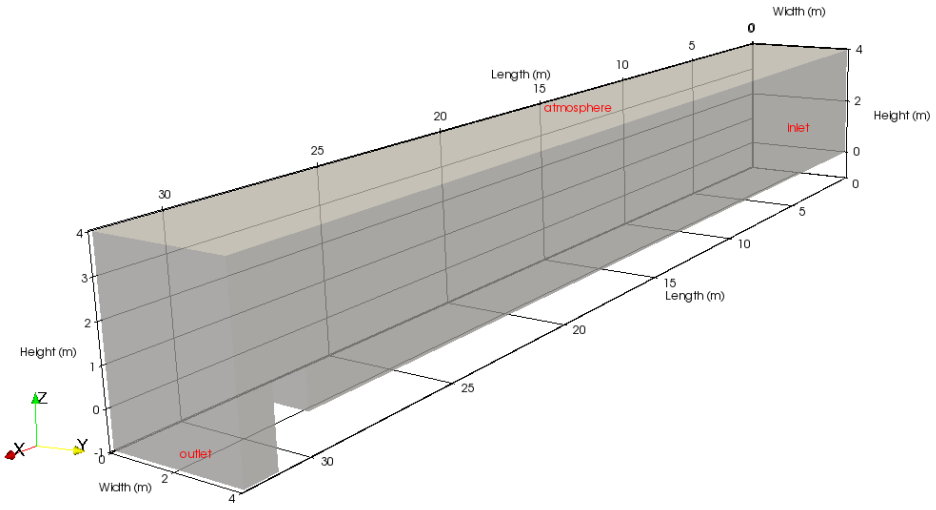

Figure 5.1: Schematic of the `veriSetA` domain. Inlet, outlet, and atmospheric outlet are labelled. Surfaces without labels are no slip walls.

where Re_L is the Reynolds number using the length scale, L.

Water was patched into the domain at time $T = 0$, at a height of $z = 1m$. Water entered the domain through the inlet, located at $x = 0m$, with a defined streamwise velocity profile, equation 5.3. The inlet spanned the entire channel width and extended between $0m \leq z \leq 1m$. This resulted in a parabolic velocity profile with a maximum of 1.0 ms^{-1} at the centre of the channel, falling to a minimum of 0.2 ms^{-1} at the near-wall channel sides. This parabolic profile was used as `veriSetA` was designed to verify the `followFlow` rule and to test the `minMaxEnergy` rule when biasing towards the local minimum energy pathway. This velocity profile is conducive to verification of `minMaxEnergy` as the minimum energy pathway was easily identified (i.e. near-wall).

$$U = 1.0 - 0.2(y - 2.0)^2 \ ms^{-1} \tag{5.3}$$

Water and air could leave the domain through either the downstream outlet or via the atmospheric outlet along the top of the domain. Furthermore, only air could enter from these locations if required for mass continuity. A weir (height, $z = 1m$) is placed at the downstream end of the domain ($x = 30m$) to control the downstream water level. The simulation was executed for $150s$ of flow time. The initial timestep was set to $0.05s$ and was automatically varied to ensure stability (following the CFL condition)

Table 5.1: Details of CFD schemes and parameters used throughout all verification domains.

Name	Type	Accuracy
Interface Capturing Scheme	Volume of Fluid	-
Pressure-Velocity Coupling	PIMPLE*	-
Timestep Scheme	Crank Nicolson	Second Order
Gradient Scheme	Gauss Linear	Second Order
Divergence Scheme	Gauss Linear	Second Order
Laplacian Scheme	Gauss Linear	Second Order

*PIMPLE is a combination of the PISO and SIMPLE algorithms.

using the `adjustTimestep` function in openFOAM.

The velocity and water surface heights were monitored along a vertical line located at $x = 20m, y = 2m$, which spanned the total height of the domain. Cross-stream and vertical velocities were found to be near-zero and therefore the streamwise velocity component dominated. After 120 seconds of flow time, the streamwise velocity profile along this line entered into a psuedo-steady state wherein the maximum velocity along the line began to oscillate between 0.69 and 0.76 ms^{-1}, with a time period of approximately 12 s, figure 5.2. Furthemore, the water surface location varied negligibly with time, between 1.595 and 1.6 m. Throughout these oscillations, the velocity profile maintained approximately the same shape, wherein the streamwise velocity rapidly increased to a maximum at a height of approximately 0.25 m. The velocity then decreased to a value of approximately 0.5 ms^{-1} at the water surface ($z \approx 1.6m$), and then subsequently decreased further to approximately zero at the atmospheric outlet ($z = 4m$). In order to create a domain which could be input into `fishPy`, the results were temporally averaged across 30 seconds of flow time; from 120 to 150 s, using a temporal resolution of 1 s. A comparison of the velocity profile of the temporally averaged result at $x = 20m$ and the velocity profile at $T = 150s, x = 20m$ shows minimal differences, figure 5.3. This, coupled with the small variations seen between $T = 120$ to $150s$, suggests the temporally averaged results are representative of the flow in the channel.

The temporally-averaged free surface location exists at approximately $z = 1.6m$, figure 5.4, and is approximately independent of x upstream of the weir, figure 5.5. This increase in the free surface height compared to the initial state is due to the influence

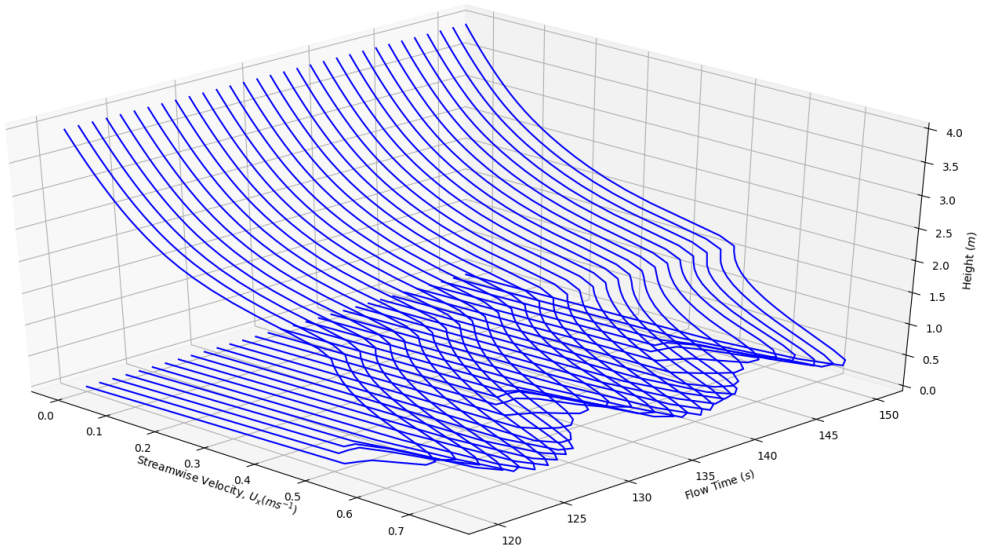

Figure 5.2: Streamwise velocity profiles over a vertical line located at $x = 20m, y = 2m$ within the `veriSetA` domain extracted for timesteps between $120s$ and $150s$ of flow time, inclusive, with a temporal resolution of $1s$.

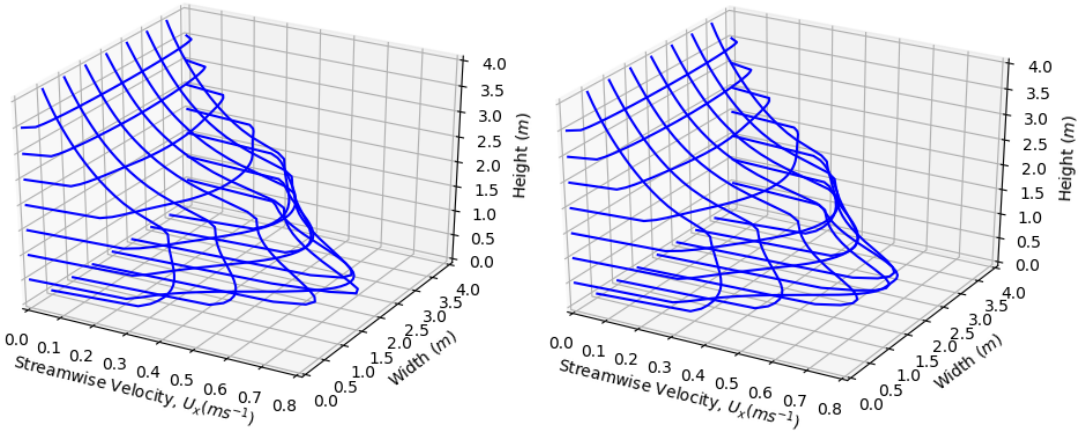

(a) (b)

Figure 5.3: Streamwise velocity profiles on the plane $x = 20m$ within `veriSetA` for a) $T = 150s$ and b) temporally averaged from 120 to $150s$, inclusive. Data were extracted along vertical and horizontal lines spaced $0.5m$ apart.

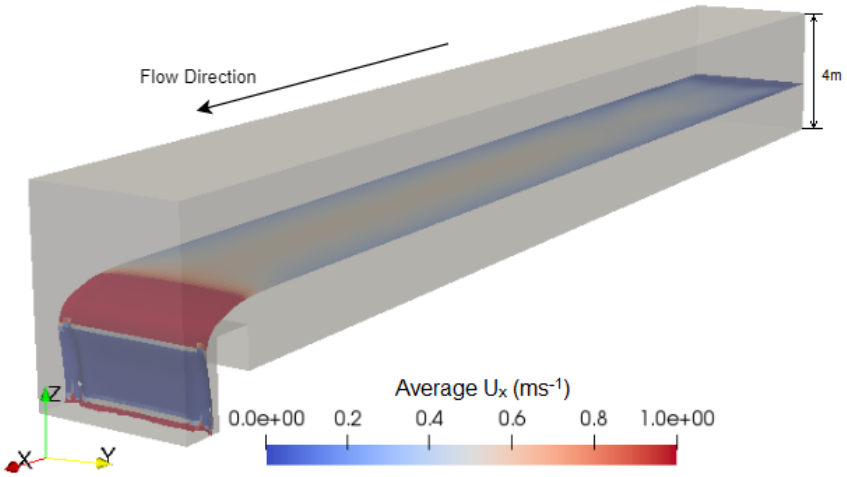

Figure 5.4: Temporally averaged isosurface at $\alpha = 0.5$ with contours of temporally averaged streamwise velocity. Colourbar fixed between 0 and 1 ms^{-1} for clarity. No negative streamwise velocities exist within the channel. Flow moves in the positive x direction. Gravitational acceleration acts in the negative z direction.

of the weir, restricting flow rate out of the domain. The velocity profile at the surface is parabolic, with a maximum existing at the centre and minima existing at either side of the channel, figure 5.4. This is corroborated by figures 5.5 and 5.6, which show that the velocity profile is parabolic throughout the domain. This parabolic profile is strongest close to the inlet and reduces with increasing x due to energy lost to the surrounding water; particularly due to the water that exists above the inlet, figures 5.5 and 5.6.

Data downstream of the weir is discarded before preparing the domain for use with `fishPy` [see section 5.3], as the weir was included purely to determine the water height within the channel. This verification dataset provides a simple domain for testing of `fishPy` as the velocity field is dominated by U_x at all locations, meaning that no recirculation zones exist. A modified version of `veriSetA` was created, termed `veriSetAK` in order to verify the `tkeAvoidance` rule. This domain is a copy of the final, temporally-averaged `veriSetA` domain, with a modified turbulence kinetic energy field. Within the new `veriSetAK` domain, the artificial TKE is set to maxima of $0.9m^2s^{-2}$ along either cross-stream wall, and decrease linearly to a value of $0.0m^2s^{-2}$ along the centreline ($y = 2m$). This is not the output of a computational fluid dynamic simulation and is an artificial domain created solely to verify the function of the `tkeAvoidance` rule.

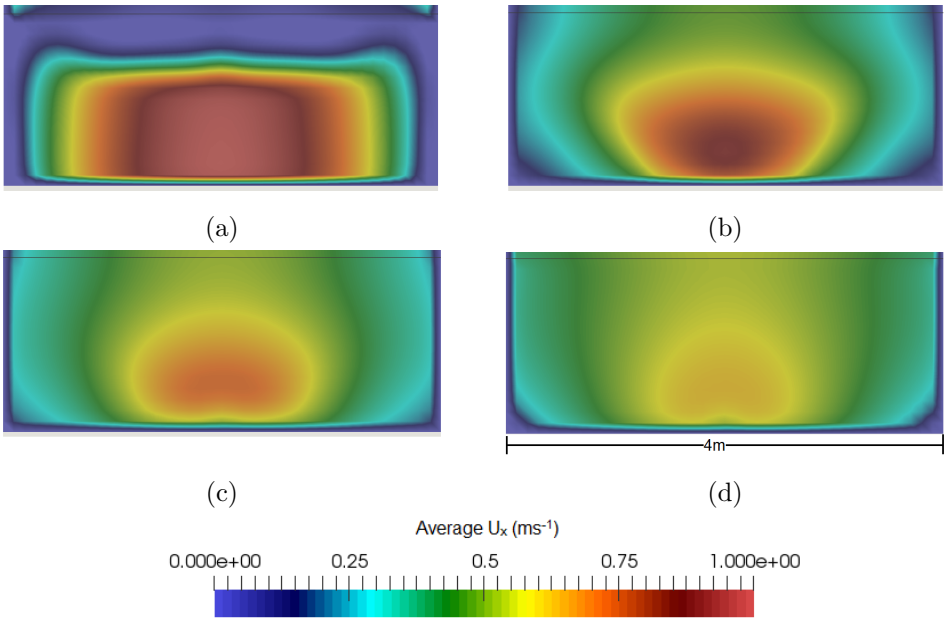

Figure 5.5: View looking upstream at yz planes taken at a) $x = 1m$; b) $x = 10m$; c) $x = 19m$; and d) $x = 28m$. Each plane is contoured with U_x and the black lines denote the free surface location in each case. All presented data are temporally-averaged.

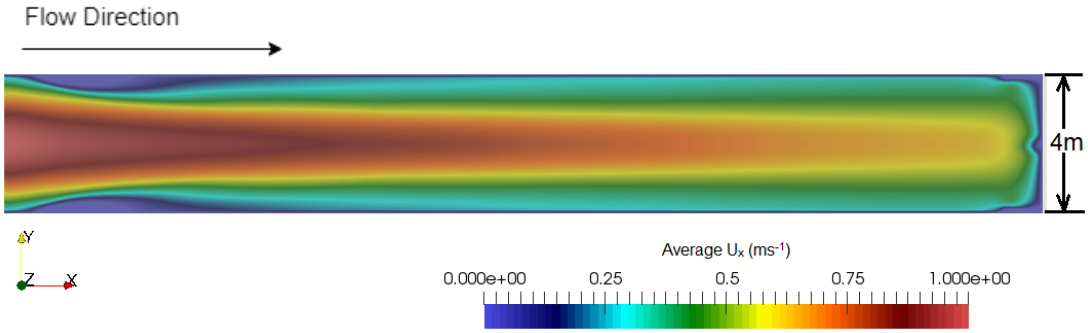

Figure 5.6: Planform view of the `veriSetA` domain, with contours of temporally-averaged U_x extracted along the xy plane $z = 0.5m$. Contour values are fixed between 0 and 1 ms^{-1} for clarity. No negative streamwise velocities exist within the channel.

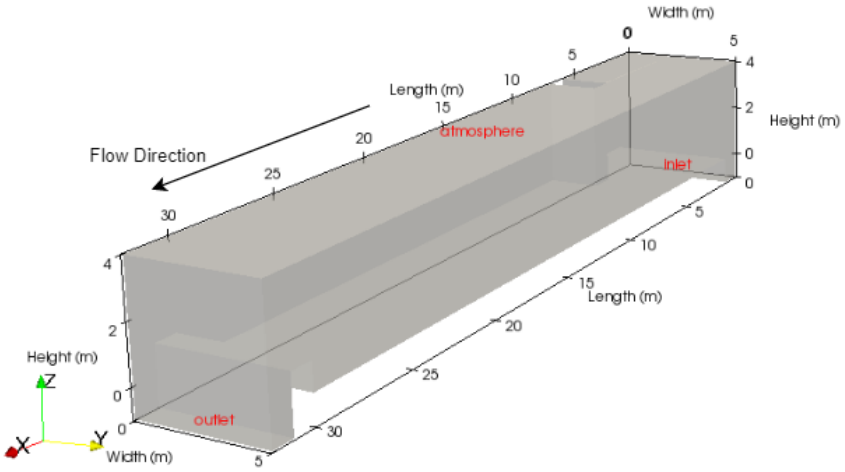

Figure 5.7: Schematic of the `veriSetB` domain. Inlet, outlet, and atmospheric outlet are labelled. Surfaces without labels are no slip walls. Flow moves in the positive x direction. Gravitational acceleration acts in the negative z direction.

5.2.2 Verification Domain 2: `veriSetB`, `veriSetB2`, and `veriSetB3`

The second verification dataset takes on three distinct forms, named `veriSetB`, `veriSetB2`, and `veriSetB3`. Each considers a similar open channel domain; 32 metres long, 5 metres wide, and 4 metres deep, figure 5.7. However, each of these domains feature a blockage approximately $5m$ downstream of the inlet. The blockages are present on one side of the channel (negative y) and extend through the entire domain in z and $1m$ in x. The `veriSetB` domain considers a blockage which extends 2 metres into the channel in y. The `veriSetB2` and `veriSetB3` domains consider blockages which extend $3m$ and $1m$ into the channel in y, respectively. The `veriSetB` domain was created to demonstrate the ability of an individual to navigate an obstacle and the turbulence it produces. Furthermore, the `veriSetB2` and `veriSetB3` variants were created to ensure that parameters used in behavioural rules were not over-fitted to a single obstacle size or turbulent wake, particularly for the `minMaxEnergy` rule.

In each case, the geometry was created and meshed using the `blockMesh` utility within openFOAM with a regular, uniform grid of hexhedral elements with a spatial resolution of $0.1m$, resulting in a mesh sizes of approximately 650000 cells. As in `veriSetA`, water could exit the domain via either the downstream outlet or via the atmospheric outlet along the top of the channel. However, water entered the domain

with a constant vertical velocity, $U_z = 0.5$ as the inlet was moved to the XY plane, figure 5.7. Water was patched into the domain at $T = 0s$ at a constant height of $z = 1m$. The same CFD approach employed in solving `veriSetA` was used to solve the `veriSetB`, `veriSetB2`, and `veriSetB3` domains [see table 5.1].

For the `veriSetB` domain, streamwise velocity and water surface height were monitored along vertical lines located at $x = 6.5m, y = 3m$ and $x = 8m, y = 2.5m$. These monitor lines were chosen as it was assumed temporal variations would be greatest in this region due to the wake of the obstacle. After 120 s of flow time, the streamwise velocity profile along the line located at $x = 6.5m, y = 3m$ was seen to vary little with additional flow time, figure 5.8a. The water surface at this location was $1.465m$ and found to be independent of time after $T = 120s$. The velocity profile along the line located at $x = 8m, y = 2.5m$, was seen to enter into a pseudo-steady state wherein, while maintaining the same shape, the maximum velocity began to oscillate between a maximum of $0.41ms^{-1}$ and a minimum of $0.37ms^{-1}$, with a time period of approximately $10s$, figure 5.8b. The water surface at $x = 8m, y = 2.5m$ was found to be $1.460m$ and did not vary with time after $T = 120s$. The streamwise velocity along an xy plane located at $z = 0.5m$ was also monitored and seen to vary little with time with the exception of the region nearest the weir [see appendix D for figures]. However, this region is of little importance compared to the region containing the obstacle. Therefore, given that little variation was seen throughout most of the `veriSetB` domain, the results were averaged from $T = 120$ to $150s$ to create an appropriate input for `fishPy`, which was assumed to be representative of the flow in the channel.

The temporally-averaged data show that the velocity in `veriSetB` is independent of y until approximately $2m$ upstream of the obstacle (negative y), at which point U_x decreases, and U_y and U_z increase in the region directly upstream of the obstacle, figure 5.9. Furthermore, the obstacle introduces a constriction in the channel resulting in an increase in U_x. The free surface is located at approximately $z = 1.5m$ and is independent of x upstream of the weir. A large recirculation zone is present in the wake of the obstacle. An additional recirculation region is present near the downstream weir and is located at a higher vertical location, figure 5.9. These recirculation zones are significant for adequate verification of the `fishPy` model as recirculation zones and their associated turbulence are known to disorientate passing individuals and are subsequently avoided by fish.

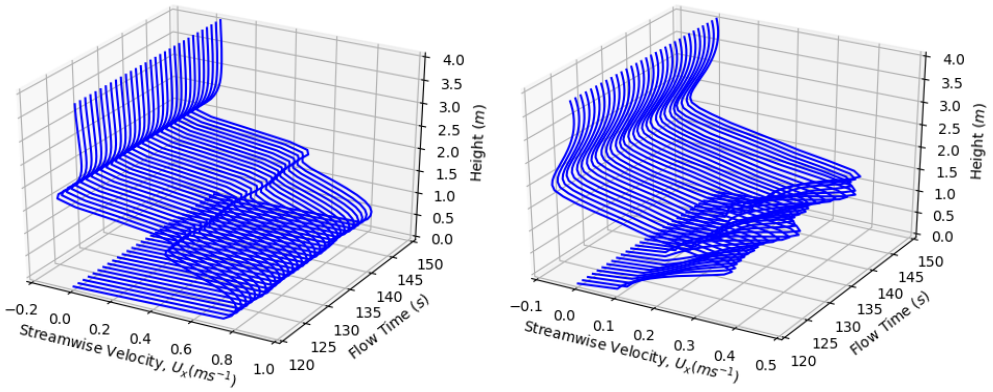

Figure 5.8: Streamwise velocity profiles along vertical lines located at a) $x = 6.5m, y = 3m$ and b) $x = 8m, y = 2.5m$ within the `veriSetB` domain for timesteps between $120s$ and $150s$ of flow time, inclusive, with a temporal resolution of $1s$.

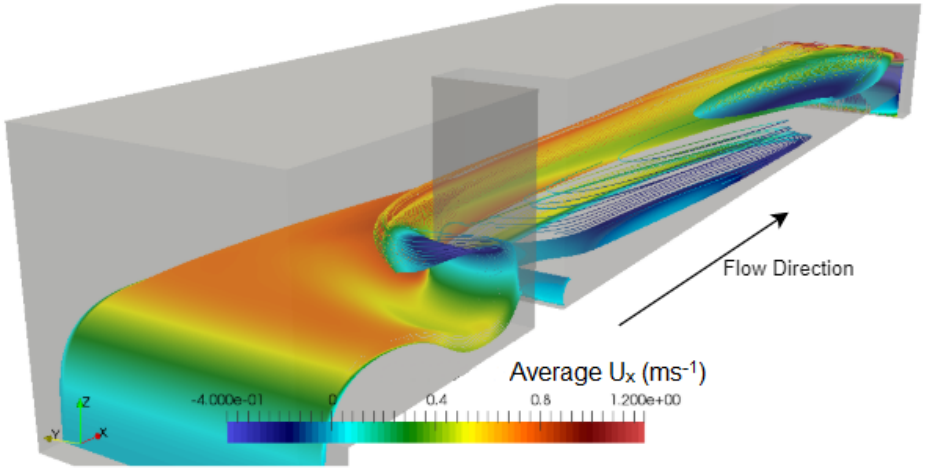

Figure 5.9: 3D view of the `veriSetB` domain with streamlines contoured with U_x. Note the negative lower bound on the legend, denoting regions of reversed flow. All presented data are temporally-averaged.

For the `veriSetB2` domain, streamwise velocity and cross-stream velocity were monitored along horizontal lines located at $x = 8m, z = 0.5m$ and $x = 9m, z = 1m$. These monitor lines were chosen as it was assumed temporal variations would be greatest in this region due to the wake of the obstacle. After $120s$ of flow time, streamwise velocities along both lines were seen to vary negligibly with time, figure 5.10. Cross-stream velocity profiles were found to be less stable, but were a small in comparison to the streamwise velocity and maintained the same profile throughout the $30s$ period, figure 5.11. These velocity fluctuations represent the increased turbulence present within the wake of the obstacle. As with `veriSetB`, the streamwise velocity along an xy plane located at $z = 0.5m$ within the `veriSetB2` domain was monitored [see appendix D for figures] and found to vary little with time. Therefore, given that little variation was seen throughout the domain, the results were averaged from $T = 120$ to $150s$ to create an input for `fishPy`, which was assumed to be representative of the flow in the channel.

For the `veriSetB3` domain, streamwise velocity and cross-stream velocity were monitored along horizontal lines located at $x = 8m, z = 0.5m$ and $x = 9m, z = 1m$. These monitor lines were chosen as it was assumed temporal variations would be greatest in this region due to the wake of the obstacle. Streamwise velocities were seen to vary little with increasing time, figure 5.12. The cross-stream velocity profile was found to be less stable, entering into an oscillation immediately downstream of the obstacle in both monitor lines [see figure 5.13, width $\approx 4.5m$]. This oscillation was larger closer to the obstacle where it moved between a minimum of $-0.08ms^{-1}$ to a maximum of $0.04ms^{-1}$ with a time period of approximately $20s$, figure 5.13a. The strength of the oscillation reduced with distance from the obstacle where it moved between a minimum of $-0.05ms^{-1}$ to a maximum of $0.01ms^{-1}$ with the same time period. The streamwise velocity along an xy plane located at $z = 0.5m$ within the `veriSetB3` domain was also monitored [see appendix D for figures] and was found to vary little with time. Therefore, given that little variation was seen throughout the domain, the results were averaged from $T = 120$ to $150s$ to create an input for `fishPy`, which is assumed to be representative of the flow in the channel.

In each `veriSetB` variant domain, the streamwise velocity dominated the flow field. Increasing the size of the obstacle resulted in an increase in the velocity near the obstacle as the flow became more constricted, figure 5.14. The recirculation zones produced in the wake of the obstacles scaled with the size of the obstacle, figure 5.14.

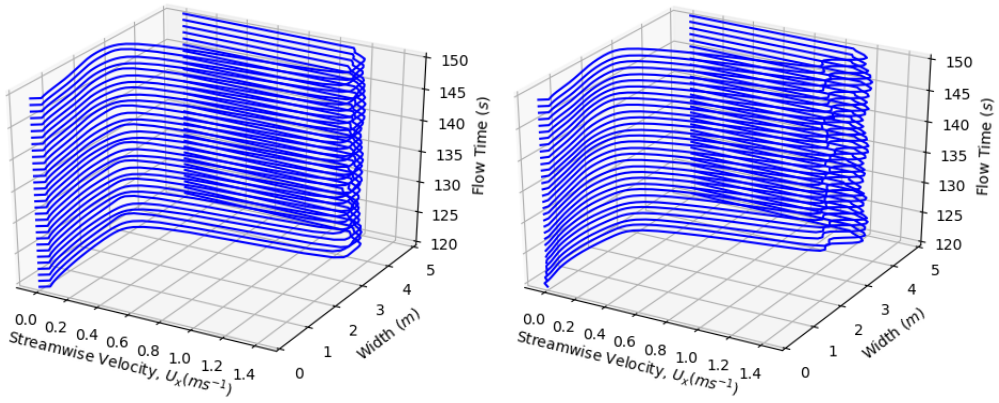

(a) (b)

Figure 5.10: Streamwise velocity profiles along horizontal lines located at a) $x = 8.0m, y = 0.5m$ and b) $x = 9.0m, y = 1.0m$ within the `veriSetB2` domain for timesteps between 120 and 150 s of flow time, inclusive, with a temporal resolution of 1 s.

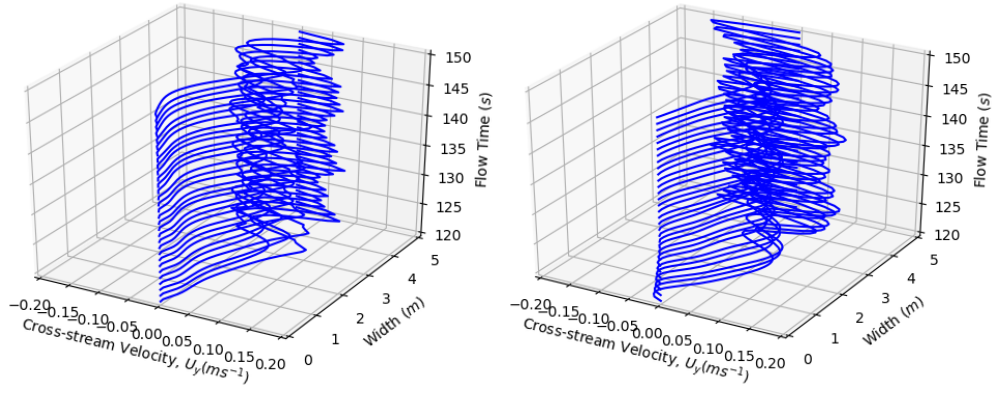

(a) (b)

Figure 5.11: Cross-stream velocity profiles along horizontal lines located at a) $x = 8.0m, y = 0.5m$ and b) $x = 9.0m, y = 1.0m$ within the `veriSetB2` domain for timesteps between 120 and 150 s of flow time, inclusive, with a temporal resolution of 1 s.

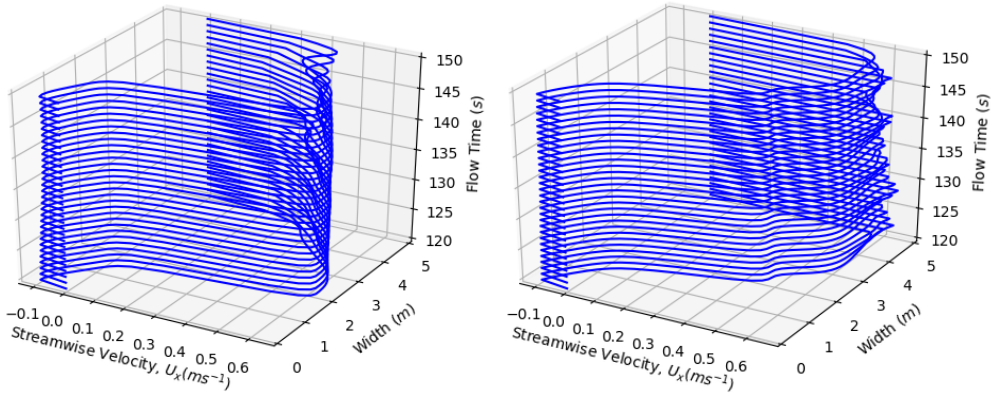

(a) (b)

Figure 5.12: Streamwise velocity profiles along horizontal lines located at a) $x = 8.0m, y = 0.5m$ and b) $x = 9.0m, y = 1.0m$ within the `veriSetB3` domain for timesteps between 120 and 150 s of flow time, inclusive, with a temporal resolution of 1 s.

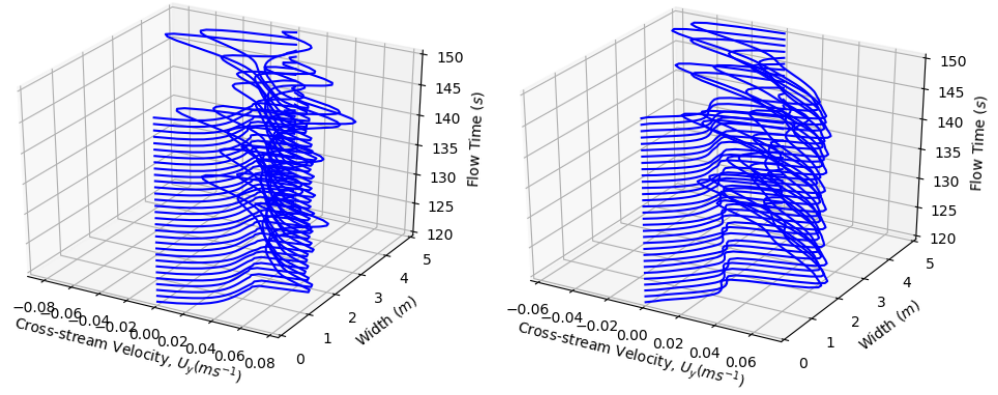

(a) (b)

Figure 5.13: Cross-stream velocity profiles along horizontal lines located at a) $x = 8.0m, y = 0.5m$ and b) $x = 9.0m, y = 1.0m$ within the `veriSetB3` domain for timesteps between 120 and 150 s of flow time, inclusive, with a temporal resolution of 1 s.

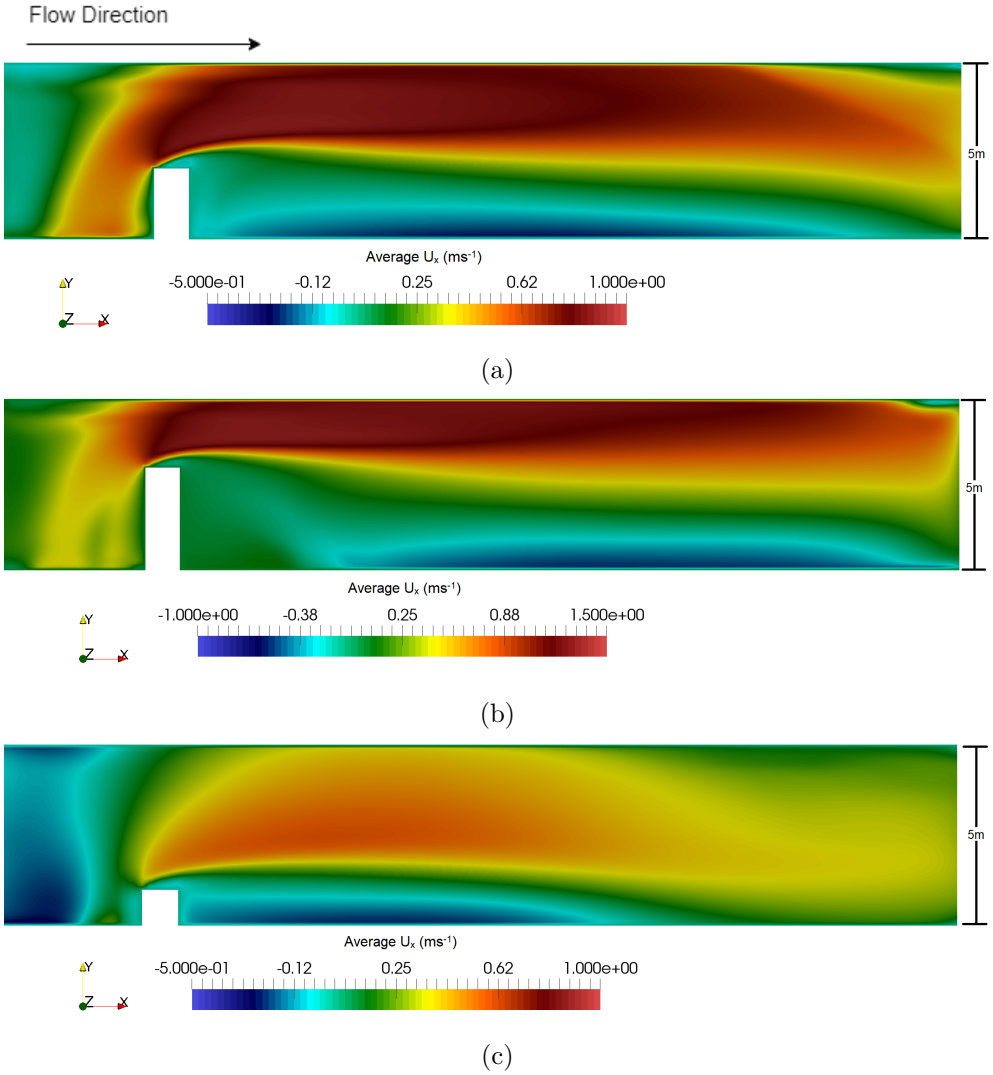

Figure 5.14: Planform views of the a) `veriSetB` domain, b) `veriSetB2` domain, and c) `veriSetB3` domain; with overlain contours of temporally averaged U_x taken at a plane $z = 0.5m$ in each case. Note the different contour scale in each case.

5.2.3 Verification Domain 3: `veriSetC`

The third verification dataset, `veriSetC`, considers an open channel measuring $30m$ long, $5m$ wide, and $4m$ deep. This domain features a vertical cylinder of diameter $2m$ placed in the centre of the channel approximately $5m$ downstream of the inlet, figure 5.15. This dataset features a similar hydrodynamic environment to that of `veriSetB`, with an heterogeneous velocity field and an increased level of turbulence in the region downstream of the obstacle. The geometry was meshed using the `snappyHexMesh` utility within openFOAM, with an initial `blockMesh` with a spatial resolution of $0.25m$. Three levels of surface refinement was specified around the obstacle to ensure the increased velocity and turbulence near the obstacle was effectively captured. Similarly, two levels of region refinement was specified to any cell within $0.75m$ of the obstacle surface, and one level of region refinement was specified to cells within $1.5m$ of the obstacle surface. In `snappyHexMesh`, refinement is implemented by selecting cells that intersect the given surface .stl file, or are within the specified region, in 3D space and splitting them into two equal halves in each axis (i.e. one cell is split into 8 equal cells), repeated for each level of surface refinement. This cell refinement ensured a smooth transition in cell size between the far field and close to the obstacle surface. The resulting mesh is a mixture of hexahedral, polyhedral, and prismatic cells and a total mesh size of approximately 700000 cells. The same parabolic velocity profile was specified at the inlet as was used in `veriSetA` (equation 5.3). The same CFD methodology employed in solving `veriSetA` was used to solve the `veriSetC` domain [see table 5.1].

The velocity was monitored along a horizontal monitor line located at $x = 8m, z = 0.5m$. This line was chosen as water velocities were greatest in the near-bed region and it was expected that velocity variations would be largest in this area due to the wake of the obstacle. The streamwise velocity profile maintained the same shape throughout the sampled time period with two approximately-equal maxima located either side of the centre of the channel (approximately $y = 2m, and y = 4m$) and fell to zero at the boundaries on either side [see figure 5.16a]. The cross-stream velocity profile maintained the same shape throughout the sampled time period, figure 5.16b. The cross-stream velocities either side of the centreline of the channel were approximately equal and opposite with both sides featuring maxima of $\approx 0.2ms^{-1}$ towards the centre of the channel, figure 5.16b. Therefore, given that little variation was seen throughout the domain, the results were averaged from $T = 120$ to $150s$ to create an appropriate input

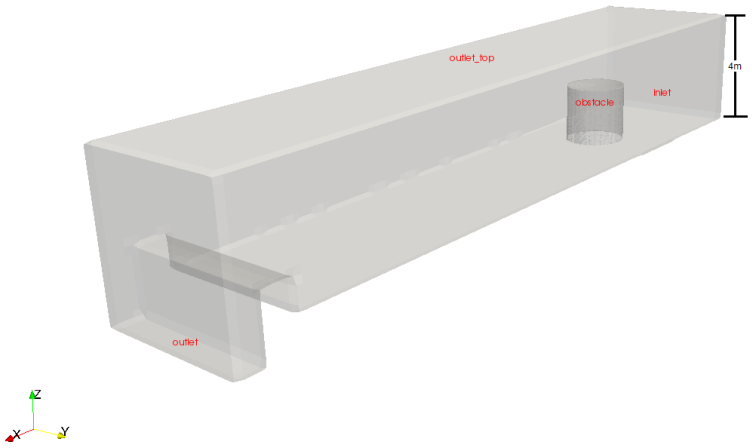

Figure 5.15: Schematic of the `veriSetC` domain. The inlet, outlets are labelled. The obstacle is also labelled. Surfaces without labels are no slip walls. Flow moves in the positive x direction. Gravitational acceleration acts in the negative z direction.

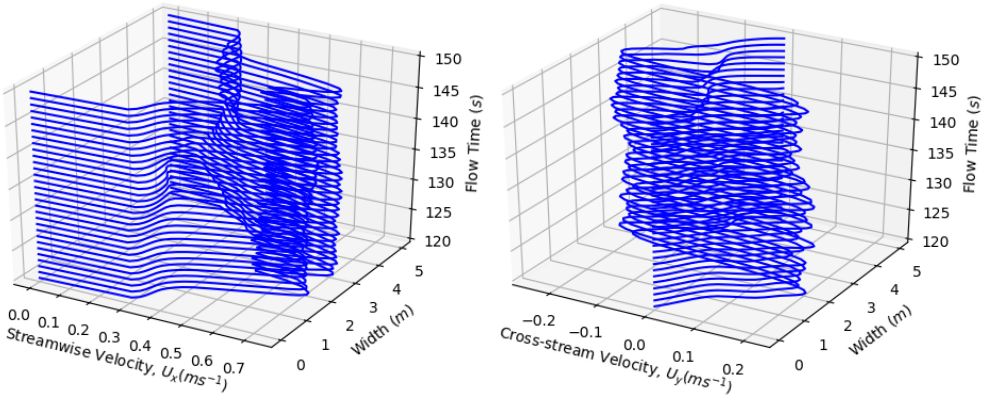

(a) (b)

Figure 5.16: Velocity profiles along the horizontal monitor line located at $x = 8.0m, z = 0.5m$ within the `veriSetC` domain for a) streamwise velocity, and b) cross-stream velocity for timesteps between 120 and 150 s of flow time, inclusive, with a temporal resolution of 1 s.

for `fishPy`, which is assumed to be representative of the flow in the channel.

Figure 5.17 shows that the presence of the obstacle causes a stagnation zone immediately upstream of the obstacle with an associated increase in free surface height. Furthermore, similarly to `veriSetB`, the presence of the obstacle constricts the flow resulting in acceleration either side of the obstacle, which results in an increase in local velocity, figure 5.17. A wake is created immediately downstream of the obstacle with an associated reduction in the free surface height, figure 5.17. The recirculation seen within the wake is smaller and weaker than that of `veriSetB`.

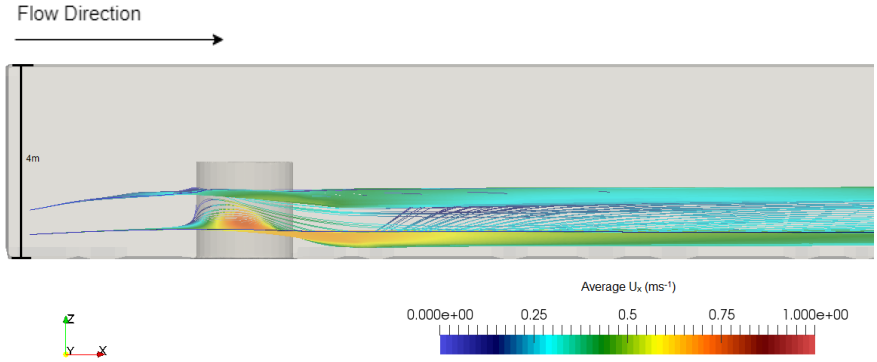

(a)

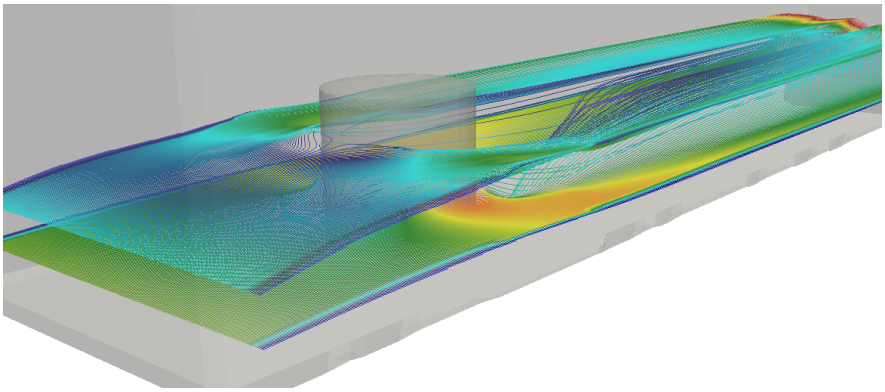

(b)

Figure 5.17: a) Side view and b) 3D view of the `veriSetC` domain. Streamlines are created at horizontal lines at $x = 0.5m$, and $z = 0.5m$ and $1.0m$, contoured with the U_x restricted to between 0 and 1.0 ms^{-1} for clarity. Data are temporally-averaged from 120 to 150s of flow time.

5.3 Preparing the Datasets for fishPy

Once the verification simulations were completed, the datasets required additional modification in order to prepare them for use with the fishPy code. As fishPy requires spatially uniform grids in the form of multiple three dimensional matrices, it was necessary to interpolate the resulting flow fields. A custom MATLAB script was written to import a .csv file of temporally-averaged flow results and then output the required three dimensional matrices. This was done by first using the meshgrid function within MATLAB to create a regular gridded mesh of the bounding box. Each of the variables were then interpolated onto the regular grid. The geometry matrix, G3D, was then created by looping through each point and interrogating whether the point was within the polyhedron defining the domain using the function inpolyhedron. This function required an .stl file to define the polyhedral domain, which was supplied by the surfaceMeshTriangulate utility within OpenFOAM. This MATLAB script is available from the University of Leeds Data Repository, [Padgett, 2020].

5.4 Verification of Behavioural Ruleset

This section presents calculated trout trajectories through the verification datasets. Verification is handled on a rule-by-rule basis. In the following subsections, each rule is considered individually and the parameters and agent attributes used are denoted for each case. Both the results and the discussion are presented together for each rule.

5.4.1 Verification of Rule 1: followFlow

The followFlow rule forms the basis of the movement of an individual. The rule uses local hydraulic information to determine the local upstream direction and then moves the individual in that direction. Two test cases were used to verify the successful function of this rule. First, a single individual was created along the centreline of the veriSetA domain at mid-depth near the downstream boundary of the domain (coordinates $[25.0m, 2.0m, 0.5m]$). This location was chosen to eliminate the impact of the downstream weir on the local hydrodynamic environment. The individual moved based only on the output of the followFlow rule. The following parameters were used to verify the followFlow rule: fishTimestep was set to $0.5s$, Tmax was set to 1000, sensoryRange was set to 1. Furthermore, the bodylength_mean was set to $0.15m$, and

`bodylength_deviation` was set to $0m$, effectively ensuring that any created individual was of length $0.15m$. It was expected that the individual would move in the direction against the average local velocity, which in the `veriSetA` domain is dominated by flow in the positive x direction. Figure 5.18a shows that, with only the `followFlow` rule enabled, the individual moves in a straight line through the domain in the negative x direction. This is expected as U_x completely dominates the velocity field throughout the domain.

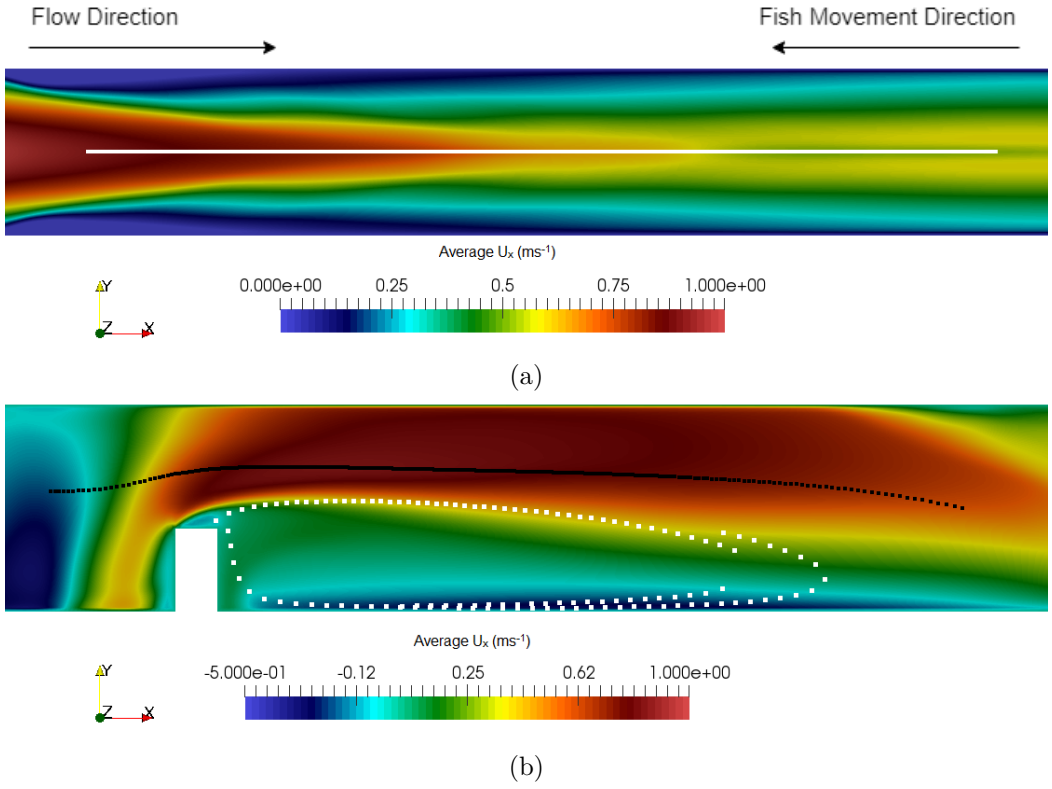

Figure 5.18: Planform view of calculated fish trajectories through the a) `veriSetA` and b) `veriSetB` domain with overlain contours of U_x, extracted along the $z = 0.4m$ plane. The individuals were created at a) $[25.0m, 2.0m, 0.5m]$ and b) $[25.0m, 2.5m, 0.5m]$ (black) and $[11.5m, 0.15m, 0.4m]$ (white). All individuals moved based on the output of the `followFlow` rule only.

Second, two individuals were created within the `veriSetB` domain at mid-depth, one along the centreline of the domain near the downstream boundary ($[25.0m, 2.5m, 0.5m]$), and the other created within the wake of the obstacle ($[11.5m, 0.15m, 0.4m]$). It can be

seen that an individual is capable of successfully navigating the obstacle and its wake, if created at $[25.0m, 2.5m, 0.5m]$, denoted in black, figure 5.18b. However, the individual created within the wake region of the obstacle (denoted in white, $[11.5, 0.15, 0.4m]$) becomes trapped within the recirculation zone. This is an unnatural movement, and shows that this rule alone, while working as intended, does not capture real fish movements.

5.4.2 Verification of Rule 2: `minMaxEnergy`

The `minMaxEnergy` rule biases the movement of an individual towards either the minimum or maximum local energy pathway, or neither, based on the current preference of the individual. By default, an individual will search for the local minimum energy path (i.e. tend towards lower velocities). However, upon encountering an average velocity magnitude less than `minEnergyThreshold` or a local fluid shear less than `gradThresholdMin`, the individual will switch to having no energy preference. Furthermore, upon encountering an average velocity magnitude less than `maxEnergyThreshold`, a local fluid shear less than `gradThresholdMax`, or an obstacle, the individual will switch to searching for the maximum energy pathway [see figure 4.5, section 4.6.2].

To verify the function of the `minMaxEnergy` rule two cases were investigated. First, a single individual was created near the centreline of the `veriSetA` domain at mid-depth near the downstream boundary of the domain (coordinates $[25.0m, 2.5m, 0.5m]$). The individual moved based only on the output of the `followFlow` and `minMaxEnergy` rules. The individual was not created along the centreline, as the velocity profile in the channel is symmetrical in y and therefore an individual exactly in the centre will have equal and opposite attraction to the lower velocities on both sides of the channel, which will cancel each other out. For verifying the `minMaxEnergy` rule; `fishTimestep` was set to $0.5s$, `Tmax` was set to 1000, `sensoryRange` was set to 1. Furthermore, the `bodylength_mean` was set to $0.15m$, and `bodylength_deviation` was set to $0m$, effectively ensuring any created individual was of length $0.15m$. Furthermore, `minEnergyThreshold` was set to $0.2ms^{-1}$, `maxEnergyThreshold` was set to $0.05ms^{-1}$, `gradThresholdMin` was set to $-0.35s^{-1}$, and `gradThresholdMax` was set to $-1.25s^{-1}$ [see section 5.5.1 for a sensitivity analysis of the `minMaxEnergy` parameters]. It was expected that an individual following the `followFlow` and `minMaxEnergy` rules in a simple domain dominated by flow in a single direction, such as `veriSetA`, will move upstream, tending towards the lower

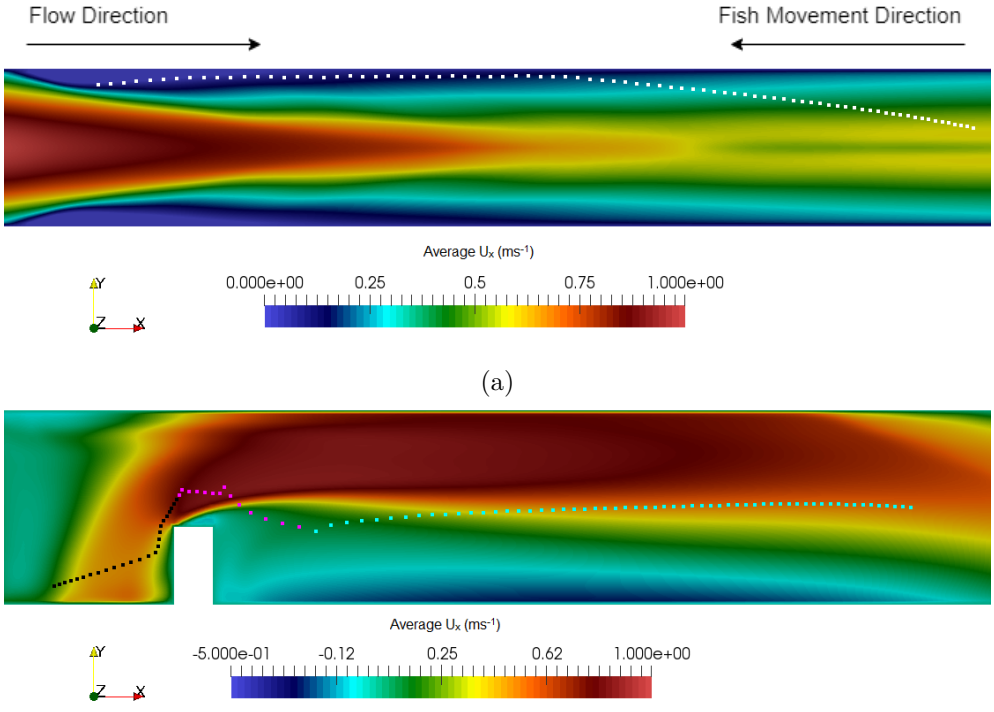

Figure 5.19: a) Planform view of a calculated fish trajectory through the `veriSetA` domain with overlain contours of U_x, extracted along the $z = 0.4m$ plane. The fish was created at $[25.0m, 2.5m, 0.5m]$ and moved in accordance with the `followFlow` and `minMaxEnergy` rules. b) Planform view of a calculated fish trajectory through the `veriSetB` domain with overlain contours of U_x, taken at a plane $z = 0.4m$. The fish was created at $[25.0m, 2.5m, 0.5m]$ and moved in accordance with the `followFlow` and `minMaxEnergy` rules. The individual's energy search preference changes throughout the trajectory first starting with minimum energy (teal), then maximum energy (pink), then returning to minimum energy (black).

velocities near the walls of the channel. Invoking the `minMaxEnergy` rule caused an individual passing the `veriSetA` domain to tend to one side of the channel, figure 5.19a, compared to using only the `followFlow` rule, figure 5.18a. This is due to the individual seeking lower velocities. Once a sufficiently low velocity region had been located, the individual switches to neither searching for a minima nor a maxima. The individual is then seen switching between searching for the minimum energy path and

not searching while close to the channel wall; as, when not searching, the `followFlow` rule naturally causes the individual to move back into faster velocities, figure 5.19a.

Second, a single individual was along the centreline of the `veriSetB` domain at mid-depth near the downstream boundary of the domain (coordinates $[25.0m, 2.5m, 0.5m]$). The individual moved based only on the output of the `followFlow` and `minMaxEnergy` rules. It was expected that the individual would tend to lower velocities near the side of the channel (i.e. $y < 2.5m$), but would avoid the wake of the obstacle due to the associated fluid shear. Enabling the `minMaxEnergy` rule on the individual moving through the `veriSetB` domain caused the individual to tend towards the wake region due to its average velocity being lower than that of the bulk flow [shown in teal in figure 5.19b]. As the individual tended towards the low velocity wake region, the individual switched to searching for maximum velocities [shown in pink in figure 5.19b]. This is expected as the local fluid shear dropped below `gradThresholdMax`. The individual operates in this mode for a number of timesteps ($\geq$`minEnergyItMax`) before successfully navigating the obstacle and reverting back to searching for the local minimum energy path [shown in black in figure 5.19b]. This is expected as none of the thresholds were triggered upstream of the obstacle. In this example, the local hydrodynamic environment changes quickly causing the individual to forgo the case of not searching for either minimum or maximum velocity. These results show that in both test cases the `minMaxEnergy` rule is functioning as intended.

5.4.3 Verification of Rule 3: `randomWalk`

The `randomWalk` rule is a simple but important addition to the ruleset as it adds stochasticity. To verify the function of this rule, four fish of `bodylength` $0.15m$ were created along the centreline of the `veriSetA` domain at mid-depth ($[25.0m, 2.0m, 0.5m]$). Each of the four fish moved based only on the output of the `randomWalk` rule. For verifying the `randomWalk` rule, `fishTimestep` was set to $0.5s$, `Tmax` was set to 1000, `sensoryRange` was set to 1. Further verification was carried out by creating an individual within the `veriSetB` domain, off-centre and at mid-depth ($[25.0m, 3.0m, 0.5m]$). This rule returns a random direction each timestep and does not influence swim speed. Therefore, it is expected that each fish will move randomly within each timestep, but overall will follow the local water direction. In each verification case, fish were seen to move approximately with the local water velocity direction (i.e. positive x), with

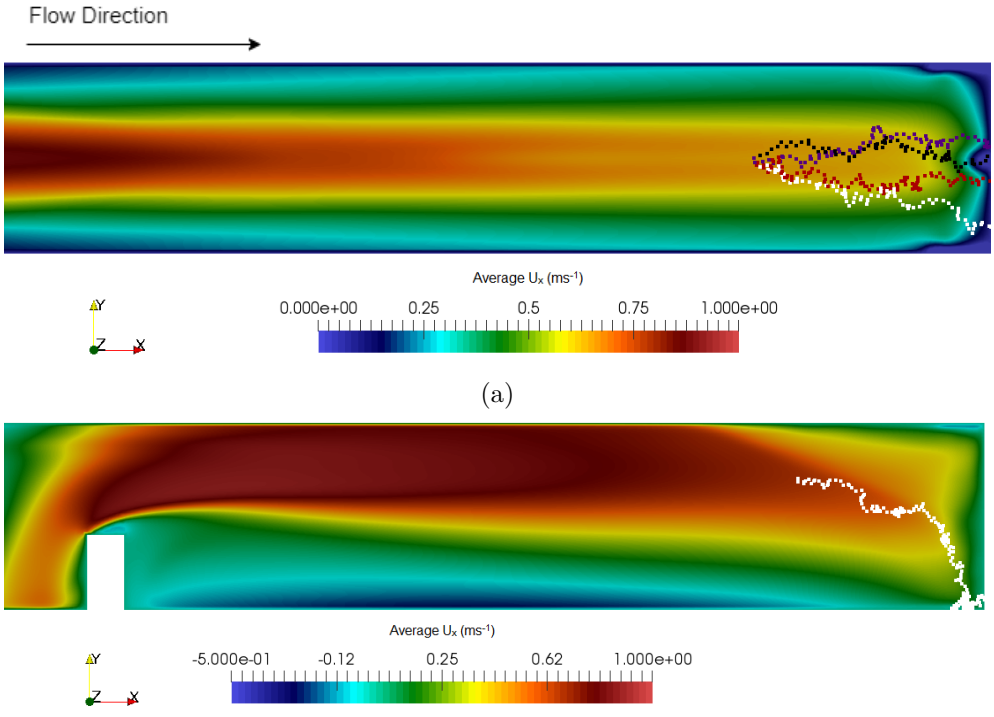

Figure 5.20: Top down views of calculated fish trajectories moving through a) the `veriSetA` domain, and b) the `veriSetB` domain. Both with overlain contours of U_x taken at planes $z = 0.3m$. In both cases, the individuals were created at $[25.0m, 2.0m, 0.5m]$ and moved based only on the `randomWalk` rule.

random perturbations within each timestep, until each individual left the domain via the downstream outlet, figure 5.20. This is the expected result as the individual has an equal chance of moving in each direction. Therefore if it is present within a velocity field dominated by a single component of velocity, it will always eventually move in the direction of flow.

5.4.4 Verification of Rule 4: `obAvoidance`

The obstacle avoidance rule is used to determine whether an obstacle is present in front of the individual. This is used in the `minMaxEnergy` rule as a trigger to switch the energy seeking case of the individual. However, it is also used to directly tend the individual away from an obstacle.

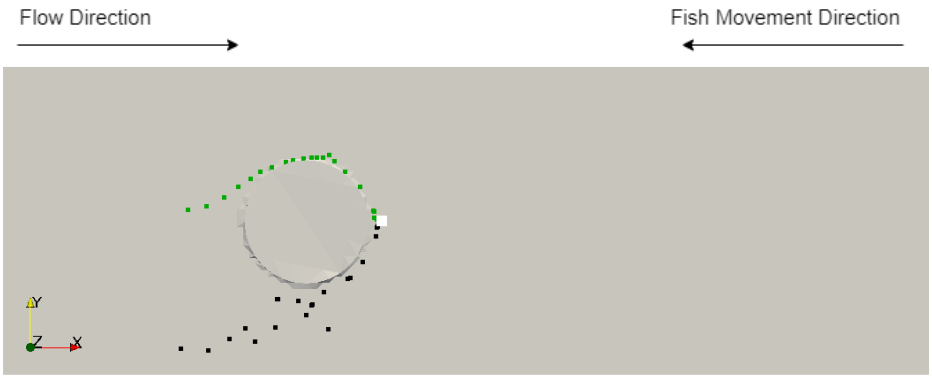

Figure 5.21: Planform view of two calculated fish trajectories moving through the `veriSetC` domain. Both trajectories originate at $[6.15m, 2.5m, 0.4m]$, denoted by the white square. Black points denote the trajectory calculated with the `followFlow` and `minMaxEnergy` rules. Green points denote the trajectory calculated with the `followFlow`, `minMaxEnergy`, and `obAvoidance` rules. For clarity, no velocity field is included.

To verify the `obAvoidance` rule, two fish were created within the `veriSetC` domain along the centreline, immediately downstream of the obstacle ($[6.15m, 2.5m, 0.4m]$). This location was selected to ensure that the obstacle was within the sensory ovoid of each individual and therefore the `obAvoidance` rule would be activated. For verifying the `obAvoidance` rule; `fishTimestep` was set to $0.5s$, `Tmax` was set to 1000, `sensoryRange` was set to 1. Furthermore, the `bodylength_mean` was set to $0.15m$, and `bodylength_deviation` was set to $0m$, effectively ensuring any created individual was of length $0.15m$. Without the `obAvoidance` rule, the individual was seen to slowly and inefficiently passes the obstacle when compared to with the `obAvoidance` rule enabled, figure 5.21.

5.4.5 Verification of Rule 5: `colAvoidance`

The `colAvoidance` rule ensures that individuals do not occupy the same space. For verifying the `colAvoidance` rule, `fishTimestep` was set to $0.5s$, `Tmax` was set to 1000, `sensoryRange` was set to 1. Furthermore, the `bodylength_mean` was set to $0.15m$, and `bodylength_deviation` was set to $0m$. The `repulsionDist` is a function of the maximum `bodylength` of the simulated population [see table 4.4], and was cal-

culated as $0.075m$. To verify the `colAvoidance` rule, two individuals were created near the centreline of the `veriSetA` domain at mid-depth within $0.05m$ of each other ($[25.0m, 2.5m, 0.5m]$ and $[25.0m, 2.55m, 0.5m]$). This ensured that the `colAvoidance` rule was triggered.

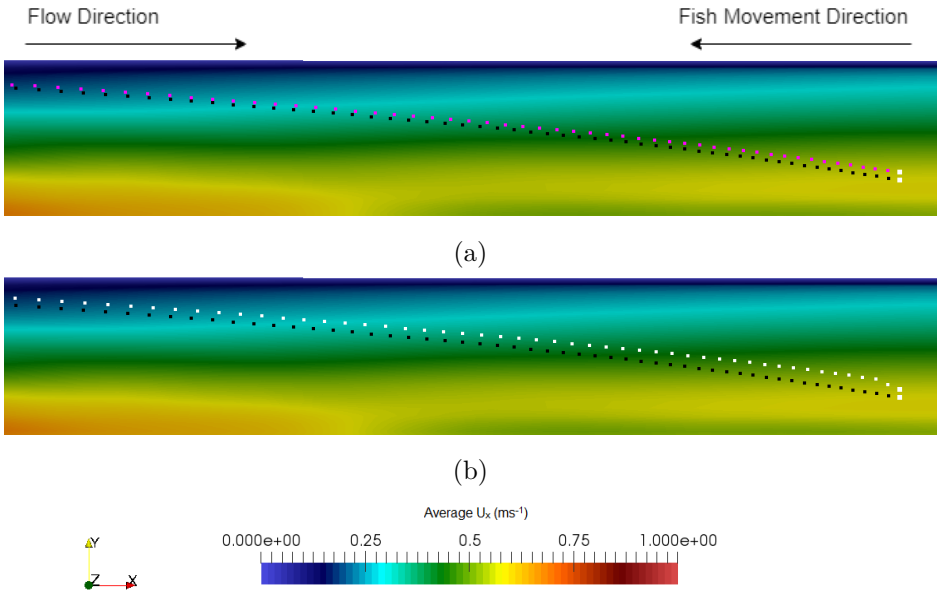

Figure 5.22: Cropped views of two individuals moving through the `veriSetA` domain with overlain contours of U_x, taken at a plane $z = 0.4m$. Both fish use the `followFlow` and `minEnergy` rules without (a) and with (b) the `colAvoidance` rule. In both cases the two fish were created at $[25.0m, 2.5m, 0.5m]$ and $[25.0m, 2.55m, 0.5m]$, denoted by the large white squares.

The test case was first executed using the `followFlow` and `minEnergy` rules. Figure 5.22a showed that, without the `colAvoidance` rule, the simulated fish occupied the same space. The test case was then executed using the `followFlow`, `minEnergy`, and `colAvoidance` rules, figure 5.22b. Activating the `colAvoidance` rule caused the first simulated fish, determined via the `initative` list [denoted in white in figure 5.22b] to immediately moved away from the other fish in the domain. The `colAvoidance` rule of the second simulated fish [denoted in black in figure 5.22b] does not trigger as the Euclidean distance between the two fish in already greater than `repulsionDist`. Therefore, inclusion of the `colAvoidance` rule was seen to successfully push the two fish away from each other, figure 5.22. This showed that the rule was working as expected.

5.4.6 Verification of Rule 6: `memory`

The `memory` rule influences the movement of an individual at the current timestep based on past knowledge of the local water velocity direction. An individual remembers the average local upstream direction for a period of time equal to the `memoryTime` variable. Setting this value to zero effectively disables the rule. For verifying the `memory` rule, `fishTimeStep` was set to $0.5s$, `Tmax` was set to 1000, `sensoryRange` was set to 1. Furthermore, the `bodylength_mean` was set to $0.15m$, and `bodylength_deviation` was set to $0m$.

To verify the `memory` rule, two test cases were considered. First, three individuals were created within the `veriSetA` domain at mid-depth ($[25.0m, 1.5m, 0.4m]$), and allowed to move based on the outputs of the `followFlow`, `minMaxEnergy`, and `memory` rules. The first fish, denoted in blue in figure 5.23, was assigned a `memoryTime` of $0s$. The second fish, denoted in pink, was assigned a memory time of $10s$. The third fish, denoted in orange, was assigned a `memoryTime` of $20s$. It was expected that activation of the `memory` rule would result in smaller changes to the initial `heading`. Enabling the `memory` rule was seen to increase the tendency for an individual to continue in its current direction rather than deviate, figure 5.23. Furthermore, increasing the `memoryTime` from $10s$ to $20s$ was not found to cause a significant difference in individuals moving through `veriSetA`, figure 5.23.

Second, three individuals were created along the centreline of the `veriSetB` domain at mid-depth ($[25.0m, 2.5m, 0.5m]$), and allowed to move based on the outputs of the `followFlow`, `minMaxEnergy`, and `memory` rules. The first fish, denoted in black in figure 5.24, was assigned a `memoryTime` of $0s$. The second fish, denoted in yellow, was assigned a `memoryTime` of $20s$. The third fish, denoted in blue, was assigned a `memoryTime` of $40s$. The fourth fish, denoted in pink, was assigned a `memoryTime` of $60s$. Without the `memory` rule the individual successfully passed the domain, but the route taken features a number of sharp changes of direction, figure 5.24. Enabling the `memory` rule eliminated these sharp changes in direction by giving influence to the upstream direction sensed over previous timesteps. In contrast to figure 5.23, increasing the `memoryTime` value above $20s$ altered the pathway. This is due to a change in the point at which the individual is triggered to search for the local maximum energy pathway, rather than directly due to the influence of the output of the `memory` rule. The results show that the `memory` rule functions as intended. However, it is unclear whether there

is a globally optimal value of `memoryTime`, and therefore this parameter may need to be used as a calibration parameter against measured fish track data in future applications of the `fishPy` model.

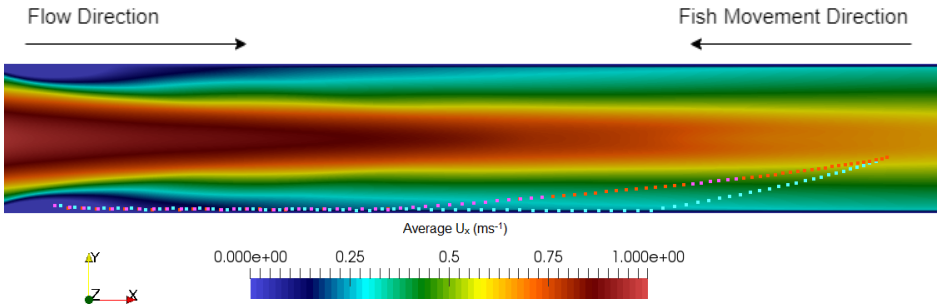

Figure 5.23: Planform view of three individuals, created at $[25.0m, 1.5m, 0.4m]$, moving through the `veriSetA` domain with overlain contours of U_x, extracted along the xy plane $z = 0.35m$. Each fish used the `followFlow`, `minEnergy`, and `memory` rules with `memoryTime` values of: $0s$, denoted by blue; $10s$, denoted by pink; and $20s$ denoted by orange.

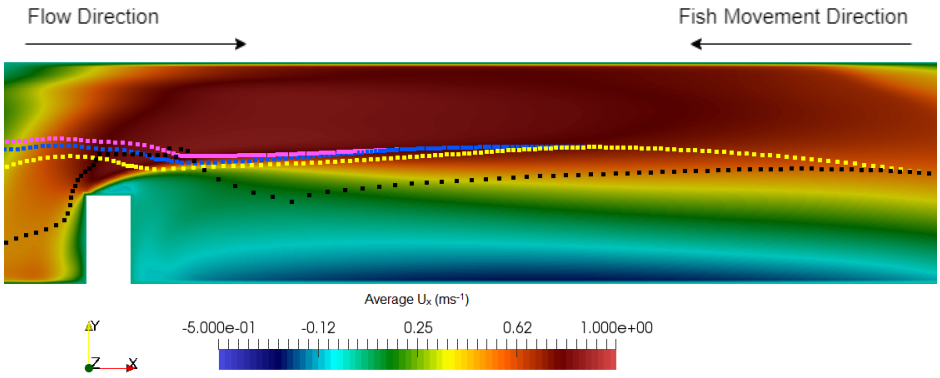

Figure 5.24: Planform view of four individuals, created at $[25.0m, 2.5m, 0.5m]$, moving through the `veriSetB` domain with overlain contours of U_x, extracted along the xy plane $z = 0.4m$. Each fish used the `followFlow`, `minEnergy`, and `memory` rules with `memoryTime` values of: $0s$, denoted by black; $20s$, denoted by yellow; $40s$ denoted by blue; and $60s$, denoted by pink.

5.4.7 Verification of Rule 7: `tkeAvoidance`

The `tkeAvoidance` rule repels individuals away from high values of turbulence kinetic energy, TKE. This rule only triggers if the individual senses a TKE value above $0.35\,m^2s^{-2}$, based on the findings of Gao et al. [2016] and Tan et al. [2018]. For verifying the `tkeAvoidance` rule, `fishTimeStep` was set to $0.5s$, `Tmax` was set to 1000, `sensoryRange` was set to 1. Furthermore, the `bodylength_mean` was set to $0.15m$, and `bodylength_deviation` was set to $0m$.

To verify the `tkeAvoidance` rule, two individuals were created within a high TKE region of the verisetAK domain at mid-depth ($[25.0m, 3.0m, 0.5m]$). The first fish, denoted in black in figure 5.25, moved based on the output of the `followFlow` rule. The second fish, denoted in red, moved based on the output of `followFlow` and `tkeAvoidance` rules. It was expected that enabling the `tkeAvoidance` rule would result in the fish actively avoiding high TKE regions of the domain. Without the `tkeAvoidance` rule, the individual moved in an approximately straight line due to the domination of the velocity field by U_x, figure 5.25. Enabling the `tkeAvoidance` rule led the individual to move towards the centre of the channel where the TKE eventually fell below the threshold value, and the `tkeAvoidance` rule ceased to be triggered, figure 5.25. This shows that the `tkeAvoidance` rule functions as intended.

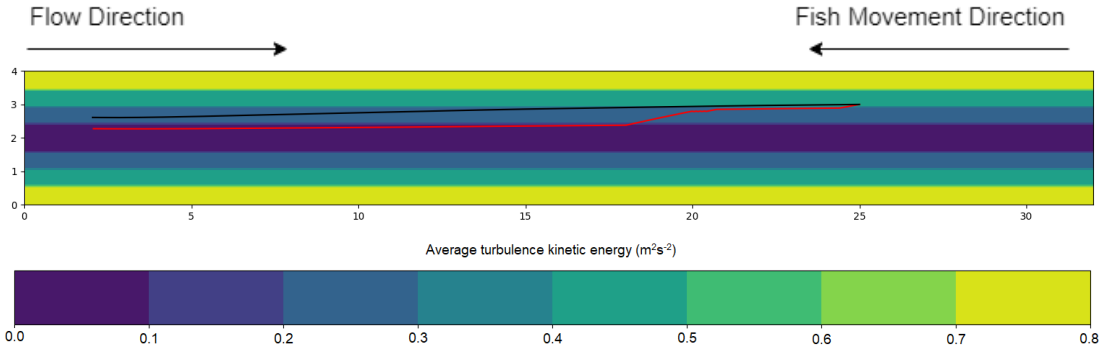

Figure 5.25: Planform view of the trajectories of two individuals moving through the `veriSetAK` domain with overlain contours of TKE, extracted from the xy plane $z = 0.4m$. Both fish were created at $[25.0m, 3.0m, 0.5m]$. Black denotes the individual with only the `followFlow` rule enabled. Red denotes the individual with the `followFlow` and `tkeAvoidance` rules enabled.

5.5 Sensitivity Analyses

This section explores the sensitivity of calculated fish trajectories to the `minMaxEnergy` thresholds, decision timestep, the individual sensory range, and the environment grid density. To allow for repeatability and ensure a like-for-like comparison between individuals, `fishPy` was executed using all rules with the exception of `randomWalk` and `colAvoidance` and the trigger to switch between burst speed and sustained swim speed was disabled. Furthermore, `bodylength_mean` was set to $0.15m$, `bodylength_deviation` was set to $0.0m$, `fishTimestep` was set to $0.25s$, `Tmax` was set to 5000, and `sensoryRange` was set to 1.0 throughout the sensitivity analyses except where the parameter is the subject of the study or where otherwise noted.

5.5.1 Sensitivity of `minMaxEnergy` Parameters

The `minMaxEnergy` rule relies on four thresholds that act as triggers to switch the behavioural case of the individual. No data are available to derive values for these thresholds therefore a sensitivity study is presented to understand the ranges of values for these four thresholds. The default behavioural case considers the individual searching for the local minimum energy pathway. If the individual encounters a velocity magnitude less than `minEnergyThreshold` or a lateral fluid shear less than `gradThresholdMin`, the case is switched and the individual ceases searching for the local minimum energy pathway. Moreover, if the individual encounters a velocity magnitude less than `maxEnergyThreshold` or a lateral fluid shear less than `gradThresholdMax`, the case is switched and the individual will begin searching for the local maximum energy pathway. The presence of an obstacle also acts as a trigger to switch an individual to searching for the maximum energy pathway. This trigger is turned off in the following analyses. In order to ensure functionality, the thresholds must satisfy the following inequalities:

$$\texttt{minEnergyThreshold} > \texttt{maxEnergyThreshold}$$

$$\texttt{gradThresholdMin} > \texttt{gradThresholdMax}$$

In all cases, three individuals were considered. These individuals were created in specific locations in each domain: $[25.0m, 2.5m, 0.5m]$, $[25.0m, 4.5m, 0.4m]$, and $[25.0m, 1.0m, 0.5m]$. In the `veriSetA` domain individuals were created at $[25.0m, 2.5m, 0.5m]$, $[25.0m, 3.5m, 0.4m]$, and $[25.0m, 1.0m, 0.5m]$ due to the narrower channel featured in

this domain. The timestep was fixed at $0.25s$ for the duration of the `minMaxEnergy` sensitivity study, the `bodylength_mean` was set to $0.35m$, and the `bodylength_deviation` was set to $0.0m$. Where multiple individuals are presented in the same domain, they are identified by their initial location in terms of the domain channel looking downstream; left, centre, and right. In order to ensure clarity, only the trajectories of individuals that demonstrate key results are shown. Many trajectories corroborated the conclusions drawn from other simulations and therefore are not presented. Multiple domains and creation locations were considered to ensure that the thresholds were not over-fitted to particular scenarios.

Velocity Magnitude Thresholds

The velocity magnitude thresholds were assessed independently to the lateral fluid shear thresholds. This was done by setting both shear thresholds to large negative number (-10^9) to effectively disable them. The `minEnergyThreshold` was considered first, and therefore the `maxEnergyThreshold` was set to a negative number to disable it. The `minEnergyThreshold` determines the velocity at which the individual switches from having a preference for lower local velocities to not having a preference. This threshold represents the velocity at which the individual gains only a small benefit from searching for lower velocities. A range of `minEnergyThreshold` value were assessed from 0.1 to 0.5 ms^{-1}.

A higher value of `minEnergyThreshold` causes the behavioural switch, from seeking the local minimum energy pathway to not seeking, to occur earlier as the individual tends towards the wall, figure 5.26a. In both cases of individuals moving through the `veriSetA` domain, only a value of $0.4ms^{-1}$ consistently allowed individuals to successfully pass. This was due to early triggering of the behavioural switch that resulted in the individual avoiding the near-zero velocity regions found upstream in `veriSetA`, rather than specific avoidance behaviour. Decreasing the threshold value resulted in later triggering of the behavioural switch, resulting in the individual becoming trapped in the near-zero velocity regions found upstream in `veriSetA`, figure 5.26b. This illogical behaviour occurs due to the individual being unable to determine the upstream direction due to the near-zero local velocity magnitude. Applying a value greater than $0.4ms^{-1}$ would effectively eliminate the case of seeking the local minimum energy pathway. Therefore, this constitutes the upper limit of the threshold range for this test case.

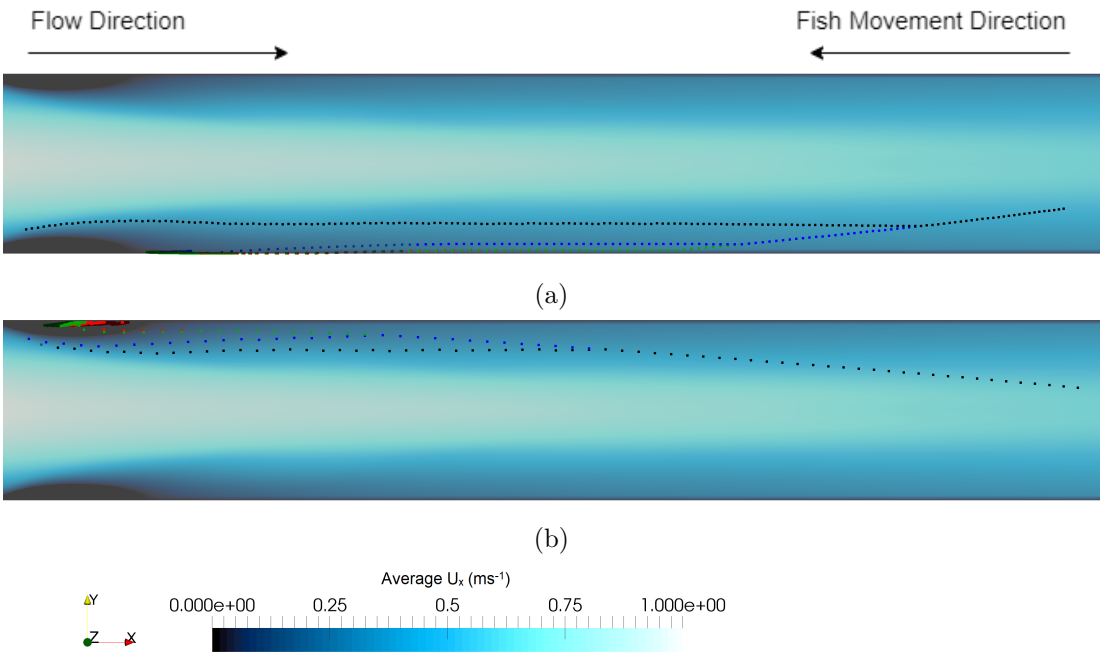

Figure 5.26: Sensitivity of the `minMaxEnergy` rule to the `maxEnergyThreshold` parameter; assessed on $0.35m$ individuals moving through the `veriSetA` domain with overlain contours of U_x, taken at a plane $z = 0.4m$. Fish used only the `followFlow` and `minMaxEnergy` rules. The individuals were created at a) $[25.0m, 1.0m, 0.5m]$, and b) $[25.0m, 2.5m, 0.5m]$; with the following `minEnergyThreshold` values: $0.1ms^{-1}$ (red), $0.2ms^{-1}$ (green), $0.3ms^{-1}$ (blue), $0.4ms^{-1}$ (black).

When the `veriSetB` domain is considered, all values of `minEnergyThreshold` results in the individual becoming confused and trapped within the recirculation region downstream of the obstacle, figure 5.27. A value of $0.4ms^{-1}$ resulted in a successful passage, but the individual was considerably delayed by the obstacle. This result was expected as the combination of the `followFlow` and `minMaxEnergy` rules, with only the `minEnergyThreshold` gives the individual only the option of moving in the local upstream direction and/or seek lower local velocities. Therefore, if an individual enters a recirculation zone, it has no behavioural option to allow it to escape.

The lower limit of the `minEnergyThreshold` range is $0.0ms^{-1}$, because the velocity magnitude cannot be negative. However, since the `maxEnergyThreshold` must be less than the `minEnergyThreshold`, a value of $0.4ms^{-1}$ was chosen as this allowed successful passage through `veriSetA` and `veriSetB` and allowed for the exploration of a range

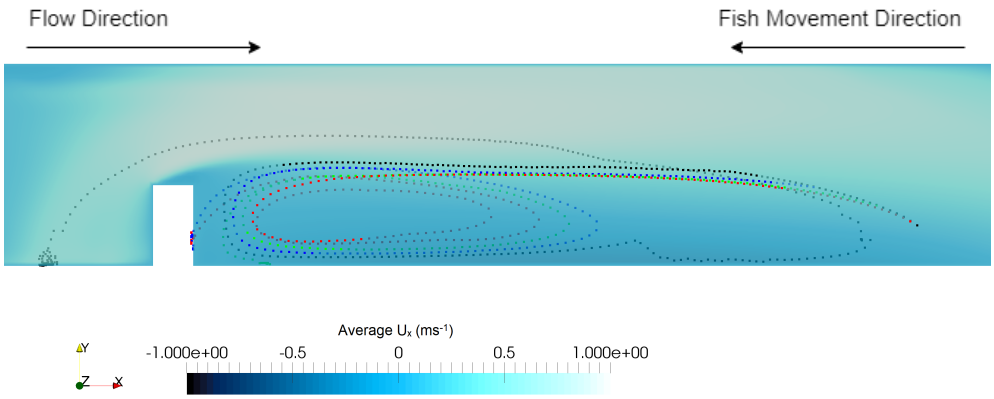

Figure 5.27: Sensitivity of the `minMaxEnergy` rule to the `minEnergyThreshold` parameter; assessed on $0.35m$ individuals moving through the `veriSetB` domain with overlain contours of U_x, taken at a plane $z = 0.4m$. Only the `followFlow` and `minMaxEnergy` rules were enabled. The individuals were created at $[25.0m, 1.0m, 0.5m]$; with the following `minEnergyThreshold` values: $0.1ms^{-1}$ (red), $0.2ms^{-1}$ (green), $0.3ms^{-1}$ (blue), $0.4ms^{-1}$ (black).

of `maxEnergyThreshold` values. The `maxEnergyThreshold` was then considered over a range from 0.01 to 0.15 ms^{-1}.

The addition of the `maxEnergyThreshold` gives an individual a behavioural ability to avoid near-zero velocity magnitude regions. Sensitivity analysis of `maxEnergyThreshold` using `veriSetA` shows that a value of $0.01ms^{-1}$ is too low and results in the individual becoming trapped in the near-zero velocity regions, figure 5.28a. However, values of 0.05 and $0.1ms^{-1}$ resulted in successful passage.

The addition of the `maxEnergyThreshold` parameter has no impact on individuals moving through `veriSetB`, all of which fail in a manner similar to only using the `minEnergyThreshold` [compare figures 5.27 and 5.28b]. This suggests that switching of the behavioural case using the local velocity magnitude is likely to be only successful for simple domains dominated by the U_x component of velocity, such as `veriSetA`. However, when applied to a more complex domain such as `veriSetB`, which features large spatial changes in velocity, controlling behaviour based solely on the local velocity magnitude is insufficient.

This limitation is due to the velocity magnitude lacking directional and gradient information, and therefore is insufficient to quantitatively capture flow recirculation

zones. This could be overcome by instead using the U_x and U_y components of flow, but this encroaches on the developmental principle of a generalised model [see tables 1.1 and 4.6 in chapters 1 and 4, respectively]. Therefore, it was decided that spatial gradients of velocity (i.e. fluid shear) would be explored as an additional trigger to switch behavioural cases, as is used in the NFS model [Goodwin et al., 2014].

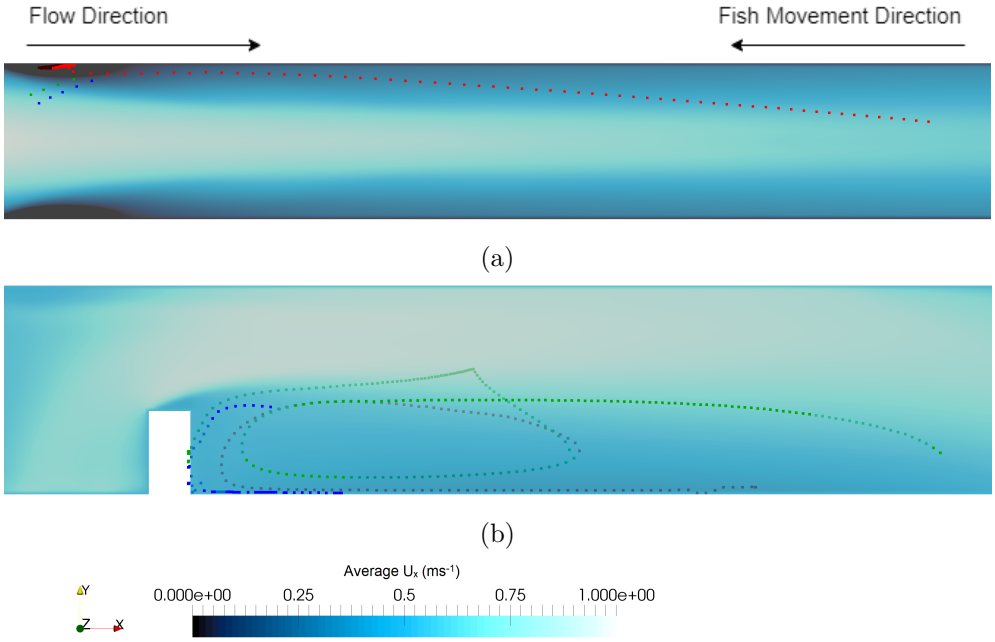

Figure 5.28: Sensitivity of the `minMaxEnergy` rule to the `maxEnergyThreshold` parameter; assessed on $0.35m$ individuals moving through the a) `veriSetA` domain and b) `veriSetB` domain with overlain contours of U_x, extract along the xy plane $z = 0.4m$. Only the `followFlow` and `minMaxEnergy` rules were enabled. The individuals were created at a) $[25.0m, 2.5m, 0.5m]$ and b) $[25.0m, 1.0m, 0.5m]$. The following `maxEnergyThreshold` values were used in each case: $0.01ms^{-1}$ (red), $0.05ms^{-1}$ (green), $0.1ms^{-1}$ (blue). The result for a `maxEnergyThreshold` value of $0.15ms^{-1}$ is not shown as it coincides with the result for a value of $0.1ms^{-1}$.

Lateral Fluid Shear Thresholds

The sensitivity of the predicted fish trajectories to the fluid shear thresholds was assessed. To do this, both velocity thresholds were effectively disabled by setting them to negative numbers, since the velocity magnitude cannot be less than zero. The

`gradThresholdMin` value was considered first, and the `gradThresholdMax` value was thus set to a large negative number (-10^9) to effectively disable it. The simulation used only the `followFlow` and `minMaxEnergy` rules. A range of `gradThresholdMin` values were considered from $-0.7s^{-1}$ to $0.0s^{-1}$. Decreasing `gradThresholdMin` from $-0.3s^{-1}$ to $-0.7s^{-1}$ delayed the transition from preferring the local minimum energy to having no preference, figure 5.29. A value of $-0.7s^{-1}$ results in a severe delay to the transition, resulting in the individual moving through the `veriSetB` domain becoming trapped inside the recirculation regions downstream of the obstacle, figure 5.29a. Furthermore, a value of $-0.2s^{-1}$ results in the transition occurring so early for the individual in the `veriSetA` domain, that the individual never seeks the minimum energy pathway, figure 5.29b. This gives an appropriate range of values between $-0.7s^{-1}$ and $-0.2s^{-1}$. A value of `gradThresholdMin` was required to assess the threshold range for `gradThresholdMax`, therefore a value of $-0.35s^{-1}$ was chosen to enable further sensitivity tests as this value lies within the established acceptable range. The `gradThresholdMax` value was considered over a range from -2.5 to $-0.5s^{-1}$, noting that it must be $< -0.35s^{-1}$. Furthermore, there must be a region between `gradThresholdMin` and `gradThresholdMax` to facilitate the behavioural case of an individual not having an energy pathway preference. Decreasing the value of `gradThresholdMax` delayed the transition between behavioural cases. However, whereas `gradThresholdMin` delayed the transition between preferring for the local minimum energy pathway and having no preference, `gradThresholdMax` delayed the transition between having no preference and preferring the local maximum energy pathway, figure 5.30. A threshold value $\leq -1.0s^{-1}$ had little effect on the trajectories through `veriSetA`, figure 5.30a. Setting the threshold to a value of $-0.5s^{-1}$ for passage through `veriSetB` resulted in early triggering of the behavioural switch, and likely denoted an over-sensitivity to the lateral fluid shear, figures 5.30b and 5.30c. Decreasing `gradThresholdMax` to $-1.0s^{-1}$ and $-1.75s^{-1}$ resulted in triggering of the behavioural switch to a preference for larger velocities closer to the obstacle, which resulted in smoother, more efficiency trajectories that successfully navigated the obstacle, figures 5.30b and 5.30c. However, decreasing to a value of $-2.5s^{-1}$ caused the switch to occur particularly late, causing the individual to move back downstream before reverting to moving upstream again, with very harsh changes of direction, figure 5.30b. This trajectory also featured significant changes in vertical height, whereas none of the

other trajectories vary significantly in z. This suggests that a value of $-2.5s^{-1}$ is too low and renders the individual under-sensitive to the lateral fluid shear. Therefore, the acceptable range for the `gradThresholdMax` parameter was determined to be between $-1.0s^{-1}$ and $-1.75s^{-1}$. A value of $-1.25s^{-1}$ was selected, as this lies in the established acceptable range. The results presented herein show that the recirculation zone featured in `veriSetB` can be avoided through using lateral fluid shear as the trigger to control the switching of energy searching behaviour from seeking minimum energy pathways to seeking maximum energy pathways.

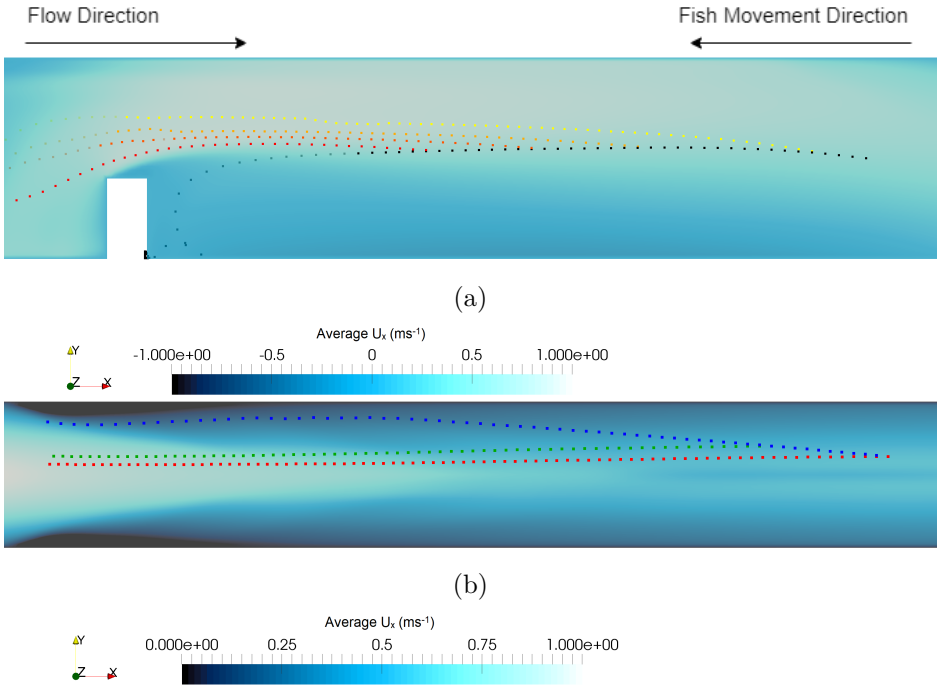

Figure 5.29: Sensitivity of the `minMaxEnergy` rule to the `gradThresholdMin` parameter; assessed on $0.35m$ individuals moving through the a) `veriSetB` and b) `veriSetA` domains both with overlain contours of U_x, extracted along the xy plane at a) $z = 0.4m$ and b) $z = 0.3m$. Only the `followFlow` and `minMaxEnergy` rules were enabled. In each case, the individuals are created at $[25.0m, 2.5m, 0.5m]$. The `gradThresholdMin` values are a) -0.3s^{-1} (yellow), -0.4s^{-1} (orange), -0.5s^{-1} (light red), -0.6s^{-1} (dark red), and -0.7s^{-1} (black) and b) -0.2s^{-1} (red), -0.3s^{-1} (green), and -0.4s^{-1} (blue).

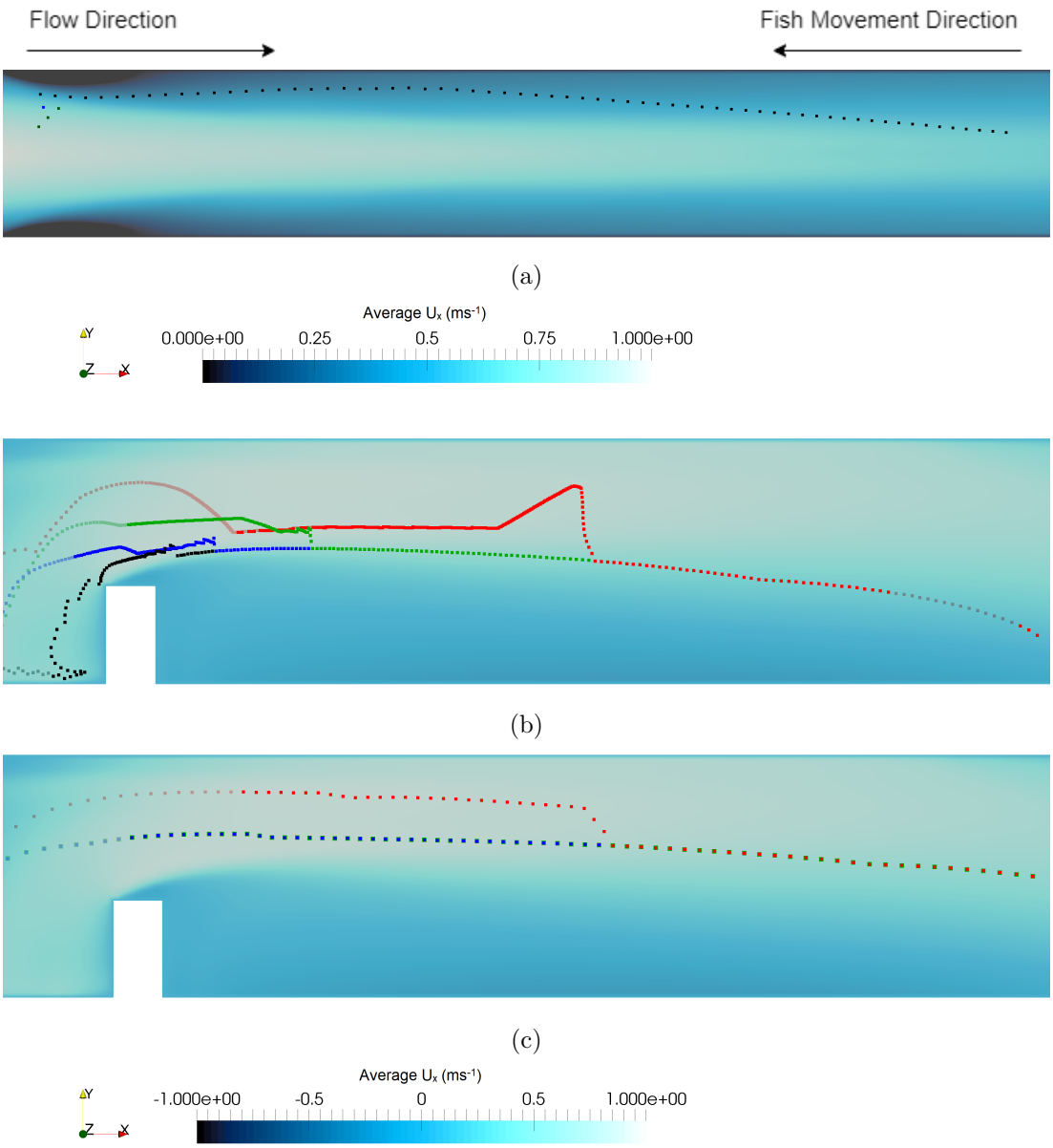

Figure 5.30: Sensitivity of the `minMaxEnergy` rule to the `gradThresholdMax` parameter; assessed on $0.35m$ individuals moving through the a) `veriSetA` domain with overlain contours of U_x at $z = 0.3m$, and b),c) `veriSetB` domains with overlain contours of U_x, taken at a plane $z = 0.4m$. Only the `followFlow` and `minMaxEnergy` rules enabled. In both a) and c) the individuals are created at $[25.0m, 2.5m, 0.5m]$. In b) the individual was created at $[25.0m, 1.0m, 0.5m]$. The `gradThresholdMax` values are a) -1.0s^{-1} (red), -1.25s^{-1} (green), -1.5s^{-1} (blue), and -1.75s^{-1} (black), b),c) -0.5s^{-1} (red), -1.0s^{-1} (green), -1.75s^{-1} (blue), and -2.5s^{-1} (black).

Combination of Velocity Magnitude and Fluid Shear Thresholds

Chosen thresholds were tested all together on the following domains: `veriSetA`, `veriSetB`, `veriSetB2`, `veriSetB3`. This was done to ensure that the chosen threshold values were appropriate and not over-fitted to a given domain, obstacle size, creation location, or a combination of these. Three individuals were created at $[25.0m, 2.5m, 0.5m]$, $[25.0m, 4.5m, 0.4m]$, and $[25.0m, 1.0m, 0.5m]$ within each domain ($[25.0m, 3.5m, 0.4m]$ in `veriSetA` rather than $[25.0m, 4.5m, 0.4m]$). The final selected thresholds are:

- `minEnergyThreshold` $= 0.4ms^{-1}$
- `maxEnergyThreshold` $= 0.05ms^{-1}$
- `gradThresholdMin` $= -0.35s^{-1}$
- `gradThresholdMax` $= -1.25s^{-1}$

Applying the `followFlow` rule and the full `minMaxEnergy` rule to the `veriSetA` domain shows that, regardless of initial placement, individuals were able to successfully navigate through the domain, figure 5.31a. In particular, each of the individuals moved towards, or stayed near, the walls, showing that some timesteps were spent searching for the local minimum energy pathway. However, the individual created in the centre of the channel ceased searching for the minimum energy pathway earlier than the other individuals, figure 5.31a. This switch in behaviour was due to the lateral shear experienced by the individual and the fact that lateral shear is calculated based on the `heading` of the individual. This explains why the right individual did not behave in the same way, at the same point, as the centre individual, figure 5.31a. Applying the same rules to individuals moving through the `veriSetB` domain also yielded successful passages in all cases, figure 5.31b. All individuals successfully avoided the recirculation region downstream of the obstacle, figure 5.31b.

In order to test the validity of the chosen threshold values and ensure that they were not over-fitted to a single domain, the `minMaxEnergy` parameters were also applied to two different domains, `veriSetB2` and `veriSetB3`, which had not been used in the calibration of the parameters. The same methodology and parameters were applied to individuals in the `veriSetB2` and `veriSetB3` domains, figures 5.31c and 5.31d. In both cases, all three individuals passed successfully.

When applied to the `veriSetB2` domain, the left individual followed a simple pathway directly upstream and successfully passed the obstacle, figure 5.31c. The trajectory of the centre individual approximately followed the edge of the recirculation zone down-

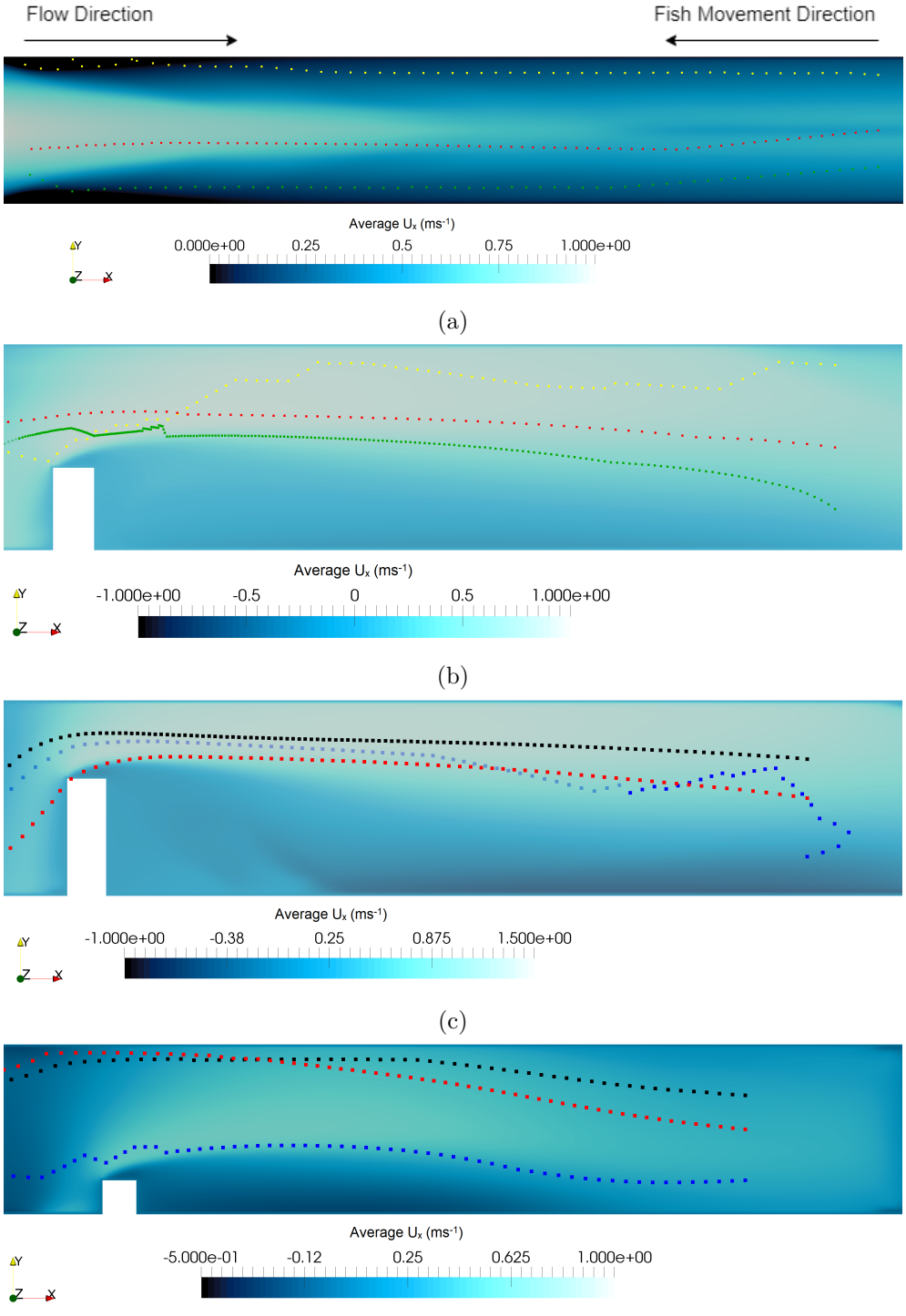

Figure 5.31: Planform view of trajectories of three individuals through the a) `veriSetA`, b) `veriSetB`, c) `veriSetB2`, d) `veriSetB3` domains with overlain contours of U_x, extracted along the xy plane for a) $z = 0.3m$ and b,c,d) $z = 0.4m$. Only the `followFlow` and `minMaxEnergy` rules were enabled.

stream of the obstacle and passed close to the obstacle, figure 5.31c. Furthermore, the right individual, created within the recirculation zone, immediately moved downstream due to the local velocity vector pointing in approximately the positive x direction; i.e. the local upstream direction was not representative of the global upstream direction, figure 5.31c. The right individual also immediately began seeking higher velocities due to the local fluid shear, causing the individual to move towards the centre of the channel. After approximately 3 timesteps, the right individual left the recirculation zone, continued to seek higher velocities, reassessed the local upstream direction, and began to move in the correct direction to pass the domain, figure 5.31c. The right individual then consistently moved upstream, approximately along the edge of the recirculation zone downstream of the obstacle, and then successfully passed the domain, figure 5.31c. When applied to the `veriSetB3` domain, the left and centre individuals tended to the left side of the channel (positive y) while seeking lower velocities, and both successfully passed the domain. The right individual immediately moved usptream and moved along the edge of the recirculation zone downstream of the obstacle, and successfully passed the domain. These results give confidence to the values of the `minMaxEnergy` thresholds, and show that the rule parameters are not over-fitted to specific hydrodynamic domains.

5.5.2 Sensitivity to the Decision Timestep

The user-defined decision timestep (`fishTimestep`) controls the temporal discretisation and therefore controls the distance moved by an individual within each timestep as well as the frequency at which an individual samples its local environment. As discussed in section 4.3.5, the decision timestep has a theoretical maximum value that ensures that an individual does not ignore relevant environmental data. Although, exceeding this maximum value does not result in failure, it will affect results and potentially cause model instabilities and unnatural behaviour.

The `fishPy` model was applied to the `veriSetA` and `veriSetB` domains for a variety of decision timesteps ranging from $0.05s$ to $2.0s$, figure 5.32. The `bodylength` was set to $0.15m$ for all simulations. Application of equation 4.7 suggests that the theoretical maximum timestep value for the `veriSetA` and `veriSetB` domains are $0.32s$ and $0.25s$ respectively. The calculated trajectories through `veriSetA` show near independence to the decision timestep, figure 5.32d. However, as the timestep is increased, the calculated

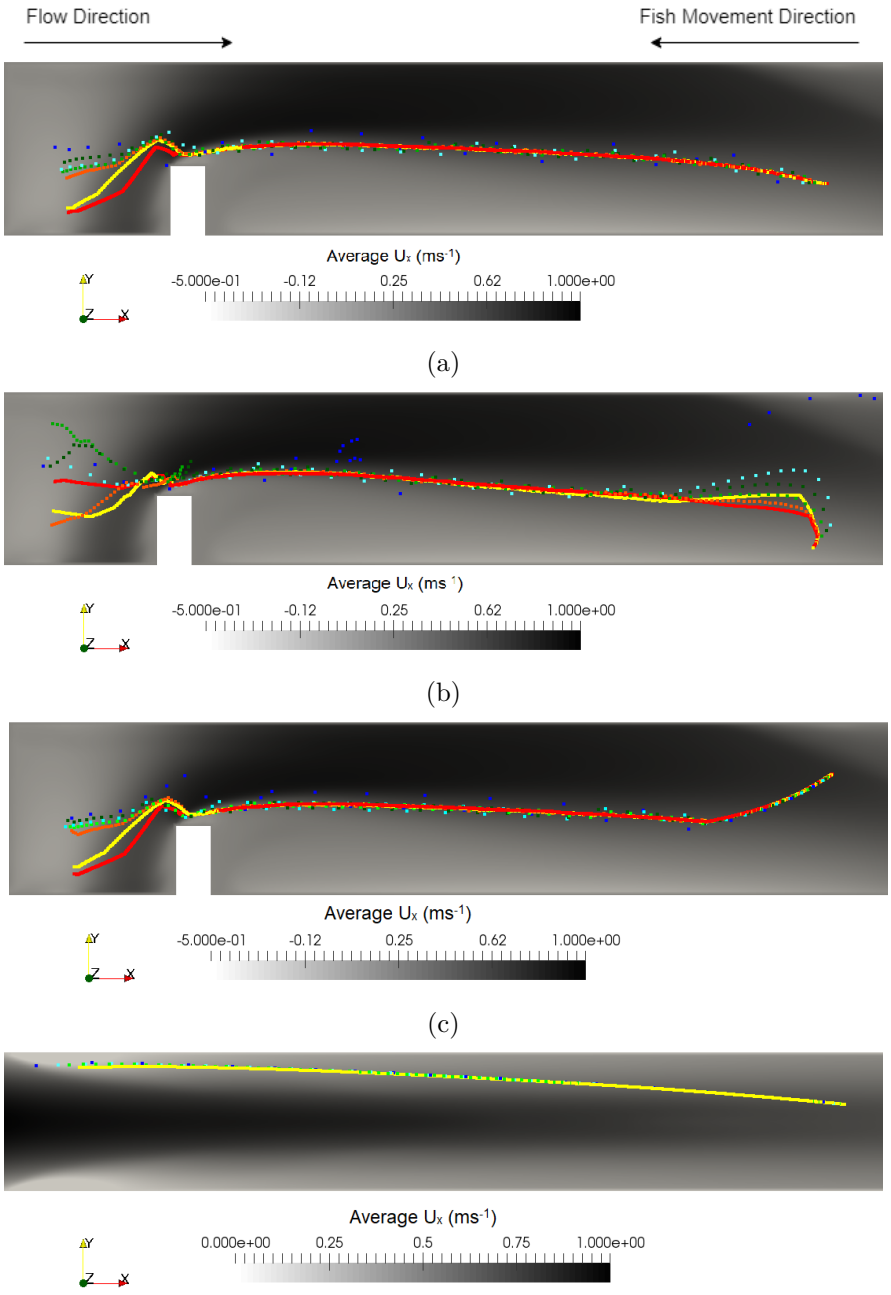

Figure 5.32: Calculated fish trajectories through a), b), and c) the `veriSetB` domain with overlain contours of U_x at $z = 0.5m$ and d) the `veriSetA` domain with overlain contours of U_x at $z = 0.4m$. Decision timestep is varied with values of: $0.05s$ (Red), $0.1s$ (Yellow), $0.25s$ (Orange), $0.5s$ (Light Green), $0.75s$ (Dark Green), $1.0s$ (Light Blue), $2.0s$ (Dark Blue). Individuals were created at a) $[25.0m, 1.5m, 0.6m]$, b) $[25.0m, 0.5m, 0.6m]$, c) $[25.0m, 3.5m, 0.6m]$, and d) $[25.0m, 2.5m, 0.45m]$.

trajectories through `veriSetB` become progressively "noisier", figures 5.32a and 5.32c. However, for these two results, the trajectories still follow the same pathway before encountering the obstacle. For individuals created within low velocity magnitude regions, increasing the timestep causes an increase to the curvature of the initial trajectories due to the decrease in the sampling frequency, figure 5.32b. Furthermore, increasing the timestep above $0.75s$ caused large deviations from the other trajectories and severe unnatural movements in the first timesteps, figure 5.32b (see trajectory for timestep $= 2s$). These unnatural movements seen in the trajectory for timestep $= 2s$ caused the individual to move into high velocity regions where it struggled to overcome the local velocity, figure 5.32b. After encountering the obstacle present in `veriSetB`, the trajectories diverge in all cases. This is likely caused by a combination of the change in sampling frequency, the increased velocity shear in the region adjacent to the obstacle, and the formulation of the `memory` rule, discussed in section 5.6.

5.5.3 Sensitivity to the Sensory Range

Throughout development of the `fishPy` model, the `sensoryRange` value was set to 1.0 bodylength, as it is suggested that it is a function of bodylength, but the exact value is unclear [see Goodwin et al. 2014 and Montgomery et al. 1997]. As noted in section 4.7.1, the sensory ovoid is significant to modelling from the perspective of the individual, but exact quantification of the size of the sensory ovoid is challenging. This section considers the sensitivity of the predicted trajectories to the `sensoryRange` value.

To investigate the sensitivity of predicted fish trajectories to the `sensoryRange`, two test cases were explored. First, an individual was created near the downstream boundary of the `veriSetB` domain near the centreline and at mid-depth ($[27.0m, 2.0m, 0.45m]$), figure 5.33a. The `sensoryRange` for this individual was varied from 0.5 to 2.0. It was found that the trajectories varied negligibly with the `sensoryRange`, figure 5.33a. Second, an individual was created within the wake region downstream of the obstacle within the `veriSetB` domain ($[26.0m, 1.0m, 0.3m]$), figure 5.33b. The `sensoryRange` of this individual was varied between 0.0 and 2.0, where a value of 0.0 effectively disabled the sensory ovoid. The results showed that, for a `sensoryRange` ≥ 0.5, the trajectories showed the same general pathway, figure 5.33b. However, disabling the sensory ovoid (`sensoryRange` $= 0.0$) caused the individual to move downstream and fail to pass the domain after 1000 timesteps, figure 5.33b. This demonstrates the significance of the

sensory ovoid to enable individuals to sample environmental data within their extended local area.

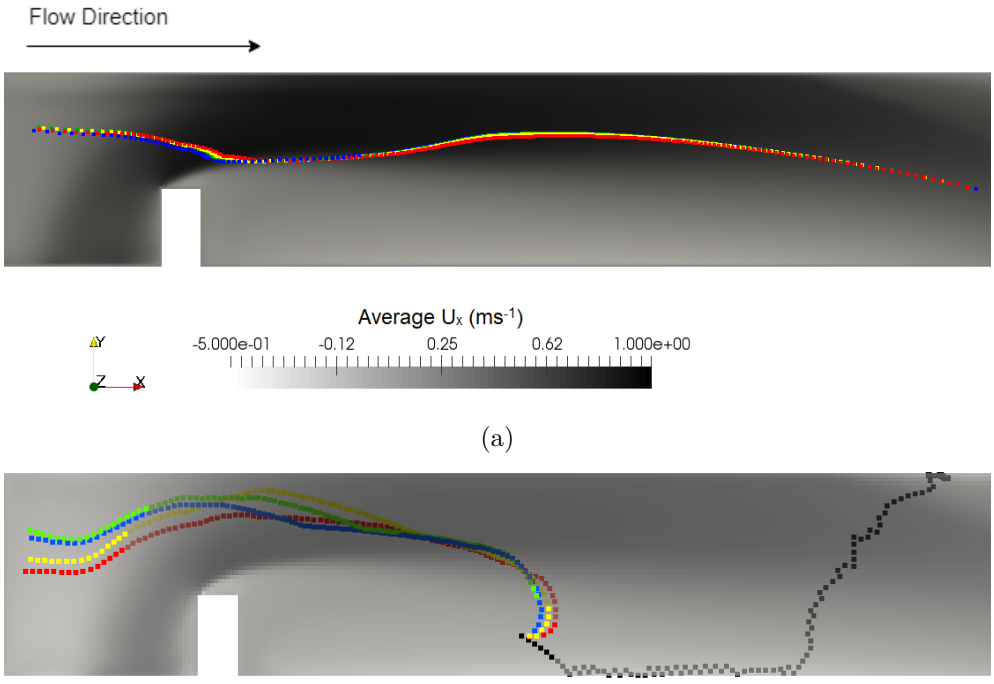

(a)

(b)

Figure 5.33: Planform views of calculated fish trajectories for individuals moving through the `veriSetB` domain with overlain contours of U_x extracted along the xy plane at a) $z = 0.4m$ and b) $z = 0.2m$. Fish created at a) $[27.0m, 2.0m, 0.45m]$ and b) $[26.0m, 1.0m, 0.3m]$, with values of sensory range measured in bodylengths: 0.0 (black), 0.5 (red), 1.0 (yellow), 1.5 (green), 2.0 (blue).

5.5.4 Spatial Resolution Sensitivity

Owing to the spatially continuous nature of the model and the interpolation functions used, the `fishPy` model requires a uniform, hexahedral, 3D mesh containing all environmental data. Therefore, CFD (or measured) data need to be preprocessed before they can be input into `fishPy` [see section 5.3]. During preprocessing, the spatial resolution for the new 3D matrices is determined. This section considers the dependency of `fishPy` to the selected spatial resolution. Note that this resolution refers to the

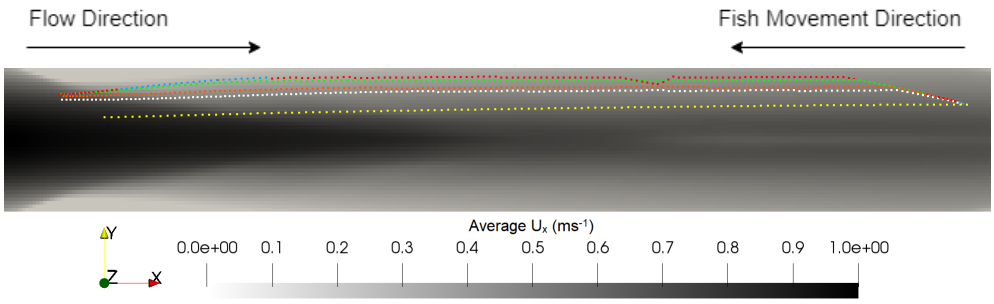

Figure 5.34: An individual, created at $[27.0m, 3.0m, 0.4m]$, moving through the `veriSetA` domain with overlain contours of U_x, extracted along the xy plane $z = 0.3m$ with varying spatial resolutions of: $0.05m$ (red), $0.1m$ (blue), $0.2m$ (green), $0.4m$ (orange), $0.5m$ (white), and $1.0m$ (yellow).

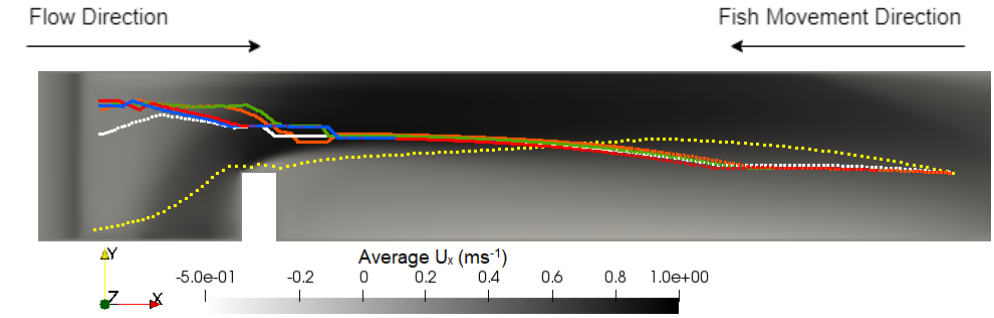

Figure 5.35: An individual, created at $[27.0m, 2.0m, 0.4m]$, moving through the `veriSetB` domain with overlain contours of U_x extracted along the xy plane $z = 0.4m$ with varying spatial resolutions of: $0.05m$ (red), $0.1m$ (blue), $0.2m$ (green), $0.4m$ (orange), $0.5m$ (white), and $1.0m$ (yellow).

interpolated grids of the same underlying CFD simulation and does not consider any modification to the CFD mesh.

The sensitivity of `fishPy` to the spatial resolution was investigated by interpolating the CFD results of flow through the `veriSetA` and `veriSetB` domains onto regular grids of varying spatial resolution. These grids were then input into the `fishPy` model. In the first case, the trajectory of an individual created at $[27.0m, 3.0m, 0.4m]$ within the `veriSetA` domain was predicted using each spatial resolution, figure 5.34. The trajectories show that larger resolutions dampened the effect of the `minMaxEnergy` rule when seeking the minimum energy route, figure 5.34. In the second case, the trajectory of an individual created at $[27.0m, 2.0m, 0.4m]$ within the `veriSetB` domain

was predicted using each spatial resolution, figure 5.35. The trajectories show little variation between spatial resolutions of 0.05 and $0.1m$, figure 5.35. Above a value of $0.1m$ the individual begins searching for the local maximum energy pathway at later points, resulting in different trajectories. However, each trajectory between $0.05m$ and $0.5m$ have approximately the same form. A spatial resolution of $1.0m$ resulted in a vastly different trajectory, figure 5.35.

Variations in trajectories through both domains are likely due to a loss of geometry and near-boundary velocity data due to the spatial interpolation, which assumes a spatially-linear variation between grid points. This results in two unwanted behaviours. First, the interpolated velocity was less than the actual velocity causing the individual to cease seeking the minimum energy pathway earlier. Secondly, the passability value in the `G3D` matrix is smoothed causing the boundary between passable and impassable locations to move further from the wall [`passabilityThreshold`= 0.1; see section 4.3.4]. Predicted trajectories through both domains can be seen to tend towards a particular path with increasing spatial resolution (i.e. the smallest differences in trajectories are seen between spatial resolutions of $0.05m$ and $0.1m$). This result suggests that increasing the spatial resolution of a given domain decreases the sensitivity of the predicted trajectories to the spatial resolution. Therefore, the highest possible spatial resolution should be used within practical limitations of time and computational resources.

5.6 Discussion of Model Verification and Sensitivity Analyses

This chapter has shown the development of a number of verification datasets as well as the process and results of applying each rule of the `fishPy` model to these datasets. The verification datasets are produced in order to test that each individual rule works as intended and to facilitate studies on the sensitivity of the model to various parameters and therefore the CFD results are not validated.

5.6.1 Discussion of Verification of Behavioural Rules

This chapter has applied each rule to the developed verification datasets and shown that each rule is functioning as intended. Due to the fact that verification is integral to

the development of any piece of software, the verification work presented in this chapter was carried out in parallel the work presented in chapter 4. Each section of code that was written was immediately verified to ensure correct formulation and function.

The result of the verification process for each behavioural rule are:

- Rule 1: `followFlow` - Individuals were found to move in the opposite direction to the local velocity direction.
- Rule 2: `minMaxEnergy` -
  - a) Individuals moved with bias towards regions of smaller velocity when seeking local minimum energy pathway.
  - b) Individual moved without bias when neither seeking the local minimum or maximum energy pathway.
  - c) Individuals moved with bias towards regions of larger velocity when seeking local maximum energy pathway.
- Rule 3: `randomWalk` - Individuals moved in random patterns, limited to 10° in the vertical, and ultimately left the domain after being pushed by the local velocity vector.
- Rule 4: `obAvoidance` - Individuals efficiently and actively avoided obstacles when they were detected.
- Rule 5: `colAvoidance` - Individuals within proximity to other individuals, moved away from each other until out of the range defined by `repulsionDist`.
- Rule 6: `memory` - Individuals biased movements towards the direction of the average upstream direction detected over previous timesteps, resulting in a reduction in sensitivity to variations in the local velocity direction.
- Rule 7: `tkeAvoidance` - Individuals moved with bias against regions with TKE values above `tkeThreshold`.

The verification process for the `followFlow`, `randomWalk`, `obAvoidance`, `colAvoidance`, `memory`, and `tkeAvoidance` rules was simple due to the simple formulation of the rules. For example, the `followFlow` rule should move an individual in the local upstream direction, which should be a straight, on-axis line when applied to a domain where the

velocity field is dominated by a single component of velocity (i.e. `veriSetA`). Verification of the `minMaxEnergy` rule was more difficult due to the complexity of the rule; i.e. the rule contains three behavioural cases with five triggers. Verification of this rule required interrogation of each domain and each trajectory to determine fluid shear values, velocity magnitudes, and obstacle data to ensure each threshold was appropriately triggered and the corresponding behavioural case was activated.

5.6.2 Discussion of Sensitivity Analyses

This section discusses each of the sensitivity analyses carried out within this chapter.

Discussion of Sensitivity to `minMaxEnergy` Thresholds

The `minMaxEnergy` rule is complex, containing three distinct behavioural cases controlled by four threshold values. This chapter has presented an investigation in the value of each of these thresholds, and identified that the following values consistently produce qualitatively agreeable trajectories through `veriSetA`, `veriSetB`, `veriSetB2`, and `veriSetB3`:

- `minEnergyThreshold` $= 0.4ms^{-1}$
- `maxEnergyThreshold` $= 0.05ms^{-1}$
- `gradThresholdMin` $= -0.35s^{-1}$
- `gradThresholdMax` $= -1.25s^{-1}$

These sensitivity studies demonstrated that using only the velocity magnitude thresholds (`minEnergyThreshold` and `maxEnergyThreshold`) was sufficient for an individual to navigate the `veriSetA` domain, but insufficient for passage of the `veriSetB` domain [see figures 5.27 and 5.28]. This was due to the inability to determine flow direction from velocity magnitude, and therefore individuals became trapped within recirculation zones, wherein they follow the local flow indefinitely. This limitation could be mitigated against by using the horizontal components of flow (i.e. U_x or U_y), but this requires *a priori* knowledge of the global upstream direction and would encroach on the developmental principle of a generalised model and would severely limit the utility of `fishPy` [see table 1.1 in chapter 1].

The sensitivity studies also showed that it was possible for an individual to successfully pass both the `veriSetA` and `veriSetB` domains using only the spatial velocity gradient thresholds [see figure 5.30]. However, regions of near-zero velocity flow can

be detrimental to up-migrating salmonidae, since exposure to relatively significant flow velocities (i.e. attraction flow) is required to determine the upstream direction [see section 2.7]. Furthermore, both food and olfactory information are transported by fluid flow within rivers and therefore it is beneficial for up-migrating fish to locate themselves within the bulk flow to collect this information. A comparison of predicted trajectories using a combination of velocity magnitude and fluid shear thresholds against using only the velocity magnitude thresholds or only the fluid shear thresholds, shows that using all four thresholds led to more qualitatively agreeable results, figures 5.31, 5.30, and 5.28. Therefore, the inclusion of all four thresholds is important as each threshold controls the attraction and repulsion from different hydraulic information.

Discussion of Sensitivity to the Decision Timestep

In chapter 4, the theoretical maximum `fishTimestep` was determined based on model stability criteria and the CFL criterion. Within section 5.5.2, the sensitivity of predicted trajectories to the `fishTimestep` was investigated. The results demonstrated that the predicted trajectories through the `veriSetB` domain were sensitive to the `fishTimestep`, even when less than the maximum theoretical value, figure 5.32. Conversely, the predicted trajectories through the `veriSetA` domain were independent of the `fishTimestep`, figure 5.32d. The spatial velocity gradients in the `veriSetA` domain were small when compared to the `veriSetB` domain. Therefore, the frequency at which an individual can sample the environment and make movement decisions (i.e. `fishTimestep`) must be smaller when considering the `veriSetB` domain, due to the increased spatial variation of the environmental data. This suggests that, much like the maximum theoretical `fishTimestep`, the required `fishTimestep` to ensure independence of predicted pathways depends upon the domain being investigated. In particular, it depends upon the minimum velocity in the domain and the spatial velocity gradients. It is interesting that neither Goodwin et al. [2014], Gao et al. [2016], nor Tan et al. [2018] consider sensitivity to the timestep and instead choose unjustified, constant values of $2s$, $1s$, and $0.3s$, respectively. Gisen [2018] briefly mentioned sensitivity of the ELAM-de model to the timestep and concluded that the model is near-independent of the chosen timestep. However, Gisen [2018] did not present any sensitivity testing methodology or results and therefore it is difficult to have confidence in this conclusion.

Discussion of Sensitivity to the Sensory Range

A study was undertaken to determine the sensitivity of the predicted fish paths against varying sensory ranges of individuals. This study revealed that varying the sensory range of a $0.3m$ individual from 0.5 to 4.0 (measured in bodylengths) did not significantly alter the predicted paths through the `veriSetA` and `veriSetB` domains, figure 5.33. This could be due to the spatial averaging processes within `fishPy`, although it is a surprising result given the complex, spatially-varying fluid environment within the `veriSetB` domain. This is an interesting result as there is no clear agreement on the size of the sensory ovoid within the literature. For example, Goodwin et al. [2014] used a randomly varying sensory range between 6.0 and 10.0 bodylengths. Whereas Gao et al. [2016] and Tan et al. [2018] used randomly varying values between 1 to 1.5, and 1 to 1.75 bodylengths, respectively. Zielinski et al. [2018] used a value of 0.5 bodylengths, which was doubled in coarse mesh regions, and Gilmanov et al. [2019] used a value of 2.0 bodylengths. However, disabling the sensory ovoid by setting the `sensoryRange` to zero, resulted in the individual moving downstream and failing to pass the domain within 1000 timesteps, , figure 5.33b. These results suggest that, while trajectories are near-independent to the size of the sensory ovoid, the existence of the sensory ovoid is significant and crucial for enabling individuals to sample the environment, make informed decisions, and escape from undesirable flow regions.

Discussion of Sensitivity to the Spatial Resolution

A study on the sensitivity of predicted fish paths to the spatial resolution of the environment data was undertaken. The results showed that the predicted trajectory through the `veriSetA` domain varied little when the spatial resolution was varied between $0.05m$ and $0.2m$, figure 5.34. However, when the spatial resolution was increased above $0.2m$, the trajectories tended towards the centre of the channel rather than the edges, figure 5.34. This is likely due to a loss of geometry and near-boundary velocity data due to the spatial interpolation, which assumes a spatially-linear variation between grid points. Predicted trajectories through the `veriSetB` domain showed little variation between spatial resolutions of $0.05m$ and $0.1m$, but increasing to $0.2m$, $0.4m$, and $0.5m$ caused individuals to seek local maximum energy pathways earlier, figure 5.35. A spatial resolution of $1.0m$ resulted in a vastly different trajectory compared to finer resolutions, suggesting that the hydraulics were not accurately represented, figure 5.35.

It is likely that the required spatial resolution of the interpolated environment data is dependent upon the spatial variation of the pre-interpolated data and the complexity of the domain geometry. For example, domains with more complex geometries will require finer spatial resolutions to ensure the geometry is accurately captured. Similarly, hydrodynamic environments with large variations in environment data (such as large spatial velocity gradients) will require finer spatial resolutions to capture these variations. Interestingly, none of the established fish path prediction models consider any dependency upon the resolution of the environmental data used.

It is interesting that the threshold for variation in trajectories occurred at roughly $0.2m$ in each domain, despite their differences in hydraulics and geometry. Given that trajectories are dependent upon the ability for an individual to sense surrounding hydraulic data, and the sensory ovoid of the individual is a function of the bodylength; it is possible that there is an interaction between the spatial resolution of the input data required to ensure independence, and the minimum bodylength of the individuals considered. For example, smaller fish may require finer mesh resolutions, due to their reduced sensory ovoid, to adequately sense spatial variations in environmental data.

Limitations of Sensitivity Analyses

The sensitivity studies undertaken in this chapter are not without limitation. Firstly, there are limited data in the literature that can be used to compare, contrast, or validate threshold values against. This is due to the significant difficulties involved in experimentally determining behavioural responses to hydraulic variables, which remains an area of active research. Due to this, in each sensitivity analysis, appropriate ranges are identified for each parameter as well as the exact values used. Secondly, variations in bodylength are not considered within any of the sensitivity analyses, and it is unclear whether these parameters are sensitive to the bodylength of each individual. In the case of the `minMaxEnergy` rule, it is possible that the velocity and fluid shear thresholds that control the switch between behavioural cases are a function of bodylength. For example, smaller fish may be more sensitive to relatively high velocities compared to larger fish, due to the difference in swimming ability. However, the thresholds that define the behavioural switch to seeking higher velocities depend more upon repulsion from both turbulent regions and low velocity regions and therefore likely depend less on the swimming ability of the individual. Moreover, regardless of bodylength or swimming

ability, fish have been found to prefer higher velocity regions to higher turbulence regions [Smith et al., 2005, 2006].

The sensitivity studies presented in this chapter consider key `fishPy` parameters, but is non-exhaustive. However, of the established fish path prediction models in the literature [see Blank 2008, Abdelaziz 2013, Plymesser 2014, Goodwin et al. 2014, Gao et al. 2016, Gisen 2018, Tan et al. 2018, Zielinski et al. 2018, Gilmanov et al. 2019, Finger et al. 2020], only Gisen [2018] considered any form of model sensitivity. Yet the sensitivity studies presented by Gisen [2018] lack context, methodology, or thorough results, although calibration of some parameters against flume studies was undertaken. Therefore, it is challenging to compare the sensitivity studies undertaken herein with any of the published fish path prediction models in the literature.

5.7 Conclusion

This chapter has presented work towards the aim outlined in section 5.1.1. First, the development and execution of five OpenFOAM CFD simulations to create six verification datasets was presented. Each dataset was solved using the `interFoam` solver within OpenFoam, using the k-ω SST turbulence closure model. Each of the verification datasets contained varying hydraulic environments, particularly with respect to the spatial-variations of the velocity fields. These variations in hydraulics ensured that the verification and sensitivity analyses were not over-fitted to a specific hydrodynamic domain. Second, each behavioural rule within `fishPy` was verified using multiple verification domains. Verification was undertaken independently of other rules where possible. Each rule was successfully verified, ensuring that they are functioning as intended. Third, a number of sensitivity analyses were performed to understand the dependency of `fishPy`-predicted trajectories to: `minMaxEnergy` parameters, `fishTimestep`, `sensoryRange`, and the spatial resolution of the environmental input.

The sensitivity analysis of the `minMaxEnergy` thresholds demonstrated that using thresholds of both velocity magnitude and fluid shear resulted in more qualitatively agreeable results than using thresholds of only one hydraulic parameter. The sensitivity analysis of the timestep suggests that the required timestep should be small ($\mathcal{O}0.1s$) and is dependent upon the domain. This finding does not agree with the constant timestep formulation of Goodwin et al. [2014] and Gao et al. [2016]. Furthermore, domain-dependency of the timestep is not considered within any of the publish fish

path prediction models. The sensitivity study of the `sensoryRange` showed that, while the predicted trajectories were near-independent of the `sensoryRange`, disabling the sensory ovoid (`sensoryRange` = 0.0) resulted in the individual failing to pass.

Chapter 6

Application of the `fishPy` model: Ruswarp Weir Case Study

6.1 Introduction

Chapter 3 demonstrated how agent-based modelling can be applied to ecohydraulic problems. Furthermore, chapters 4 and 5 have described the development and verification of the `fishPy` tool. This chapter considers the application of the `fishPy` tool to a newly created hydraulic domain to assess fish trajectories, fish passage metrics, and to facilitate comparisons with measured fish track data.

The application of the `fishPy` tool facilitates the validation of the outputs of the model. Validation of agent-based models is important to achieve a fully realised model and understand its function [Ngo and See, 2012]. For example, Heppenstall et al. [2006] developed a hybrid agent-based model of petrol prices across the county of West Yorkshire, initialised with real data. Heppenstall et al. [2006] found that the model reproduced the spatial patterns of the real market and was successful in predicting the prices and profitability of individual retailers over a number of years. However, validation is a challenging process [see Ngo and See 2012 and Crooks et al. 2008] and Crooks and Heppenstall [2012] stated that a model should not be considered as valid or invalid, but instead be viewed as having a certain degree of validity.

The validation process considers a comparison of simulated outputs to measured data. In the context of the `fishPy` model, this requires a comparison of predicted and measured brown trout trajectories. Many experimental studies use passive integrated transponder (PIT) tags together with reader antennas [see Gibbons and Andrews 2004] to track the movements of fish [e.g. Castro-Santos et al. 1996, Peterson and Neville 2019, and Kammerlander et al. 2020]. This method collects binary present/absent data which allows for macro-scale metrics such as passage efficiency, but does not elucidate the precise pathway selected by an individual (micro-scale); i.e. the spatio-temporal resolution of the technique is insufficient. Dodd et al. [2018] utilised acoustic measurement systems to collect spatial data of individual sea trout (anadromous *Salmo trutta*) approaching and passing Ruswarp Weir; located on the River Esk. These spatial data were a mixture of 2D fish tracks (depth not measured) and binary present/absent data depending upon the number of acoustic receivers within range. This methodology yielded a higher spatio-temporal resolution compared to the use of PIT tags. This trajectory dataset has not yet been published, although findings using the dataset have been published [Dodd et al., 2018]. However for the purposes of this study, Dodd [2019] kindly shared this dataset with the author. Ruswarp Weir, henceforth the study

site, features a number of complexities important in the modelling procedure which are described in detail in section 6.2.

Securing this dataset meant that predicted fish paths and bulk passage metrics could be compared against measured bulk passage data as well as individual measured fish paths. To calculate simulated trajectories, the `fishPy` model required a dataset quantifying the hydrodynamic environment at the study site. This chapter details the collection and post-processing of the required data at the study site, the subsequent development of the CFD model to provide high resolution environment data, the validation of the CFD model, and finally the application of the `fishPy` tool to the Ruswarp domain.

6.1.1 Aim

The aim of this chapter is to apply the `fishPy` tool to Ruswarp Weir to enable comparisons of predicted and measured fish tracks using the Dodd et al. [2018] dataset. This aim is achieved through the following objectives:

- Collection, assessment, and unification of topographic bathymetry and hydraulic data at the study site.
- Development, execution, and validation of computational fluid dynamics simulations of two flow conditions at the study site.
- Application of `fishPy` to the study site to predict fish pathways and bulk passage metrics, and subsequent comparisons against the Dodd et al. [2018] dataset.

6.2 Study Site

The River Esk rises upstream of Westerdale, and flows for approximately 45 km through Eskdale, until draining into the North Sea at Whitby, figure 6.1. Ruswarp Weir lies on the River Esk, approximately $1.6km$ upstream of Whitby and marks the tidal limit. The broad-crested weir at Ruswarp was originally constructed to divert water through a now inactive mill, and is $270m$ long and positioned oblique to the river at approximately a 15° angle, figure 6.1. The River Esk is approximately 50 m wide as it approaches Ruswarp Weir. The weir features three fish passage facilities: a smolt pass at the downstream-most point on the weir, a diagonal V notch baulk pass in the centre of the

weir, and a Larinier pass at the upstream-most point on the weir. The Larinier pass features 150mm baffles, an installation angle of 8.53° (15% gradient), and is co-located with a low-head Archimedes screw hydropower turbine. This hydropower facility is licensed to abstract a maximum of 4.0m^3s^{-1} and is not allowed to function when the river level is below 3.492 metres above ordnance datum (mAOD) or the discharge is less than 0.92m^3s^{-1} [Dodd et al., 2018]. This ensures sufficient water flow through both fish passes at low flow. For reference, the weir crest is located at 3.555 mAOD.

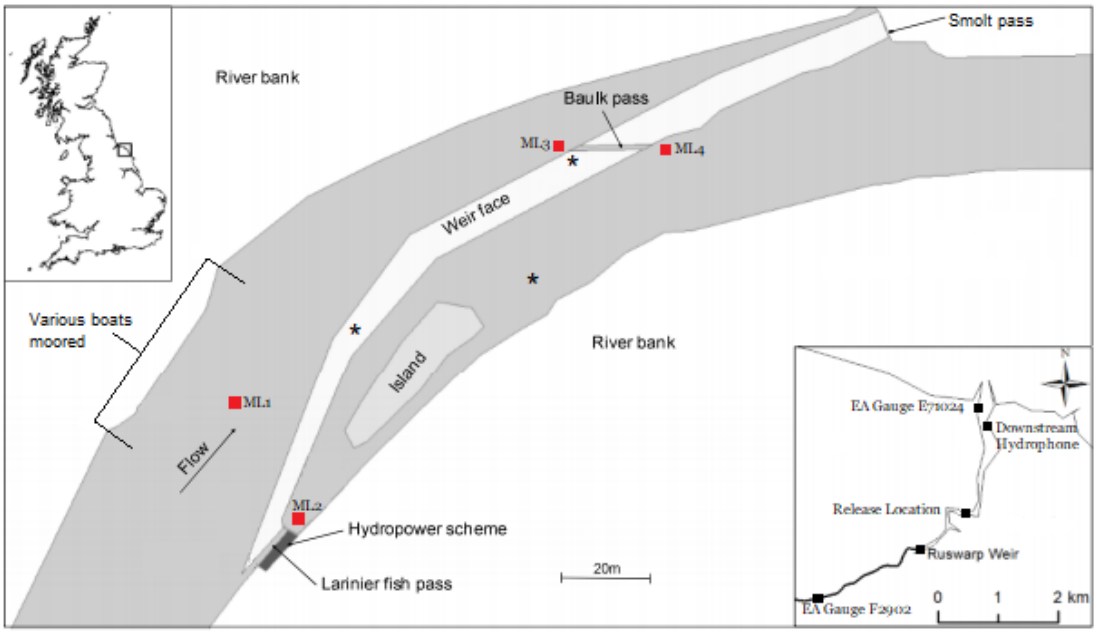

Figure 6.1: Schematic of Ruswarp Weir on the Yorkshire Esk, including location of the Larinier fish pass, baulk pass, hydropower scheme, and smolt pass. Asterisks denote terrestrial laser scanner locations. Red squares denote approximate monitor line locations used in section 6.3.3. Figure modified from Dodd et al. [2018].

6.2.1 The Study of Dodd et al. [2018]

Dodd et al. [2018] used acoustic telemetry to quantify the performance of a co-located Larinier fish pass located at Ruswarp Weir, and to understand the effect of hydropower operation of fish passage. Dodd et al. [2018] used electrofishing to catch 131 sea trout (anadromous *Salmo trutta*) between the 24th of September 2013 and the 23rd of November 2015. Fish were caught approximately 0.5km downstream of Ruswarp Weir,

surgically implanted with acoustic tags (Model 795LG; Hydroacoustic Technology Inc., Seattle, USA), and transported approximately 1.5 km downstream of Ruswarp Weir where they were released. The acoustic tags, together with an array of river-bank-mounted hydrophones, enabled the collection of two dimensional fish locations (i.e. no depth data). The temporal resolution of the data varied between $\approx 1.6s$ and $\approx 10.1s$. A single hydrophone was placed downstream of the release location, another was placed approximately $30m$ downstream of Ruswarp Weir, and seven were placed immediately downstream of the Larinier fish pass. A further three hydrophones were placed upstream of the weir. The Larinier fish pass and baulk pass were open throughout the study, and the smolt pass was closed throughout the study. River discharge was obtained from the Environment Agency gauge F2902, River Esk at Briggswath which is located $1.6km$ upstream of Ruswarp Weir, and the through-turbine flow rate, obtained from Whitby Esk Energy, at 15 minute intervals throughout the study period. Furthermore, water levels were monitored at 5 minute intervals at the Environment Agency gauge E71024 at Whitby Harbour.

Dodd et al. [2018] reported that 84 of the 131 fish approached Ruswarp Weir, with a median of 6 approaches each. A total of 61 fish ascended the weir, with 53 passing via the fish pass. This gave an impediment passage efficiency of 72.6% and a fish pass efficiency of 63.1%. Dodd et al. [2018] recorded significant variation in river discharge throughout the study from $0.44m^3s^{-1}$ to $88.00m^3s^{-1}$. These discharge values show that the weir is subject to flood conditions and overtopping of the weir is possible. Tidal variations, together with these discharge variations, caused the downstream river level to vary from 1.68 to 4.24 mAOD throughout the study. Dodd et al. [2018] reported that fish ascended the Larinier fish pass when the river discharge was between $1.65m^3s^{-1}$ and $31.00m^3s^{-1}$, and that no significant difference in discharge was seen between when fish successfully ascended the Larinier fish pass (median discharge $6.22m^3s^{-1}$) and when fish approached but did not ascend (median discharge $6.48m^3s^{-1}$). Dodd et al. [2018] reported that over half of the approaches to the Larinier fish pass occurred when the downstream river level was between 2.00 and 2.19 mAOD. No fish approached the Larinier fish pass when the flow was below the lower limit for hydropower operation (3.492 mAOD and $0.92m^3s^{-1}$). The data collected by Dodd et al. [2018] were kindly provided to the author including: measured fish tracks, downstream water levels, river discharges, hydropower discharges, and lengths and weights of tagged fish.

Dodd et al. [2018] reported that the Archimedes screw hydropower turbine was active for 76% of the study period and fish ascended the co-located Larinier fish pass across the operating range of the hydropower turbine ($0.11 - 3.83 m^3 s^{-1}$), as well as when the hydropower turbine was inactive. Furthermore, Dodd et al. [2018] reported that the through-turbine flow rate had little influence over the probability of successful passage through the Larinier fish pass. Since modelling of an Archimedes screw turbine is complex and computationally challenging, it was decided that fish tracks measured while the turbine was active would be discarded. Furthermore, tracks measured during flood conditions, where discharge was in excess of 500% of the average, were discounted. This left a total of 60 fish tracks measured for 15 tagged sea trout to compare against the predicted outputs. Data on the tagged individuals and specific tracks are given in tables E.3, E.4, E.5, and E.6 in Appendix E, and are discussed later in this chapter.

6.2.2 Environmental Data

Since Dodd et al. [2018] did not collect high resolution bathymetry and hydraulic flow data, fieldwork was undertaken between the 10^{th} and 13^{th} of September 2018. This period coincided with the largest Spring tide of 2018, which afforded the advantage that the dry bed area was maximised at low tide. Further data were also collected on the 4^{th} of April 2019. The corresponding river discharge and stage data from the Environment Agency gauge 27902, River Esk at Briggswath were provided by the Environment Agency [Lindsay, 2019]. Furthermore, upstream and downstream river levels at the weir were provided by Whitby Esk Energy [Ford, 2019]. These data showed that the river discharge varied from 0.46 to $0.86 m^3 s^{-1}$, with an average of $0.57 m^3 s^{-1}$, and the downstream river level varied from approximately 1.75 to 3.35 mAOD.

Permission from the Environment Agency was obtained to close the Larinier fish pass, the smolt pass, and the hydropower scheme throughout data collection. This meant that the only flow across the weir was through the baulk pass. This was done to reduce the downstream water level as much as possible to aid in collecting bathymetry data. Since the environmental conditions during the fieldwork were different to those reported by Dodd et al. [2018], the collected data were used to parametrise and validate a CFD model of the same environmental conditions before its application to the conditions reported by Dodd et al. [2018].

6.2.3 Data Collection Methodology

Data collection was divided into two components. The first considered the collection of topography of the subaerial regions of the study site using LIDAR. The LIDAR system was unable to penetrate water and therefore, to maximise the area that could be measured, the fish pass was closed on arrival to minimise the downstream water level. It was not possible to reduce the upstream water level by an amount that would allow for collection of the upstream bathymetry using the LIDAR system. Thus a second component was included to collect subaqueous bathymetry and velocity data using an Acoustic Doppler Current Profiler (ADCP) mounted underneath a remote-controlled boat. The two datasets were coupled through the use of real-time kinetic Global Positioning System data. This section details the data collection methodology and the extensive manipulation and filtering processes employed, which is summarised in figure 6.2.

Collection and Post-Processing of Real-time Kinematic Global Positioning System Data

Leica Geosystems 1200 real-time kinematic (RTK) Global Positional System (GPS) surveying instrument was used to collect three dimensional positions of 107 key points across the weir. In particular, data were collected around and within the fish pass and baulk pass, along the upper and lower limits of the weir face, and at five targets spaced across the weir face.

All base data were post-processed using Geo Office version 7 [Leica Geosystems, 2020]. Simultaneous same-satellite observations collected at publicly accessible reference stations and local base stations were combined during post-processing. In order to accomplish this task, precise satellite ephemeris and reference station data were downloaded from NASA [NASA, 2020] and the Ordnance Survey, respectively [Ordnance Survey, 2020]. Data from publicly accessible reference stations at Catterick (ID:CATT), Scarborough (ID:SCAU) and Yearsley (ID:YEAL) were used. During baseline post-processing, three-dimensional vectors were computed between reference sites and local base stations; triangulation yielded highly accurate three-dimensional coordinates of the local base stations. For the two base stations occupied during surveys, Geo Office estimated standard deviations in the X-, Y- and Z-coordinates of $\pm 0.0001m$, $\pm 0.0001m$ and $\pm 0.0001m$, respectively.

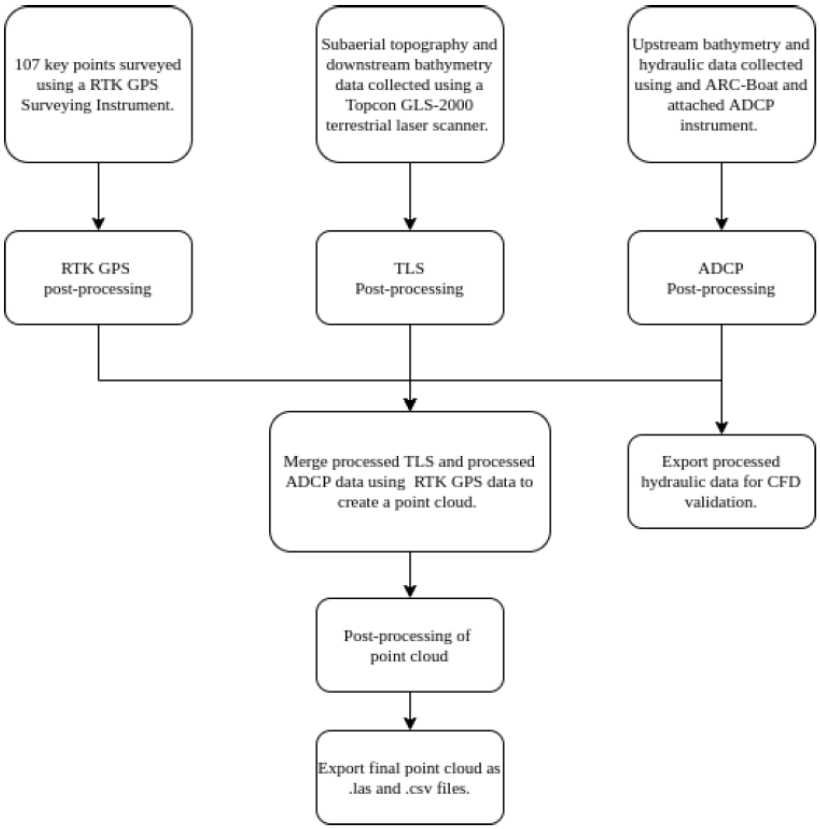

Figure 6.2: Flowchart outlining the parallel data collection process, post-processing, and subsequent creation of the final point cloud through the integration of the TLS, ADCP, and RTK GPS data.

After post-processing, all GPS coordinates were projected from the WGS84 coordinate system to the Universal Transverse Mercator Zone 30 North coordinate system and ellipsoidal heights were converted to altitudes by subtracting geoid heights computed by the HSYNTH WGS84 tool created by the National Geospatial-Intelligence Agency [NGA, 2020]. In addition, it was found that there was an offset of $0.883m$ between estimated altitudes and Ordnance Datum Newlyn.

Collection and Post-Processing of Terrestrial Laser Scanner Data

A Topcon GLS-2000 terrestrial laser scanner was used to collect three dimensional point data of the dry bed and surrounding geometry [see Hohenthal et al. 2011]. Thorough

manual removal of flora was undertaken around the study site prior to data collection to reduce the required post-processing. Throughout data collection: the camera resolution was set to high (2560 x 1920 pixels), the laser resolution was set to $3.1mm$ at a range of $10m$ and the "detail" mode was selected, pulse selection was set to "last" to maximise the laser penetration of the water surface and any vegetation. Three separate scanning locations were used to ensure full coverage of the weir face and downstream dry bed [denoted by the asterisks in figure 6.1]. Individual laser scans each had their own local coordinate system and thus need to be subject to a five variable (three translation and two rotation) coordinate transfer. To compute this transform for each laser scan, the position of five targets distributed over a range of three dimensional positions were surveyed using the Leica RTK GPS.

Data from five separate laser scans and the location data of the five targets were imported into TopCon ScanMaster 3.06. For scans that could see the targets, the tie point registration method was used to compute the 3D coordinate transformation to shift the local scans into UTM coordinate system. For the scan position that could not see the targets, the occupy and backsight method was used. Outliers were removed from the data within ScanMaster 3.06. The data were then imported into CloudCompare v2.9.1, where vegetation on the weir face was filtered using a Cloth Simulation Filter [see Zhang et al. 2016]. Optimal settings were determined through trial and error by assessing the numbers of points removed and most accurate identification of vegetation as opposed to the weir face or river banks. In particular, "Relief" with "Slope processing" was enabled, with a cloth resolution of $0.5m$ and a classification threshold of $0.2m$.

Collection and Post-Processing of Acoustic Doppler Current Profiler Data

A SonTek RiverSurveyor M9 [SonTek, 2011] mounted underneath a remote-controlled ARCboat [HR Wallingford, 2020] was used to collect bathymetry and hydraulic data upstream of the weir. The SonTek RiverSurveyer M9 is an acoustic Doppler current profiler (ADCP) that uses four acoustic beams to evaluate three dimensional velocity data and five acoustic beams to measure bathymetry. Velocity data are measured in up to 128 equally- spaced bins through the acoustic beam. This results in an instantaneous three dimensional velocity profile along a vertical line from the probe to the bed. The SonTek RiverSurveyor M9 has a measurement resolution of $0.001ms^{-1}$ and $0.001m$ for

Table 6.1: Acoustic Doppler current profiler data quality categories based on measurement parameters

Quality Category	NVS	HDOP	Q_in
A	≥ 6	≤ 3	4
B	≥ 6	> 3	3
C	≥ 6	≤ 3	-
D	≥ 6	> 3	-

velocity and depth measurements, respectively [SonTek, 2011]. Similarly, the SonTek RiverSurveyor M9 has a reported accuracy of $\pm 0.002 ms^{-1}$ (or 0.25%) and $\pm 0.001 m$ (or 1%) for velocity and depth measurements, respectively [SonTek, 2011]. The M9 is fitted with an on-board compass and two-axis tilt sensor to enable computation of the x,y,z location of the sample bins. The ARCboat is also equipped with an on-board GPS, which gave spatial locations and facilitated integration with the other geospatial datasets. The compass and tilt sensor required daily calibration, achieved through manual simulation of roll, pitch, and yaw movements. Measurements were taken along a series of transects, spaced approximately $5m$ apart, upstream of the weir. Transects were repeated three times to lessen the impact of noise in the data. The ARCboat was moved at slow speeds to ensure high quality measurements [SonTek, 2011]. Furthermore, measurements were taken along three additional streamwise lines to compliment the transects.

Measured ADCP data were exported to a modified version of the Velocity Mapping Toolbox [Parsons et al., 2013] that permitted export of bathymetry computed using all ADCP beams together with the central depth-sounding transceiver. These data were categorised based on their assessed quality using multiple parameters: the number of visible satellites (`NVS`), the Horizontal Dilution of Precision (`HDOP`), and the internal "Quality" value (`Q_in`). An `HDOP` value of 4 to 6 represents the minimum level appropriate for discharge measurements, whereas an `HDOP` value ≤ 3 represents excellent quality [SonTek, 2011]. The `Q_in` value is defined as: zero denotes a lack of GPS data, one denotes a non-differential GPS signal, two denotes a differential GPS signal (submetre accurate), and four denotes a full RTK GPS signal (accurate to 30 mm or less) [SonTek, 2011]. The quality categories used to process the ADCP data are defined in table 6.1.

All category C and D data were discarded. All category A data were retained. Category B data were retained only if surrounding data points were category A and no significant changes in xy location were observed. 80.8% of measurement data points were retained (66347 out of 82123 data points). Measured depths were then converted to altitudes through reference to upstream water surface elevations and Ordnance Datum, provided by Whitby Esk Energy. These upstream water surface elevations were linearly interpolated to determine elevations at the exact collection time of each ADCP measurement.

Creation and Post-Processing of Point Cloud Data

Processed sub-aerial elevation data collected via LIDAR and processed subaqueous elevation data collected via ADCP were imported into CloudCompare and merged to create a single point cloud dataset. These were then compared to the measured GPS point data, collected around key features of the weir, to ensure accuracy, and then subsequently merged. This resulted in a point cloud of approximately 6.3 million points. To reduce the point cloud to a more manageable size, the sub sample tool within CloudCompare was used to select the points with a minimum spacing of $0.1m$ between data points. The final processed point cloud was then exported as a .las file and as a .csv file.

6.3 Computational Fluid Dynamics of Ruswarp Case Study

Two computational fluid dynamics simulations were developed. The first, named `valSet`, simulated the flow conditions during the present fieldwork. This case allows for direct comparisons of velocity measurements between the CFD and the collected ADCP data, providing some evidence of the validity of the use of CFD on the geometry. The second, named `fishSet`, simulated the flow for the conditions under which the Dodd et al. [2018] fish tracks were measured. This dataset is designed to be used as an input to the `fishPy` model to predict the fish pathways.

For each case, a separate CFD mesh was required. This was due to the fish pass being closed during the fieldwork, yet open during the collection of fish tracks. Furthermore, the implementation of the downstream boundary condition, detailed in section 6.3.2, required a separate CFD mesh for each.

6.3.1 Creation of the Computational Fluid Dynamics Meshes

In order to create computational fluid dynamic simulations of the study site, the geometric data was first converted into a high quality CFD mesh. This was a laborious and complex process. Furthermore, no published methodology or protocol detailing the conversion from TLS data to CFD mesh was found. Therefore, to aid future researchers, the method used is thoroughly detailed within this section. The methodology briefly consisted of the following steps:

1. Creation of the .tin file.
2. Creation of the initial .stl file.
3. Quality control of the .stl file.
4. Preparation of the manifold surface file for openFOAM.
5. Creation of CFD mesh.

Creation of the .tin File

The final point cloud, exported in both .las and .csv file formats, was converted into a .tin file. This was done using `las2tin`, a tool which is part of the `LAStools` suite [Isenburg, 2019]. The `las2tin` tool is designed to read in TLS point cloud data and create a .tin through incremental Delaunay triangulation based on the work of Bowyer [1981] and Watson [1981]. Thus, regions of the domain that did not contain surveyed points, were filled using linear interpolation between surveyed points. This is an appropriate approach for natural river channels since elevation gradients are low, with slopes up to the angle of repose [e.g. Nicholas et al. 2012].

Creation of the Initial .stl File

The newly created .tin file was then imported into MATLAB using the `dlmread` function. As all position data was in UTM coordinates, the resultant origin location was approximately 6×10^6 m from the nearest data in the point cloud. A new coordinate system was developed by subtracting the minimum position value in each axis from the position vectors. termed the `UTM_RUS` coordinate system. This translated the origin of the new domain to the southwest corner of the original domain. The .tin and .csv

files were then converted into a surface file using a combination of the MATLAB functions `surf2solid` [Holcombe, 2014], `stlwrite` [Holcombe, 2018], and `geom3d` [Legland, 2019]. This resulted in a large .stl file of the entire Ruswarp domain [see figures 6.3a and 6.4a, for selected regions].

Quality Control of the .stl File

The initial .stl file was imported into Blender, where it was thoroughly interrogated using the 3D Print Toolbox Add-on for Blender [Blender Foundation, 2019]. This included identification and rectification of intersecting faces, zero area faces, zero length edges, non-flat faces, thin faces, sharp faces, and holes within the surface. This also identified issues with the initial geometry that had to be rectified. Specifically, sections of the bed between measured points were in-filled by linearly interpolating data from the surrounding area. This was particularly necessary along the upstream bed since the only measured elevations were from the ADCP data collected along transects at $5m$ intervals. Additionally, the weir face was particularly rough, likely due to the presence of flora in the original point cloud. Therefore, any remaining influence of flora on the surface file was reduced by smoothing the surface to simplify CFD meshing. Finally, the fish pass and baulk pass were rebuilt using the GPS locations measured with the Leica Geosystems 1200 and from photographs taken during the fieldwork. In particular, the crest heights of the baulk pass, fish pass, and weir were corrected based on known and collected data.

The CFD meshing process employed later required a manifold surface. Therefore, a lid was constructed to cover the domain, and the river banks were extended vertically to connect to the lid. This lid was chosen to be $4m$ above the highest point in the domain, as it was decided that this was far enough away from the expected free surface to not impact upon the flow. The 3D Print Toolbox Add-On was then used to identify non-manifold edges to aid in ensuring that the .stl file was completely manifold. Before and after views of the surface file are shown in figures 6.3 and 6.4.

Preparation of Surface File for OpenFOAM

The `valSet` and `fishSet` domains feature some fundamental geometric differences because the downstream boundary condition (downstream water height) was implemented through the creation of an artificial weir at the downstream end of the surface file for

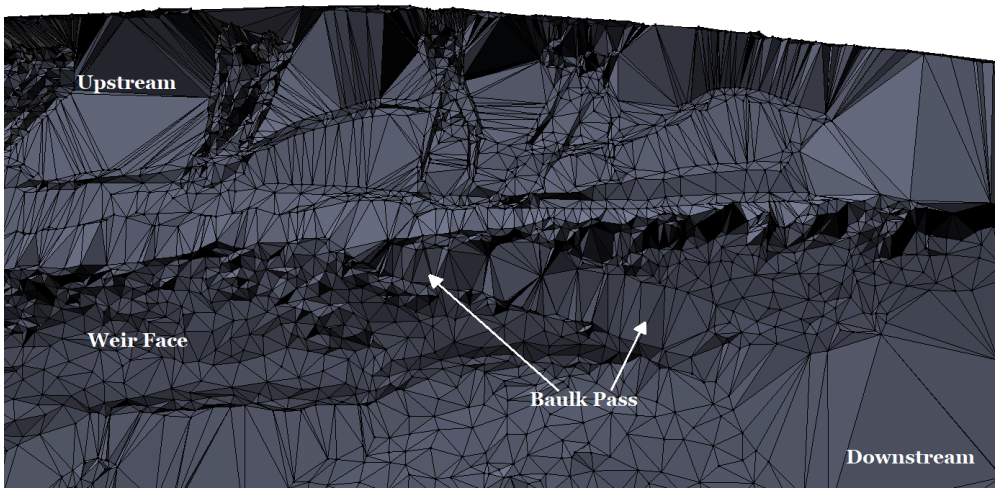

(a)

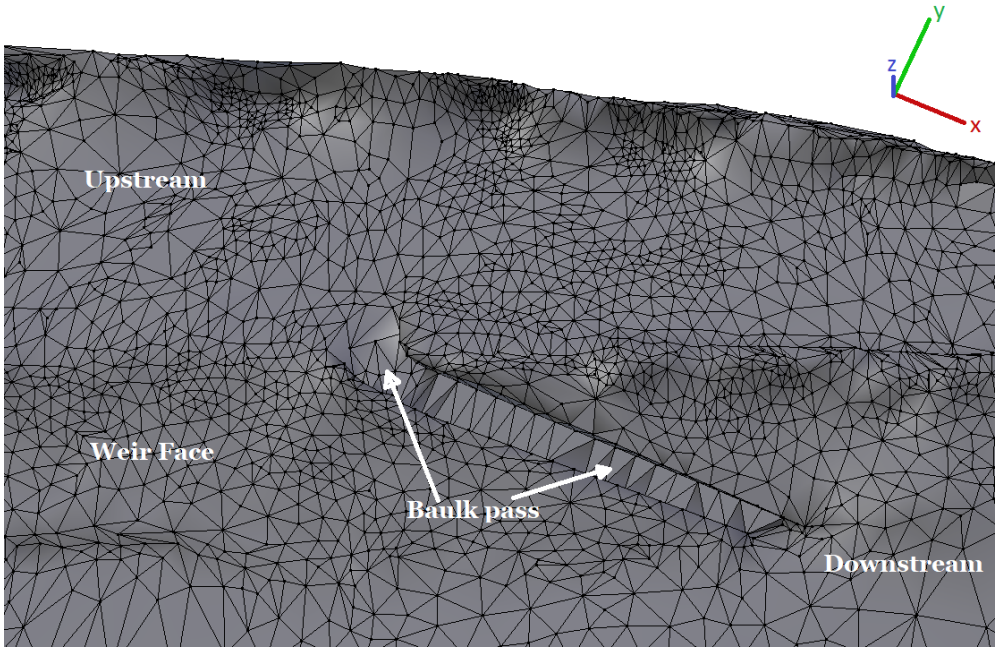

(b)

Figure 6.3: Annotated planform view of the baulk pass within the .stl file a) before and b) after extensive cleaning, smoothing, and interpolation.

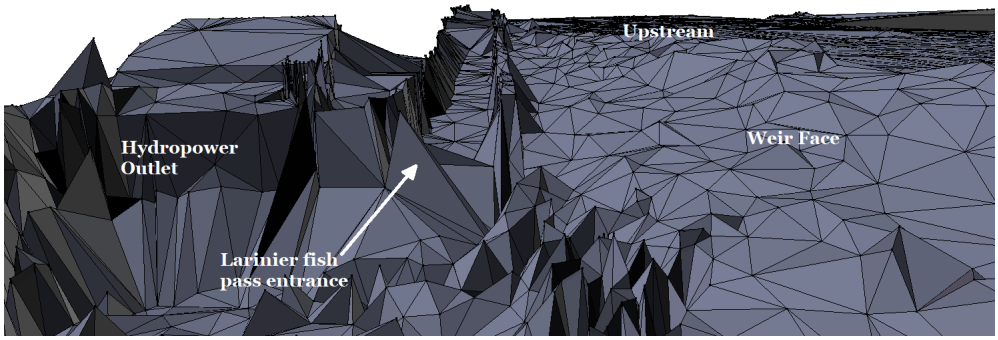

(a)

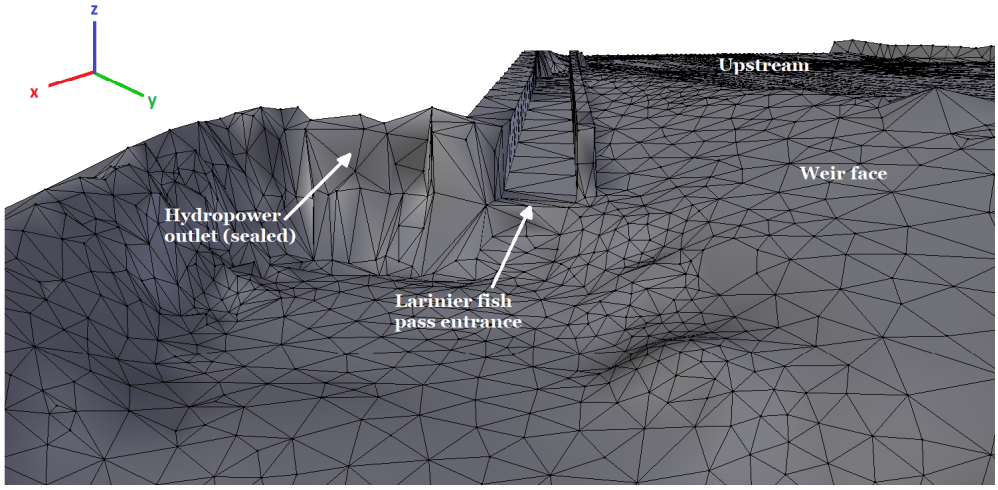

(b)

Figure 6.4: Annotated view looking up the fish pass within the .stl file a) before and b) after extensive cleaning, smoothing, and interpolation.

each of the two flow conditions, detailed in section 6.3.2. Therefore, the .stl file was duplicated to create separate surface files for each flow case.

The `snappyHexMesh` tool within OpenFOAM requires an input of a manifold ASCII .stl file of the entire domain. It also requires multiple additional ASCII .stl files which define each boundary condition and each cell refinement region (i.e. for inflation layers). This was done in Blender by duplicating the final .stl and then subsequently sectioning the surface into the required regions.

Creation of CFD Mesh

The manifold ASCII .stl file and the sectioned ASCII .stl files were used as inputs utilising openFOAM v4.1 and the `blockMesh` and `snappyHexMesh` tools. The `blockMesh` tool was used to create a three dimensional hexahedral mesh within the bounding box that encompassed the manifold surface. This bounding box mesh provided the starting point for the `snappyHexMesh` tool, and was required to feature elements with an aspect ratio of 1. This is known as the background mesh and featured approximately 300,000 cells with a cell characteristic length of roughly $1m$. The meshing algorithm then incrementally refined the background mesh by splitting hexahedral cells that were intersected by the input surface files into 8 (2^n; where n is the number of spatial dimensions) new hexahedral cells of equal size. The amount of refinement (cell splitting) is determined by the `level` associated with each `refinementSurface` within `snappyHexMeshDict`. For each flow condition, the `level` was set to 2 for the full manifold surface, with an additional `level` for both the fish pass and baulk pass. This was done to ensure accurate modelling of the passes, as these control the movement of water from above the weir to below the weir.

Once the desired refinement had taken place, unnecessary cells were automatically removed. This was done by removing regions that were either inside or outside of the manifold surface. This is controlled by the `locationInMesh` variable; if the specified point was inside the manifold surface, any regions outside the manifold surface were removed and *vice versa*. Cells were retained if $\geq 50\%$ of their volume was within the desired region. The mesh was then smoothed to remove the resultant jagged cell edges at the intersection with the input surfaces. This was done within the meshing algorithm by incrementally moving cell vertices onto the surface of the manifold surface. The mesh quality was tracked to ensure that moving a cell vertex did not compromise

Table 6.2: Defined `snappyHexMesh` quality parameters for mesh generation for both Ruswarp flow cases.

Control	Value	Description
`maxNonOrtho`	45	Maximum non-orthogonality allowed (degrees).
`maxBoundarySkewness`	10	Maximum skewness allowed.
`maxInternalSkewness`	4	Maximum skewness allowed.
`maxConcave`	60	Maximum concaveness allowed (degrees).
`minVol`	10^{-9}	Minimum cell volume.
`minTetQuality`	10^{-30}	Minimum quality of tetrahedral cells from cell decomposition.
`minArea`	10^{-6}	Minimum cell face area.
`minTwist`	0.02	Minimum cell face twist.
`minDeterminant`	0.001	Minimum normalised cell determinant.

mesh quality. The snapping process is controlled by the `nSmoothPatch`, `tolerance`, `nSolveIter`, and `nRelaxIer` variables within `snappyHexMeshDict`. The `nSmoothPatch` variable controls the number of smoothing iterations undertaken before attempting to move cell vertices. The `tolerance` variable defines the maximum distance for a cell vertex to be attracted to a surface. This is defined with units of local maximum edge length. The `nSolveIter` variable defines the number of mesh displacement relaxation iterations undertaken. The `nRelaxIter` variable defines the maximum number of snap relaxation iterations. After trial and error, the following snapping controls were used for each flow condition: `nSmoothPatch` was set to 5, `tolerance` was set to 2, `nSolveIter` was set to 30, and `nRelaxIter` was set to 5.

Once the mesh snapping process was complete, the `snappyHexMesh` tool allowed for additional mesh layers to be applied. These were specified by the input sectioned .stl files. In each flow condition, inflation layers were applied to both the fish pass and the baulk pass. The `expansionRatio` was set 1.2. The `finalLayerThickness` variable, which describes the size of the final layer cell relative to the nearest undistorted, non-layer cell, was set to 0.4. Similarly, the `minThickness` variable, which describes the smallest acceptable cell thickness relative to the nearest undistorted, non-layer cell, was set to 0.05. The mesh quality requirements were defined as given in table 6.2. The final

meshes for the `valSet` and `fishSet` domains contain approximately 5.2 million and 4.7 million elements, respectively. The possibility of applying additional mesh layers to the entire bed was investigated but it was found that this would drastically increase the size of the mesh due to the large scale of the domain ($\approx 200m$ by $\approx 60m$ by $\approx 10m$).

6.3.2 Computational Fluid Dynamics Methodology

Solver Settings

A RANS approach was used to model the flow under both environmental conditions. Both the `fishSet` and `valSet` domains are large and time-dependent, making solving them, even with a RANS approach, challenging. Therefore, more complex modelling approaches such as LES or DNS were not considered due to their increased complexity, time requirements, and computational demands. Furthermore, it was doubtful that the additional complexities would affect the outputs of the `fishPy` tool, due to the spatio-temporal resolution of the tool and the spatial-averaging of data undertaken by individuals.

The Reynolds numbers for the `fishSet` and `valSet` were estimated using equation 2.25, using the expected bulk velocity and the maximum expected flow depth, and were found to be 19000 and 12500, respectively. This demonstrated the need for turbulence modelling within the computational fluid dynamics approach. The `interFoam` solver within OpenFOAM v4.1 was used. This solver makes use of the Volume of Fluid (VOF) method [see section 2.5.4]. Second order numerical schemes were used and residual tolerances were set to 10^{-8}. The gravitational acceleration vector was applied to the domain in the negative z direction (vertically downwards). Values of ω and k at the inlet were chosen based on equations 6.1 and 6.2 [Menter, 1993]. The freestream velocity, U_∞ was estimated at 0.5 ms^{-1}. The turbulence intensity was estimated at 10%, which is acceptable for moderately turbulent domains (e.g. Jensen 2007). This gave initial k and ω values of approximately 0.01 m^2s^{-2} and 0.006 s^{-1} for each flow case.

$$k = \frac{3}{2}(U_\infty I)^2 \tag{6.1}$$

Where: U_∞ is the freestream velocity; and I is the turbulence intensity.

$$\omega = \frac{\sqrt{k}}{L} \tag{6.2}$$

Where L is the turbulence length scale.

Boundary Conditions & Initial Conditions

A river discharge and downstream river level were required to implement meaningful boundary conditions for each CFD model. For the `fishSet`, these were taken as average values over the time period that the selected measured fish were active. This resulted in a value of 2.58 mAOD and $2.41m^3s^{-1}$. For the `valSet`, the upstream boundary condition was taken as the average fish discharge across the window of time that the ADCP measurements were taken, giving a value of 0.648 m^3s^{-1}. As all ADCP measurements were taken upstream, the downstream boundary condition was unimportant as the flow across the weir was supercritical. Therefore, a downstream river level of 1.63 mAOD was selected as this was within the range present during fieldwork.

To model the inflow discharge entering the domain without specifying a flow depth, a velocity inlet was created along an xy plane. This meant that water entered the domain in the positive z direction, and therefore the upstream flow depth was determined solely by the mass balance of the water entering through the inlet versus the water passing down the baulk and fish passes. The upstream discharge conditions for `fishSet` and `valSet` were $2.41m^3s^{-1}$ and $0.648m^3s^{-1}$, respectively. These equated to inlet velocities of $0.045ms^{-1}$ and $0.0108ms^{-1}$, respectively. Both cases also featured an atmospheric outlet along the top of the domain, which allowed air to enter and exit the domain. The remaining walls were defined with a no-slip boundary condition. As the baffles within the fish pass were not modelled, the roughness value within the pass was inflated using the `nutkRoughWallFunction` boundary condition. This was done to simulate the effect of the baffles by slowing the water within the pass.

The boundary condition at the downstream-most end of the domain was implemented to ensure that downstream water height was equal to the measured data. The measured downstream water heights were 2.58 and 1.63 mAOD for the `fishSet` and `valSet`, respectively. This boundary condition was implemented through the creation of an artificial broad-crested weir at the downstream end of the surface file for each of the two flow conditions, as the VOF methodology is known to accurately capture flow heights over broad-crested weirs [Sarker and Rhodes, 2004]. The heights of each

of these artificial weirs were calculated using the known downstream water level and the weir equation for a broad-crested weir, equation 6.3 [Swamee, 1988]. Application of equation 6.3 yielded a depth over the crest of the weir, but did not elucidate the required weir height. Therefore, the minimum weir height required to ensure critical depth was calculated using equation 6.4, which is formulated as a balance of energy.

$$Q = CBH^{\frac{3}{2}} \tag{6.3}$$

where: Q is the discharge ($m^3 s^{-1}$; C is the weir coefficient, estimated as 1.7 $m^{0.5} s^{-1}$, B is the crest width of the weir (m), and H is the vertical distance from the weir crest to the water surface (m).

$$p = y_1 + \frac{v_1^2}{2g} - y_2 - \frac{v_2^2}{2g} \tag{6.4}$$

where: y_1 is the flow depth upstream of the artificial weir (m), $\frac{v_1^2}{2g}$ is the velocity head upstream of the artificial weir (m), y_2 is the flow depth on the artificial weir where critical depth is achieved (m), $\frac{v_2^2}{2g}$ is the velocity head on the artificial weir where critical depth is achieved (m), and p is the required minimum height of the weir from the bed (m).

The velocity upstream of the artificial weir was calculated based on the continuity equation:

$$v_1 = \frac{Q}{By_1} \tag{6.5}$$

The critical depth over the weir,y_2, was calculated using:

$$y_2 = (\frac{Q^2}{gB^2})^{\frac{1}{3}} \tag{6.6}$$

Lastly, the critical velocity was determined using:

$$v_2 = \frac{Q}{By_2} = \sqrt{gy_2} \tag{6.7}$$

This analysis showed that the `fishSet` and `valSet` cases required minimum artificial weir heights of 1.54 and 0.70 metres above the bed, respectively. These values equated

Table 6.3: Inlet and outlet boundary conditions for each Ruswarp flow case.

Parameter	`valSet`	`fishSet`
Required discharge (m^3s^{-1})	0.648	2.41
Prescribed inlet velocity (ms^{-1})	0.0108	0.045
Downstream water level (mAOD)	1.63	2.58
Prescribed artificial weir height (mAOD)	1.48	2.24

to 2.24 and 1.56 mAOD, respectively. The values yielded for H were then summed with the artificial weir heights to give the original downstream water levels; 2.58 and 1.63 mAOD. These artificial weirs were constructed within each domain and an xy plane was constructed immediately downstream of the artificial weir which was defined as a pressure outlet with a gauge pressure of $0Pa$. This combination of artificial weir and pressure outlet meant that the downstream water height was controlled by the hydraulics of the artificial weir and any fluid overtopping the artificial weir would leave the domain via the outlet. The boundary conditions are summarised in table 6.3. Initial water surface elevation was set equal to 3.5 mAOD across the entire domain using the `setFields` tool. Patching different water surface elevations upstream and downstream of the weir was explored but difficult due to the geometry of the domain. Although this resulted in initial water levels downstream of the weir being anomalously high, this water soon drained over the artificial weir used to control the downstream water level.

Computational Requirements

In both simulated cases, it was noted that the velocities at the inlet were low relative to the size of the domain ($\mathcal{O}(0.01\ ms^{-1})$). Given the geometry of the study site and assuming this order of magnitude represented the entire domain, this meant that the residence time for a fluid parcel entering the domain at $T = 0$ was in the range of 15000 to $25000s$. This range of values may be an overestimate since fluid accelerates as it transitions from subcritical to critical conditions as it descends over the weir. In both simulated cases, the flow was simulated for $30000s$ of flow time to ensure the simulations reached a pseudo-steady state. The timestep was controlled by the `adaptiveTimestep` function within openFOAM, which varied the timestep to ensure that the CFL criterion was met.

Table 6.4: Locations of four vertical monitor lines within the `valSet` and `fishSet` domains.

Line	$[x, y]$ location (m)	Description
`ML1`	$[77.0, 125.0]$	Upstream of the weir, in the centre of the river.
`ML2`	$[85.0, 75.0]$	Within the pool downstream of the Larinier fish pass.
`ML3`	$[132.0, 159.0]$	Immediately upstream of the baulk pass.
`ML4`	$[160.0, 158.0]$	Immediately downstream of the baulk pass.

Each case was run on the University of Hull HPC facility, VIPER [University of Hull, 2020]. For each case, 32 computational nodes were used, totalling 896 processor cores and 768 GB of RAM. Despite the available computational power, both simulations took between 20 and 30 days of run time to solve to $30000s$ of flow time. Each case was then run for an additional $180s$ of flow time, sampling at $0.5s$ intervals. These additional 361 timesteps were used to determine whether the results from both cases had reached a pseudo-steady state.

6.3.3 Convergence of `valSet` and `fishSet` to Pseudo-steady States

To enable the results from the `valSet` case to be validated against field-measured velocity data and to enable the results from the `fishSet` case to be input into the `fishPy` tool so that it could be compared against the measured fish tracks of Dodd et al. [2018], the final `valSet` and `fishSet` domains must be temporally-averaged. The residence time was calculated to define the minimum flow time that must be simulated to ensure that the inlet affects the outlet. However, due to the required temporal-averaging, it is important to ensure that the results have reached a pseudo-steady state. This was accomplished by tracking the flow parameters along four vertical monitor lines strategically located within the domain [see table 6.4 and denoted by the red squares in figure 6.1]. These locations were chosen as they are diverse and represent areas where the largest fluctuations were expected. Pressure and three-component velocity were monitored along each line. Instantaneous three-component velocities as well as velocity magnitudes were tracked at $0.1m$ intervals throughout the depth of water along each monitor lines; examples can be found in appendix E.

The depth-averaged velocity magnitudes of water (i.e. $\alpha \geq 0.5$) at each of the

four monitor line locations within the `valSet` domain against flow time from 30000 to 30180 s are shown in figure 6.5. These results show that for `ML1`, within the `valSet` domain, the average velocity magnitude was approximately $0.037ms^{-1}$, and varied negligibly with time, figure 6.5a. This is expected as `ML1` is located within the bulk of the flow, upstream of the weir, and therefore significant velocity fluctuations were not expected. Depth-averaged velocity magnitudes for `ML2`, located within the pool downstream of the Larinier fish pass in the `valSet` domain, varied with time from approximately $0.039ms^{-1}$ to $0.046ms^{-1}$, with a mean value of $0.043ms^{-1}$, figure 6.5b. The depth-averaged velocity magnitude for `ML3`, located at the top of the baulk pass in the `valSet` domain, ranged from approximately $0.047ms^{-1}$ to $0.053ms^{-1}$, with a mean value of $0.049ms^{-1}$, figure 6.5c. At the downstream end of the baulk pass within the `valSet` domain, `ML4`, the depth-averaged velocity magnitudes varied from approximately $0.073ms^{-1}$ to $0.086ms^{-1}$, with a mean value of $0.08ms^{-1}$, figure 6.5d.

The depth-averaged velocity magnitudes of water at each of the four monitor line locations within the `fishSet` domain against flow time from 30000 to 30180 s are shown in figure 6.6. These results for `ML1` within the `fishSet` domain show that the average velocity magnitude was approximately $0.066ms^{-1}$, and varied negligibly with time, figure 6.6a. Depth-averaged velocity magnitude for `ML2` within the `fishSet` domain varied with time from approximately $0.04ms^{-1}5$ to $0.057ms^{-1}$, with a mean value of $0.051ms^{-1}$, figure 6.6b. The velocity fluctuations at `ML2` within the `fishSet` domain are greater than those at the same location within the `valSet` domain due to the open Larinier fish pass within the `fishSet` domain, figures 6.5b and 6.6b. The depth-averaged velocity magnitude at the top of the baulk pass within the `fishSet` domain (`ML3`) varied between $0.130ms^{-1}$ and $0.134ms^{-1}$ with a mean value of $0.132ms^{-1}$, figure 6.6c. The depth-averaged velocity magnitude at the bottom of the baulk pass within the `fishSet` domain (`ML4`) varied between $0.0655ms^{-1}$ and $0.0690ms^{-1}$ with a mean value of $0.0676ms^{-1}$, figure 6.6d.

Temporal fluctuations of depth-averaged velocity magnitudes at `ML1` were consistently smaller than those at `ML2`, `ML3`, or `ML4` for both datasets. Within the `valSet` domain, the fluctuations immediately downstream of the baulk pass were the most significant. Conversely, within the `fishSet` domain, the fluctuations immediately downstream of the Larinier fish pass were the most significant. However, for each monitor line in each domain, temporal variations in depth-averaged velocity magnitude were

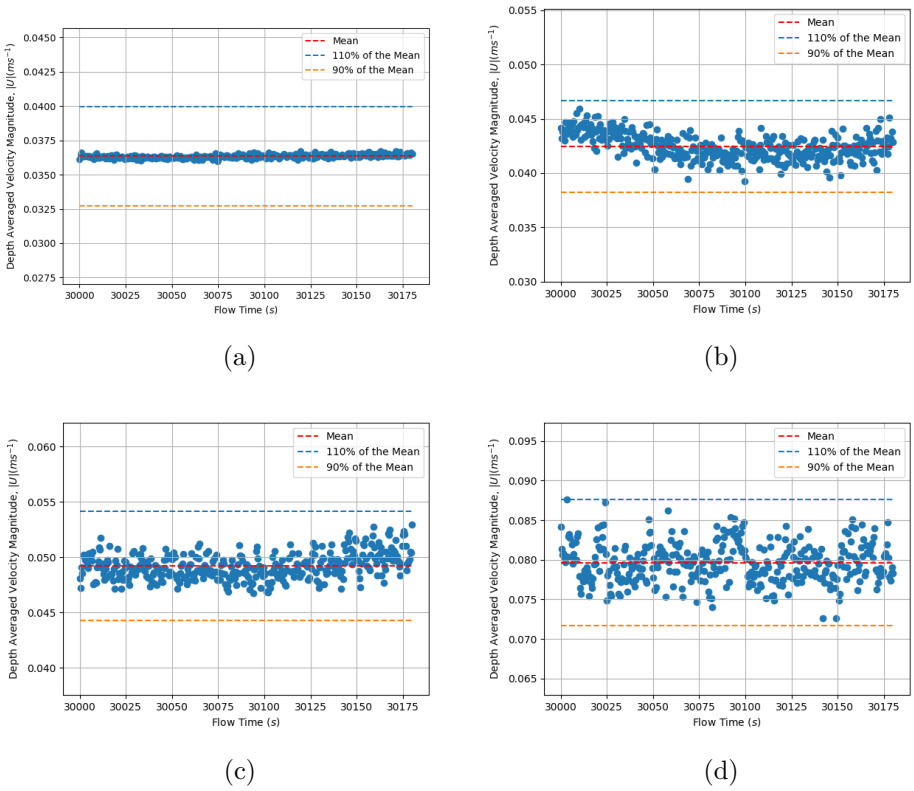

Figure 6.5: Depth-averaged velocity magnitude of water against flow time for four vertical monitor lines within the `valSet` domain located at a) $[77.0m, 125.0m]$, b) $[85.0m, 75.0m]$, c) $[132.0m, 159.0m]$, and d) $[160.0m, 158.0m]$ compared against the mean values.

consistently within 10% of the mean value, figures 6.5 and 6.6. Furthermore, the results suggest no temporal-dependency of flow magnitudes at any of the monitor locations within either domain, figures 6.5 and 6.6. Therefore, these results demonstrate that the mean values are an appropriate representation of the flow.

The flow data from 30000 to 30180 s of flow time were temporally-averaged, with a temporal resolution of 0.5 s, to enable the results from the `valSet` case to be validated against field-measured velocity data and to enable the results from the `fishSet` case to be input into the `fishPy` tool so that it could be validated against the measured fish tracks of Dodd et al. [2018].

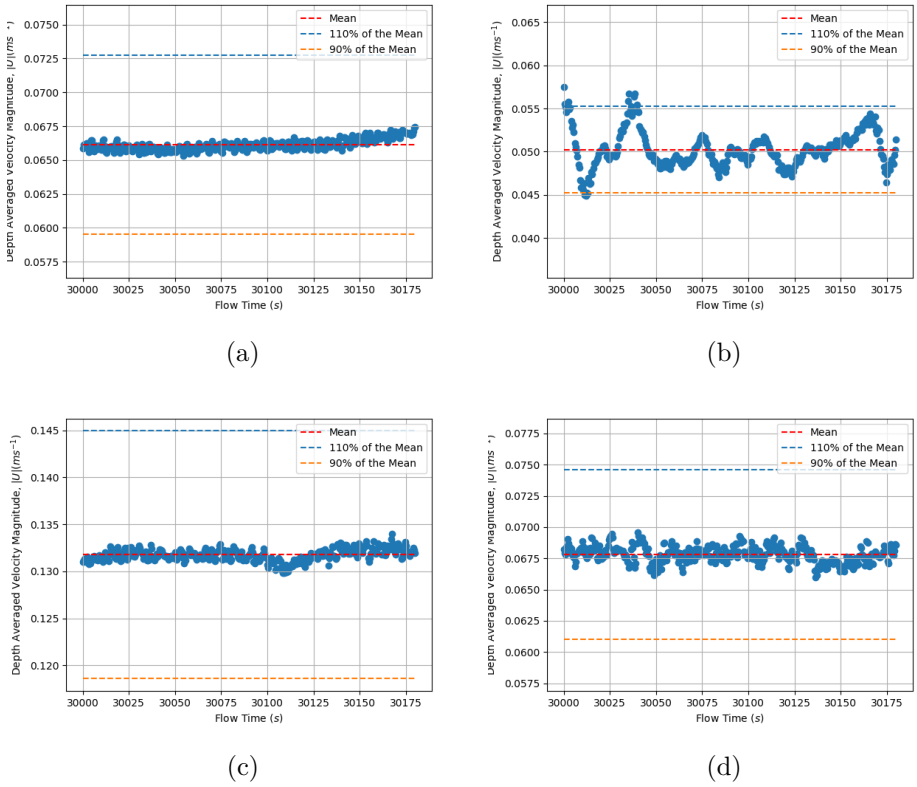

Figure 6.6: Depth-averaged velocity magnitude of water against flow time for four vertical monitor lines within the `fishSet` domain located at a) $[77.0m, 125.0m]$, b) $[85.0m, 75.0m]$, c) $[132.0m, 159.0m]$, and d) $[160.0m, 158.0m]$ compared against the mean values.

6.3.4 Mesh Independence of `valSet` and `fishSet`

As discussed in section 6.3.2, the computational requirements for solving both the `valSet` and `fishSet` cases was significant. This was due to the physical size of the domain, the size of the computational mesh, the large residence time, and the higher velocities present within either pass that decreased the allowable timestep size to satisfy the CFL condition. The creation of a finer mesh was computationally challenging. Furthermore, an attempt was made but, despite the available computational power, solving the simulation on a finer mesh required an impractical amount of time. Therefore, due to these challenges, confidence in the results is instead drawn from the validation of the `valSet` against measured data (covered in section 6.3.5).

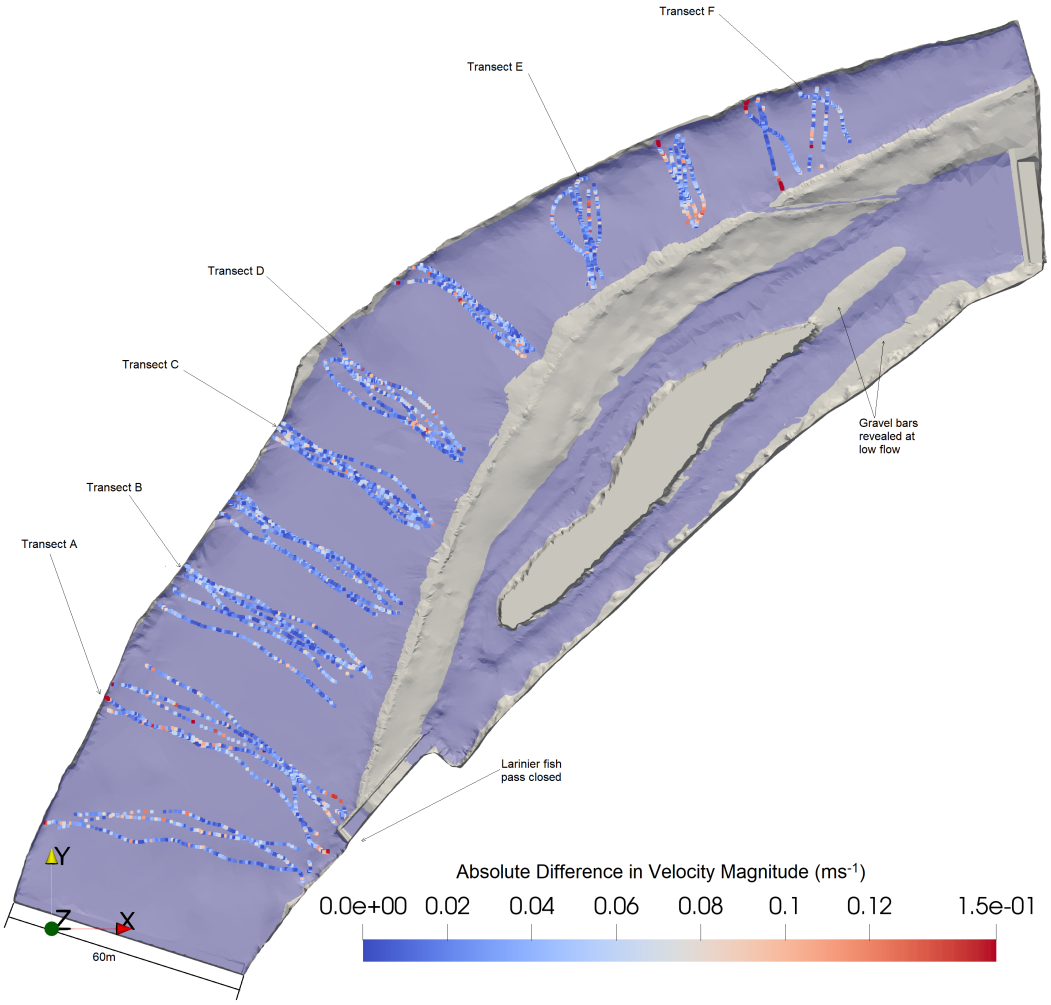

Figure 6.7: Planform view of the `valSet` domain with an overlain isosurface ($\alpha = 0.5$) depicting the free surface within the domain, coloured pale blue. Measurement transects are overlain, contoured with the absolute difference in measured and predicted velocity magnitudes.

6.3.5 Computational Fluid Dynamics Results: `valSet` Case

This section details the results of the computational fluid dynamic simulation for the `valSet` case. Firstly, the downstream water level was found to be within $0.02m$ of the measured data (2.32%). This gives confidence to the use of the artificial broad crested weir to control the downstream water level. The downstream water level was sufficiently low that gravel bars were revealed downstream of the island, which were

observed during fieldwork, figure 6.7. This gives confidence to the simulated results, the collected bathymetry, and the construction of the domain. The average water velocity magnitude in the domain was $0.0432ms^{-1}$. Water underwent significant acceleration through the baulk pass with a velocity magnitude maximum of $3.1575ms^{-1}$. The upstream water level remained below the weir crest height throughout, and therefore water only moved across the weir via the baulk pass (no over-topping). A vector plot of the temporally-averaged flow within the domain is presented in appendix E.

The velocities at each measured location within each of the 49 filtered transects were extracted from the temporally-averaged `valSet` dataset, which were then compared to the measured values. The measurement locations of each transect corresponded to simulated data with predicted α values greater than 0.5%, i.e. beneath the predicted water level. This gives confidence to the locations of the measured data and to the processing of the TLS data and subsequent creation of the CFD mesh. The predicted velocity magnitudes compared well with the measured data for the `valSet` case, figure 6.7. The measured data were seen to be noisy and therefore were filtered by removing data points more than 2 standard deviations from the transect mean. Measured and simulated transect-averaged velocity magnitudes are given in tables E.1 and E.2 in appendix E. The percentage errors tended towards infinity due to the proximity of measured and predicted data to 0.0 ms^{-1}, see i.e. figure 6.8. However, for all 49 filtered transects, the majority of the predicted velocities were within $0.03ms^{-1}$ of the measured velocity magnitudes, figure 6.7. Measured and predicted U, V, and velocity magnitude data along six example transects, shown in figure 6.7, were extracted, depth-averaged, and compared, figures 6.8, 6.9, 6.10, 6.11, 6.12, 6.13. Note that the hydraulic variables are plotted against distance from the transect starting locations along the West bank of the river (negative x in figure 6.7).

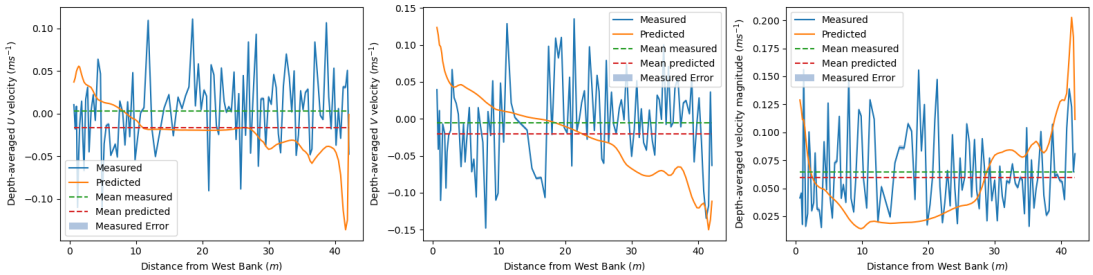

Figure 6.8: Comparison of depth-averaged U, V, and velocity magnitude of measured and simulated data for each measurement point along transect A, shown in figure 6.7. Transect means for each hydraulic variable are also shown.

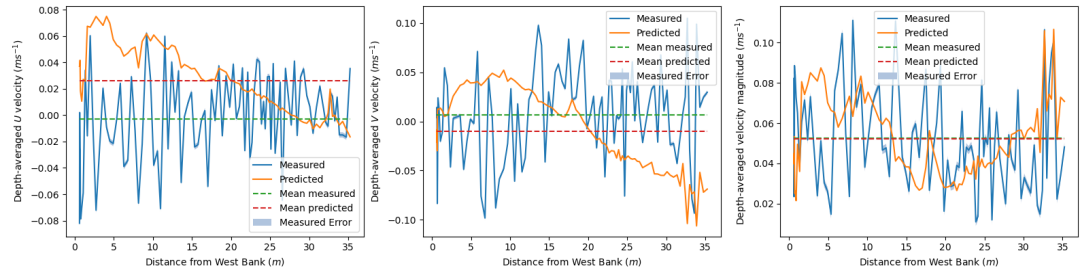

Figure 6.9: Comparison of depth-averaged U, V, and velocity magnitude of measured and simulated data for each measurement point along transect B, shown in figure 6.7. Transect means for each hydraulic variable are also shown.

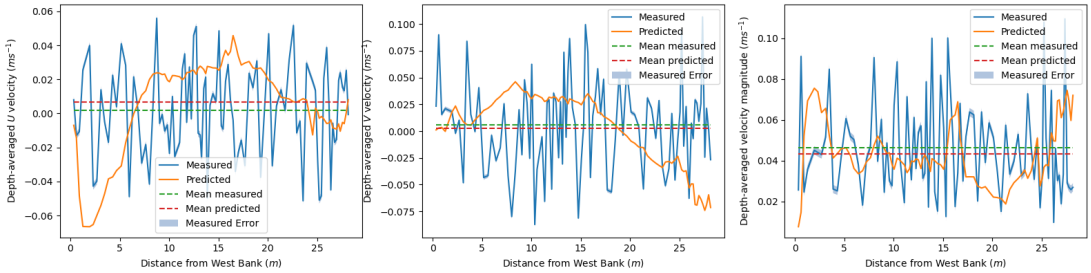

Figure 6.10: Comparison of depth-averaged U, V, and velocity magnitude of measured and simulated data for each measurement point along transect C, shown in figure 6.7. Transect means for each hydraulic variable are also shown.

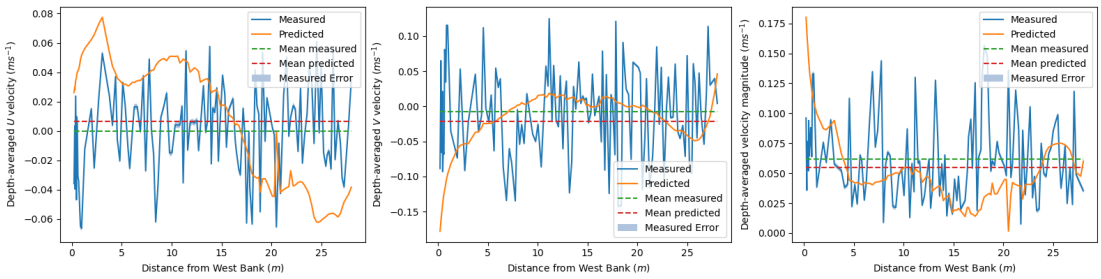

Figure 6.11: Comparison of depth-averaged U, V, and velocity magnitude of measured and simulated data for each measurement point along transect D, shown in figure 6.7. Transect means for each hydraulic variable are also shown.

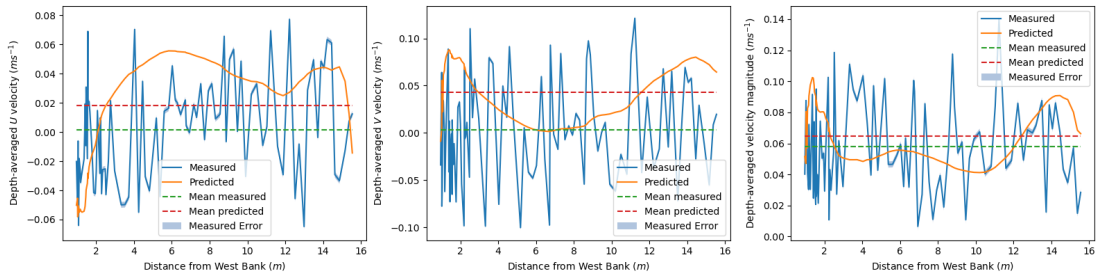

Figure 6.12: Comparison of depth-averaged U, V, and velocity magnitude of measured and simulated data for each measurement point along transect E, shown in figure 6.7. Transect means for each hydraulic variable are also shown.

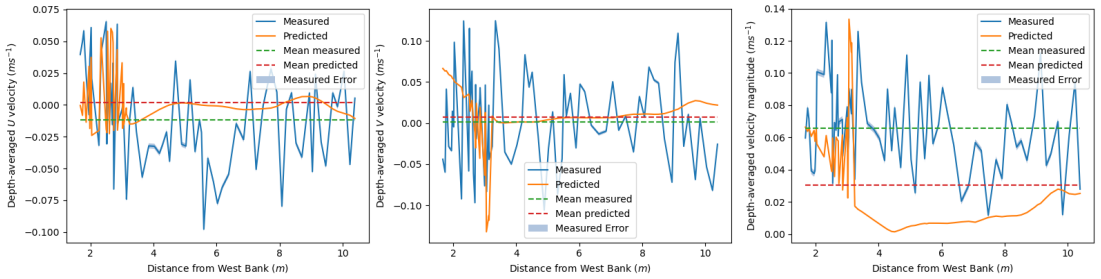

Figure 6.13: Comparison of depth-averaged U, V, and velocity magnitude of measured and simulated data for each measurement point along transect F, shown in figure 6.7. Transect means for each hydraulic variable are also shown.

A comparison of the frequency distributions of the measured three-component velocities and velocity magnitudes against the CFD results extracted along all 49 transects show good agreement, figure 6.14. A comparison of the distribution of U in the measured and predicted data show good agreement in the average value and the overall distribution of data, figure 6.14a. The CFD results suggest a narrower distribution of V values compared to the measured data, but show good agreement in the average values, figure 6.14b. A comparison of the W distributions for the measured and predicted data shows that the average predicted W value was approximately zero compared to the wider distribution and larger, positive average value seen in the measured data, figure 6.14c.

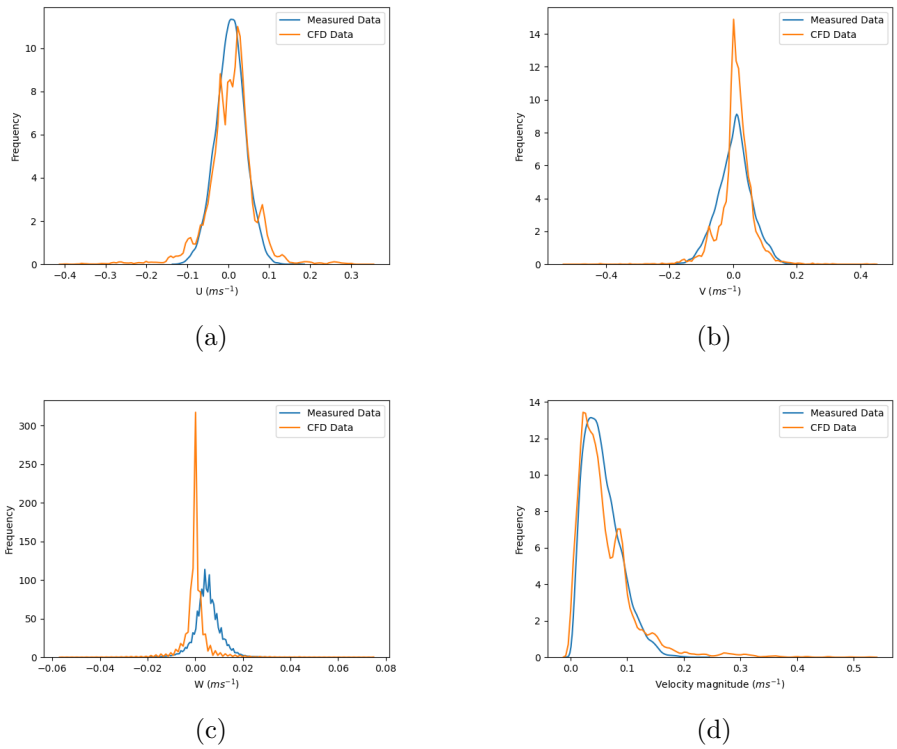

Figure 6.14: Graphs of frequency of occurrence against a) U, b) V, c) W, and d) velocity magnitude for measured and simulated data at each measurement location across all transects.

6.3.6 Computational Fluid Dynamics Results: `fishSet` Case

This section details the results of the computational fluid dynamic simulation for the `fishSet` case. First, the downstream water level was found to be within $0.02m$ of the measured data (1.30%). Second, the average water velocity magnitude within the domain was $0.08661ms^{-1}$, figure 6.15. Third, water accelerated to a maximum of $2.4151ms^{-1}$ within the baulk pass. Fourth, a discharge of approximately $0.81m^3s^{-1}$ was calculated immediately upstream of the Larinier pass, which accelerated to a maximum of $4.2250ms^{-1}$ within the Larinier pass, with an average velocity magnitude of $1.4652ms^{-1}$. Lastly, the upstream water level remained below the weir crest throughout, and therefore water only moved across the weir via the baulk pass and the Larinier fish pass, figure 6.15. A vector plot of the temporally-averaged flow within the domain is presented in appendix E.

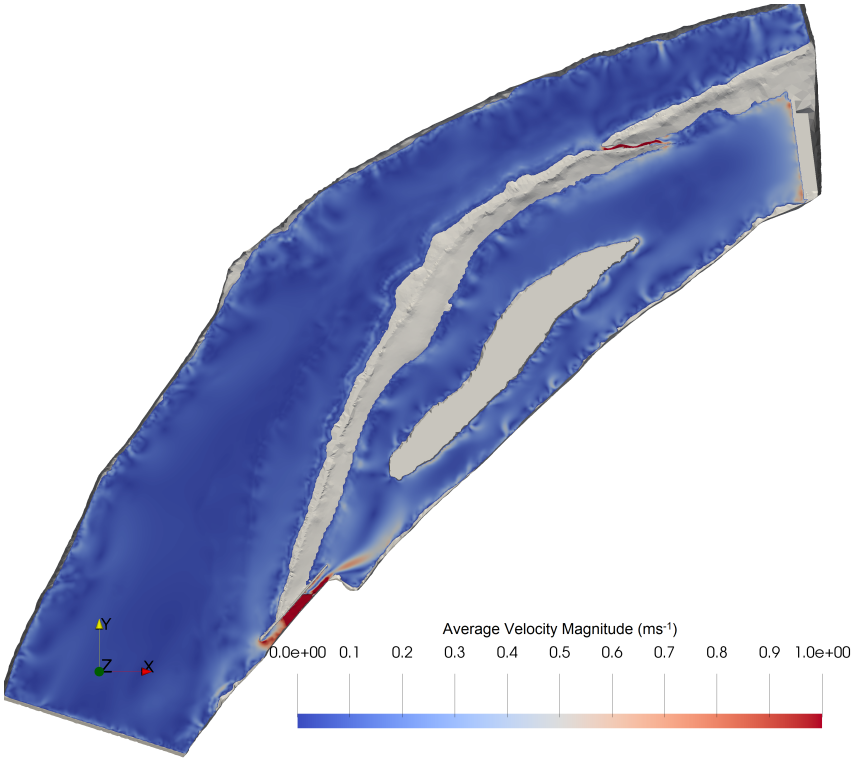

Figure 6.15: Planform view of the `fishSet` domain with an overlain isosurface of $\alpha = 0.5$ denoting the free surface location and contoured with velocity magnitude, limited $0.0ms^{-1}$ and $1.0ms^{-1}$ for clarity.

6.3.7 Discussion of the Computational Fluid Dynamic Simulations at the Ruswarp Study Site

Discussion of the Data Collection & Geometry Construction Processes

The process of collecting bathymetry and converting the measured geometric data into an adequate CFD mesh was laborious and complex. The process presented in this chapter covers only the last attempt. Many other methods and software were used and each resulted in either unusable meshes or impractical computational requirements to produce the mesh.

A TLS system and an ADCP system were used, coupled with RTK GPS, to capture subaerial and subaqueous topography of the study site. The TLS system allowed for the collection of high resolution ($\approx 0.1m$) geometric data of the study site. However, this approach had a number of limitations. Firstly, the TLS was unable to penetrate water, and therefore the dry bed area was maximised by closing the Larinier fish pass and hydropower scheme upon arrival at the study site. Furthermore, the ADCP system was used to collect subaqueous topography in regions inaccessible to the TLS, such as upstream of the weir. Secondly, the TLS required line of sight for measurements, and therefore scans were taken from three different scanning locations to maximise the visible regions of the study site, to ensure redundancy, and to ensure the accuracy of the scans. These limitations meant that the TLS and ADCP were unable to capture topographic data within either the baulk pass or the Larinier fish pass. To overcome this, the baulk pass and Larinier pass were rebuilt within Blender using the TLS data, the RTK GPS data points, photographs taken of the study site, and engineering drawings of the Larinier fish pass. The geometry of these passes, particularly respective crest heights, were significant as they controlled the follow of water across the weir.

These limitations also meant that no TLS data were available for the wetted surfaces of the domain, i.e. the river bed upstream and downstream of the weir. Upstream of the weir, bathymetry data were collected via ADCP along transects spaced approximately $5m$ apart, which enabled the upstream bed to be approximated using linear interpolation between the measured ADCP data. Wetted areas downstream of the weir were similarly approximated using linear interpolation between the measured TLS data. It was assumed that the river bed would be relatively smooth and therefore Gaussian smoothing was employed within Blender to remove sharp changes in the surface normal direction of the interpolated beds. It is possible that wood or other debris could have

been present on the river bed and would not be captured within this methodology. Therefore, there is some uncertainty associated with the bed topography, although this is not thought to be significant.

An additional option for modelling the study site would have been to collect flow rate, depth, and velocity data over the crest of the baulk pass and the fish pass. These data would allow for the modelling of only the section of the study site downstream of the weir by using two separate inlets: one at the top of each pass. This would vastly reduce the residence time, physical size, and subsequently the mesh size of the fluid domain. However, this approach would require collection of velocity data downstream of the weir in order to validate the CFD approach, which would increase the complexity of data collection due to the limited space and water depths downstream of the weir. This approach was not employed in the current study and it was impossible to determine the ratio of flow down each pass from the available data.

Discussion of the CFD Methodology & Results

In both the `valSet` and `fishSet` cases the downstream water levels were found to be within $0.02m$ of the average measured levels, equating to 2.32% and 1.30%, respectively. This result gives confidence to the implementation of the downstream boundary condition, the inlet condition, and the accuracy of both fish pass geometries. Furthermore, free surface results of the `valSet` case showed no over-topping of the weir and revealed downstream gravel bars, which are both results that reflect the conditions seen during data collection. The baffles of the Larinier fish pass were not modelled within either simulation, therefore it is likely that the peak velocities seen within the simulated pass are an overestimate. Furthermore, as the Larinier fish pass was closed throughout data collection, it was not possible to collect any data within or downstream of the fish pass to validate against. However, an approximate discharge of $0.81m^3s^{-1}$ was calculated immediately upstream of the Larinier fish pass, which results in an approximate discharge per unit width of $0.443m^2s^{-1}$. Application of equation 2.1 for this discharge per unit width yields a predicted average through-pass velocity of $1.379ms^{-1}$. Therefore, the CFD-derived, average velocity magnitude within the Larinier fish pass of $1.4652ms^{-1}$ compares well to empirical prediction of $1.379ms^{-1}$.

Predicted velocity magnitudes and three-component velocities of the `valSet` case compared well to the measured ADCP data [see figures 6.7 and 6.14]. Calculated per-

centage errors tended to infinity due to the proximity of measured and predicted data to $0.0ms^{-1}$, however absolute errors were less than $0.03ms^{-1}$ for the majority of measurement locations, figure 6.7. The largest differences between measured and predicted data occurred near the inlet and close to the upstream entrance to the baulk pass, figure 6.7. This is likely due to the implementation of the upstream boundary condition (i.e. water entering the domain in the positive z direction), which may not accurately emulate the velocity profile in the upstream-most region of the domain. However, predicted data agreed well with measured data in the middle regions of the domain [i.e. figures 6.9, 6.10, and 6.11], and therefore it can be surmised that the impact of the inlet boundary condition reduced as water progressed through the domain and became fully developed. Larger errors immediately upstream of the baulk pass are thought to be due to the large velocities and spatial velocity gradients in the region caused by the entrance to the baulk pass, which meant that small differences in location (due to GPS and/or interpolation errors) can cause large differences in velocity. Additionally, this region may be more acutely affected by temporal variations in the flow, not captured by the temporally-averaged CFD.

Filtered depth-averaged measured U, V, and velocity magnitude data were particularly noisy compared to the corresponding predicted data, figures 6.8, 6.9, 6.10, 6.11, 6.12, 6.13. However, the measured data are instantaneous whereas the predicted data are temporally-averaged, and therefore the smoother appearance of the predicted data was expected. Predicted transect-averaged U and V data did not always compare well to the corresponding measured data, although predicted transect-averaged velocity magnitudes consistently compared well (within $0.01ms^{-1}$) [see tables E.1 and E.2 in appendix E]. This suggests possible errors in coordinate conversions causing a small misalignment in the x and y axes, which would result in weaker comparisons of U and V but would not affect comparisons of velocity magnitude. Furthermore, although SonTek [2011] reported ADCP accuracies of $0.002ms^{-1}$ (or 0.25%), Rennie [2008] found an average ADCP velocity error of $0.22 \pm 0.18ms^{-1}$ (mean $\pm$ standard deviation) when applied to a $6km$ river reach featuring velocities between $0.0ms^{-1}$ and $3.0ms^{-1}$ (corresponding to $\approx$ 1.3 to 13.3% of maximum velocity). It is not clear from the work of Rennie [2008] exactly how the error scales with measured velocity, although Rennie [2008] reported that the error increased with distance from the ADCP (i.e. deeper profiles result in increased error).

Comparisons of the frequency distributions of all measured and predicted U, V, W, and velocity magnitude data showed good agreement, figure 6.14, particularly in velocity magnitude. A comparison of the W distributions for the measured and predicted data, figure 6.14c, shows that the average predicted W value was approximately zero compared to the wider distribution and positive average value seen in the measured data. This may be due to the presence of waves in the measured data which were seen at the study site. These waves were likely caused by the moored boats [see figure 6.1], wind shear, or the Arc-Boat itself. Wind shear and the moored boats were not measured nor modelled and therefore their affect on the data collected is not quantified. It is possible that both of these factors may have influenced the river flow. However, given the dominance of U and V within the domain, small changes in W are not significant to the overall velocity field. Furthermore, given that the predicted data are temporally-averaged, it is possible that these small variations in W may have been averaged out within the CFD data.

The boundary conditions used within the CFD were averages throughout the fieldwork and the average time of measured fish passage, for the `valSet` and `fishSet` cases, respectively. Throughout the fieldwork the upstream river discharge was naturally varying ($0.46m^3s^{-1}$ to $0.86m^3s^{-1}$, with an average of $0.57m^3s^{-1}$). The fish pass was closed upon arrival each day during the fieldwork, and the hydropower was disabled throughout, which meant the capacity for flow across the weir was significantly reduced. Even though the discharges were low, this meant that the upstream water level was slowly rising throughout the fieldwork. The exact river discharge for each measured transect is not known and therefore the averaged conditions used in the CFD models may not reflect the exact conditions for a given measured data point, although the differences are not thought to be significant.

In summary, downstream water levels compared well to averaged measure levels in both cases. Furthermore, the average velocity magnitude within the Larinier pass in the `fishSet` case compared well to analytical predictions. Despite the limitations of the study, predicted velocity data compared well to measured data, particularly velocity magnitudes. Errors were largest near the inlet and are attributed to the implementation of the inlet boundary condition which was not fully developed and introduced a vertical component to the flow. The dissimilarities near the baulk pass inlet may be due to differences in the bed topography, greater spatial velocity gradients, or larger temporal

variation. For all transects, measured instantaneous data were noisy compared to temporally-averaged predicted data. Comparisons of overall distributions of predicted velocities for all measured data points showed good agreement against measured data.

The chapter has so far detailed the collection of high resolution ($\approx 0.1m$) subaerial and subaqueous topography of the study site, as well as instantaneous three-component velocities measured along 49 transects. This was achieved through the use of a TLS system and an ADCP system coupled with RTK GPS. These collected data were post-processed to produce a point cloud with an approximate spatial resolution of $0.1m$. This post-processed data was then converted to a manifold surface representing the entire study site through a combination of `LAStools`, MATLAB, and Blender. This manifold surface was converted to a computational mesh using the OpenFOAM function `snappyHexMesh`. Simulations were executed using the `interFoam` solver within OpenFOAM and using the VIPER HPC facility [University of Hull, 2020]. Despite the limitations of the data collection and geometry construction, the computationally-derived flow fields of the `valSet` case compared favourably to the measured instantaneous velocity data. In addition, a second environment case, `fishSet`, has been developed which is representative of the average flow field present during the study of Dodd et al. [2018], which enables the application of `fishPy` and subsequent comparisons of predicted and measured fish tracks.

6.4 Application of `fishPy` to the `fishSet` Dataset

This section considers the application of the `fishPy` tool to the `fishSet` dataset in order to predict up-migration pathways of brown trout. These predicted trajectories were then compared to the Dodd et al. [2018] dataset. The `fishSet` dataset was prepared for use with the `fishPy` tool using the custom MATLAB script detailed in section 5.3. This process was computationally intensive due to the size of the domain relative to the spatial resolution, and therefore required use of the VIPER HPC facility [University of Hull, 2020]. The MATLAB script was run on one computational node containing 28 processor cores and 24 GB of RAM. Additional computational nodes could not be used due to parallelisation issues and licensing restrictions. The temporally-averaged `fishSet` data were interpolated onto a 3D, regular grid with a specified spatial resolution of $0.25m$. This spatial resolution represents the finest spatial resolution that was practically attainable throughout the domain. The following sections consider the

application of fishPy to the Ruswarp dataset, and is split into three cases:

- Case A - This case considers the creation of individuals at the downstream-most end of the domain and their subsequent movement through the domain. This case is used to demonstrate the applicability and generalised form of the fishPy tool by applying the tool to a dataset not used during the development of the tool. Furthermore, this case is used to predict the attraction efficiency of the Larinier pass.
- Case B - This case considers the creation of individuals both immediately downstream of the Larinier fish pass and at the downstream-most end of the domain, and is used to investigate the applicability of the fishPy tool when applied to a fish pass facility. Furthermore, this case is used to predict the passage efficiency of the Larinier pass.
- Case C - This case considers a comparison of the predicted pathways versus selected measured pathways.

6.4.1 Results of fishPy applied to Ruswarp: Case A

The fishPy tool was applied to the fishSet dataset to predict the trajectories of five individuals created at the downstream-most end of the domain. The bounding box described by [161.0m,141.0m,0.0m] and [163.0m,164.0m,4.0m] was used to define the creationZone. The targetZone was defined as the pool downstream of the Larinier fish pass, defined by the bounding box described by $[74.0m, 70.0m, 0.0m]$ and $[90.0m, 86.0m, 3.0m]$. The fishTimestep was set to 0.05s, and Tmax was set to 5000. The bodylength_mean was set to 0.3m and the bodylength_deviation was set to 0.05m. This range of bodylengths represented the smallest length of the fish measured by Dodd et al. [2018] and is assumed to represent the worse swimming performance of up-migrating brown trout at the site.

All individuals successfully moved from the creationZone to the targetZone and therefore successfully passed the domain, figure 6.16. The time taken ranged from 1534 to 6617 timesteps (76.7s to 330.85s). None of the individuals approached the baulk pass, and instead opted to approach the Larinier fish pass. While these trajectories are not explicitly compared against measured data, none of the predicted tracks show any obvious unnatural motions, such as significant movement in the downstream direction

or movement into dry cells. No modifications were made to fishPy before applying it to the fishSet dataset, which was not used during the development of the tool. This demonstrates the successful generalisation of the tool and gives confidence to the prescribed rules and model parameters.

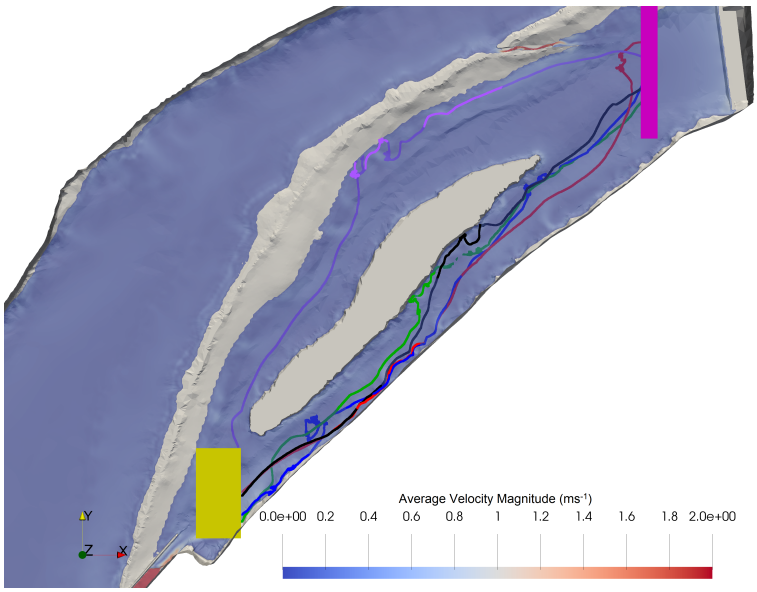

Figure 6.16: Top down view of the fishSet dataset overlain with an isosurface of $\alpha = 0.5$, denoting the free surface location with contours of velocity magnitude limited to $2.0ms^{-1}$ for clarity. The trajectories of five virtual individuals are overlain. The creationZone is shown in magenta and the targetZone is shown in yellow.

The fishPy tool was then used to predict the attraction efficiency of the Larinier fish pass. This was done by assessing the trajectories of 1000 individuals. The targetZone and creationZone remained as previously defined. The fishTimestep was set to $0.05s$, and Tmax was set to 5000. The bodylength_mean and bodylength_deviation were set to $0.532m$ and $0.0578m$, respectively, to mirror the bodylength distribution of the selected Dodd et al. [2018] data. The colAvoidance rule was disabled, which meant there were no fish-fish interactions modelled. An individual that passed the domain was deemed to have successfully located the Larinier fish pass. All 1000 individuals successfully passed the domain, suggesting an attraction efficiency of the Larinier fish pass of 100%, which compares favourably to the value of 96% reported by Dodd et al. [2018].

6.4.2 Results of fishPy applied to Ruswarp: Case B

Case B considers the predicted passage of five individuals through the Larinier fish pass, after it was found in case A that each simulated individual chose to approach the Larinier fish pass. The targetZone defined for Case A was moved to upstream of the weir (defined by $[0.0m, 40.0m, 0.0m]$ and $[70.0m, 120.0m, 10.0m]$). The creationZone remained defined as the bounding box described by $[161.0m, 141.0m, 0.0m]$ and $[163.0m$, $164.0m$, $4.0m]$. The fishTimestep was set to $0.05s$ and Tmax was set to 1000. The bodylength_mean was set to $0.8m$ and the bodylength_deviation was set to $0.00m$. This bodylength distribution gave increased swimSust and swimBurst values, ensuring that passage through the Larinier pass was not limited by the swimming capacity of the individuals.

The predicted trajectories show that all the individuals moved within the Larinier pass, but none successfully ascended the pass in the given time, figure 6.17. Further increasing the value of Tmax did not result in successful passage. The swimming ability of individuals was known to not limit passage, therefore it was thought that the spatial resolution of the domain was too coarse to allow for passage. A new domain was created with a higher spatial resolution, termed the fishSetLFP domain [see section 5.3]. This was done by cutting the original temporally-averaged CFD results to consider only the area immediately surrounding the Larinier fish pass. This drastically reduced the size of the domain and allowed for a spatial resolution of $0.05m$.

The fishPy tool was applied to the fishSetLFP datset to predict the trajectories of five individuals through the Larinier fish pass. The targetZone was defined as the bounding box described by $[60.0m, 50.0m, 0.0m]$ and $[71.0m, 62.0m, 10.0m]$, which lies immediately upstream of the Larinier fish pass. The creationZone was defined as the bounding box described by $[76.0m, 66.0m, 2.0m]$ and $[77.5m$,$67.5m$,$3.0m]$, which lies immediately downstream of the Larinier fish pass. The fishTimestep was set to $0.05s$, and Tmax was set to 5000. The bodylength_mean was set to $0.8m$ and the bodylength_deviation was set to $0.00m$. The predicted trajectories show that each individual successfully passed through the Larinier fish pass when the fishPy tool was applied to the fishSetLFP domain, figure 6.18. This result demonstrates that the more intricate geometry and more spatially-varying flow field of the Larinier fish pass required an increased spatial resolution during the interpolation step to accurately capture the flow.

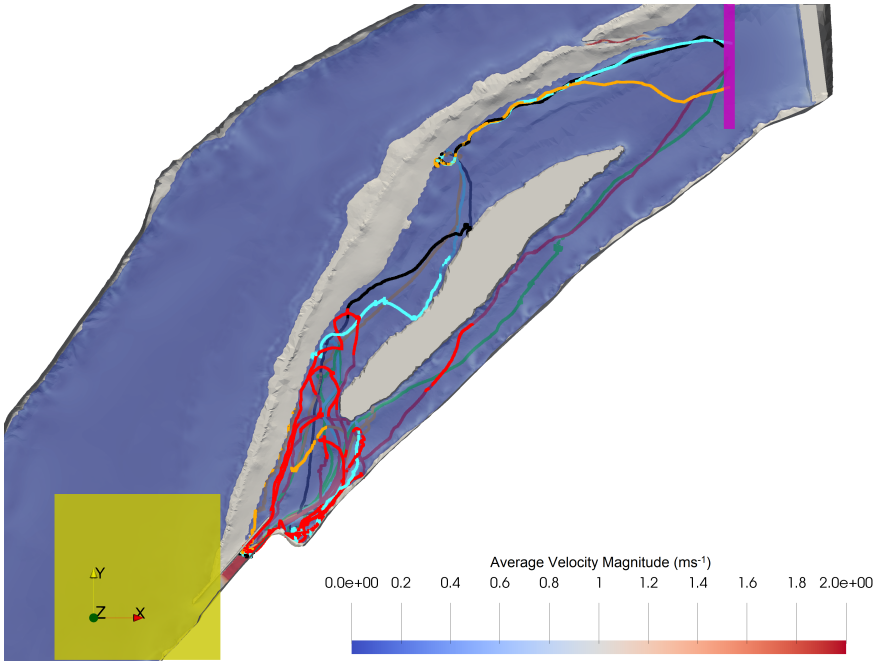

Figure 6.17: Planform view of the `fishSet` dataset overlain with an isosurface of $\alpha = 0.5$, denoting the free surface location with contours of velocity magnitude limited to $2.0ms^{-1}$ for clarity. Predicted trajectories of five individuals are shown, determined by applying `fishPy` to the `fishSet` dataset. The `creationZone` is shown in pink, the `targetZone` is shown in yellow.

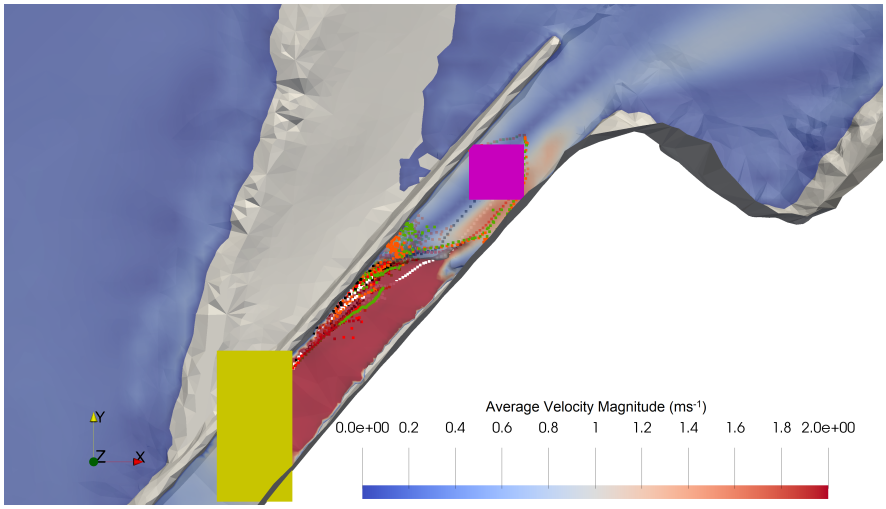

Figure 6.18: Planform view of the `fishSet` dataset overlain with an isosurface of $\alpha = 0.5$, denoting the free surface location with contours of velocity magnitude limited to $2.0ms^{-1}$ for clarity. Predicted trajectories of five individuals are shown, determined by applying `fishPy` to the `fishSetLFP` dataset. The `creationZone` is shown in pink, the `targetZone` is shown in yellow.

Applying the fishPy tool to the fishSet and fishSetLFP datasets in series allowed for a prediction of movements through the entire study site. This was demonstrated by determining the trajectory of a single individual of bodylength $0.8m$, created at [$169.0m$,$160.0m$,$1.0m$], moving through the fishSet dataset. Once the individual reached the downstream end of the Larinier fish pass, the location was saved and used as the starting location for an additional simulation using the fishSetLFP dataset. The combined predicted trajectory is shown in figure 6.19. These results further demonstrate the successful generalisation of the tool and give more confidence to the prescribed rules and model parameters.

The creation of the fishSetLFP dataset allowed for an approximation of the passage efficiency of the Larinier fish pass for the specific hydraulic condition modelled in the CFD. To achieve this, the fishPy tool was applied to the fishSetLFP dataset to assess the passage attempts of 1000 individuals. The targetZone and creationZone remained as previously defined, immediately upstream and downstream of the Larinier fish pass. The fishTimestep was set to $0.05s$, and Tmax was set to 5000. The bodylength_mean and bodylength_deviation were set to $0.532m$ and $0.0578m$, respectively, to mirror the bodylength distribution of the selected Dodd et al. [2018] data. All rules were enabled with the exception of the colAvoidance rule, which meant there were no agent-agent interactions modelled.

A total of 750 individuals successfully passed the domain within the given time, resulting in a passage efficiency of 75.0%. This result suggests that a motivated individual within the selected bodylength distribution that has found the Larinier fish pass had an 75% chance of successfully passing for the modelled hydraulic condition. In comparison, Dodd et al. [2018] reported a passage efficiency of 65% ($n = 53/81$) for the Larinier fish pass. However, Dodd et al. [2018] determined this value using data across the entire study period and therefore it includes passage attempts made over a range of river discharges, downstream water levels, and with a range of hydropower operating parameters. Whereas the value determined by fishPy considers only a single hydraulic environment. Therefore, while these passage efficiencies cannot be directly compared, their similarities give confidence to the fishPy tool.

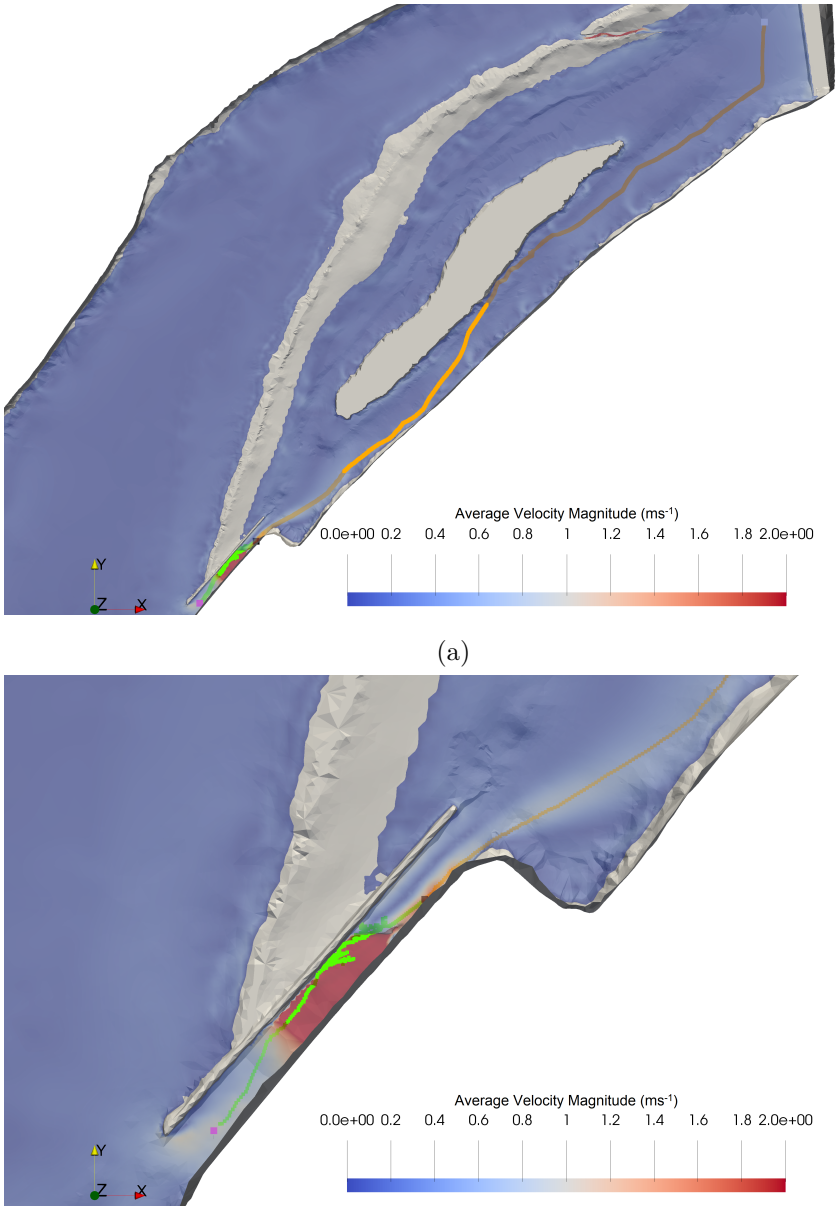

Figure 6.19: a) Full, and b) zoomed in planform views of the `fishSet` domain overlain with an isosurface of $\alpha = 0.5$, denoting the free surface location with contours of velocity magnitude limited to $2.0ms^{-1}$ for clarity. The total predicted trajectory of a single $0.8m$ individual is shown. The creation location of the individual is denoted by the white square. The orange line denotes the trajectory predicted using the `fishSet` dataset, which ends at the black square. The green line denotes the trajectory predicted using the `fishSetLFP` dataset, beginning at the black square. The successful end location of the individual is denoted by the pink square.

6.4.3 Results of fishPy applied to Ruswarp: Case C

This case considers an explicit comparison of fishPy-predicted fish trajectories against the measured fish tracks collected by Dodd et al. [2018]. However, this is included for completeness and it is not suggested that the fishPy tool predicts individual behaviours, but rather aggregate behaviours.

As discussed in section 6.2.1, Dodd et al. [2018] provided measured data of 84 sea trout (anadromous *Salmo trutta*) broken down into each approach of each individual, totalling approximately 500 fish tracks. As the fishSet represented the study site fluid environment without the hydropower activated, only fish tracks with a hydropower discharge of zero were considered. Furthermore, tracks measured during flood conditions, where discharge was in excess of 500% of the average, were discounted. This left a total of 68 fish tracks measured for 17 tagged sea trout to compare against the predicted outputs [see tables E.3 in Appendix E]. These fish tracks were provided in the OSGB1936 coordinate system and were converted to the UTM_RUS coordinate system via a custom written python script. Coordinate system conversions were handled using the convertbng and utm python packages [see Hugel 2020 and Bieniek 2020, respectively]. The track IDs, start and end locations, start and end times, number of measurement points, average downstream water level, and average river discharge for each track are given in tables E.4, E.5, and E.6 in Appendix E. The temporal resolution of the track measurements varied between $\approx 1.6s$ and $\approx 10.1s$, and the time period of each track varied from $3s$ to $\approx 1920s$.

The three longest measured fish tracks are shown in figure 6.20 to serve as an example. As the measured tracks were two dimensional (i.e. no measured depth), the tracks are presented at approximately mid-depth. Tracks 2612_02 and 2689_09, denoted in red and yellow respectively, show two individuals that make multiple attempts to ascend the Larinier pass before instead retreating downstream. Track 2661_15, denoted in green, shows an individual that maintained station within a small section of the domain and made no attempt to pass within the measured track ($>$ 30 minutes). Track 2612_ 02 suggests that, while attempting to ascend the Larinier fish pass, the individual moves out of the domain. It is assumed that these measurements are erroneous and due to the acoustic spikes and decreasing accuracy of the measurements as the individual moves further from the hydrophones placed downstream of the Larinier pass.

The fishPy tool was applied to the fishSet dataset for each of the measured tracks,

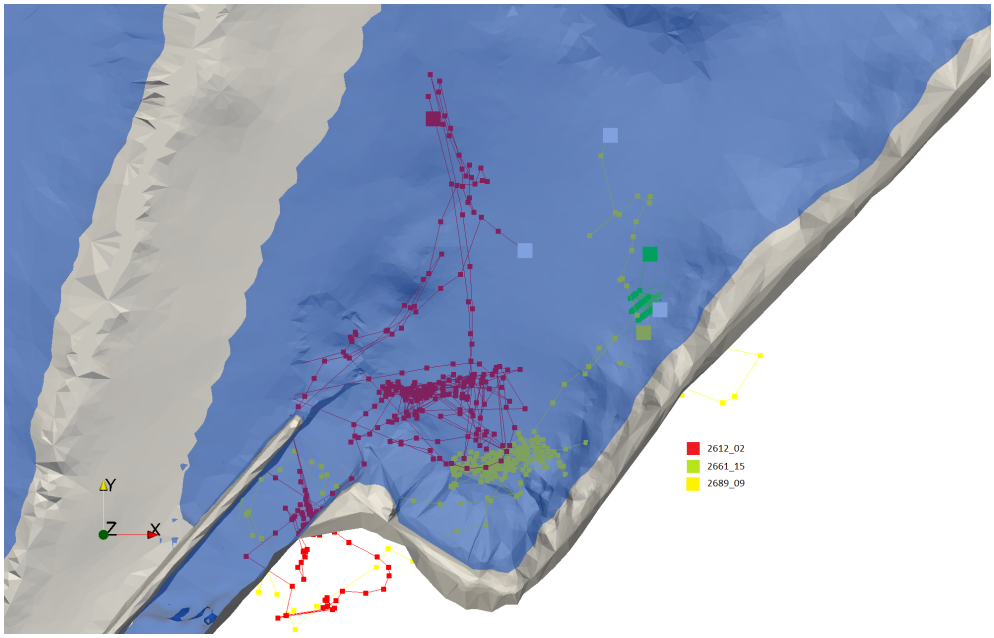

Figure 6.20: Planform view of the Ruswarp study site geometry with overlain water surface location coloured blue, and with multiple overlain two dimensional fish tracks, each coloured individually. The start location of each track is denoted in white, and the end locations are denoted by the large coloured squares. Lines are drawn between discrete measurement points to portray the order of locations and the direction of travel.

specifying the initial location and bodylength of each tagged individual. Figures 6.21 and 6.22 show two example comparisons between measured and predicted fish tracks. In each case, 10 individuals were simulated to demonstrate the variability in predicted paths. Each virtual individual was created at the same initial xy location as the corresponding tagged individual, but evenly spaced in z throughout the water column due to the lack of measured z location. Track 2661_15 denotes an individual with an associated length of $0.42m$, mass of $0.75kg$, and an initial location of $[89.35m, 73.73m]$. The track shows that the individual holds station within a small space throughout the track, before moving approximately $1.5m$ downstream, before the measured track ends, figure 6.21. Conversely, the predicted tracks for the virtual individuals of the same length and starting at the same initial xy location, immediately move upstream, attracted to the large flows immediately downstream of the Larinier fish pass. The

predicted paths shows the majority of the virtual individuals entering the Larinier pass and, subsequently, the `targetZone` where the track ends, figure 6.21. However, one virtual individual, denoted in orange, took a less direct route into the Larinier pass due to the recirculation at the base of the Larinier pass which initially repelled the individual. A comparison of these tracks suggests that the tagged individual was either not motivated to migrate at this particular time or could not locate the pass. Although the individual displays little in the way of exploratory behaviour which would be expected if it were searching for the pass.

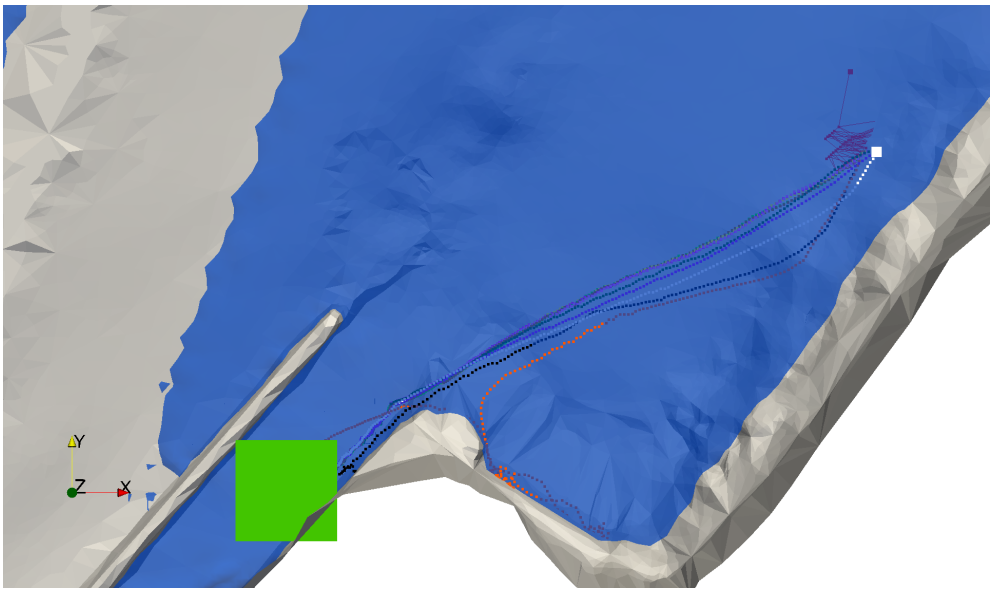

Figure 6.21: Planform view of the Ruswarp study site geometry with overlain water surface location denoted in blue. Track 2661_15 is denoted in red, and the end location of the track is denoted by the large red square. The predicted fish tracks are denoted in various colours, with the `targetZone` denoted by the large green square. The white square denotes the initial location of both tracks.

Track 2668_06 shows an individual with an associated length of $0.42m$, mass of $0.75kg$ and an initial location of $[88.53m, 73.99m]$, figure 6.22. This track shows the individual moving towards the downstream-end of the Larinier pass indirectly, before making an unsuccessful passage attempt, figure 6.22. The virtual individuals, created at the same initial xy location and evenly spaced in z, immediately moved towards the Larinier pass and began passage attempts wherein each individual moved into

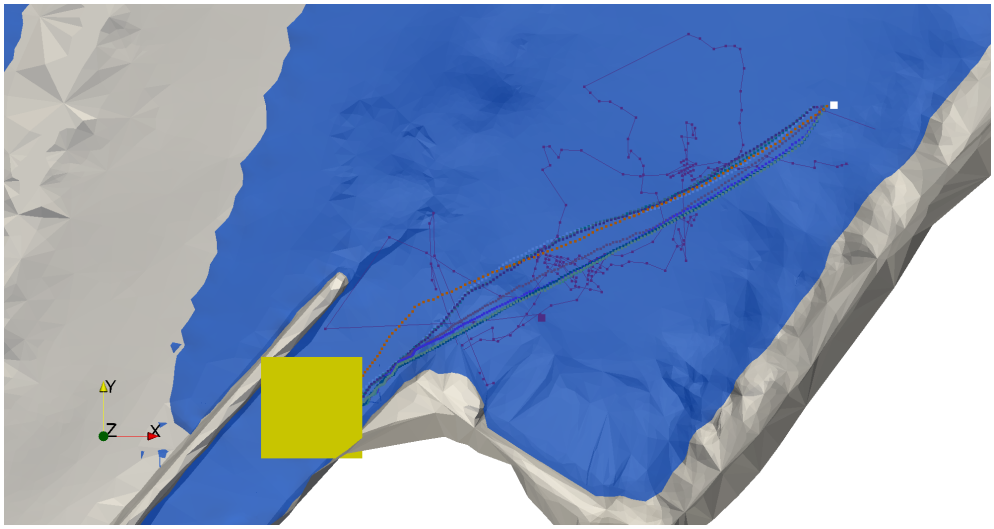

Figure 6.22: Planform view of the Ruswarp study site geometry with overlain water surface location denoted in blue. Track 2668_06 is denoted in red, and the end location of the track is denoted by the large red square. The predicted fish tracks are denoted in various colours, with the `targetZone` denoted by the large yellow square. The white square denotes the initial location of both tracks.

the `targetZone` where their track ends, figure 6.22. Although, the predicted tracks suggest more direct paths to the Larinier pass, they compare well to the measured track, and qualitatively appear as smoother, averaged versions of the measured track. Track 2668_06 also suggests that the tagged individual moves out of the domain near the beginning of the track. This could be due to the interpolation of the measured geometric data during the creation of the CFD domain, or due to the accuracy of the measurement technique employed by Dodd et al. [2018].

6.5 Discussion on the Application of `fishPy` to Ruswarp Weir

The previous sections have presented a number of cases of the `fishPy` tool applied to the `fishSet` dataset, representative of the Ruswarp study site. Case A demonstrated that the `fishPy` tool can be applied to a previously unseen dataset and yield sensible, qualitatively agreeable results. Case A also demonstrated the use of the `fishPy` tool to predict the ability of individuals to find a fish pass within a river reach. Setting

the fishPy bodylength distribution to that of the Dodd et al. [2018] data yielded an attraction efficiency of the Larinier fish pass of 100%, compared to 96% reported by Dodd et al. [2018]. This result is unsurprising given the oblique nature of the weir and the strategic positioning of the Larinier pass at the upstream-most point of the weir. Furthermore, the small discrepancy between predicted and measured values is very likely due to environmental factors not captured within the fishPy model, such as predation by grey seals, which is known to have occurred at the study site [Dodd, 2019]. Interestingly, this result also suggests that the baulk pass had an attraction efficiency of 0%. Dodd et al. [2018] did not quantify the attraction or passage efficiency of the baulk pass and therefore comparisons cannot be made. The results of case A show the successful generalisation of the fishPy tool and its applicability to domains representative of river reaches rather than the flume-based domains as seen in chapter 5, and give confidence to the prescribed rules and model parameters.

Case B demonstrated the importance of the spatial resolution of the input hydraulic dataset. A spatial resolution of $0.25m$ suggested that five $0.8m$ individuals, while attracted to the Larinier fish pass and able to overcome the water velocities within the pass, were unable to ascend. Increasing the spatial resolution to $0.05m$ while retaining all other model parameters, resulted in successful passage of all five individuals through the Larinier fish pass. Increasing the spatial resolution increased the required computational power to create the domain and to execute the fishPy tool, and therefore only a small region of the original fishSet domain could be re-interpolated onto the higher resolution fishSetLFP domain.

Case B also demonstrated the use of the fishPy tool to approximate the passage efficiency of the Larinier fish pass for the specific hydraulic condition modelled within the fishSet CFD simulation, using the fishSetLFP dataset. Setting the fishPy bodylength distribution to that of the Dodd et al. [2018] data yielded a passage efficiency of 75.0%, compared to 65% reported by Dodd et al. [2018]. There are a number of differences between the methods of determining these two passage efficiencies. First, the Dodd et al. [2018] value was determined using data from their entire study period and therefore it includes passage attempts made over a range of river discharges (1.59 to $41.50m^3s^{-1}$), downstream water levels (1.68 to 4.24 mAOD), and with a range of hydropower operating parameters (0.00 to $3.83m^3s^{-1}$). The values yielded from fishPy considered only a single hydraulic case where the hydropower turbine was inoperative

($0.00m^3s^{-1}$), the river discharge was $2.41m^3s^{-1}$, and the downstream water level was 2.58 mAOD. Second, the fishPy tools utilises an implicit motivation, discussed more in section 6.5.1. This formulation has the effect of overestimating the number of passage attempts, and subsequently the passage efficiency, by neglecting individuals that are not immediately motivated to migrate. Conversely, one can assume that the Dodd et al. [2018] dataset is representative of the full spectrum motivation within the population. Third, Dodd et al. [2018] suggest that it is possible that the 27% of fish that approached the Larinier fish pass but did not ascend could have been predated upon or caught by fishermen. Neither of these factors are considered within the fishPy model, which may act to inflate the predicted passage efficiency. Lastly, there are a number of environmental factors not considered within the fishPy model such temperature, time of day, scent, and light/shade which are inherent to the Dodd et al. [2018] dataset, and which may play a role in expediting or delaying passage [see section 6.5.1]. Therefore, while these passage efficiencies cannot be directly compared, their similarities give confidence to the fishPy tool.

Case C considered explicit comparisons between fishPy-predicted fish tracks and the measured tracks of Dodd et al. [2018]. A comparison to track 2661_15 showed distinct differences in measured and predicted tracks, figure 6.21. Namely, the measured track made no attempt to pass the Larinier pass and, within the measured time period ($>$ 30 minutes), made no move towards the Larinier pass. This suggested that either the tagged individual could not locate the pass, although it does not display searching behaviour, or it was not motivated to attempt to pass. Conversely, 9 of the 10 virtual individuals immediately moved to the base of the Larinier pass, before entering and making an attempt to pass. One of the virtual individuals moved towards the base of the Larinier pass and was initially repelled by the recirculation region downstream of the pass, causing it to move towards the bank before making a passage attempt. The predicted trajectories of the virtual individuals demonstrate the variability in predicted tracks due to the heterogeneity within the population and the stochastic nature of the model. A comparison to track 2668_06 showed that both the tagged and virtual individuals moved towards the base of the Larinier pass, although the virtual individuals took more direct paths, regardless of initial depth, figure 6.22. It is challenging to determine the exact reason for the indirect path of the tagged individual. A comparison of the predicted tracks and track 2668_06 suggests that the fishPy model predicts

aggregate and/or averaged trajectories, figure 6.22. This is demonstrable in the distinct differences apparent in explicit comparisons compared to the agreeable predictions of bulk passage metrics.

6.5.1 Limitations of the Application of the fishPy model to Ruswarp Weir

Discussion on Motivation & Environmental Cues in Migration

The fishPy model, like the majority of fish path prediction models, assumes an inherent, persistent motivation of fish to migrate upstream. Although Castro-Santos and Haro [2010] suggest that this approach is well-justified for salmonidae, consideration of fish track 2661_15 shows an individual choosing to hold station immediately downstream of the Larinier fish pass for in excess of 30 minutes, figure 6.20. This is in contrast to the corresponding predicted fish paths, which suggests immediate movement towards the base of the Larinier fish pass followed by successful passage, figure 6.21. It is not clear why this tagged individual (fish no. 2661) chose to hold station immediately downstream of the pass when model predictions suggest that the individual would have been able to successfully ascend. This suggests that the tagged individual was not motivated to ascend, and instead was waiting for an additional stimulus to trigger the motivation to migrate.

It is possible that motivation for river-scale migration is governed by exposure to environmental stimuli such as scent or temperature, rather than purely hydraulic stimuli. For example, light level is known to influence the initiation of large-scale migratory activities [Binder et al., 2011]. However, Dodd et al. [2018] found that time of day (and hence light level) was not a significant factor in the number of attempts or the number of successful passages. Similarly, Binder et al. [2011] state that temperature influences the onset of spawning migrations, particularly when the migration is short in duration. It is unclear if temperature played a role within the Dodd et al. [2018] study as it was not monitored. Furthermore, there is little literature on the role of water temperature on river-scale migratory activities. Moreover, while correlations between many environmental triggers and large-scale migration initiation have been identified [see Binder et al. 2011], they are not well-understood at river-scale. Furthermore, exact causation is difficult to determine due to the high inter-correlation between environmental triggers (i.e. light level and temperature). This ambiguity makes fine-scale predic-

tions of fish behaviour challenging. Nevertheless, the modular nature of the fishPy model and its combination with CFD facilitates easy expansion of environmental data inputs to include static stimuli such as light/shade, as well as computationally-derived spatially-varying data such as temperature, salinity, or chemical tracers.

Discussion on Spatial Resolution Requirements for the Application of the fishPy model to Ruswarp Weir

As discussed in chapter 5, the spatial resolution required to appropriately capture spatial variations of data within a given domain is dependent upon the spatial variations of the original data and the complexity of the domain geometry. This is evident in the work presented in this chapter. Applying the fishPy tool to the fishSet dataset ($0.25m$ spatial resolution) yielded a Larinier passage efficiency of 0%. Conversely, applying the tool to the fishSetLFP dataset ($0.05m$ spatial resolution) yielded a value of 75%. These differences in fishPy-predicted passage efficiencies between the fishSet and the fishSetLFP datasets highlight the importance of the spatial resolution of the interpolated data.

The fishPy tool requires input data in the form of regular, uniform, 3D matrices due to the spatially-continuous formulation of the model and the interpolation schemes used. This restriction meant that the application of the fishPy tool to the Ruswarp domain was computationally challenging due to the large scale, complex geometry, and large spatial variations in the hydrodynamic fields. The limiting factor in computation of the interpolated data is the calculation of the G3D matrix using the inpolyhedron function within MATLAB [see section 5.3]. This computation was parallelised using one VIPER HPC node consisting of 28 processor cores [see University of Hull 2020] and took approximately 12 days to complete. Further parallelisation of this process was not possible due to licensing restrictions. For these reasons it was not practical to interpolate the entire domain at a spatial resolution higher than $0.25m$. However, although higher spatial interpolation around the Larinier fish pass ($0.05m$) had a marked affect on predicted trajectories, similar effects are not expected within the rest of the domain due to the comparatively small spatial variations in hydraulic data and comparatively simple geometry.

Discussion on the Use of the Dodd et al. [2018] Dataset for Comparisons Against fishPy-Predicted Trajectories

The Dodd et al. [2018] dataset was originally collected to quantify passage efficiency at the study site and its sensitivity to hydropower operation, rather than to measure microscale movements of individuals. While the Dodd et al. [2018] dataset was not conceived for use with the fishPy tool, the retroactive use of this data within this study was pursued as the Dodd et al. [2018] dataset represented the highest quality dataset available for this study.

Explicit comparisons between predicted and measured fish tracks were challenging for various reasons. First, comparisons were complicated by the inherent motivation assumed within the fishPy model, discussed in section 6.5.1. Second, the accuracy and spatial dimensionality of the Dodd et al. [2018] study was limited by the number of hydrophones within range of a given individual. Therefore, due to the impractical number of hydrophones required for 3D measurements throughout the domain, the Dodd et al. [2018] study did not monitor depth for tagged individuals. However, fishPy-predicted trajectories were seen to be dependent upon the initial depth of the individual during comparisons against track 2661_15. Additionally, 2D measurements were only taken immediately downstream of the Larinier pass, which limited comparisons to a small section of the domain. Successful passage through the Larinier pass was determined solely by a single binary present/absent hydrophone placed immediately upstream of the Larinier fish pass. This facilitated comparisons between measured and predicted bulk passage metrics, but did not provide sufficient data for comparisons of fish paths through the Larinier pass.

The Dodd et al. [2018] dataset was collected in the field. Field-based collection of data has the advantage of being the closest approximation to realism. For example, field-based monitoring of fish captures environmental stimuli such as predation, temperature, scent, and salinity, all of which would be challenging within a laboratory. However, field-based experiments can increase the complexity of data collection, and reduce the scale over which data collection is attainable. Furthermore, field-based study increases the complexity of CFD modelling required to generate appropriate inputs for the application of the fishPy tool. In contrast, laboratory-, or flume-, based studies facilitate greater control over experimental processes and data collection methodologies, and can reduce the complexity of CFD modelling via the use of regular geometries.

While not available for consideration within this study, the use of flume-based measured fish tracks would facilitate the use of videometry to measure and compute 3D fish tracks with $\mathcal{O}(0.1)m$ spatial resolution and $\mathcal{O}(0.1)s$ temporal resolution [e.g. Butail and Paley 2012, Rodriguez et al. 2011, 2015, or Detert et al. 2018]. The application of videometry to the collection of fish tracks is a recent development that has only been successfully applied to low turbidity, moderately calm, flume-based flows. Application of this technique to a flume-based Larinier pass would be challenging due to the associated air entrainment and turbulence, but would remove some of the environmental stimuli not considered within the `fishPy` model and allow for fine-scale comparisons of fish movements. Furthermore, such a dataset would facilitate calibration of the `fishPy` tool to fit the measured fish tracks. Therefore, as the use of videometry in the collection of fish tracks develops and datasets become available, the `fishPy` tool should be applied to one such dataset to further assess the validity of the model.

6.6 Conclusion

The work presented in this chapter has demonstrated the successful application of the `fishPy` tool to a newly created hydraulic dataset representing the Ruswarp weir study site. The work described herein has shown the data collection, assessment, and unification processes, CFD mesh creation processes, and subsequent development and execution of CFD simulations to create the hydraulic dataset of Ruswarp Weir for two hydraulic cases. Resulting velocity fields for the validation case (`valSet`) compared favourably to measured ADCP data. The `fishPy` tool was applied to the Ruswarp domain and used to predict individual fish tracks based on the size and initial location of tagged fish. Predicted fish trajectories compared fairly well to measured tracks, but highlighted the need for further understanding of river-scale migration motivation within diadromous fish species. The `fishPy` tool was used to predict two bulk metrics of the Larinier fish pass within the domain: the attraction efficiency and the passage efficiency, using a population of 1000 individuals. Both predicted bulk metrics compared favourably with the values reported by Dodd et al. [2018] (attraction efficiency 100% vs 96%, passage efficiency 75% vs 65%). The work herein considered only comparisons for a single hydraulic condition of a river reach. However, now that the `fishPy` model has been developed, it can be applied to other hydraulic conditions and other river reaches in future studies. Trajectories predicted using the `fishPy` model could be compared

to other published models of up-migration [i.e. Gao et al. 2016, Gisen 2018, Zielinski et al. 2018]. Fine-scale comparisons of predicted and measured fish tracks could be facilitated through the use of flume-based videometry, which would enable 3D spatial tracking of individuals, reduce CFD modelling complexity, increase the obtainable spatial interpolation resolution, and allow for greater control over hydraulic conditions.

Chapter 7

Discussion & Conclusion

7.1 Individual-based Modelling for the Assessment of Passage Efficiencies for Up-Migrating Fauna

Anthropogenic alteration of rivers is ubiquitous and leads to fragmented river systems that restrict the passage of aquatic fauna [Nilsson et al., 2005]. Current policy mandates unhindered longitudinal migration of aquatic species through the installation of fish passage facilities or, where practical, the total removal of barriers [Armstrong et al., 2010, European Commission, 2012]. However, fish pass efficiencies are consistently reported as low [Roscoe et al., 2011, Brown et al., 2013]. Furthermore, there is a distinct lack of recommended performance criteria in the literature and the current methodology to assess fish passage facilities is cost-prohibitive, time- and resource-intensive, and often invasive [Silva et al., 2018].

It was hypothesised that the ecological efficiency of fish passage facilities could be computationally-assessed through the development and application of agent-based models of up-migrating fish behaviour. The passage efficiency of juvenile European eels (*Anguilla anguilla*) through various configurations of eel tiles was assessed through the development of multiple 2D CA and IBMs. The trajectories of up-migrating brown trout (*Salmo trutta*) through 3D domains was assessed through the development of the `fishPy` tool, and its subsequent application to a real-world ecohydraulic domain.

7.1.1 Predicting the Upstream Passage of Juvenile European Eels through Eel Tiles

The work presented in chapter 3 is the first to computationally assess the passability of eel tiles for up-migrating juvenile European eels (*Anguilla anguilla*). The European eel is a catadromous species and therefore up- and down-migration are integral to their survival. Furthermore, the recruitment of elvers across Europe is down 95% compared to levels seen in the early 1980s [Moriarty, 1996], resulting in IUCN Red list status [Jacoby and Gollock, 2014]. Recently, purpose-built anguilliform-specific passage facilities have been developed but independent assessment of their performance is lacking in the literature.

Development of Computational Metrics of Elver Passability

The work presented in chapter 3 considered various computational metrics to determine passability. These can be grouped in landscape connectivity metrics, cellular automata, and individual-based models. No previous studies of the application of landscape connectivity metrics or the use of CA for fish passage were found in the literature. Each metric relied upon 2D temporally-independent flow fields of the eel tile and on the critical burst speed of the passing elvers.

Three-dimensional flow fields were computationally determined for a range of discharges and installation angles using CFD with the unsteady, incompressible, Reynolds Averaged Navier-Stokes (RANS) equations , the VOF methodology, and using the k–ω SST turbulence closure. This methodology yielded results agreeable with those reported by Vowles et al. [2015]. The validated results were then temporally-averaged and 2D flow fields were extracted. This approach to obtaining 2D flow fields had a larger computational expense compare to using 2D, steady simulations [e.g. Gao et al. 2016, Tan et al. 2018] but yielded greater accuracy due to the inclusion of 3D flow features and a deeper understanding of the temporal-dependency of the flow. The use of Reynolds stress models, LES, or DNS could have yielded more accurate results [see Benhamadouche and Laurence 2003], but this level of complexity is not necessary as elvers have been shown to react to larger-scale flow structures [Piper et al., 2012, 2015]. Furthermore, various ABMs in the literature have demonstrated the utility of using the RANS approach to generate flow field inputs [i.e. Goodwin et al. 2014, Gisen 2018, Zielinski et al. 2018, Finger et al. 2020].

The critical burst speeds for the passing elvers were extracted from the SWIM-IT programme [Clough and Turnpenny, 2001]. Use of the critical burst speed over a variable swim speed, such as that used by Goodwin et al. [2014] or Gisen [2018], or a static sustained swim speed, such as that used by Gao et al. [2016] or Tan et al. [2018], was crucial in implementing exhaustion, and the subsequent calculation of theoretical maximum passable pass lengths. However, use of the critical burst speed was only practical due to observations by Vowles et al. [2015] of passing elvers opting to ascend the pass as quickly as possible. If this was not the case, or the models were applied to domains were passing elvers chose a different approach, modelling exhaustion would require implementation of discrete fatigue increments, akin to that used by Zielinski et al. [2018].

Outcomes of the Computational Metrics for Elver Passability

The landscape connectivity metrics were able to predict trends within passage efficiencies for different configurations of eel tile. However, they offered little practical results to accurately determine passage efficiencies. Modifications to the landscape connectivity metrics may yield more accurate results but, given the scarcity of data with which to calibrate and the utility of individual-based models, further use of the landscape connectivity metrics for fish passage is not recommended.

The CA (`SEPM`, `FEPM`, and `EEPM`) correctly predicted trends within passage efficiencies for different configurations of eel tile, but suffered from polarised results due to their usage of an homogeneous population of elvers. The `HEPM` overcame this issue through the use of a heterogeneous population, and compared well to the results of Vowles et al. [2015] (75.50% vs. 73.82%). Comparisons to the wider literature is difficult, as no other computational assessment of anguilliform-specific passage facilities is available in the literature.

Current UK guidance for eel tile-type passes suggests installation angles up to 45° are appropriate [Environment Agency, 2011]. Results of the `HEPM` show that passage efficiency reduced significantly with increasing installation angle, resulting in less than 40% passage efficiency for all but the largest populations for an angle of 20°. This result is well below the recommended threshold of 90% made by Lucas and Baras [2008]. Furthermore, the significance of passing eel size and discharge are not considered in current policy, but are demonstrated in the results of this work. For example, the maximum allowable installation angle to facilitate a passage efficiency of 75% reduces considerably with increasing discharge per unit width and decreasing elver length, table 7.1.

Application of the `HEPM` yielded a time to ascend the $1.25m$ pass for each elver, which was used to determine theoretical maximum passage lengths through assuming the velocity field was not significantly dependent on passage length and that passing elver became exhausted after $20s$, figure 3.22. These results demonstrate the significant of pass length in facilitating adequate passage efficiency. However, current guidance suggests that the pass length is only a function of the surrounding geometry (i.e. the hydraulic head that must be overcome).

It is curious that none of these topics appear in current guidance [Environment Agency, 2011] yet are discussed in-depth in previous guidance that has since been

Table 7.1: Installation angle required to allow for a 75% passage efficiency for each discharge per unit width, Q. Calculated based on the results of the `HEPM`. Note that ^{a} denotes a case for which the passage efficiency was never determined to be $< 75\%$, regardless of the installation angle, and ^{b} denotes cases for which the passage efficiency was never determined to be $\geq 75\%$, regardless of the installation angle.

	Req. Installation Angle (°) for $Q =$		
Elver Length (m)	$1.6\dot{7}\times10^{-3}m^2s^{-1}$	$3.3\dot{3}\times10^{-3}m^2s^{-1}$	$5.0\times10^{-3}m^2s^{-1}$
0.05	≤12.7	≤9.3	$< 8.0^b$
0.06	≤14.1	≤11.0	$< 8.0^b$
0.07	≤15.3	≤14.8	$< 8.0^b$
0.08	≤16.4	≤15.9	≤12.0
0.09	≤18.9	≤17.6	≤15.1
0.1	$> 20.0^a$	≤19.7	≤17.2

withdrawn [Solomon and Beach, 2004]. It is therefore recommended that policy is updated as a matter of urgency to reconsider the compounding effects of installation angle, expected eel length, pass length, and installation angle on passage efficiency. This could be achieved through the inclusion of results such as figure 3.22 and table 7.1, which provide immediate, simple resources for practitioners. This is of particular importance as current guidance unfairly biases against smaller eel sizes, which [Solomon and Beach, 2004, p 18] previously suggested were "first priority, as the stock of the whole catchment is dependent upon them".

7.1.2 Predicting Trajectories of Up-Migrating Brown Trout

The work presented in chapter 4 detailed the development, structure, and function of the `fishPy` tool. In addition, the work presented in chapter 5 detailed verification of the `fishPy` code and sensitivity studies of selected parameters. A number of development principles were outlined in the early stages of this research and have guided the development of the software tool [table 1.1, chapter 1].

The work presented in chapter 6 detailed the collection and filtering of high resolution velocity and bathymetry data for a real world ecohydraulic domain, the develop-

ment and execution of CFD simulations of the domain, the application of the `fishPy` tool to the new dataset, and a comparison of the predicted passages to published measured fish tracks.

Development of the `fishPy` Model

The `fishPy` tool is a three-dimensional, spatially-continuous, temporally-discrete individual-based model, which predicts up-migration pathways of brown trout through computation of fish responses to hydraulic stimuli. The `fishPy` model combines high spatial ($\mathcal{O}(0.1)m$) and temporal ($\mathcal{O}(0.1)s$) resolutions. The underlying ruleset that governs the `fishPy` tool is a novel combination of rheotaxis, energy pathway selection, obstacle avoidance, and turbulence avoidance, and assumes an inherent, persistent motivation to migrate. This ruleset was developed based on a thorough literature review and was implemented in a modular manner to facilitate future expansion of the model.

Adequate simulation of rheotaxis is shown to be significant in the literature, and has increased significance due to the spatially-continuous, generalised formulation of the `fishPy` model, which facilitates its application to any domain. This model formulation is novel compared to the other published up-migration fish path prediction models.

The `fishPy` tool uses a combination of biasing towards locally slower velocities and biasing towards locally faster velocities, dependent upon the local flow environment (`minMaxEnergy` rule). The behavioural case is determined by the local velocity magnitude and fluid strain, inspired by the work of Goodwin et al. [2014]. This is a novel formulation which combines the concept of the minimum energy pathway as used by Blank [2008], Abdelaziz [2013], Plymesser [2014], Zielinski et al. [2018] and Gilmanov et al. [2019], and the concept of attraction flow used in the ecology community [see Armstrong et al. 2010] and within the ELAM-de model [Gisen, 2018].

Outcomes of the Application of the `fishPy` Model

The work presented in chapter 6 showed that, when applied to the CFD-derived flow fields used to represent Ruswarp Weir, the `fishPy` model was able to accurately predict the attraction efficiency (100% vs. 96%) and passage efficiency (75% vs. 65%) of the Larinier fish pass compared to published, measured data. This finding gives confidence to the data collection and filtering processes, CFD methodology, and to the novel formulation and behavioural ruleset of the `fishPy` model. Furthermore, unlike all

Table 7.2: Resulting behaviours emergent from usage of the `minMaxEnergy` rule within `fishPy`.

Predicted Behaviour	Supporting Literature
Attraction to lower velocities such as near-wall regions.	Larinier [2002b], Blank [2008]
Obstacle avoidance through attraction to high velocity streamlines round obstacles	Dabiri [2017]
A preference for high velocity regions over high turbulence regions, where turbulence is quantified using fluid shear.	Smith et al. [2005, 2006], Nestler et al. [2008]
Attraction to higher velocity flows (i.e. bulk flow)	Lundqvist et al. [2008], Thorstad et al. [2008], Armstrong et al. [2010]

published models in the literature [i.e. Goodwin et al. 2014, Gisen 2018, or Zielinski et al. 2018; see section 2.8], the `fishPy` model is able to yield accurate results when applied to previously-unseen, generalised domains without domain-specific calibration. Eliminating the need for domain-specific calibration vastly increases the utility of the tool and its ease-of-use, increasing its accessibility to practitioners.

The results presented in chapters 5 and 6 demonstrate the utility of the `fishPy` rule-set, which depends significantly on the energy pathway selection rule, `minMaxEnergy`. This rule is novel in its formulation and is the result of a synthesis of theories from the literature. Use of this rule results in a multitude of behaviours depending upon the extended local fluid velocity magnitude and fluid shear, which correlate to behaviours identified in the literature, table 7.2. This shows that, while simple energy saving rules are not sufficient [Gisen, 2018], an energy pathway selection rule is able to reproduce observed fish behaviours using only the local velocity field, as turbulence is quantified using the fluid shear (i.e. the spatial velocity gradient), which implicitly includes the Reynolds shear stress.

Work presented in chapter 5 demonstrated the sensitivity of predicted fish tracks to the spatial resolution of the input data and the chosen timestep. However, implementing a maximum timestep based upon the established CFL criterion was found to not be sufficient to eliminate spatial and temporal dependencies. Furthermore, the required spatial resolution was found to be dependent upon the domain geometry, the spatial variation of the flow field, and the smallest bodylength of the simulated population, and

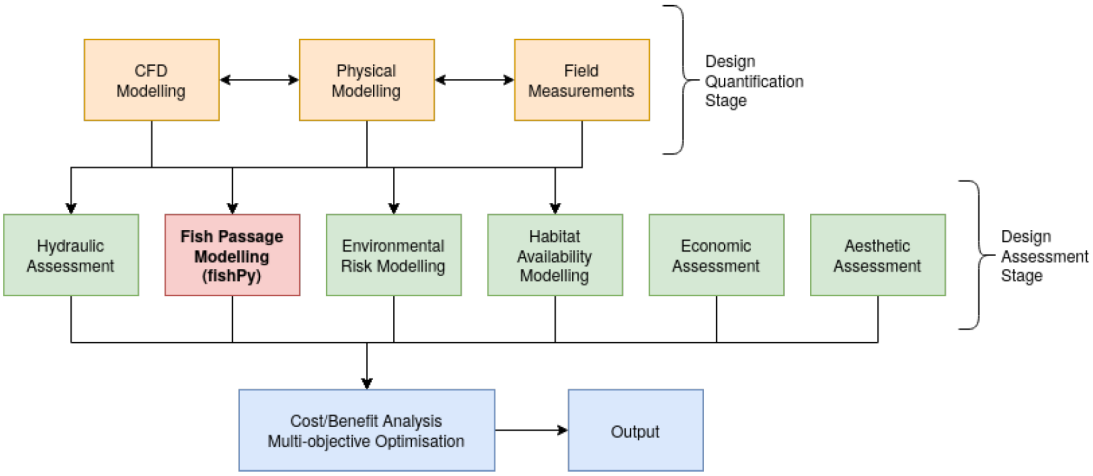

Figure 7.1: Schematic showing an outline of the proposed wider decision-making framework. This framework could be used to computationally assess and compare hydraulic, ecological, economic, and aesthetic factors when designing fish passage facilities. The location of the `fishPy` model is highlighted within the model.

the required temporal resolution was found to be dependent upon the minimum velocity in the domain and the spatial velocity gradients. The significance of these dependencies was demonstrated in the results presented in chapter 6. Therefore, it is recommended that the highest possible spatial resolution should be used within practical limitations of time and computational resources, and a spatial resolution dependency study may be required when the `fishPy` model is applied to new domains. Interestingly, no other model in the literature considers model sensitivity to spatial resolution or to temporal resolution over differing domains.

The `fishPy` tool facilitates a policy-driven, computational metric which can be used to computationally assess fish passage at existing or future hydraulic sites. With additional development, the `fishPy` tool can be incorporated into a wider decision-making framework to computationally assess the hydraulic, ecological, economic, and aesthetic factors of different designs of in-stream structures such as fish passes, i.e. figure 7.1. This framework could include a cost/benefit analysis to assess and optimise designs based on a number of criteria, for example: successful fish passage, power generation of hydropower facilities, flood capacity, installation costs, or fish habitat availability. This framework would provide a tangible, practical tool for practitioners

and the wider ecological community, aid in the reduction of invasive experiments, and provide a foundation for new, firm guidance from policy-makers on the design and installation of future fish passage facilities.

7.1.3 Limitations & Future Work

Future Work in Predicting Eel Passage

The HEPM has shown to be able to produce accurate predictions of passage efficiency through an eel tile for a single combination of discharge per unit width, installation angle, pass length, and elver size. As more experimental data become available, the HEPM should be further validated to ensure its validity when applied to other configurations of eel tile.

The HEPM is spatially-2D and considers only temporally-independent data. Therefore, the model could be further developed into a spatially-3D formulation, which may allow passing elver to exploit additional route options through the domain. However, it is unclear if the increased complexity of transitioning to a fully 3D model would yield greater results given the tendency for passing elver to remain near the bed throughout passage.

The HEPM could be expanded to consider temporally-varying data, which would facilitate the use of velocity fluctuations within the model and potentially allow passing elver to exploit lower velocity regions, particularly if coupled with the implementation of resting behaviours. This would enable the model to be used on more complex eel passes with larger velocity fluctuations and more complex geometry. However, the introduction of temporally-varying inputs is likely to result in temporally-varying outputs, which drastically increase the complexity of the interpretation of the results.

The HEPM considers a single behavioural type where an individual uses their burst swimming ability to rapidly ascend the pass in one attempt. However, while not seen in the study of Vowles et al. [2015], elvers are known to exhibit crawling and climbing behaviour as well as rest during a passage attempt [Legault, 1988]. Therefore, the HEPM could be further developed to consider these additional behavioural cases. Podgorniak et al. [2015a,b] suggest that cognitive processes have more influence than metabolic ability for climbing elvers. Furthermore, Podgorniak et al. [2016] suggest that climbing elvers display inherent personality types, which determine how aggressive the individual is, and that those that displayed the best climbing ability tended to have more

aggressive personalities. Therefore, if climbing behaviour was implemented, an inherent "aggression factor" could be developed to give the model further heterogeneity and control climbing behaviour.

The `HEPM` considered only the pass geometry and therefore the influence of the upstream and downstream reaches of the wider domain is not considered. However, the ability for passing elvers to locate the pass within a timely manner is known to be important in successful passage [Environment Agency, 2011]. Therefore, the `HEPM` could be applied to wider domains which consider the pass geometry *in situ*, rather than the pass in isolation, which would facilitate quantification of the attraction efficiency of a given anguilliform pass.

Future Development of `fishPy`

The `fishPy` tool has shown to be able to produce qualitatively sensible predictions of fish trajectories through various artificial domains with differing geometries and flow fields, and accurately predict the attraction efficiency and passage efficiency of a Larinier pass. However, as more experimental data become available, the `fishPy` tool should be further applied to new flume- and field-based datasets to ensure its validity and applicability to generalised domains.

The modular nature of the `fishPy` tool facilitates development of new species "modules" that contain new species-specific attributes and behavioural rules. Implementation of new species modules will increase the utility of the `fishPy` tool, allow for the parallel computation of fish pathways for multiple fish species, and allow for inter-species interactions such as predation to be modelled. The modular nature of the `fishPy` model means that future species modules could be added to a "species library" and future researchers could utilise only those species required. This would vastly increase the utility of the `fishPy` tool and aid in the reduction of resource-intensive, invasive experiments.

The `fishPy` tool considers only hydraulic stimuli when predicting fish behaviour. However, environmental stimuli such as light level, temperature, salinity, and scent have all been shown to correlate to behavioural patterns. In particular, light level and temperature have both been identified as stimuli correlated to the onset of large-scale migratory movements [Binder et al., 2011]. Therefore, additional environment data could be added to the model along with additional rules to capture these additional

facets of behavioural responses. Furthermore, modelling of these environmental stimuli may elucidate the drivers for motivation at river-scale, which remains unanswered in the literature. This would facilitate the expansion of `fishPy` to incorporate non-salmonidae species, where the assumption of an inherent, persistent motivation to migrate upstream is no longer justified.

The `fishPy` tool depend significantly on the formulation of the `minMaxEnergy` rule and the thresholds used for switching between behavioural cases. Within chapter 5, the thresholds were estimated based on numerous sensitivity analyses within multiple artificial domains. However, high spatio-temporal resolution ($\mathcal{O}(0.1m)$,$\mathcal{O}(0.1s)$) experimental data were not available to validate the `minMaxEnergy` rule, nor its parameters. Future development should centre on comprehensive validation and calibration of the `minMaxEnergy` rule. This could be achieved through the development of a flume-based testing framework, utilising state-of-the-art three-dimensional videometry to produce the required high spatio-temporal resolution fish tracks ($\mathcal{O}(0.1m)$,$\mathcal{O}(0.1s)$). Furthermore, ADV or PIV instrumentation should be used to collect accurate velocity data ($\mathcal{O}(0.001ms^{-1})$ with a high spatial resolution ($\mathcal{O}(0.1m)$) within the flume. This testing framework would facilitate observations of brown trout, and other species, through domains of varying geometry, through the installation of structures within the domain. In particular, observations of brown trout moving through flume-based versions of the artificial domains developed throughout chapter 5 would facilitate the validation and calibration of the `minMaxEnergy` rule. Once calibration of the parameters for a single size of individual is completed, a subsequent investigation into the relationship between the `minMaxEnergy` thresholds and the bodylength of the individual should be performed to understand the potential sensitivity of the model.

7.2 Conclusion

The work presented herein has detailed the development and application of multiple cellular automata and individual-based models to predict the up-migration pathways of British fish through lowland rivers, including:

- An investigation into the applicability of agent-based modelling to predict the passage efficiency of up-migrating juvenile European eels through eel tiles.
- The development of the `fishPy` software tool to predict the up-migration path-

ways of brown trout based on fish responses to hydraulic stimuli.

- The rule-by-rule verification of the `fishPy` tool using purpose-built, artificial, CFD-derived flow fields.
- Sensitivity studies on a number of key model parameters to determine appropriate parameter ranges and quantified model dependencies.
- Application of the `fishPy` tool to a real ecohydraulic domain with comparisons between predicted fish trajectories with measured bulk passage metrics.

References

Aarestrup, K., Økland, F., Hansen, M. M., Righton, D., Gargan, P., Castonguay, M., Bernatchez, L., Howey, P., Sparholt, H., Pedersen, M. I., et al. (2009). Oceanic spawning migration of the European eel (*Anguilla anguilla*). *Science*, 325(5948):1660–1660.

Abdelaziz, S., Bui, M. D., Atsushi, N., and Rutschmann, P. (2013). Numerical simulation of flow and upstream fish movement inside a pool-and-weir fishway. In *The Wise Find Pleasure in Water: Meandering through Water Science and Engineering. Proceedings of the 35th IAHR World Congress, Chengdu, China*, volume 8.

Abdelaziz, S. M. A. (2013). *Numerical simulation of fish behavior and fish movement through passages*. Unpublished PhD Thesis. TUM, Lehrstuhl für Wasserbau und Wasserwirtschaft.

Abebea, Y. A., Ghorbanib, A., Vojinovica, Z., Nikolicb, I., and Sancheza, A. (2016). Institutional analysis for flood risk reduction: A coupled agent-based–flood model method. In *iEMSs 2016 Conference*, volume 4, page 974.

Ackefors, H., Johansson, N., and Wahlberg, B. (1991). The Swedish compensatory programme for salmon in the Baltic: An action plan with biological and economic implications. In *ICES Marine Science Symposium*, volume 192, pages 109–119. Oxford University Press.

Alam, S. J. and Geller, A. (2012). Networks in agent-based social simulation. In *Agent-based models of geographical systems*, pages 199–216. Springer.

Alexander, R. (1966). Physical aspects of swimbladder function. *Biological Reviews*, 41(1):141–176.

Alexander, R. (1971). Swimbladder gas secretion and energy expenditure in vertically migrating fishes. In *Proceedings of an International Symposium on Biological Sound Scattering in the Ocean. Maury Center for Ocean Science, Washington DC*, pages 74–85.

Alexander, R. M. (1990). Size, speed and buoyancy adaptations in aquatic animals. *American Zoologist*, 30(1):189–196.

Alo, D. and Turner, T. F. (2005). Effects of habitat fragmentation on effective population size in the endangered Rio Grande silvery minnow. *Conservation Biology*, 19(4):1138–1148.

Anderson, J. (1995). *Computational Fluid Dynamics*. Computational Fluid Dynamics: The Basics with Applications. McGraw-Hill Education.

Andersson, A. G., Andreasson, P., and Staffan Lundström, T. (2013). CFD-modelling and validation of free surface flow during spilling of reservoir in down-scale model. *Engineering Applications of Computational Fluid Mechanics*, 7(1):159–167.

Andersson, A. G., Lindberg, D.-E., Lindmark, E. M., Leonardsson, K., Andreasson, P., Lundqvist, H., and Lundström, T. S. (2012). A study of the location of the entrance of a fishway in a regulated river with CFD and ADCP. *Modelling and Simulation in Engineering*, 2012. Article ID 327929.

ANSYS (2016). *ANSYS Fluent 18.2 User Guide*.

Archer, G. C. (1979). *The Skin and Mucous Secretion of the European Eel, Anguilla anguilla. L.* Unpublished PhD Thesis. University of Plymouth.

Arenas, A., Politano, M., Weber, L., and Timko, M. (2015). Analysis of movements and behavior of smolts swimming in hydropower reservoirs. *Ecological Modelling*, 312:292–307.

Armstrong, G., Aprahamian, M., Fewings, G. A., Gough, P. J., Reader, N. A., and Varallo, P. V. (2010). Environment Agency Fish Pass Manual. Environment Agency RND report. UK Government Publishing House, London.

Arnold, G. (1974). Rheotropism in fishes. *Biological reviews*, 49(4):515–576.

Atsushi, N. (2009). Studies on design of pool-and-weir type fishway focusing flow structure in the fishway. *Institute for Rural Engineering Report*, 49. National Institute for Rural Engineering. Tsukuba, Japan.

Atsushi, N., Masahiro, G., and Hiroyasu, K. (2008). The flow pattern of the pool-and-weir-fishway in the pool and the swimming behaviour of *leuciscus hakonensis*. *Japanese Journal of Hydraulic Engineering*, 52:1191–1196.

Banks, J. (1969). A review of the literature on the upstream migration of adult salmonids. *Journal of Fish Biology*, 1(2):85–136.

Baras, E. and Lucas, M. C. (2001). Impacts of man's modifications of river hydrology on the migration of freshwater fishes: A mechanistic perspective. *International Journal of Ecohydrology & Hydrobiology*, 1(3):291–304.

Barton, A. F., Keller, R. J., and Katopodis, C. (2009). Verification of a numerical model for the prediction of low slope vertical slot fishway hydraulics. *Australian Journal of Water Resources*, 13(1):53–60.

Bates, P., Lane, S., and Ferguson, R. (2005). *Computational Fluid Dynamics: Applications in Environmental Hydraulics*. Wiley.

Beach, M. (1984). Fish pass design-criteria for the design and approval of fish passes and other structures to facilitate the passage of migratory fish in rivers. Ministry of Agriculture, Fisheries and Food - Directorate of Fisheries Research. Fisheries Research Technical Report No. 78.

Beamish, F. (1979). Swimming capacity. *Fish physiology*, 7:101–187.

Bednarek, A. T. (2001). Undamming rivers: A review of the ecological impacts of dam removal. *Environmental Management*, 27(6):803–814.

Behlke, C. E. (1991). Power and energy implications of passage structures for fish. In *Fisheries Bioengineering Symposium: American Fisheries Society Symposium 10*, page 289.

Benenson, I. and Torrens, P. (2004). *Geosimulation: Automata-based modeling of urban phenomena*. John Wiley & Sons.

Benhamadouche, S. and Laurence, D. (2003). LES, coarse LES, and transient RANS comparisons on the flow across a tube bundle. *International Journal of Heat and Fluid Flow*, 24(4):470–479.

Bennett, D. A. and Tang, W. (2006). Modelling adaptive, spatially aware, and mobile agents: Elk migration in yellowstone. *International Journal of Geographical Information Science*, 20(9):1039–1066.

Bermúdez, M., Puertas, J., Cea, L., Pena, L., and Balairón, L. (2010). Influence of pool geometry on the biological efficiency of vertical slot fishways. *Ecological Engineering*, 36(10):1355–1364.

Bernard, R. N. et al. (1999). Using adaptive agent-based simulation models to assist planners in policy development: The case of rent control. *Rutgers University, Department of Urban Planning and Policy Development*.

Berry & Escott Engineering (2017). Berry & Escott Engineering: Eel Tile Product Page. Available at `http://www.berryescott.co.uk/eel-tile/`. [Accessed 07/02/17].

Bian, L. (2003). The representation of the environment in the context of individual-based modeling. *Ecological Modelling*, 159(2-3):279–296.

Bieniek, T. (2020). utm 0.5.0. Available at `https://pypi.org/project/utm/`. [Accessed 09/07/2020].

Binder, T., Cooke, S., and Hinch, S. (2011). Fish Migrations: The Biology of Fish Migration.

Blank, M. D. (2008). Advanced studies of fish passage through culverts: 1-D and 3-D hydraulic modeling of velocity, fish energy expenditure, and a new barrier assessment method. Unpublished PhD Thesis. Montana State University, Bozeman, Montana.

Blazek, J. (2015). *Computational fluid dynamics: principles and applications*. Butterworth-Heinemann.

Bleckmann, H. and Zelick, R. (2009). Lateral line system of fish. *Integrative Zoology*, 4(1):13–25.

Blender Foundation (2019). 3d printing toolbox. Available at `https://archive.blender.org/wiki/index.php/Extensions:2.6/Py/Scripts/Modeling/PrintToolbox/`. [Accessed 03/12/19].

Bolland, J. (2018). Discussion on eel and elver fallback within passes. Personal communication.

Bombač, M., Novak, G., Rodič, P., and Četina, M. (2014). Numerical and physical model study of a vertical slot fishway. *Journal of Hydrology and Hydromechanics*, 62(2):150–159.

Bonabeau, E. (2002). Agent-based modeling: Methods and techniques for simulating human systems. *Proceedings of the National Academy of Sciences*, 99(suppl 3):7280–7287.

Boussinesq, J. (1877). *Essai sur la théorie des eaux courantes*. Impr. nationale.

Bowyer, A. (1981). Computing dirichlet tessellations. *The computer journal*, 24(2):162–166.

Braun, C. B. and Coombs, S. (2000). The overlapping roles of the inner ear and lateral line: The active space of dipole source detection. *Philosophical Transactions of the Royal Society of London B: Biological Sciences*, 355(1401):1115–1119.

Brawn, V. M. (1962). Physical properties and hydrostatic function of the swimbladder of herring (*Clupea harengus L.*). *Journal of the Fisheries Board of Canada*, 19(4):635–656.

Briand, C., Fatin, D., Fontenelle, G., and Feunteun, E. (2005). Effect of re-opening of a migratory pathway for eel (*Anguilla anguilla, L.*) at a watershed scale. *Bulletin Français de la Pêche et de la Pisciculture*, (378-379):67–86.

Brönmark, C., Hulthén, K., Nilsson, P., Skov, C., Hansson, L.-A., Brodersen, J., and Chapman, B. (2014). There and back again: migration in freshwater fishes. *Canadian Journal of Zoology*, 92(6):467–479.

Brown, C. and Laland, K. N. (2003). Social learning in fishes: a review. *Fish and fisheries*, 4(3):280–288.

Brown, J. J., Limburg, K. E., Waldman, J. R., Stephenson, K., Glenn, E. P., Juanes, F., and Jordaan, A. (2013). Fish and hydropower on the US Atlantic coast: Failed fisheries policies from half-way technologies. *Conservation Letters*, 6(4):280–286.

Brown, R. (1828). XXVII. A brief account of microscopical observations made in the months of June, July and August 1827, on the particles contained in the pollen of plants; and on the general existence of active molecules in organic and inorganic bodies. *The Philosophical Magazine*, 4(21):161–173.

Burnett, N., Hinch, S., Bett, N., Braun, D., Casselman, M., Cooke, S., Gelchu, A., Lingard, S., Middleton, C., Minke-Martin, V., et al. (2016). Reducing carryover effects on the migration and spawning success of Sockeye Salmon through a management experiment of dam flows. *River Research and Applications*.

Butail, S. and Paley, D. A. (2012). Three-dimensional reconstruction of the fast-start swimming kinematics of densely schooling fish. *Journal of the Royal Society Interface*, 9(66):77–88.

Calles, E. O. and Greenberg, L. A. (2005). Evaluation of nature-like fishways for re-establishing connectivity in fragmented salmonid populations in the River Emån. *River Research and Applications*, 21(9):951–960.

Carling, P. and Dobson, J. (1992). Fish pass design and evaluation: phase 1.

Cassan, L., Tien, T. D., Courret, D., Laurens, P., and Dartus, D. (2014). Hydraulic resistance of emergent macroroughness at large froude numbers: design of nature-like fishpasses. *Journal of Hydraulic engineering*, 140(9):04014043.

Castro-Santos, T. (2005). Optimal swim speeds for traversing velocity barriers: an analysis of volitional high-speed swimming behavior of migratory fishes. *Journal of Experimental Biology*, 208(3):421–432.

Castro-Santos, T. (2006). Modeling the effect of varying swim speeds on fish passage through velocity barriers. *Transactions of the American Fisheries Society*, 135(5):1230–1237.

Castro-Santos, T., Cotel, A., and Webb, P. (2009). Fishway evaluations for better bioengineering: an integrative approach. In *Challenges for diadromous fishes in a*

dynamic global environment. American Fisheries Society, Symposium, volume 69, pages 557–575.

Castro-Santos, T. and Haro, A. (2010). Fish guidance and passage at barriers. In *Fish Locomotion: An Eco-ethological Perspective*. Science Publishers: Enfield, NH.

Castro-Santos, T., Haro, A., and Walk, S. (1996). A passive integrated transponder (PIT) tag system for monitoring fishways. *Fisheries research*, 28(3):253–261.

Caudill, C. C., Daigle, W. R., Keefer, M. L., Boggs, C. T., Jepson, M. A., Burke, B. J., Zabel, R. W., Bjornn, T. C., and Peery, C. A. (2007). Slow dam passage in adult Columbia River salmonids associated with unsuccessful migration: Delayed negative effects of passage obstacles or condition-dependent mortality? *Canadian Journal of Fisheries and Aquatic Sciences*, 64(7):979–995.

Cea, L., Pena, L., Puertas, J., Vázquez-Cendón, M., and Peña, E. (2007). Application of several depth-averaged turbulence models to simulate flow in vertical slot fishways. *Journal of Hydraulic Engineering*, 133(2):160–172.

Chen, C. (1997). *Fundamentals Of Turbulence Modelling*. Combustion (New York). Taylor & Francis.

Chittenden, C., Sura, S., Butterworth, K., Cubitt, K., Plantalech Manel-la, N., Balfry, S., Økland, F., and McKinley, R. (2008). Riverine, estuarine and marine migratory behaviour and physiology of wild and hatchery-reared Coho Salmon (*Oncorhynchus kisutch*) (Walbaum) smolts descending the Campbell River, BC, Canada. *Journal of Fish Biology*, 72(3):614–628.

Chorda, J., Cassan, L., and Laurens, P. (2019). Modeling steep-slope flow across staggered emergent cylinders: Application to fish passes. *Journal of Hydraulic Engineering*, 145(11):04019038.

Chorda, J., Maubourguet, M. M., Roux, H., Larinier, M., Tarrade, L., and David, L. (2010). Two-dimensional free surface flow numerical model for vertical slot fishways. *Journal of Hydraulic Research*, 48(2):141–151.

Clay, C. (1994). *Design of Fishways and Other Fish Facilities*. CRC Press, Florida, USA.

Clough, S. and Turnpenny, A. (2001). *Swimming speeds in fish: Phase 1*. Environment Agency. R&D Technical Report W2-026/TR1.

Codling, E. A., Plank, M. J., and Benhamou, S. (2008). Random walk models in biology. *Journal of the Royal Society Interface*, 5(25):813–834.

Conte, R. and Paolucci, M. (2014). On agent-based modeling and computational social science. *Frontiers in Psychology*, 5:668.

Costanza, R., d'Arge, R., De Groot, R., Farber, S., Grasso, M., Hannon, B., Limburg, K., Naeem, S., O'neill, R. V., Paruelo, J., et al. (1997). The value of the world's ecosystem services and natural capital. *Nature*, 387(6630):253–260.

Cotel, A. J., Webb, P. W., and Tritico, H. (2006). Do brown trout choose locations with reduced turbulence? *Transactions of the American Fisheries Society*, 135(3):610–619.

Courant, R., Friedrichs, K., and Lewy, H. (1967). On the partial difference equations of mathematical physics. *IBM journal of Research and Development*, 11(2):215–234.

Coutant, C. C. (1998). *Turbulent attraction flows for juvenile salmonid passage at dams*. Environmental Sciences Division, Oak Ridge National Laboratory, Oak Ridge, TN. Report ORNL/TM- 13608.

Cowx, I., O'Grady, K., Knights, B., and White, E. (1998a). Enhancing immigration and recruitment of eels: The use of passes and associated trapping systems. *Fisheries Management and Ecology*, 5(6):459–471.

Cowx, I., Welcomme, R., and European Inland Fisheries Advisory Commission (1998b). *Rehabilitation of Rivers for Fish*. Fishing News Books. Wiley, Chichester.

Crisp, T. (2008). *Trout and salmon: ecology, conservation and rehabilitation*. John Wiley & Sons.

Crooks, A., Castle, C., and Batty, M. (2008). Key challenges in agent-based modelling for geo-spatial simulation. *Computers, Environment and Urban Systems*, 32(6):417–430.

Crooks, A. T. and Heppenstall, A. J. (2012). Introduction to agent-based modelling. In *Agent-based models of geographical systems*, pages 85–105. Springer.

Dabiri, J. O. (2017). Biomechanics: How fish feel the flow. *Nature*, 547(7664):406–407.

Deelder, C. L. (1984). *Synopsis of biological data on the eel, Anguilla anguilla (Linnaeus, 1758)*. FAO Fisheries Synopsis No. 80, Revision I.

Denil, G. (1909). Les échelles a poissons et leur application aux barrages des Meuse et d'Ourthe. *Annales des Travaux Publics de Belgique*, 66:1221–1224.

Detert, M., Schütz, C., and Czerny, R. (2018). Development and tests of a 3D fish-tracking videometry system for an experimental flume. In *River Flow 2018-Ninth International Conference on Fluvial Hydraulics*, volume 40, page 03018. EDP Sciences.

Deutscher Verband für Wasserwirtschaft und Kulturbau (1996). *Fish Passes: Design, Dimensions and monitoring*. Food and Agriculture Organization of the United Nations, Rome.

Dickinson, M. H., Farley, C. T., Full, R. J., Koehl, M., Kram, R., and Lehman, S. (2000). How animals move: an integrative view. *science*, 288(5463):100–106.

Dijkgraaf, S. (1963). The functioning and significance of the lateral-line organs. *Biological Reviews*, 38(1):51–105.

Dodd, J. (2019). Fish tracking dataset for brown trout migration through Ruswarp weir. Personal communication.

Dodd, J. R., Bolland, J. D., Hateley, J., Cowx, I. G., Walton, S. E., Cattaneo, M. E., and Noble, R. A. (2018). Upstream passage of adult sea trout (*Salmo trutta*) at a low-head weir with an archimedean screw hydropower turbine and co-located fish pass. *Marine and Freshwater Research*, 69(12):1822–1833.

Duarte, B. A. d. F., Ramos, I. C. R., et al. (2012). Reynolds shear-stress and velocity: positive biological response of neotropical fishes to hydraulic parameters in a vertical slot fishway. *Neotropical Ichthyology*, 10(4):813–819.

Ducrocq, T., Cassan, L., Chorda, J., and Roux, H. (2017). Flow and drag force around a free surface piercing cylinder for environmental applications. *Environmental Fluid Mechanics*, 17(4):629–645.

Duguay, J., Lacey, R., and Gaucher, J. (2017). A case study of a pool and weir fishway modeled with openfoam and flow-3d. *Ecological Engineering*, 103:31–42.

Dynesius, M. and Nilsson, C. (1994). Fragmentation and flow regulation of river systems in the Northern third of the world. *Science*, 266(5186):753–762.

Ead, S., Katopodis, C., Sikora, G., and Rajaratnam, N. (2004). Flow regimes and structure in pool and weir fishways. *Journal of environmental engineering and science*, 3(5):379–390.

Einstein, A. (1905). Über die von der molekularkinetischen theorie der wärme geforderte bewegung von in ruhenden flüssigkeiten suspendierten teilchen. *Annalen der physik*, 322(8):549–560.

Environment Agency (2011). Elver and eel passes: A guide to the design and implementation of passage solutions at weirs, tidal gates and sluices. Environment Agency RND report. UK Government Publishing House, London.

Eriksson, T. and Eriksson, L.-O. (1993). Biological interactions of natural and enhanced stocks of salmon: The status of wild and hatchery propagated Swedish salmon stocks after 40 years of hatchery releases in the Baltic rivers. *Fisheries Research*, 18(1):147 – 159.

European Commission (2012). Report from the Commission to the European Parliament and the Council on the Implementation of the Water Framework Directive (2000/60/EC). Brussels, EU.

Fagiolo, G., Moneta, A., and Windrum, P. (2007). A critical guide to empirical validation of agent-based models in economics: Methodologies, procedures, and open problems. *Computational Economics*, 30(3):195–226.

Fenwick, N., Griffin, G., and Gauthier, C. (2009). The welfare of animals used in science: How the "Three Rs" ethic guides improvements. *The Canadian Veterinary Journal*, 50(5):523–530.

Ferrari, G. E., Politano, M., and Weber, L. (2009). Numerical simulation of free surface flows on a fish bypass. *Computers & Fluids*, 38(5):997–1002.

Feunteun, E. (2002). Management and restoration of European eel population (*Anguilla anguilla*): An impossible bargain. *Ecological Engineering*, 18(5):575–591.

Feurich, R., Boubée, J., and Olsen, N. R. B. (2012). Improvement of fish passage in culverts using CFD. *Ecological Engineering*, 47:1–8.

Finger, J. S., Riesgraf, A. T., Zielinski, D. P., and Sorensen, P. W. (2020). Monitoring upstream fish passage through a Mississippi River lock and dam reveals species differences in lock chamber usage and supports a fish passage model which describes velocity-dependent passage through spillway gates. *River Research and Applications*, 36(1):36–46.

Fish Counters In Action (2008). Sea Lamprey swims through a fish pass. Accessed 18th January 2017. Available at `https://www.youtube.com/watch?v=oKEPoy9Fp60`.

Ford, M. (2019). Upstream and downstream river levels at Ruswarp Weir. Personal Communication. [25/04/2019].

Forman, R. (2014). *Land Mosaics: The ecology of landscapes and regions (1995)*. Springer.

Foulds, W. L. and Lucas, M. C. (2013). Extreme inefficiency of two conventional, technical fishways used by European river lamprey (*Lampetra fluviatilis*). *Ecological Engineering*, 58:423–433.

Froese, R. and Pauly, D. (2019). FishBase version 12/2019. Internet Database. Accessible at `www.fishbase.org`.

Fuller, M. R., Doyle, M. W., and Strayer, D. L. (2015). Causes and consequences of habitat fragmentation in river networks. *Annals of the New York Academy of Sciences*, 1355(1):31–51.

Fulton, L. A., Gangmark, H. A., and Bair, S. H. (1953). *Trial of Denil-type fish ladder on Pacific salmon*, volume 99. US Department of the Interior, Fish and Wildlife Service.

Gao, Z., Andersson, H. I., Dai, H., Jiang, F., and Zhao, L. (2016). A new Eulerian-Lagrangian Agent Method to model fish paths in a vertical slot fishway. *Ecological Engineering*, 88:217–225.

Gardner, M. (1970). Mathematical games - the fantastic combinations of john conway's new solitaire game "life". *Scientific American*, 223.

Gardner, R. H. and O'Neill, R. V. (1991). Pattern, process, and predictability: the use of neutral models for landscape analysis. *Ecological Studies*, 82:289–307.

Gauld, N., Campbell, R., and Lucas, M. (2013). Reduced flow impacts salmonid smolt emigration in a river with low-head weirs. *Science of the total environment*, 458:435–443.

Gergel, S. E. and Turner, M. G. (2017). *Learning landscape ecology: a practical guide to concepts and techniques*. Springer.

Gibbons, W. J. and Andrews, K. M. (2004). PIT tagging: simple technology at its best. *Bioscience*, 54(5):447–454.

Gilmanov, A., Zielinski, D., Voller, V., and Sorensen, P. (2019). The effect of modifying a CFD-AB approach on fish passage through a model hydraulic dam. *Water*, 11(9):1776.

Gisen, D. (2018). Modeling upstream fish migration in small-scale using the Eulerian-Lagrangian-Agent method (elam). PhD Thesis.

Gisen, D. C., Weichert, R. B., and Nestler, J. M. (2016). Optimizing attraction flow for upstream fish passage at a hydropower dam employing 3-D Detached-Eddy Simulation. *Ecological Engineering*, 100:344–353.

Goettel, M. T., Atkinson, J. F., and Bennett, S. J. (2015). Behavior of western blacknose dace in a turbulence modified flow field. *Ecological Engineering*, 74:230–240.

Goodwin, R. A. (2004). Hydrodynamics and juvenile salmon movement behaviour at lower granite dam: Decoding the relationship using 3-D space-time (Celagent IBM) simulation. Unpublished PhD Thesis. Cornell University, Ithaca, NY.

Goodwin, R. A., Nestler, J. M., Anderson, J. J., Weber, L. J., and Loucks, D. P. (2006). Forecasting 3-D fish movement behavior using a Eulerian–Lagrangian–agent method (ELAM). *Ecological Modelling*, 192(1):197–223.

Goodwin, R. A., Politano, M., Garvin, J. W., Nestler, J. M., Hay, D., Anderson, J. J., Weber, L. J., Dimperio, E., Smith, D. L., and Timko, M. (2014). Fish navigation of large dams emerges from their modulation of flow field experience. *Proceedings of the National Academy of Sciences*, 111(14):5277–5282.

Grimm, V. and Railsback, S. F. (2005). *Individual-based modeling and ecology*, volume 8. Princeton University Press.

Gustafson, E. J. (1998). Quantifying landscape spatial pattern: what is the state of the art? *Ecosystems*, 1(2):143–156.

Haefner, J. W. and Bowen, M. D. (2002). Physical-based model of fish movement in fish extraction facilities. *Ecological Modelling*, 152(2):227–245.

Hall, C. J., Jordaan, A., and Frisk, M. G. (2012). Centuries of anadromous forage fish loss: consequences for ecosystem connectivity and productivity. *BioScience*, 62(8):723–731.

Harden Jones, F. R. and Scholes, P. (1985). Gas secretion and resorption in the swimbladder of the cod *gadus morhua*. *Journal of Comparative Physiology B*, 155(3):319–331.

Haro, A., Odeh, M., Castro-Santos, T., and Noreika, J. (1999). Effect of slope and headpond on passage of American shad and blueback herring through simple Denil and deepened Alaska steeppass fishways. *North American Journal of Fisheries Management*, 19(1):51–58.

Hayashida, K., Honda, T., Kayaba, Y., and Shimatani, Y. (2000). The characteristic of the plunging flow and the streaming flow in the pool-weir-fishway and the swimming behaviour of *Leuciscus Hakonensis*. *Environmental Systems Research*, 28:333–338.

Heimerl, S., Hagmeyer, M., and Echteler, C. (2008). Numerical flow simulation of pool-type fishways: New ways with well-known tools. *Hydrobiologia*, 609(1):189.

Heppenstall, A., Evans, A., and Birkin, M. (2006). Using hybrid agent-based systems to model spatially-influenced retail markets. *Journal of Artificial Societies and Social Simulation*, 9(3).

Hinch, S. G. and Rand, P. S. (2000). Optimal swimming speeds and forward-assisted propulsion: energy-conserving behaviours of upriver-migrating adult salmon. *Canadian Journal of Fisheries and Aquatic Sciences*, 57(12):2470–2478.

Hirt, C. and Nichols, B. (1981). Volume of fluid (VOF) method for the dynamics of free boundaries. *Journal of Computational Physics*, 39(1):201 – 225.

Hohenthal, J., Alho, P., Hyyppä, J., and Hyyppä, H. (2011). Laser scanning applications in fluvial studies. *Progress in Physical Geography*, 35(6):782–809.

Holcombe, S. (2014). surf2solid - make a solid volume from a surface for 3d printing. Available at `https://uk.mathworks.com/matlabcentral/fileexchange/42876-surf2solid-make-a-solid-volume-from-a-surface-for-3d-printing`. [Accessed 03/12/19].

Holcombe, S. (2018). stlwrite - write ascii or binary stl files. Available at `https://uk.mathworks.com/matlabcentral/fileexchange/20922-stlwrite-write-ascii-or-binary-stl-files`. [Accessed 03/12/19].

Holthe, E., Lund, E., Finstad, B., Thorstad, E., and McKinley, R. (2005). A fish selective obstacle to prevent dispersion of an unwanted fish species, based on leaping capabilities. *Fisheries Management and Ecology*, 12(2):143–147.

HR Wallingford (2020). Arcboat product page. Available at `http://equipit.hrwallingford.com/products/arc-boat/the-arc-boat`. [Accessed 12/06/2020].

Hugel, S. (2020). convertbng 0.6.17. Available at `https://pypi.org/project/convertbng/`. [Accessed 09/07/2020].

Humborg, C., Ittekkot, V., Cociasu, A., and Bodungen, B. v. (1997). Effect of Danube River dam on Black Sea biogeochemistry and ecosystem structure. *Nature*, 386(6623):385–388.

Iltanen, S. (2012). Cellular automata in urban spatial modelling. In *Agent-based models of geographical systems*, pages 69–84. Springer.

Ingham, D. and Ma, L. (2005). Fundamental equations for CFD in river flow simulations. *Computational Fluid Dynamics: Applications in Environmental Hydraulics*, page 19.

Isenburg, M. (2019). las2tin readme. Available at `https://www.cs.unc.edu/~isenburg/lastools/download/las2tin_README.txt`. [Accessed 03/12/19].

Jackman, G., Larson, M., and Ruzicka, V. (2009). American eel passage enhancement plan for the bronx river. Report for Park & Recreation department, City of New York, NY.

Jacoby, D. and Gollock, M. (2014). *Anguilla anguilla*. the iucn red list of threatened species 2014:e.t60344a45833138. Available at: http://dx.doi.org/10.2305/IUCN.UK.2014-1.RLTS.T60344A45833138.en. Accessed 2nd of November 2018.

Jaeger, J. A. (2000). Landscape division, splitting index, and effective mesh size: new measures of landscape fragmentation. *Landscape ecology*, 15(2):115–130.

Janssen, J. and Corcoran, J. (1993). Lateral line stimuli can override vision to determine sunfish strike trajectory. *Journal of Experimental Biology*, 176(1):299–305.

Jensen, B. B. B. (2007). Numerical study of influence of inlet turbulence parameters on turbulence intensity in the flow domain: incompressible flow in pipe system. *Proceedings of the Institution of Mechanical Engineers, Part E: Journal of Process Mechanical Engineering*, 221(4):177–186.

Johnston, I. (1981). Structure and function of fish muscles. In *Symposia Zoological Society London*, volume 48, pages 71–113.

Jones, F. R. H. (1951). The swimbladder and the vertical movement of teleostean fishes. *Journal of Experimental Biology*, 28(4):553–566.

Jones, J., Börger, L., Tummers, J., Jones, P., Lucas, M., Kerr, J., Kemp, P., Bizzi, S., Consuegra, S., Marcello, L., et al. (2019). A comprehensive assessment of stream fragmentation in great britain. *Science of the total environment*, 673:756–762.

Jones, W. and Launder, B. (1972). The prediction of laminarization with a two-equation model of turbulence. *International journal of heat and mass transfer*, 15(2):301–314.

Kammerlander, H., Schlosser, L., Zeiringer, B., Unfer, G., Zeileis, A., and Aufleger, M. (2020). Downstream passage behavior of potamodromous fishes at the fish protection and guidance system “flexible fish fence”. *Ecological Engineering*, 143:105698.

Kamula, R. (2001). Flow over weirs with application to fish passage facilities. Unpublished PhD Thesis. Department of Process and Environmental Engineering, University of Oulu, Finland.

Kane, D. L., Belke, C. E., Gieck, R. E., and McLean, R. F. (2000). Juvenile fish passage through culverts in Alaska: A field study. Technical report. Publication Number FHWA-AK-RD-00-03.

Katopodis, C. (1992). *Introduction to Fishway Design.* Freshwater Institute, Central and Arctic Region, Department of Fisheries and Oceans, Ottawa, Canada.

Katopodis, C. (2005). Developing a toolkit for fish passage, ecological flow management and fish habitat works. *Journal of Hydraulic Research*, 43(5):451–467.

Keefer, M. L., Caudill, C. C., Peery, C. A., and Lee, S. R. (2008). Transporting juvenile salmonids around dams impairs adult migration. *Ecological Applications*, 18(8):1888–1900.

Kerr, J. R., Manes, C., and Kemp, P. S. (2016). Assessing hydrodynamic space use of brown trout, *Salmo trutta*, in a complex flow environment: a return to first principles. *Journal of Experimental Biology*, 219(21):3480–3491.

Khan, L. A. (2006). A three-dimensional Computational Fluid Dynamics (CFD) model analysis of free surface hydrodynamics and fish passage energetics in a vertical-slot fishway. *North American Journal of Fisheries Management*, 26(2):255–267.

Kim, S., Yu, K., Yoon, B., and Lim, Y. (2012). A numerical study on hydraulic characteristics in the Ice Harbor-type fishway. *KSCE Journal of Civil Engineering*, 16(2):265–272.

Klopries, E.-M. and Schüttrumpf, H. (2020). Mortality assessment for adult european eels (*Anguilla anguilla*) during turbine passage using CFD modelling. *Renewable Energy*, 147:1481–1490.

Knights, B. and White, E. M. (1998). Enhancing immigration and recruitment of eels: the use of passes and associated trapping systems. *Fisheries Management and Ecology*, 5(6):459–471.

Kopec, J. A., Finès, P., Manuel, D. G., Buckeridge, D. L., Flanagan, W. M., Oderkirk, J., Abrahamowicz, M., Harper, S., Sharif, B., Okhmatovskaia, A., et al. (2010). Validation of population-based disease simulation models: a review of concepts and methods. *BMC public health*, 10(1):710.

Kremmydas, D. (2012). Agent based modeling for agricultural policy evaluation: A. Technical report, AUA Working Paper Series.

Kröger, R., Cooper, C., and Moore, M. (2008). A preliminary study of an alternative controlled drainage strategy in surface drainage ditches: low-grade weirs. *Agricultural water management*, 95(6):678–684.

Kwan, S., Vasquez, J., Millar, R., and Steffler, P. (2011). A fast method for 3D CFD modeling of a long river reach. In *World Environmental and Water Resources Congress 2011: Bearing Knowledge for Sustainability*, pages 2095–2103.

Lacey, R. J., Neary, V. S., Liao, J. C., Enders, E. C., and Tritico, H. M. (2012). The IPOS framework: linking fish swimming performance in altered flows from laboratory experiments to rivers. *River Research and Applications*, 28(4):429–443.

Laffaille, P., Acou, A., Guillouët, J., and Legault, A. (2005). Temporal changes in European eel, *Anguilla anguilla*, stocks in a small catchment after installation of fish passes. *Fisheries Management and Ecology*, 12(2):123–129.

Lai, Y. G. (2000). Unstructured grid arbitrarily shaped element method for fluid flow simulation. *American Institute of Aeronautics and Astronautics Journal*, 38(12):2246–2252.

Lamperti, F., Roventini, A., and Sani, A. (2018). Agent-based model calibration using machine learning surrogates. *Journal of Economic Dynamics and Control*, 90:366–389.

Larinier, M. (1992). Les passes à ralentisseurs. *Bulletin Français de la Pêche et de la Pisciculture*, (326-327):73–94.

Larinier, M. (2002a). Baffle fishways. *Bulletin FranÃ§ais de la PÃªche et de la Pisciculture*, 6:83–101. Available at `https://www.researchgate.net/profile/Michel_Larinier/publication/27335345_Baffle_fishways/links/5416fa560cf2788c4b35f9e0.pdf`.

Larinier, M. (2002b). Location of fishways. *Bull. Fr. Peche Piscic.*, (364):39–53.

Larinier, M. and Marmulla, G. (2004). Fish passes: types, principles and geographical distribution - an overview. In *Proceedings of the second international symposium on the management of large rivers for fisheries*, volume 2, pages 183–206. RAP Publication.

Larinier, M. and Miralles, A. (1981). Caracteristiques hydrauliques des passes a ralentisseurs. Report, Institut National de Recherche en Sciences et Technologies pour l'Environnement et l'Agriculture (IRSTEA), Paris, France.

Larinier, M. and Travade, F. (2002a). The design of fishways for shad. *Bulletin Francais de la Peche et de la Pisciculture*, (364):135–146.

Larinier, M. and Travade, F. (2002b). Downstream migration: problems and facilities. *Bulletin Français de la Pêche et de la Pisciculture*, 364(Supplément):181–207. Available at `https://www.researchgate.net/profile/Michel_Larinier/publication/27335350_Downstream_migration_Problems_and_facilities/links/5416f9090cf2788c4b35f986.pdf`.

Larinier, M., Travade, F., Porcher, J., and Gosset, C. (1994). Passes à poissons: expertise et conception des ouvrages de franchissement. Conseil Superieur de la Pêche. Paris, France.

Launder, B. E. and Spalding, D. B. (1974). The numerical computation of turbulent flows. *Computer Methods in Applied Mechanics and Engineering*, 3(2):269 – 289.

Lee, C., Farrell, A., Lotto, A., MacNutt, M., Hinch, S., and Healey, M. (2003). The effect of temperature on swimming performance and oxygen consumption in adult sockeye (oncorhynchus nerka) and coho (o. kisutch) salmon stocks. *Journal of Experimental Biology*, 206(18):3239–3251.

Legault, A. (1988). Le franchissement des barrages par l'escalade de l'anguille. Etude en Sèvre Niortaise. *Bulletin Français de la Pêche et de la Pisciculture*, (308):1–10.

Legland, D. (2019). geom3d. Available at `https://uk.mathworks.com/matlabcentral/fileexchange/24484-geom3d?s_tid=prof_contriblnk`. [Accessed 03/12/19].

Leica Geosystems (2020). Leica Geo Office - one integrated Office Software. Available at `https://leica-geosystems.com/products/total-stations/software/leica-geo-office`. [Accessed 12/06/2020].

Li, H. and Reynolds, J. F. (1993). A new contagion index to quantify spatial patterns of landscapes. *Landscape ecology*, 8(3):155–162.

Liao, J. C. (2007). A review of fish swimming mechanics and behaviour in altered flows. *Philosophical Transactions of the Royal Society of London B: Biological Sciences*, 362(1487):1973–1993.

Liao, J. C., Beal, D. N., Lauder, G. V., and Triantafyllou, M. S. (2003). Fish exploiting vortices decrease muscle activity. *Science*, 302(5650):1566–1569.

Lindberg, D.-E., Leonardsson, K., Andersson, A. G., Lundström, T. S., and Lundqvist, H. (2013). Methods for locating the proper position of a planned fishway entrance near a hydropower tailrace. *Limnologica-Ecology and Management of Inland Waters*, 43(5):339–347.

Lindsay, D. (2019). Environment Agency gauge 27902. Briggswath data. Personal Communication. [30/04/2019].

Liu, M., Rajaratnam, N., and Zhu, D. Z. (2006). Mean flow and turbulence structure in vertical slot fishways. *Journal of Hydraulic Engineering*, 132(8):765–777.

Lucas, M. and Baras, E. (2008). *Migration of Freshwater Fishes*. John Wiley & Sons, Chichester.

Lucas, M. and Frear, P. (1997). Effects of a flow-gauging weir on the migratory behaviour of adult barbel, a riverine cyprinid. *Journal of fish biology*, 50(2):382–396.

Lucas, M. C. and Baras, E. (2000). Methods for studying spatial behaviour of freshwater fishes in the natural environment. *Fish and fisheries*, 1(4):283–316.

Lundqvist, H., Rivinoja, P., Leonardsson, K., and McKinnell, S. (2008). Upstream passage problems for wild Atlantic salmon (*Salmo salar L.*) in a regulated river and its effect on the population. In *Fish and Diadromy in Europe (ecology, management, conservation)*, pages 111–127. Springer.

Macal, C. M. and North, M. J. (2010). Tutorial on agent-based modelling and simulation. *Journal of simulation*, 4(3):151–162.

Maeno, S. and Miyauchi, Y. (2001). Flow analysis in pool and weir type fishway using VOF method. *Proceedings of Hydraulic Engineering*, 45:421–426.

Mallen-Cooper, M. and Stuart, I. (2007). Optimising Denil fishways for passage of small and large fishes. *Fisheries Management and Ecology*, 14(1):61–71.

Marjoribanks, T. I., Hardy, R. J., Lane, S. N., and Parsons, D. R. (2014). High-resolution numerical modelling of flow-vegetation interactions. *Journal of Hydraulic Research*, 52(6):775–793.

Marjoribanks, T. I., Hardy, R. J., Lane, S. N., and Tancock, M. J. (2017). Patch-scale representation of vegetation within hydraulic models. *Earth surface processes and landforms*, 42(5):699–710.

Marriner, B. A., Baki, A. B., Zhu, D. Z., Cooke, S. J., and Katopodis, C. (2016). The hydraulics of a vertical slot fishway: A case study on the multi-species Vianney-Legendre fishway in Quebec, Canada. *Ecological Engineering*, 90:190–202.

Marriner, B. A., Baki, A. B. M., Zhu, D. Z., Thiem, J. D., Cooke, S. J., and Katopodis, C. (2014). Field and numerical assessment of turning pool hydraulics in a vertical slot fishway. *Ecological Engineering*, 63:88 – 101.

Masters, J., Welton, J., Beaumont, W., Hodder, K., Pinder, A., Gozlan, R., and Ladle, M. (2002). Habitat utilisation by pike (*esox lucius l.*) during winter floods in a Southern English chalk river. In Thorstad, E. B., Fleming, I. A., and Naesje, T. F., editors, *Aquatic Telemetry*, pages 185–191. Springer, Berlin.

Matsumoto, M. and Nishimura, T. (1998). Mersenne twister: a 623-dimensionally equidistributed uniform pseudo-random number generator. *ACM Transactions on Modeling and Computer Simulation (TOMACS)*, 8(1):3–30.

McElroy, B., DeLonay, A., and Jacobson, R. (2012). Optimum swimming pathways of fish spawning migrations in rivers. *Ecology*, 93(1):29–34.

McGarigal, K. (2015). Fragstats v4.2: User manual.

McGarigal, K., Cushman, S., and Ene, E. (2012). Fragstats v4: Spatial pattern analysis program for categorical and continuous maps. *Computer software program produced by the authors at the University of Massachusetts, Amherst*. Available at `http://www.umass.edu/landeco/research/fragstats/fragstats.html` [Accessed 24/07/18].

McLeod, A. M. and Nemenyi, P. (1941). An investigation of fishways. Conducted for the Iowa State Conservation Commission by the Iowa Institute of Hydraulic Research.

Menter, F. (1993). Zonal two-equation k–ω turbulence models for aerodynamic flows. *23rd Fluid Dynamics, Plasmadynamics, and Lasers Conference*.

Menter, F. R. (1994). Two-equation eddy-viscosity turbulence models for engineering applications. *AIAA journal*, 32(8):1598–1605.

Menter, F. R. (2009). Review of the shear-stress transport turbulence model experience from an industrial perspective. *International journal of computational fluid dynamics*, 23(4):305–316.

Milewski, C. L. and Brown, M. L. (1994). Proposed standard weight (Ws) equation and length-categorization standards for stream-dwelling brown trout (*Salmo trutta*). *Journal of Freshwater Ecology*, 9(2):111–116.

Milieu Inc. (2017). Milieu Products: Substrates for Elvers. Available at `http://www.milieuinc.com/products`. [Accessed 07/02/17].

Mills, D. (1989). *Ecology and management of Atlantic salmon*. Springer Science & Business Media.

Moin, P. and Mahesh, K. (1998). Direct numerical simulation: a tool in turbulence research. *Annual review of fluid mechanics*, 30(1):539–578.

Montgomery, J., Coombs, S., and Halstead, M. (1995). Biology of the mechanosensory lateral line in fishes. *Reviews in Fish Biology and Fisheries*, 5(4):399–416.

Montgomery, J. C., Baker, C. F., and Carton, A. G. (1997). The lateral line can mediate rheotaxis in fish. *Nature*, 389(6654):960–963.

Moriarty, C. (1986). Variations in elver abundance at European catching stations from 1938 to 1985 (*Anguilla anguilla*). *Vie et Milieu (France)*.

Moriarty, C. (1996). The decline in catches of european elver 1980-1992. *Archiwum Rybactwa Polskiego*, 4(2a):245–248.

Moriarty, C. and Dekker, W. (1997). Management of the European eel. Technical report, Marine Institute.

Moulinec, C., Hunt, J., and Nieuwstadt, F. (2004). Disappearing wakes and dispersion in numerically simulated flows through tube bundles. *Flow, Turbulence and Combustion*, 73(2):95–116.

NASA (2020). Satellite ephemeris data. Available at `ftp://cddis.nasa.gov/gnss/data/daily/`. [Accessed 12/06/2020].

Nathan, R., Getz, W. M., Revilla, E., Holyoak, M., Kadmon, R., Saltz, D., and Smouse, P. E. (2008). A movement ecology paradigm for unifying organismal movement research. *Proceedings of the National Academy of Sciences*, 105(49):19052–19059.

Nestler, J., Goodwin, R., Smith, D., Anderson, J., and Li, S. (2008). Optimum fish passage and guidance designs are based in the hydrogeomorphology of natural rivers. *River Research and Applications*, 24(2):148–168.

NGA (2020). HSYNTH WGS84 Tool Download. Available at `https://earth-info.nga.mil/GandG/wgs84/gravitymod/egm2008/hsynth_WGS84.exe`. [Accessed 12/06/2020].

Ngo, T. A. and See, L. (2012). Calibration and validation of agent-based models of land cover change. In *Agent-based models of geographical systems*, pages 181–197. Springer.

Nicholas, A. P., Sandbach, S. D., Ashworth, P. J., Amsler, M. L., Best, J. L., Hardy, R. J., Lane, S. N., Orfeo, O., Parsons, D. R., Reesink, A. J., et al. (2012). Modelling hydrodynamics in the Rio Paraná, Argentina: An evaluation and inter-comparison of reduced-complexity and physics based models applied to a large sand-bed river. *Geomorphology*, 169:192–211.

Nicola, G., Elvira, B., and Almodovar, A. (1996). Dams and fish passage facilities in the large rivers of Spain: Effects on migratory species. *Archiv für Hydrobiologie. Supplementband. Large rivers*, 113(10):375–379.

Nilsson, C. and Berggren, K. (2000). Alterations of riparian ecosystems caused by river regulation: Dam operations have caused global-scale ecological changes in riparian ecosystems. how to protect river environments and human needs of rivers remains one of the most important questions of our time. *BioScience*, 50(9):783–792.

Nilsson, C., Reidy, C. A., Dynesius, M., and Revenga, C. (2005). Fragmentation and flow regulation of the world's large river systems. *Science*, 308(5720):405–408.

Noonan, M. J., Grant, J. W., and Jackson, C. D. (2012). A quantitative assessment of fish passage efficiency. *Fish and Fisheries*, 13(4):450–464.

Northcote, T. G. (1997). Potamodromy in salmonidae - living and moving in the fast lane. *North American Journal of Fisheries Management*, 17(4):1029–1045.

Noss, R. F. (1991). Landscape connectivity: different functions at different scales. *Landscape linkages and biodiversity. Island Press, Washington, DC, USA*, pages 27–39.

Nourinejad, M. and Roorda, M. J. (2016). Agent based model for dynamic ridesharing. *Transportation Research Part C: Emerging Technologies*, 64:117–132.

Odeh, M., Noreika, J. F., Haro, A., Maynard, A., Castro-Santos, T., and Cada, G. F. (2002). Evaluation of the effects of turbulence on the behavior of migratory fish. *Final Report to the Bonneville Power Administration, Contract*, 22.

Oldani, N. O., Baigun, C. R. M., Nestler, J. M., and Goodwin, R. A. (2007). Fish passage technology saving fish resources in the lower La Plata River basin. *Neotropical Ichthyology*, 5(2):89–102. International Symposium on Fish Passages in South America, Fed Univ Lavras, Lavras, Brazil, July 30th - August 3rd, 2007.

Ona, E. (1990). Physiological factors causing natural variations in acoustic target strength of fish. *Journal of the Marine Biological Association of the United Kingdom*, 70(1):107â€“127.

O'neill, R., Krummel, J., Gardner, R. e. a., Sugihara, G., Jackson, B., DeAngelis, D., Milne, B., Turner, M. G., Zygmunt, B., Christensen, S., et al. (1988). Indices of landscape pattern. *Landscape ecology*, 1(3):153–162.

Ordnance Survey (2020). OS Net RINEX Data. Available at `https://www.ordnancesurvey.co.uk/gps/os-net-rinex-data/`. [Accessed 12/06/2020].

Padgett, T. E. (2020). The `fishPy` tool: An individual-based model to predict upstream movements of brown trout (*Salmo trutta*). University of Leeds. [Dataset]. `https://doi.org/10.5518/861`.

Padgett, T. E. and Thomas, R. E. (2019). Models of upstream movement of juvenile European eels (*Anguilla anguilla*) through studded eel tiles. University of Leeds. [Dataset]. `https://doi.org/10.5518/710`.

Padgett, T. E., Thomas, R. E., Borman, D. J., and Mould, D. C. (2020). Individual-based model of juvenile eel movement parametrized with computational fluid dynamics-derived flow fields informs improved fish pass design. *Royal Society Open Science*, 7(1):191505.

Parsons, D. R., Jackson, P., Czuba, J. A., Engel, F., Rhoads, B. L., Oberg, K., Best, J. L., Mueller, D., Johnson, K., and Riley, J. (2013). Velocity Mapping Toolbox (VMT): A processing and visualization suite for moving-vessel ADCP measurements. *Earth Surface Processes and Landforms*, 38(11):1244–1260.

Patankar, S. V. and Spalding, D. B. (1972). A calculation procedure for heat, mass and momentum transfer in three-dimensional parabolic flows. *International journal of heat and mass transfer*, 15(10):1787–1806.

Paxton, J. R. (2000). Fish otoliths: Do sizes correlate with taxonomic group, habitat and/or luminescence? *Philosophical Transactions of the Royal Society of London B: Biological Sciences*, 355(1401):1299–1303.

Peake, S. J. (2008). Swimming performance and behaviour of fish species endemic to Newfoundland and Labrador: A literature review for the purpose of establishing design and water velocity criteria for fishways and culverts.

Pearson, K. (1905). The problem of the random walk. *Nature*, 72(1867):342.

Pedlosky, J. (2013). *Geophysical Fluid Dynamics*. Springer New York.

Peterson, D. P. and Neville, H. M. (2019). Comparison of methods to verify upstream passage by trout at remediated culverts in four rocky mountain streams. *North American Journal of Fisheries Management*, 39(4):738–752.

Piper, A. T., Manes, C., Siniscalchi, F., Marion, A., Wright, R. M., and Kemp, P. S. (2015). Response of seaward-migrating european eel (*Anguilla anguilla*) to manipulated flow fields. In *Proc. R. Soc. B*, volume 282, page 20151098. The Royal Society.

Piper, A. T., Svendsen, J. C., Wright, R. M., and Kemp, P. S. (2017). Movement patterns of seaward migrating european eel (*Anguilla anguilla*) at a complex of riverine barriers: implications for conservation. *Ecology of Freshwater Fish*, 26(1):87–98.

Piper, A. T., Wright, R. M., and Kemp, P. S. (2012). The influence of attraction flow on upstream passage of european eel (*Anguilla anguilla*) at intertidal barriers. *Ecological Engineering*, 44:329–336.

Plymesser, K. and Cahoon, J. (2017). Pressure gradients in a steeppass fishway using a computational fluid dynamics model. *Ecological Engineering*, 108:277–283.

Plymesser, K. E. (2014). *Modeling fish passage and energy expenditure for American Shad in a steeppass fishway using computational fluid dynamics model.* Unpublished PhD Thesis. Montana State University, Bozman, Montana.

Podgorniak, T., Angelini, A., Blanchet, S., De Oliveira, E., Pierron, F., and Daverat, F. (2015a). Climbing experience in glass eels: A cognitive task or a matter of physical capacities? *Physiology & Behavior*, 151:448–455.

Podgorniak, T., Blanchet, S., De Oliveira, E., Daverat, F., and Pierron, F. (2016). To boldly climb: behavioural and cognitive differences in migrating European glass eels. *Royal Society open science*, 3(1):150665.

Podgorniak, T., Milan, M., Pujolar, J. M., Maes, G. E., Bargelloni, L., De Oliveira, E., Pierron, F., and Daverat, F. (2015b). Differences in brain gene transcription profiles advocate for an important role of cognitive function in upstream migration and water obstacles crossing in European eel. *BMC genomics*, 16(1):378.

Poole, W. R. and Reynolds, J. D. (1998). Variability in growth rate in European eel *anguilla anguilla (l.)* in a western Irish catchment. In *Biology and Environment: Proceedings of the Royal Irish Academy*, pages 141–145. JSTOR.

Popper, A. N., Fay, R. R., Platt, C., and Sand, O. (2003). Sound detection mechanisms and capabilities of teleost fishes. In Collin, S. P. and Marshall, N. J., editors, *Sensory processing in aquatic environments*, pages 3–38. Springer, Berlin.

Popper, A. N., Ramcharitar, J., and Campana, S. E. (2005). Why otoliths? Insights from inner ear physiology and fisheries biology. *Marine and freshwater Research*, 56(5):497–504.

Porcher, J. (2002). Fishways for eels. *Bulletin Français de la Pêche et de la Pisciculture*, (364):147–155.

Pyke, G. H. (1984). Optimal foraging theory: a critical review. *Annual review of ecology and systematics*, 15(1):523–575.

Quaranta, E., Comoglio, C., Christos, K., and Roberto, R. (2016). Numerical simulations of flow field in vertical slot fishways. Dipartimento Ingegneria Civile, Chimica, Ambientale E Dei Materiali, Università di Bologna, Bologna.

Quaranta, E., Katopodis, C., Revelli, R., and Comoglio, C. (2017). Turbulent flow field comparison and related suitability for fish passage of a standard and a simplified low-gradient vertical slot fishway. *River Research and Applications*.

Quaresma, A. and Pinheiro, A. (2014). Analysis of flows in pool-type fishways using acoustic doppler velocimetry (ADV) and computational fluid dynamics (CFD). Presented at 10th International Symposium on Ecohydraulics, Trondheim, Norway.

Quinn, T. P. (2018). *The behavior and ecology of Pacific salmon and trout*. University of Washington Press.

Rajaratnam, N., Katopodis, C., and Mainali, A. (1988). Plunging and streaming flows in pool and weir fishways. *Journal of Hydraulic Engineering*, 114(8):939–944.

Rajaratnam, N., Katopodis, C., and Solanki, S. (1992). New designs for vertical slot fishways. *Canadian Journal of Civil Engineering*, 19(3):402–414.

Rajaratnam, N., Van der Vinne, G., and Katopodis, C. (1986). Hydraulics of vertical slot fishways. *Journal of Hydraulic Engineering*, 112(10):909–927.

Randall, D. and Daxboeck, C. (1984). Oxygen and carbon dioxide transfer across fish gills. In *Fish physiology*, volume 10, pages 263–314. Elsevier.

Rayleigh, L. (1905). The problem of the random walk. *Nature*, 72(1866):318.

Rennie, C. D. (2008). Uncertainty of ADCP spatial velocity distributions. In *Proceedings of the 6th International Symposium on Ultrasonic Doppler Method for Fluid Mechanics and Fluid Engineering, Prague, Czech Republic*, volume 911, page 147150.

Rodriguez, A., Bermudez, M., Rabunal, J. R., and Puertas, J. (2015). Fish tracking in vertical slot fishways using computer vision techniques. *Journal of Hydroinformatics*, 17(2):275–292.

Rodriguez, Á., Bermúdez, M., Rabuñal, J. R., Puertas, J., Dorado, J., Pena, L., and Balairón, L. (2011). Optical fish trajectory measurement in fishways through computer vision and artificial neural networks. *Journal of Computing in Civil Engineering*, 25(4):291–301.

Rodriguez, J. F., Bombardelli, F. A., Garcia, M. H., Frothingham, K. M., Rhoads, B. L., and Abad, J. D. (2004). High-resolution numerical simulation of flow through a highly sinuous river reach. *Water Resources Management*, 18(3):177–199.

Rodríguez, T. T., Agudo, J. P., Mosquera, L. P., and González, E. P. (2006). Evaluating vertical-slot fishway designs in terms of fish swimming capabilities. *Ecological Engineering*, 27(1):37–48.

Roscoe, D., Hinch, S., Cooke, S., and Patterson, D. (2011). Fishway passage and post-passage mortality of up-river migrating Sockeye Salmon in the Seton River, British Columbia. *River Research and Applications*, 27(6):693–705.

Roscoe, D. W. and Hinch, S. G. (2010). Effectiveness monitoring of fish passage facilities: Historical trends, geographic patterns and future directions. *Fish and Fisheries*, 11(1):12–33.

Rudnick, D. A., Ryan, S. J., Beier, P., Cushman, S. A., Dieffenbach, F., Epps, C. W., Gerber, L. R., Hartter, J., Jenness, J. S., Kintsch, J., et al. (2012). The role of landscape connectivity in planning and implementing conservation and restoration priorities. *Issues in Ecology. 16 (Fall): 1-20.*, pages 1–20.

Russell, W. and Burch, R. (1992). *Principles of humane experimental technique*. Methuen, Online.

Russon, I., Kemp, P., and Lucas, M. (2011). Gauging weirs impede the upstream migration of adult river lamprey *Lampetra fluviatilis*. *Fisheries Management and Ecology*, 18(3):201–210.

Sagaut, P. (2006). *Large eddy simulation for incompressible flows: an introduction*. Springer Science & Business Media.

Saloniemi, I., Jokikokko, E., Kallio-Nyberg, I., Jutila, E., and Pasanen, P. (2004). Survival of reared and wild Atlantic salmon smolts: size matters more in bad years. *ICES Journal of Marine Science: Journal du Conseil*, 61(5):782–787.

Sarker, M. and Rhodes, D. (2004). Calculation of free-surface profile over a rectangular broad-crested weir. *Flow measurement and Instrumentation*, 15(4):215–219.

Schumaker, N. H. (1996). Using landscape indices to predict habitat connectivity. *Ecology*, 77(4):1210–1225.

Scruton, D., Goosney, R., McKinley, R., Booth, R., and Peake, S. (1998). Evaluation of swimming capability and potential velocity barrier problems for fish. part a: Swimming performance of selected warm and cold water fish species relative to fish passage and fishway design. Fisheries and Oceans Canada.

Serrano, I., Larsson, S., and Eriksson, L.-O. (2009). Migration performance of wild and hatchery sea trout (*Salmo trutta L.*) smolts - Implications for compensatory hatchery programs. *Fisheries Research*, 99(3):210 – 215.

Shepard, E. L., Wilson, R. P., Rees, W. G., Grundy, E., Lambertucci, S. A., and Vosper, S. B. (2013). Energy landscapes shape animal movement ecology. *The American Naturalist*, 182(3):298–312.

Shotzberger, S. and Strait, K. (2002). Successful migration of juvenile American eels (*Anguilla rostrata*) at two experimental eel ladders on small Delaware impoundments. 132nd Annual Meeting of the American Fisheries Society, Baltimore, MD.

Silva, A., Katopodis, C., Tachie, M., Santos, J., and Ferreira, M. (2016). Downstream swimming behaviour of catadromous and potamodromous fish over spillways. *River Research and Applications*, 32(5):935–945.

Silva, A., Santos, J., Ferreira, M., Pinheiro, A., and Katopodis, C. (2010). Passage efficiency of offset and straight orifices for upstream movements of Iberian barbel in a pool-type fishway. *River research and applications*, 28(5):529–542.

Silva, A., Santos, J., Franco, A., Ferreira, M., and Pinheiro, A. (2009). Selection of Iberian barbel *Barbus bocagei* (steindachner, 1864) for orifices and notches upon different hydraulic configurations in an experimental pool-type fishway. *Journal of Applied Ichthyology*, 25(2):173–177.

Silva, A. T., Katopodis, C., Santos, J. M., Ferreira, M. T., and Pinheiro, A. N. (2012). Cyprinid swimming behaviour in response to turbulent flow. *Ecological Engineering*, 44:314–328.

Silva, A. T., Lucas, M. C., Castro-Santos, T., Katopodis, C., Baumgartner, L. J., Thiem, J. D., Aarestrup, K., Pompeu, P. S., O'Brien, G. C., Braun, D. C., et al. (2018). The future of fish passage science, engineering, and practice. *Fish and Fisheries*, 19(2):340–362.

Silva, A. T., Santos, J. M., Ferreira, M. T., Pinheiro, A. N., and Katopodis, C. (2011). Effects of water velocity and turbulence on the behaviour of Iberian barbel (*Luciobarbus bocagei*, Steindachner 1864) in an experimental pool-type fishway. *River Research and Applications*, 27(3):360–373.

Smagorinsky, J. (1963). General circulation experiments with the primitive equations: I. the basic experiment. *Monthly weather review*, 91(3):99–164.

Smith, D. L., Brannon, E. L., and Odeh, M. (2005). Response of juvenile rainbow trout to turbulence produced by prismatoidal shapes. *Transactions of the American Fisheries Society*, 134(3):741–753.

Smith, D. L., Brannon, E. L., Shafii, B., and Odeh, M. (2006). Use of the average and fluctuating velocity components for estimation of volitional rainbow trout density. *Transactions of the American Fisheries Society*, 135(2):431–441.

Solomon, D. and Beach, M. (2004). Fish pass design for Eel and Elver (*Anguilla anguilla*). *R&D Technical Report W2-070TR*. Environment Agency RND report. UK Government Publishing House, London.

SonTek (2011). RiverSurveyor S5/M9 System Manual Firmware Version 2.00. Available at https://www.tttenviro.com/wp-content/uploads/Manual-M9-Acoustic-Doppler-Profiler-ADP.pdf. [Accessed 12/06/2020].

Speziale, C. G. and Thangam, S. (1992). Analysis of an RNG based turbulence model for separated flows.

Stamou, A. I., Mitsopoulos, G., Rutschmann, P., and Bui, M. D. (2018). Verification of a 3D CFD model for vertical slot fish-passes. *Environmental Fluid Mechanics*, 18(6):1435–1461.

Stanley, E. H. and Doyle, M. W. (2003). Trading off: The ecological effects of dam removal. *Frontiers in Ecology and the Environment*, 1(1):15–22.

Strand, E., Jørgensen, C., and Huse, G. (2005). Modelling buoyancy regulation in fishes with swimbladders: bioenergetics and behaviour. *Ecological Modelling*, 185(2-4):309–327.

Swamee, P. K. (1988). Generalized rectangular weir equations. *Journal of Hydraulic Engineering*, 114(8):945–949.

Tan, J., Tao, L., Gao, Z., Dai, H., and Shi, X. (2018). Modeling fish movement trajectories in relation to hydraulic response relationships in an experimental fishway. *Water*, 10(11):1511.

Tang, W. and Bennett, D. A. (2010). Agent-based modeling of animal movement: A review. *Geography Compass*, 4(7):682–700.

Tansley, C. E. and Marshall, D. P. (2001). Flow past a cylinder on a β plane, with application to gulf stream separation and the antarctic circumpolar current. *Journal of Physical Oceanography*, 31(11):3274–3283.

Terraqua Environmental Solutions (2017). Terraqua: Eel Substrates. Available at http://terraqua-es.co.uk/fish-pass/eel-substrates/. [Accessed 07/02/17].

Tesch, F. (2004). The Eel. *Journal of Fish Biology*, 65(3):893–893. Edited by J. E. Thorpe.

The World Commission on Dams (2000). *Dams and Development: A New Framework for Decision-making : the Report of the World Commission on Dams*. Earthscan.

Thorstad, E. B., Økland, F., Aarestrup, K., and Heggberget, T. G. (2008). Factors affecting the within-river spawning migration of Atlantic salmon, with emphasis on human impacts. *Reviews in Fish Biology and Fisheries*, 18(4):345–371.

Tong, F., Cheng, L., Zhao, M., Zhou, T., and Chen, X.-b. (2014). The vortex shedding around four circular cylinders in an in-line square configuration. *Physics of Fluids*, 26(2):024112.

Tonkin, J. D., David, B. O., and Brooke, N. (2013). Some morphometric measurements of juvenile rainbow trout (*Oncorhynchus mykiss*) and inanga (*Galaxias maculatus*) relevant to fish passage remediation.

Tran, T. D., Chorda, J., Laurens, P., and Cassan, L. (2016). Modelling nature-like fishway flow around unsubmerged obstacles using a 2D shallow water model. *Environmental Fluid Mechanics*, 16(2):413–428.

Tucker, V. A. et al. (1970). Energetic cost of locomotion in animals. *Comparative Biochemistry and Physiology*, 34:841–846.

Tullos, D. and Walter, C. (2015). Fish use of turbulence around wood in winter: physical experiments on hydraulic variability and habitat selection by juvenile Coho salmon, *Oncorhynchus kisutch*. *Environmental Biology of Fishes*, 98(5):1339–1353.

Turner, M. G. (1989). Landscape ecology: the effect of pattern on process. *Annual review of ecology and systematics*, 20(1):171–197.

University of Hull (2020). VIPER. High Performance Computing. Available at `http://hpc.wordpress.hull.ac.uk/`. [Accessed 11/06/2020].

van Ginneken, V. J. and Maes, G. E. (2005). The european eel (Anguilla anguilla, linnaeus), its lifecycle, evolution and reproduction: A literature review. *Reviews in Fish Biology and Fisheries*, 15(4):367–398.

van Puijenbroek, P. J., Buijse, A. D., Kraak, M. H., and Verdonschot, P. F. (2019). Species and river specific effects of river fragmentation on european anadromous fish species. *River Research and Applications*, 35(1):68–77.

Versteeg, H. K. and Malalasekera, W. (2007). *An introduction to computational fluid dynamics: the finite volume method*. Pearson education.

Voegtle, B. and Larinier, M. (2000). Etude sur les capacités de franchissement des civelles et anguillettes: Site hydroélectrique de Tuilières sur la Dordogne (24) barrage estuarien d'Arzal sur la Vilaine (56). Groupe d'Hydraulique AppliquÃ©e aux AmÃ©nagements Piscicoles et Ã la Protection de l'Environnement (GHAAPPE).

Vogel, S. (1994). *Life in Moving Fluids: The Physical Biology of Flow*. Princeton paperbacks. Princeton University Press.

Vowles, A. S., Don, A., Karageorgopoulos, P., Worthington, T., and Kemp, P. (2015). Efficiency of a dual density studded fish pass designed to mitigate for impeded upstream passage of juvenile European eels (*Anguilla anguilla*) at a model Crump weir. *Fisheries Management and Ecology*, 22(4):307–316.

Wall, J., Douglas-Hamilton, I., and Vollrath, F. (2006). Elephants avoid costly mountaineering. *Current Biology*, 16(14):R527–R529.

Wanke, T., Brämick, U., and Mehner, T. (2016). Early detection of reproduction deficits and the compensatory potential of enhancement stocking for vendace, *Coregonus albula*, fisheries in German lakes. *Fisheries Management and Ecology*, 23(1):55–65.

Watson, D. F. (1981). Computing the n-dimensional Delaunay tessellation with application to Voronoi polytopes. *The computer journal*, 24(2):167–172.

Webb, P. (1971a). The swimming energetics of trout: Ii. oxygen consumption and swimming efficiency. *Journal of Experimental Biology*, 55(2):521–540.

Webb, P. (1975). *Hydrodynamics and Energetics of Fish Propulsion*. Bulletin (Fisheries Research Board of Canada). Department of the Environment Fisheries and Marine Service.

Webb, P. W. (1971b). The swimming energetics of trout: I. thrust and power output at cruising speeds. *Journal of experimental biology*, 55(2):489–520.

Weber, E. D. and Fausch, K. D. (2003). Interactions between hatchery and wild salmonids in streams: Differences in biology and evidence for competition. *Canadian Journal of Fisheries and Aquatic Sciences*, 60(8):1018–1036.

Weber, L. J., Goodwin, R. A., Li, S., Nestler, J. M., and Anderson, J. J. (2006). Application of an Eulerian–Lagrangian–Agent method (ELAM) to rank alternative designs of a juvenile fish passage facility. *Journal of Hydroinformatics*, 8(4):271–295.

Weichert, R., Kampke, W., Deutsch, L., and Scholten, M. (2013). Zur frage der dotationswassermenge von fisch auf stiegs anlagen an großen fließgewässern. *Biologische Durchgängigkeit von Fließgewässern*, page 111.

White, C. and Nemenyi, P. (1942). Report on hydraulic research on fish passes. *Report of the Committee on Fish Passes.*, pages 32–61. Clowes and Sons, London, UK.

Wilcox, D. C. (1988). Reassessment of the scale-determining equation for advanced turbulence models. *AIAA journal*, 26(11):1299–1310.

Wilcox, D. C. (1993). Turbulence modeling. *DCW Industries*.

Williams, J. G., Armstrong, G., Katopodis, C., Larinier, M., and Travade, F. (2012). Thinking like a fish: A key ingredient for development of effective fish passage facilities at river obstructions. *River Research and Applications*, 28(4):407–417.

Williams, J. G., Smith, S. G., Zabel, R., Muir, W., Scheuerell, M., Sandford, B., Marsh, D. M., McNatt, R., and Achord, S. (2005). Effects of the Federal Columbia River power system on salmon populations. *NOAA Technical Memorandum, NMFS-NWFSC*, 63.

Wilson, R. P., Quintana, F., and Hobson, V. J. (2012). Construction of energy landscapes can clarify the movement and distribution of foraging animals. *Proceedings of the Royal Society B: Biological Sciences*, 279(1730):975–980.

Wu, S., Rajaratnam, N., and Katopodis, C. (1999). Structure of flow in vertical slot fishway. *Journal of Hydraulic Engineering*, 125(4):351–360.

Yakhot, V., Orszag, S., Thangam, S., Gatski, T., and Speziale, C. (1992). Development of turbulence models for shear flows by a double expansion technique. *Physics of Fluids A: Fluid Dynamics*, 4(7):1510–1520.

Youngs, D. (1982). Time-dependent multi-material flow with large fluid distortion. *Num. Method Fluid Dyn.*, 24:273–285.

Zhang, W., Qi, J., Wan, P., Wang, H., Xie, D., Wang, X., and Yan, G. (2016). An easy-to-use airborne lidar data filtering method based on cloth simulation. *Remote Sensing*, 8(6):501.

Zielinski, D., Voller, V. R., and Sorensen, P. W. (2018). A physiologically inspired agent-based approach to model upstream passage of invasive fish at a lock-and-dam. *Ecological Modelling*, 382:18–32.

Ziemer, G. (1962). Steeppass fishway development. Alaska Department of Fish and Game. Division of Engineering and Services. Informational Leaflet No. 12.

Zottoli, S. J. and Danielson, P. D. (1989). Lateral line afferent and efferent systems of the goldfish with special reference to the Mauthner cell. In Coombs, S., Görner, P., and Münz, H., editors, *The Mechanosensory Lateral Line*, pages 461–478. Springer, Berlin.

Appendices

Appendix A

Example Table of British Fish Species

Table A.1: A non-exhaustive list of example British freshwater fish species, their migration type, and the corresponding IUCN Red List status. Data compiled using the FishBase database [see Froese and Pauly 2019].

Common name	**Taxonomic name**	**IUCN Status**	**Family**	**Migration type**	**Habitation zone**
Allis shad	*Alosa alosa*	LC	Clupeidae	Anadromous	Pelagic-neritic
Atlantic salmon	*Salmo salar*	LC	Salmonidae	Anadromous	Benthopelagic
Brown Trout	*Salmo trutta*	LC	Salmonidae	Potamodromous	Benthopelagic
Bullhead	*Cottus gobio*	LC	Cottidae	Potamodromous	Demersal
Common Barbel	*Barbus barbus*	LC	Cyprinidae	Potamodromous	Benthopelagic
Common Bream	*Abramis brama*	LC	Cyprinidae	Potamodromous	Benthopelagic
Common Chub	*Squalius cephalus*	LC	Cyprinidae	Potamodromous	Benthopelagic
Crucian Carp	*Carassius carassius*	LC	Cyprinidae	Potamodromous	Demersal
Common Roach	*Rutilus rutilus*	LC	Cyprinidae	Potamodromous	Benthopelagic
European Brook lamprey	*Lampetra planeri*	LC	Petromyzontidae	Potamodromous	Demersal
European Eel	*Anguilla anguilla*	CR	Anguillidae	Catadromous	Benthic
Rainbow trout	*Oncorhynchus mykiss*	NE	Salmonidae	Anadromous	Benthopelagic
River lamprey	*Lampetra fluviatilis*	LC	Petromyzontidae	Anadromous	Demersal
Sea lamprey	*Petromyzon marinus*	LC	Petromyzontidae	Anadromous	Demersal
Sea Trout	*Salmo trutta**	LC	Salmonidae	Anadromous	Pelagic-neritic
Sturgeon	*Acipenser sturio*	CR	Acipenseridae	Anadromous	Demersal
Tench	*Tinca tinca*	LC	Cyprinidae	Potamodromous	Demersal

Appendix B

Supplementary Data for Predicting Passage of Juvenile Eels through Eel Tiles

B.1 Supplementary Binary Maps

This section presents additional binary maps for each configuration of eel pass for elver between 0.05 and 0.1 m bodylength for the 10%, 50%, and 90% burst swimming speed confidence intervals.

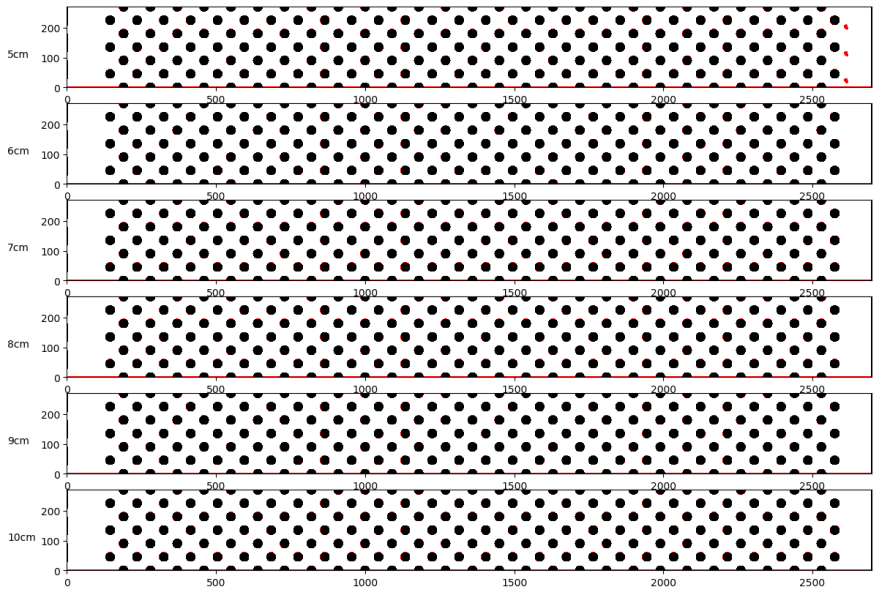

Figure B.1: Binary maps for an eel pass installed at 8° with a discharge per unit width of $1.6\dot{7}\times10^{-3}m^2s^{-1}$ for elver between 0.05 and 0.1 m bodylength, using the mean burst swimming speed.

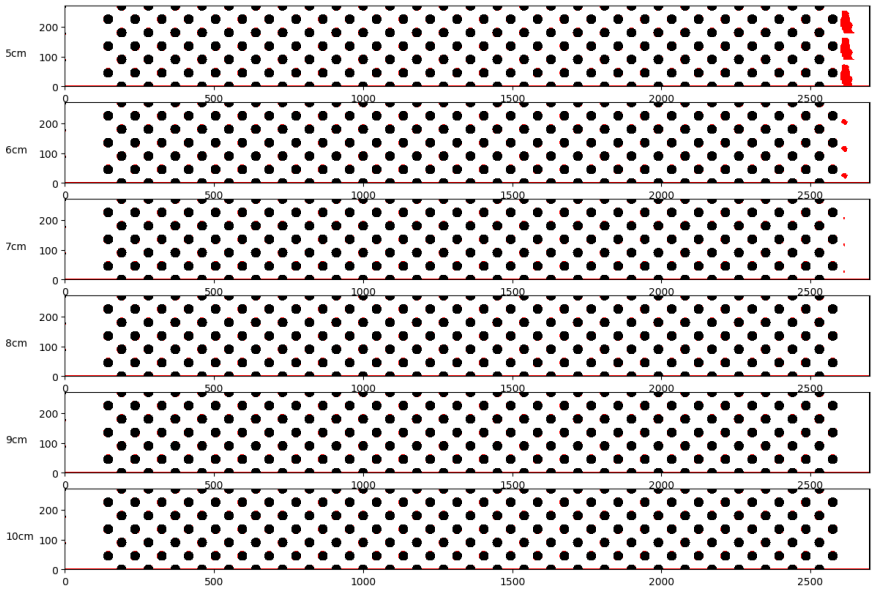

Figure B.2: Binary maps for an eel pass installed at 11° with a discharge per unit width of $1.6\dot{7}\times10^{-3}m^2s^{-1}$ for elver between 0.05 and 0.1 m bodylength, using the mean burst swimming speed.

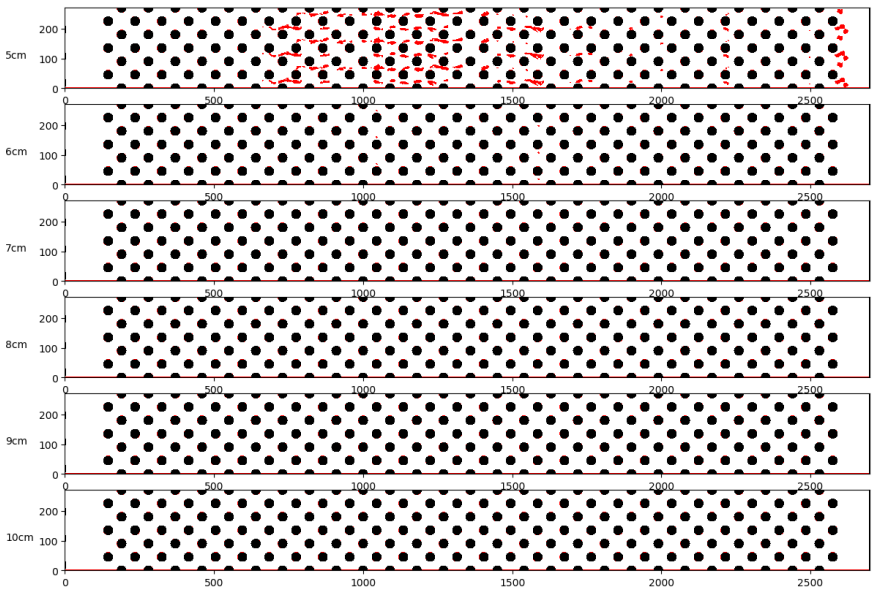

Figure B.3: Binary maps for an eel pass installed at 14° with a discharge per unit width of $1.6\dot{7}\times10^{-3}m^2s^{-1}$ for elver between 0.05 and 0.1 m bodylength, using the mean burst swimming speed.

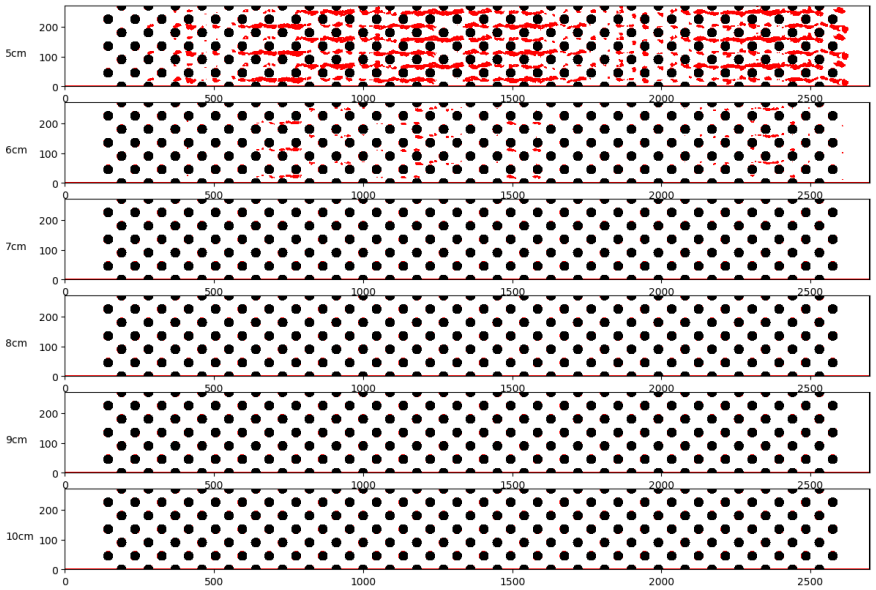

Figure B.4: Binary maps for an eel pass installed at 17° with a discharge per unit width of $1.6\dot{7}\times10^{-3}m^2s^{-1}$ for elver between 0.05 and 0.1 m bodylength, using the mean burst swimming speed.

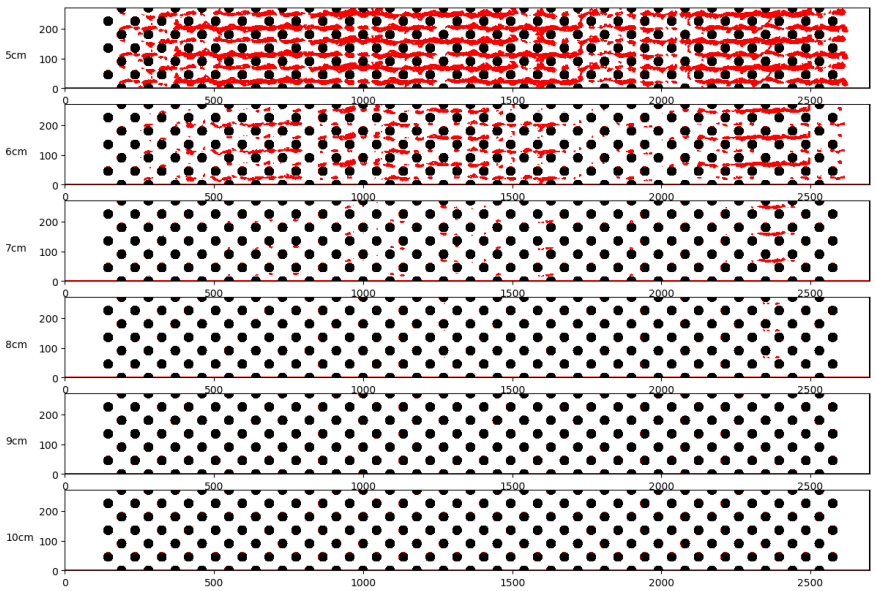

Figure B.5: Binary maps for an eel pass installed at 20° with a discharge per unit width of $1.6\dot{7}\times10^{-3}m^2s^{-1}$ for elver between 0.05 and 0.1 m bodylength, using the mean burst swimming speed.

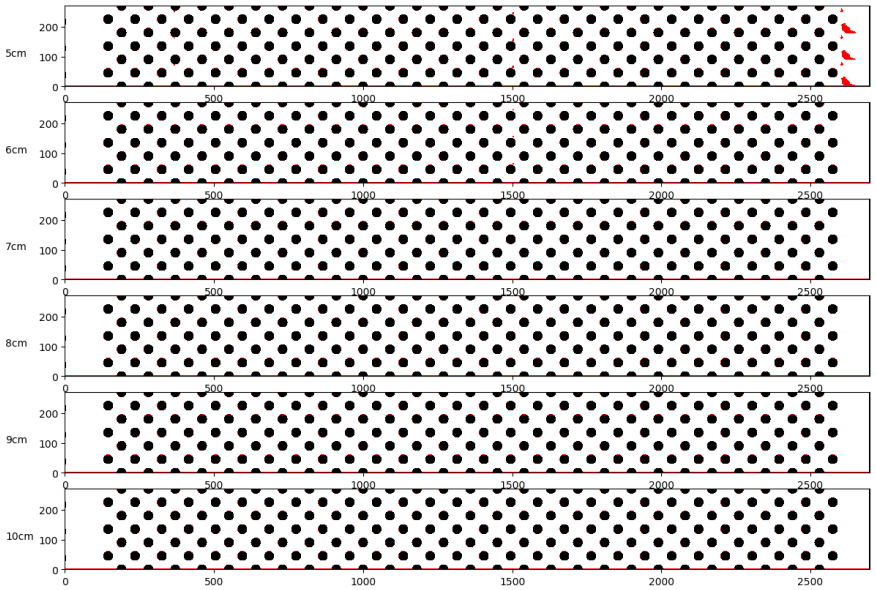

Figure B.6: Binary maps for an eel pass installed at 8° with a discharge per unit width of $3.3\dot{3}\times10^{-3}m^2s^{-1}$ for elver between 0.05 and 0.1 m bodylength, using the mean burst swimming speed.

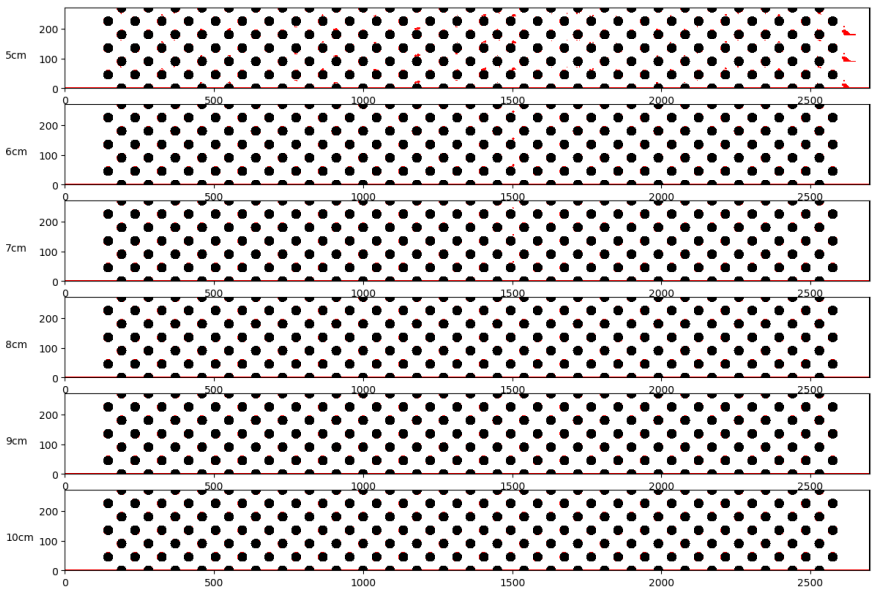

Figure B.7: Binary maps for an eel pass installed at 11° with a discharge per unit width of $3.3\dot{3}\times10^{-3}m^2s^{-1}$ for elver between 0.05 and 0.1 m bodylength, using the mean burst swimming speed.

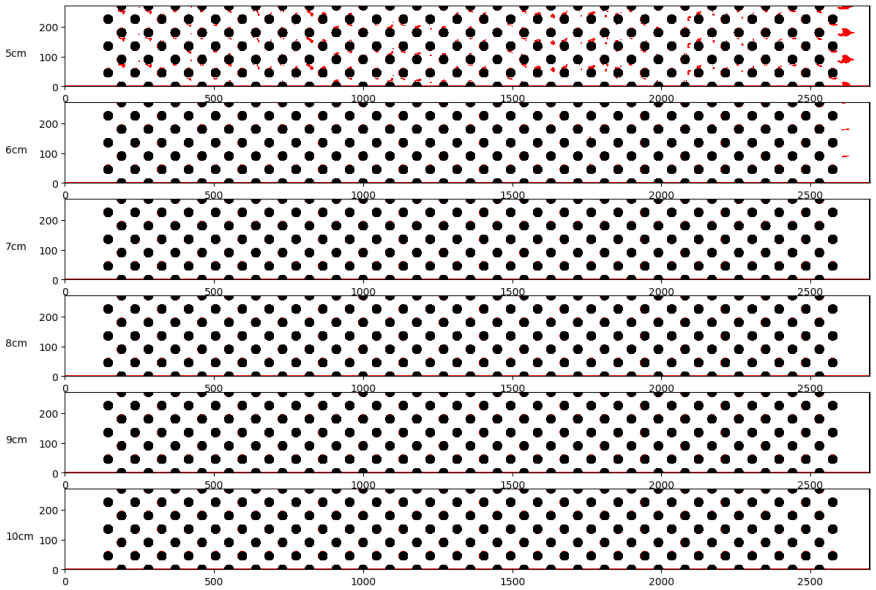

Figure B.8: Binary maps for an eel pass installed at 14° with a discharge per unit width of $3.3\dot{3}\times10^{-3}m^2s^{-1}$ for elver between 0.05 and 0.1 m bodylength, using the mean burst swimming speed.

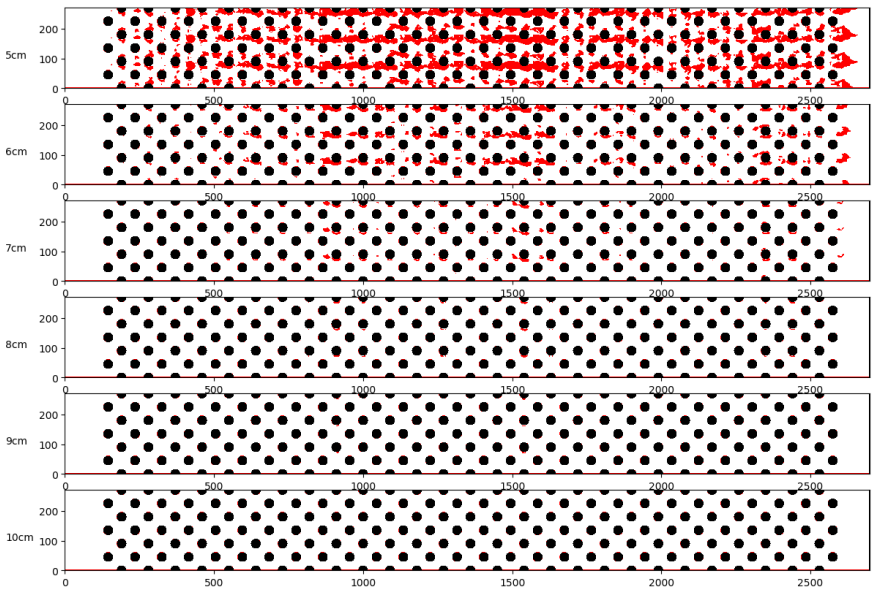

Figure B.9: Binary maps for an eel pass installed at 17° with a discharge per unit width of $3.3\dot{3}\times10^{-3}m^2s^{-1}$ for elver between 0.05 and 0.1 m bodylength, using the mean burst swimming speed.

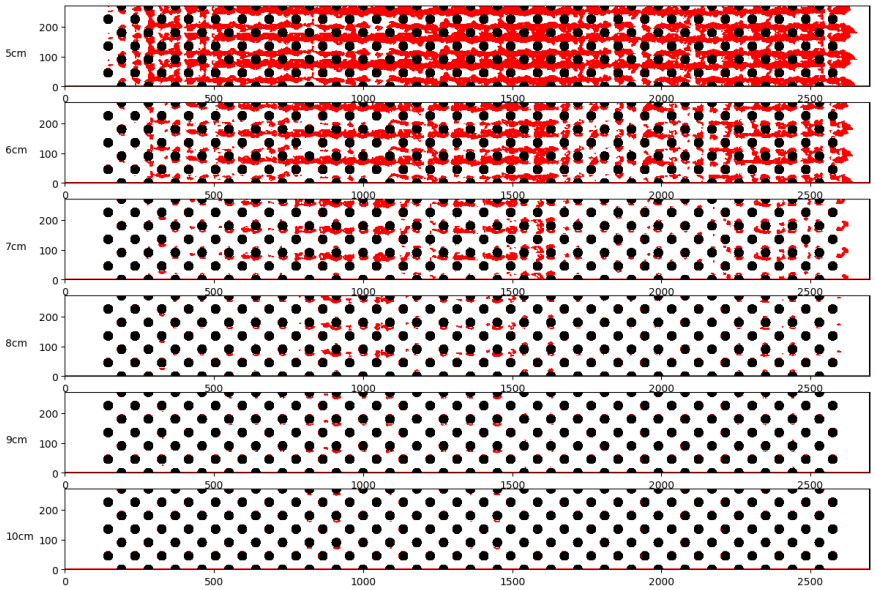

Figure B.10: Binary maps for an eel pass installed at 20° with a discharge per unit width of $3.3\dot{3}\times10^{-3}m^2s^{-1}$ for elver between 0.05 and 0.1 m bodylength, using the mean burst swimming speed.

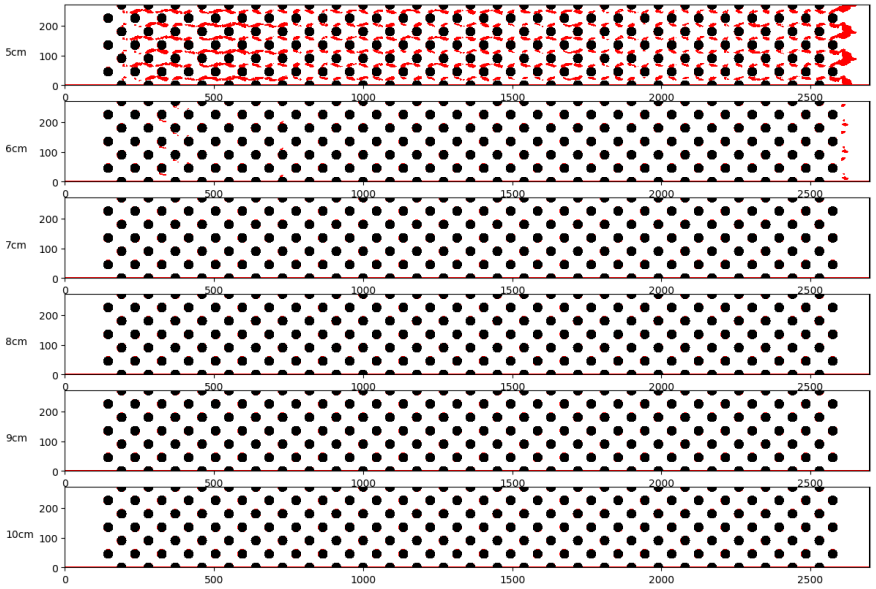

Figure B.11: Binary maps for an eel pass installed at 8° with a discharge per unit width of $5.0\times10^{-3}m^2s^{-1}$ for elver between 0.05 and 0.1 m bodylength, using the mean burst swimming speed.

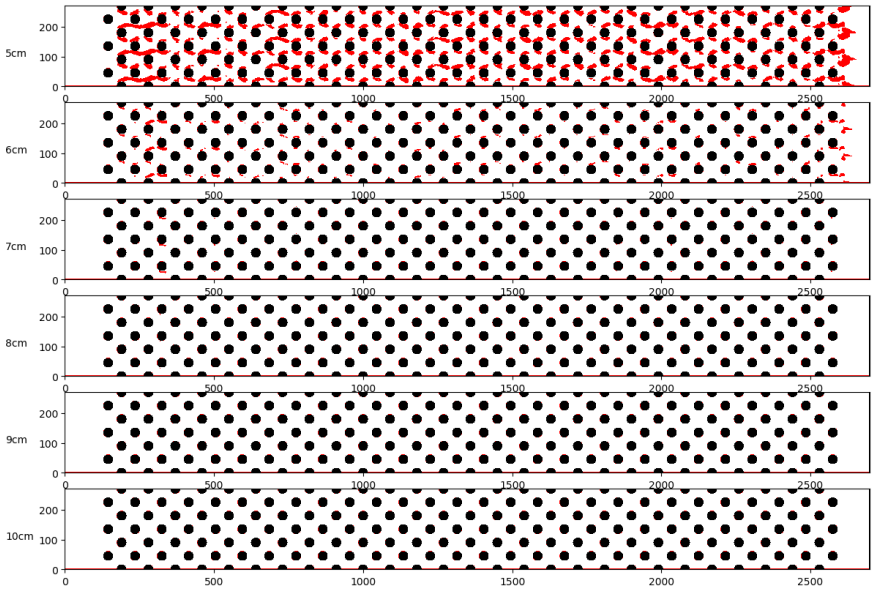

Figure B.12: Binary maps for an eel pass installed at 11° with a discharge per unit width of $5.0\times10^{-3}m^2s^{-1}$ for elver between 0.05 and 0.1 m bodylength, using the mean burst swimming speed.

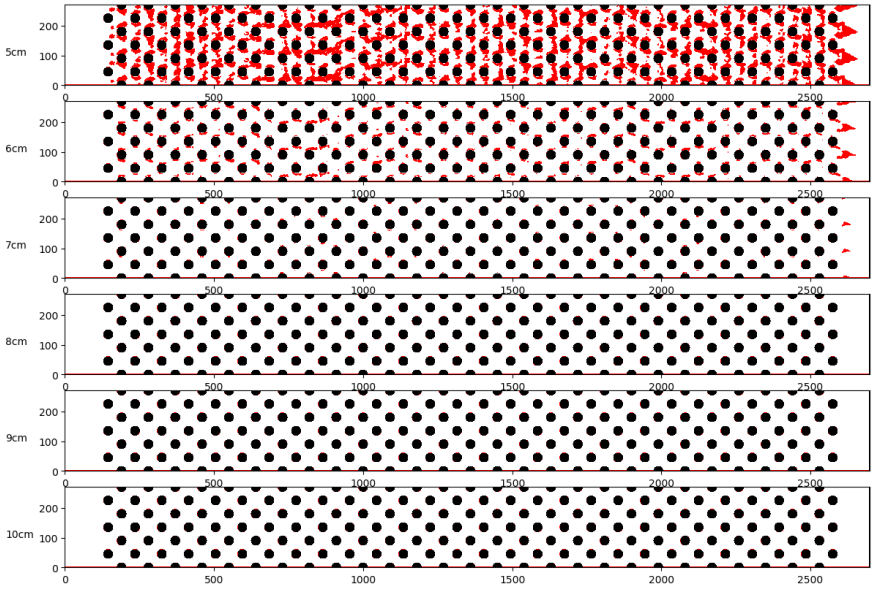

Figure B.13: Binary maps for an eel pass installed at 14° with a discharge per unit width of $5.0\times10^{-3}m^2s^{-1}$ for elver between 0.05 and 0.1 m bodylength, using the mean burst swimming speed.

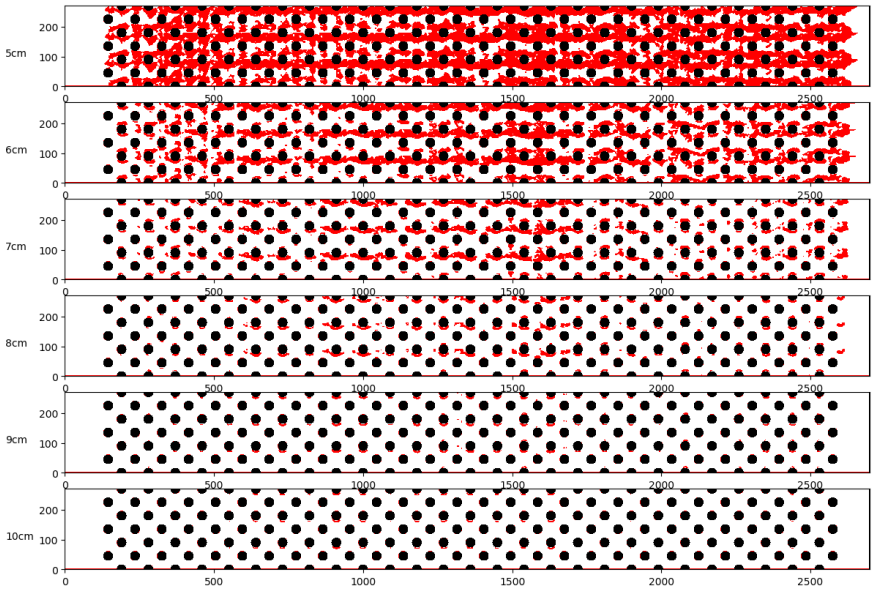

Figure B.14: Binary maps for an eel pass installed at 17° with a discharge per unit width of $5.0{\times}10^{-3}m^2s^{-1}$ for elver between 0.05 and 0.1 m bodylength, using the mean burst swimming speed.

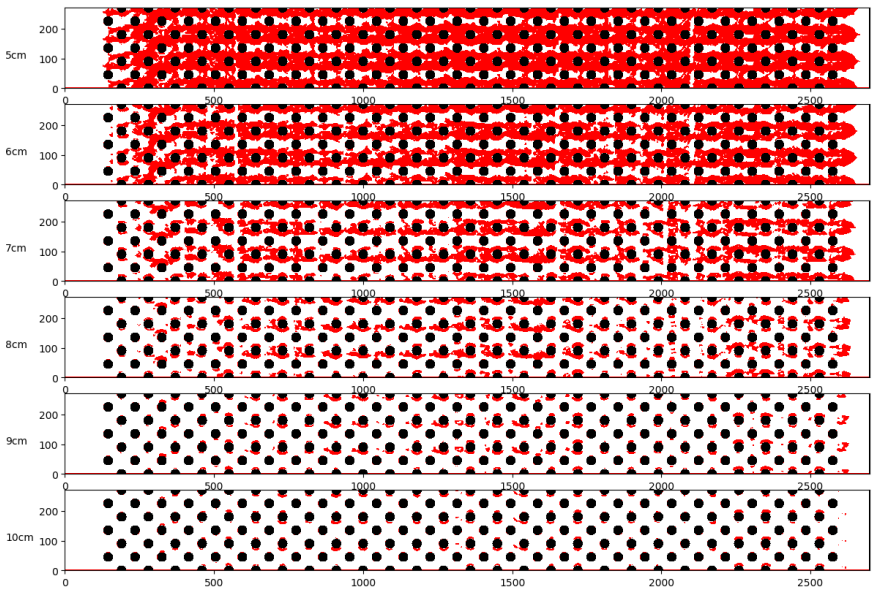

Figure B.15: Binary maps for an eel pass installed at 20° with a discharge per unit width of $5.0{\times}10^{-3}m^2s^{-1}$ for elver between 0.05 and 0.1 m bodylength, using the mean burst swimming speed.

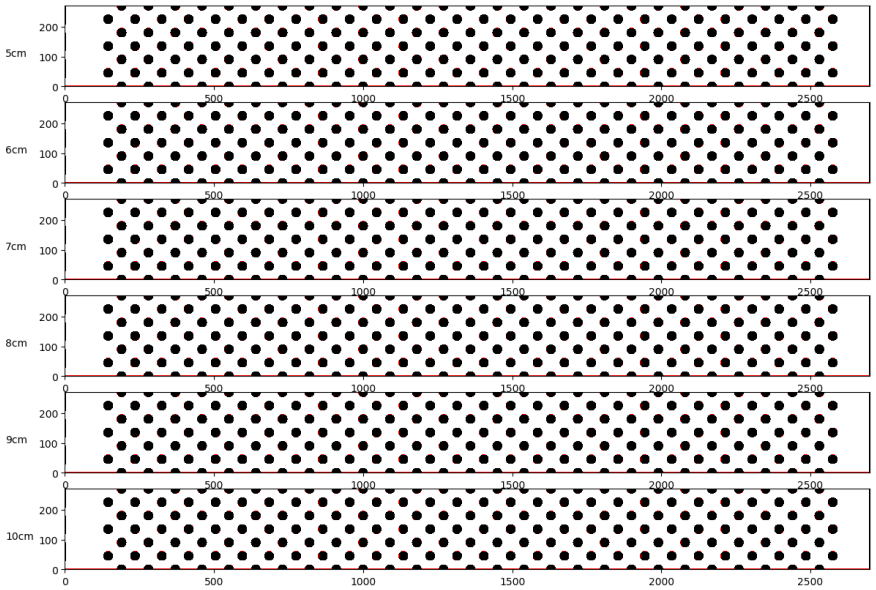

Figure B.16: Binary maps for an eel pass installed at 8° with a discharge per unit width of $1.6\dot{7}\times10^{-3}m^2s^{-1}$ for elver between 0.05 and 0.1 m bodylength, using the 10% confidence interval of the burst swimming speed.

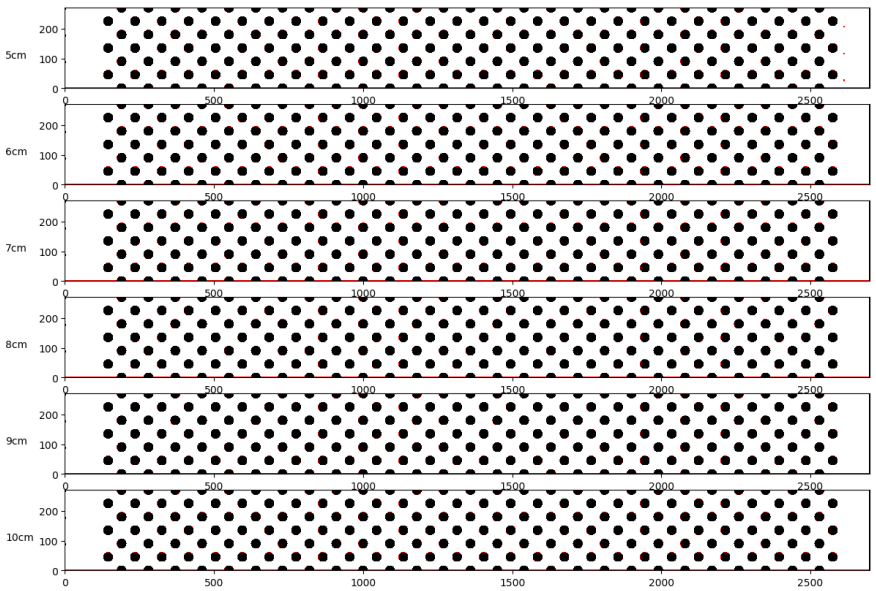

Figure B.17: Binary maps for an eel pass installed at 11° with a discharge per unit width of $1.6\dot{7}\times10^{-3}m^2s^{-1}$ for elver between 0.05 and 0.1 m bodylength, using the 10% confidence interval of the burst swimming speed.

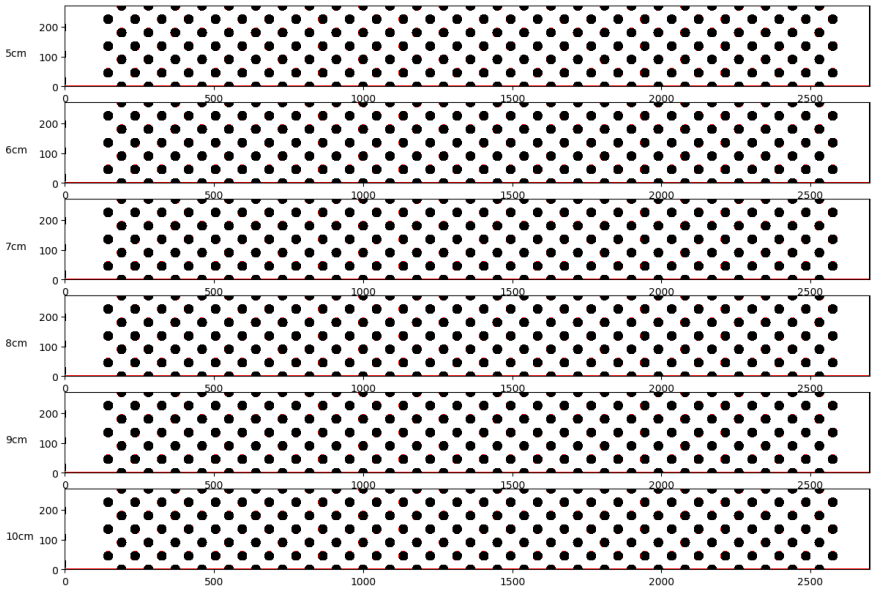

Figure B.18: Binary maps for an eel pass installed at 14° with a discharge per unit width of $1.6\dot{7}\times10^{-3}m^2s^{-1}$ for elver between 0.05 and 0.1 m bodylength, using the 10% confidence interval of the burst swimming speed.

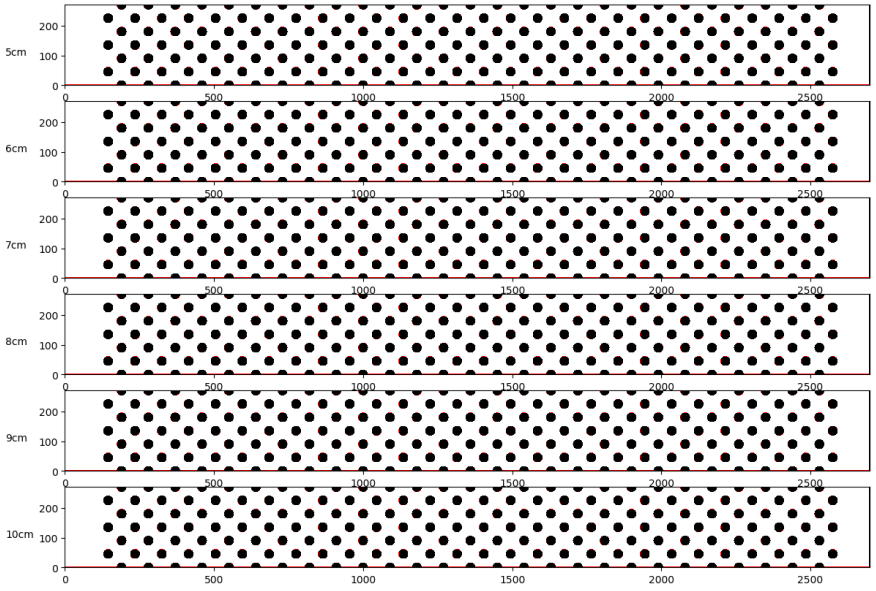

Figure B.19: Binary maps for an eel pass installed at 17° with a discharge per unit width of $1.6\dot{7}\times10^{-3}m^2s^{-1}$ for elver between 0.05 and 0.1 m bodylength, using the 10% confidence interval of the burst swimming speed.

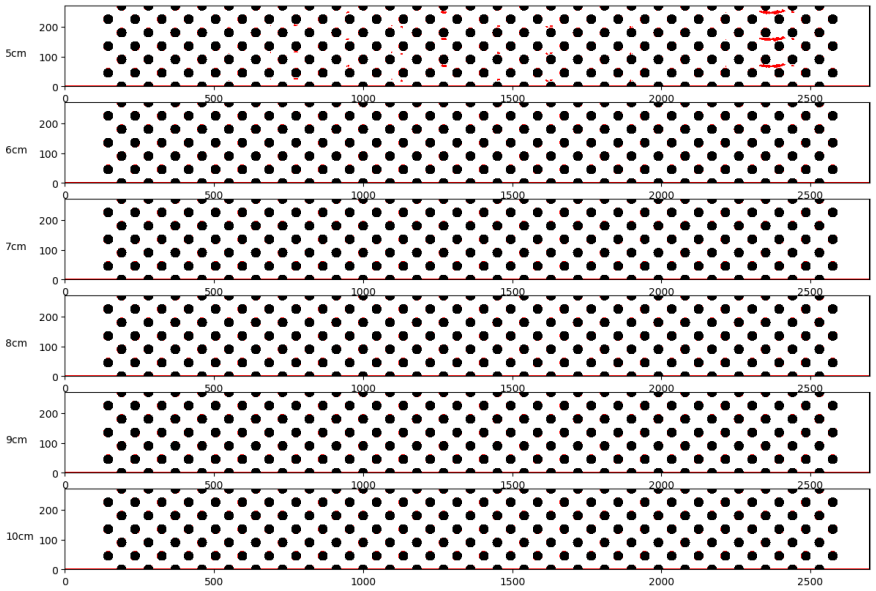

Figure B.20: Binary maps for an eel pass installed at 20° with a discharge per unit width of $1.6\dot{7}\times10^{-3}m^2s^{-1}$ for elver between 0.05 and 0.1 m bodylength, using the 10% confidence interval of the burst swimming speed.

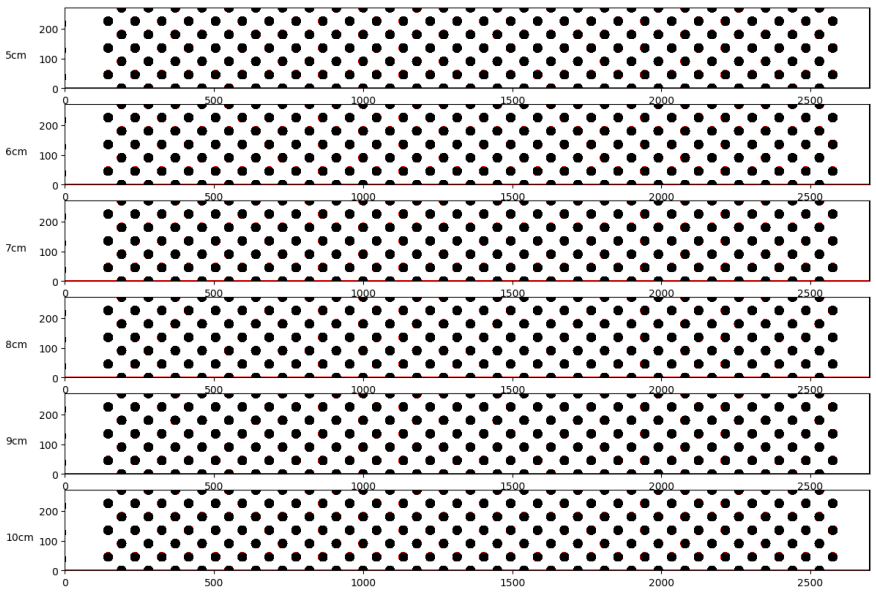

Figure B.21: Binary maps for an eel pass installed at 8° with a discharge per unit width of $3.3\dot{3}\times10^{-3}m^2s^{-1}$ for elver between 0.05 and 0.1 m bodylength, using the 10% confidence interval of the burst swimming speed.

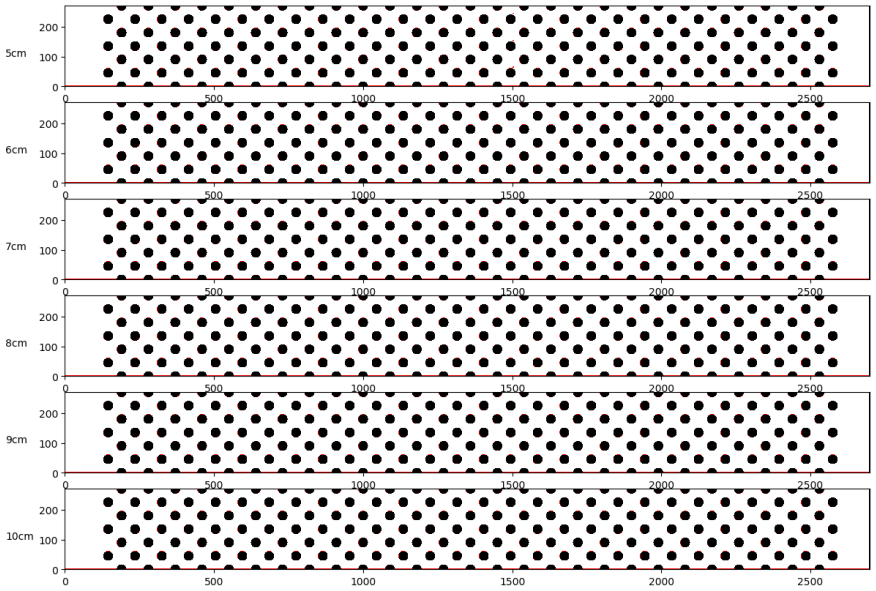

Figure B.22: Binary maps for an eel pass installed at 11° with a discharge per unit width of $3.3\dot{3}\times10^{-3}m^2s^{-1}$ for elver between 0.05 and 0.1 m bodylength, using the 10% confidence interval of the burst swimming speed.

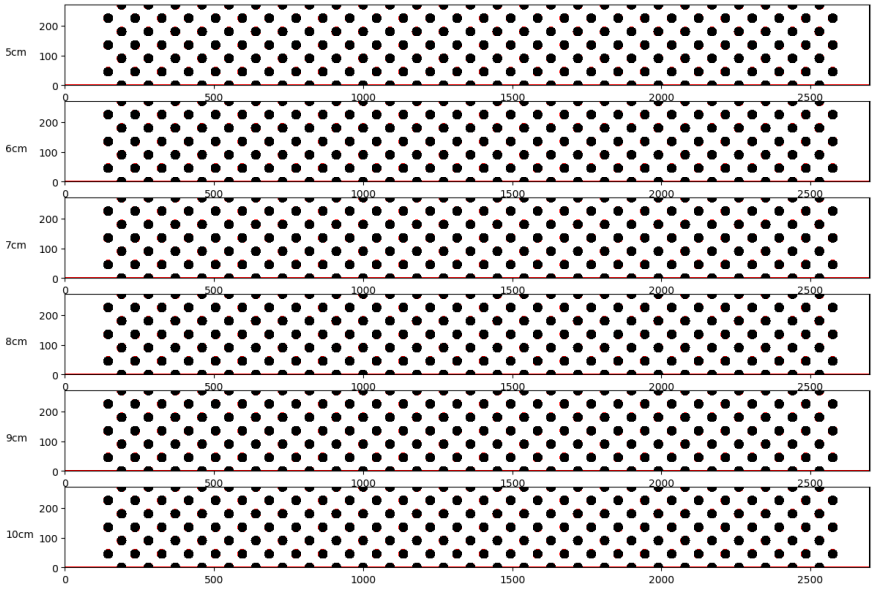

Figure B.23: Binary maps for an eel pass installed at 14° with a discharge per unit width of $3.3\dot{3}\times10^{-3}m^2s^{-1}$ for elver between 0.05 and 0.1 m bodylength, using the 10% confidence interval of the burst swimming speed.

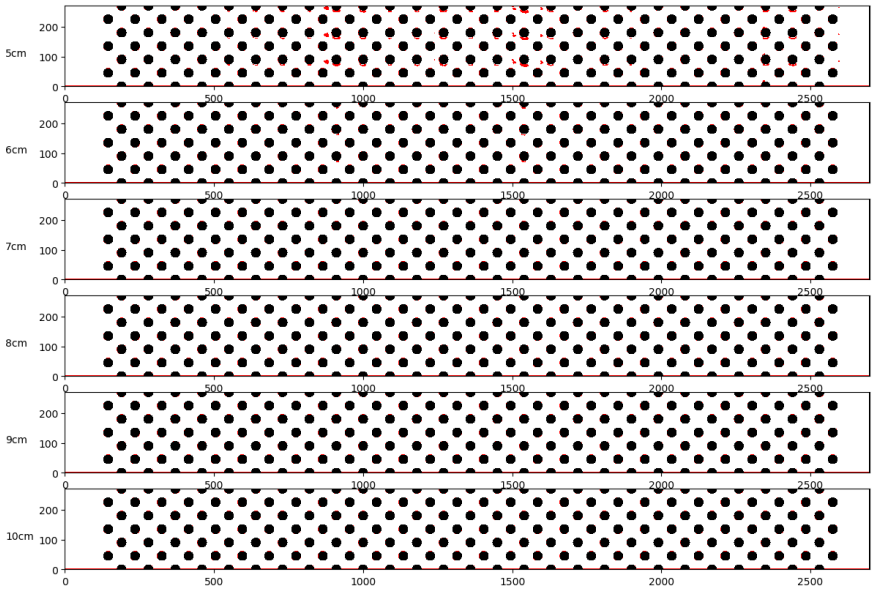

Figure B.24: Binary maps for an eel pass installed at 17° with a discharge per unit width of $3.3\dot{3}\times10^{-3}m^2s^{-1}$ for elver between 0.05 and 0.1 m bodylength, using the 10% confidence interval of the burst swimming speed.

Figure B.25: Binary maps for an eel pass installed at 20° with a discharge per unit width of $3.3\dot{3}\times10^{-3}m^2s^{-1}$ for elver between 0.05 and 0.1 m bodylength, using the 10% confidence interval of the burst swimming speed.

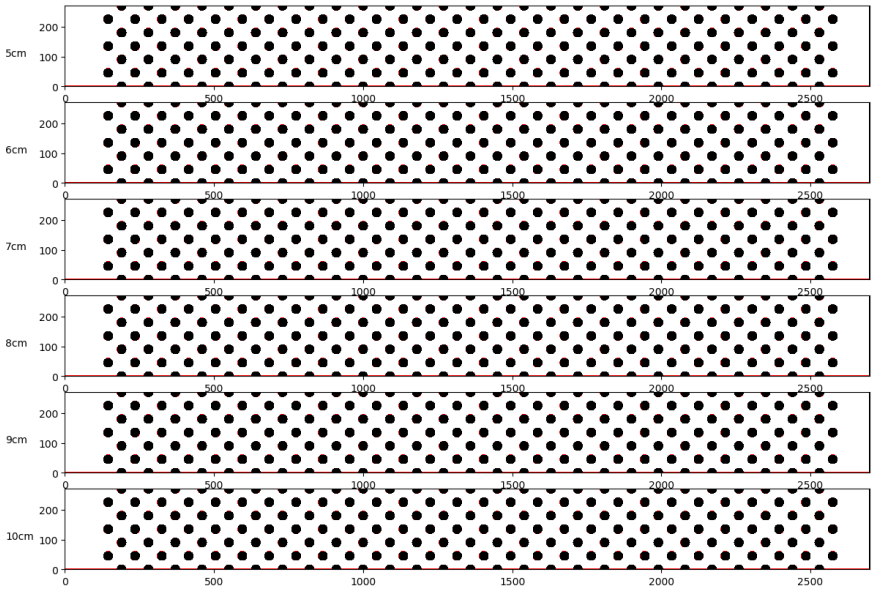

Figure B.26: Binary maps for an eel pass installed at 8° with a discharge per unit width of $5.0{\times}10^{-3} m^2 s^{-1}$ for elver between 0.05 and 0.1 m bodylength, using the 10% confidence interval of the burst swimming speed.

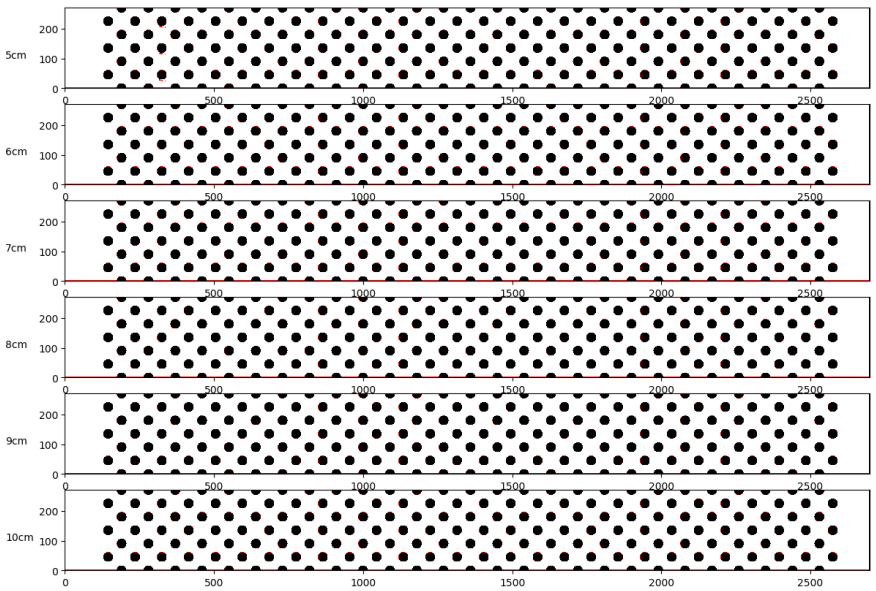

Figure B.27: Binary maps for an eel pass installed at 11° with a discharge per unit width of $5.0{\times}10^{-3} m^2 s^{-1}$ for elver between 0.05 and 0.1 m bodylength, using the 10% confidence interval of the burst swimming speed.

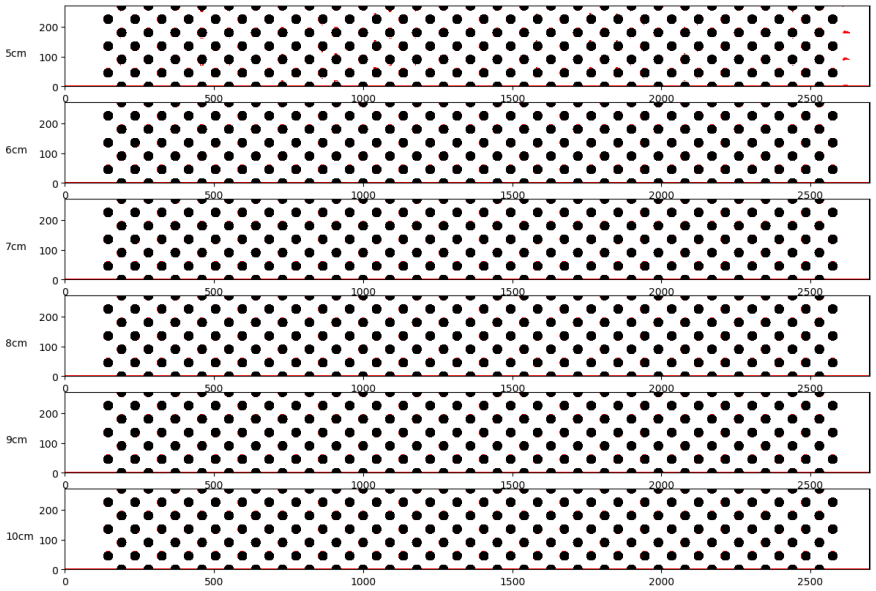

Figure B.28: Binary maps for an eel pass installed at 14° with a discharge per unit width of $5.0\times10^{-3}m^2s^{-1}$ for elver between 0.05 and 0.1 m bodylength, using the 10% confidence interval of the burst swimming speed.

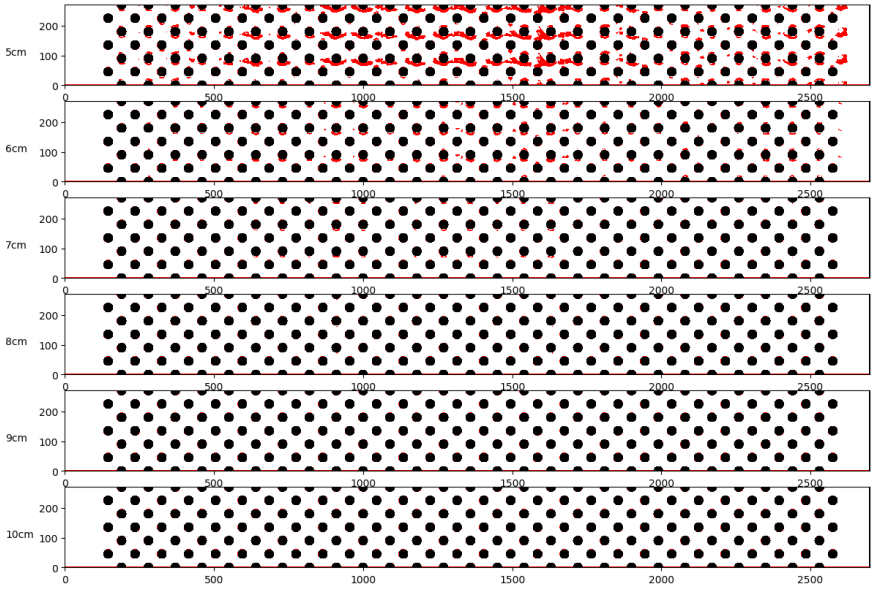

Figure B.29: Binary maps for an eel pass installed at 17° with a discharge per unit width of $5.0\times10^{-3}m^2s^{-1}$ for elver between 0.05 and 0.1 m bodylength, using the 10% confidence interval of the burst swimming speed.

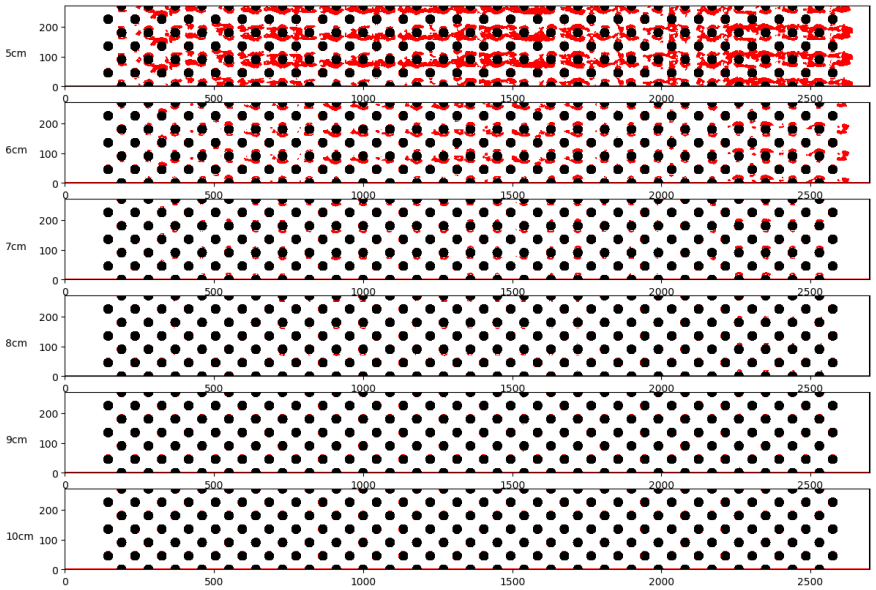

Figure B.30: Binary maps for an eel pass installed at 20° with a discharge per unit width of $5.0\times10^{-3}m^2s^{-1}$ for elver between 0.05 and 0.1 m bodylength, using the 10% confidence interval of the burst swimming speed.

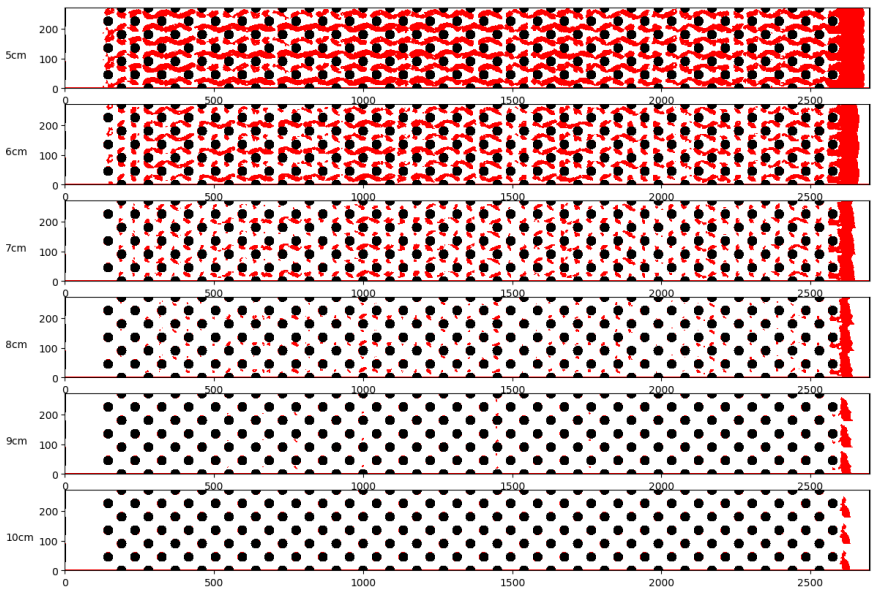

Figure B.31: Binary maps for an eel pass installed at 8° with a discharge per unit width of $1.6\dot{7}\times10^{-3}m^2s^{-1}$ for elver between 0.05 and 0.1 m bodylength, using the 90% confidence interval of the burst swimming speed.

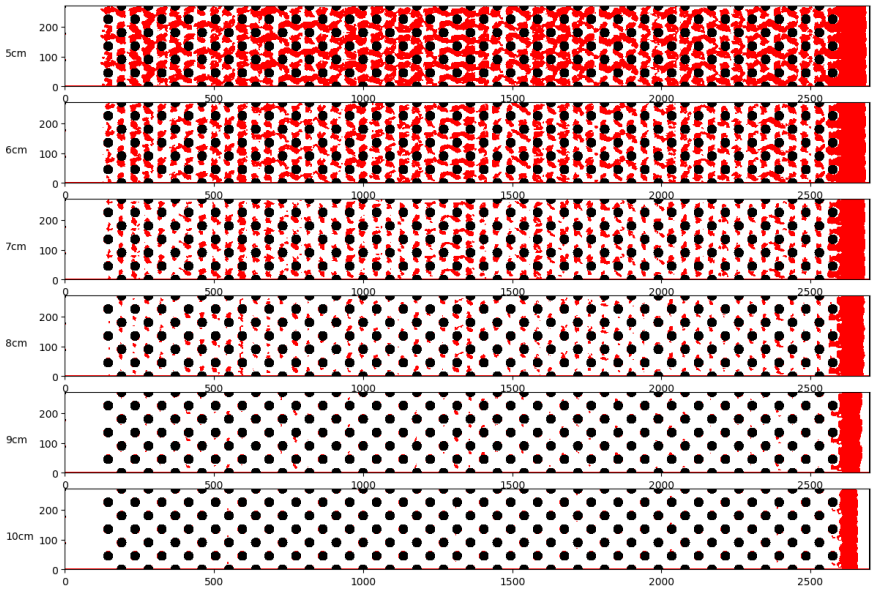

Figure B.32: Binary maps for an eel pass installed at 11° with a discharge per unit width of $1.6\dot{7}\times10^{-3}m^2s^{-1}$ for elver between 0.05 and 0.1 m bodylength, using the 90% confidence interval of the burst swimming speed.

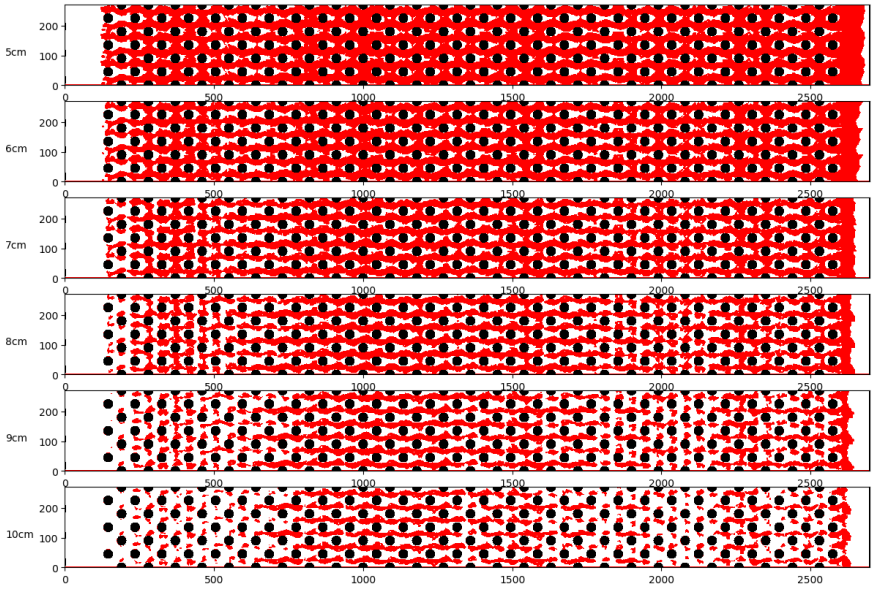

Figure B.33: Binary maps for an eel pass installed at 14° with a discharge per unit width of $1.6\dot{7}\times10^{-3}m^2s^{-1}$ for elver between 0.05 and 0.1 m bodylength, using the 90% confidence interval of the burst swimming speed.

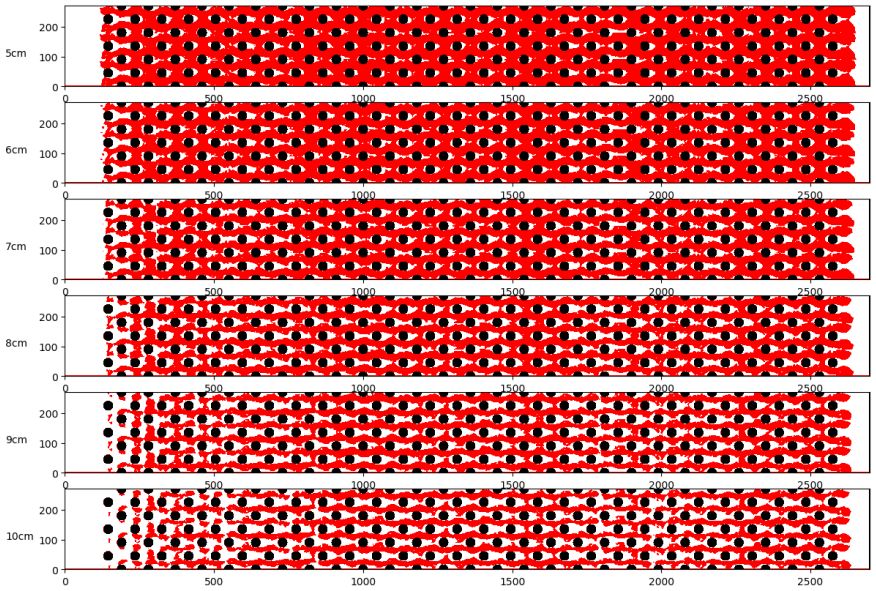

Figure B.34: Binary maps for an eel pass installed at 17° with a discharge per unit width of $1.6\dot{7}\times10^{-3}m^2s^{-1}$ for elver between 0.05 and 0.1 m bodylength, using the 90% confidence interval of the burst swimming speed.

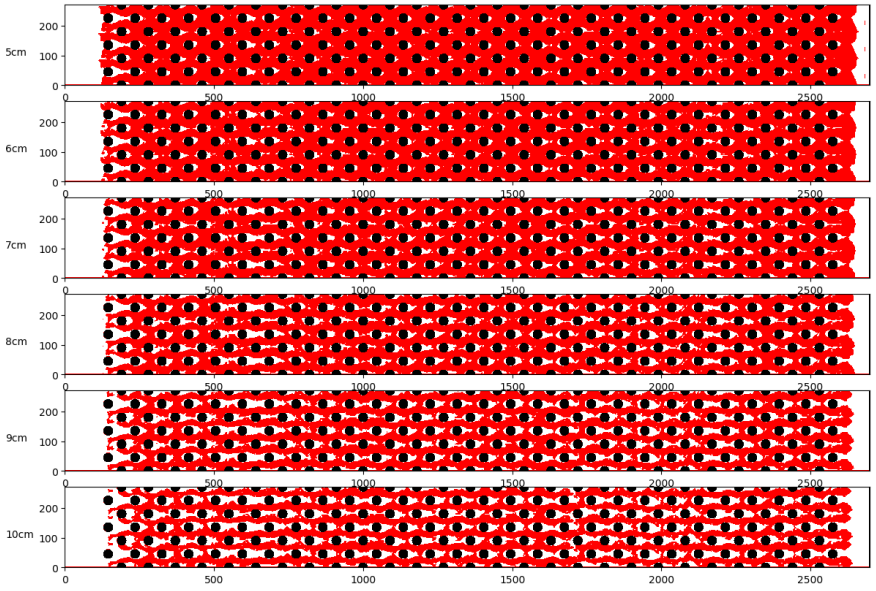

Figure B.35: Binary maps for an eel pass installed at 20° with a discharge per unit width of $1.6\dot{7}\times10^{-3}m^2s^{-1}$ for elver between 0.05 and 0.1 m bodylength, using the 90% confidence interval of the burst swimming speed.

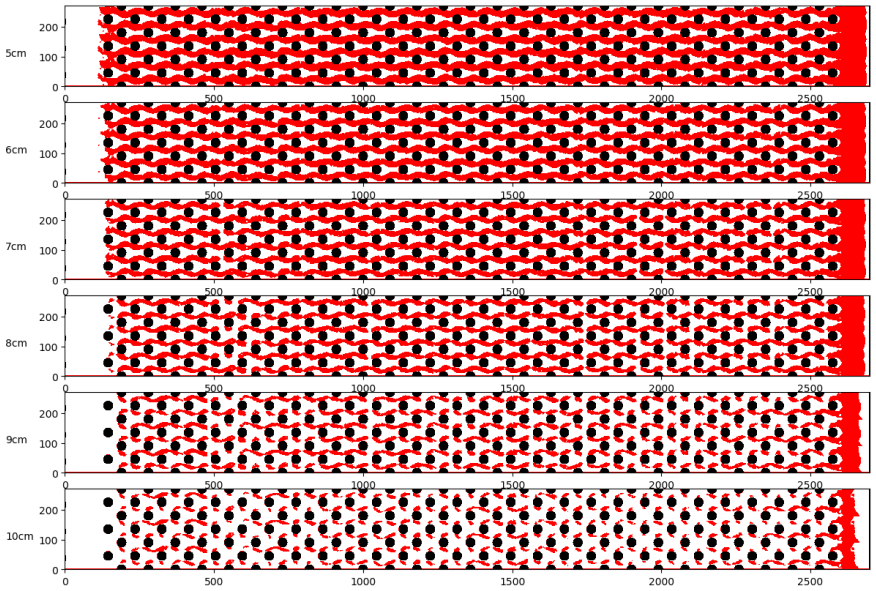

Figure B.36: Binary maps for an eel pass installed at 8° with a discharge per unit width of $3.3\dot{3}\times10^{-3}m^2s^{-1}$ for elver between 0.05 and 0.1 m bodylength, using the 90% confidence interval of the burst swimming speed.

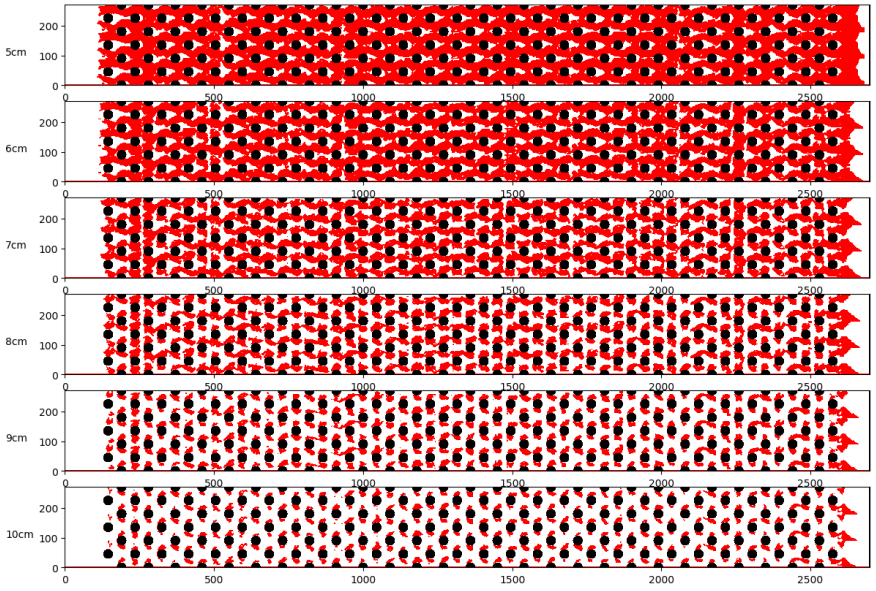

Figure B.37: Binary maps for an eel pass installed at 11° with a discharge per unit width of $3.3\dot{3}\times10^{-3}m^2s^{-1}$ for elver between 0.05 and 0.1 m bodylength, using the 90% confidence interval of the burst swimming speed.

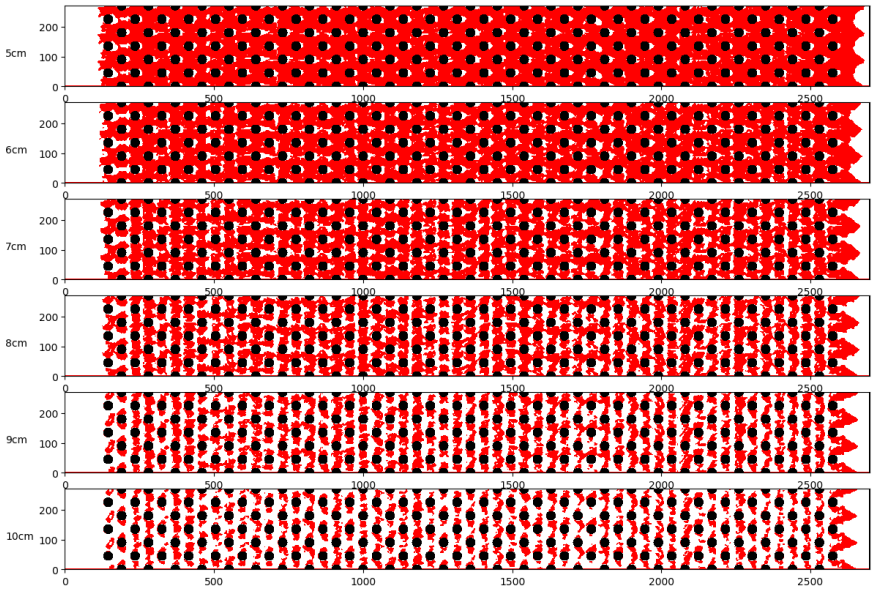

Figure B.38: Binary maps for an eel pass installed at 14° with a discharge per unit width of $3.3\dot{3}\times10^{-3}m^2s^{-1}$ for elver between 0.05 and 0.1 m bodylength, using the 90% confidence interval of the burst swimming speed.

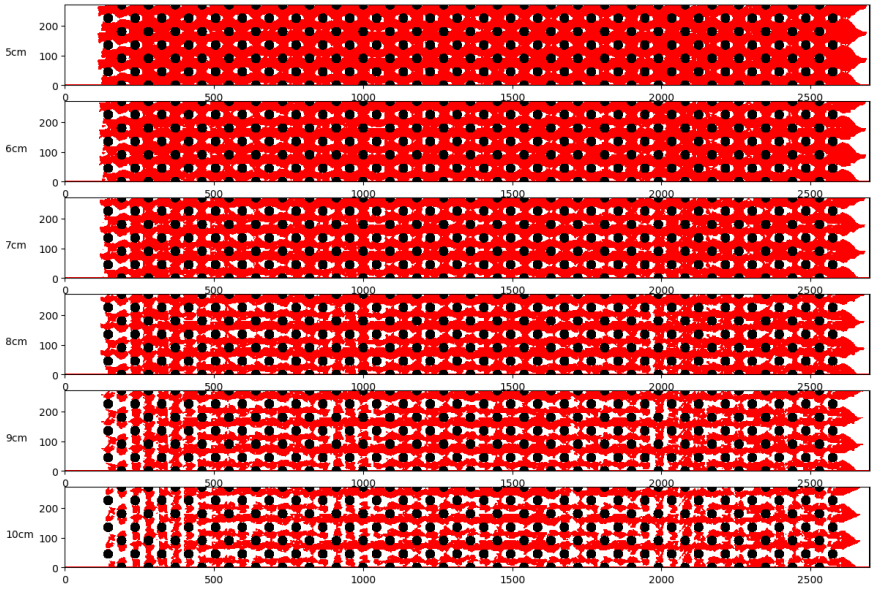

Figure B.39: Binary maps for an eel pass installed at 17° with a discharge per unit width of $3.3\dot{3}\times10^{-3}m^2s^{-1}$ for elver between 0.05 and 0.1 m bodylength, using the 90% confidence interval of the burst swimming speed.

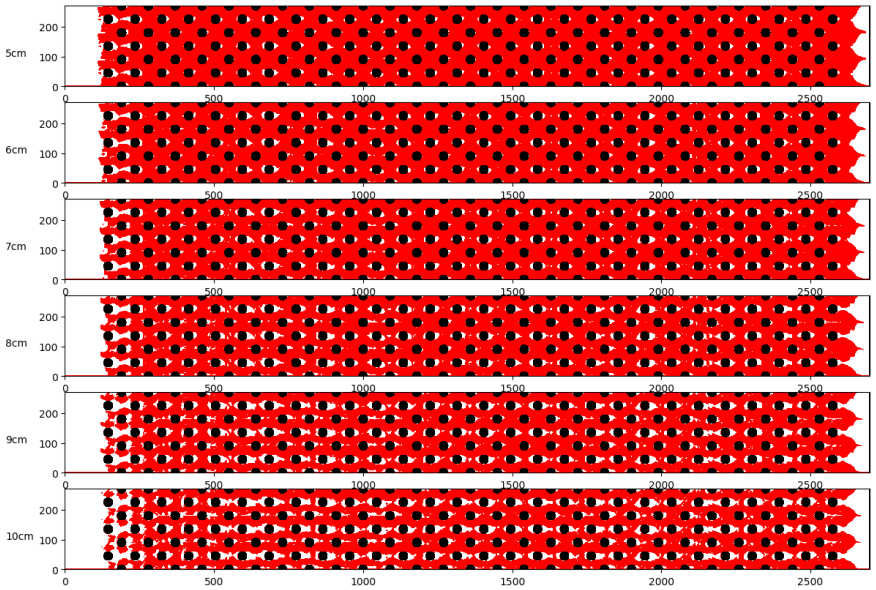

Figure B.40: Binary maps for an eel pass installed at 20° with a discharge per unit width of $3.3\dot{3}\times10^{-3}m^2s^{-1}$ for elver between 0.05 and 0.1 m bodylength, using the 90% confidence interval of the burst swimming speed.

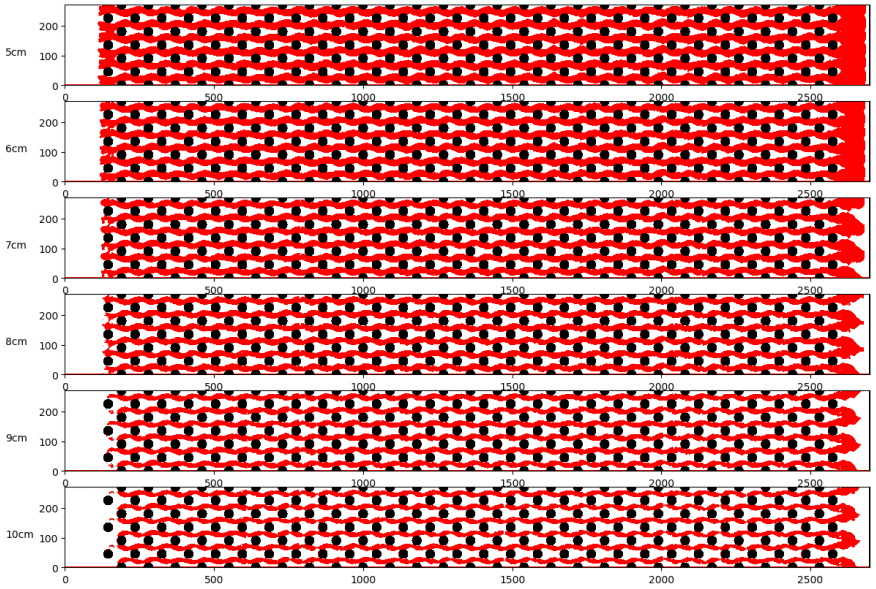

Figure B.41: Binary maps for an eel pass installed at 8° with a discharge per unit width of $5.0\times10^{-3}m^2s^{-1}$ for elver between 0.05 and 0.1 m bodylength, using the 90% confidence interval of the burst swimming speed.

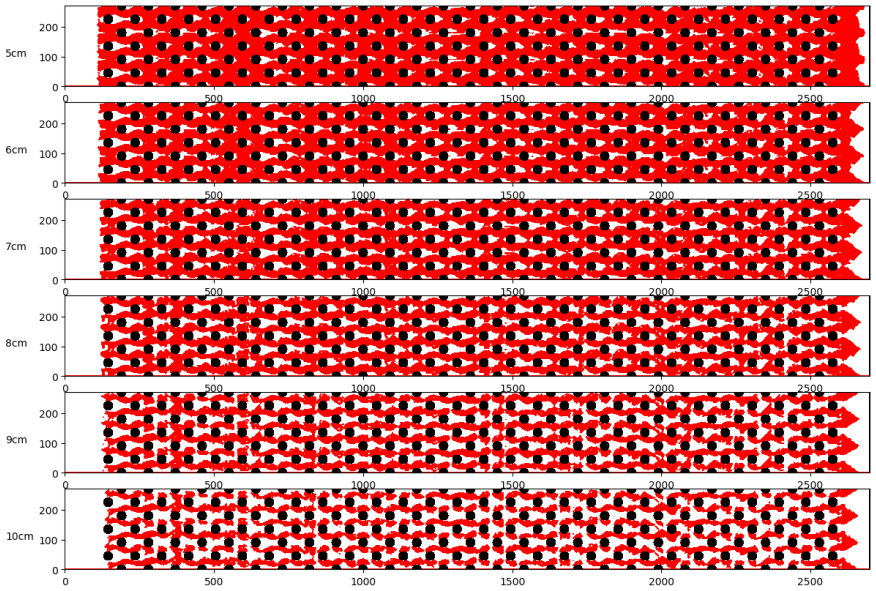

Figure B.42: Binary maps for an eel pass installed at 11° with a discharge per unit width of $5.0\times10^{-3}m^2s^{-1}$ for elver between 0.05 and 0.1 m bodylength, using the 90% confidence interval of the burst swimming speed.

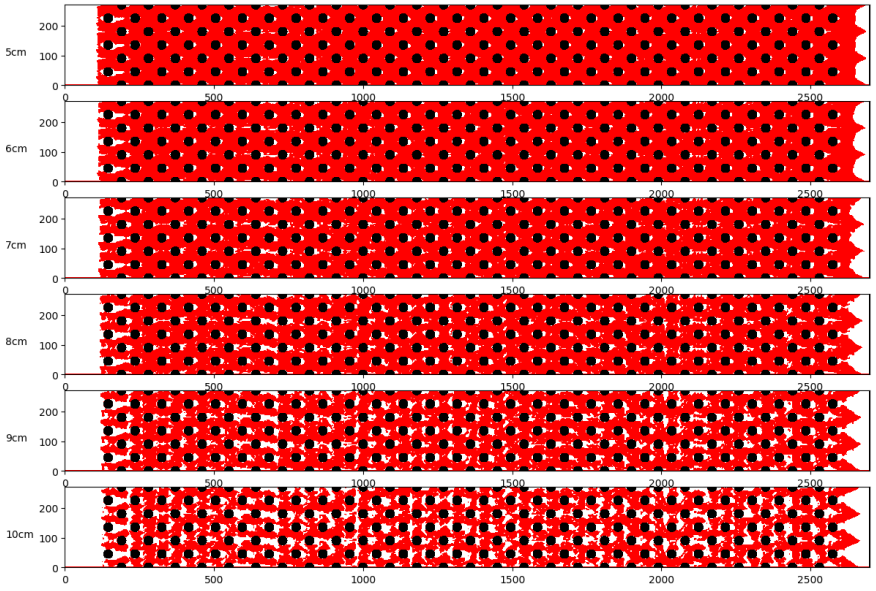

Figure B.43: Binary maps for an eel pass installed at 14° with a discharge per unit width of $5.0\times10^{-3}m^2s^{-1}$ for elver between 0.05 and 0.1 m bodylength, using the 90% confidence interval of the burst swimming speed.

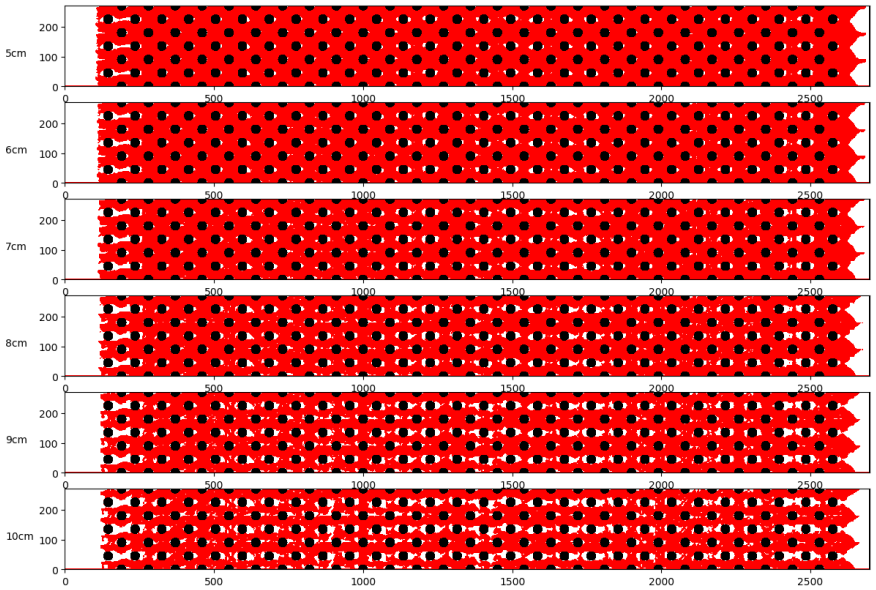

Figure B.44: Binary maps for an eel pass installed at 17° with a discharge per unit width of $5.0{\times}10^{-3} m^2 s^{-1}$ for elver between 0.05 and 0.1 m bodylength, using the 90% confidence interval of the burst swimming speed.

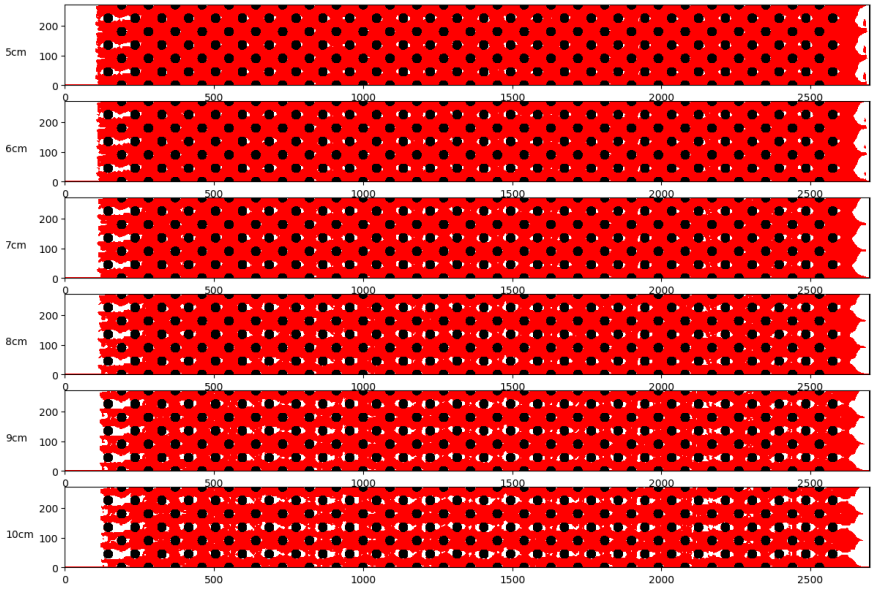

Figure B.45: Binary maps for an eel pass installed at 20° with a discharge per unit width of $5.0{\times}10^{-3} m^2 s^{-1}$ for elver between 0.05 and 0.1 m bodylength, using the 90% confidence interval of the burst swimming speed.

B.2 Supplementary Velocity Maps

This section presents the velocity maps created for each configuration of eel pass, used as inputs to the `HEPM`.

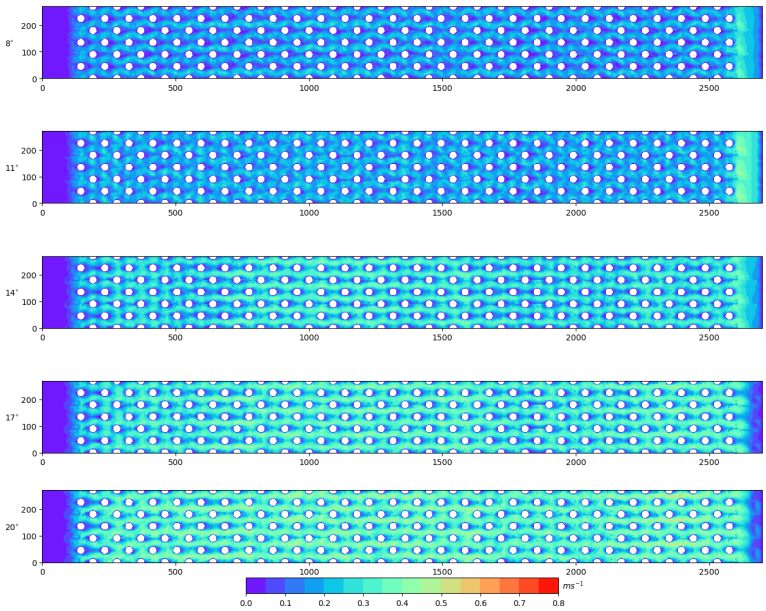

Figure B.46: Velocity maps for an eel pass with a discharge per unit width of $1.6\dot{7}\times10^{-3}m^2s^{-1}$ for installation angles ranging between 8° and 20°.

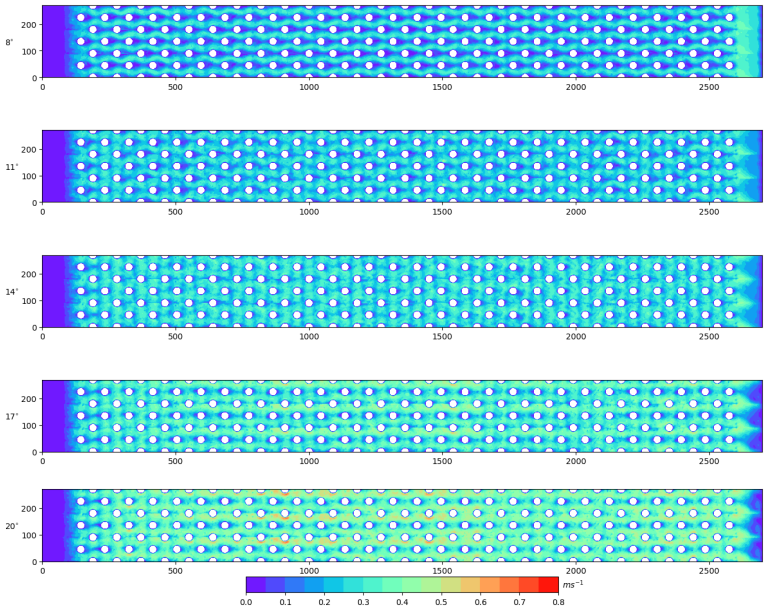

Figure B.47: Velocity maps for an eel pass with a discharge per unit width of $3.3\dot{3}\times10^{-3}m^2s^{-1}$ for installation angles ranging between 8° and 20°.

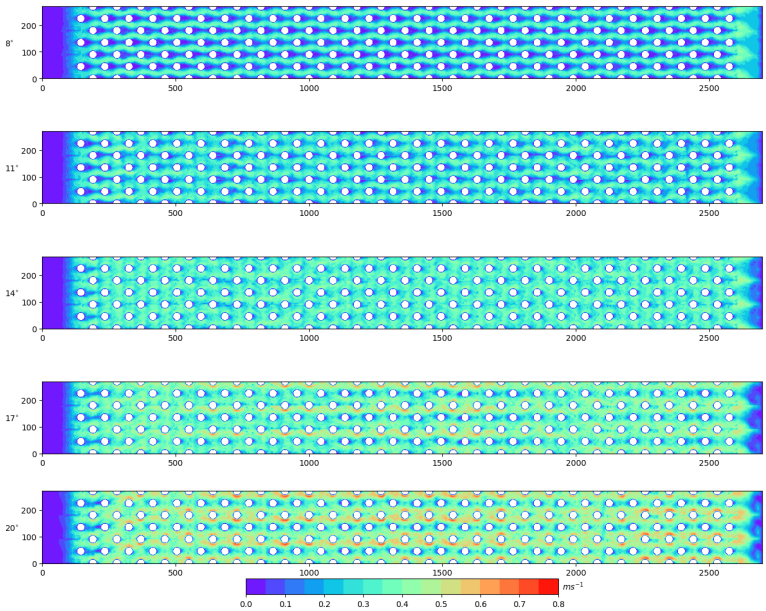

Figure B.48: Velocity maps for an eel pass with a discharge per unit width of $5.0\times10^{-3}m^2s^{-1}$ for installation angles ranging between 8° and 20°.

B.3 Supplementary Landscape Connectivity Results

This section presents additional results of the landscape connectivity metrics applied to the binary maps for the 10% and 90% confidence intervals of the burst swimming speeds for all lengths of elvers and all configurations of eel pass.

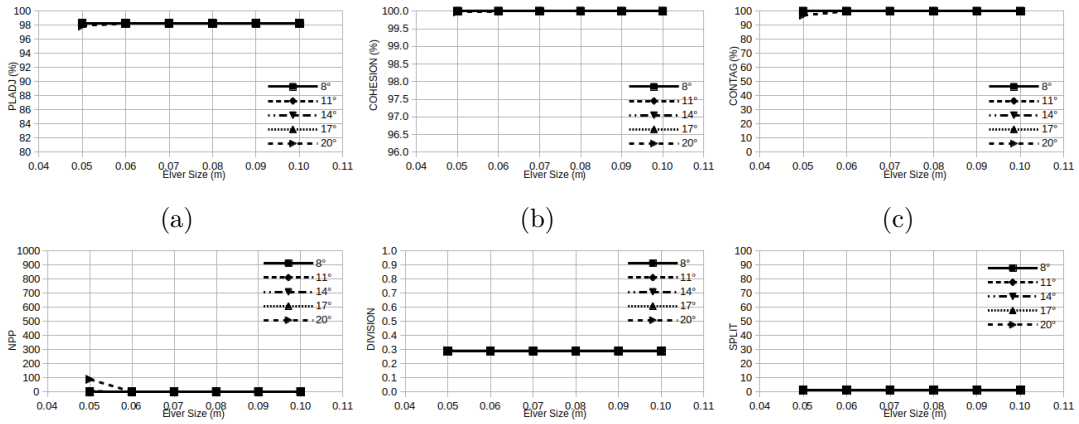

(a) (b) (c)

(d) (e) (f)

Figure B.49: Six landscape connectivity metrics applied to an eel pass for 5 installation angles using a) `PLADJ`, b) `COHESION`, c) `CONTAG`, d) `NPP`, e) `DIVISION`, and f) `SPLIT`. Results shown are for a discharge per unit width of $1.6\dot{7}\times10^{-3}m^2s^{-1}$ and for elver between 0.05 and 0.1 m bodylength, using the 10% confidence interval of the burst swimming speeds.

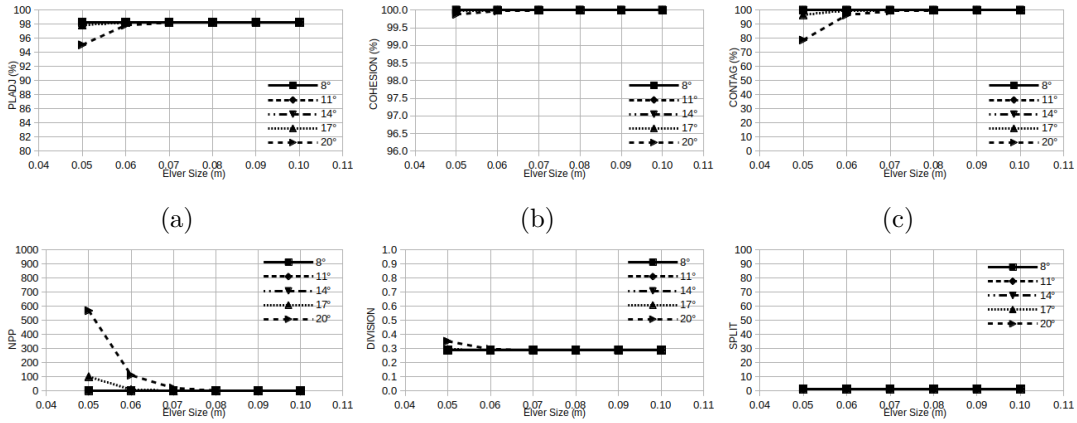

Figure B.50: Six landscape connectivity metrics applied to an eel pass for 5 installation angles using a) `PLADJ`, b) `COHESION`, c) `CONTAG`, d) `NPP`, e) `DIVISION`, and f) `SPLIT`. Results shown are for a discharge per unit width of $3.3\dot{3}\times10^{-3}m^2s^{-1}$ and for elver between 0.05 and 0.1 m bodylength, using the 10% confidence interval of the burst swimming speeds.

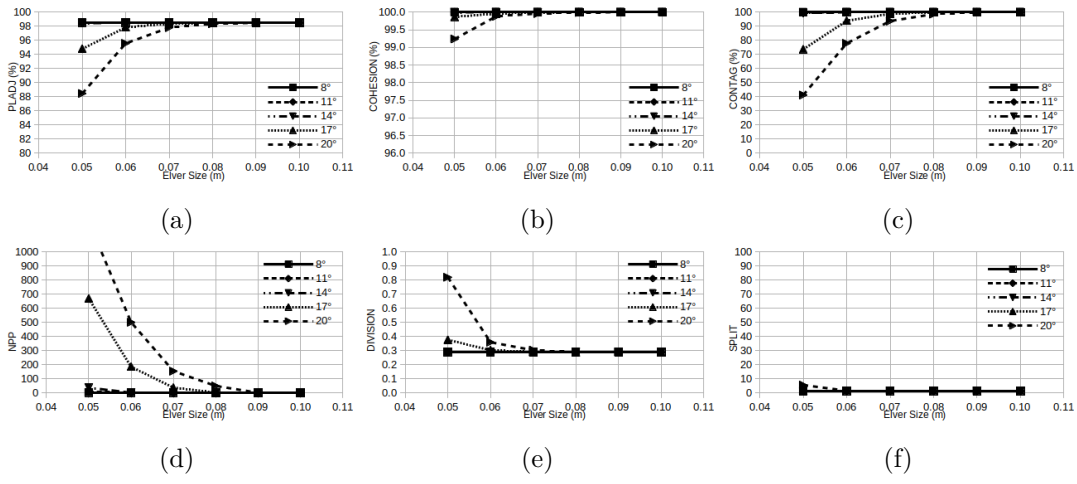

Figure B.51: Six landscape connectivity metrics applied to an eel pass for 5 installation angles using a) `PLADJ`, b) `COHESION`, c) `CONTAG`, d) `NPP`, e) `DIVISION`, and f) `SPLIT`. Results shown are for a discharge per unit width of $5.0\times10^{-3}m^2s^{-1}$ and for elver between 0.05 and 0.1 m bodylength, using the 10% confidence interval of the burst swimming speeds.

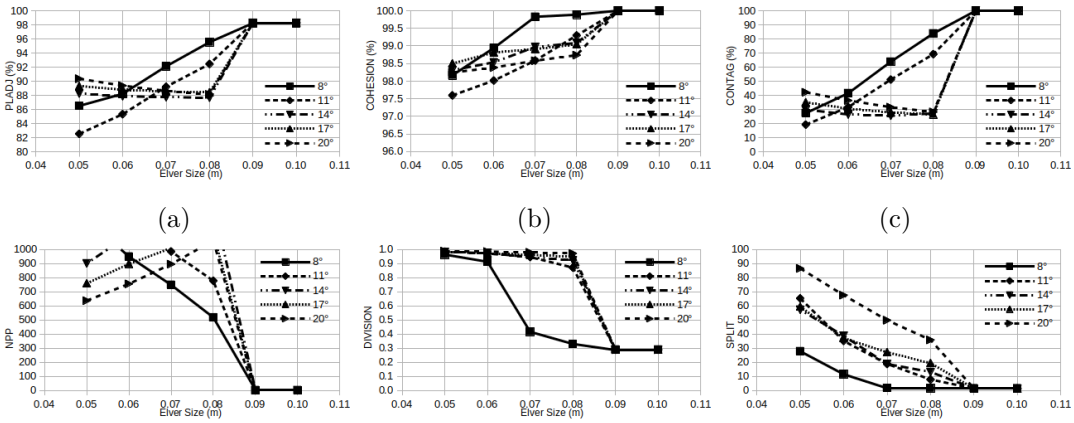

Figure B.52: Six landscape connectivity metrics applied to an eel pass for 5 installation angles using a) `PLADJ`, b) `COHESION`, c) `CONTAG`, d) `NPP`, e) `DIVISION`, and f) `SPLIT`. Results shown are for a discharge per unit width of $1.6\dot{7}\times10^{-3}m^2s^{-1}$ and for elver between 0.05 and 0.1 m bodylength, using the 90% confidence interval of the burst swimming speeds.

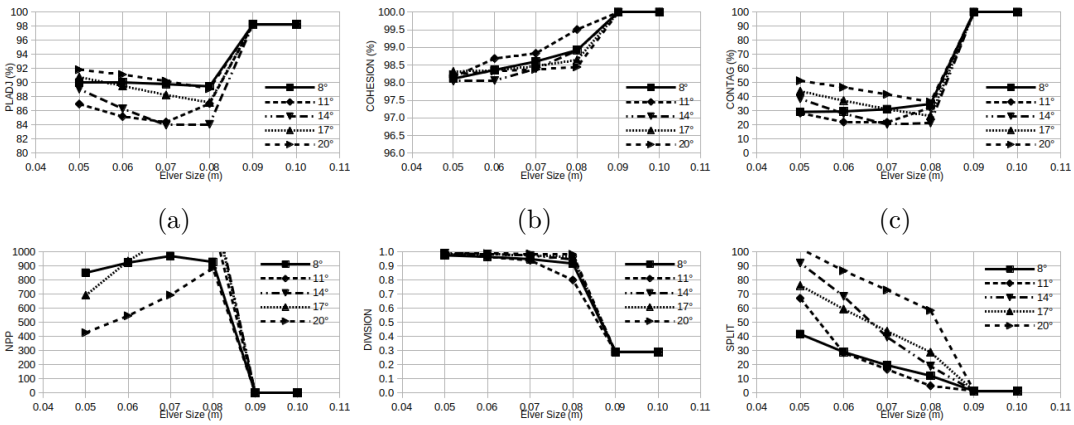

Figure B.53: Six landscape connectivity metrics applied to an eel pass for 5 installation angles using a) `PLADJ`, b) `COHESION`, c) `CONTAG`, d) `NPP`, e) `DIVISION`, and f) `SPLIT`. Results shown are for a discharge per unit width of $3.3\dot{3}\times10^{-3}m^2s^{-1}$ and for elver between 0.05 and 0.1 m bodylength, using the 90% confidence interval of the burst swimming speeds.

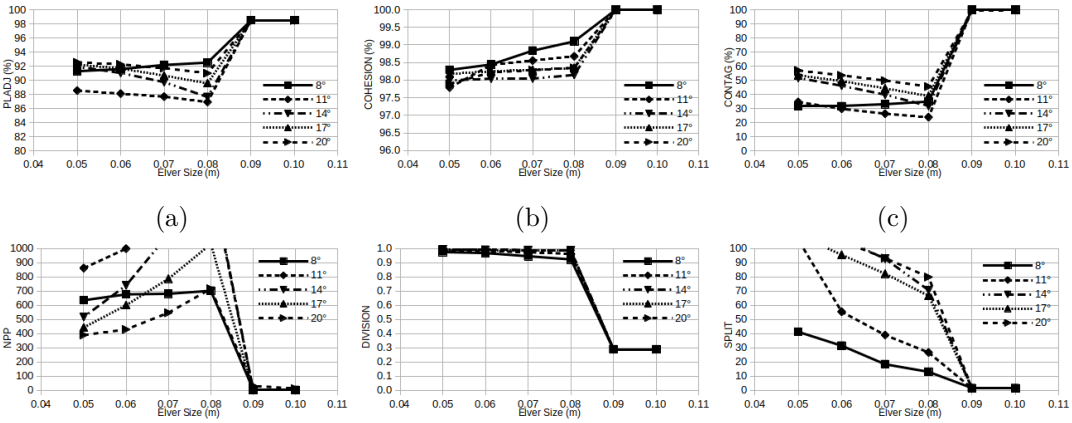

Figure B.54: Six landscape connectivity metrics applied to an eel pass for 5 installation angles using a) `PLADJ`, b) `COHESION`, c) `CONTAG`, d) `NPP`, e) `DIVISION`, and f) `SPLIT`. Results shown are for a discharge per unit width of $5.0{\times}10^{-3}m^2s^{-1}$ and for elver between 0.05 and 0.1 m bodylength, using the 90% confidence interval of the burst swimming speeds.

B.4 Supplementary Cellular Automata Results

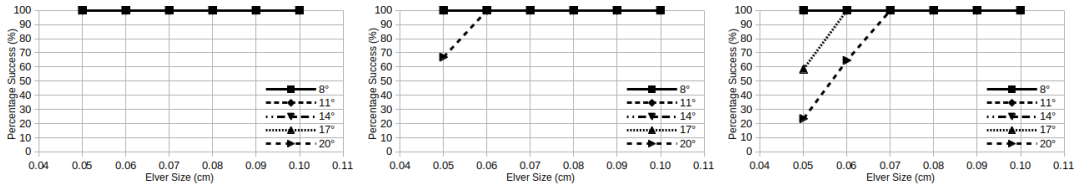

(a) (b) (c)

Figure B.55: Results of the SEPM applied to each eel pass configuration for the passage of elver between 0.05 and 0.1 m using the 10% confidence interval of the burst swimming speed, for discharges per unit width of a)$1.6\dot{7}\times10^{-3}m^2s^{-1}$, b) $3.3\dot{3}\times10^{-3}m^2s^{-1}$, and c) $5.0\times10^{-3}m^2s^{-1}$.

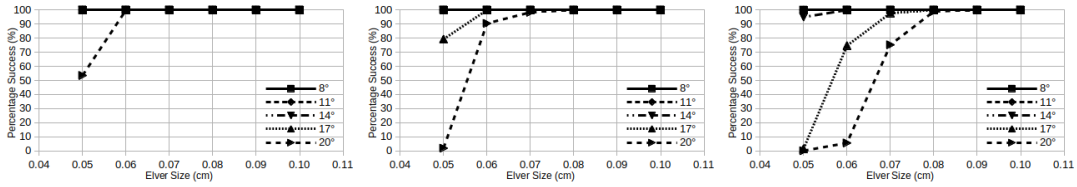

(a) (b) (c)

Figure B.56: Results of the EEPM applied to each eel pass configuration for the passage of elver between 0.05 and 0.1 m using the 10% confidence interval of the burst swimming speed, for discharges per unit width of a)$1.6\dot{7}\times10^{-3}m^2s^{-1}$, b) $3.3\dot{3}\times10^{-3}m^2s^{-1}$, and c) $5.0\times10^{-3}m^2s^{-1}$.

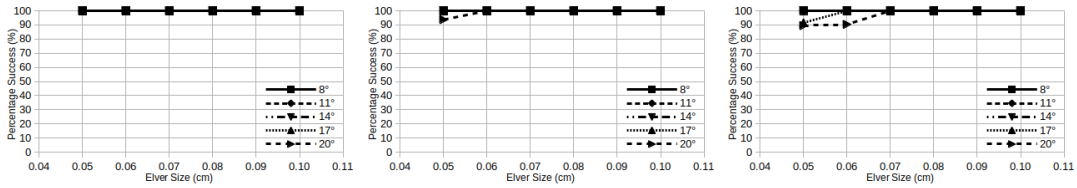

(a) (b) (c)

Figure B.57: Results of the FEPM applied to each eel pass configuration for the passage of elver between 0.05 and 0.1 m using the 10% confidence interval of the burst swimming speed, for discharges per unit width of a)$1.6\dot{7}\times10^{-3}m^2s^{-1}$, b) $3.3\dot{3}\times10^{-3}m^2s^{-1}$, and c) $5.0\times10^{-3}m^2s^{-1}$.

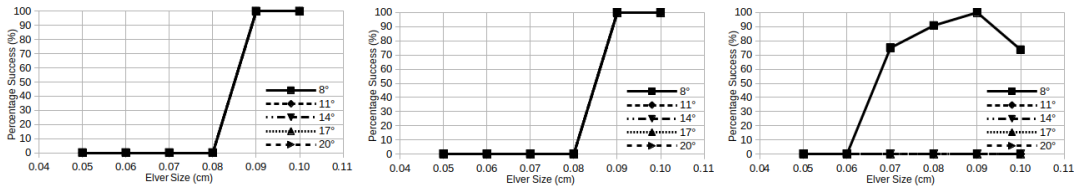

(a) (b) (c)

Figure B.58: Results of the SEPM applied to each eel pass configuration for the passage of elver between 0.05 and 0.1 m using the 90% confidence interval of the burst swimming speed, for discharges per unit width of a)$1.6\dot{7}\times10^{-3}m^2s^{-1}$, b) $3.3\dot{3}\times10^{-3}m^2s^{-1}$, and c) $5.0\times10^{-3}m^2s^{-1}$.

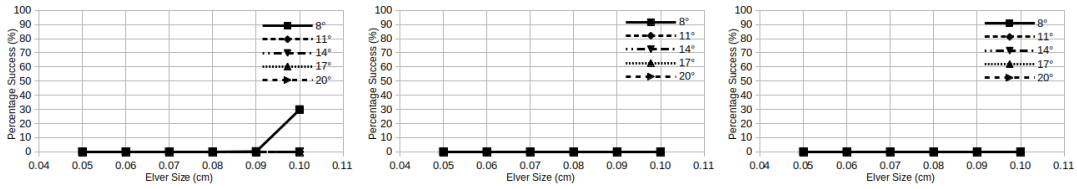

(a) (b) (c)

Figure B.59: Results of the EEPM applied to each eel pass configuration for the passage of elver between 0.05 and 0.1 m using the 90% confidence interval of the burst swimming speed, for discharges per unit width of a)$1.6\dot{7}\times10^{-3}m^2s^{-1}$, b) $3.3\dot{3}\times10^{-3}m^2s^{-1}$, and c) $5.0\times10^{-3}m^2s^{-1}$.

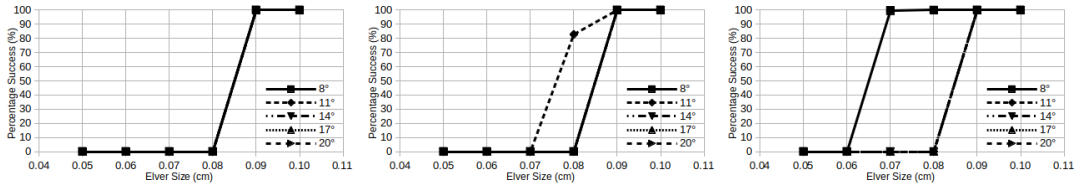

(a) (b) (c)

Figure B.60: Results of the FEPM applied to each eel pass configuration for the passage of elver between 0.05 and 0.1 m using the 90% confidence interval of the burst swimming speed, for discharges per unit width of a)$1.6\dot{7}\times10^{-3}m^2s^{-1}$, b) $3.3\dot{3}\times10^{-3}m^2s^{-1}$, and c) $5.0\times10^{-3}m^2s^{-1}$.

Appendix C

Supplementary Data for the Development of `fishPy`

C.1 Supplementary Data for Modelling the Swim Bladder

This section presents the modelling of the swim bladder based on the work of Alexander [1966] and Strand et al. [2005]. Although complex modelling of the swim bladder was not included in `fishPy`, details of the Strand et al. [2005] method are included hereinfor prudence. This is done to aid future users who may wish to further develop the model to incorporate full modelling of the swim bladder in order to predict vertical migrations, such as that detailed by Strand et al. [2005]. Similarly, the simple implementation of the swim bladder was retained within `fishPy` to demonstrate the negligible effect of buoyancy. This is in line with the developmental principles of transparency and code modularity, and facilitates development of future species modules and application of `fishPy` to marine datasets.

The Strand et al. [2005] approach calculates the buoyancy as a function of the actual volume of the individual's swim bladder compared to the volume required for neutral buoyancy. The volume required to cause the individual to be neutrally buoyant is calculated using Archimedes' principle, equation C.1.

$$V_n = \frac{M(1 - \frac{\rho_w}{\rho_f})}{\rho_w} \tag{C.1}$$

Where V_n is the neutral swim bladder volume in m^{-3}; M is the mass of the individual in kg; ρ_w is the density of the water in kgm^{-3}; and ρ_f is the density of the individual in kgm^{-3}.

Strand et al. [2005] based their calculation on Atlantic cod (*Gadus morhua*), and used a ρ_f value of 1081 kgm^{-3}, taken from Harden Jones and Scholes [1985]. Similar values for brown trout could not be found in the literature. The authors stipulate that if the actual swim bladder volume, V_s, differs from the neutral volume, V_n, a buoyancy force, B, will be experienced by the individual, equation C.2.

$$B = (V_s - V_n)\rho_w g \tag{C.2}$$

This approach would allow for the calculation of the buoyancy force at any timestep but requires an additional equation to model the change in volume of the swim bladder over time, $\frac{\partial V_s}{\partial t}$. Strand et al. [2005] suggest that this value can be calculated as a balance of leakage, secretion, and absorption of gases through the swim bladder wall,

equation C.3.

$$\frac{\partial V_s}{\partial t} = \frac{\partial V_{Leakage}}{\partial t} + \frac{\partial V_{Secretion}}{\partial t} + \frac{\partial V_{Absorption}}{\partial t} \tag{C.3}$$

The passive leakage of gases out of the swim bladder is due to constant diffusion across its walls, and is a function of the surface area of the swim bladder which is estimated to be a perfect ellipsoid [Strand et al., 2005]. However, x-rays of swim bladders have revealed that while this is not the case, it is a close approximation [Ona, 1990]. The rate of leakage, with units $mols^{-1}$, is given by equation C.4. As the rate of leakage is a function of the pressure differential, it depends upon the depth of the individual compared to its previous depth.

$$\frac{\partial V_{Leakage}}{\partial t} = \frac{GS_s(P - P_0)}{RT} \tag{C.4}$$

Where: G is the oxygen conductance of the swim bladder wall with units $m^3O_2m^{-2}atm^{-1}s^{-1}$; S_s is the surface area of the swim bladder in m^2 (equation C.5); P is the pressure currently experienced by the individual; P_0 is the original pressure, both in Pa; R is the universal gas constant; and T is the temperature in K.

$$S_s = 2\pi b^2\left(1 + \frac{(a/b)\arcsin(e)}{e}\right) \tag{C.5}$$

Where a is the polar radius of the bladder in m; b is the equatorial radius of the bladder in m; and e is the eccentricity of the swim bladder (given by C.6).

$$e = \sqrt[2]{1 - \frac{b^2}{a^2}} \tag{C.6}$$

For a known length to width ratio, $\frac{a}{b}$; b can be expressed as in equation C.7.

$$b = \left(\frac{3V_s(\frac{a}{b})^2}{4\pi}\right)^{\frac{1}{3}} \tag{C.7}$$

The buoyancy of the individual is regulated via the rates of absorption and secretion. If an individual would like to ascend, it will increase its rate of absorption. Conversely, if the individual would like to descend, it will increase its rate of secretion. The maximum rates of secretion and absorption are presented by Strand et al. [2005], equations C.8 and C.9.

$$\frac{\partial V_{Secretion}}{\partial t}|_{max} = \frac{C_{out}C_{rete}O_{2a}R_{eff}P_0}{RT\delta_{O_2}} \tag{C.8}$$

Table C.1: Parameters used by Strand et al. [2005] to model the swim bladder variance of Atlantic cod (*Gadus morhua*) with respect to time.

Variable	Description	Value	Units
C_{out}	Cardiac output	-	-
C_{oval}	Fraction of C_{out} to *oval*	0.25	-
C_{rete}	Fraction of C_{out} to *rete*	0.1	-
R_{eff}	Rete Efficiency*	0.2	-
O_{2a}	O_2 content of arterial blood by volume	0.1	-
O_{2sol}	Solubility of O_2	0.04	$m^3O_2m^3blood^{-1}atm^{-1}$
δ_{02}	Fraction of oxygen in gas	0.63	-
G	Oxygen conductance	1.5×10^{-9}	$m^3O_2m^{-2}atm^{-1}s^{-1}$
ΔHb	Fraction of haemoglobin available for O_2	0.15	-
$\frac{a}{b}$	Length-width ratio of bladder	10	-

*Taken for *Anguilla anguilla*.

Where: C_{out} is the cardiac output with units m^3s^{-1}; C_{rete} is the percentage of C_{out} diverted to the *rete*; O_{2a} is the volume fraction of O_2 in the blood; R_{eff} is the efficiency of the *rete*; δ_{O_2} is the fraction of oxygen in the secreted gases.

$$\frac{\partial V_{Absorption}}{\partial t}|_{max} = \frac{C_{out}C_{oval}P_0}{RT}\left(\frac{O_{2sol}(P-P_0)}{\delta_{O_2}} + O_{2a}\Delta Hb\right) \tag{C.9}$$

Where C_{oval} is the fraction of the cardiac output that flows through the oval; O_{2sol} is the solubility of oxygen, with units $m^3\ O_2\ m^{-3}\ blood\ atm^{-1}$; ΔHb is the fraction of available haemoglobin binding sites within the gas gland; and all other variables are as previously defined.

Using the data of Strand et al. [2005] (table C.1) the leakage, secretion, and absorption rates are calculated for depths of 1 and 10 metres. The surface area of the swim bladder, assuming a ratio $\frac{a}{b} = 10$, can be reduced to equation C.10.

$$S_s = 8.218834V_s^{2/3} \tag{C.10}$$

Appendix D

Supplementary Data for the Verification and Sensitivity Analyses of `fishPy`

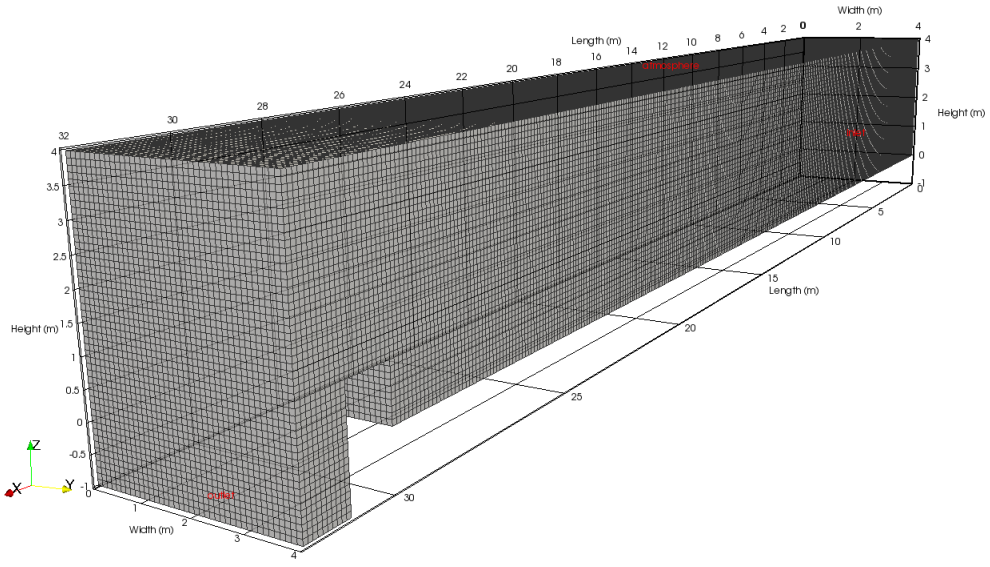

Figure D.1: Schematic of the `veriSetA` domain showing the regular mesh employed. Inlet, outlet, and atmospheric outlet are labelled. Surfaces without labels are no slip walls.

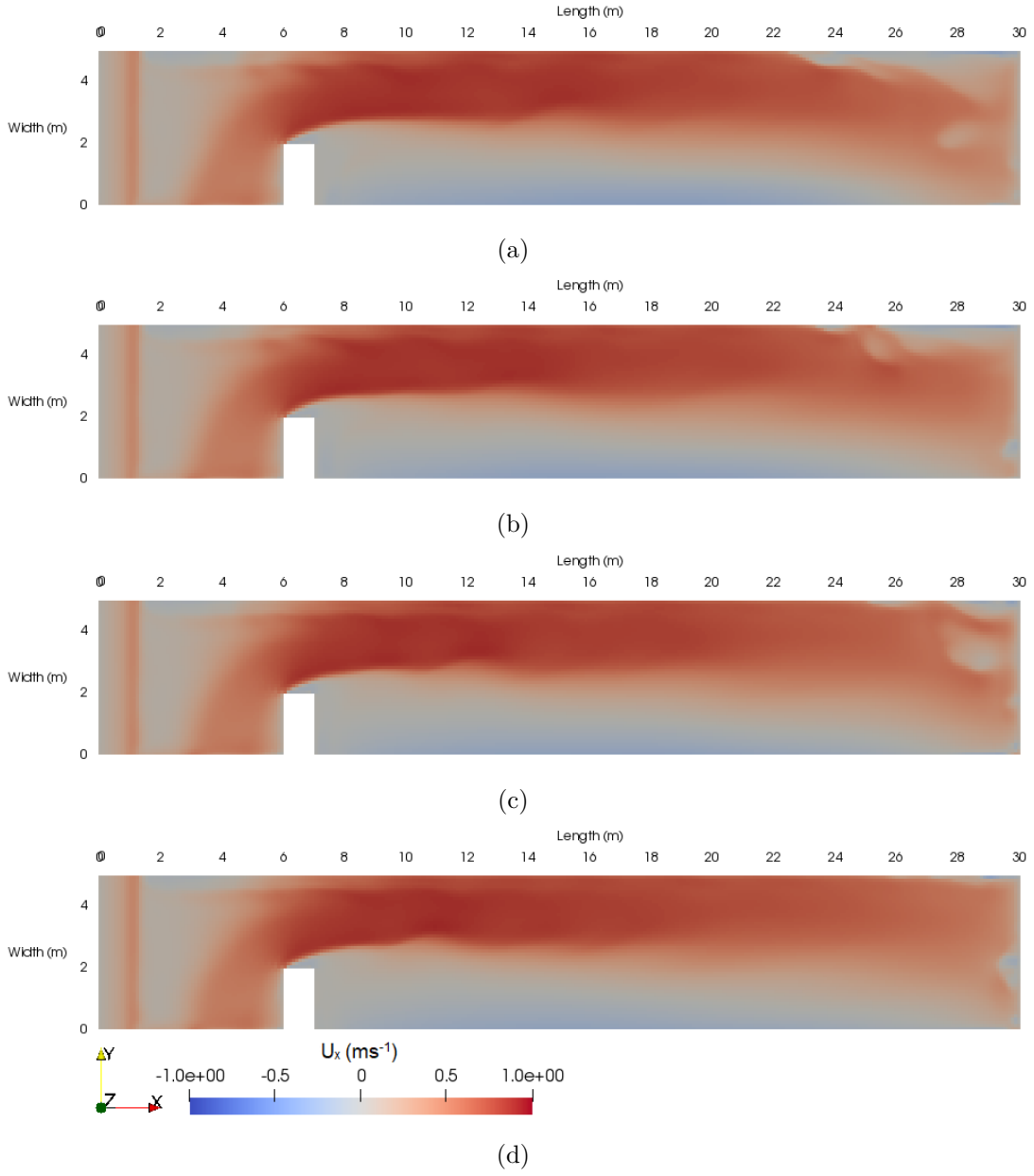

Figure D.2: Contours of streamwise velocity taken along an xy plane at $z = 0.5m$ within the `veriSetB` domain for a) $T = 120s$, b) $T = 130s$, c) $T = 140s$, d) $T = 150s$

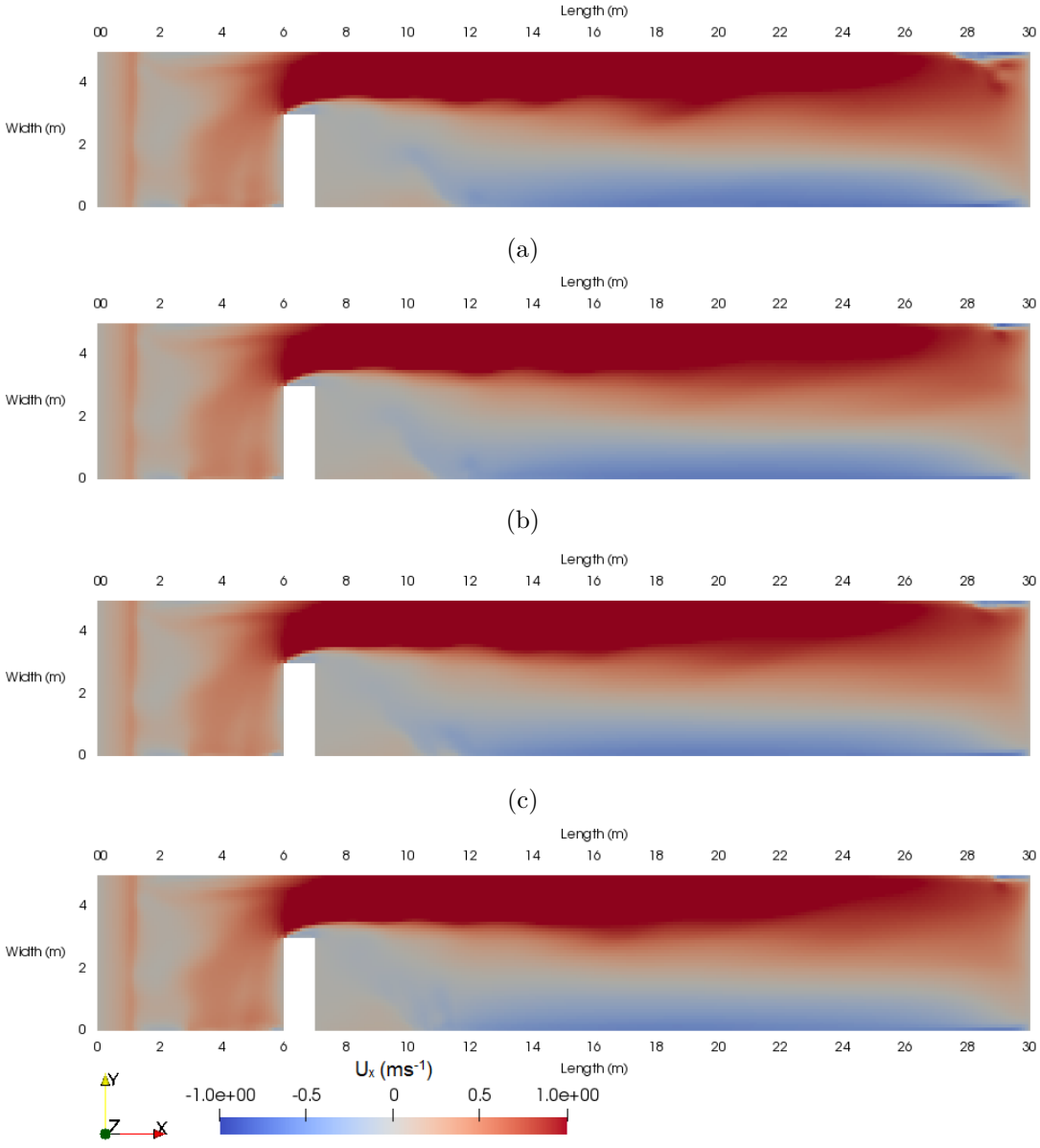

Figure D.3: Contours of streamwise velocity taken along an xy plane at $z = 0.5m$ within the `veriSetB2` domain for a) $T = 120s$, b) $T = 130s$, c) $T = 140s$, d) $T = 150s$

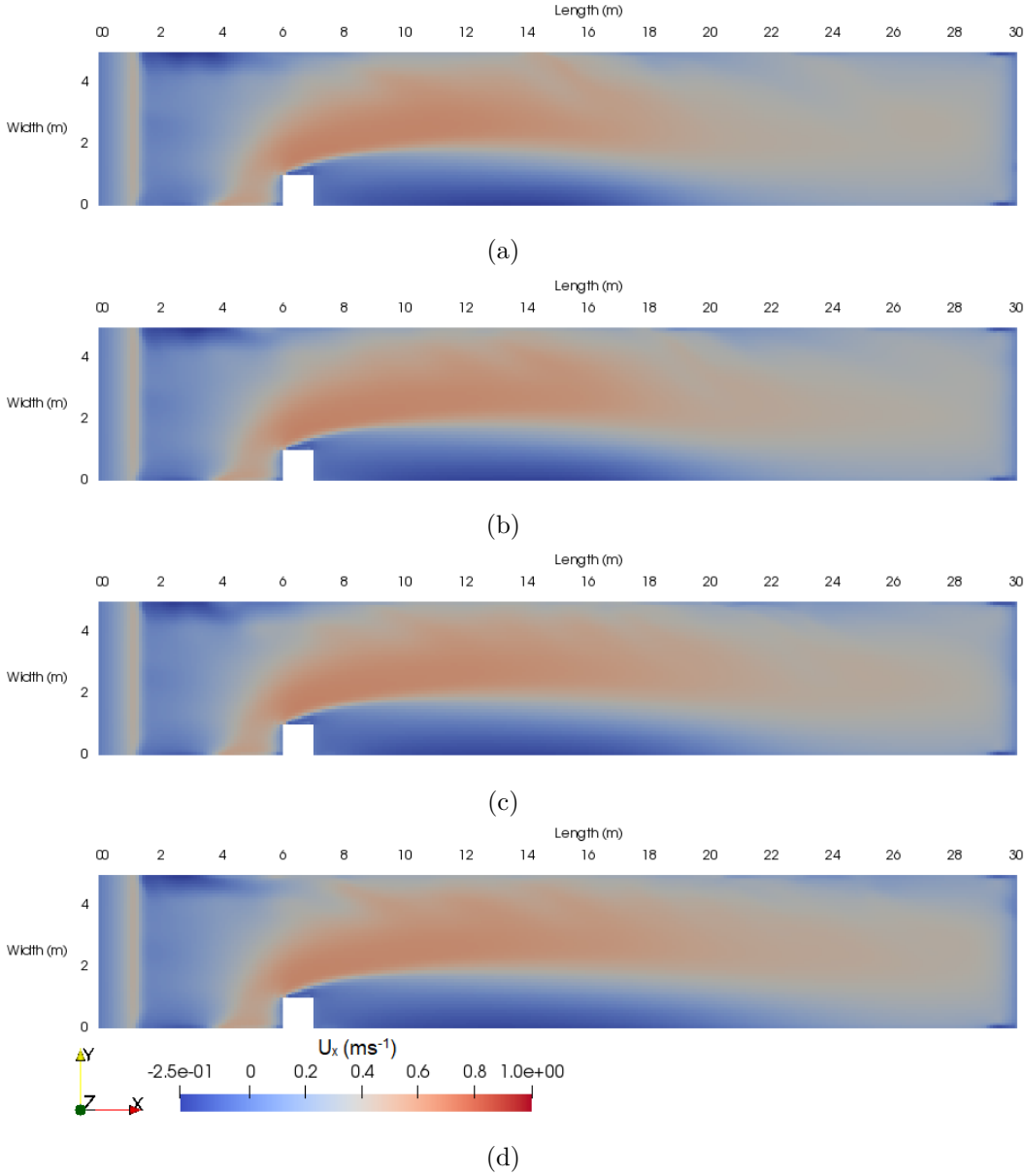

Figure D.4: Contours of streamwise velocity taken along an xy plane at $z = 0.5m$ within the `veriSetB3` domain for a) $T = 120s$, b) $T = 130s$, c) $T = 140s$, d) $T = 150s$

Appendix E

Supplementary Data for the Application of the `fishPy` model to Ruswarp Weir

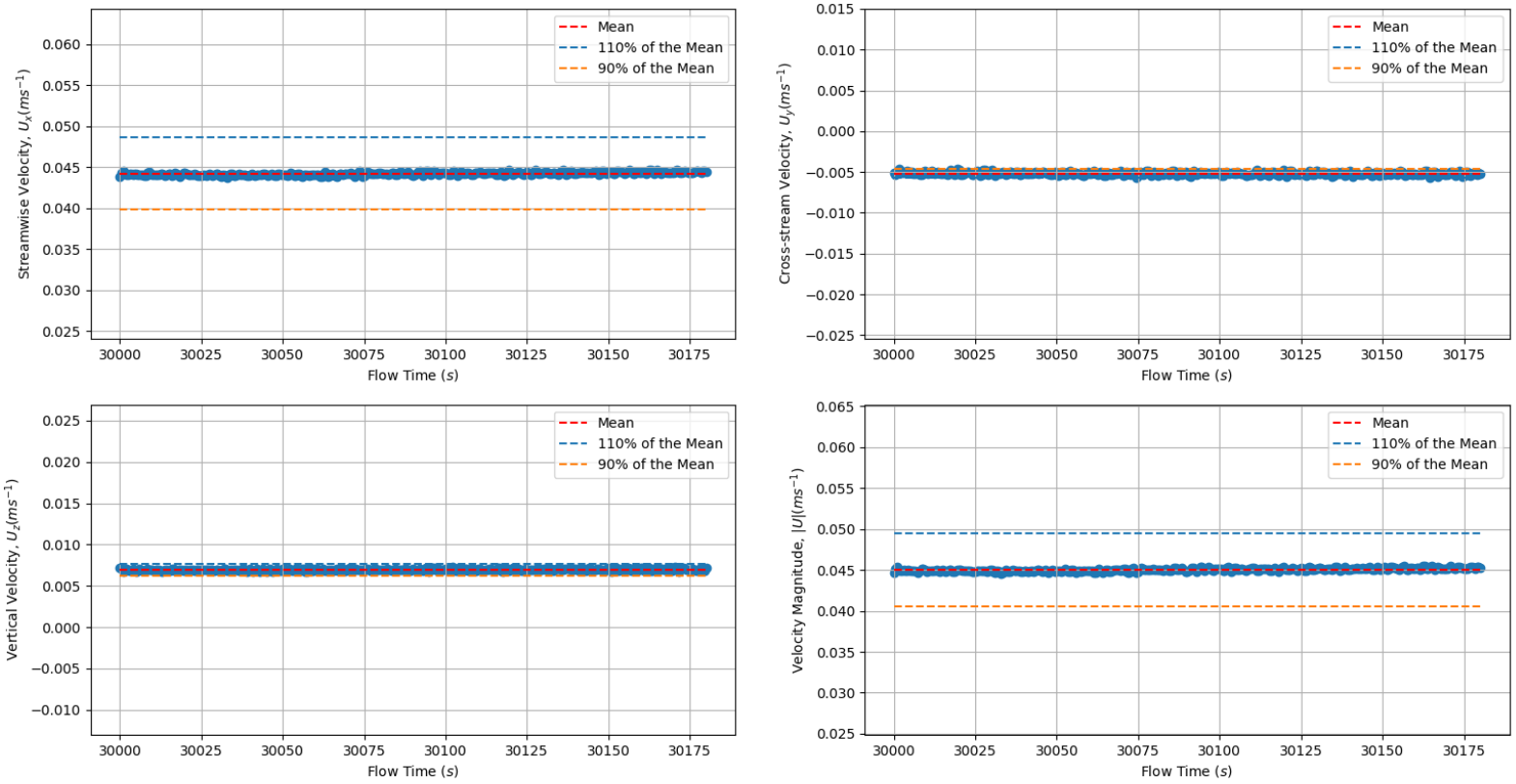

Figure E.1: Three-component velocity and velocity magnitude extracted from the `valSet` domain at `ML1` ($[77.0m, 125.0m]$) at mid-depth ($z = 2.6m$).

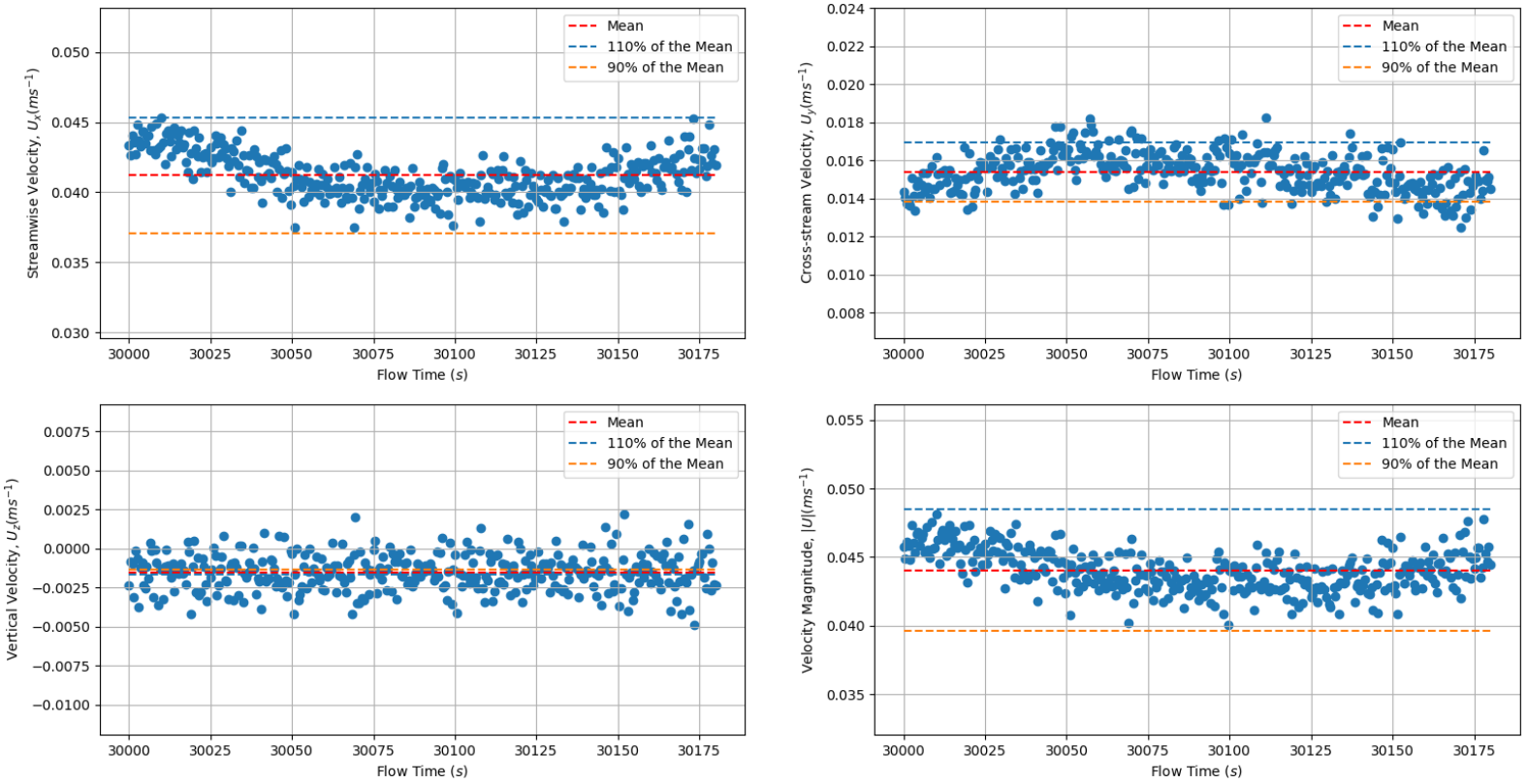

Figure E.2: Three-component velocity and velocity magnitude extracted from the `valSet` domain at `ML2` ($[85.0m, 75.0m]$) at mid-depth ($z = 1.2m$).

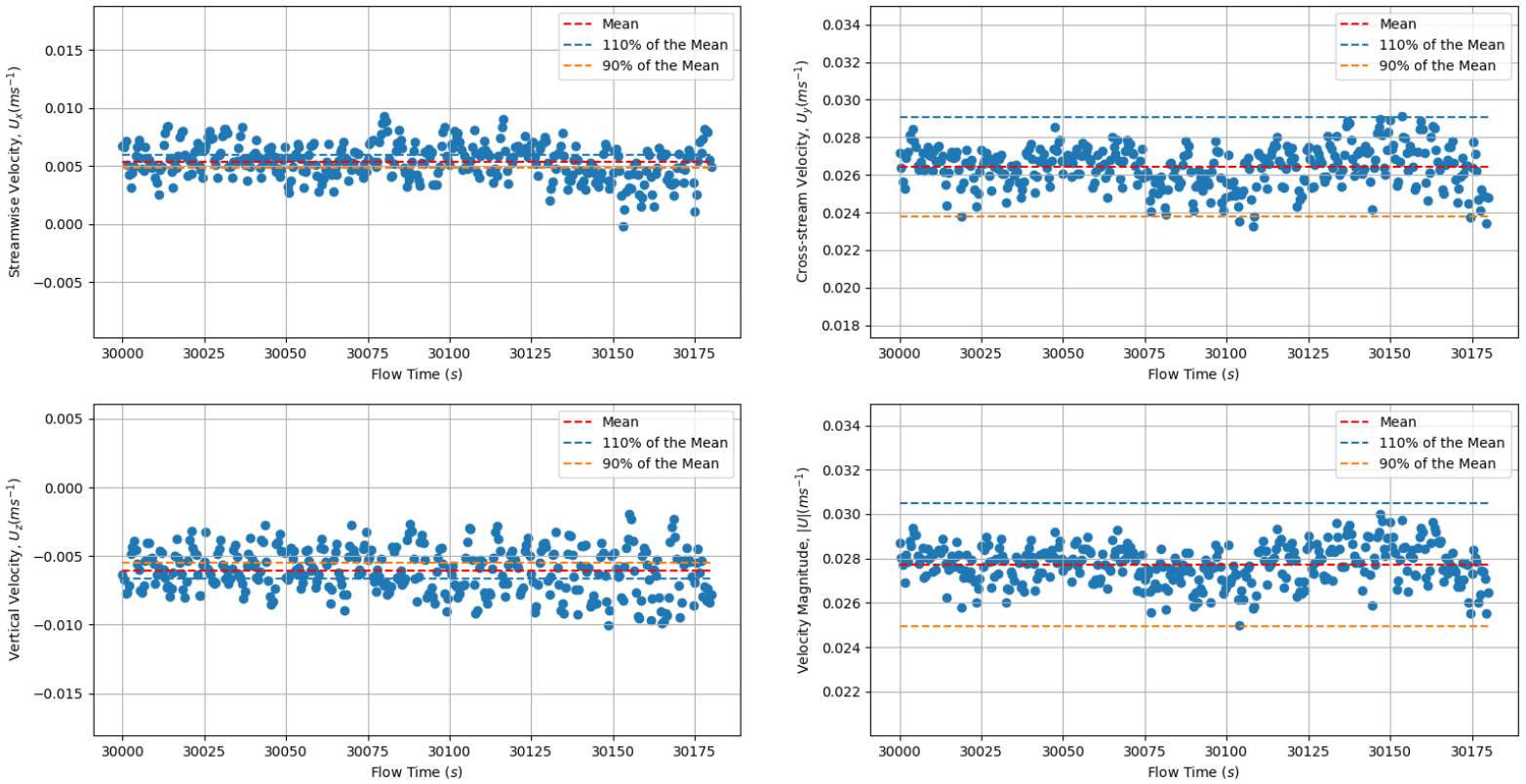

Figure E.3: Three-component velocity and velocity magnitude extracted from the `valSet` domain at `ML3` ($[132.0m, 159.0m]$) at mid-depth ($z = 2.7m$).

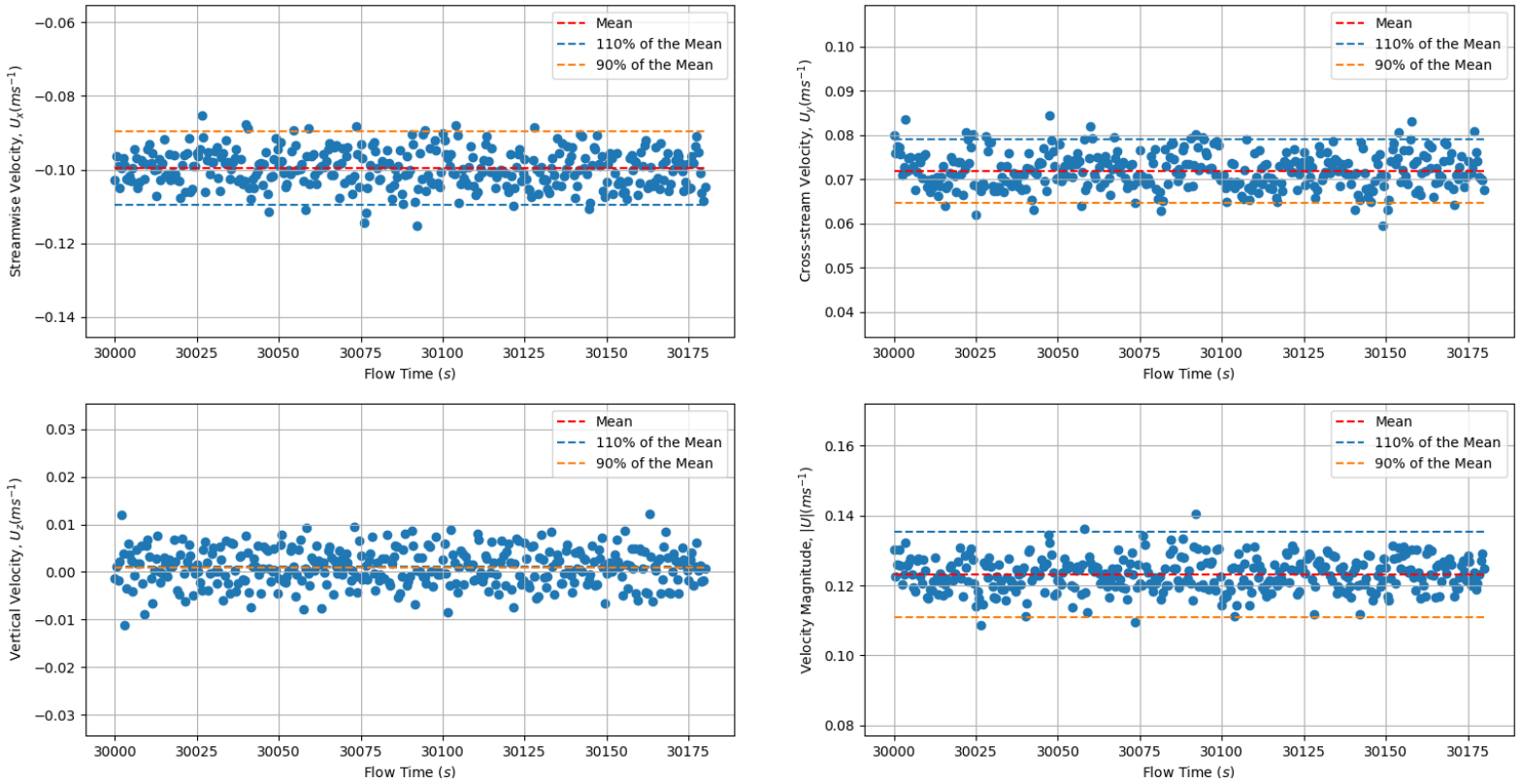

Figure E.4: Three-component velocity and velocity magnitude extracted from the `valSet` domain at `ML4` ($[160.0m, 158.0m]$) at mid-depth ($z = 1.4m$).

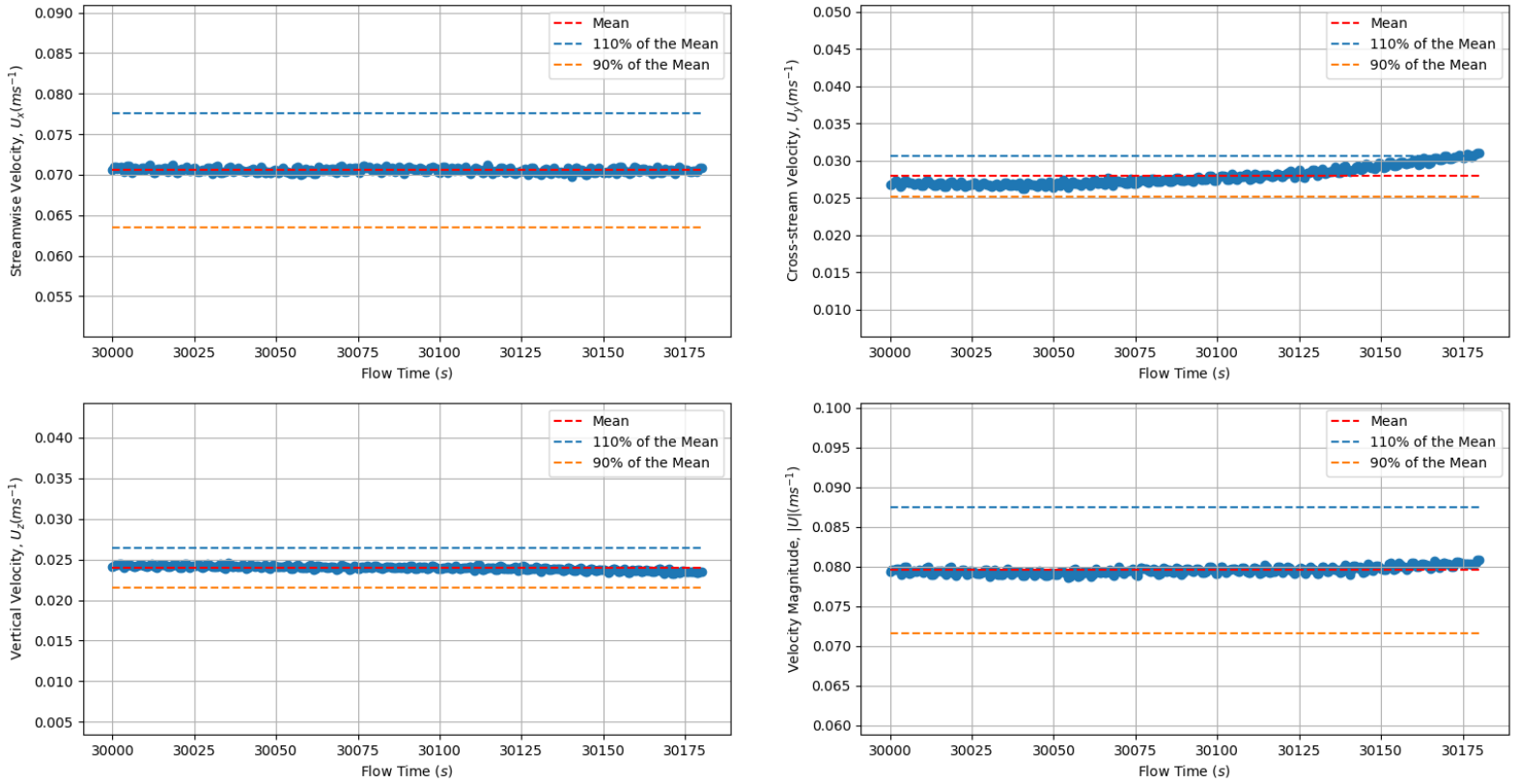

Figure E.5: Three-component velocity and velocity magnitude extracted from the `fishSet` domain at `ML1` ($[77.0m, 125.0m]$) at mid-depth ($z = 2.6m$).

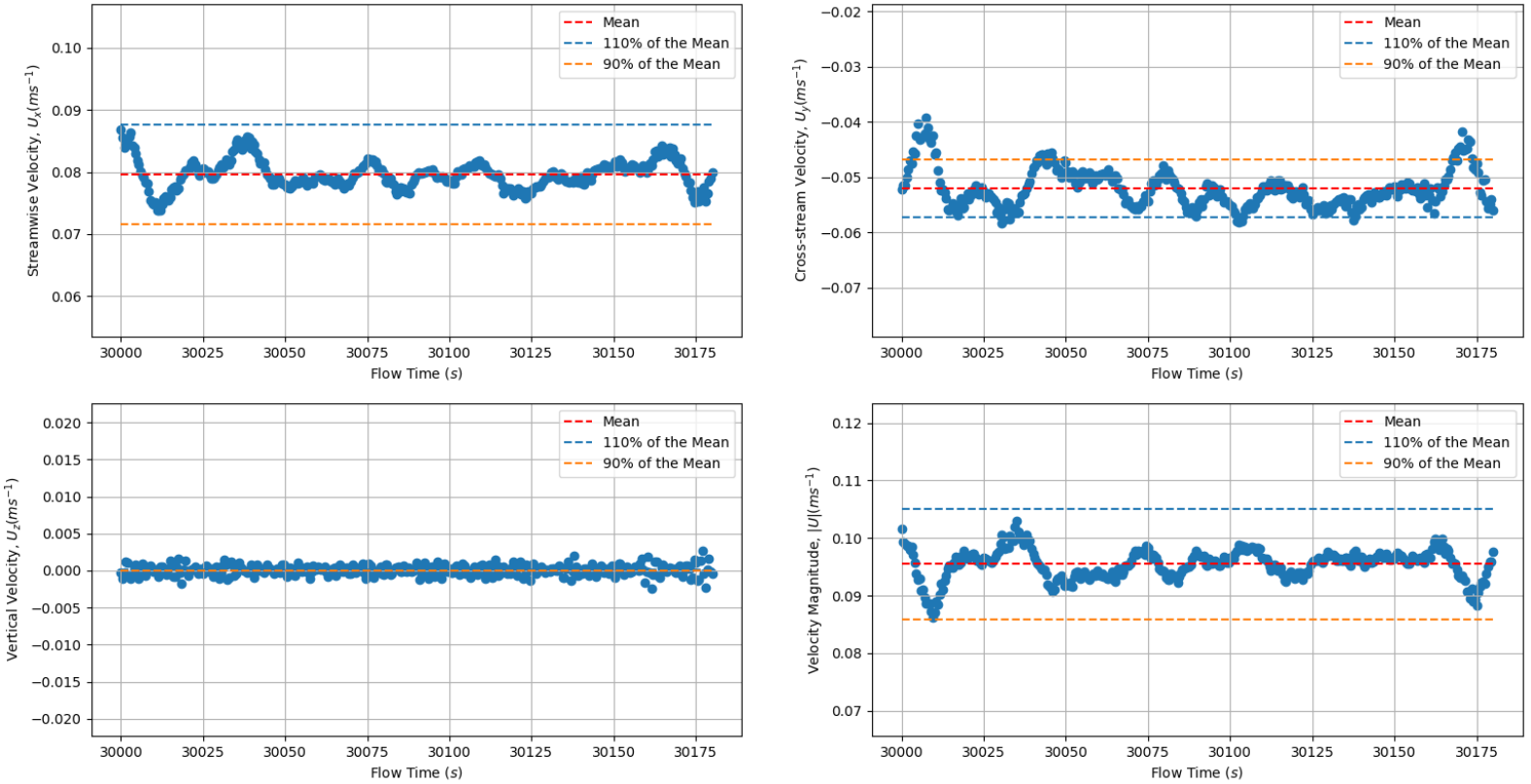

Figure E.6: Three-component velocity and velocity magnitude extracted from the `fishSet` domain at `ML2` ($[85.0m, 75.0m]$) at mid-depth ($z = 2.3m$).

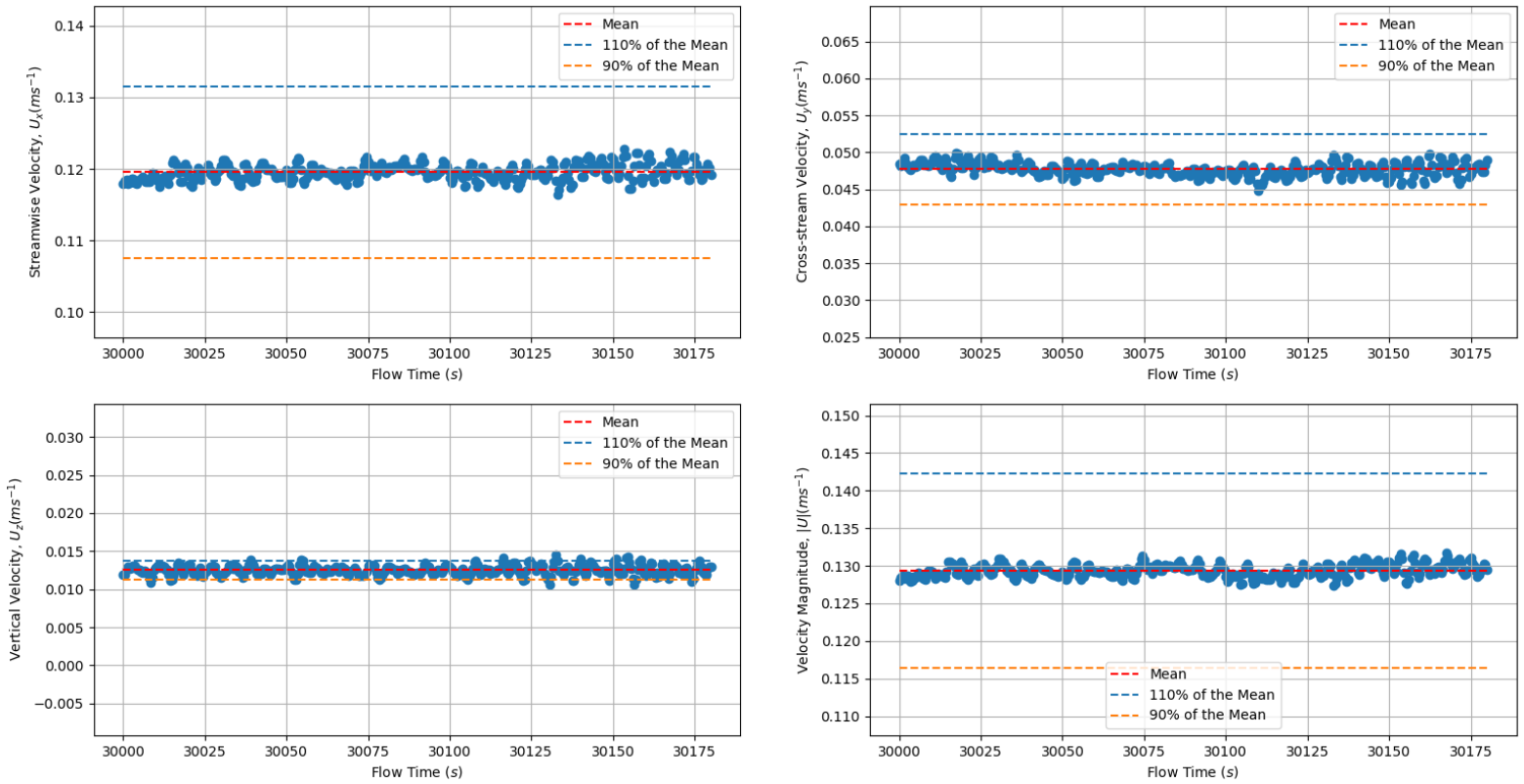

Figure E.7: Three-component velocity and velocity magnitude extracted from the `fishSet` domain at `ML3` ($[132.0m, 159.0m]$) at mid-depth ($z = 2.7m$).

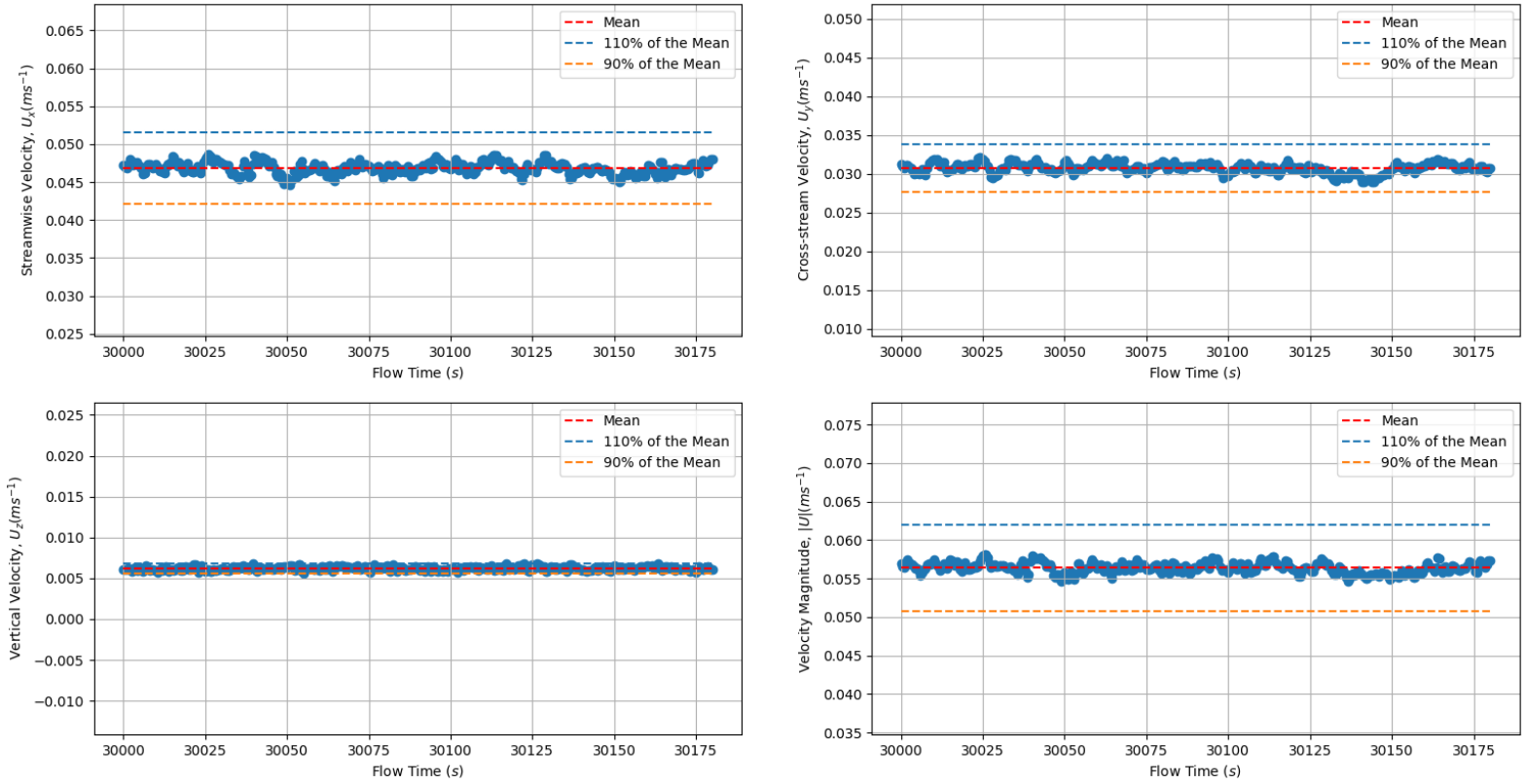

Figure E.8: Three-component velocity and velocity magnitude extracted from the `fishSet` domain at `ML4` ($[160.0m, 158.0m]$) at mid-depth ($z = 1.4m$).

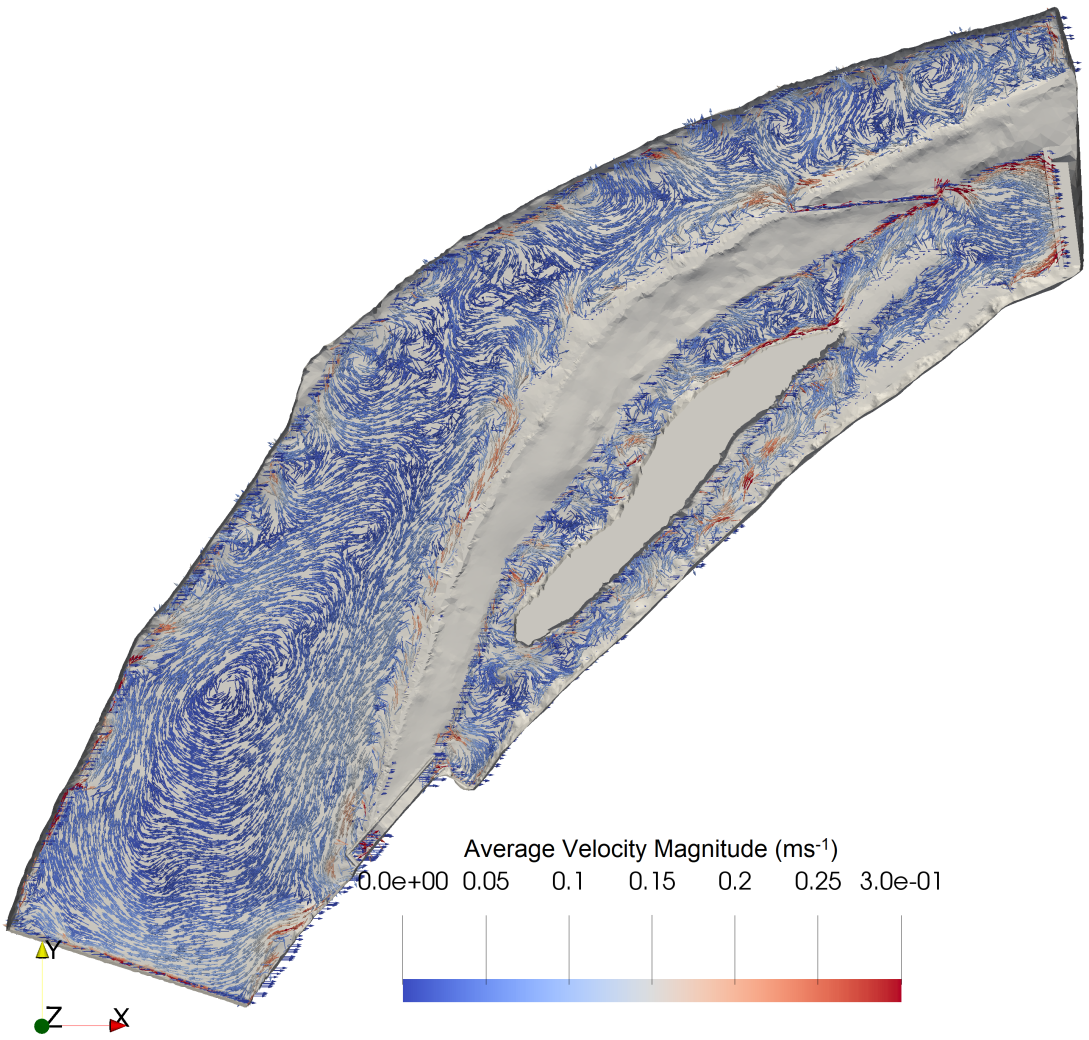

Figure E.9: Planform view of the `valSet` domain with overlain vectors displayed over the isosurface $\alpha = 0.5$, which denotes the free surface. The vectors are equally scaled due to the overwhelming dominance of the flow velocity within the baulk pass compared to the bulk flow. Vectors are coloured with velocity magnitude, limited to a maximum of $0.3ms^{-1}$ for clarity.

Table E.1: Transect-averaged velocity magnitudes of measured and predicted data (Table 1/2)

Transect Number	Transect-averaged measured velocity magnitude (ms^{-1})	Transect-averaged predicted velocity magnitude (ms^{-1})	Note
10	0.0580	0.0414	
11	0.0556	0.0523	
12	0.0524	0.0523	Transect B
13	0.0524	0.0357	
14	0.0520	0.0427	
15	0.0471	0.0525	
16	0.0547	0.0330	
17	0.0518	0.0377	
18	0.0547	0.0347	
19	0.0566	0.0493	
20	0.0546	0.0419	
21	0.0502	0.0361	
22	0.0461	0.0432	Transect C
23	0.0550	0.0379	
24	0.0530	0.0380	
25	0.0711	0.0431	
26	0.0682	0.0399	
27	0.0570	0.0374	
28	0.0777	0.0312	
29	0.0618	0.0547	Transect D
30	0.0662	0.0396	
31	0.0634	0.0452	
32	0.0633	0.0629	
33	0.0662	0.0462	
34	0.0692	0.0648	
35	0.0540	0.0514	

Table E.2: Transect-averaged velocity magnitudes of measured and predicted data Table (2/2)

Transect Number	Transect-averaged measured velocity magnitude (ms^{-1})	Transect-averaged predicted velocity magnitude (ms^{-1})	Note
36	0.0895	0.0520	
37	0.0842	0.0894	
38	0.0795	0.0678	
39	0.0670	0.0731	
40	0.0684	0.0541	
41	0.0579	0.0645	Transect E
42	0.0692	0.1011	
43	0.0706	0.1311	
44	0.0723	0.0757	
45	0.0581	0.0869	
46	0.0659	0.0827	
47	0.0455	0.0766	
49	0.0249	0.0521	
50	0.0719	0.0570	
51	0.0657	0.0303	Transect F
52	0.0645	0.0504	
53	0.0564	0.0589	
54	0.0646	0.0598	Transect A
55	0.0812	0.0722	
56	0.0654	0.0621	
57	0.0621	0.0740	
58	0.0760	0.0311	
59	0.0595	0.0395	
60	0.0665	0.0416	

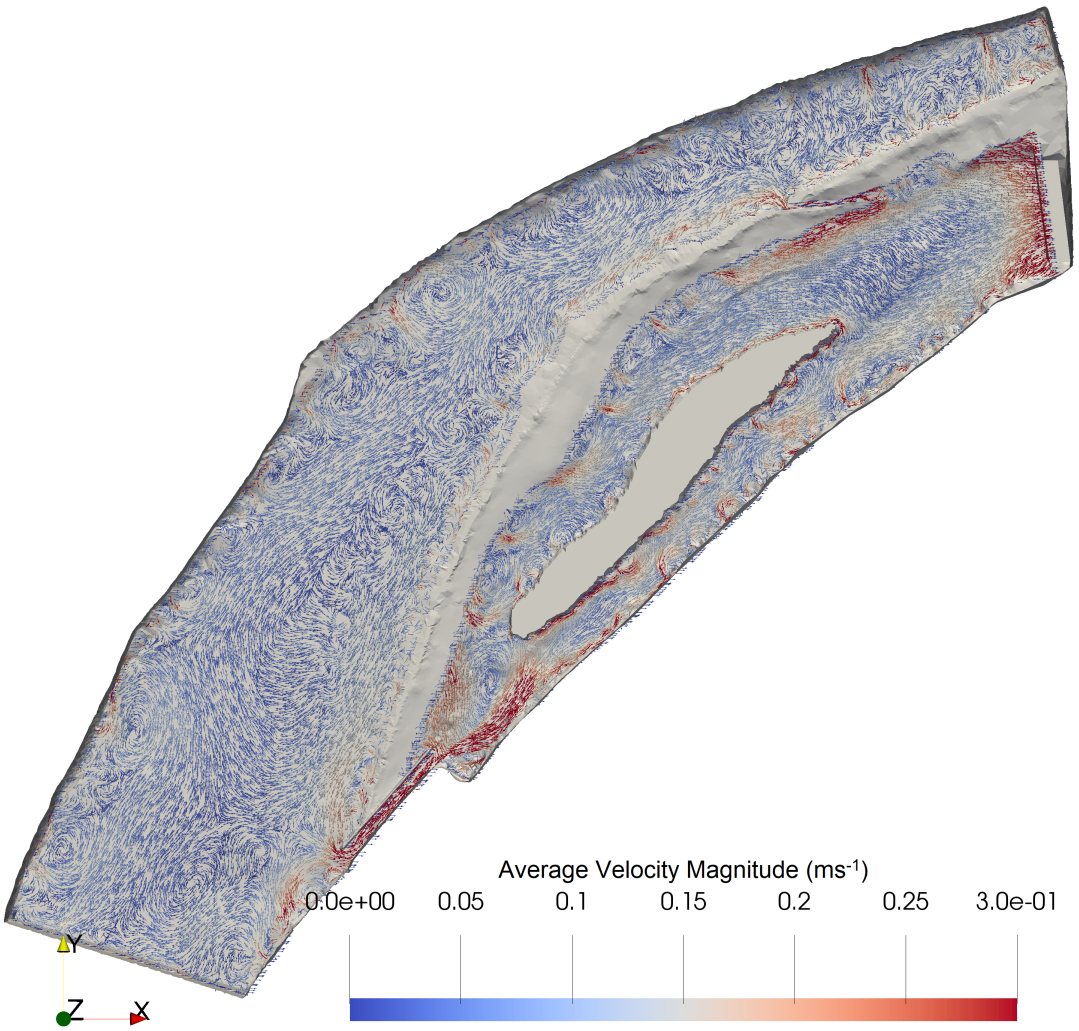

Figure E.10: Planform view of the `fishSet` domain with overlain vectors displayed over the isosurface $\alpha = 0.5$, which denotes the free surface. The vectors are equally scaled due to the overwhelming dominance of the flow velocity within the baulk pass compared to the bulk flow. Vectors are coloured with velocity magnitude, limited to a maximum of $0.3ms^{-1}$ for clarity.

Table E.3: Selected tagged fish data provided by Dodd [2019].

Fish ID	Tag ID	Sex	Length (mm)	Mass (kg)
1	2013_2563	F	650	3.075
2	2013_2640	M	540	1.3
3	2013_2654	M	550	1.8
4	2013_2668	F	420	0.75
5	2013_2689	M	620	2.15
6	2013_2738	F	460	0.95
8	2014_2535	F	530	1.55
9	2014_2542	F	520	1.425
10	2014_2612	F	540	1.7
11	2014_2654	M	550	1.875
12	2014_2661	F	420	0.75
13	2014_2689	F	530	1.35
14	2014_2731	M	530	1.25
15	2014_2752	M	590	1.75
16	2014_2794	F	540	1.5

Table E.4: Selected measured fish track data provided by Dodd [2019] (Table 1/3)

Track ID	Start Location	End Location	No. Points	Start Time	End Time	Date	Level (m)	$Q(m^3s^{-1}$
2013_2563_61	[88.14, 74.37]	[88.39, 72.51]	12	07:00:55	07:03:09	2013-10-21	2.424	3.8
2013_2563_62	[88.31, 73.45]	[87.84, 74.21]	6	08:08:15	08:08:28	2013-10-21	1.911	3.7
2013_2563_63	[85.34, 74.23]	[81.90, 66.83]	106	08:28:30	08:33:32	2013-10-21	1.946	3.5
2013_2640_52	[85.02, 74.78]	[83.03, 74.66]	11	08:30:03	08:33:06	2013-10-21	1.946	3.5
2013_2654_24	[84.42, 70.65]	[85.10, 72.82]	54	22:02:07	22:06:14	2013-10-16	2.003	6.9
2013_2668_4	[85.69, 75.13]	[85.13, 76.15]	41	06:11:52	06:14:00	2013-10-19	2.035	3.5
2013_2668_5	[83.84, 74.23]	[94.52, 72.46]	55	06:19:23	06:22:11	2013-10-19	1.895	3.5
2013_2668_6	[88.53, 73.99]	[82.59, 69.55]	298	07:13:42	07:28:14	2013-10-19	1.927	3.4
2013_2689_9	[87.86, 78.98]	[88.94, 73.01]	289	02:23:48	02:37:34	2013-11-02	2.688	2.6
2013_2689_10	[89.39, 74.23]	[88.59, 75.50]	38	03:00:19	03:02:34	2013-11-02	2.735	2.5
2013_2689_11	[88.69, 73.62]	[87.85, 74.07]	31	03:05:53	03:08:21	2013-11-02	2.735	2.5
2013_2689_12	[88.44, 73.65]	[87.58, 76.45]	12	03:16:22	03:16:52	2013-11-02	2.64	2.5
2013_2689_13	[86.43, 77.71]	[88.29, 76.49]	19	03:20:40	03:21:31	2013-11-02	2.64	2.5
2013_2689_14	[83.10, 73.73]	[85.34, 79.93]	21	03:24:31	03:27:21	2013-11-02	2.54	2.5
2013_2689_15	[91.38, 72.84]	[88.76, 74.59]	11	03:32:03	03:32:35	2013-11-02	2.54	2.5
2013_2689_16	[88.81, 72.85]	[88.67, 74.50]	9	03:45:27	03:45:59	2013-11-02	2.403	2.5
2013_2689_17	[88.46, 73.88]	[88.39, 76.46]	10	04:13:48	04:14:12	2013-11-02	2.05	2.5
2013_2689_18	[88.23, 72.84]	[83.49, 72.02]	20	04:17:34	04:18:52	2013-11-02	2.05	2.5
2013_2689_19	[84.89, 70.27]	[85.77, 74.55]	24	04:32:40	04:34:09	2013-11-02	1.95	2.5
2013_2738_13	[87.24, 78.08]	[88.71, 80.10]	77	03:21:22	03:26:42	2013-11-02	2.54	2.5
2013_2738_14	[88.23, 76.37]	[88.68, 73.91]	18	03:52:34	03:54:43	2013-11-02	2.285	2.5
2013_2738_15	[88.89, 73.37]	[88.16, 74.86]	2	04:30:06	04:30:42	2013-11-02	1.95	2.5
2013_2738_16	[89.66, 73.48]	[90.49, 73.53]	2	04:33:26	04:33:29	2013-11-02	1.95	2.5
2013_2738_22	[87.96, 72.22]	[88.32, 72.06]	2	15:51:18	15:51:21	2013-11-03	2.907	7.1

Table E.5: Selected measured fish track data provided by Dodd [2019] (Table 2/3)

Track ID	Start Location	End Location	No. Points	Start Time	End Time	Date	Level (m)	$Q(m^3s^{-1}$
2013_2738_23	[91.20, 72.25]	[75.30, 67.70]	29	15:54:16	15:55:46	2013-11-03	2.906	7.1
2014_2535_6	[89.68, 73.38]	[88.57, 75.31]	10	15:15:07	15:16:20	2014-10-21	2.62	3.3
2014_2535_16	[85.57, 83.77]	[84.83, 80.52]	264	02:12:00	02:26:50	2014-10-22	2.792	3.3
2014_2535_17	[89.12, 84.73]	[85.17, 73.84]	25	02:50:32	02:51:38	2014-10-22	2.676	3.3
2014_2535_18	[86.77, 78.43]	[87.02, 77.63]	65	03:01:03	03:03:45	2014-10-22	2.714	3.3
2014_2535_19	[84.93, 80.12]	[90.10, 70.34]	27	03:12:22	03:13:51	2014-10-22	2.796	3.3
2014_2542_1	[87.63, 77.81]	[86.83, 77.22]	3	14:56:02	14:56:07	2014-10-21	2.728	3.1
2014_2542_3	[79.94, 70.71]	[87.85, 82.94]	68	07:00:04	07:02:59	2014-10-29	2.383	1.8
2014_2612_2	[85.26, 75.52]	[82.54, 79.49]	398	05:02:26	05:21:01	2014-05-11	1.825	1.6
2014_2612_3	[84.00, 78.20]	[84.55, 77.34]	5	05:23:15	05:23:25	2014-05-11	1.825	1.7
2014_2654_1	[89.24, 75.01]	[88.50, 74.24]	4	01:20:00	01:21:30	2014-05-11	2.454	0.6
2014_2654_2	[87.62, 84.61]	[87.66, 85.61]	5	03:13:20	03:13:30	2014-05-11	2.242	1.6
2014_2654_3	[85.66, 83.01]	[85.38, 80.63]	28	03:17:13	03:20:22	2014-05-11	2.242	1.6
2014_2654_4	[90.08, 80.00]	[90.12, 77.73]	44	03:24:34	03:29:47	2014-05-11	2.166	1.6
2014_2654_5	[89.93, 80.90]	[88.11, 75.23]	32	03:35:56	03:38:09	2014-05-11	2.166	1.6
2014_2654_6	[84.44, 82.05]	[83.39, 81.39]	9	03:50:08	03:50:42	2014-05-11	2.04	1.6
2014_2654_7	[83.58, 79.36]	[73.66, 77.65]	3	03:54:12	03:54:57	2014-05-11	1.865	1.6
2014_2661_1	[86.74, 78.32]	[86.74, 78.32]	2	02:10:36	02:10:39	2014-05-11	2.678	1.5
2014_2661_2	[92.03, 90.25]	[90.72, 87.75]	12	02:13:21	02:14:52	2014-05-11	2.678	1.5
2014_2661_4	[91.52, 88.40]	[92.56, 89.40]	102	02:19:31	02:36:46	2014-05-11	2.639	1.6
2014_2661_5	[93.25, 91.54]	[93.25, 91.54]	4	02:39:10	02:39:34	2014-05-11	2.639	1.6
2014_2661_6	[92.56, 89.40]	[93.25, 91.54]	3	02:42:30	02:42:38	2014-05-11	2.65	1.6
2014_2661_7	[91.52, 88.40]	[90.39, 86.36]	2	02:48:23	02:49:06	2014-05-11	2.65	1.6

Table E.6: Selected measured fish track data provided by Dodd [2019] (Table 3/3)

Track ID	Start Location	End Location	No. Points	Start Time	End Time	Date	Level (m)	$Q(m^3s^{-1}$
2014_2661_8	[87.33, 78.37]	[86.61, 78.53]	8	02:52:10	02:54:20	2014-05-11	2.502	1.6
2014_2661_9	[86.51, 76.77]	[86.81, 78.19]	7	02:56:28	02:56:44	2014-05-11	2.502	1.6
2014_2661_10	[86.96, 84.77]	[88.03, 85.58]	186	03:00:03	03:08:15	2014-05-11	2.502	1.6
2014_2661_12	[88.39, 77.94]	[88.13, 74.40]	17	05:20:40	05:21:23	2014-05-11	1.752	1.7
142014_2661_	[90.73, 73.70]	[88.66, 74.94]	5	06:04:06	06:04:17	2014-05-11	1.759	1.6
2014_2661_15	[89.35, 73.73]	[89.11, 75.38]	515	06:08:51	06:40:39	2014-05-11	1.758	1.5
2014_2661_16	[89.79, 74.08]	[88.60, 74.43]	75	06:42:23	06:52:48	2014-05-11	1.759	1.5
2014_2661_17	[88.46, 73.88]	[88.58, 73.73]	139	07:06:46	07:14:32	2014-05-11	1.825	1.7
2014_2689_1	[83.25, 74.21]	[86.26, 76.08]	65	00:32:56	00:35:48	2014-11-11	1.899	5.1
2014_2689_2	[85.00, 77.21]	[86.77, 73.46]	78	00:39:15	00:44:32	2014-11-11	1.974	4.8
2014_2731_43	[78.46, 62.71]	[78.46, 62.71]	2	07:46:00	07:46:03	2014-12-11	1.991	4.3
2014_2752_29	[82.48, 74.04]	[84.17, 72.61]	41	09:06:43	09:10:51	2014-11-20	2.043	8.62
2014_2794_1	[85.81, 77.08]	[81.88, 73.55]	71	06:04:39	06:08:14	2014-11-19	2.064	7.2